

Final Technical Report
on the
Surface Electrical Properties
Experiment

report prepared by
The University of Toronto

and submitted to MIT
in fulfillment of the
subcontract on NASA
contract NAS9-11540

Personnel

D.W. Strangway
A.P. Annan
J.D. Redman
J.R. Rossiter
J.A. Rylaarsdam
R.D. Watts

Part III of III Parts

SEP Final Theory Report

A.P. Annan

Table of Contents

1. Introduction	1
2. Basic Physics & Mathematical Descriptions	2
3. Hertz Potentials, Point Sources & Particular solutions	6
4. Plane Wave Spectrum Representation	10
5. Plane Stratified Medium	14
6. Solution of Wave Equation in Plane- Stratified Medium	16
7. Transmission Matrices & N-layered Structure Reflection Coefficients	19
8. Point Dipole Sources over an N-layered Earth	26
9. 1 and 2-Layer Earth Reflection Coefficients	33
10. Normalization & Tabulation of HED Fields for SEP Application	37
11. Radiation Patterns of a HED on the Surface of a Half-Space	38
12. Surface Fields about a HED on the Surface of a Half-Space	53
13. HED on the Surface of a 2-Layer Earth	59
14. N-Layered Earth Response: The "Fast" Hankel Transform	82
Appendix 1 Numerical Evaluation of Saddle Point Contour	91
Appendix 2 Table of Useful Hankel Transforms	98

1. Introduction

This report is intended to give a complete unified discussion of the electromagnetic response of a plane stratified structure. The geophysical literature is full of various bits and pieces of analysis. Most often these papers deal with very specific problems, i.e. vertical magnetic dipole over a conductive 2 layer earth. The objective of this report is two-fold. First a detailed and comprehensive analysis of the theoretical parts of the electromagnetic response is given with the emphasis on the physical meaning of the somewhat messy mathematical expressions. An attempt is also made to use a meaningful notation, which, hopefully, is not too cluttered. With a clean compact development of the theory in hand, the more interesting and much more difficult problem of actually using it will be tackled. It is at this point where the particular problem at hand must be considered. The actual theoretical expressions for the fields in a stratified medium can be obtained in closed form and take the form of Hankel transforms or 2-dimensional Fourier transforms. The numerical problem of actually computing numbers for the electromagnetic field strengths is that of performing some type numerical or approximate quadrature technique to evaluate the integrals describing the fields. The particular context of most interest here is the response of low-loss dielectric media. Much of the numerical analysis is, therefore,

devoted to problems in this area. The analysis of conductive media, while quite different in behaviour and geophysical interest, is not very far removed from the theoretical analysis and the numerical difficulties are not as acute as for the low-loss problem. While these problems will not be analysed in detail, a few side excursions into some interesting points will be made.

2. Basic Physics & Mathematical Descriptions

The basic physics of electromagnetic theory is totally wrapped up mathematically when Maxwell's equations and the constitutive equations are written down. While the details from this point on are usually specific, a wide variety of interesting, and at first glance, unrelated phenomena pop out when these equations are manipulated about. It is the physical interpretation and understanding of the results obtained from the mathematically simple basic equations which are exciting. In fact, in the last eighty years, these basic equations have provided food for thought and controversy of some of the most brilliant minds. Even many of these people have missed the beauty of the analysis and have gotten too wrapped up in the details to appreciate the subtle unity of the various facets of Maxwell's mathematical description of basic electromagnetic phenomena.

The analysis from here on will be conducted using the rationalized ~~MKS~~ system of units. The time dependent form of Maxwell's equations is

$$\bar{\nabla} \times \bar{E} = -\frac{\partial \bar{B}}{\partial t} \quad (2-1) \quad \bar{\nabla} \times \bar{H} = \bar{J} + \frac{\partial \bar{D}}{\partial t} \quad (2-2)$$

$$\bar{\nabla} \cdot \bar{D} = q \quad (2-3) \quad \bar{\nabla} \cdot \bar{B} = 0 \quad (2-4)$$

In order to completely define an electromagnetic problem (no-mechanical coupling here) the constitutive equation introducing the electromagnetic properties of media when treated on the continuum scale are required. These equations are

$$\bar{B} = \mu' \bar{H} + \mu_o \bar{M}_S \quad (2-5)$$

$$\bar{J} = \sigma' \bar{E} + \bar{J}_S \quad (2-6)$$

$$\bar{D} = \epsilon' \bar{E} + \bar{P}_S \quad (2-7)$$

\bar{E} , \bar{D} , \bar{B} , \bar{H} , \bar{J} have their conventional meanings; q is the electric charge density; μ' , ϵ' , σ' are the permeability, permittivity and electrical conductivity subscripts o (i.e. μ_o) are used to indicate free space values ; \bar{M}_S , \bar{P}_S are impressed magnetic and electric dipole moment densities and \bar{J}_S is an impressed electric current density.

For time-varying problems it is convenient to define generalized electric and magnetic source current densities namely

$$\bar{J}'_S = \bar{J}_S + \frac{\partial \bar{P}_S}{\partial t} \quad (2-8)$$

$$\bar{M}'_S = \mu_o \frac{\partial \bar{M}_S}{\partial t} \quad (2-9)$$

Now, combining Maxwell's equations with the linear isotropic

constitutive equations (2-5, -6 and -7) one has

$$\bar{\nabla} \times \bar{E} = -\mu' \frac{\partial \bar{H}}{\partial t} + \bar{M}_s \quad (2-10) \quad \bar{\nabla} \times \bar{H} = \sigma' \bar{E} + \epsilon' \frac{\partial \bar{E}}{\partial t} + \bar{J}_s \quad (2-11)$$

plus the continuity equations

$$\frac{\partial q}{\partial t} = -\bar{\nabla} \cdot \bar{J}_s - \bar{\nabla} \cdot \sigma' \bar{E} = -\bar{\nabla} \cdot \bar{J}_s - \sigma' \bar{\nabla} \cdot \bar{E} - \bar{E} \cdot \bar{\nabla} \sigma' \quad (2-12)$$

$$\bar{\nabla} \cdot \bar{M}_s + \frac{\partial}{\partial t} \bar{\nabla} \cdot \mu \bar{H} = 0 \quad (2-13)$$

or
$$\mu_0 \bar{\nabla} \cdot \bar{M}_s + \bar{\nabla} \cdot \mu \bar{H} = 0$$

For most applications, the response of sinusoidally time varying fields is of most interest. The individual sinusoidal responses can be built into transient responses with the aid of the Fourier integral. The following time-frequency Fourier transform pair is adopted for the rest of the analysis

$$f(t) = \frac{1}{2\pi} \int_{-\infty}^{\infty} f(\omega) e^{-j\omega t} d\omega \quad (2-14)$$

$$f(\omega) = \int_{-\infty}^{\infty} f(t) e^{j\omega t} dt \quad (2-15)$$

Upon Fourier transformation, the frequency domain equations become

$$\bar{\nabla} \times \bar{E} = j\omega \mu \bar{H} + \bar{M}_s \quad (2-16) \quad \bar{\nabla} \times \bar{H} = (\sigma' - j\omega \epsilon') \bar{E} + \bar{J}_s \quad (2-17)$$

$$q = + \frac{\bar{\nabla} \cdot \bar{J}}{j\omega} + \frac{\bar{\nabla} \cdot \sigma' \bar{E}}{j\omega} \quad (2-18)$$

$$\bar{\nabla} \cdot \bar{M}_s - j\omega \bar{\nabla} \cdot \mu \bar{H} = 0 \quad (2-19)$$

For time-varying field analysis, it is convenient to lump electrical conduction and displacement currents into one term by defining the complex permittivity

$$\epsilon = \epsilon' \left(1 + j \frac{\sigma'}{\omega \epsilon'} \right) \quad (2-20)$$

or the complex conductivity

$$\zeta = (\sigma' - j\omega\epsilon')$$
(2-21)

In the following, the complex permittivity is adapted since the primary applications will be to low-loss dielectrics. The electric loss-tangent is defined as

$$\tan\delta_e = \frac{\zeta}{\omega\epsilon'}$$
(2-22)

Therefore

$$\epsilon = \epsilon'(1 + j \tan\delta_e)$$
(2-23)

In addition, time-varying magnetic losses are introduced by defining a complex permeability with an analogous form to ϵ , namely,

$$\mu = \mu'(1 + j \tan\delta_m)$$
(2-24)

With this formalism of getting notations clear, one can now get down to the business at hand.

The frequency domain wave equations for the \vec{E} and \vec{H} field are obtained by taking the curl of equations (2-16) and (2-17) with the result.

$$\vec{\nabla} \times \vec{\nabla} \times \vec{E} - k^2 \vec{E} + j\omega \vec{H} \times \vec{\nabla} \mu = j\omega \mu \vec{J}_s + \vec{\nabla} \times \vec{M}_s$$
(2-25)

and

$$\vec{\nabla} \times \vec{\nabla} \times \vec{H} - k^2 \vec{H} - j\omega \vec{E} \times \vec{\nabla} \epsilon = -j\omega \epsilon \vec{M}_s + \vec{\nabla} \times \vec{J}_s$$
(2-26)

where $k = \omega \sqrt{\epsilon \mu}$ is the propagation constant. The symmetrical form of equations 2-25 and 2-26 is a result of the careful choice of definitions developed above.

The terms $\vec{H} \times \vec{\nabla} \mu$ and $\vec{E} \times \vec{\nabla} \epsilon$ enter since μ and ϵ may be functions of spatial position. In the following analysis μ and ϵ will always

be taken as constant in various spatial regions with step discontinuities between the regions. The terms $\bar{H} \times \bar{\nabla} \mu$ and $\bar{E} \times \bar{\nabla} \epsilon$ are dropped from the equations. These terms are essentially replaced by the usually boundary conditions at the interfaces between the two regions, namely, continuity of normal \bar{B} , \bar{D} , \bar{J} and tangential \bar{E} and \bar{H} fields.

3. Hertz Potentials, Point Sources and Particular Solutions

a) Hertz Vector Potentials

At this point in the analysis it is of interest to consider the case of a source in a whole-space of constant material properties. This leads immediately to the concept of Hertz-potentials. The natural manner to progress is to consider the electric field from electric currents and the magnetic fields for magnetic currents.

$$\bar{\nabla} \times \bar{\nabla} \times \bar{E} - k^2 \bar{E} = +j\omega\mu \bar{J}_s \quad (3-1)$$

$$\bar{\nabla} \times \bar{\nabla} \times \bar{H} - k^2 \bar{H} = -j\omega\epsilon \bar{M}_s \quad (3-2)$$

These equations are mathematically equivalent and are transverse vector wave equations.

Since a vector field can be split into transverse and longitudinal components,

$$\bar{E} = \bar{E}_l + \bar{E}_t \quad (3-3)$$

$$\bar{\nabla} \times \bar{E}_l = 0 \quad \bar{\nabla} \cdot \bar{E}_t = 0 \quad (3-4)$$

one has

$$\bar{\nabla} \times \bar{\nabla} \times \bar{E}_t - k^2 \bar{E}_t = j\omega\mu \bar{J}_{s_t} \quad (3-5)$$

$$-k^2 \bar{E}_l = j\omega\mu \bar{J}_{s_l} \quad (3-6)$$

A similar decomposition of the \bar{H} field and \bar{M}_s can be written down.

In this context, the transverse component of E satisfies the transverse vector wave equation while \bar{E}_l and \bar{J}_s are linearly related. A much more expedient way of developing \bar{E} is to define with its longitudinal and transverse components in terms of a single vector field, namely,

$$\bar{E} = (\bar{I} + \frac{\bar{\nabla}\bar{\nabla}}{k^2}) \cdot \bar{\Pi}_e \quad (3-7)$$

where
$$\bar{E}_l = \frac{\bar{\nabla}\bar{\nabla}}{k^2} \cdot \bar{\Pi}_e + \bar{\Pi}_e \quad (3-8)$$

$$\bar{E}_t = \bar{\Pi}_e \quad (3-9)$$

(Note: \bar{I} is the unity dyadic or tensor)

$\bar{\Pi}_e$ is known as the electric Hertz potential and satisfies the total vector wave equation

$$\bar{\nabla} \times \bar{\nabla} \times \bar{\Pi}_e - \bar{\nabla} \bar{\nabla} \cdot \bar{\Pi}_e - k^2 \bar{\Pi}_e = j\omega\mu \bar{J}_s \quad (3-10)$$

or
$$\nabla^2 \bar{\Pi}_e + k^2 \bar{\Pi}_e = -j\omega\mu \bar{J}_s \quad (3-11)$$

where $\nabla^2 = -\bar{\nabla} \times \bar{\nabla} \times + \bar{\nabla} \bar{\nabla} \cdot$ is the Laplacian operator

Thus $\bar{\Pi}_e$ satisfies the vector Helmholtz equation (wave equation with time dependence transformed out).

Similarly, \bar{H} can be expressed in terms of a magnetic Hertz potential

$$\bar{H} = (\bar{I} + \frac{\bar{\nabla}\bar{\nabla}}{k^2}) \cdot \bar{\Pi}_m \quad (3-12)$$

and
$$\nabla^2 \bar{\Pi}_m + k^2 \bar{\Pi}_m = j\omega\epsilon \bar{M}_e \quad (3-13)$$

The electric and magnetic fields associated with the magnetic and electric currents are obtained from the Hertz potentials as follows

$$\bar{H}_{\mathcal{J}_S} = \frac{\bar{\nabla} \times \bar{E}}{j\omega\mu} = \frac{\bar{\nabla} \times \bar{\Pi}_e}{j\omega\mu} \quad (3-14)$$

and similarly

$$\bar{E}_{M_S} = \frac{\bar{\nabla} \times \bar{H}}{-j\omega\epsilon} = \frac{\bar{\nabla} \times \bar{\Pi}_m}{-j\omega\epsilon} \quad (3-15)$$

The total electric and magnetic fields are then given by

$$\bar{E} = \left(\hat{I} + \frac{\bar{\nabla} \bar{\nabla}}{k^2} \right) \cdot \bar{\Pi}_e + \frac{\bar{\nabla} \times \bar{\Pi}_m}{-j\omega\epsilon} \quad (3-16)$$

$$\bar{H} = \left(\hat{I} + \frac{\bar{\nabla} \bar{\nabla}}{k^2} \right) \cdot \bar{\Pi}_m + \frac{\bar{\nabla} \times \bar{\Pi}_e}{j\omega\mu} \quad (3-17)$$

(b) Point Sources

The development of the response of a system to an arbitrary excitation is most easily done using the Green's theory approach. In other words, the response of the system to excitation at a point is used to develop the solution for arbitrary excitation. In the electromagnetic context, the point excitation function are point electric and magnetic dipoles.

Thus

$$\bar{\mathcal{J}}_S = \delta(\bar{r} - \bar{r}') \hat{s} \quad (3-18)$$

$$\bar{M}_S = \delta(\bar{r} - \bar{r}') \hat{s} \quad (3-19)$$

where \bar{r}' is the location of the point source, \hat{s} is the direction of the dipole moment and δ is the three dimensional Dirac delta function.

Examples:

The point source are basic building blocks for analysing any other source configurations.

Electrical Current:

A wire of infinitesimal cross section carrying I amps of current can be composed of point dipoles each representing an infinitesimal section of the wire

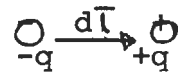
$$\vec{J}_s = \vec{J} = \sum_i I d\vec{l}; \delta(\vec{r} - \vec{r}'_i) \quad (3-20)$$



Time Varying Electric Dipole Moment

The electric dipole moment is

$$\vec{P}_s = q d\vec{l} \delta(r - r') \quad (3-21)$$

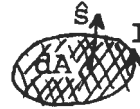


$$\begin{aligned} \vec{J}_s &= \frac{\partial P_s}{\partial t} = -j\omega q d\vec{l} \delta(r - r') \\ &= I d\vec{l} \delta(r - r') \quad (3-22) \quad I = -j\omega q \quad (3-23) \end{aligned}$$

Time Varying Magnetic Dipole Moment

A point magnetic dipole can be visualized as an infinitesimally small loop of wire carrying I amps.

The magnetic dipole moment density is defined as



$$\vec{M} = I dA \delta(r - r') \hat{s} \quad (3-24) \quad \hat{s} - \text{unit normal to } dA$$

where IdA remains finite as dA → 0 in the usually point source sense.

The associated magnetic current is

$$\begin{aligned} \vec{m}_s &= -j\omega\mu_0 \vec{M}_s \\ &= -j\omega\mu_0 I dA \delta(r - r') \hat{s} \end{aligned} \quad (3-25)$$

Particular Solutions

The first stage of analysis before continuing to more

complex problems is to find the solution for the electric and magnetic Hertz potentials for a point source excitation. These are denoted as the particular or inhomogeneous solution to the vector Helmholtz equation. The basic partial differential equation is

$$\nabla^2 \begin{Bmatrix} \bar{\Pi}_e \\ \bar{\Pi}_m \end{Bmatrix} + k^2 \begin{Bmatrix} \bar{\Pi}_e \\ \bar{\Pi}_m \end{Bmatrix} = \begin{Bmatrix} -j\omega\mu \\ j\omega\epsilon \end{Bmatrix} \delta(\mathbf{r} - \mathbf{r}') \hat{\mathbf{s}} \quad (3-26)$$

It is obvious that the particular solution can be expressed as

$$\bar{\Pi} = \Pi_p \hat{\mathbf{s}} \quad (3-27)$$

and that Π_p satisfies the scalar Helmholtz equation

$$\nabla^2 \Pi_p + k^2 \Pi_p = -c \delta(\mathbf{r} - \mathbf{r}') \quad (3-28)$$

The particular solution is the well known spherical wave form

$$\Pi_p = c \frac{e^{jk|\bar{\mathbf{r}} - \bar{\mathbf{r}}'|}}{4\pi|\bar{\mathbf{r}} - \bar{\mathbf{r}}'|} \quad (3-29)$$

4. Plane Wave Spectrum Representation

In the analysis of plane stratified media, the plane wave spectrum approach is applied to obtain the solution of the boundary value. This is the physical interpretation of the mathematical manipulations. The mathematical basis for the development are the Fourier transform and Hankel transform integrals.

The basic coordinate systems to be used in the later analysis are shown in figure 4-1. The Cartesian coordinates are denoted by $(x_1 \ x_2 \ x_3)$ and the associated unit vectors are $(\hat{\mathbf{e}}_1 \ \hat{\mathbf{e}}_2 \ \hat{\mathbf{e}}_3)$. The cylindrical coordinates are denoted by (ρ, φ, z) and the associate unit vector $(\hat{\rho}, \hat{\varphi}, \hat{z})$. The coordinates are related by

$$\begin{bmatrix} x_1 \\ x_2 \\ x_3 \end{bmatrix} = \begin{bmatrix} \rho \cos \varphi \\ \rho \sin \varphi \\ z \end{bmatrix} \quad (4-1)$$

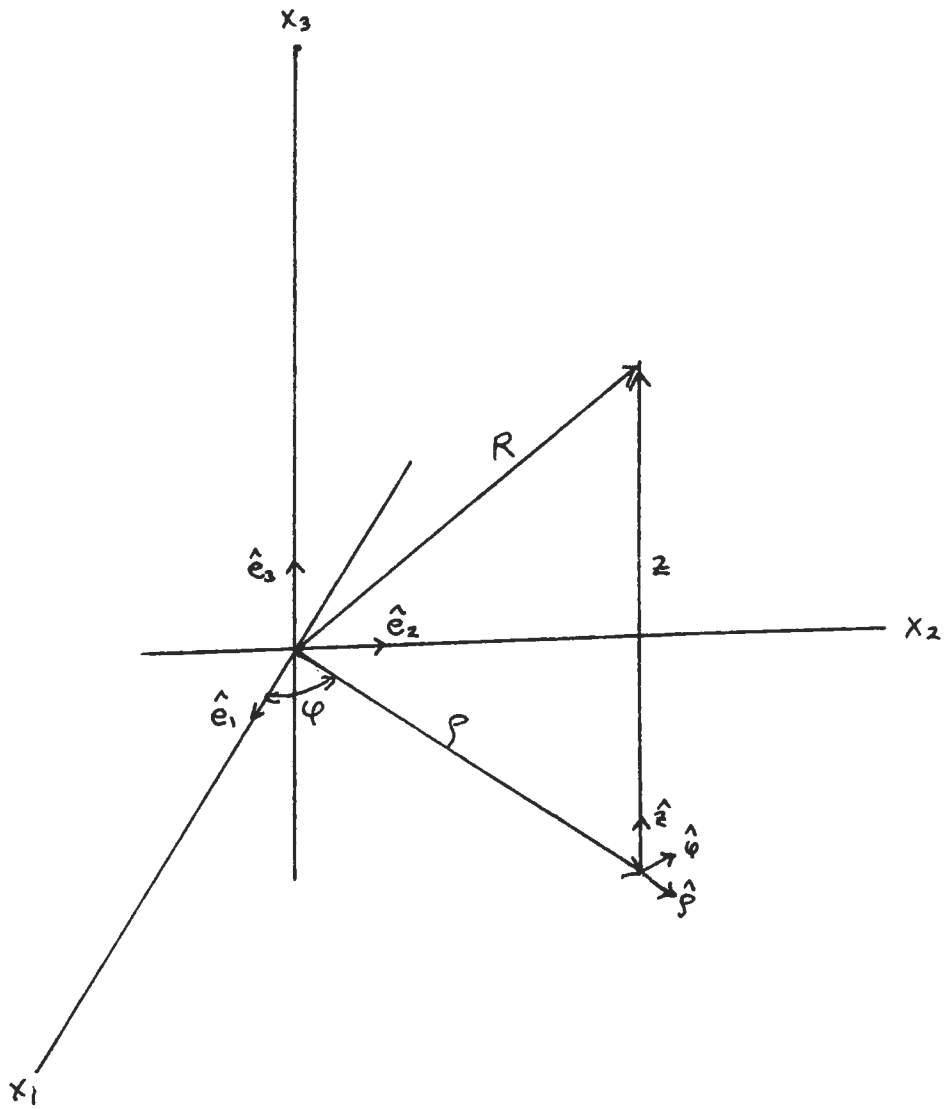


Fig. 4-1

The plane wave spectrum is developed from the Fourier integral starting with the scalar Helmholtz equation of the last section

$$\nabla^2 \Pi_p + k^2 \Pi_p = -(\delta C(\bar{r} - \bar{r}'))$$

and taking \bar{r}' to be the origin, the 2-dimensional Fourier transform pair are

$$\Pi_p(x_1 x_2 x_3) = \frac{1}{4\pi^2} \iint_{-\infty}^{\infty} \Pi(\lambda_1 \lambda_2 x_3) e^{j(\lambda_1 x_1 + \lambda_2 x_2)} d\lambda_1 d\lambda_2 \quad (4-3)$$

$$\Pi_p(\lambda_1 \lambda_2 x_3) = \iint_{-\infty}^{\infty} (x_1 x_2 x_3) e^{-j(\lambda_1 x_1 + \lambda_2 x_2)} dx_1 dx_2 \quad (4-4)$$

Combining 4-2 with 4-3, the p.d.e. reduces to the ordinary differential equation

$$\frac{d^2 \Pi_p}{dx_3^2} + (k^2 - \lambda^2) \Pi_p = -C \delta(x_3) \quad (4-5)$$

where $\lambda^2 = \lambda_1^2 + \lambda_2^2$

The homogeneous solutions to 4-5 have the form

$$e^{\pm j(k^2 - \lambda^2)^{1/2} x_3} \quad (4-6)$$

while the particular solution to 4-5 is

$$\Pi_p = \frac{e^{j(k^2 - \lambda^2)^{1/2} |x_3|}}{(k^2 - \lambda^2)^{1/2}} \quad (4-7)$$

Defining $\gamma = (k^2 - \lambda^2)^{1/2}$, 4-3 can be written as

$$\Pi_p(x_1 x_2 x_3) = \frac{1}{4\pi^2} \iint_{-\infty}^{\infty} \frac{e^{j(\lambda_1 x_1 + \lambda_2 x_2 + \gamma |x_3|)}}{-2j\gamma} e^{-j\omega t} d\lambda_1 d\lambda_2 \quad (4-8)$$

The rationale for the plane wave spectrum terminology is from the form of 4-8. The integrand is a plane wave (the final factor in curly brackets is to emphasize the wave nature of the integrand) and the integral is over all possible wave numbers in the $\hat{e}_1 - \hat{e}_2$ plane. In factor $\frac{1}{2j\gamma}$ is the spectral amplitude of

Π_p in X_1 - X_2 ($X_3=0$) plane and the amplitude can be continued upward or downward in space by multiplication by the factor $e^{j\kappa |X_3|}$. It is readily seen that κ is the vertical component of the propagation vector $\bar{k} = (\lambda_1, \lambda_2, \kappa)$.

The double Fourier transform 4-8 is the Fourier form of the well-known Sommerfeld integral (1909, 1949), Watson (1966). Since the Sommerfeld integral is most often given as a Hankel transform, 4-8 will be rewritten in this notation.

Defining \bar{k} in cylindrical coordinates $(\lambda, \theta, \kappa)$, 4-8 becomes

$$\Pi_p (X_1 X_2 X_3) = \frac{1}{4\pi^2} \int_0^\infty \int_0^{2\pi} \frac{e^{j(\lambda \rho \cos(\varphi - \theta) + \kappa |Z|)}}{2j\kappa} \lambda d\lambda d\theta \quad (4-9)$$

Noting that the integral definition of $J_n(Z)$ is

$$\begin{aligned} J_n(Z) &= \frac{i^{-n}}{\pi} \int_0^{\pi/2} \cos n\varphi e^{iZ \cos \varphi} d\varphi \\ &= \frac{(i)^{-n}}{2\pi} \int_0^{2\pi} \cos \varphi e^{iZ \cos \varphi} d\varphi \end{aligned} \quad (4-10)$$

4-9 can be rewritten as_∞

$$\Pi_p (X_1 X_2 X_3) = \frac{1}{4\pi} \int_0^\infty \frac{\lambda e^{j\kappa |Z|}}{j\kappa} J_n(\lambda \rho) d\lambda \quad (4-11)$$

which is the Hankel transform representation of the Sommerfeld integral. The evaluation of 4-11 is given by Watson (1966)

13.47.4, namely,

$$\int_0^\infty J_0(bt) \frac{e^{-a(t^2 - y^2)^{1/2}}}{(t^2 - y^2)^{1/2}} t dt = \frac{e^{-iy\sqrt{a^2 + b^2}}}{\sqrt{a^2 + b^2}} \quad (4-12)$$

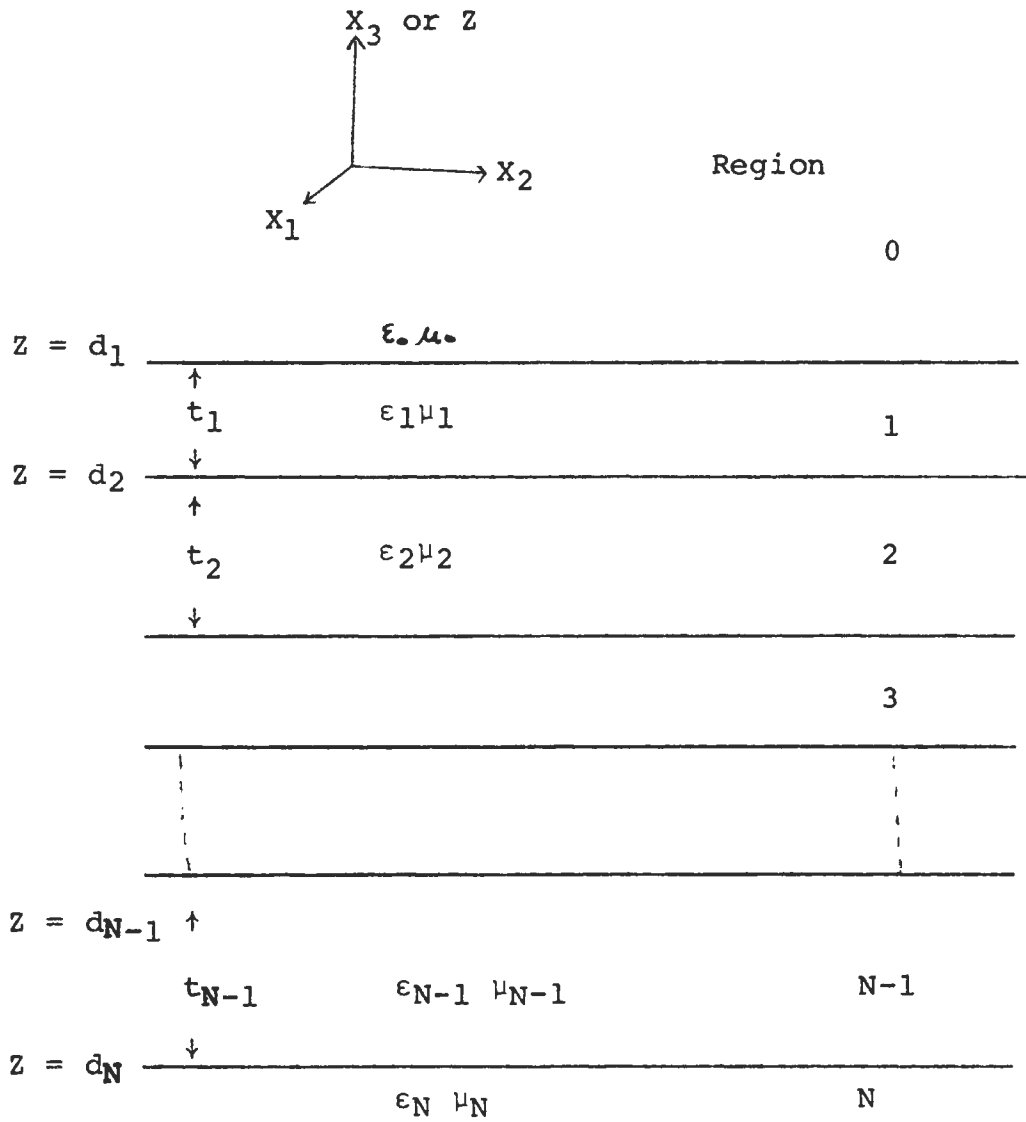
In the remaining discussions the Hankel transform notation is adopted since the point dipole sources of interest have particularly simple angular symmetries.

5. Plane-Stratified Medium

Much of the remaining discussions revolve around the response of point dipole sources in a plane stratified environment. At this point, the stratification, notation, and geometrics will be briefly outlined in order that these details are available for use later.

In the geophysical context, it is common to denote a structure as consisting of N plane layers. The N layer notation here is used to imply that there are $N + 1$ regions of different material properties with $N-1$ of these regions sandwiched between 2 half-spaces. Thus a whole-space is a 0 layer structure, 2 adjoining halfspaces are a 1 layer structure and a thin strip between 2 halfspaces is a 2 layer structure.

The general geometry is shown in Fig. 5-1. The planar symmetry is parallel to the $X_1 - X_2$ coordinates. The upper most region is denoted region 0 while the lowest layer (half-space bounding the structure on the bottom) is region N . The N -plane interfaces between the regions are located at depths $Z = d_i$. Each layer is assigned a pair of constant complex material properties (permittivity and permeability) ϵ_i, μ_i . An additional parameter which is useful is the thickness of the individual layers t_i . The structure just described has cylindrical symmetry about the X_3 or Z axis



Layer thickness $t_i = |d_{i+1} - d_i| = d_i - d_{i+1}$ since z upward.

Layer propagation constant $k_i = \sqrt{\omega^2 \epsilon_i \mu_i}$

Fig. 5-1

6. Solution of Wave Equation in Plane-Stratified Medium;

TE and TM Fields

6-1 Hertz Potentials and TE-TM Fields

The basic wave equations for the electric and magnetic fields in a whole-space were discussed in section 3. As was discussed in that section, it is most convenient to express the fields in terms of electric and magnetic Hertz potentials which satisfy the vector Helmholtz equations

$$\nabla^2 \begin{Bmatrix} \bar{\Pi}_e \\ \bar{\Pi}_m \end{Bmatrix} + k^2 \begin{Bmatrix} \bar{\Pi}_e \\ \bar{\Pi}_m \end{Bmatrix} = \begin{Bmatrix} \text{source term} \\ 0 \end{Bmatrix} \quad (6-1)$$

with the electric and magnetic fields given by 3-16 and -17.

At this point it is best to get a subscript notation clarified in order that the region in question is contained in the equations. Thus, the Hertz potentials will be denoted

$$\bar{\Pi}_i^e \quad \bar{\Pi}_i^m \quad (6-2)$$

where the superscript denotes electric or magnetic and the subscript denotes the region i . Thus the homogeneous electric Hertz potential satisfies

$$\nabla^2 \bar{\Pi}_i^e + k_i^2 \bar{\Pi}_i^e = 0 \quad (6-3)$$

in regions.

For the electromagnetic problem, the Hertz potentials have only \hat{z} components. As a result one has to work with only 2 scalar potentials rather than 2 vector potentials

$$\bar{\Pi}_i^e = \Pi_i^e \hat{z} \quad (6-4)$$

$$\bar{\Pi}_i^m = \Pi_i^m \hat{z} \quad (6-5)$$

and 6-3 reduces to the scalar Helmholtz equation.

Examination of the electric and magnetic fields associated with the 2 components of the Hertz potentials shows physically why the potentials with only \hat{z} components are appropriate. From 3-16 and -17 the fields of Π_i^e are

$$\frac{\Pi_i^e \text{ Fields}}{\Pi_i^e} \quad \bar{E}_i = \hat{z} \Pi_i^e + \frac{\nabla_{\perp}^2}{k_i^2} \frac{\partial \Pi_i^e}{\partial z} \quad (6-6)$$

$$\bar{H}_i = \frac{\hat{z} \times \nabla_{\perp} \Pi_i^e}{-j\omega\mu_i} \quad (6-7)$$

$$\frac{\Pi_i^m \text{ Fields}}{\Pi_i^m} \quad \bar{H}_i = \hat{z} \Pi_i^m + \frac{\nabla_{\perp}^2}{k_i^2} \frac{\partial \Pi_i^m}{\partial z} \quad (6-8) \quad \bar{E}_i = \frac{\hat{z} \times \nabla_{\perp} \cdot \Pi_i^m}{j\omega\epsilon_i} \quad (6-9)$$

Examination of 6-7 and 6-9 shows that Π_i^e generates an electromagnetic field which always has its magnetic field in a plane perpendicular to the \hat{z} axis. In other words $\hat{z} \cdot \bar{H}$ is zero at all the planar interfaces in the structure. Similarly, Π_i^m generates the analogous electromagnetic field which has $\hat{z} \cdot \bar{E} \equiv 0$. Referring back to section 4 and the description of fields as superpositions of plane waves, the fact that Π_i^e and Π_i^m have only \hat{z} components has a physical significance. From basic electromagnetic theory, a plane wave incident on a plane interface can be split into two components, one with $\bar{E} \cdot \hat{u} \equiv 0$ and one with $\bar{H} \cdot \hat{u} \equiv 0$ where \hat{u} is the normal to the planar interface. The selection of the above description for the Hertz potentials yields the generalized form of this result.

An alternate notation for the two types of fields is now

adopted. In accordance with waveguide analysis, the Π_i^e fields are denoted transverse magnetic (TM) fields while the Π_i^m fields are denoted transverse electric (TE) fields. In instance where the both types of field appear, the two components are denoted as

$$\begin{aligned} & (\text{TE } \bar{E}, \text{ TM } \bar{E}) \\ & (\text{TE } \bar{H}, \text{ TM } \bar{H}) \end{aligned} \tag{6-10}$$

6-2 General Form of the Hertz Potentials

The general, homogeneous solution of the Helmholtz equation for the problem at hand can be written down immediately. Using the cylindrical symmetry of the boundaries, the potentials are

$$\Pi_i^e = \frac{\cos(n\phi)}{\sin(n\phi)} \left\{ \frac{C_{SA}^e}{n_i} (\lambda) e^{j\chi_i Z} + \frac{C_{SB}^e}{n_i} (\lambda) e^{-j\chi_i Z} \right\} J_n(\lambda r) + C_n(\lambda) Y_n(\lambda r) \tag{6-11}$$

The subscripts and superscripts should be self-explanatory. For the problems at hand only waves propagating radially outward from a source at the center are excited and $C_n(\lambda) = 0$. In the above, λ is the radial wavenumber as discussed briefly in section 4, while $\chi = (k_i^2 - \lambda^2)^{1/2}$ is the vertical wavenumber in the i th medium.

The general solution will take the form, for example,

$$\Pi_i^e = \sum_n \frac{\cos(n\phi)}{\sin(n\phi)} \int_0^\infty \left(\frac{C_{SA}^e}{n_i} (\lambda) e^{j\chi_i Z} + \frac{C_{SB}^e}{n_i} (\lambda) e^{-j\chi_i Z} \right) J_n(\lambda r) d\lambda \tag{6-12}$$

which is reminiscent of the particular solution in the form of 4-11.

7 Transmission Matrices and N-Layered Structure Reflection Coefficients

7-1 General Boundary Conditions

In the last section, the basic mathematical formalism for the fields in the layered structure. From 6-12, the problem at hand is that of finding the coefficients $A_i^m(\lambda)$ and $B_i^m(\lambda)$. Once these coefficients are determined the formal mathematical part of the analysis is complete.

The exact form of the coefficients depends on the nature of the source. In this section, the relationships between the A_i^m and B_i^m in different regions are developed. The results of this section then lead to the determination of particular form of the coefficients for different excitations which are discussed in section 9.

The boundary conditions on electromagnetic fields at the interface between any two regions are that the tangential components of the \vec{E} and \vec{H} fields must be continuous. Thus

$$\hat{z} \times \vec{E}_i = \hat{z} \times \vec{E}_{i\pm 1} \quad (7-1)$$

$$\hat{z} \times \vec{H}_i = \hat{z} \times \vec{H}_{i\pm 1}$$

In terms of TE and TM fields, the tangential components of the fields are

TM Fields

$$\text{Transverse } \vec{E}_i^{\text{TM}} = \frac{1}{k^2} \nabla_t \frac{\partial \Pi_i^e}{\partial z} \quad (7-2)$$

$$\text{Transverse } \vec{H}_i^{\text{TM}} = \frac{\hat{z} \times \nabla_t \Pi_i^e}{-j\omega\mu} \quad (7-3)$$

TE Fields Transverse ${}^{\text{TE}}\bar{E}_i = \hat{z} \times \bar{\nabla} \Pi_i^m$ (7-3)

Transverse ${}^{\text{TE}}\bar{H}_i = \frac{1}{k_i^2} \bar{\nabla}_t \frac{\partial \Pi_i^m}{\partial z}$ (7-4)

where $\bar{\nabla}_t = \hat{\rho} \frac{d}{d\rho} + \frac{1}{\rho} \frac{d}{d\phi} \hat{\phi}$

7-2 TM Boundary Conditions

The boundary conditions on the TM fields yield constraints on the Π_i^e which in turn relate the A_i^e and B_i^e from one region to another. Combining 7-1, 2, and -3 one obtains the result that

$$\frac{\Pi_i^e}{\epsilon_i} = \frac{\Pi_{i\pm 1}^e}{\epsilon_{i\pm 1}} \quad (7-5)$$

and $\frac{1}{\epsilon_i \mu_i} \frac{\partial \Pi_i^e}{\partial z} = \frac{1}{\epsilon_{i\pm 1} \mu_{i\pm 1}} \frac{\partial \Pi_{i\pm 1}^e}{\partial z}$ (7-6)

when

$$z = d_{(i)}^{(i+1)}$$

7-3 TE Boundary Conditions

In the same manner as for the TM fields, the boundary conditions for the magnetic Hertz potential can be derived in the form

$$\frac{\Pi_i^m}{\mu_i} = \frac{\Pi_{i\pm 1}^m}{\mu_{i\pm 1}} \quad (7-7)$$

$$\frac{1}{\epsilon_i \mu_i} \frac{\partial \Pi_i^m}{\partial z} = \frac{1}{\epsilon_{i\pm 1} \mu_{i\pm 1}} \frac{\partial \Pi_{i\pm 1}^m}{\partial z} \quad (7-8)$$

for $z = d_{(i)}^{(i+1)}$

The symmetry of the two sets of boundary conditions is apparent. The material property factors ϵ_i and μ_i switch places.

7-4 Transmission Matrices

The general solutions for Π_i^o and Π_i^m are of the form 6-12.

Since the $\cos(\eta z)$ and $\int_0^\infty J_n(\lambda r) d\lambda$ factors are common, the only factor which varies from region to region is

$$A_i^m(\lambda) e^{j\lambda_i z} + B_i^m(\lambda) e^{-j\lambda_i z} \quad (7-9)$$

Combining 7-9 with 7-5 through 7-8 it is possible to write the relationship for A_i^m B_i^m in terms of the coefficients in the neighbouring region. In the following the TE fields are used to illustrate the analysis

$$\frac{1}{\epsilon_i} \begin{bmatrix} 1 & 1 \\ j\lambda_i & -j\lambda_i \\ \mu_i & \mu_i \end{bmatrix} \begin{bmatrix} e^{j\lambda_i d_{i+1}} & 0 \\ 0 & e^{-j\lambda_i d_{i+1}} \end{bmatrix} \begin{bmatrix} A \\ B \end{bmatrix} = \frac{1}{\epsilon_{i+1}} \begin{bmatrix} 1 & 1 \\ j\lambda_{i+1} & -j\lambda_{i+1} \\ \mu_{i+1} & \mu_{i+1} \end{bmatrix} \begin{bmatrix} e^{j\lambda_{i+1} d_{i+1}} & 0 \\ 0 & e^{-j\lambda_{i+1} d_{i+1}} \end{bmatrix} \begin{bmatrix} A_{i+1} \\ B_{i+1} \end{bmatrix} \quad (7-10)$$

This result can be regrouped and written

$$\begin{bmatrix} A_i^m \\ B_i^m \end{bmatrix} = \begin{bmatrix} U_{i,i+1}^{TE} \\ \end{bmatrix} \begin{bmatrix} A_{i+1} \\ B_{i+1} \end{bmatrix} \quad (7-11)$$

where

$$\begin{bmatrix} U_{i,i+1}^{TE} \end{bmatrix} = \frac{\epsilon_i}{\epsilon_{i+1}} \begin{bmatrix} e^{-j\lambda_i d_{i+1}} & 0 \\ 0 & e^{+j\lambda_i d_{i+1}} \end{bmatrix} \begin{bmatrix} 1 & R_{i,i+1}^{TE} \\ T_{i,i+1}^{TE} & T_{i,i+1}^{TE} \\ R_{i,i+1}^{TE} & 1 \end{bmatrix} \begin{bmatrix} e^{j\lambda_{i+1} d_{i+1}} & 0 \\ 0 & e^{-j\lambda_{i+1} d_{i+1}} \end{bmatrix} \quad (7-12)$$

$\begin{bmatrix} U_{i,i+1}^{TE} \end{bmatrix}$ is the TE transmission matrix for the boundary at $Z = d_{i+1}$ and relates the fields in region i to those in $i + 1$. Similarly, a matrix describing region $i + 1$ in terms of i can be written down and is

$$\begin{bmatrix} U_{i,i+1}^{TE} \end{bmatrix}^{-1} = \begin{bmatrix} U_{i+1,i}^{TE} \end{bmatrix} \quad (7-13)$$

The coefficients $R_{i,i+1}^{TE}$ and $T_{i,i+1}^{TE}$ are the Fresnel TE plane wave reflection and transmission coefficient.

$$R_{i,i+1}^{TE} = \frac{\mu_{i+1}\gamma_i - \mu_i\gamma_{i+1}}{\mu_{i+1}\gamma_i + \mu_i\gamma_{i+1}} \quad (7-14)$$

$$T_{i,i+1}^{TE} = 1 + R_{i,i+1}^{TE} = \frac{2\mu_{i+1}\gamma_i}{\mu_{i+1}\gamma_i + \mu_i\gamma_{i+1}} \quad (7-15)$$

In a similar fashion the TM coefficients can be transmitted across an interface using the TM transmission matrix which takes the form

$$\begin{bmatrix} A_i^e \\ B_i^e \end{bmatrix} = \begin{bmatrix} U_{i,i+1}^{TM} \end{bmatrix} \begin{bmatrix} A_{i+1}^e \\ B_{i+1}^e \end{bmatrix} \quad (7-16)$$

where

$$\begin{bmatrix} U_{i,i+1}^{TM} \end{bmatrix} = \frac{\mu_i}{\mu_{i+1}} \begin{bmatrix} e^{-j\gamma_i d_{i+1}} & 0 \\ 0 & e^{j\gamma_i d_{i+1}} \end{bmatrix} \begin{bmatrix} \frac{1}{T_{i,i+1}^{TM}} & \frac{R_{i,i+1}^{TM}}{T_{i,i+1}^{TM}} \\ \frac{R_{i,i+1}^{TM}}{T_{i,i+1}^{TM}} & \frac{1}{T_{i,i+1}^{TM}} \end{bmatrix} \begin{bmatrix} e^{j\gamma_{i+1} d_{i+1}} & 0 \\ 0 & e^{-j\gamma_{i+1} d_{i+1}} \end{bmatrix} \quad (7-17)$$

$R_{i,i+1}^{TM}$ and $T_{i,i+1}^{TM}$ are the Fresnel TM plane reflection and transmission coefficients which have the form

$$R_{i,i+1}^{TM} = \frac{\epsilon_{i+1}\gamma_i - \epsilon_i\gamma_{i+1}}{\epsilon_{i+1}\gamma_i + \epsilon_i\gamma_{i+1}} \quad (7-18)$$

$$T_{i,i+1}^{TM} = 1 + R_{i,i+1}^{TM} = \frac{2\epsilon_{i+1}\gamma_i}{\epsilon_{i+1}\gamma_i + \epsilon_i\gamma_{i+1}} \quad (7-19)$$

The matrix notation can be extended to relate region i with region 0 or region N.

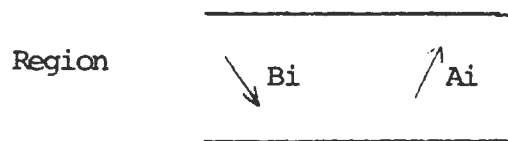
$$\begin{bmatrix} A_i \\ B_i \end{bmatrix} = \begin{matrix} U_{i,i+1} & U_{i+1,i+1} & \dots & U_{N-1,N} \end{matrix} \begin{bmatrix} A_N \\ B_N \end{bmatrix} \quad (7-20)$$

$$\begin{bmatrix} A_i \\ B_i \end{bmatrix} = \begin{matrix} U_{i,i-1} & U_{i-1,i-2} & \dots & U_{1,0} \end{matrix} \begin{bmatrix} A_0 \\ B_0 \end{bmatrix} \quad (7-21)$$

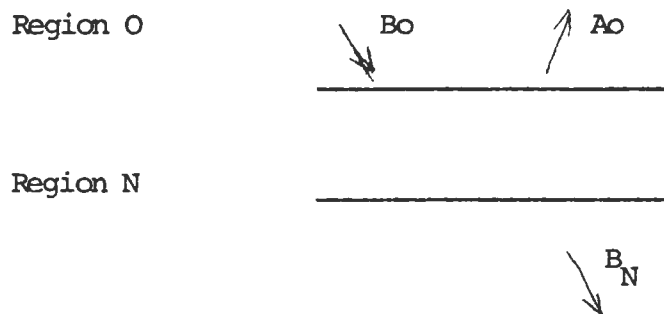
Any other pair of layers can be related in a similar fashion.

N-Layer Reflection Coefficient

In the same manner as one expresses the response of a single interface by a Fresnel reflection coefficient, a more generalized reflection coefficient can be defined for a stack of an arbitrary number of layers. From examination 7-9 and 6-12, it becomes readily apparent that the $A_i^{\hat{e}_m}$ coefficients are the amplitudes of waves propagating in the positive Z direction while the $B_i^{\hat{e}_m}$ are the amplitudes of waves propagating in the negative Z direction



Now consider the simplest case of a wave incident on the stack N-layers from region 0. B_0 is the amplitude of the incident wave and A_0 is the amplitude of the wave reflected from the stack



A generalized reflection coefficient is defined as

$$R = \frac{A_0}{B_0} \quad (7-22)$$

It should be noted that in the wave number domain, a fixed λ corresponds to a plane wave incident on the stack in the FT domain and a single cylindrical wave in the Henkel Transform domain.

i.e. $B_0(\lambda) = \delta(\lambda - \lambda_0)$ (7-23)

A very useful representation for R is obtained from the transmission matrix formalism. For the example at hand one can write

$$\begin{bmatrix} A_0 \\ B_0 \end{bmatrix} = \begin{bmatrix} w_{11}^1 & w_{12}^1 \\ w_{21}^1 & w_{22}^1 \end{bmatrix} \begin{bmatrix} A_1 \\ B_1 \end{bmatrix} \quad (7-24)$$

(Note that the development is the same for both TE and TM type fields so no distinction is made here). Thus the reflection coefficient becomes

$$\begin{aligned} R = \frac{A_0}{B_0} &= \frac{w_{11}^1 A_1 + w_{12}^1 B_1}{w_{21}^1 A_1 + w_{22}^1 B_1} \\ &= \frac{w_{11}^1}{w_{21}^1} + \left(\frac{\frac{w_{12}^1}{w_{22}^1} - \frac{w_{11}^1}{w_{21}^1}}{1 + \frac{w_{21}^1}{w_{22}^1} \left(\frac{A_1}{B_1} \right)} \right) \end{aligned} \quad (7-25)$$

Thus $R = A_0/B_0$ is expressible in terms of (A_1/B_1) plus some parameters depending on the electrical properties. Now the

same thing can be done to represent (A_1/B_1) in terms of (A_2/B_2) etc. down to region (A_{N-1}/B_{N-1}) . Since there is no source in region N , only downward propagating waves can exist and

$(A_N/B_N) = 0$. Thus

$$R = \frac{w_{11}^1}{w_{21}^1} + \frac{\left(\frac{w_{12}^1}{w_{22}^1} - \frac{w_{11}^1}{w_{21}^1} \right)}{\left(1 + \frac{w_{21}^1}{w_{22}^1} \left(\frac{w_{11}^2}{w_{21}^2} + \left(\frac{w_{12}^2}{w_{22}^2} - \frac{w_{11}^2}{w_{21}^2} \right) \right) \right)} \dots \dots \dots \frac{\left(1 + \frac{w_{21}^{N-1}}{w_{22}^{N-1}} \frac{w_{11}^N}{w_{21}^N} \right)}{\left(1 + \frac{w_{21}^{N-1}}{w_{22}^{N-1}} \frac{w_{12}^N}{w_{22}^N} \right)} \quad (7-26)$$

which is known in mathematical terminology as a continued fraction expansion for R of length N with the member elements being independent of the excitation field and dependent only on the electrical properties and their distribution with depth in the stack.

If, for example, a particular source distribution exists in region o , the fields to this source if the layered structure were not present would simply be of the form

$$B e^{-j\gamma_o z} \quad (7-27)$$

plus the appropriate integral over X_1 the angular symmetry etc. The effect of the stack of layers can then be represented by

$$R B e^{j\gamma_o z} \quad (7-28)$$

and the total field by

$$B (e^{-j\gamma_o z} + R e^{j\gamma_o z}) \quad (7-29)$$

While the particular case of the source in region has been considered here, the source could actually exist in any layer and reflection from below and above would have to be considered. In the above, the problem of solving the response in a stack boils down to finding the particular excitation for the given source in a homogeneous wholespace. The layered structure appears as an additive homogeneous solution to the origin P.D.E. and is just a factor times the whole-space of particular solution. The application of these results to some particular cases is discussed in the next section where a number of examples are worked out.

8. Point Dipole Sources over an N-Layered Earth

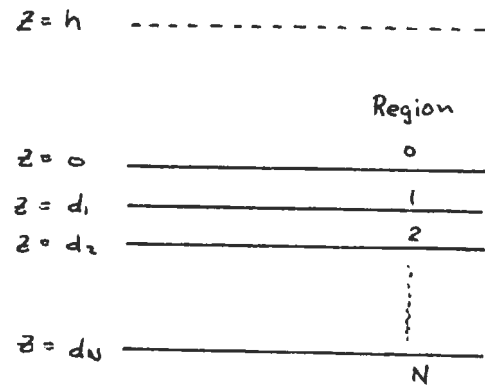
The preceding sections give all the basic mathematical developments required for this particular problem. The analysis is in three stages; first the particular excitation field is developed, secondly, the reduction of the particular solution into electric and magnetic Hertz potentials which have only vertical components is made, finally each spectral component is reflected by its N-layer reflection coefficient. In the following, the first case of a vertical electric dipole is considered in some detail. The remaining examples are very similar and as much detail is omitted as is possible.

8-1. Vertical Electric Dipole (VED)

The electric dipole has moment $Id\ell$ and is located at a

height h above the surface of an N -layer earth. From section three

$$\vec{J}_s = I dl \frac{\delta(\rho)}{2\pi\rho} \delta(z-h) \hat{z} \quad (8-1)$$



and the particular Hertz potential is an electric Hertz potential with a component only in the \hat{z} direction.

$$\bar{\Pi}_p = j\omega\mu_0 I dl \frac{e^{jk_0|\vec{r}-\vec{r}'|}}{4\pi|\vec{r}-\vec{r}'|} \hat{z} \quad (8-2)$$

In Hankel transform notation, using 4-11,

$$\bar{\Pi}_p = j\omega\mu_0 \hat{z} \frac{I dl}{4\pi} \int_0^\infty j \frac{\lambda}{\gamma_0} e^{j\gamma_0(z-h)} J_0(\lambda\rho) d\lambda \quad (8-3)$$

From section 6, it is apparent that the only excitation in this problem is circularly symmetric and $n \equiv 0$. In the region $0 \leq z \leq h$, the excitation 8-3 gives

$${}_0B_o^e = j \frac{\lambda}{\gamma_0} e^{j\gamma_0 h} \quad (8-4)$$

It is apparent from the source and structure symmetry that only TM waves are excited and the reflected wave is defined in region 0 by

$${}_0A_o^e = j \frac{\lambda}{\gamma_0} R^{TM} e^{j\gamma_0 h} \quad (8-5)$$

Table 8-1. TE and TM Field Components

	TE	TM
E_r	$-\frac{1}{j\omega\epsilon} \frac{1}{r} \frac{\partial}{\partial \phi} \pi^m$	$\frac{1}{k^2} \frac{\partial^2}{\partial r \partial z} \pi^e$
E_ϕ	$\frac{1}{j\omega\epsilon} \frac{\partial}{\partial r} \pi^m$	$\frac{1}{k^2} \frac{1}{r} \frac{\partial^2}{\partial \phi \partial z} \pi^e$
E_z	0	$\pi^e + \frac{1}{k^2} \frac{\partial^2}{\partial z^2} \pi^e$
H_r	$\frac{1}{k^2} \frac{\partial^2}{\partial r \partial z} \pi^m$	$\frac{1}{j\omega\mu} \frac{1}{r} \frac{\partial}{\partial \phi} \pi^e$
H_ϕ	$\frac{1}{k^2} \frac{1}{r} \frac{\partial^2}{\partial \phi \partial z} \pi^m$	$-\frac{1}{j\omega\mu} \frac{\partial}{\partial r} \pi^e$
H_z	$\pi^m + \frac{1}{k^2} \frac{\partial^2}{\partial z^2} \pi^m$	0

where R^{TM} is the TM reflection coefficient for the N-layer stack. The total field in region 0 is described ^{by} the electric Hertz potential

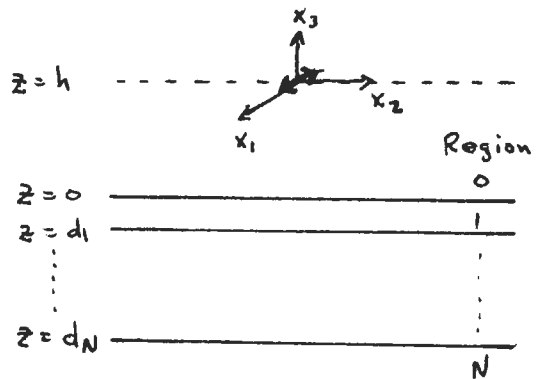
$$\pi_o^e = j\omega\mu_o \frac{I dl}{4\pi} \int_0^\infty j \frac{\lambda}{\gamma_o} \left\{ e^{j\gamma_o(z-h)} + R^{TM} e^{j\gamma_o(z+h)} \right\} J_o(\lambda \rho) d\lambda \quad (8-6)$$

The fields in other regions can be obtained using the transmission matrices of section 7 and continuing ${}_oA_o^e$ and ${}_oB_o^e$ downward.

8-2. Horizontal Electric Dipole (HED)

The other orientation for the electric dipole is in the horizontal plane. Combination of the VED and HED solutions yields the solution for an arbitrarily oriented dipole. For convenience in the following, the HED is assumed aligned in the \hat{e}_1 or $\phi \equiv 0$ direction. The electric source current is then

$$\vec{J}_s = I \delta l \frac{\delta(\rho)}{2\pi \rho} \delta(z-h) \hat{e}_1 \quad (8-7)$$



The particular solution for this current distribution is an electric Hertz potential aligned in the \hat{e}_1 direction.

$$\pi_p = j\omega\mu_o I dl \frac{e^{jk_o|\vec{r}-\vec{r}'|}}{4\pi|\vec{r}-\vec{r}'|} \hat{e}_1 \quad (8-8)$$

Now the problem of solving for the effect of the layered stack requires reducing $\bar{\Pi}_p$ into electric and/or magnetic Hertz potentials with only a vertical component. This is achieved by examining the TE and TM electric and magnetic fields in order to find Π_p^e and Π_p^m .

From Table 8-1 it is readily apparent that the vertical electric field is associated with Π_i^e (since Π_i^m generates a totally TE field). Similarly the vertical magnetic field is totally associated with Π_i^m . This then gives the key as to how to break Π_p into its Π_o^e and Π_o^m components.

From section 3, E_z and H_z associated with $\bar{\Pi}_p$ are given by

$$E_z = \frac{1}{k_0^2} \frac{\partial^2}{\partial z \partial x_1} \Pi_p \quad (8-9)$$

$$H_z = -\frac{1}{j\omega\mu_0} \frac{\partial \Pi_p}{\partial x_2} \quad (8-10)$$

Using the Sommerfeld integral discussed in section 4,

$$E_z = -\frac{I dl}{j\omega\epsilon_0 4\pi} \cos\varphi \int_0^\infty \text{sign}(z-h) \lambda^2 e^{j\gamma_0(z-h)} J_1(\lambda\rho) d\lambda \quad (8-11)$$

In order to obtain Π_o^e , E_z has to be regrouped to the form analogous to that in Table 8-1 namely

$$E_z = \mathcal{F} + \frac{1}{k_0^2} \frac{\partial^2}{\partial z^2} \mathcal{F} \quad (8-12)$$

Noting that $\gamma^2 = k^2 - \lambda^2$, 8-11 can be written as

$$\begin{aligned} E_z &= j \frac{\omega \mu_0 I d l}{4\pi} \cos \varphi \int_0^\infty \text{sign}(z-h) \left(1 - \frac{\gamma_0^2}{k_0^2}\right) e^{j\gamma_0(z-h)} J_1(\lambda \rho) d\lambda \\ &= j \frac{\omega \mu_0 I d l}{4\pi} \left[1 + \frac{1}{k_0^2} \frac{\partial^2}{\partial z^2}\right] \cos \varphi \int_0^\infty \text{sign}(z-h) e^{j\gamma_0(z-h)} J_1(\lambda \rho) d\lambda \end{aligned} \quad (8-13)$$

and Π_p^e is readily identified as

$$\Pi_p^e = j \frac{\omega \mu_0 I d l}{4\pi} \cos \varphi \int_0^\infty \text{sign}(z-h) e^{j\gamma_0(z-h)} J_1(\lambda \rho) d\lambda \quad (8-14)$$

In a similar manner, H_z is given by

$$\begin{aligned} H_z &= \frac{I d l}{4\pi} \sin \varphi \int_0^\infty j \frac{\lambda}{\gamma_0} e^{j\gamma_0(z-h)} \lambda J_1(\lambda \rho) d\lambda \\ &= \frac{I d l}{4\pi} \sin \varphi \int_0^\infty j \frac{(k_0^2 - \gamma_0^2)}{\gamma_0} e^{j\gamma_0(z-h)} J_1(\lambda \rho) d\lambda \\ &= \frac{I d l}{4\pi} \left[1 + \frac{1}{k_0^2} \frac{\partial^2}{\partial z^2}\right] \sin \varphi \int_0^\infty j \frac{k_0^2}{\gamma_0} e^{j\gamma_0(z-h)} J_1(\lambda \rho) d\lambda \end{aligned} \quad (8-15)$$

The magnetic Hertz potential associated with $\bar{\Pi}_p$ is readily identified as

$$\Pi_p^m = \frac{I d\ell}{4\pi} \sin\phi \int_0^\infty j \frac{k_0^2}{\gamma_0} e^{j\gamma_0|z-h|} J_1(\lambda\rho) d\lambda \quad (8-16)$$

Analysis of Π_p^e and Π_p^m shows that $\bar{\Pi}_p$ has been split into a TE field which has a sinusoidal variation with azimuth and a TM field which has a cosinusoidal angular variation. In order to find the total field in region 0, the integrands of 8-16 and 8-14 must be multiplied by the TE and TM N-layer Fresnel coefficients and then added to the solution. The total solution is the

$$\Pi_0^e = j\omega\mu_0 \frac{I d\ell}{4\pi} \cos\phi \int_0^\infty \left\{ \text{sign}(z-h) e^{j\gamma_0|z-h|} - R^{TM} e^{j\gamma_0(z+h)} \right\} J_1(\lambda\rho) d\lambda \quad (8-17)$$

$$\Pi_0^m = \frac{I d\ell}{4\pi} \sin\phi \int_0^\infty j \frac{k_0^2}{\gamma_0} \left\{ e^{j\gamma_0|z-h|} + R^{TE} e^{j\gamma_0(z+h)} \right\} J_1(\lambda\rho) d\lambda \quad (8-18)$$

The fields in the other regions are obtained by the transmission matrix analysis of section 7.

8-3. Vertical Magnetic Dipole (VMD)

The vertical magnetic dipole problem is analogous to the vertical electric dipole problem and can be obtained directly by replacing $j\omega\mu$ by $-j\omega\epsilon$, Idl , by $-j\omega\mu_0 IdA$ and R^{TM} and R^{TE} . From section 3, the fields can be expressed in terms of a magnetic Hertz potential

$$\overline{\Pi}_p = -\omega^2 \epsilon_0 \mu_0 IdA \hat{z} \frac{e^{jk_0 |\vec{r}-\vec{r}'|}}{4\pi |\vec{r}-\vec{r}'|} \quad (8-19)$$

Now, Π_p^m is identical to $\overline{\Pi}_p$ and

$$\Pi_0^m = -\frac{\omega^2 \epsilon_0 \mu_0 IdA}{4\pi} \int_0^\infty j \frac{\lambda}{\gamma_0} \left\{ e^{j\gamma_0 |z-h|} + R^{TE} e^{j\gamma_0 (z+h)} \right\} J_0(\lambda \rho) d\lambda \quad (8-20)$$

The response is purely one composed of TE waves as to be expected.

8-4. Horizontal Magnetic Dipole (HMD)

The last point source to be considered is the HMD. As with the VMD, the solution can be obtained by analogy with the HED result. The roles of Π_0^e and Π_0^m interchange with the result that

$$\Pi_0^e = \frac{-j\omega\mu_0 IdA \sin\varphi}{4\pi} \int_0^\infty \frac{j k_0^2}{\gamma_0} \left\{ e^{j\gamma_0 |z-h|} + R^{TM} e^{j\gamma_0 (z+h)} \right\} J_1(\lambda \rho) d\lambda \quad (8-21)$$

$$\pi_0^m = -\frac{\omega^2 \epsilon_0 \mu_0 I d A}{4\pi} \cos \varphi \int_0^\infty \left\{ \text{sign}(z-h) e^{j\gamma_0(z-h)} - R^{TE} e^{j\gamma_0(z+h)} \right\} J_1(\lambda \rho) d\lambda \quad (8-22)$$

8-5. Summary

The last four subsections, completely cover most of the use geophysical source models. While it has not been discussed here, the addition of a stack of layers above the source can be accomplished in a similar manner to the above derivations. For earth bound applications this can be used to describe ionospheric effects.

9. 1 and 2 Layer Earth Reflection Coefficients

For the preliminary analysis of the SEP problem, the response of a half-space and of a 2-layer earth are discussed in detail since these special cases contain all the particular features of a general N layer system. The reflection coefficient for a 2-layer earth are obtained from the continued fraction expansion of section 7. The physical interpretation of the mathematical form of the reflection coefficients are discussed.

The 2-layer earth is sketched below. The stack TE reflection coefficient is

$$R^{TE} = \frac{A_0^m}{B_0^m} \quad (9-1)$$

The transmission matrix for the $z = d$ interface is

$$\left[U_{01}^{TE} \right] = \frac{\epsilon_0}{\epsilon_1} \frac{1}{T_{01}^{TE}} \begin{bmatrix} 1 & R_{01}^{TE} \\ R_{01}^{TE} & 1 \end{bmatrix} \quad (9-2)$$

and

$$R^{TE} = \frac{1}{R_{01}^{TE}} + \frac{(R_{01}^{TE} - 1/R_{01}^{TE})}{1 + R_{01}^{TE} \left(\frac{A_1}{B_1} \right)} \quad (9-3)$$

The $z = d_2 = -t_1$ transmission matrix becomes

$$\left[U_{12}^{TE} \right] = \frac{\epsilon_1}{\epsilon_2} \frac{1}{T_{12}^{TE}} \begin{bmatrix} e^{j(\gamma_1 - \gamma_2)t_1} & R_{12}^{TE} e^{j(\gamma_1 + \gamma_2)t_1} \\ R_{12}^{TE} e^{-j(\gamma_1 + \gamma_2)t_1} & e^{-j(\gamma_1 - \gamma_2)t_1} \end{bmatrix} \quad (9-4)$$

Now since $A_2/B_2 \equiv 0$,

$$\frac{A_1}{B_1} = R_{12}^{TE} e^{j2\gamma_1 t_1} \quad (9-5)$$

and

$$R^{TE} = \frac{1}{R_{01}^{TE}} + \frac{(R_{01}^{TE} - 1/R_{01}^{TE})}{(1 + R_{01}^{TE} R_{12}^{TE} e^{j2\gamma_1 t_1})} \quad (9-6)$$

The TM reflection coefficient for the 2-layer earth is obtained in a similar manner and is identical to (9-6) with the TE superscripts replaced by TM.

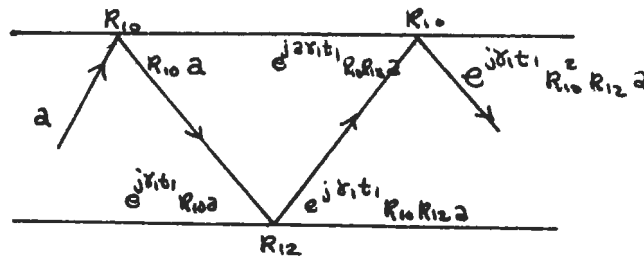
The most important part of 9-6 is the denominator of the second term. Taking

$$\alpha = -R_{01}^{TE} R_{12}^{TE} e^{2j\gamma_1 t_1} \quad (9-7)$$

The multiple reflection back and forth between $d = 0$ and $d = -t_1$, in region 1 appear by expanding

$$\frac{1}{1-\alpha} = \sum_{n=0}^{\infty} \alpha^n \quad (9-8)$$

in a geometric series. Each term of the series represents an additional reflection at the two boundaries with appropriate reflection amplitude change plus a "phase" change $2\gamma_1 t_1$, corresponding to the two way path through the layer 1 as sketched below.



Note: $R_{10} = -R_{01}$

The half space reflection coefficient can be obtained in three manners, in the limits as $R_{12} \rightarrow 0$ (i.e. $\mu_1 \rightarrow \mu_2$, $\epsilon_1 \rightarrow \epsilon_2$) $t_1 \rightarrow \infty$ and $t_1 \rightarrow 0$.

Case 1: When $R_{12} \equiv 0$

$$R^{TE} = R_{01}^{TE} \quad (9-9)$$

as expected.

Case 2: When $t_1 \rightarrow \infty$, any infinitesimal loss in region 1 will cause

$$e^{j\gamma_1 t_1} \rightarrow 0 \quad t_1 \rightarrow \infty \quad (9-10)$$

and

$$R^{TE} = R_{01}^{TE} \quad (9-11)$$

Case 3: In the limit as $t_1 \rightarrow 0$, one obtains a half space with material properties ϵ_2, μ_2 .

$$R^{TE} = \frac{R_{01}^{TE} + R_{12}^{TE}}{1 + R_{01}^{TE} R_{12}^{TE}} \quad (9-12)$$

Using the fact that

$$R_{ij}^{TE} = \frac{\mu_j \gamma_i - \mu_i \gamma_j}{\mu_j \gamma_i + \mu_i \gamma_j}$$

one can show that

$$R^{TE} = R_{02}^{TE} \quad (9-13)$$

Note:

$$\begin{aligned} \frac{R_{01}^{TE} + R_{12}^{TE}}{1 + R_{01}^{TE} R_{12}^{TE}} &= \frac{(\mu_1 \gamma_0 - \mu_0 \gamma_1)(\mu_2 \gamma_1 + \mu_1 \gamma_2) - (\mu_1 \gamma_0 + \mu_0 \gamma_1)(\mu_2 \gamma_1 - \mu_1 \gamma_2)}{(\mu_1 \gamma_0 + \mu_0 \gamma_1)(\mu_2 \gamma_1 + \mu_1 \gamma_2) + (\mu_1 \gamma_0 - \mu_0 \gamma_1)(\mu_2 \gamma_1 - \mu_1 \gamma_2)} \\ &= \frac{\mu_2 \gamma_0 - \mu_0 \gamma_2}{\mu_2 \gamma_0 + \mu_0 \gamma_2} \\ &= R_{02}^{TE} \end{aligned} \quad (9-14)$$

In the above the emphasis has been placed on the TE reflection coefficient only as far as it illustrates the nature of the stack

reflection coefficient. All the analysis also holds for the TM reflection coefficients.

One other important feature of the 2-layer reflection coefficient is the resonant wave numbers for the waveguide formed by the slab placed between two media of differing properties. In most instances, the guide is leaky. These resonances occur when

$$1 - R_{10} R_{12} e^{j 2\gamma_1 t_1} = 0$$

which is the general form of the normal mode equation.

Solution of 9-15 plays an important role in the analysis of the 2-layer earth response. This will be discussed in detail later.

10 - Normalization and Tabulation of HED Fields for SEP Application

In this section, the formal mathematical solution for the HED derived in section 8 is rewritten in a normalized format which facilitates computation aspects of the evaluation of the fields numerically. Since the primary source of interest for the SEP application is the HED, it is used as the example in the following sections. The other dipole sources can be treated in exactly the same manner so there is no real ~~loss~~ of generality.

In the MKS system of units, the electric and magnetic fields have units of volt/m. and amp/m.; the spatial dimensions are in m. and wavenumbers in m^{-1} . For computation

Table 10-1

Normalized Field and Parameter Definitions

$$\overline{H} = \frac{\overline{H}}{\left(\frac{\Gamma d (k_0^2)}{4\pi} \right)}$$

$$\overline{E} = \frac{\overline{E}}{\left(\frac{j \omega \mu_0 \Gamma d (k_0)}{4\pi} \right)}$$

$$W = \text{free space wavelength} = \frac{2\pi}{k_0}$$

$$\Delta = \frac{\lambda}{k_0} \quad \bullet \quad \text{normalized radial wavenumber}$$

$$\Gamma_i = \frac{\gamma_i}{k_0} \quad - \quad \text{normalized vertical wavenumber}$$

$$P = k_0 \rho = 2\pi \frac{\rho}{W} \quad - \quad \text{normalized radial distance}$$

$$Z = k_0 z = 2\pi \frac{z}{W} \quad - \quad \text{normalized vertical distance}$$

$$H = k_0 h = 2\pi \frac{h}{W} \quad - \quad \text{normalized HED elevation}$$

$$D_i = k_0 d_i = 2\pi \frac{d_i}{W} \quad - \quad \text{normalized interface depths}$$

Table 10-2

Normalized HED TE Field Components

$$E_p = \frac{\cos \varphi}{\rho} \int_0^{\infty} \frac{j}{\Gamma_0} \left\{ e^{j\Gamma_0 |z-H|} + R^{TE} e^{j\Gamma_0 (z+H)} \right\} J_1(\Delta \rho) d\Delta$$

$$E_\varphi = -\sin \varphi \int_0^{\infty} \frac{j\Delta}{\Gamma_0} \left\{ e^{j\Gamma_0 |z-H|} + R^{TE} e^{j\Gamma_0 (z+H)} \right\} J_1'(\Delta \rho) d\Delta$$

$$E_z = 0$$

$$H_p = \sin \varphi \int_0^{\infty} -\Delta \left\{ \text{sign}(z-H) e^{j\Gamma_0 |z-H|} + R^{TE} e^{j\Gamma_0 (z+H)} \right\} J_1'(\Delta \rho) d\Delta$$

$$H_\varphi = \frac{\cos \varphi}{\rho} \int_0^{\infty} - \left\{ \text{sign}(z-H) e^{j\Gamma_0 |z-H|} + R^{TE} e^{j\Gamma_0 (z+H)} \right\} J_1(\Delta \rho) d\Delta$$

$$H_z = \sin \varphi \int_0^{\infty} \frac{j\Delta^2}{\Gamma_0} \left\{ e^{j\Gamma_0 |z-H|} + R^{TE} e^{j\Gamma_0 (z+H)} \right\} J_1(\Delta \rho) d\Delta$$

$$J_1'(z) = \frac{dJ_1(z)}{dz} = J_0(z) - \frac{1}{z} J_1(z)$$

$$\begin{aligned} \text{sign}(z) &= -1 & z < 0 \\ &= 0 & z = 0 \\ &= 1 & z > 0 \end{aligned}$$

Table 10-3

Normalized HED TM Field Components

$$\mathcal{E}_r = -\cos\varphi \int_0^\infty j \Lambda T_0 (e^{j\Gamma_0 |z-H|} - R^{TM} e^{j\Gamma_0 (z+H)}) J_1'(\Lambda\rho) d\Lambda$$

$$\mathcal{E}_\varphi = \frac{\sin\varphi}{\rho} \int_0^\infty j T_0 (e^{j\Gamma_0 |z-H|} - R^{TM} e^{j\Gamma_0 (z+H)}) J_1(\Lambda\rho) d\Lambda$$

$$\mathcal{E}_z = -\cos\varphi \int_0^\infty \Lambda^2 (\text{sign}(z-H) e^{j\Gamma_0 |z-H|} - R^{TM} e^{j\Gamma_0 (z+H)}) J_1(\Lambda\rho) d\Lambda$$

$$\mathcal{H}_r = \frac{\sin\varphi}{\rho} \int_0^\infty (\text{sign}(z-H) e^{j\Gamma_0 |z-H|} - R^{TM} e^{j\Gamma_0 (z+H)}) J_1(\Lambda\rho) d\Lambda$$

$$\mathcal{H}_\varphi = \cos\varphi \int_0^\infty \Lambda (\text{sign}(z-H) e^{j\Gamma_0 |z-H|} - R^{TM} e^{j\Gamma_0 (z+H)}) J_1'(\Lambda\rho) d\Lambda$$

$$\mathcal{H}_z = 0$$

Table 10-4

Normalized HED Radiation FieldsTE

$$E_{\phi} = -\sin\varphi \int_0^{\infty} j \frac{\Delta}{\Gamma_0} \left(e^{j\Gamma_0|z-H|} + R^{TE} e^{j\Gamma_0(z+H)} \right) J_0(\Delta\rho) d\Delta$$

$$H_{\rho} = \sin\varphi \int_0^{\infty} -\Delta \left(\text{sign}(z-H) e^{j\Gamma_0|z-H|} + R^{TE} e^{j\Gamma_0(z+H)} \right) J_0(\Delta\rho) d\Delta$$

$$H_z = \sin\varphi \int_0^{\infty} \frac{j\Delta^2}{\Gamma_0} \left(e^{j\Gamma_0|z-H|} + R^{TE} e^{j\Gamma_0(z+H)} \right) J_1(\Delta\rho) d\Delta$$

$$E_{\rho} = E_z = H_{\phi} = 0$$

TM

$$H_{\phi} = \cos\varphi \int_0^{\infty} \Delta \left(\text{sign}(z-H) e^{j\Gamma_0|z-H|} - R^{TM} e^{j\Gamma_0(z+H)} \right) J_0(\Delta\rho) d\Delta$$

$$E_{\rho} = -\cos\varphi \int_0^{\infty} j\Delta\Gamma_0 \left(e^{j\Gamma_0|z-H|} - R^{TM} e^{j\Gamma_0(z+H)} \right) J_0(\Delta\rho) d\Delta$$

$$E_z = -\cos\varphi \int_0^{\infty} \Delta^2 \left(\text{sign}(z-H) e^{j\Gamma_0|z-H|} - R^{TM} e^{j\Gamma_0(z+H)} \right) J_1(\Delta\rho) d\Delta$$

$$H_{\rho} = H_z = E_{\phi} = 0$$

purposes it is convenient if all these quantities are normalized in such a manner as to make them dimensionless. Examination of the HED electric and magnetic Hertz potentials of section 8 yields a convenient set of factors for normalizing the \bar{E} and \bar{H} fields. The wavenumbers are normalized w.r.t. the freespace wavenumber and spatial dimensions are normalized w.r.t. to the freespace wavelength.

A summary of the normalization procedure is given in Table 10-1. Combining the definitions of Table 10-1 with expressions for the fields in Table 8-1 and the forms of the electric and magnetic Hertz potentials 8-17 and 8-18, one obtains the normalized expressions for the TE and TM fields given in Table 10-2 and 10-3. For analysis of fields at large distances from the source, the fields take a simpler form since only the radiation fields have to be considered. The radiation fields are summarized in Table 10-4.

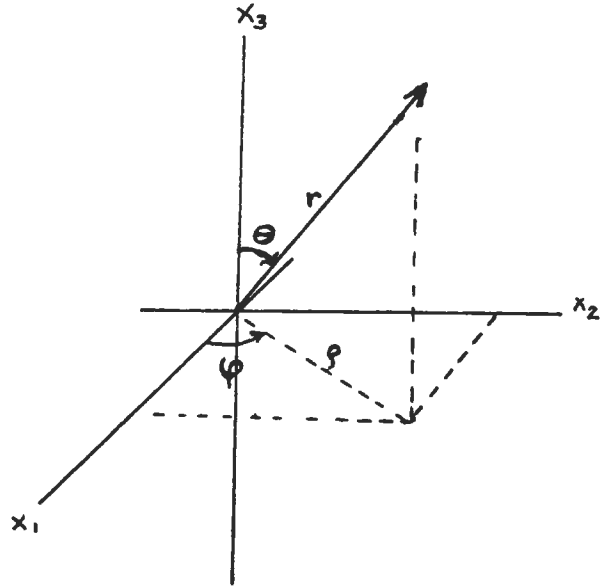
11 - Radiation Patterns of a HED on the Surface of a Half-Space

11-1. Basic Formalism for Radiation Fields

One of the more important aspects of SEP method is the manner in which the presence of a nearby halfspace modifies the energy radiated by the dipole. In this section, a general discussion of radiated power is followed and it is

applied to the particular case of a HED on a loss-free halfspace.

In the discussion of energy radiation and radiation patterns, it is most convenient to adopt a spherical polar coordinate system as sketched to the right. For any finite size source, the fields at large distances from the source are the radiation fields and the fields are of the form



$$f(\theta, \varphi) \frac{e^{jkr}}{r} \quad (11-1)$$

All higher order terms in $1/r$ become negligible as far as radiated power is concerned where $r \rightarrow \infty$.

For the layered earth problem at hand, it was discussed in section 6, that the fields can be split into two independent types namely the TE and TM fields. This convention is continued here in order to facilitate later analysis. At very large distances one has the fields

$$\vec{E}^{TE} = \hat{\varphi} E_{\varphi}(\theta, \varphi) \frac{e^{jkr}}{r} \quad (11-2)$$

$$\begin{aligned} \vec{H}^{TE} &= (\hat{\rho} H_{\rho}(\theta, \varphi) + \hat{e}_3 H_z(\theta, \varphi)) \frac{e^{jkr}}{r} \\ &= H_{\theta}(\theta, \varphi) \hat{\theta} \frac{e^{jkr}}{r} \end{aligned} \quad (11-3)$$

$$\begin{aligned} \bar{E}^{TM} &= (\hat{\rho} E_{\rho}(\theta, \varphi) + \hat{e}_3 E_z(\theta, \varphi)) \frac{e^{jkr}}{r} \\ &= E_{\theta}(\theta, \varphi) \hat{\theta} \frac{e^{jkr}}{r} \end{aligned} \quad (11-4)$$

$$\bar{H}^{TM} = \hat{\varphi} H_{\varphi}(\theta, \varphi) \frac{e^{jkr}}{r} \quad (11-5)$$

E_{θ} and \bar{H}_{φ} as well as E_{φ} and H_{θ} are simply related by Maxwell's equations

$$\bar{H}^{TE} = \frac{\bar{\nabla} \times \bar{E}^{TE}}{j\omega\mu} \quad (11-6)$$

$$= \frac{E_{\varphi}(\theta, \varphi)}{r} \bar{\nabla} \times \hat{\varphi} e^{jkr} \quad (11-7)$$

It should be noted that to remain consistent with the concept of radiation fields, higher order terms in $1/r$ must be neglected. Hence in all operations of the form 11-6, the $\bar{\nabla}$ operator acts only on e^{jkr} term in the field as written in 11-7.

Further

$$\bar{\nabla} \times \hat{\varphi} e^{jkr} = \frac{1}{r^2 \sin \theta} \begin{bmatrix} \hat{r} & r \hat{\theta} & r \sin \theta \hat{\varphi} \\ \frac{\partial}{\partial r} & \frac{\partial}{\partial \theta} & \frac{\partial}{\partial \varphi} \\ 0 & 0 & r \sin \theta e^{jkr} \end{bmatrix} \quad (11-8)$$

$$= + \frac{\hat{r}}{r \sin \theta} \frac{\partial}{\partial \theta} \sin \theta e^{jkr} = \frac{\hat{\theta}}{r} \frac{\partial}{\partial r} r e^{jkr}$$

$$\Rightarrow -jk e^{jkr} \hat{\theta}$$

Once again only $1/r$ terms may be retained for the radiation field analysis and it is permissible to write

$$\bar{\nabla} \times \hat{a} e^{jkr} \Rightarrow -\hat{a} \times \bar{\nabla} \cdot e^{jkr} = -\hat{\theta} j k e^{jkr} \quad (11-9)$$

although this is not mathematically correct. In a similar manner

$$\begin{aligned} \bar{\nabla} \times \hat{\theta} e^{jkr} &\rightarrow -\hat{\theta} \times \bar{\nabla} e^{jkr} \\ &= -\hat{\phi} j k e^{jkr} \end{aligned} \quad (11-10)$$

With these basic formalities settled one has

$$\begin{aligned} \bar{H}^{TE} &= \frac{E_{\phi}(\theta, \varphi)}{j\omega\mu r} (-\hat{\theta} j k) e^{jkr} \\ &= -\hat{\theta} \sqrt{\frac{\epsilon}{\mu}} E_{\phi}(\theta, \varphi) \frac{e^{jkr}}{r} \end{aligned} \quad (11-11)$$

$\sqrt{\frac{\epsilon}{\mu}}$ is identified as the intrinsic admittance of the medium in which the waves are propagating and is denoted by Y . The intrinsic impedance is given by

$$Z = \frac{1}{Y} = \sqrt{\frac{\mu}{\epsilon}} \quad (11-12)$$

In free space $Z = 120\pi$ ohms. Thus 11-11 gives

$$H_{\theta} = -Y E_{\phi} \quad (11-13)$$

In a similar manner, analysis of TM fields yields

$$\begin{aligned} \bar{E}^{TM} &= \frac{\bar{\nabla} \times \bar{H}^{TM}}{-j\omega\epsilon} \\ &= \sum H_{\phi} \hat{\theta} \frac{e^{jkr}}{r} \end{aligned} \quad (11-14)$$

and

$$E_{\theta} = \sum H_{\phi} \quad (11-15)$$

11-2. Poynting Theorem

For a general distribution of electric and magnetic currents, Poynting theorem summarizes the energy balance of the electromagnetic system. For continuity, the general form of Poynting's theorem will be reviewed. The power supplied by the source is given by

$$P = \iiint_{V_{ob}} (\bar{J}_s^* \cdot \bar{E} - \bar{M}_s^* \cdot \bar{H}) dV = \iiint_V (\bar{J}_s^* \cdot \bar{E} - \bar{M}_s^* \cdot \bar{H}) dV \quad (11-16)$$

where V is the volume containing the electric and magnetic current systems \bar{J}_s and \bar{M}_s .

Now from Ampere's law

$$\bar{J}_s^* \cdot \bar{E} = \bar{E} \cdot \nabla \times \bar{H}^* - j\omega \epsilon^* \bar{E}^* \cdot \bar{E} \quad (11-17)$$

and Faraday's law

$$\bar{M}_s^* \cdot \bar{H} = \bar{H} \cdot \nabla \times \bar{E}^* + j\omega \mu^* \bar{H} \cdot \bar{H}^* \quad (11-18)$$

Using the vector identity

$$\nabla \cdot (\bar{A} \times \bar{B}) = \bar{B} \cdot \nabla \times \bar{A} - \bar{A} \cdot \nabla \times \bar{B} \quad (11-19)$$

one obtains

$$\bar{J}_s^* \cdot \bar{E} = \bar{H}^* \cdot \nabla \times \bar{E} - \nabla \cdot (\bar{E} \times \bar{H}^*) - j\omega \epsilon^* \bar{E} \cdot \bar{E}^* \quad (11-20)$$

$$\bar{M}_s^* \cdot \bar{H} = \bar{E}^* \cdot \nabla \times \bar{H} + \nabla \cdot (\bar{E}^* \times \bar{H}) + j\omega \mu^* \bar{H} \cdot \bar{H}^* \quad (11-21)$$

Now

$$\bar{J}_s^* \cdot \bar{E} = j\omega\mu \bar{H} \cdot \bar{H}^* + \bar{H}^* \cdot \bar{M}_s - \bar{\nabla} \cdot (\bar{E} \times \bar{H}^*) - j\omega\epsilon^* \bar{E} \cdot \bar{E}^* \quad (11-22)$$

$$\bar{M}_s^* \cdot \bar{H} = -j\omega\epsilon \bar{E} \cdot \bar{E}^* + \bar{E}^* \cdot \bar{J}_s + \bar{\nabla} \cdot (\bar{E}^* \times \bar{H}) + j\omega\mu^* \bar{H} \cdot \bar{H}^*$$

and

$$\begin{aligned} \bar{J}_s^* \cdot \bar{E} - \bar{M}_s^* \cdot \bar{H} &= -(\bar{J}_s \cdot \bar{E}^* - \bar{M}_s \cdot \bar{H}^*) + j\omega(\epsilon \bar{E} \cdot \bar{E}^* - \epsilon^* \bar{E} \cdot \bar{E}^*) \\ &\quad + j\omega(\mu \bar{H} \cdot \bar{H}^* - \mu^* \bar{H} \cdot \bar{H}^*) - \bar{\nabla} \cdot (\bar{E} \times \bar{H}^* + \bar{E}^* \times \bar{H}) \end{aligned} \quad (11-23)$$

Thus one obtains

$$\text{Real } P = \iiint_{V_\infty} -\omega\epsilon' \tan\delta_e \bar{E} \cdot \bar{E}^* - \omega\mu' \tan\delta_m \bar{H} \cdot \bar{H}^* - \text{Re} \bar{\nabla} \cdot (\bar{E} \times \bar{H}^*) dV$$

$$= -\omega \iiint_{V_\infty} (\epsilon' \tan\delta_e \bar{E} \cdot \bar{E}^* + \mu' \tan\delta_m \bar{H} \cdot \bar{H}^*) dV \quad (11-24)$$

$$- \text{Real} \iint_{S_\infty} (\bar{E} \times \bar{H}^*) \cdot \hat{n} dS$$

and

$$\text{Imag } P = \iiint_{V_\infty} (-\omega\epsilon'' \bar{E} \cdot \bar{E}^* + \omega\mu'' \bar{H} \cdot \bar{H}^*) dV$$

$$(11-25)$$

$$- \text{Im} \iint_{S_\infty} (\bar{E} \times \bar{H}^*) \cdot \hat{n} dS$$

It is not difficult to show that if $\tan \delta_e$ and $\tan \delta_m$ are not identically zero, the surface integrals over the infinite sphere will vanish identically since the fields will be of the form

$$\frac{e^{-\alpha r + j\beta r}}{r} \quad (11-26)$$

for large r and go to zero exponentially with $r \rightarrow \infty$. Thus for a finite loss in the media

$$\text{Real } P = - \omega \iiint_{V_{\infty}} (\epsilon' \tan \delta_e \bar{\mathbf{E}} \cdot \bar{\mathbf{E}}^* + \mu' \tan \delta_m \bar{\mathbf{H}} \cdot \bar{\mathbf{H}}^*) dV \quad (11-27)$$

$$\text{Imag } P = \omega \iiint_{V_{\infty}} (-\epsilon' \bar{\mathbf{E}} \cdot \bar{\mathbf{E}}^* + \mu' \bar{\mathbf{H}} \cdot \bar{\mathbf{H}}^*) dV \quad (11-28)$$

For loss-free media

$$\text{Real } P = - \iint_{S_{\infty}} (\bar{\mathbf{E}} \times \bar{\mathbf{H}}^*) \cdot \hat{\mathbf{n}} dS \quad (11-29)$$

$$\text{Imag } P = \omega \iiint_{V_{\infty}} (-\epsilon' \bar{\mathbf{E}} \cdot \bar{\mathbf{E}}^* + \mu' \bar{\mathbf{H}} \cdot \bar{\mathbf{H}}^*) dV \quad (11-30)$$

One minor point to note is the rationale for retention of one field of the order $1/r$ in the radiation analysis. This is readily obtained by examination of the real power dissipated in a loss free medium. It has the form

$$\text{Real } P = - \iint_{S_{\infty}} (\bar{\mathbf{E}} \times \bar{\mathbf{H}}^*) \cdot \hat{\mathbf{n}} dS \quad (11-31)$$

If $|E| \sim 1/r^n$ and $|H| \sim 1/r^m$, on the infinite sphere so

$$\text{Real } P = \lim_{r \rightarrow \infty} - \int_0^{2\pi} \int_0^\pi \frac{1}{r^{n+m-2}} \sin \theta \, d\theta \, d\varphi \quad (11-32)$$

$$\rightarrow 0 \quad \text{unless} \quad n+m-2 = 0$$

Thus n and m equal 1 and higher order values yield no radiated power. Higher powers of n and m describe the energy stored in the reactive inductive and capacitive fields.

11-3. TE and TM Radiated Power

The energy radiated in TE and TM fields is now formulated in terms of the field components which are transverse into the planar surfaces of the system. The radiated TE power takes the form

$$\begin{aligned} P^{TE} &= - \iint_{S_\infty} (\vec{E} \times \vec{H}^*) \cdot \hat{n} \, ds \\ &= -Y \int_0^{2\pi} \int_0^\pi |E_\theta(\theta, \varphi)|^2 \sin \theta \, d\theta \, d\varphi \end{aligned} \quad (11-33)$$

The TM radiated power is expressed in the same manner and takes the form

$$P^{TM} = -Z \int_0^{2\pi} \int_0^\pi |H_\theta(\theta, \varphi)|^2 \sin \theta \, d\theta \, d\varphi \quad (11-34)$$

11-4. TE and TM Power Radiated in A Whole-Space by a HED

The power radiated by a HED is readily expressed by

combining the results of 11-3 and section 10. The E_φ TE electric field has the form

$$E_\varphi = -\sin\varphi \int_0^\infty \frac{j\Delta}{T_0} e^{jT_0(z-H)} J_0(\Delta\rho) d\Delta$$

$$= -\sin\varphi \frac{e^{jkR}}{R} \quad R = ((z-H)^2 + \rho^2)^{1/2}$$
(11-35)

Thus

$$E_\varphi(\theta, \varphi) = -\sin\varphi$$
(11-36)

and

$$P^{TE} = -Y \int_0^{2\pi} \int_0^\pi \sin^2\varphi \sin\theta \, d\theta d\varphi$$

$$= -2\pi Y$$
(11-37)

The true power in watts must be obtained by multiplying the above P^{TE} for the normalized fields by the scaling factors for the E and H fields of Table 10-1. For the following discussions, only the relative power is of interest.

The TM power is determined from the H_φ TM field

$$H_\varphi = \cos\varphi \int_0^\infty \Delta \operatorname{sign}(z-H) e^{jT_0|z-H|} J_0(\Delta\rho) d\Delta$$

$$= -j \cos\varphi \cos\theta \frac{e^{jkR}}{R}$$
(11-38)

and therefore

$$H_\varphi(\theta, \varphi) = -j \cos\varphi \cos\theta$$
(11-39)

The TM power is then expressed by

$$P^{TM} = -Z \int_0^\pi \cos^2 \theta \sin \theta d\theta \int_0^{2\pi} \cos^2 \phi d\phi \quad (11-40)$$

$$= -\frac{2\pi}{3} Z$$

As for the TE power, the true power 11-40 is obtained by multiplication by the normalizing factor for the fields. The true total power radiated by the HED is then

$$P = \frac{P^{TE}}{k_0^2} \frac{\omega^2 \mu_0 I^2 d^2 k_0^2}{(4\pi)^2} + \frac{P^{TM}}{k_0^2} \frac{I^2 d^2 k_0^4}{(4\pi)^2} \quad (11-41)$$

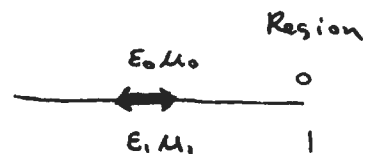
The addition $1/k_0^2$ factors appear since the normalized fields are given as $1/R$ while the integrals 11-33 and 11-34 are based on the use of $1/r$ hence a difference of $1/k_0^2$ in the magnitude. Regrouping 11-41 yields

$$P = -\frac{Z I^2 d^2 k_0^2}{8\pi} \left(\frac{K_e}{K_m} + \frac{1}{3} \right) \text{ watts} \quad (11-42)$$

where $K_e = \epsilon/\epsilon_0$ and $K_m = \mu/\mu_0$.

11-5. Radiation Patterns for a HED on the Surface of a Half-Space

The radiation patterns for a HED on the surface of a halfspace are obtained from H^{TM} and E^{TE} by finding the angular dependence of the $1/r$ term fields. The general picture is sketched at the right. The radiation pattern



in region 0 will be derived. The pattern in region 1 is obtained by the fact the solution is the same as for region 0 with material properties interchanged $\epsilon_0 \rightarrow \epsilon_1$, $\epsilon_1 \rightarrow \epsilon_0$ etc.

From Table 10-4

$$E_{\phi} = -\sin\psi \int_0^{\infty} j \frac{\Lambda}{\pi_0} (1 + R_{01}^{TE}) e^{j\pi_0 z} J_0(\Lambda \rho) d\Lambda \quad (11-43)$$

$$H_{\phi} = \cos\psi \int_0^{\infty} \Lambda (1 - R_{01}^{TM}) e^{j\pi_0 z} J_0(\Lambda \rho) d\Lambda \quad (11-44)$$

The exact analytical evaluation of these Hankel transforms is not possible. For the analysis of the radiation patterns, however, an exact form for the integral can be obtained by obtaining an asymptotic expansion for the fields. This requires that P and Z be large. This is a compatible condition since analysis of radiation patterns and power radiated is carried out at "infinite" distances from the source.

The first step in reducing 11-43 and -44 is to note that

$$1 + R_{01}^{TE} = T_{01}^{TE} \quad (11-45)$$

$$1 - R_{01}^{TM} = T_{10}^{TM} \quad (11-46)$$

Next the integral from 0 to ∞ is transformed into an integral from $-\infty$ to ∞ . This can be done for all order Hankel transforms with the aid of the identities in Table 11-1. Thus

$$E_{\phi} = -\frac{\sin\psi}{2} \int_{-\infty}^{\infty} j \frac{\Lambda}{\pi_0} T_{01}^{TE} e^{j\pi_0 z} H_0^1(\Lambda \rho) d\Lambda \quad (11-47)$$

$$H_0 = \frac{\cos \varphi}{2} \int_{-\infty}^{\infty} \Delta T_{10}^{TM} e^{j\tau_0 z} H_0'(\Delta \rho) d\Delta \quad (11-48)$$

To this point, no approximations have been made.

At this point the contour of integration will be changed and the asymptotic form of the Hankel function introduced.

Thus

$$E_0 = -\frac{\sin \varphi}{2} \int_{-\infty}^{\infty} j \frac{\Delta}{\tau_0} T_{01}^{TE} e^{j(\tau_0 z + \Delta \rho)} e^{-j\pi/4} \sqrt{\frac{z}{\pi \Delta \rho}} d\Delta \quad (11-49)$$

$$H_0 = \frac{\cos \varphi}{2} \int_{-\infty}^{\infty} \Delta T_{10}^{TM} e^{j(\tau_0 z + \Delta \rho)} e^{-j\pi/4} \sqrt{\frac{z}{\pi \Delta \rho}} d\Delta \quad (11-50)$$

Examination of 11-50 and -51 are in the form which admits evaluation in terms of an asymptotic series by the saddle point method. The contour C is the saddle point contour in the complex Δ . In changing the integration path from along the real axis to C, the effect of any singularities lying between the real axis and C must be considered. Fortunately, the integrands in 11-49 and -50 have only branch point singularities but no poles. The effect of the branch point singularities is the generation of second order effects. These effects will be discussed later. For radiation patterns, the branch points may be safely ignored. The rationale for this will be seen in a moment.

The exponential in the integrand

$$e^{j(\Gamma_0 z + \Delta \rho)} \quad (11-51)$$

and the definition of the saddle point and saddle point contour are dealt with in detail in Appendix 1. Transforming from the Δ plane to the μ plane 11-49 and -50 take the form

$$E_{\psi} = -\frac{\sin \psi}{2} \sqrt{\frac{2}{\pi \rho}} e^{j(R-\pi/4)} \int_{-\infty}^{\infty} F_1(u) e^{-u^2} du \quad (11-52)$$

$$H_{\psi} = \frac{\cos \psi}{2} \sqrt{\frac{2}{\pi \rho}} e^{j(R-\pi/4)} \int_{-\infty}^{\infty} F_2(u) e^{-u^2} du \quad (11-53)$$

where

$$F_1(u) = j \frac{\Delta^{1/2}(u)}{\Gamma_0(u)} T_{01}^{TE}(u) \frac{d\Delta}{du} \quad (11-54)$$

and

$$F_2(u) = j \frac{\Delta^{1/2}(u)}{\Gamma_0(u)} T_{10}^{TM}(u) \frac{d\Delta}{du} \quad (11-55)$$

Now in the vicinity of Δ_p , the saddle point of the exponent,

$$\Delta \approx \Delta_p + C\mu \quad (11-56)$$

where $C \propto 1/R$. In the limit as $R \rightarrow \infty$, $\Delta \rightarrow \Delta_p$. Since the integrands of 11-52 and -53 are exponential integrals, an asymptotic series can be developed by expanding F_1 and F_2 in Taylor series. For present purposes, only the 0 order term of the series will be retained and

$$\begin{aligned} F_1(u) &\approx j \frac{\Delta^{1/2}(0)}{\Gamma_0(0)} T_{01}^{TE}(\Delta(0)) \frac{d\Delta}{du} \Big|_0 \\ &= j \frac{\Delta_p^{1/2}}{\Gamma_0(\Delta_p)} T_{01}^{TE}(\Delta_p) C \end{aligned} \quad (11-57)$$

and

$$\int_{-\infty}^{\infty} F_1(u) e^{-u^2} du \approx F_1(0) \int_{-\infty}^{\infty} e^{-u^2} du \quad (11-58)$$

$$= \sqrt{\pi} F_1(0)$$

If higher order terms in the asymptotic expansion of F_1 were required then terms of $\frac{d^{2n}F}{d\mu^{2n}}$ in the Taylor series would be required. It is not difficult to show that terms of $\frac{d^{2n}F}{d\mu^{2n}}$ will contain factors of c^{2n} since

$$\frac{d^2 F}{d u^2} = c^2 \left. \frac{d^2 F}{d \Delta^2} \right|_{\lambda = \lambda_0} \quad (11-59)$$

since $\frac{d^2 \Delta}{d u^2} \approx 0$. In the limit as $R \rightarrow \infty$, all these relations become exact and the asymptotic series is in powers $(1/R)^n$. At the branch points of F , the function derivation become singular. Since this only affects terms in \mathcal{E} and \mathcal{H} of higher order than $1/R$, the branch point effects may be safely ignored in radiation pattern analysis.

Putting all the pieces together one obtains

$$\mathcal{E}_\varphi \approx -\sin\varphi T_{01}^{TE} \left(\frac{P}{R}\right) \frac{e^{jR}}{R} \quad (11-60)$$

$$\mathcal{H}_\varphi \approx -j \cos\varphi \cos\theta T_{10}^{TM} \left(\frac{P}{R}\right) \frac{e^{jR}}{R} \quad (11-61)$$

Thus the radiation pattern is just that of the whole-space

modified by a Fresnel transmission coefficient. The radiation patterns for a dielectric half-space with dielectric constant K_e take the form

$z > 0$

$$|E_\psi(\theta, \psi)|^2 = \sin^2 \psi \left(\frac{2\alpha}{\alpha + n \left(\left(1 - \frac{1}{n^2}\right) + \frac{\alpha^2}{n^2} \right)^{1/2}} \right)^2 \quad (11-62)$$

$$|H_\psi(\theta, \psi)|^2 = \cos^2 \psi \left(\frac{2 \left(\left(1 - \frac{1}{n^2}\right) + \frac{\alpha^2}{n^2} \right)^{1/2}}{\left(\left(1 - \frac{1}{n^2}\right) + \frac{\alpha^2}{n^2} \right)^{1/2} + n\alpha} \right)^2 \quad (11-63)$$

$z < 0$

$$|E_\psi(\theta, \psi)|^2 = \frac{\sin^2 \psi}{n} \left(\frac{2\alpha}{\alpha + \frac{1}{n} \left((1-n^2) + n^2 \alpha^2 \right)^{1/2}} \right)^2 \quad (11-64)$$

$$|H_\psi(\theta, \psi)|^2 = \frac{\cos^2 \psi}{n} \left(\frac{2 \left((1-n^2) + n^2 \alpha^2 \right)^{1/2}}{\left((1-n^2) + n^2 \alpha^2 \right)^{1/2} + \frac{\alpha}{n}} \right)^2 \quad (11-65)$$

$$\alpha = \cos \theta \quad n = \sqrt{K_1} \quad \text{- refractive index of the earth.}$$

The resulting radiation patterns are plotted in Fig. 11-1, through 12 for various values of dielectric constant for the halfspace.

The particular feature to note is the strong directionality of the TE pattern into the earth. This peak in the pattern occurs in the direction of the critical angle of the air-earth interface.

$$\theta_c = \sin^{-1} \frac{1}{n}$$

The TM pattern exhibits a null in the θ_c direction but shows

Table 11 - 1

Useful Bessel & Hankel Function Identities & Properties

$$J_n(z) = \frac{1}{2} (H_n^1(z) + H_n^2(z))$$

$$H_n^2(z) = -e^{jn\pi} H_n^1(z)$$

$$C_n'(z) = C_{n-1}(z) - \frac{n}{z} C_n(z)$$

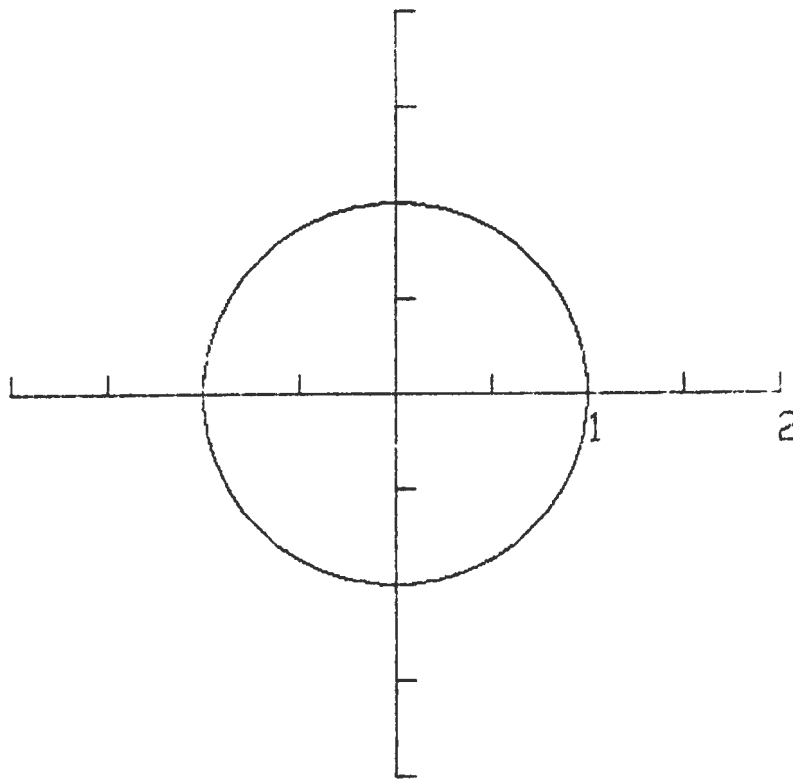
Asymptotic Forms

$$J_n(z) \approx \sqrt{\frac{2}{\pi z}} \cos\left(z - \frac{n\pi}{2} - \frac{\pi}{4}\right)$$

$$H_n^1(z) \approx \sqrt{\frac{2}{\pi z}} e^{j\left(z - \frac{n\pi}{2} - \frac{\pi}{4}\right)}$$

TE

$K = 1.0EO$



TM

$K = 1.0EO$

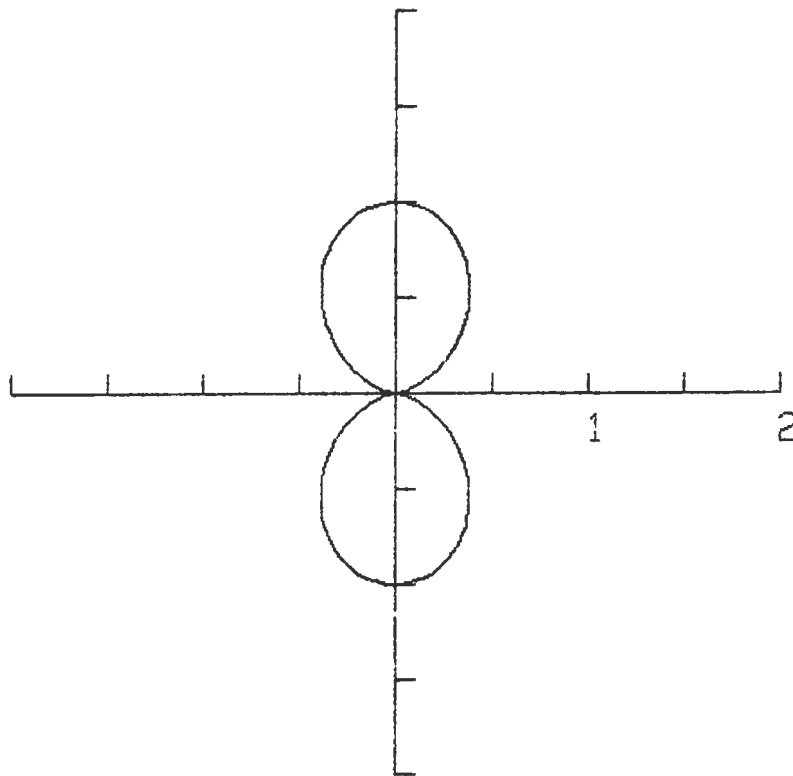


Fig 11-1

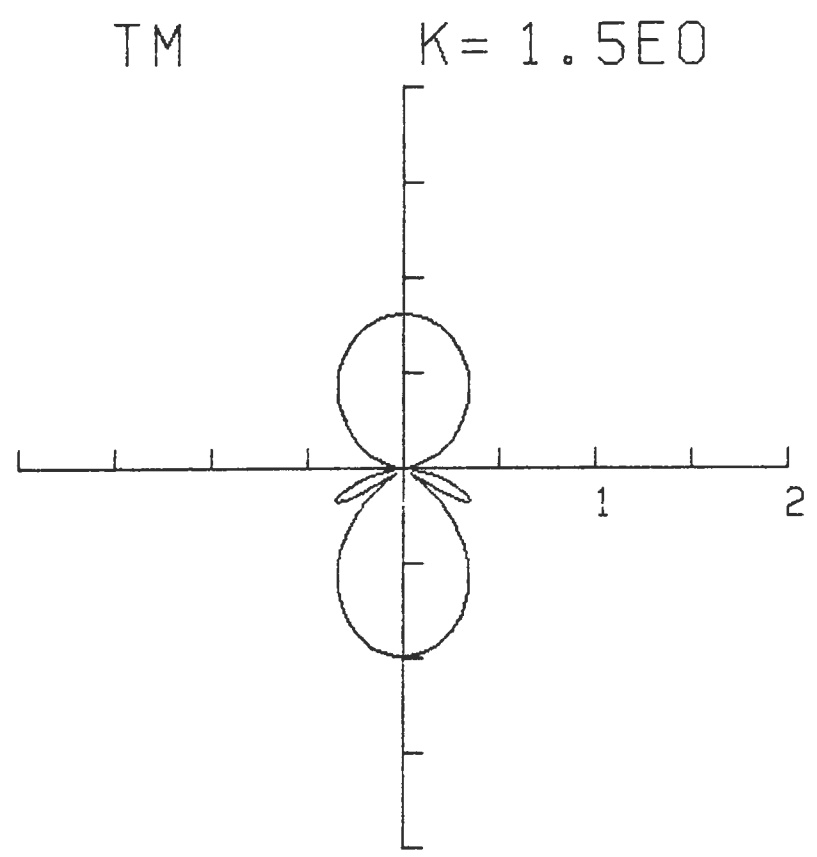
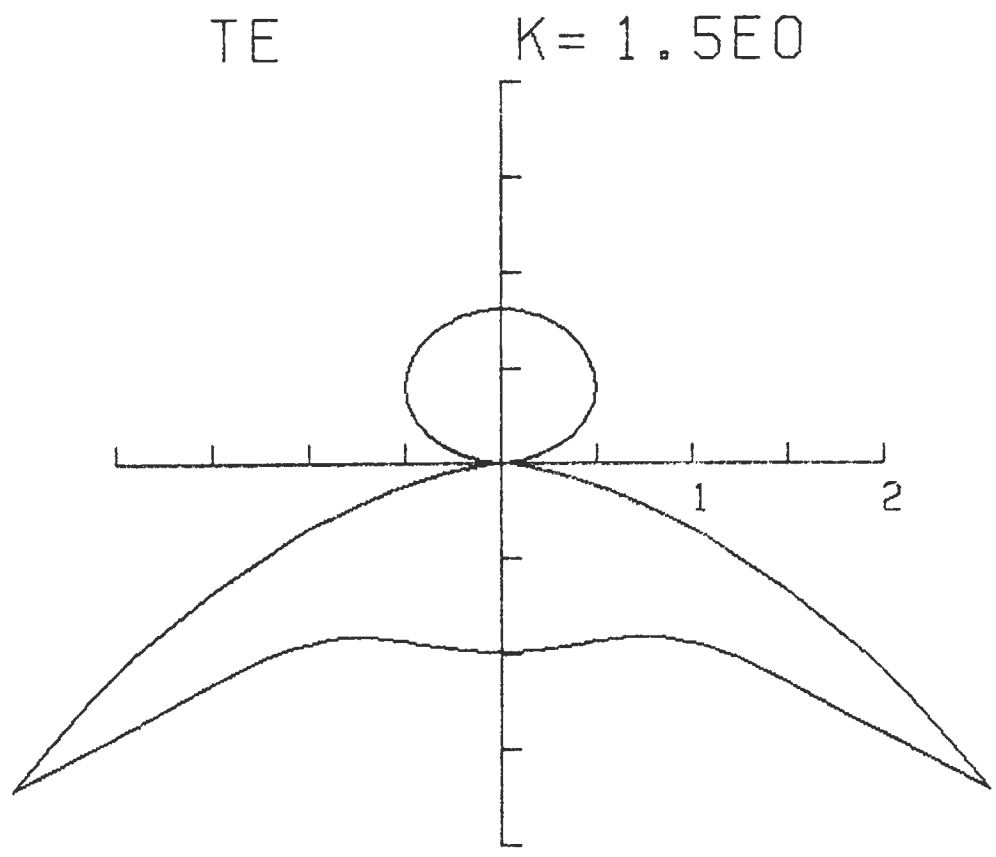


Fig. 11-2

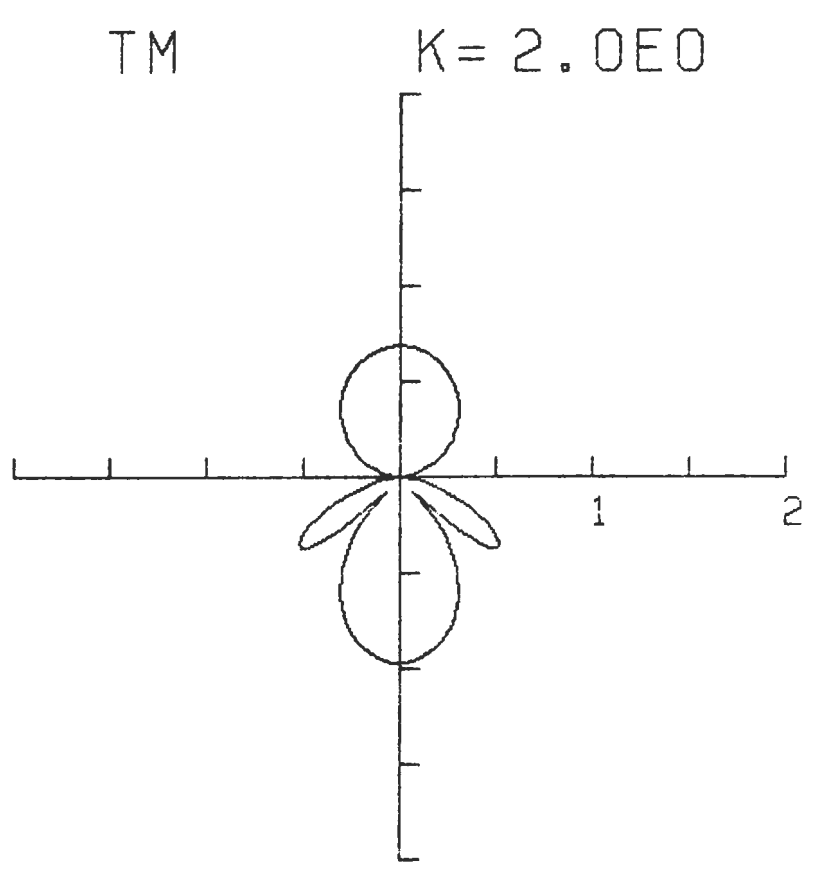
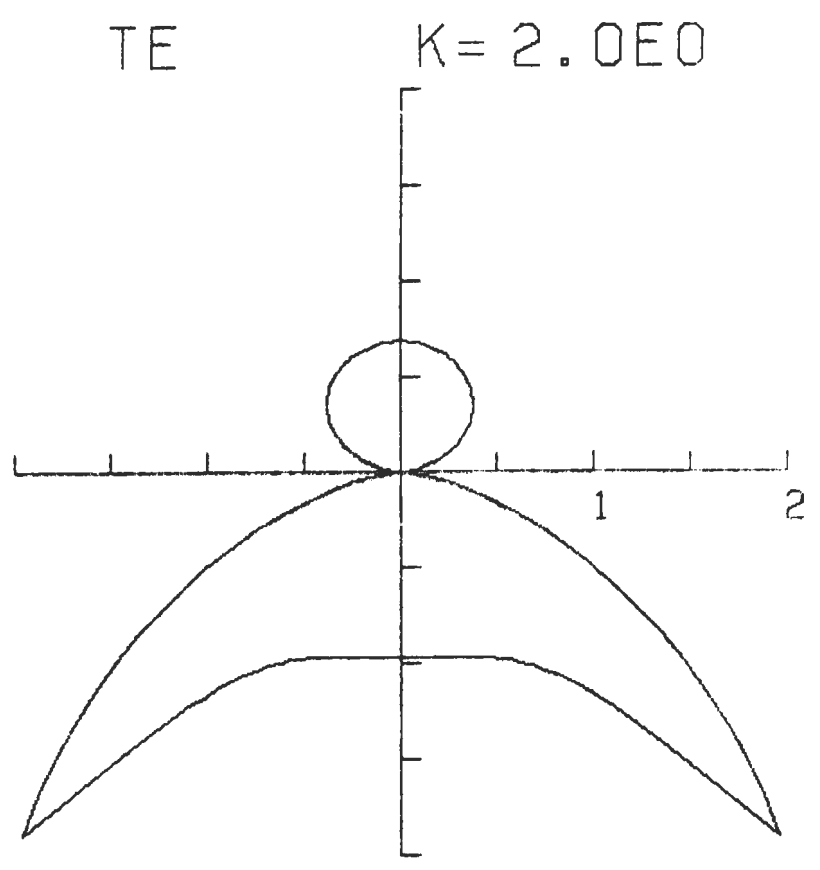
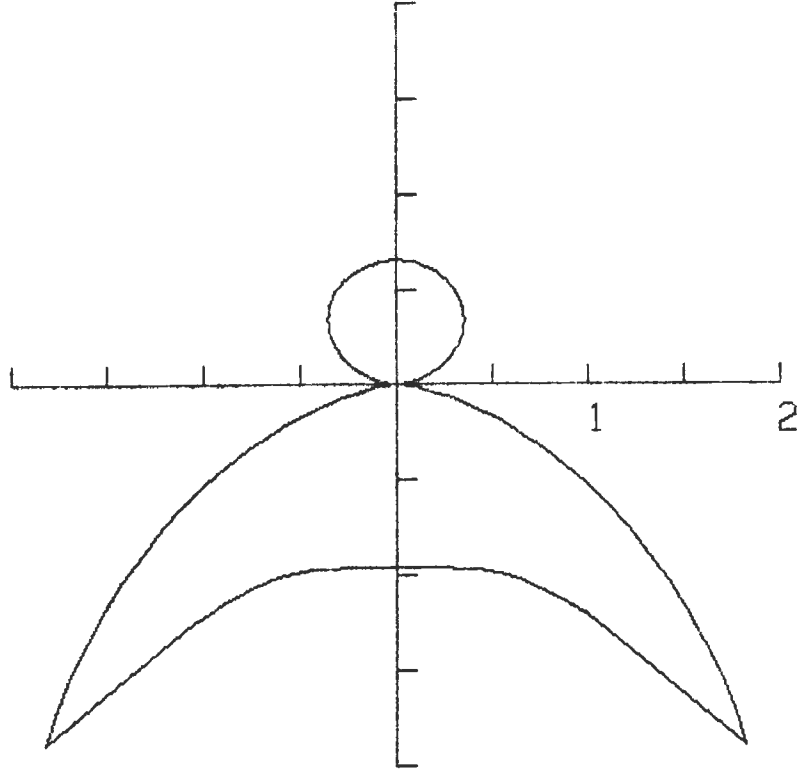


FIG. 11-3

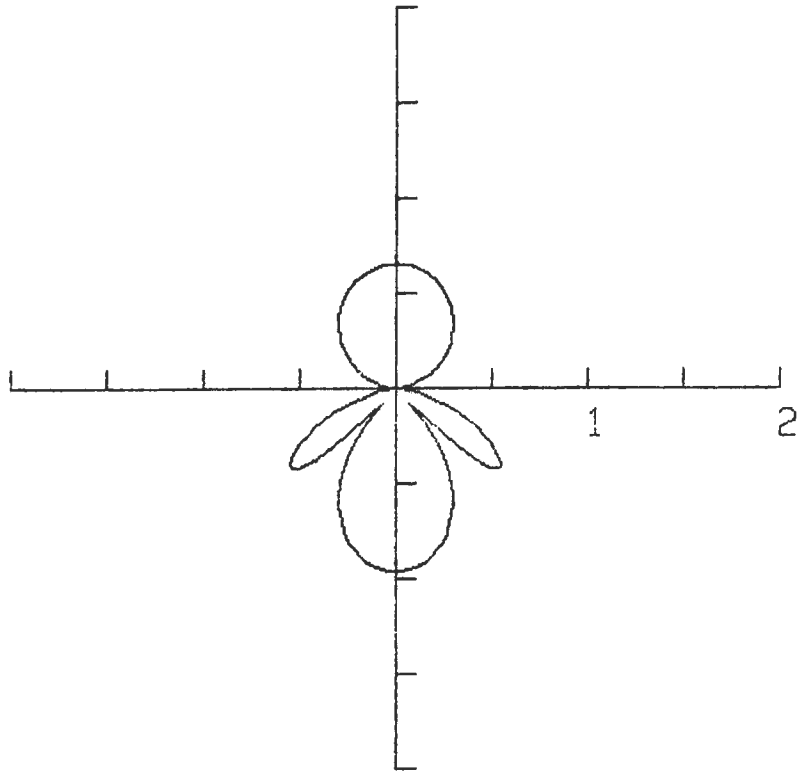
TE

$K = 2.2E0$



TM

$K = 2.2E0$



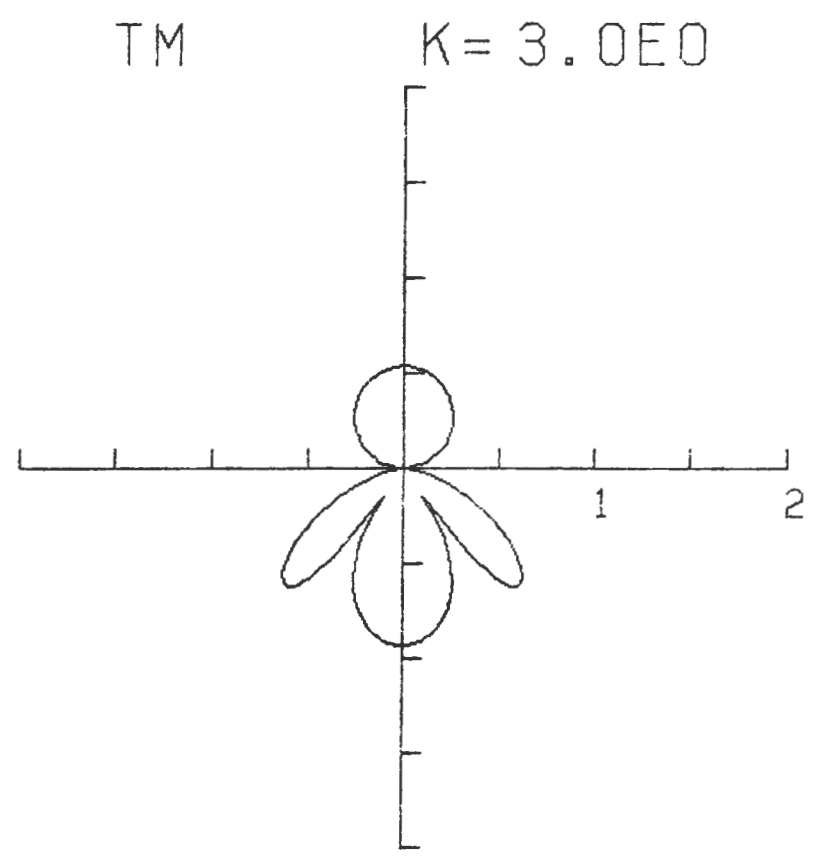
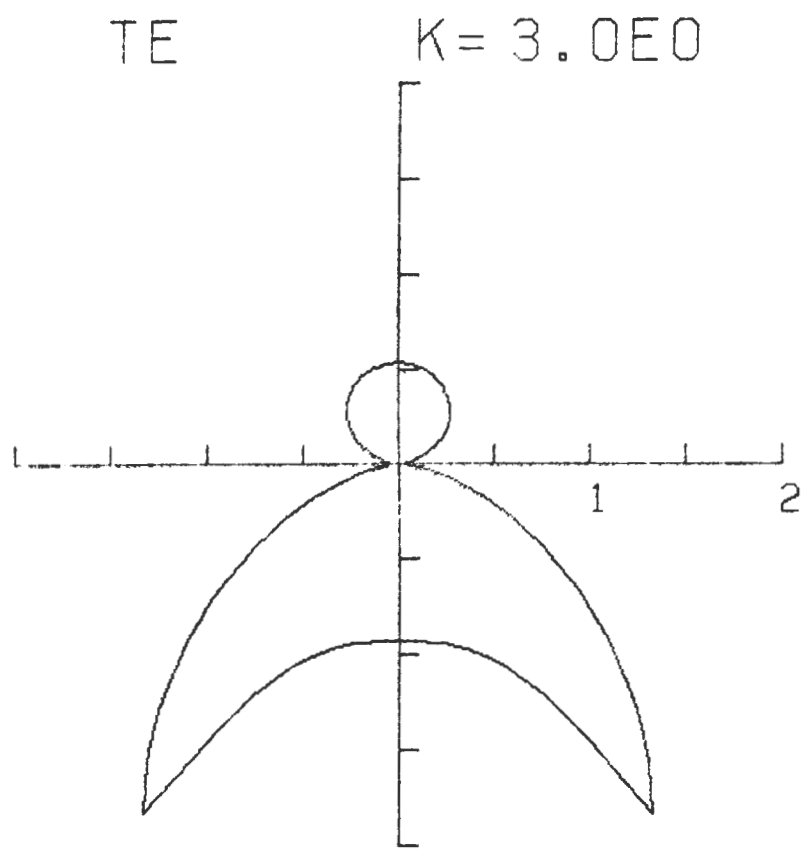
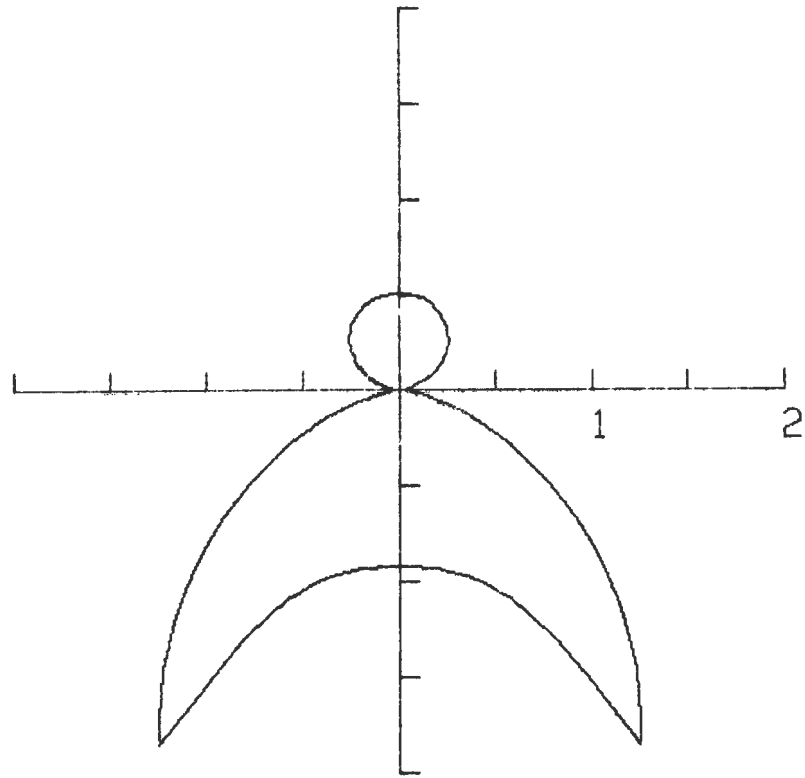


Fig. 11-5

TE

$K = 3.2E0$



TM

$K = 3.2E0$

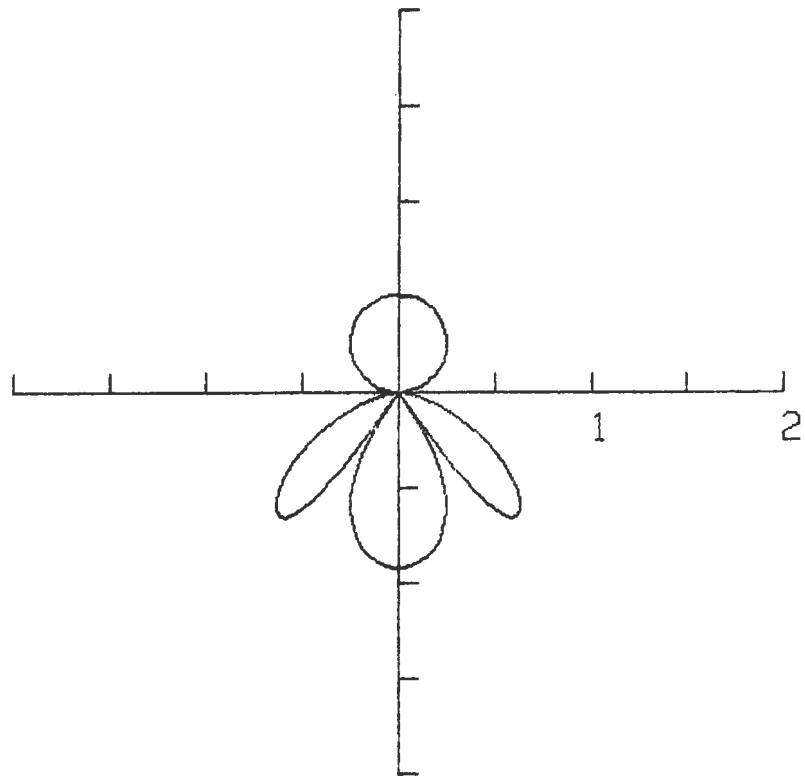
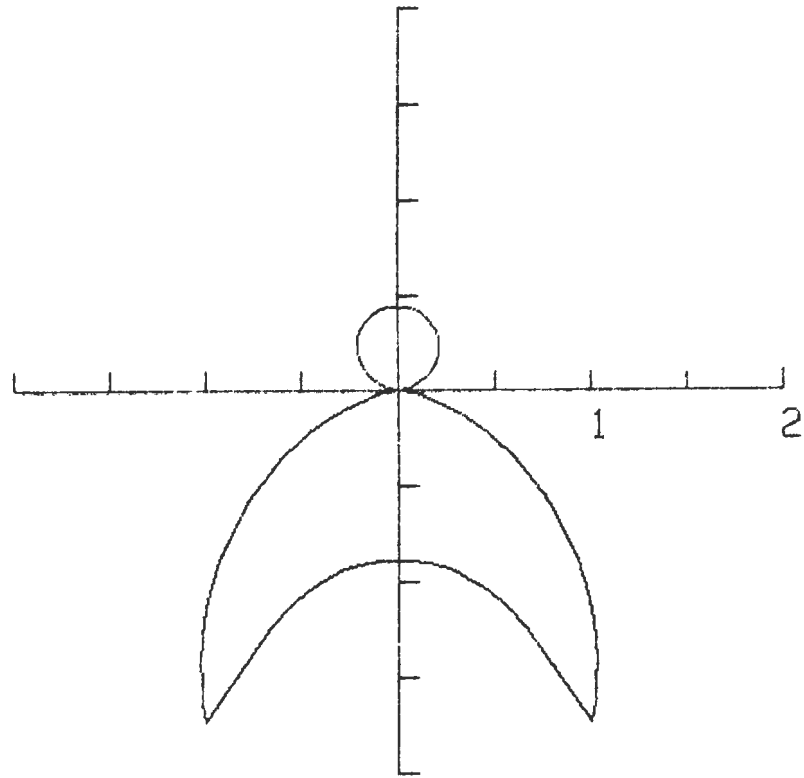


Fig. 11-6

TE

$K = 4.0E0$



TM

$K = 4.0E0$

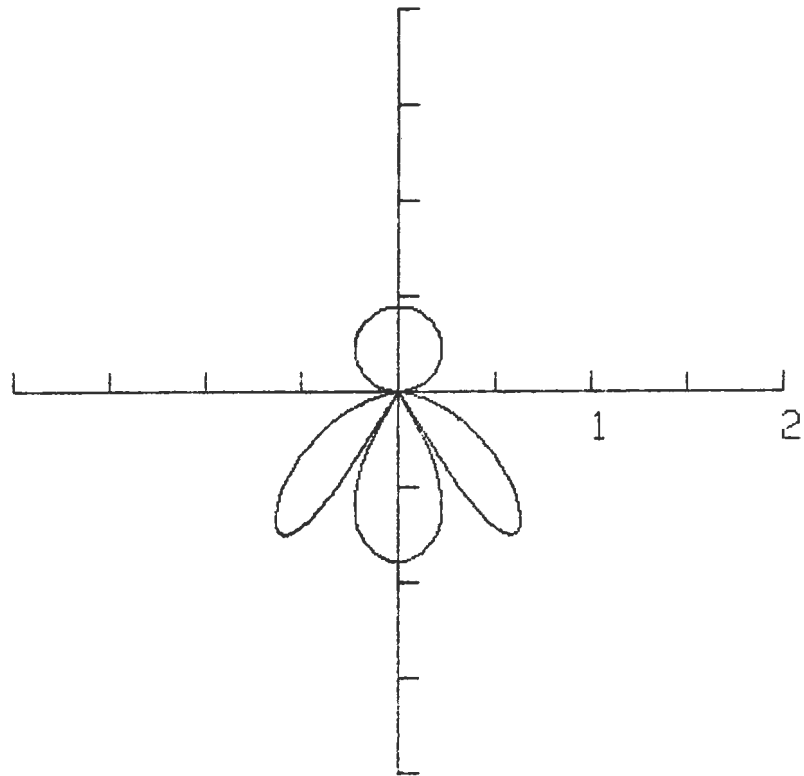
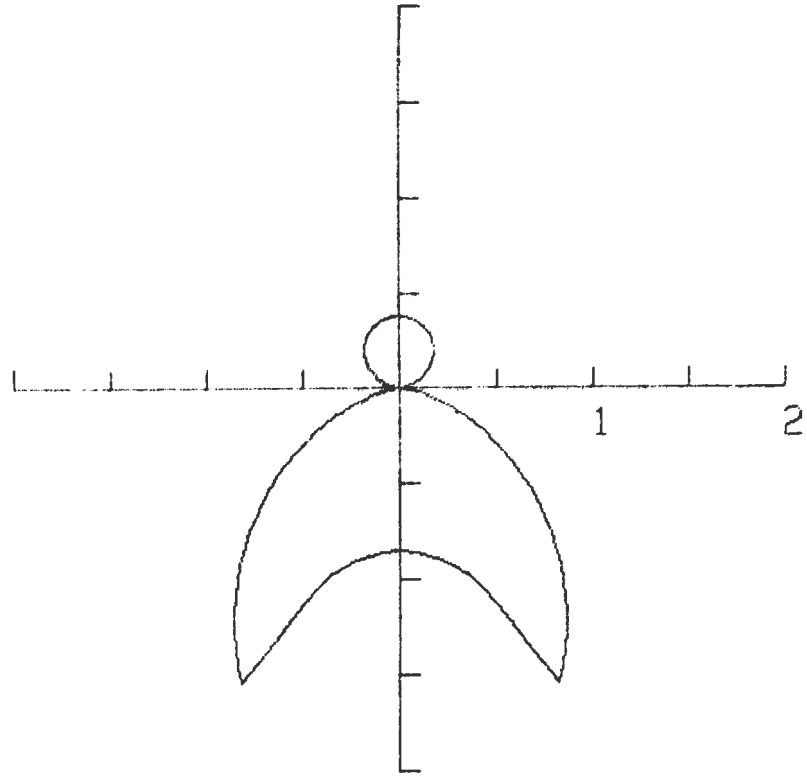


Fig. 11-7

TE

$K = 5.0E0$



TM

$K = 5.0E0$

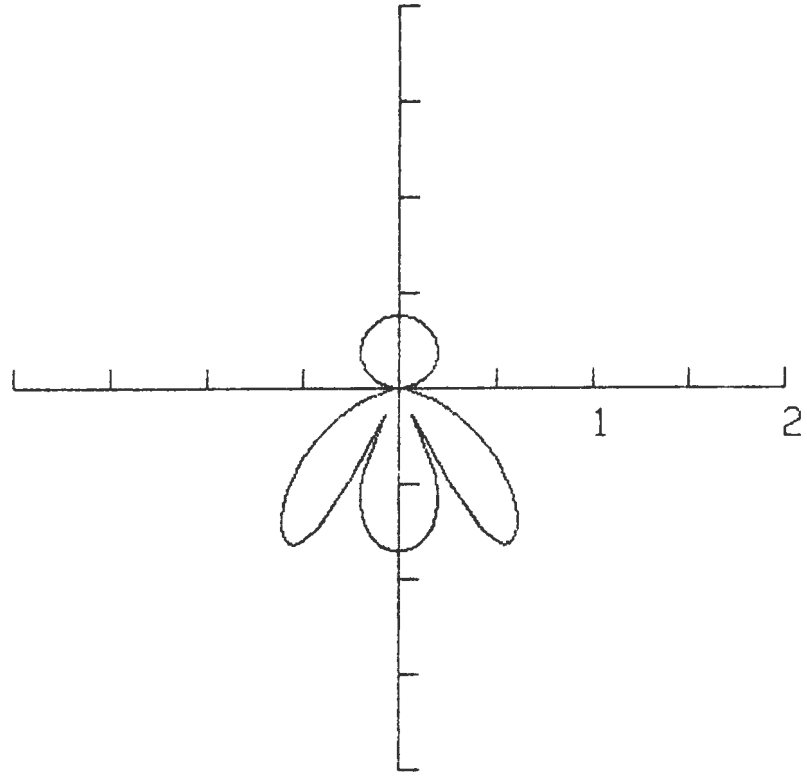


Fig. 11-8

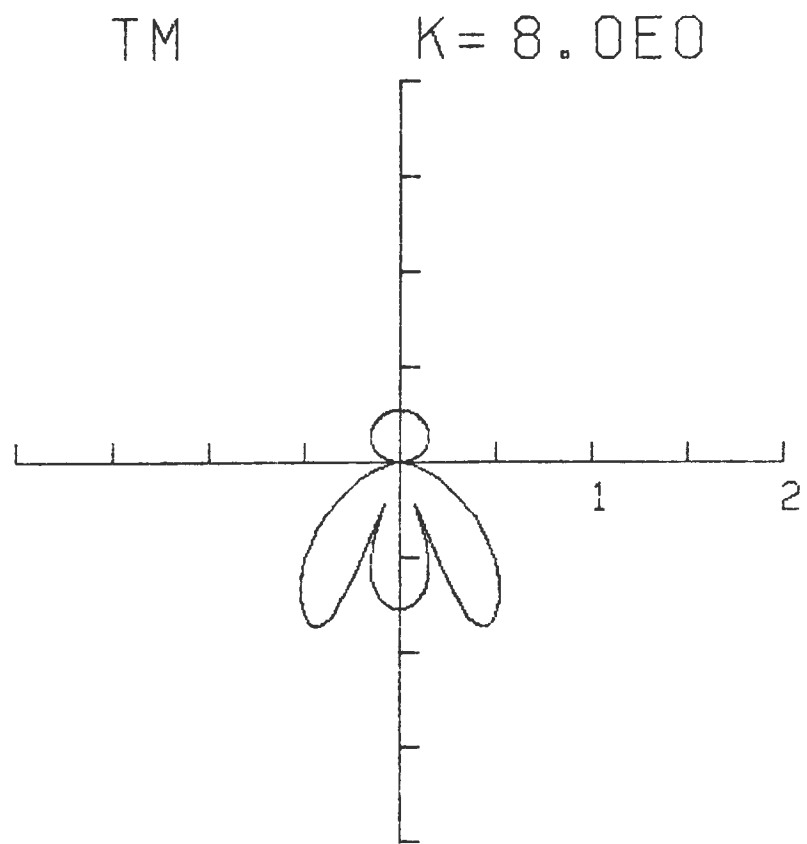
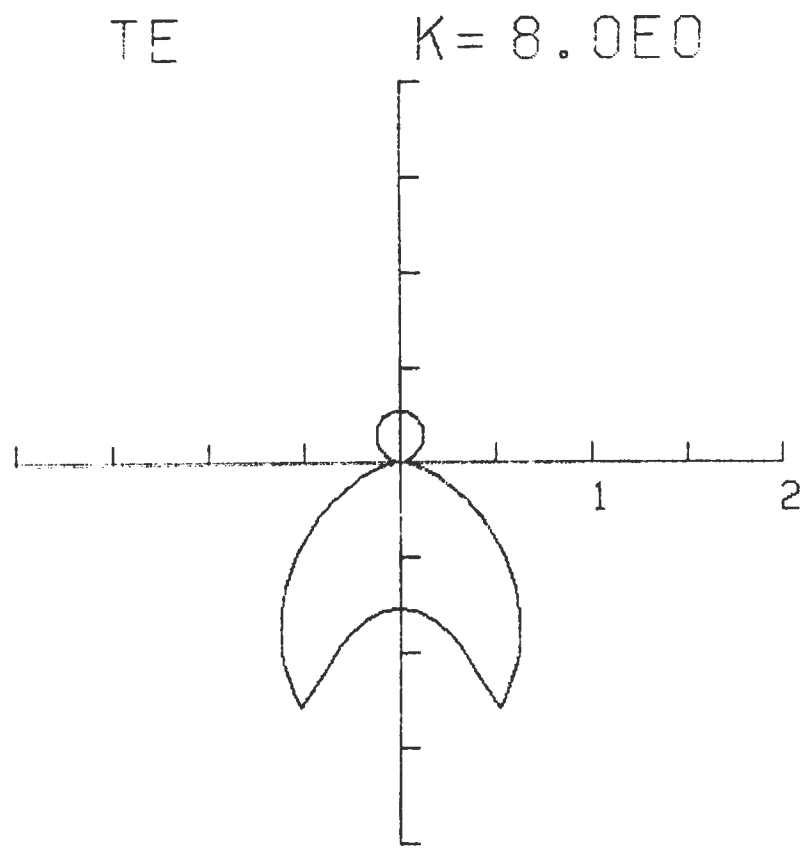
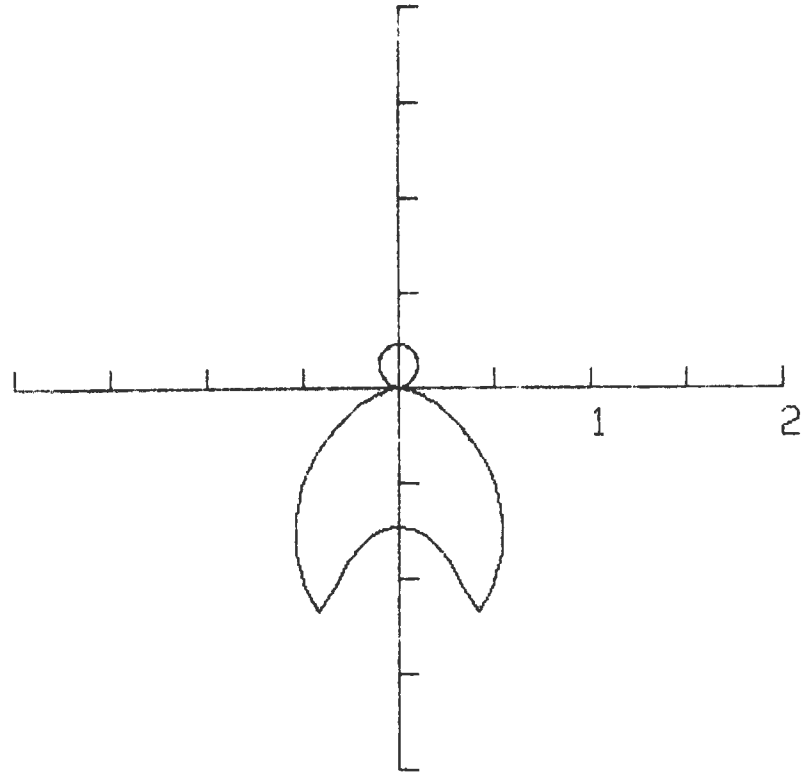


Fig. 11-9

TE

$K = 10.0E0$



TM

$K = 10.0E0$

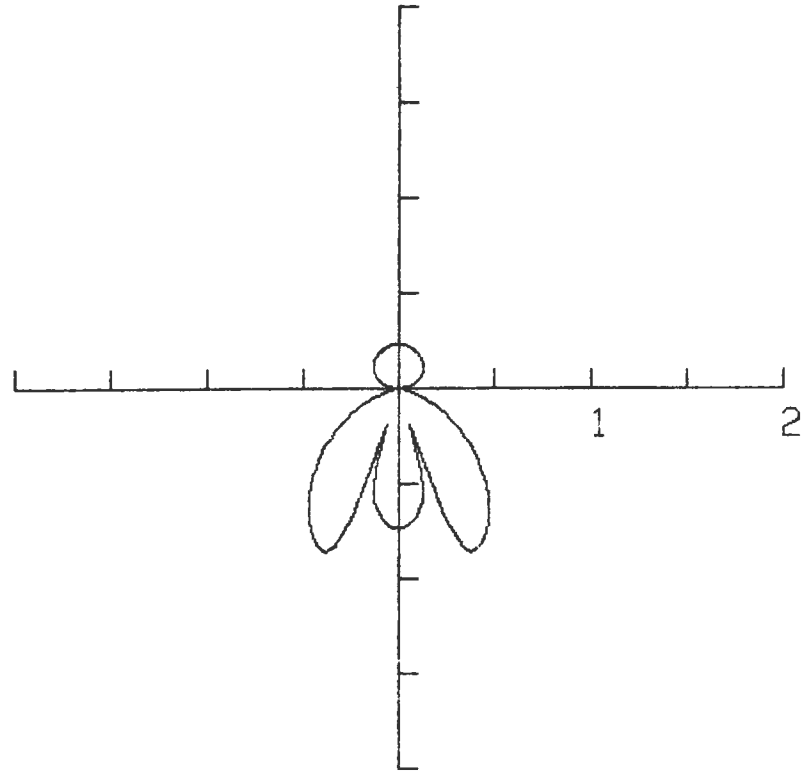
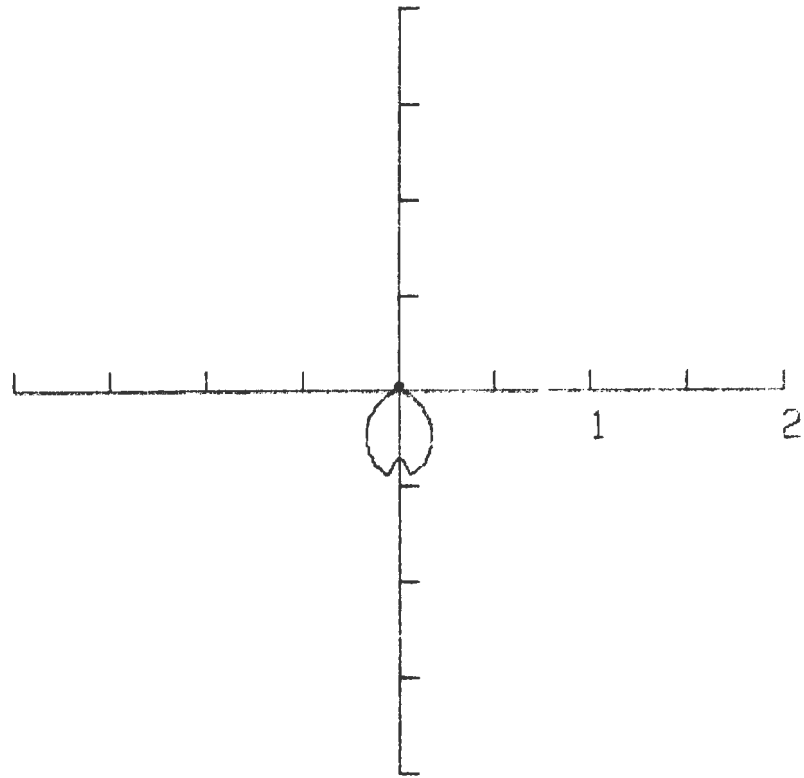


Fig. 11-10

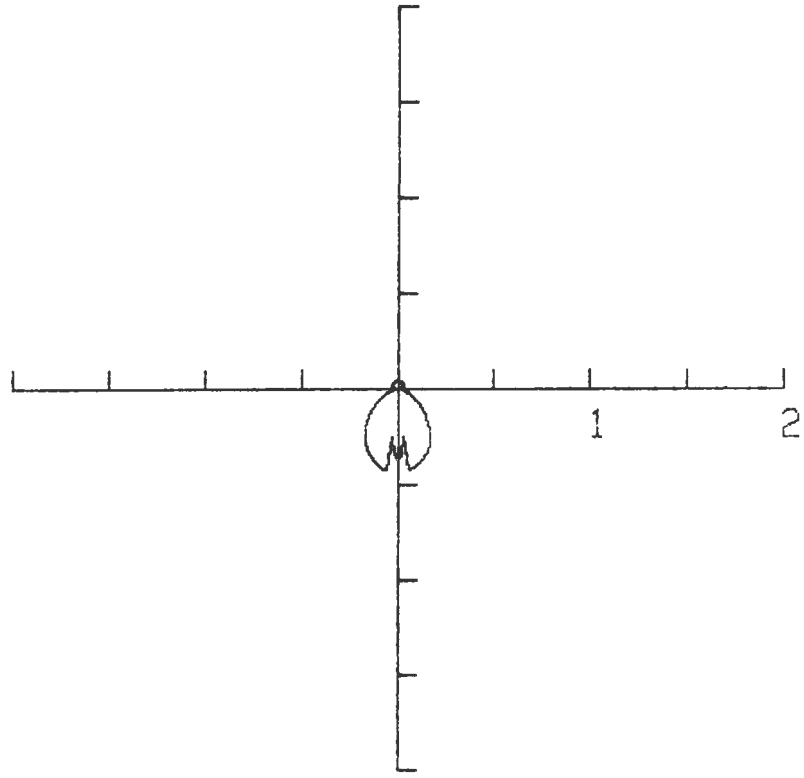
TE

$K = 8.1E1$



TM

$K = 8.1E1$



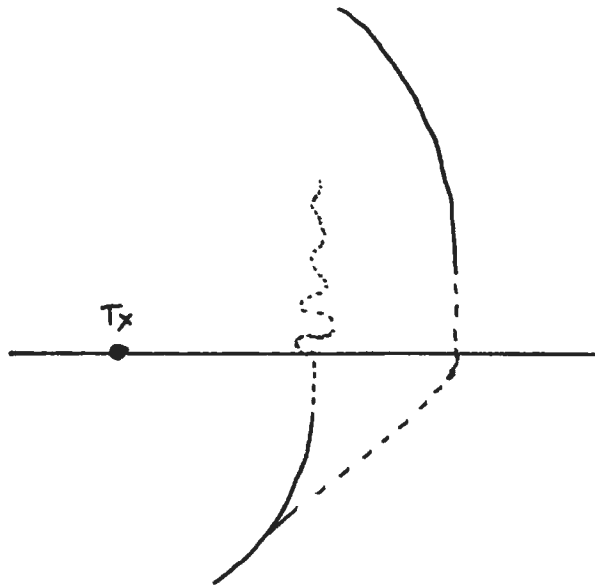
a lobe of increasing strength at angles of $\theta > \theta_c$
for increasing K_e .

12. Surface Fields about a HED on the Surface of a Half-space

In the previous section the radiation patterns for the HED on the surface of a half-space were developed. Examination of the pattern in the plane of the interface shows that both the TE and TM patterns have a null in this direction. The fields in this direction must^{be} of second order at large distances from the source.

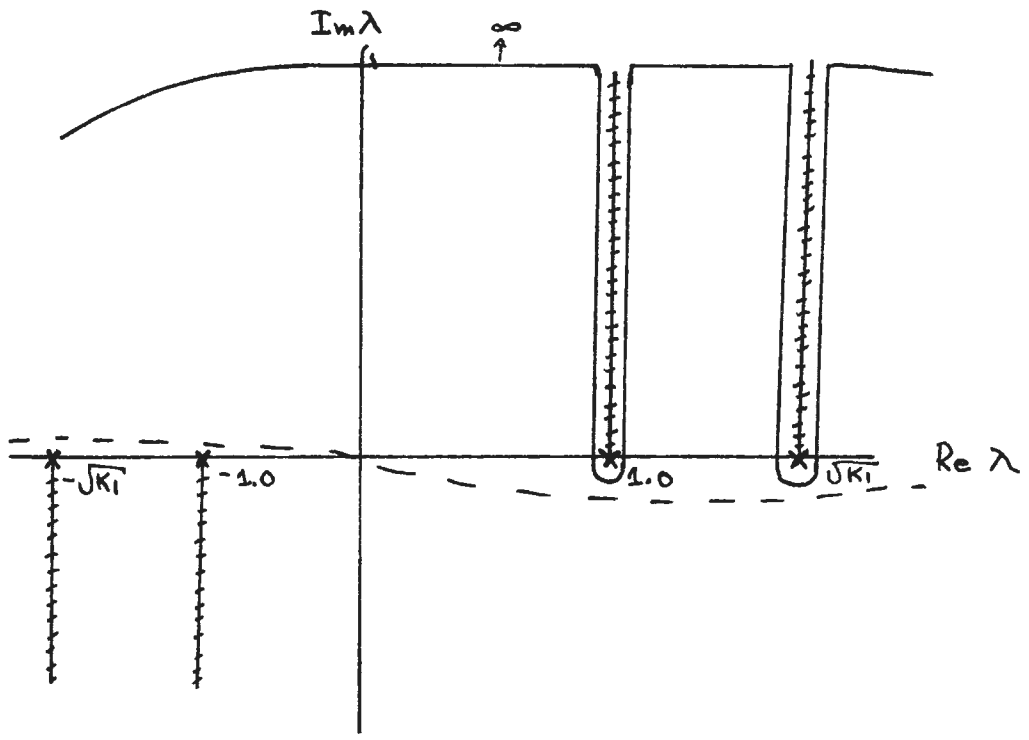
In the SEP experiments, the fields about a HED are measured on the earth or lunar surface. It is therefore instructive and useful to^{develop} expressions for the fields near the interface. For these applications distances of 1 to 20 wavelengths from the source are most interesting and use asymptotic expansions to estimate the second order fields is feasible. The general nature of the fields is discussed by Annan (1973) and is sketched in Figure 12-1. Near the interface the fields are composed of two parts, one which propagates outward with the phase velocity of the air and one which has the phase velocity of the earth.

In this section the asymptotic expressions for these second order fields are developed for the case of a half-space with free space magnetic properties, but arbitrary



— Radiation or $1/R$ fields
----- Second order or $1/R^2$ fields

Fig. 12-1



- Branch-cut
- x Branch point
- - - - Original Hankel transform path
- Saddle point contour

Fig. 12-2

dielectric constant and loss tangent. The expansions are obtained by analysis of the limiting case of the saddlepoint expansion of the last section in the limit as $Z/P \rightarrow 0$. This limiting case of the saddlepoint curve is sketched in Fig. 12-2 and is essentially two integrals about the branchlines from the branch points at the right of the imaginary Λ axis. The branch point at $\Lambda = 1$ and the saddlepoint merge as $Z/P \rightarrow 0$.

As an example of how the solutions are developed, the TE H_z component will be analysed in detail. The other solutions are developed in like manner and the results will be tabulated. For the development Z will be taken to be finite, but such that $(Z)/P \ll 1$. The H_z field is then expressed as

$$H_z = \frac{\sin \varphi}{2} \int_{-\infty}^{\infty} j \frac{\Lambda^2}{P_0} T_{01}^{TE} e^{j P_0(z+h)} \sqrt{\frac{z}{\pi \Lambda P}} e^{j P \Lambda - 3\pi/4} d\Lambda \quad (12-1)$$

Regrouping the integrand and deforming the contour of integration to that of the limiting steepest descent form, 12-1 becomes

$$H_z = \frac{\sin \varphi}{2} \left[\int_{\sqrt{k_0}}^{\sqrt{k_0 + j\infty}} F_0(\Lambda) e^{j \Lambda P} + \int_{\sqrt{k_0}}^{\sqrt{k_0 + j\infty}} F_1(\Lambda) e^{j \Lambda P} d\Lambda \right] \quad (12-2)$$

where

$$\begin{aligned} F_0 &= F_{R_0}(\Lambda) - F_{L_0}(\Lambda) \\ F_1 &= F_{R_1}(\Lambda) - F_{L_1}(\Lambda) \end{aligned} \quad (12-3)$$

where F_{R_i} is the value of the integrand at the right of the branch line and F_{L_i} is the value it takes at the left of the branch line. Defining

$$j p \Lambda = j p - u \quad (k_0 = 1) \quad (12-4)$$

the first integral of 12-2 becomes

$$j \frac{e^{j p}}{p} \int_0^{\infty} F_0 \left(1 + j \frac{u}{p} \right) e^{-u} du \quad (12-5)$$

Similarly letting

$$j \Lambda p = j \sqrt{k_1} p - \beta \quad (12-6)$$

the second term of 12-2 has the form

$$j \frac{e^{j \sqrt{k_1} p}}{p} \int_0^{\infty} F_0 \left(\sqrt{k_1} + j \frac{\beta}{p} \right) e^{-\beta} d\beta \quad (12-7)$$

The basic wave nature of the two branch-cut integrals is now apparent. It only remains to evaluate the wave amplitudes. The steepest descent technique is now applied to obtain the asymptotic series expansion of the integrals in p^{-1} and the first non-zero term in the expansions yields ^{the} amplitudes required here. Higher order terms may be retained; however, their contributions are not significant for SEP applications.

To obtain the asymptotic expansion, p is assumed $\gg 1$ and non-exponent part of the integrand is expanded in ^a Taylor

series about μ and $\beta \equiv 0$. In the vicinity of the branch points, F_1 and F_2 take the form

$$u^c g(u) \approx u^c \left(g(0) + g'(0)u + \frac{g''(0)}{2}u^2 - \dots \right) \quad (12-8)$$

where the function g is expanded into a Taylor series about $\mu = 0$. Thus the integrals in 12-2 take the form

$$\begin{aligned} \Gamma &= \int_0^{\infty} u^c g(u) e^{-u} du \\ &= \sum_{n=0}^{\infty} \frac{1}{n!} g^n(0) \Gamma(n+c+1) \end{aligned} \quad (12-9)$$

where $\Gamma(x)$ is the gamma function. For the present purposes only the first non-vanishing term is retained in order to obtain the second order fields. In order to obtain the amplitudes of $g^n(0)$, it is necessary to examine the behaviour F_0 and F_1 near $\Lambda = 1$ and $\Lambda = \sqrt{K_1}$, respectively.

$$F_0 = j \Lambda^2 \left\{ \frac{T_{01}^{TE-}}{\Gamma_0^-} - \frac{T_{01}^{TE+}}{\Gamma_0^+} \right\} \sqrt{\frac{z}{\pi \Delta \rho}} e^{-j 3\pi/4} \quad (12-10)$$

The \pm superscripts denote the (left / right) side value of the radical near branch line

$$\Gamma_0^- = -\Gamma_0^+ \quad (12-11)$$

Since

$$T_{01}^{TE} = \frac{2\Gamma_0}{\Gamma_0 + \Gamma_1} \quad (12-12)$$

12-10 becomes

$$F_0 = 4j \Lambda^{3/2} \frac{\pi_0^+}{\pi_1^2 - \pi_0^2} \sqrt{\frac{z}{\pi p}} e^{-j\pi/4} \quad (12-13)$$

and the first term of 12-8 is obtained by noting that

$$\begin{aligned} \pi_0^+ &= (1 - (1 + j \frac{u}{p})^2)^{1/2} \\ &\approx (-2j \frac{u}{p})^{1/2} \\ &= \sqrt{\frac{2u}{p}} e^{-j\pi/4} \end{aligned} \quad (12-14)$$

with result

$$g(0) = -\frac{8j}{p\sqrt{\pi}} \frac{1}{(k_1 - 1)} \quad (12-15)$$

and $C = 1/2$

Similarly about $\Lambda = \sqrt{k_1}$, F_1 becomes

$$F_1 = 4j \Lambda^{3/2} \sqrt{\frac{z}{\pi p}} e^{-j\pi/4} \frac{\pi_1}{(\pi_0^2 - \pi_1^2)} e^{j(1 - k_1)^{1/2} z} \quad (12-16)$$

which yields

$$g(0) = \frac{8j k_1}{p\sqrt{\pi}} \frac{e^{-(k_1 - 1)^{1/2} z}}{(k_1 - 1)} \quad (12-17)$$

and $C = 1/2$. Since $T(3/2) = \sqrt{\frac{\pi}{2}}$, the resulting expression for the H field becomes

$$\frac{H}{H_0} = \frac{2 \sin \omega}{(k_1 - 1) p^2} \left\{ e^{jp} - k_1 e^{j\sqrt{k_1} p - (k_1 - 1)^{1/2} z} \right\} \quad (12-18)$$

The approximate forms for the HED on a half-space second order fields are listed in Table 12-1. Before leaving this

section it is important to note some mathematical and intrinsic physical points in the development of the TM response. The applicability of the TM expressions in Table 12-1 is highly dependent on K , not being extremely large.

While the difficulties cannot be dealt with in detail here, the basic mathematical problem stems from the Taylor series expansion 12-8. For the TM reflection coefficient, a pole located on the lower Riemann surface of the reflection coefficient approaches $\Delta = 1$ as $K_1 \rightarrow \infty$. This limits the radius of convergence of the 12-8 Taylor series. This pole may be handled by application of the modified saddle point or steepest descent method (van der Waerden (1950)) in which the effect of the pole is subtracted from the integrand and evaluated separately while the remaining portion of the integrand is evaluated as above. For K_1 in the range of SEP applications ($1 < K_1 \leq 15$). There is no need to go through this extra step. The role of this pole and its effect on evaluation the integrals has been a source of controversy since Sommerfeld's original discussion of the problem in (1909). A good discussion of this problem is given by Banos (1966).

Table 12-1

Asymptotic Form of Second Order Fields about a HED on the
Surface of a Half-space

TE

$$E_y = -\frac{2j \sin \phi}{(\kappa_1 - 1) p^2} \left[e^{jP} - \sqrt{\kappa_1} e^{j\sqrt{\kappa_1} P - (\kappa_1 - 1)^{1/2} z} \right]$$

$$H_z = \frac{-2j \sin \phi}{(\kappa_1 - 1)^{1/2} p^2} \left[e^{jP} + j \sqrt{\kappa_1} e^{j\sqrt{\kappa_1} P - (\kappa_1 - 1)^{1/2} z} \right]$$

$$H_y = \frac{2 \sin \phi}{(\kappa_1 - 1) p^2} \left[e^{jP} - \kappa_1 e^{j\sqrt{\kappa_1} P - (\kappa_1 - 1)^{1/2} z} \right]$$

TM

$$H_y = \frac{-2j \cos \phi}{(\kappa_1 - 1)^{1/2} p^2} \left[\kappa_1 e^{jP} + j \frac{e^{j\sqrt{\kappa_1} P - (\kappa_1 - 1)^{1/2} z}}{\sqrt{\kappa_1}} \right]$$

$$E_x = \frac{2 \cos \phi}{p^2} \left[e^{jP} + \frac{e^{j\sqrt{\kappa_1} P - (\kappa_1 - 1)^{1/2} z}}{\sqrt{\kappa_1}} \right]$$

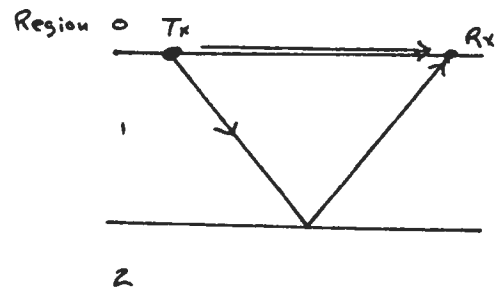
$$E_z = \frac{2 \cos \phi}{(\kappa_1 - 1)^{1/2} p^2} \left[\kappa_1 e^{jP} + j e^{j\sqrt{\kappa_1} P - (\kappa_1 - 1)^{1/2} z} \right]$$

Note: $z/p \ll 1$ & $p \gg 1$

13 HED on the Surface of a 2-Layer Earth

13-1 Introduction

One of the first objectives of the SEP experiment was the detection and delineation of a planar reflector buried at depth in a low-loss dielectric earth. The fields at the surface of the earth should be those generated by energy transmitted parallel to the earth's surface plus energy reflected from the underlying interface. As it turns out, the reflected signal, in many instances, is stronger than the direct one. For some field components, the reflected signals are weak and the direct signal dominates.



There are two techniques for obtaining mathematically useful expressions for the fields in the vicinity of the region 0-region 1 interface. The one technique is known as the geometrical optics solution while the other is the normal mode solution. The two solutions for the fields in region of $(z) \leq 0$ will be developed here. The two techniques are based on the properties of the 2-layer earth reflection coefficient discussed in section 9. In particular, the two types of solutions are contingent on the applicability of

equation 9-8, the geometrical series expansion of the denominator of the reflection coefficient. The effect of magnetic properties will not be considered here and the permeability of each region is taken to be the freespace value.

13-2 Geometrical Optics Solution

Examination of the HED radiation fields in Table 10-4 shows all the TE fields contain the factor $(H \equiv 0)$

$$1 + R^{TE} \tag{13-1}$$

while the TM fields contain the factor

$$1 - R^{TM} \tag{13-2}$$

Upon substitution of the 2-layer earth TE reflection coefficient given by equation 9-6 and the equivalent TM coefficient, equations 13-1 and 2 become

$$\frac{T_{01} (1 + R_{12}^{TE} \beta)}{(1 - R_{10}^{TE} R_{12}^{TE} \beta)} \tag{13-3}$$

$$\frac{T_{10}^{TM} (1 - R_{12}^{TM} \beta)}{(1 - R_{10}^{TM} R_{12}^{TM} \beta)} \tag{13-4}$$

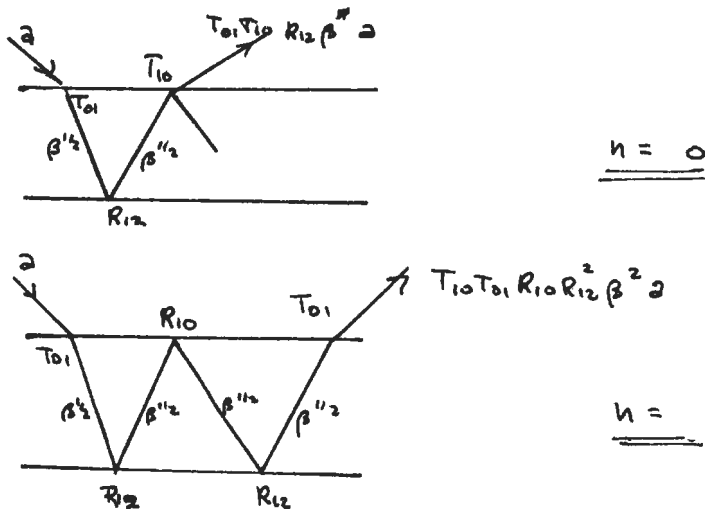
where $\beta = e^{j2\Gamma_1 t_1}$ is the phase shift (and attenuation) for a 2 way pass through region 1. If the interfaces are poor reflectors and region 1 has a finite loss then the terms $R_{10}^{TE} R_{12}^{TE} \beta$ and $R_{10}^{TM} R_{12}^{TM} \beta$ have amplitudes less than unity. When this condition is satisfied 13-3 and -4 can be written

with the aid of 9-8 as

$$T_{01}^{TE} + T_{01}^{TE} T_{10}^{TE} \sum_{n=0}^{\infty} (R_{10}^{TE})^n (R_{12}^{TE})^{n+1} (\beta)^{n+1} \quad (13-5)$$

$$T_{10}^{TM} - T_{10}^{TM} T_{01}^{TM} \sum_{n=0}^{\infty} (R_{10}^{TM})^n (R_{12}^{TM})^{n+1} \beta^{n+1} \quad (13-6)$$

The nth term in the series represents a wave which has made (n+1) 2 way passes through region 1 before being detected at the receiver. For example, a TE wave for n = 0 and n = 1 is sketched below



The final step in the geometrical optics analysis is the evaluation of the Hankel transform integral. The solution is obtained by saddle-point contour integration on each term of the above series and retention of the first order term. The half-space solution which is the term independent of the

series in 17-5 and -6 is obtained by retention of the second order terms. The field expressions are those developed in section 12 and given in Table 12-1. As an example, the H_z TE field will be derived here.

$$H_z = H_z \text{ (H.S.)} + \sum_{n=0}^{\infty} H_z^n \quad (13-7)$$

where H_z (H.S.) indicates the half-space solution and

$$H_z^n = \sin \varphi \int_0^{\infty} j \frac{\Delta^2}{P_0} \left\{ T_{10}^{TE} T_{01}^{TE} (R_{10}^{TE})^n (R_{12}^{TE} \beta)^{n+1} e^{j \beta_0 z} \right\} J_1(\Delta P) d\Delta \quad (13-8)$$

is the nth multiple reflection in the layer.

The individual terms H_z^n are evaluated as follows. The Bessel function is replaced by the appropriate Hankel function (see section 11) and the asymptotic form of the Hankel function is inserted into 13-10. The integrand then contains an exponential form

$$e^{j 2(n+1)t_1 + j \Delta P} \quad (\text{Note: } z \ll P \ll n t_1) \quad (13-9)$$

which is identical in form to that of the integrals discussed in section 11 and the saddlepoint contour developed in appendix 1.

Defining $R_n = (P^2 + 4(n+1)^2 t_1^2)^{1/2}$, the saddle point of the exponent in 13-14 occurs at

$$\Delta_P^n = \frac{P}{R_n} \sqrt{k_1} \quad (13-10)$$

where K is the complex dielectric constant of region 1.

Thus

$$\begin{aligned}
 H_z &\approx \frac{\sin \varphi}{2} e^{j\sqrt{K_1} R_n} \int_c \frac{j \Delta^2}{\Gamma_0} (T_{10}^{TE} T_{01}^{TE} (R_{10}^{TE})^n (R_{12}^{TE})^{n+1}) e^{j\Gamma_0 z} e^{-u^2} \sqrt{\frac{z}{\pi \Delta \rho}} e^{-j3\pi/4} d\Delta \\
 &= \frac{\sin \varphi}{2} e^{j\sqrt{K_1} R_n} \int_{-\infty}^{\infty} F_n(u) e^{-u^2} du \quad (13-11) \\
 &\approx \frac{\sin \varphi}{2} e^{j\sqrt{K_1} R_n} \sqrt{\pi} F_n(0)
 \end{aligned}$$

The $F_n(0)$ is given by setting $\Delta = \Delta_p^n$ in remaining portion of the integrand of 13-16

$$\begin{aligned}
 F_n(0) = & \frac{j \Delta_p^{n2}}{\Gamma_0(\Delta_p^n)} T_{10}^{TE}(\Delta_p^n) T_{01}^{TE}(\Delta_p^n) (R_{10}^{TE}(\Delta_p^n))^n (R_{12}(\Delta_p^n))^{n+1} e^{j\Gamma_0(\Delta_p^n)z} \\
 & \times \sqrt{\frac{z}{\pi \Delta_p^n \rho}} e^{-j3\pi/4} \left. \frac{d\Delta}{du} \right|_{\Delta=\Delta_p^n} \quad (13-12)
 \end{aligned}$$

and with

$$\left. \frac{d\Delta}{du} \right|_{\Delta=\Delta_p^n} = e^{-j\pi/4} \sqrt{2\sqrt{K_1}} \frac{z}{R_n} \frac{1}{R_n^{1/2}} \quad (13-13)$$

H_z^n is given by

$$\begin{aligned}
 H_z^n = & \sin \varphi \frac{e^{j\sqrt{K_1} R_n}}{R_n} \left(-j \frac{\Gamma_1}{\Gamma_0} \alpha_n T_{10}^{TE}(\alpha_n) T_{01}^{TE}(\alpha_n) (R_{10}^{TE}(\alpha_n))^n \times \right. \\
 & \left. (R_{12}^{TE}(\alpha_n))^{n+1} e^{j(1-\alpha_n)^{1/2} z} \right) \quad (13-14)
 \end{aligned}$$

$$\alpha = \frac{\rho}{R_n} \sqrt{k_1} \quad (13-15)$$

H_z^n appears as if generated by a spherical wave radiated from a source at a depth

$$z = -(n+1)t_1 \quad (13-16)$$

which has the radiation pattern of the half-space interface modified by the angular dependence of the n th and $n+1$ th power of $R_{10}(\alpha_n)$ and $R_{12}(\alpha_n)$, the interface Fresnel coefficients at the geometrical angle between the receiver and the n image source. This is sketched in Fig. 13-1.

The evaluation of each image contribution by the saddle point method invokes the usual assumptions that R is large and the $R_{10} R_{01} \beta$ product is considerably less than unity. The series 13-4 is rapidly convergent in this case. As in the radiation pattern development, second order effects which are additional head and unhomogeneous ^{waves} tied to the interfaces are ignored. When the geometric optics expansions are reasonably valid, neglect of these and higher order terms can be made with reasonable justification. The most important second order terms are retained in H_z (H.S.).

When $R_{10} R_{12} \beta$ approaches unity, as it does for loss free media when Δ exceeds the critical horizontal wave numbers for the two interfaces, the above expansion falls apart. In a geometrical sense this occurs when

$$\frac{P}{R_n} \approx 1 \quad (13-17)$$

or

$$\frac{2(n+1)t_1}{P} \ll 1 \quad (13-18)$$

for a large number of n.

The geometrical optics series terms for each of the TE and TM fields generated by the HED are summarized in Table 13-1. The expressions given are for the amplitude of the nth multiple. Thus, the total field at a height h (small w.r.t. P, t_1 , etc.) is given by

$$\text{Field} = \text{Field (H.S.)} + \sum_{n=0}^{\infty} A_n(\alpha_n) e^{j(1-\alpha_n^2)^{1/2} z} \frac{e^{j\sqrt{k_1} R_n}}{R_n} \quad (13-19)$$

with $A_n(\alpha_n)$ being the quantity listed in Table 13-1.

Fig. 13-1

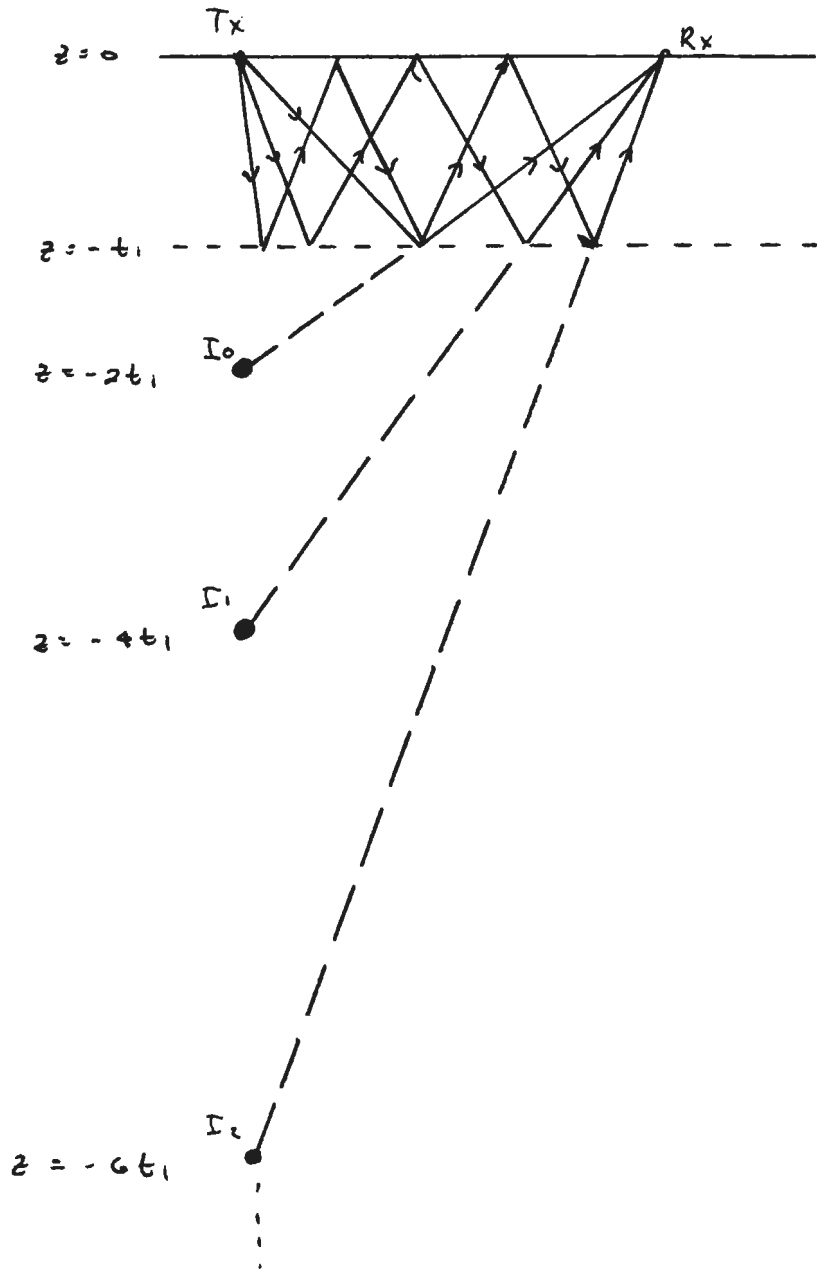


Table 13-1

nth Term of the Geometrical Optics Series for Fields about

a HED

TE

Component

A_n

\mathcal{E}_φ

$$\sin\varphi \frac{T_1}{T_0} T_{10}^{TE} T_{01}^{TE} R_{10}^{TE^n} R_{12}^{TE^{n+1}}$$

\mathcal{H}_φ

$$\sin\varphi j T_1 T_{10}^{TE} T_{01}^{TE} R_{10}^{TE^n} R_{12}^{TE^{n+1}}$$

\mathcal{H}_z

$$\sin\varphi -j \alpha_n \frac{T_1}{T_0} T_{10}^{TE} T_{01}^{TE} R_{10}^{TE^n} R_{12}^{TE^{n+1}}$$

TM

Component

A_n

\mathcal{H}_φ

$$\cos\varphi -j T_1 T_{10}^{TM} T_{01}^{TM} R_{10}^{TM^n} R_{12}^{TM^{n+1}}$$

\mathcal{E}_φ

$$\cos\varphi T_0 T_1 T_{10}^{TM} T_{01}^{TM} R_{10}^{TM^n} R_{12}^{TM^{n+1}}$$

\mathcal{E}_z

$$\cos\varphi -j \alpha_n T_1 T_{10}^{TM} T_{01}^{TM} R_{10}^{TM^n} R_{12}^{TM^{n+1}}$$

The Fresnel coefficients have the argument α_n as defined by

13-15

$$T_1 = \sqrt{k_1} \frac{z(n+1)t_1}{R_n}$$

$$T_0 = (1 - \alpha_n^2)^{1/2}$$

13-3 Normal Mode Solution

The geometrical optics solution discussed in the last section required three major assumptions. First, the expansions 13-5 and 13-6 must be valid; second, the evaluation of the integral for each term in the series was obtained by retaining only the first term of an asymptotic expansion; third, second order waves were totally neglected in all but the half-space portion of the solution. While many situations warrant these approximations, some of the most interesting geological environments may not meet criteria for this type of solution.

An alternate form of solution is the normal mode solution; this solution complements the geometrical optics solution since it is most useful in problems where the geometrical optics solution fails. The normal mode solution is applied primarily in situations where the layer thickness is small, usually on the order of the medium wavelength or less, the interfaces are highly reflective and the layer is almost loss-free. The normal mode solution can be applied in situations where the geometrical optics solution is adequate but computational efficiency is usually quite a bit less when the solution is applied.

The basis for the normal mode solution lies in manipulation of the contour of integration in the complex Λ ^{plane.} Analysis of each term in the geometrical optics solutions and the associated saddle point contour shows that the limiting contour for $P/Z \gg 1$ is as sketched in Fig. 13-2. This limiting case $P/Z \rightarrow \infty$ is defined as the normal mode integration contour. The original contour along the real Λ axis is deformed to this contour. In the process of performing this deformation, all singularities of the integrand must be accounted for. The singularities of the integrand are just the poles associated with the zeros

$$1 - R_{10} R_{12} \beta = 0 \quad (13-20)$$

(TE or TM superscripts implied). As an example of how the procedure goes, the H_2 TE field will be used as an example

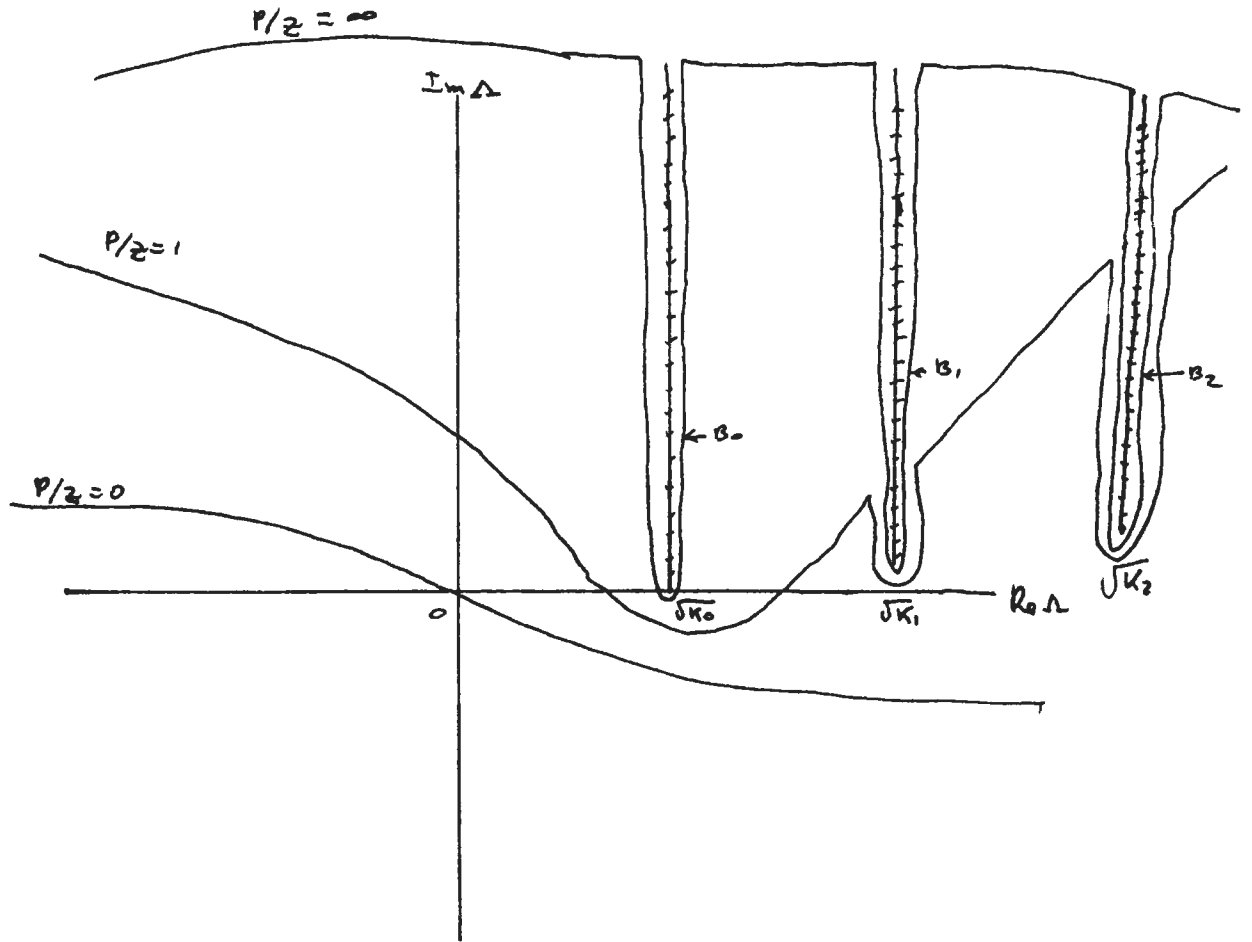
First

$$H_2 = \frac{\sin \varphi}{2} \int_{-\infty}^{\infty} j \frac{\Lambda^2}{\pi_0} (1 + R^{TE}) e^{j\pi_0 z} H_1'(\Lambda \rho) d\Lambda \quad (13-21)$$

$$= \sum \text{Residues} + \int_{B_0} + \int_{B_1} + \int_{B_2}$$

The second line is the form ^{of} the integrand after taking the integration path along the real Λ path from $-\infty$ to $+\infty$ and moving it to the limiting $P/Z \rightarrow \infty$ case shown in Fig. 13-2. The residue sum takes into

Figure 13-2



account the poles of the integrands crossed in deforming the contour and integrals are contours around the branch cuts associated with radicals $(k_i - \Lambda^2)^{1/2}$. Thus \mathcal{B}_1 implies

$$\begin{aligned} \int_{\mathcal{B}_1} F d\Lambda &= \int_{\sqrt{k_i}}^{\sqrt{k_i+j\infty}} F_L d\Lambda + \int_{\sqrt{k_i}}^{\sqrt{k_i+j\infty}} F_R d\Lambda \\ &= \int_{\sqrt{k_i}}^{\sqrt{k_i+j\infty}} (F_R - F_L) d\Lambda \end{aligned}$$

where F_R and F_L denote the values F takes on the right and left side of the branch cut. The other \mathcal{B}_i contours have the same form as 13-22.

Mode

13-3 (i) Normal Wavenumbers Λ_n

At this point it is informative to examine the singularities of the integrand. Inspection shows that the only singularities besides the branch-points are the poles associated with the solution of 13-20. The nature of the solution of 13-20 is most easily understood by considering special cases first and then working toward more complicated situations. The simplest of all models is the one used in electrical engineering waveguide analysis. Here $R_{10} = R_{12} = \pm 1$ (i.e. the walls; regions 0 and 2) are perfect reflectors (i.e. perfect conductors) and region 1 is loss free.

Then 13-20 becomes

$$1 \pm e^{j2\pi_1 t_1} = 0 \quad (13-23)$$

Taking the log of 13-23 yields

$$j2\pi_1 t_1 = \begin{cases} (2n+1)\pi j \\ 2\pi n j \end{cases} \quad n = 0, 1, 2 \quad (13-24)$$

and

$$K_1 - \Lambda_n^2 = \begin{cases} ((2n+1)\pi/2t_1)^2 \\ (\pi n/t_1)^2 \end{cases} \quad (13-25)$$

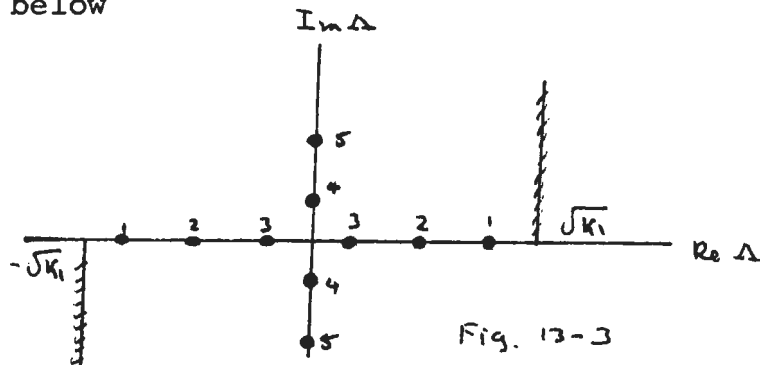
and

$$\Lambda_n = \pm \left(K_1 - \left(\frac{(2n+1)\pi}{2t_1} \right)^2 \right)^{1/2} \quad (13-26)$$

or

$$\Lambda_n = \pm \left(K_1 - \left(\frac{\pi n}{t_1} \right)^2 \right)^{1/2} \quad (13-27)$$

The solutions Λ_n of 13-23 lie in the complex Λ plane as sketched below



For $\frac{(2n+1)\pi}{2t_1}$ or $\frac{\pi n}{t_1} < \sqrt{K_1}$, the root Λ_n lies on the

real Λ axis while for values greater than $\sqrt{K_1}$ the roots lie on the imaginary axis. If one returns to the plane wave spectrum notation, it is readily seen that the real

Λ_n corresponds to waves propagating in the radial direction whereas the poles in the imaginary axis are evanescent waves decaying exponentially with the radial distance. There are a doubly infinite set of solutions Λ_n and in addition, there is a second set of roots on the other Riemann surface of the radial Γ_1 .

The next step in the discussion is to consider the situation when region 1 has a finite loss. The solution for Λ_n is identical to 13-26 and -27 with K_1 complex. The solutions Λ_n are shown below

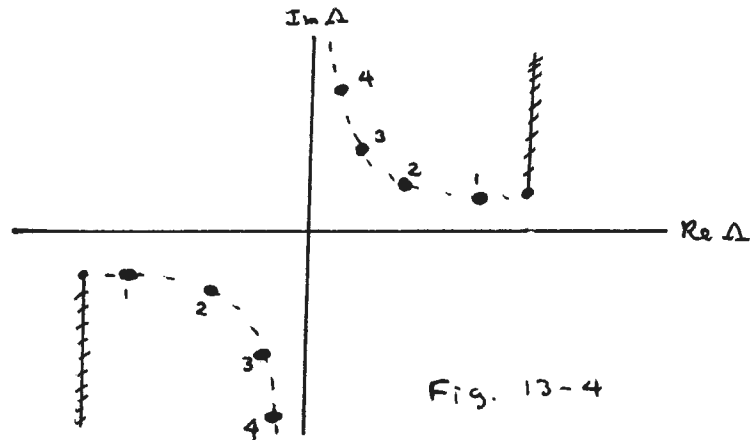


Fig. 13-4

The poles now lie on the dotted line which is the path in the complex plane where $\text{Im } \Gamma_1 \equiv 0$. It is readily seen that the no-loss case is the limiting case of the one above with two non-intersecting branches. It is also apparent that there is no clear distinction between propagating and evanescent waves. The waves which formerly were unattenuated with radial distance have a small attenuation while those exponentially decayed with radial distance. When the loss is small, the dotted line lies close to the real axis and bends

abruptly upwards near the imaginary axis so that the evanescent and propagating terminology can still be applied.

The preceding example is of little interest to SEP applications, but it does show the basic effects of finite-loss and layer thickness t_1 . As t_1 increases the Λ_n become more closely spaced and more and more move into the propagating regime.

Two last examples of the behaviour of the Λ_n solutions provide insight into the general case to be considered in a moment. First, the case of $R_{10} = C$ a constant. If $|C| < 1$, the upper boundary is leaky and some energy leaks out of the layer with every reflection at the boundary. If $|C| > 1$, the upper boundary is active or the region 0 is resonant in some way or another. In the following sketches, the Λ_n for the finite loss case are shown in the positions they would assume if $|C| > 1$, $|C| < 1$ for $\angle C = 0$ and finally $|C| = 1$ $\angle C \neq 0$.

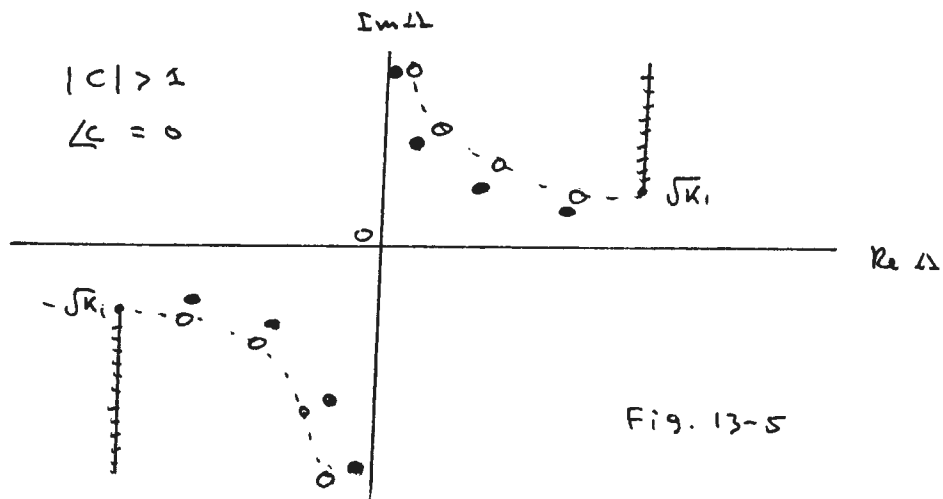


Fig. 13-5

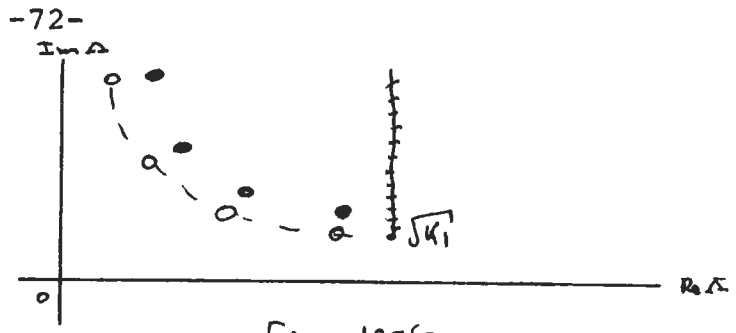


Fig. 13-6

$$|C| < 1 \quad \angle C = 0$$

$$|C| = 1 \quad \angle C \neq 0$$



The interpretation of the behaviour is simple. For $|C| > 1$, the radial Γ_1 must have an imaginary component

$$\Gamma_1 = \alpha + j\beta \tag{13-28}$$

such that

$$|C| e^{-2t_1\beta} = 1 \tag{13-29}$$

Hence $\beta > 0$ if $|C| > 1$ and Λ_n is moved left and downwards from the dotted line along which $\beta \equiv 0$. If $|C| \equiv 1$ but C has an arbitrary phase, the Λ_n slide up or down the line $\beta \equiv 0$ to yield the appropriate phase shift.

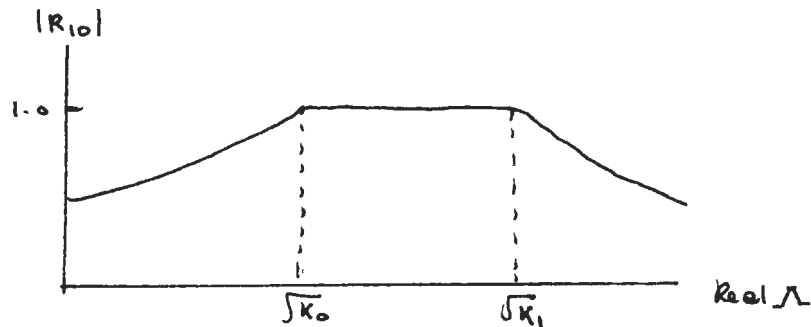
The preceding examples provide the insight as to how a real model might behave. The simplest geophysical model is the case retaining $R_{12} \equiv -1$ but taking R_{10} as the boundary between two loss-free media. Thus

$$1 + R_{10} e^{j2\Gamma_1 t_1} = 0 \tag{13-30}$$

As a demonstration, the TE case will be discussed in detail. The TE reflection coefficient has the form

$$R_{10} = \frac{\pi_1 - \pi_0}{\pi_1 + \pi_0} \quad (13-31)$$

and examination of the behaviour of R_{10} along the real Λ axis shows that $|R_{10}|$ varies as shown below



The wavenumber $\Lambda = \sqrt{k_0}$ corresponds to a ray incident at the 1-0 boundary at the critical angle; beyond the critical angle out to $\Lambda = \sqrt{k_1}$, the maximum allowable horizontal wavenumber the region 1 will permit to be non-evanescent, the reflection coefficient has an amplitude of unity. The phase of R_{10} swings from 0 to π as Λ runs from $\sqrt{k_0}$ to $\sqrt{k_1}$.

or $\Lambda < \sqrt{K_0}$, the reflection coefficient is less than 1 and has a phase of 0. The solution of 13-30 will yield the positions of Λ_n to be sketched below.

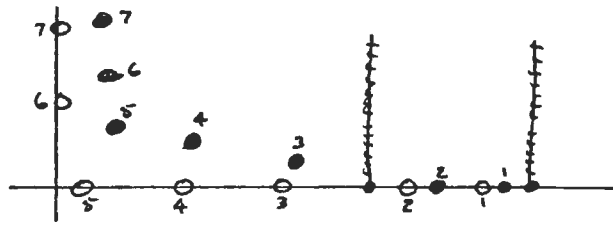


Fig. 13-9

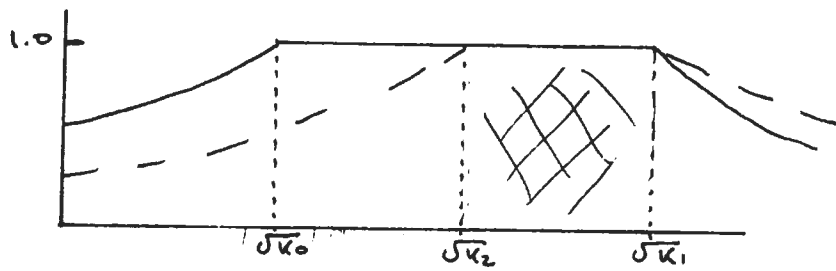
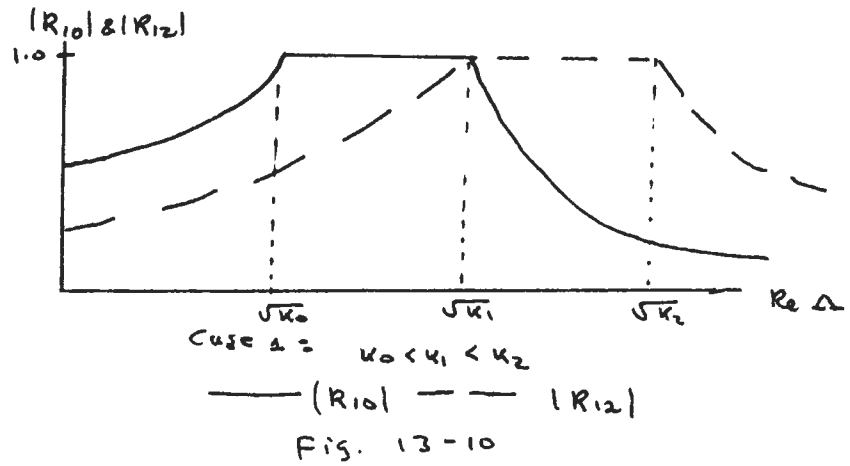
The positions of the Λ_n can be synthesized by combining Fig. 13-3, -6 and -7. For $\Lambda < \sqrt{K_0}$, $|R_{10}| < 1$ and Λ_n must be located up and to the right of the line $\text{Im } \Gamma_1 = 0$. For the region $\sqrt{K_0} < \Lambda < \sqrt{K_1}$, the Λ_n lie on the real axis but shifted along due to the finite phase of R_{10} . In the above example, $\Lambda_n, n = 1$ and 2 correspond to true guided waves while $\Lambda_n, n = 3$ to ∞ are leaky modes of the layer. These leaky modes decay exponential with radial (horizontal) distance due to finite leakage of energy upwards into region 0. If region 1 is made lossy, the behaviour is similar to that sketched in Fig. 13-4.

The solution of 13-30 has the corresponding set of Λ_n solutions not shown in Fig. 13-9. In addition each Riemann sheet of which there are now four has its own set of solutions. Thus there are four doubly infinite sets of solutions Λ_n

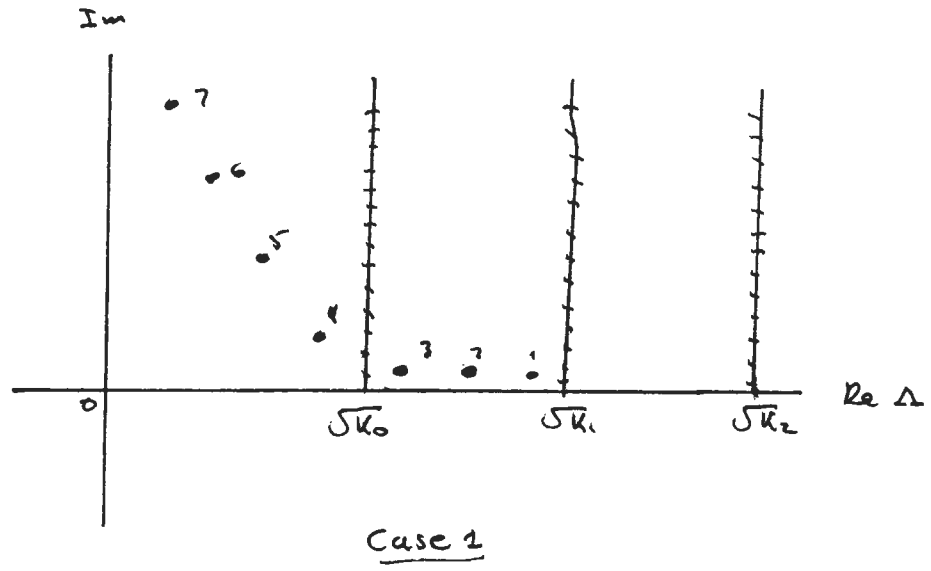
The last case to be considered is the one where regions 0 and 2 are both dielectric media. Then one must consider the effect of R_{12} which has the form

$$R_{12} = \frac{\Gamma_1 - \Gamma_2}{\Gamma_1 + \Gamma_2} \quad (13-32)$$

Along the real axis one has $|R_{12}|$ and $|R_{10}|$ being one of ^{the} two forms as shown below



For case 1, the product $|R_{10} R_{12}| < 1$ except at $\Delta = \sqrt{k_1}$ while for case 2 the product $|R_{10} R_{12}| = 1$ for $\sqrt{k_2} < \Delta < \sqrt{k_1}$. The two cases yield the schematic pole positions shown below



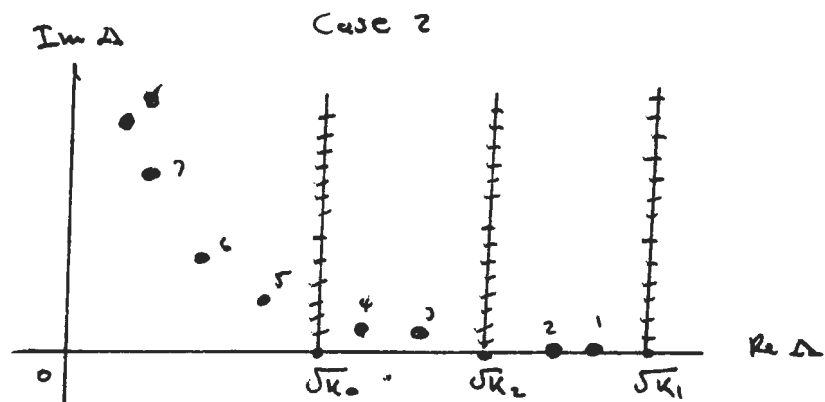


Fig. 13-12

For case 1, no truly guided mode can exist. All Δ_n are complex since there is no Δ for which $|R_{10} R_{12}| = 1$. Energy is continually leaking into the upper and/or lower halfspace.

For case 2, however, it is possible to generate unattenuated guided waves since $|R_{10} R_{12}| = 2$ for an interval of Δ . In this case $\sqrt{k_0}$ and $\sqrt{k_2} < \Delta < \sqrt{k_1}$ and Δ corresponds to rays incident at angles greater than the critical angle for the two interfaces. The slab then becomes a dielectric wave guide if the thickness is sufficiently great to move some of the Δ_n into this interval of the real axis. For finite loss in the media, the Δ_n are pushed up from the real Δ axis. In this problem, the branch cuts generate an 8 sheeted Riemann surface each with its own set of Δ_n .

13-3 (ii) Normal Mode Amplitude

In the preceding analysis, the normal mode wavenumbers were discussed in relation to the physical parameters of the problem. Returning to equation 13-21, the residue series becomes a sum over the normal mode wavenumbers Δ_n . Each Δ_n corresponds to a

simple pole in the integrand. The amplitude of the residue at each pole then yields the excitation amplitude of the mode for the given source and layer geometry.

The amplitude of a mode is obtained as follows where Hz is used to demonstrate the procedure.

The integrand of Hz has the form

$$\frac{j \Lambda^2}{2 \pi_0} \frac{T_{01}^{TE} (1 + R_{12}^{TE} \beta)}{(1 - R_{10}^{TE} R_{12}^{TE} \beta)} e^{j \pi_0 z} H_1'(\Delta \rho) \quad (13-33)$$

In the vicinity of Λ_n ,

$$R_{10}^{TE} R_{12}^{TE} \beta \approx 1 + \frac{d}{d\Lambda} (R_{10}^{TE} R_{12}^{TE} \beta) \Big|_{\Lambda = \Lambda_n} (\Lambda - \Lambda_n) \quad (13-34)$$

The residue at the pole Λ_n is obtained by multiplying 13-35 by $(\Lambda - \Lambda_n)$ and taking the limit as $\Lambda \rightarrow \Lambda_n$. Thus

$$\text{Residue } n = (2\pi j) \frac{j \Lambda_n}{2 \pi_0 (\Lambda_n)} \frac{T_{01}^{TE} (1 + R_{12}^{TE} \beta)}{(1 - R_{10}^{TE} R_{12}^{TE} \beta)} H_1'(\Lambda_n \rho) \quad (13-35)$$

$$= A_n H_1'(\Lambda_n \rho)$$

where A_n is the normal mode amplitude of excitation

factor. The asymptotic form of H_1^1 shows that the mode behaves as

$$\frac{e^{j \Delta_n P}}{\sqrt{P}} \quad (13-36)$$

Thus all modes have a characteristic distance P_n in which they exponentially decay beyond detection unless they have $\text{Im} \Delta_n \equiv 0$. In the case $\text{Im} \Delta_n \equiv 0$, $P_n \rightarrow \infty$.

The H_2 field may then be expressed as

$$H_2 = \sin \varphi \sum_{n=0}^{\infty} A_n H_1^1(\Delta_n P) + \int_{B_0} + \int_{B_1} + \int_{B_2} \quad (13-37)$$

Examination of Δ_n shows that $\Delta_n \rightarrow j\infty$ as $n \rightarrow \infty$.

Therefore, in any practical situation where P is finite, the series sum can be truncated without loss of accuracy. Thus

$$H_2 \approx \sin \varphi \sum_{n=0}^M A_n H_1^1(\Delta_n P) + \int_{B_0} + \int_{B_1} + \int_{B_2} \quad (13-38)$$

where M is primarily determined by the geometry.

In addition to the attenuation truncation of the series, there is another factor which must be considered as $t_1 \rightarrow 0$. The number of Δ_n on the upper Riemann surface used earlier actually becomes finite and $M \rightarrow 0$ as $t_1 \rightarrow 0$. Pictorially the Δ_n lie on lines determined by t_1 as

sketched in Fig. 13-12. As to $t_1 \rightarrow 0$, pole $n = 1$ moves up the contour and the contour wraps itself onto one of the lower Riemann surfaces.

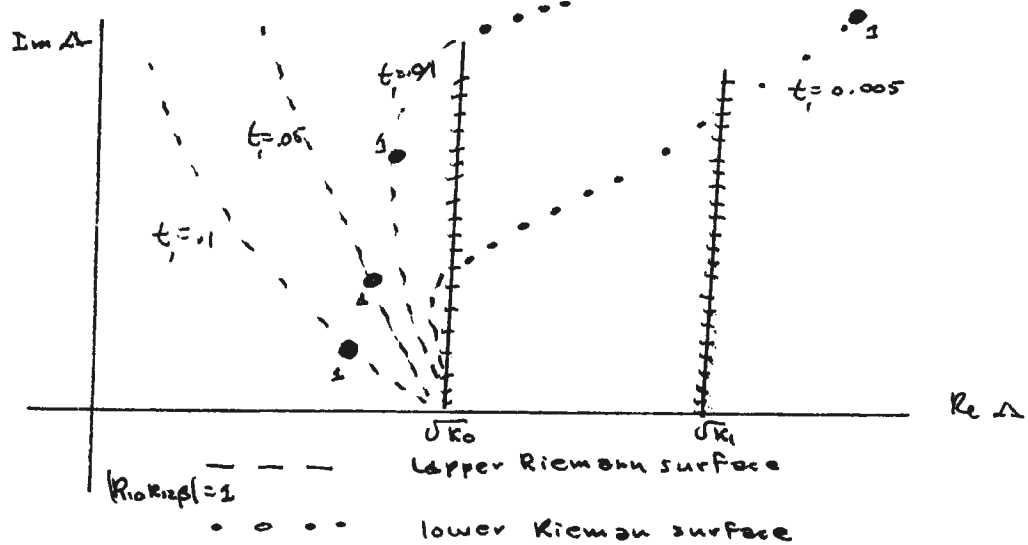


Fig. 13-13

The position of pole 1 is schematically indicated on the diagram. The layer thickness are typical values for $k_1 = 3$.

13-3(i) Branch Line Contributions

The final stage of the analysis by the normal mode technique is the evaluation of the branch-line contributions. The analysis will not be carried out in detail since it is identical in form to that considered for the half-space solutions in section 12. The integrals cannot be evaluated exactly but asymptotic forms obtained by steepest descent integration are quite often adequate.

The first thing to be noted is that the \mathcal{B}_1 integral is identically 0. The asymmetry of the integrand about the

branch-cut faces the integral to vanish. The other two integrals take the form

$$\int_{B_0} = \frac{e^{jP}}{P^2} D_0 \quad (13-39)$$

$$\int_{B_2} = \frac{e^{j\sqrt{K_2}P}}{P^2} D_2 \quad (13-40)$$

which are second order lateral and/or inhomogeneous waves tied to the interfaces.

The above solutions for the normal mode and branch line integrals are valid except for the case of $|R_{12}| \equiv 1$ and $\text{Im } K_0 = \text{Im } K_1 \equiv 0$. In this case, certain critical values of t_1 cause a pole to align itself with the branch-point. At the same time a pole in the lower Riemann surface also coalesces with $\overline{K_0}$. The result is a second order pole at the branch point. The integral in this very special case can be analysed by subtracting of the residue contribution which yields a "guided" later^{al} or leaky wave which has the form

$$\frac{e^{jP}}{P^{3/2}} \quad (13-41)$$

as D gets large. Since this situation rarely occurs in real media, its role will not be dealt with in detail.

One other point which should be briefly mentioned

is the pole associated with the Sommerfeld "surface" wave. For a dielectric layer which is very thin over a perfect reflector. This pole can appear on the upper Riemann surface. As a result, the TM energy will be channeled into a guided wave for smaller values of t_1 than will TE energy. Since the real environments of interest are quite lossy, the details of this case are primarily of academic interest.

13-3 (iv) Summary

The preceding discussions demonstrate the development of the normal mode solution. In table 13-2, the A_n , D_0 and D_2 amplitudes for the various field components listed in Table 10-4 are summarized.

Table 13-2 (a)

<u>TE</u>			
E_φ	$-\sin\varphi$	$\frac{j\Delta}{2\pi_0}$	$G^{TE}(\lambda) e^{j\pi_0 z}$
H_φ	$-\sin\varphi$	$\frac{\Delta}{2}$	$G^{TE}(\lambda) e^{j\pi_0 z}$
H_z	$\sin\varphi$	$\frac{j\Delta^2}{2\pi_0}$	$G^{TE}(\lambda) e^{j\pi_0 z}$

<u>TM</u>			
H_φ	$\cos\varphi$	$\frac{\Delta}{2}$	$G^{TM}(\lambda) e^{j\pi_0 z}$
E_φ	$\cos\varphi$	$-j\frac{\Delta\pi_0}{2}$	$G^{TM}(\Delta) e^{j\pi_0 z}$
E_z	$\cos\varphi$	$-\frac{\Delta^2}{2}$	$G^{TM}(\Delta) e^{j\pi_0 z}$

$$G^{TE} = \frac{T_{01}^{TE}}{T_{01}^{TE}} (1 + R_{12}^{TE} \beta) / \mathcal{D}^{TE}$$

$$G^{TM} = \frac{T_{10}^{TM}}{T_{10}^{TM}} (1 - R_{12}^{TM} \beta) / \mathcal{D}^{TM}$$

$$\mathcal{D}^{TE} = \frac{2\Delta}{\pi_1} \left(jt_1 - \frac{1}{\pi_0} - \frac{1}{\pi_2} \right)$$

$$\mathcal{D}^{TM} = \frac{2\Delta}{\pi_1} \left(\frac{\kappa_0 \kappa_1}{\pi_0 (\kappa_0 \kappa_1 - (\kappa_0 + \kappa_1) \lambda^2)} + \frac{\kappa_1 \kappa_2}{\pi_2 (\kappa_1 \kappa_2 - (\kappa_1 + \kappa_2) \lambda^2)} + jt_1 \right)$$

14 N-Layered Earth Response : The "Fast" Hankel Transform (FHT)

In the preceding sections, the analysis particular earth models was carried out by the use of approximate integration methods. While these results provide a useful basis to start from, the need for a more generalized model to simulate the presence of several subsurface interfaces or to model at gradational change in material properties becomes important when one must attempt to interpret real data. The next simplest model for SEP purposes is to consider N-plane layers. The most interesting models which are virtually intractable to analysis in a general way are models which exhibit both vertical and lateral variations in material properties.

The N-layered model is just an extension of the half-space and 2-layer model. The spectral forms of the fields are readily obtained and the main obstacle to determining the field strengths as a function of spatial position is the evaluation of the Hankel transform. While the approximate methods of earlier sections may be applied, it becomes very difficult to handle the approximations required at each step. As a result, a fast numerical method of determining the Hankel transform directly on a computer was sought. The result is an algorithm which

combines the Fast Fourier Transform (FFT) method and a Gaussian quadrature based on Chebychev polynomials to directly evaluate the Hankel transform. This section is devoted to the mathematical niceties required to reduce the infinite integral to an approximate form which facilitates evaluation with the afore-mentioned numerical quadrature schemes.

The general Hankel transform pair are expressed by

$$f(r) = \int_0^{\infty} \lambda F(\lambda) J_n(\lambda r) d\lambda \quad (14-1)$$

$$F(\lambda) = \int_0^{\infty} r f(r) J_n(\lambda r) dr \quad (14-2)$$

The expressions 14-1 and -2 are identical in form, so that the evaluation of one by some numerical method assumes the evaluation of the inverse transform.

The first step in the analysis is to replace the Bessel function by its integral representation.

$$J_n(z) = \frac{(j)^{-n}}{\pi} \int_0^{\pi} \cos n\varphi e^{jz \cos\varphi} d\varphi \quad (14-3)$$

Now the transformation of integration variables

$$u = \cos\varphi \quad (14-4)$$

is applied to 14-3 with the result

$$J_n(z) = \frac{(j)^{-n}}{\pi} \int_{-1}^1 \frac{\cos n \cos^{-1} u e^{jz u}}{(1-u^2)^{1/2}} du \quad (14-5)$$

Noting now that the Chebychev polynomial of the first kind and of nth degree is given by

$$T_n(x) = \cos(n \cos^{-1} x) \quad (14-7)$$

and defining

$$B(x) = \begin{cases} 0 & |x| > 1 \\ 1 & |x| \leq 1 \end{cases} \quad (14-8)$$

equation 14-5 becomes

$$J_n(z) = \frac{1}{2\pi} \int_{-\infty}^{\infty} \frac{2(j)^{-n} T_n(u) B(u)}{(1-u^2)^{1/2}} e^{j\mu z} du \quad (14-9)$$

which is readily identified as a Fourier integral transform.

The inverse transform integral associate with 14-6 is

therefore

$$\frac{2(j)^{-n} T_n(u) B(u)}{(1-u^2)^{1/2}} = \int_{-\infty}^{\infty} J_n(z) e^{-jzu} du \quad (14-10)$$

With this development complete, 14-1 can now be

rewritten in a more useful form. First, 14-5 is used to

replace $J_n(\lambda r)$ in 14-1.

$$f(r) = \int_0^{\infty} \lambda F(\lambda) \frac{(j)^{-n}}{\pi} \int_{-1}^1 \frac{T_n(u)}{(1-u^2)^{1/2}} e^{j\lambda r u} du d\lambda \quad (14-11)$$

The integration roles are now interchanged with the result

that

$$f(r) = \frac{(j)^{-n}}{\pi} \int_{-1}^1 \frac{T_n(u)}{(1-u^2)^{1/2}} \left\{ \int_0^{\infty} \lambda F(\lambda) e^{j\lambda r u} d\lambda \right\} du \quad (14-12)$$

Using the symmetry properties of the Bessel function

$$J_n(-z) = (-1)^n J_n(z) \quad (14-13)$$

14-9 finally becomes

$$f(r) = \frac{(j)^{-n}}{\pi} \int_{-1}^1 \frac{T_n(u)}{(1-u^2)^{1/2}} \left\{ \int_{-\infty}^{\infty} G(\lambda) e^{j\lambda\beta} d\lambda \right\} du \quad (14-14)$$

where

$$\begin{aligned} G(\lambda) &= \lambda F(\lambda) \quad \lambda > 0 \\ &= (-1)^n |\lambda| F(|\lambda|) \quad \lambda < 0 \\ &= F(0) + (-1)^n F(0) \quad \lambda = 0 \end{aligned} \quad (14-15)$$

and

$$\beta = \mu r \quad (14-16)$$

The interior integral in 14-11 is readily identified as a Fourier integral transform

$$\mathcal{G}(\beta) = \int_{-\infty}^{\infty} G(\lambda) e^{j\lambda\beta} d\lambda \quad (14-17)$$

and 14-11 becomes

$$f(r) = \frac{(j)^{-n}}{2\pi} \int_{-1}^1 \frac{T_n(u) \mathcal{G}(\mu r)}{(1-u^2)^{1/2}} du \quad (14-18)$$

At this stage, the transform has been reduced to the form amenable for numerical analysis. The two integration steps

14-14 and 14-15 essentially take the spectral function, map it into its two dimensional equivalent and finally do an azimuthal quadrature to obtain the three dimensional response.

In the FHT algorithm, 14-14 is evaluated by the FFT method. Under the assumption that $G(\lambda)$ can be written or reformatted in a manner that

$$G(\lambda) \rightarrow 0 \quad \lambda \rightarrow \infty \quad (14-19)$$

$$g(\beta) \approx \int_{-\omega_N}^{\omega_N} G(\lambda) e^{j\lambda\beta} d\lambda \quad (14-20)$$

where ω_N is a limit chosen such that $G(\lambda)$ may be assumed 0 for all $\lambda > \omega_N$. As an example of how G can be taylorred if it does not go to 0 as $\lambda \rightarrow \infty$ is the case where

$$G(\lambda) \rightarrow c \quad \text{as} \quad \lambda \rightarrow \infty \quad (14-21)$$

Defining $G_1 = G - c$ (14-22)

$$g(\beta) = c \delta(\beta) + \int_{-\omega_N}^{\omega_N} G_1(\lambda) e^{j\lambda\beta} d\lambda \quad (14-23)$$

In other words the limiting behaviour as $\lambda \rightarrow \infty$ can be analysed and usually an exact evaluation of the

behaviour at high wavenumber can be derived. With the integration limit to a finite interval, the next step is to digitize $G(\lambda)$ at equispaced intervals. Thus the discrete form of $G(\lambda)$ is

$$G_D = \Delta \sum_{n=-N+1}^N G(n\Delta) \delta(\lambda - n\Delta) \quad (14-24)$$

Thus 14-17 becomes

$$g(\beta) = \Delta \sum_{n=-N+1}^N G(n\Delta) e^{jn\Delta\beta} \quad (14-25)$$

If it is then decided to evaluate $g(\beta)$ at a discrete set of $2N$ points equalispaced at interval δ

$$g(m\delta) = \Delta \sum_{n=-N+1}^N G(n\Delta) e^{jnm\delta\Delta} \quad (14-26)$$

Noting now that choosing $\delta = \frac{\pi}{N\Delta}$ one has

$$g_m = \Delta \sum_{n=-N+1}^N G_n e^{j2\pi\left(\frac{nm}{2N}\right)} \quad (14-27)$$

which is the conventional form of an FFT with $2N$ points.

If one now redistributes G_n and the subscript notation by defining

$$\begin{aligned} G_n &= G_n \quad n = 0, N \\ G_n &= G_{2N-n} \quad n = N+1, 2N-1 \end{aligned} \quad (14-28)$$

One finally obtains

$$G_m = \Delta \sum_{n=0}^{2N-1} G_n e^{j2\pi\left(\frac{nm}{2N}\right)} \quad m = 0, 2N-1 \quad (14-29)$$

The second integral is reduced to a numerical quadrature by use of the general Gaussian quadrature method with weighting function $(1 - u^2)^{-1/2}$. Without delving into the details, the result (Abramowitz and Stegun (1965)) is

$$\int_{-1}^1 \frac{f(x)}{(1-x^2)^{1/2}} dx \approx \sum_{n=1}^M \omega_n f(x_n) \quad (14-30)$$

where

$$\omega_n = \pi/M \quad (14-31)$$

$$x_n = \cos \frac{(2n-1)\pi}{2M} \quad (14-32)$$

The only remaining problem is to bolt these two quadratures together. The main difficulty is that g is available only at discrete points $\beta = m\delta$ while it is required at points x_i . In order to complete the quadrature some form of interpolation scheme is required to map from $m\delta \rightarrow rx_i$.

If one uses linear interpolation, one can write the piece-wise continuous function

$$g_I(\alpha) = g_s (1 - (\alpha - s\delta)) + g_{s+1} (\alpha - s\delta) \quad (14-33)$$

where

$$s = \frac{\alpha}{\delta} \quad \text{nearest truncated integer}$$

Combining all the pieces one has

$$f(r) = \frac{(j)^{-u}}{2\pi} \left(\frac{\Delta\pi}{M}\right) \prod_{i=1}^M T_n(x_i) g_I(x_i v) \quad (14-34)$$

The basic assumptions built into this development are summarized as follows:

1. Band limiting of $G(\lambda)$ to limits $-\omega_N$ to ω_N . The ω_N are determined by considering the function G .
2. The next step is the digitization of G at interval Δ . The interval Δ must be chosen in order that it will adequately resolve the spectrum G .
3. With the spatial interval determined by Δ and N , an interpolation routine must be set up to generate g at any arbitrary value of the argument.
4. The second quadrature requires picking of the sampling density of the quadrature. This step is determined by the M for the Chebychev quadrature. The sampling occurs at the roots of the Chebychev polynomial of degree M .

With the above algorithm it is a strictly computational problem for determining the approximate field strengths over an N -layered earth for any spatial

position. There are practical limitations, however, since letting, M , N become large which is occasionally required by some awkward models makes the computational expensive far too high for routine operation.

Section 15 Summary

The development of all relevant mathematical forms required for the SEP plane-layered model is complete at this point. The application of the theoretical development appears in various papers and SEP documentation. It is hoped that a record report similar to this which would present the numerical tricks and program listings as well as sample computations which parallel the theory presented here will be completed in the future.

The preceding book contains most of the relevant mathematical tricks for analysis of geophysical electromagnetic problems. The asymptotic expansion methods and the FHT quadrature method are more amenable to conductive earth problems since all spectral singularities are smoothed out and the numerical computations are easier.

Appendix 1

Numerical Evaluation of Saddle Point Contour

The saddle point method of evaluating some of the Hankel and Fourier transform integrals is exploited to varying degrees in the body of this work. In this appendix, a brief summary of the numerical determination of the saddle point contour is considered.

The saddle point is defined by examining the kernel function

$$e^{f(\lambda)} \tag{A-1}$$

In the case at hand, $f(\lambda)$ has the form

$$f(\lambda) = j(\gamma z + \rho \lambda) \tag{A-2}$$
$$\gamma = (k^2 - \lambda^2)^{1/2}$$

The objective of the saddle point method is to find where f has a saddle point and thence to deform the integration contour into a contour of steepest descent through the saddle point.

The saddle point of f in the above discussion occurs at the point where

$$\frac{df}{d\lambda} = 0 = j \left(-\frac{\lambda}{\gamma} z + \rho \right) \tag{A-3}$$

with the result that

$$\lambda_p = \frac{\rho}{R} k \tag{A-4}$$

$$\gamma_p = \frac{z}{R} k \tag{A-5}$$

$$R = (\rho^2 + z^2)^{1/2} \tag{A-6}$$

The physical interpretation of this result should be obvious;

the maximum result a given spatial position will be received from those elements of the wavenumber spectrum which propagate in that spatial direction. Hence the saddle point can be determined directly from the geometry.

With the saddle point defined, the next step is the definition of the steepest descent contour. Along this contour

$$f(\lambda) = f(\lambda_p) - u^2 \quad A-7$$

$$f(\lambda_p) = j k R$$

where U is a real variable which is identically 0 at $\lambda = \lambda_p$. The problem now is to define a contour in the complex λ plane such that f has the functional form (7). Since the path in the λ plane corresponds to the real axis of the complex μ plane, one is attempting to find the mapping of the real μ axis in the complex λ plane.

In the vicinity of the saddle point, it is not difficult to ascertain the contour behaviour. Defining

$$\lambda = \lambda_p + \Delta \quad A-8$$

Then

$$f(\lambda) \approx f(\lambda_p) + \frac{f''(\lambda_p)}{2} \Delta^2 \quad A-9$$

Comparing (9) with (7) yields

$$\Delta = \pm \left(-\frac{f''(\lambda_p)}{2} \right)^{-1/2} u \quad A-10$$

Since

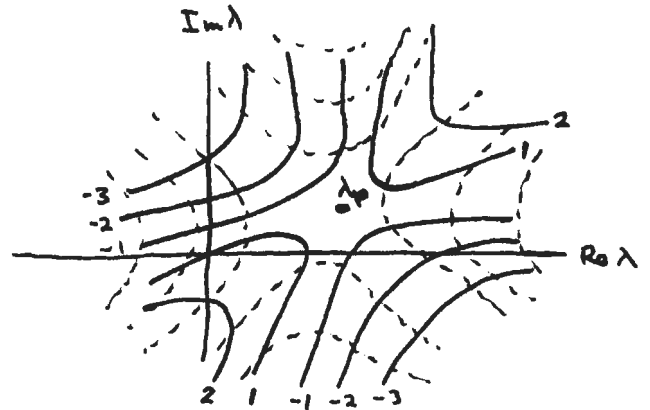
$$f''(\lambda_p) = j \left(-\frac{k^2 z}{r_p^3} \right) = -j \frac{R^3}{z^2 k} \quad A-11$$

Then

$$\Delta = \pm \left(-j \frac{2kz^2}{R^3} \right)^{1/2} \mu$$

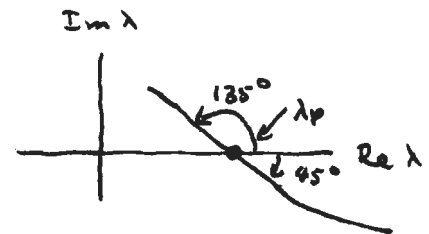
A-12

Pictorially one has the contours of $f(\lambda) - f(\lambda_p)$ sketched at the right. The steepest descent path passes through the saddle point as shown.



— Contours of $\text{Re } f(\lambda) = \text{const.}$
 - - - - Contours of $\text{Im } f(\lambda) = \text{const.}$

If k is real, the saddle point lies on the real x axis and the steepest descent contour passes through the saddle point at a 135° and -45° angle.



Case of k real.
 — Steepest descent contour near λ_p

For some numerical computations, the exact position of the steepest descent contour is important. The remainder of this section is related to determining the exact position of the steepest descent contour numerically. The most useful starting point in analysing the behaviour of the steepest descent path is to look at its asymptotic

limits since the behaviour near the saddle point is well defined. This is done by taking

$$\lambda = A e^{j\beta} \quad \text{A-13}$$

where $A \gg k, kR$ etc. (similarly for μ). In this instance

$$f(\lambda) = j(\gamma z + \lambda \rho) \rightarrow -\mu^2 \quad \text{A-14}$$

Now

$$\gamma \rightarrow (-A^2 e^{j2\beta})^{1/2} = A e^{j\beta \pm \pi/2} \quad \text{A-15}$$

thus

$$f(\lambda) \approx j A (z e^{j(\beta \pm \pi/2)} + \rho e^{j\beta}) \quad \text{A-16}$$

Since μ is real and negative the limiting angle β must be such that

$$\operatorname{Re} (z e^{j(\beta \pm \pi/2)} + \rho e^{j\beta}) = 0 \quad \text{A-17}$$

$$\operatorname{Im} (z e^{j(\beta \pm \pi/2)} + \rho e^{j\beta}) > 0 \quad \text{A-18}$$

Breaking the bracketed part of (16) into real and imaginary components and taking the $+\pi/2$ factor yields

$$-z \sin \beta + j z \cos \beta + \rho \cos \beta + j \rho \sin \beta \quad \text{A-19}$$

Now, by

$$-z \sin \beta + \rho \cos \beta = 0 \quad \lim A \rightarrow \infty \quad \text{A-20}$$

and

$$\tan \beta_+ = \rho/z \quad \text{A-21}$$

If the $-\pi/2$ factor is chosen (20) would become

$$z \sin \beta - j z \cos \beta + p \cos \beta + j r \cos \beta \quad A-22$$

and (24) would become

$$\tan \beta = -\frac{p}{z} = \tan(\pi - \beta) \quad A-23$$

The sign choice depends on the particular choice of the branch cuts for the radical $(k^2 - \lambda^2)^{1/2}$. Examples of the form of the saddle point contour are shown in Fig. 1.

The asymptotic limits are defined by

$$A = u^2/R \quad A-24$$

$$\beta = \tan^{-1}\left(\frac{p}{z}\right) \text{ or } \pi - \tan^{-1}\frac{p}{z} \quad A-25$$

$$R = p^2 + z^2 \quad A-26$$

A FORTRAN program was written to map the saddle point contour in the complex λ plane as a function of the parameters p , z , and $\tan \delta$ ($k^2 = (1 + j \tan \delta)$).

The numerical procedure is a 2 step process. For a given value of μ , an estimate of the corresponding value of λ is obtained by using a weighted combination of the small μ and asymptotic form for large μ . The estimate of λ is λ_e

$$\lambda_e = \lambda_{\text{small}} (1-b) + \lambda_{\text{asympt}} \times b \quad A-27$$

where

$$b = |u/R| / (1 + |u/R|) \quad A-28$$

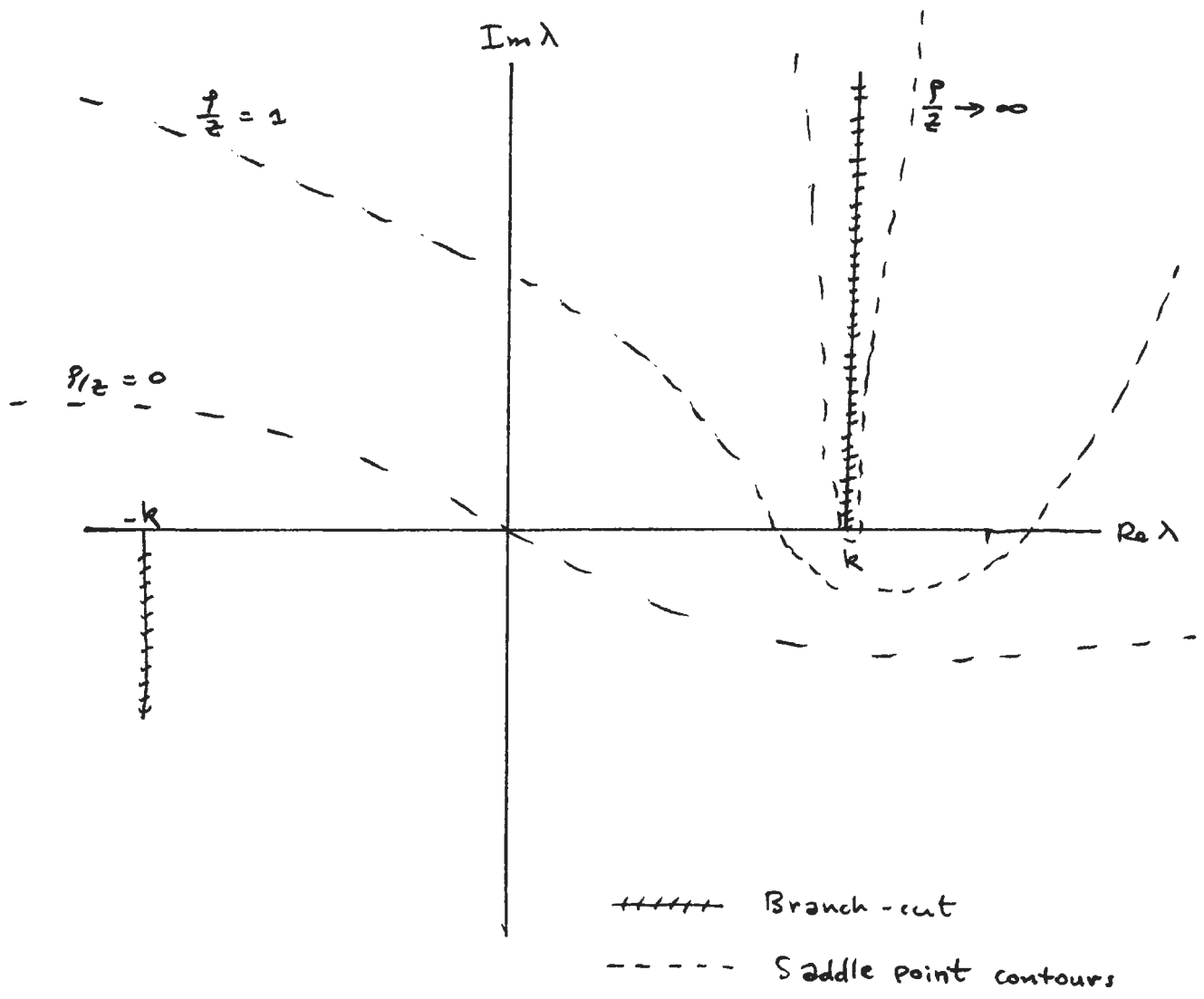


Figure 1

From the initial guess λ_e , a Newton iterative scheme is used to zero in on the correct value of λ . On the saddle point contour

$$f(\lambda_t) = f(\lambda_p) - u^2 \quad A-29$$

For λ_e one has

$$f(\lambda_e) = f(\lambda_p) - u^2 + e \quad A-30$$

where e is the error from the fact that λ_e is not the correct value of λ . On the assumption that λ_e is reasonably close to the correct value λ_t , one expands f about λ_e in a Taylor series. (f assumed analytic; in this example f is not analytic at the branch cut so a few minor computational tricks have to be used)

$$f(\lambda) \cong f(\lambda_e) + f'(\lambda_e) \Delta + \frac{f''(\lambda_e)}{2} \Delta^2 \quad A-31$$

The next estimate of λ_t is obtained by setting

$$\frac{f''}{2} \Delta^2 + f' \Delta = e \quad A-32$$

and solving for Δ yields

$$\lambda_e' = \lambda_e + \Delta$$

where

$$\Delta = \frac{-f' \pm (f'^2 - 2f''e)^{1/2}}{f''} \quad A-33$$

In the limit as $f''/f' \rightarrow 0$, 33 becomes

$$\Delta = -\frac{e}{f'} \quad A-34$$

Near the saddle point, the expression for Δ given in equation 40 is used since $f' \equiv 0$ at λ_p . The choice of sign for the radical in 40 is the one which makes the $|\Delta|$ smallest. Far from the saddle point 41 can be used since f''/f' becomes small as $|\lambda| \rightarrow \infty$.

Appendix 2

Table of Useful Hankel Transforms

$$\frac{e^{jkr}}{r} = \int_0^\infty \frac{\lambda}{p} e^{-\lambda|z|} J_0(\lambda p) d\lambda \quad \begin{array}{l} r = (p^2 + z^2)^{1/2} \\ p = (\lambda^2 - k^2)^{1/2} \end{array}$$

$$\frac{1}{p} = \int_0^\infty J_0(\lambda p) d\lambda$$

$$\delta(p) = \int_0^\infty \lambda J_0(\lambda p) d\lambda$$

$$\delta'(p) = - \int_0^\infty \lambda^2 J_1(\lambda p) d\lambda$$

$$\frac{1}{p^2} = \int_0^\infty \lambda J_1(\lambda p) d\lambda$$

$$\frac{1}{r} = \int_0^\infty e^{-\lambda|z|} J_0(\lambda p) d\lambda$$

$$-\frac{z}{r^3} = -\text{sign}(z) \int_0^\infty \lambda e^{-\lambda|z|} J_0(\lambda p) d\lambda$$

$$\frac{1}{p^3} = -\frac{1}{2} \int_0^\infty \lambda^2 J_1'(\lambda p) d\lambda$$

$$\frac{p}{r^3} = \int_0^\infty \lambda^2 e^{-\lambda|z|} J_1(\lambda p) d\lambda$$

Specific References

- Abramowitz, M. & Stegun, I.A., 1965, Handbook of Mathematical Functions, Dover Publications.
- Banos, A., 1962, Dipole Radiation in the Presence of a Conducting Half-space, Pergammon Press.
- Sommerfeld, A., 1949, Partial Differential Equations in Physics: New York, Academic Press (contains summary of 1909 paper).
- Van der Waerden, B.L., 1950, On the Method of Saddle Points, Appl. Sci. Res., vol. B2, pg. 33.

General References

- Brekhovskikh, L.M., 1960, Waves in Layered Media, New York, Academic Press.
- Jackson, J.D., 1962, Classical Electrodynamics, John Wiley and Sons.
- Kline, M., & Kay, I.W., 1965, Electromagnetic Theory and Geometrical Optics, Interscience Publishers.
- Kong, J.A., 1972, Electromagnetic Fields due to Dipole Antennas over stratified anisotropic media, Geophysics, vol. 37.
- Landau, L.D., & Lifshitz, E.M., 1960, Electrodynamics of Continuous Media, Pergammon Press.
- Ott, H., 1941, Reflexion and Brechung von Kugelwellen: Effekte Q. Ordnung: Ann. Physik, v. 41, 443-466.

Reitz, J.R. & Milford, F.J., 1960, Foundations of
Electromagnetic Theory, Addison Wesley.

Wait, J.R., 1962, Electromagnetic Waves in Stratified
Media, Pergammon Press (Revised edition 1970).

SEP References

- Annan, A.P., 1973, Radio Interferometry Depth Sounding:
Part I - Theoretical Discussion, Geophysics, v. 30,
no. 3, p. 557-580.
- Annan, A.P., 1970, Radio Interferometry Depth Sounding, M.Sc.
Thesis, University of Toronto, Toronto, Ontario,
Canada.
- Brekhovskikh, L.M., 1960, Waves in Layered Media: New York,
Academic Press.
- Cooper, W.W., 1971, Patterns of Dipole Antenna on Stratified
Medium, Technical Report TR71-3, MIT Centre for Space
Research.
- Katsube, T.J., and Collett, L.S., 1971, Electrical properties
of Apollo 11 and 12 lunar samples, in Proceedings of
the Second Lunar Science Conference, Houston, Texas,
edited by A.A. Levinson: Cambridge, Mass. Inst. Tech.
- Olhoeft, G.R., Strangway, D.W., and Frisillo, A.L., 1973,
Lunar Sample Electrical Properties, Proc. Fourth Lunar
Sci. Conf., (Suppl. 4, Geochim. Cosochim. Acta),
v. 3, p. 3133-3149.
- Rossiter, J.R., LaTorraca, G.A., Annan, A.P., Strangway, D.W.,
and Simmons, G., 1973, Radio Interferometry Depth
Sounding, Part II - Experimental Results, Geophysics,
v. 38, no. 3, p. 581-599.

- Rossiter, J.R., Strangway, D.W., Annan, A.P., Watts, R.D., and Redman, J.D., Detection of Thin Layers by Radio Interferometry, submitted to Geophysics, 1974.
- Simmons, G., Strangway, D.W., Bannister, L., Baker, R., Cubley, D., LaTorraca, G., and Watts, R., 1972, The Surface Electrical Properties Experiment, in Kopal, Z. and Strangway, D., eds., Lunar Geophysics, Proceedings of a Conference at the Lunar Science Institute, Houston, Texas, 18-21, October, 1971, D. Reidel, Dor drecht, p. 258-271.
- Strangway, D.W., Simmons, G., LaTorraca, G.A., Watts, R.D., Bannister, L., Baker, R., Redman, J.D., and Rossiter, J.R., 1974, Radio-Frequency Interferometry - A New Technique for Studying Glaciers, J. of Glaciology, in press.
- Tsang, L., Kong, J.A., and Simmons, G., Interference Patterns of a Horizontal Electric Dipole over Layered Dielectric Media, J. Geophys. Res., v. 78, p. 3287-3300, 1973.
- Wait, J.R., 1970, Electromagnetic Waves in Stratified Media, 2nd Edition: New York, The Macmillan Co.
- Waller, W.M., 1973, Surface Electrical Properties of Simulation Model, Lockheed Electronics Co. Final Report. LEC/PESD 634-TR-139 for contract NAS 9-122200, NASA-JSC, Houston, 1973.

FINAL REPORT
LEC/HASD No. 645D.21.077

SURFACE ELECTRICAL
PROPERTIES SIMULATION MODEL

Prepared By
Lockheed Electronics Company, Inc.
Houston Aerospace Systems Division
Houston, Texas

Under Contract NAS 9-12200

For
PLANETARY AND EARTH SCIENCES DIVISION



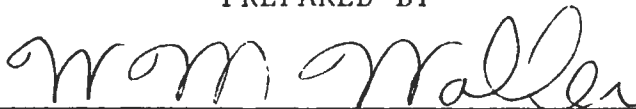
National Aeronautics and Space Administration
LYNDON B. JOHNSON SPACE CENTER
Houston, Texas
September 1973

LEC-0645

LEC/ASD 645D.21.077
Project Work Order 63-0255-2234

FINAL REPORT
SURFACE ELECTRICAL PROPERTIES
SIMULATION MODEL

PREPARED BY



W. M. Waller, Senior Scientist 5/28/74
Physics Section

APPROVED BY



N. C. Allen, Section Supervisor 5-23-74
Physics Section



W. R. Walker, Manager
Planetary and Earth Sciences Department

Produced By

Lockheed Electronics Company, Inc.

For

Planetary and Earth Sciences Division

NATIONAL AERONAUTICS AND SPACE ADMINISTRATION
LYNDON B. JOHNSON SPACE CENTER
HOUSTON, TEXAS

September 1973

LEC-0645

PREFACE

The work discussed in this report was done by Lockheed's Physics Section in support of the Planetary and Earth Sciences Division at the Johnson Space Center, Houston, Texas. The work was performed under Contract No. NAS 9-12200 for the National Aeronautics and Space Administration in compliance with Project Work Order 63-0255-2234. W. M. Waller prepared the report.

CONTENTS

Section	Page
PREFACE.	iii
ABSTRACT	ix
1.0 INTRODUCTION	1-1
2.0 TRAVERSE RECORDINGS.	2-1
2.1 Traverses Over a Metal Plate.	2-3
2.1.1 Horizontal metal plate	2-3
2.1.2 Metal plate -- lateral slopes	2-5
2.1.3 Metal plate -- forward slopes	2-5
2.2 Traverses Over a Dielectric Slab.	2-7
2.2.1 Horizontal dielectric slab	2-8
2.2.2 Dielectric slab -- forward slopes	2-8
2.2.3 Crater over dielectric slab	2-9
2.2.4 Crevasses over dielectric slab	2-10
2.2.5 Spheres over dielectric slab	2-12
2.2.6 Simulated crevasse in dielectric slab.	2-13
2.2.7 Random blocks on dielectric slab.	2-14
2.3 Variable-Loss Data.	2-15
2.3.1 Half-space at various loss-tangents	2-16

Section		Page
	2.3.2 Horizontal metal plate at various loss-tangents.	2-16
	2.3.3 Crevasses in half-space.	2-17
	2.3.4 Crevasses over metal plate	2-18
	2.3.5 Crater	2-19
	2.3.6 Mountain, step, and ridge simulations.	2-20
	2.4 Spherical Scattering Objects.	2-23
	2.5 DYE-3 Simulation.	2-25
3.0	ANTENNA PATTERNS	3-1
	3.1 Horizontal Electric Dipole.	3-1
	3.2 Vertical Electric Dipole.	3-2
	3.3 Vertical Magnetic Dipole.	3-2
4.0	EXPERIMENTAL DETAILS	4-1
	4.1 Tape Recording System	4-1
	4.2 Digital Conversion and Processing	4-2
	4.3 Power Measurement	4-4
	4.4 Dielectric Properties Test-Cell	4-6
	4.5 Antenna-Pattern Measurements.	4-9
5.0	INDEX TO DIGITIZED TRAVERSES	5-1
6.0	REFERENCES	6-1

Appendix

- A Traverses Over Metal Plate
- B Traverses Over a Dielectric Slab
- C Variable – Loss Data Traverses
- D Spherical Scattering Objects Traverses
- E DYE-3 Traverses

FIGURES

Figure		Page
1-1	The SEP experiment.	1-3
1-2	SEP scale model side view	1-4
1-3	Plate/slab -- forward slopes. Side view of tank	1-5
1-4	Plate -- lateral slopes. End view of tank.	1-6
1-5	Mélange of structures used. Side view of tank	1-7
2-1	Crater simulation	2-11
3-1	Antenna patterns.	3-3
3-2	Antenna measurement coordinate system . . .	3-4
3-3	Antenna pattern at various radii.	3-5
3-4	Antenna pattern for high loss-tangent . . .	3-6
3-5	Skirt dipole antenna patterns	3-7
3-6	Magnetic dipole antenna patterns.	3-8
4-1	Tape recording system	4-10
4-2	Comparison of filtered and unfiltered data.	4-11
4-3	Filter generation	4-12
4-4	Dielectric properties measurement	4-13
4-5	Antenna rotating fixture (simplified) . . .	4-14
4-6	Antenna measurement circuit	4-15

ABSTRACT

The Surface Electrical Properties (SEP) Experiment was performed as part of the Apollo 17 Mission. This report describes measurements made with a scale-model simulation of the experiment. Included is an extensive set of traverse patterns taken with a dielectric fluid overlying metal and dielectric plates both with and without the addition of various structures designed to simulate various features such as crevasses, craters, and buried objects. Horizontal-interface traverses are shown to generally agree with theoretical calculations. Various experimental techniques used are discussed and an index to traverses recorded on magnetic tape is given.

1.0 INTRODUCTION

This is the final report dealing with modeling activities carried out in support of the Apollo 17 Surface Electrical Properties Experiment¹. The modeling activities consisted of operation of a scale model of the SEP experiment, which utilized a technique known as radio-interferometry depth sounding^{2,3} to study the electrical properties of the upper layers of the moon's surface. Figures 1-1 and 1-2 illustrate the SEP experiment and the model respectively.

Previous reports^{4,5} have discussed in detail the general design and operation of the model and have included detailed work concerning antenna patterns and traverse patterns (recordings of signal strength vs. transmitter-receiver separation) taken without a dielectric medium present. In addition, the last report contained a preliminary set of curves taken using dielectric fluid and the metal plate.

The purpose of this final report is to exhibit the extensive set of traverse patterns which the model was designed to produce. Section 2.1 describes traverses made with a low-loss dielectric fluid over a metal plate at various depths and inclinations. Section 2.2 describes similar data collected using a lossy dielectric slab in place of the metal plate, with the addition of traverses taken using objects simulating craters, crevasses, spheres, and irregular blocks positioned in the dielectric fluid. Both the above sections contain comparisons of the experimental horizontal-interface traverses with theory; general agreement is apparent.

Section 2.3 discusses traverses made using the dielectric fluid with its loss tangent adjusted to various values. This group includes traverses taken both with and without the metal plate using objects simulating craters, crevasses, mountain-sides, and submerged steps and ridges. Section 2.4 describes data collected using spheres positioned in the low-loss fluid both with and without the metal plate. Section 2.5 details traverses collected using flat circular metal plates simulating a buried waste dump at the DYE-3 site in Greenland. Figures 1-3, 4, 5 illustrate the various complex structures used.

Section 3 describes antenna results obtained since the last report and Section 4 discusses various experimental details. Section 5 contains an index to data which has been recorded on digital tape.

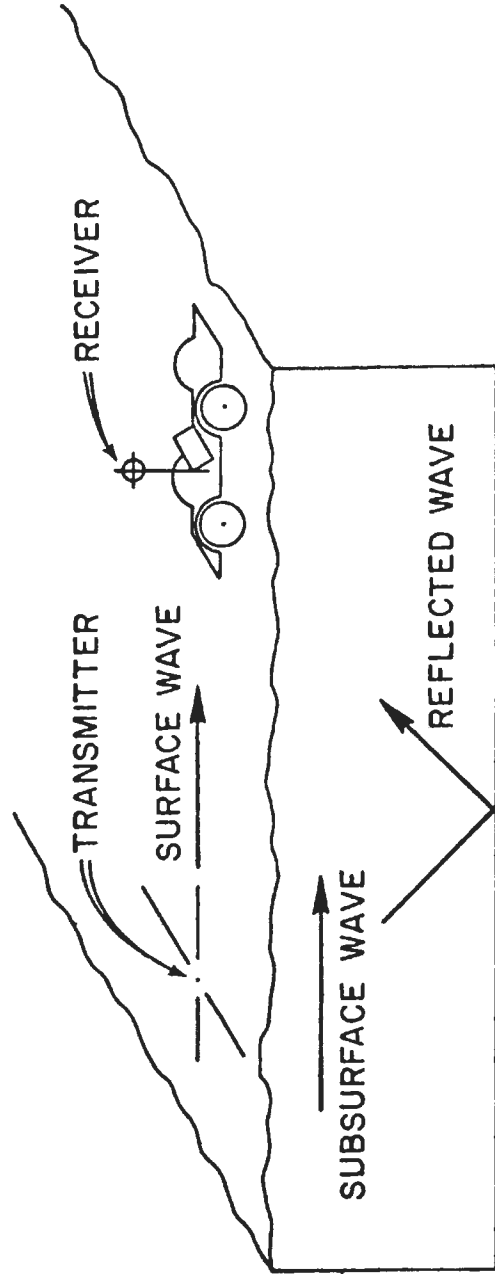


Figure 1-1. — The SEP experiment.

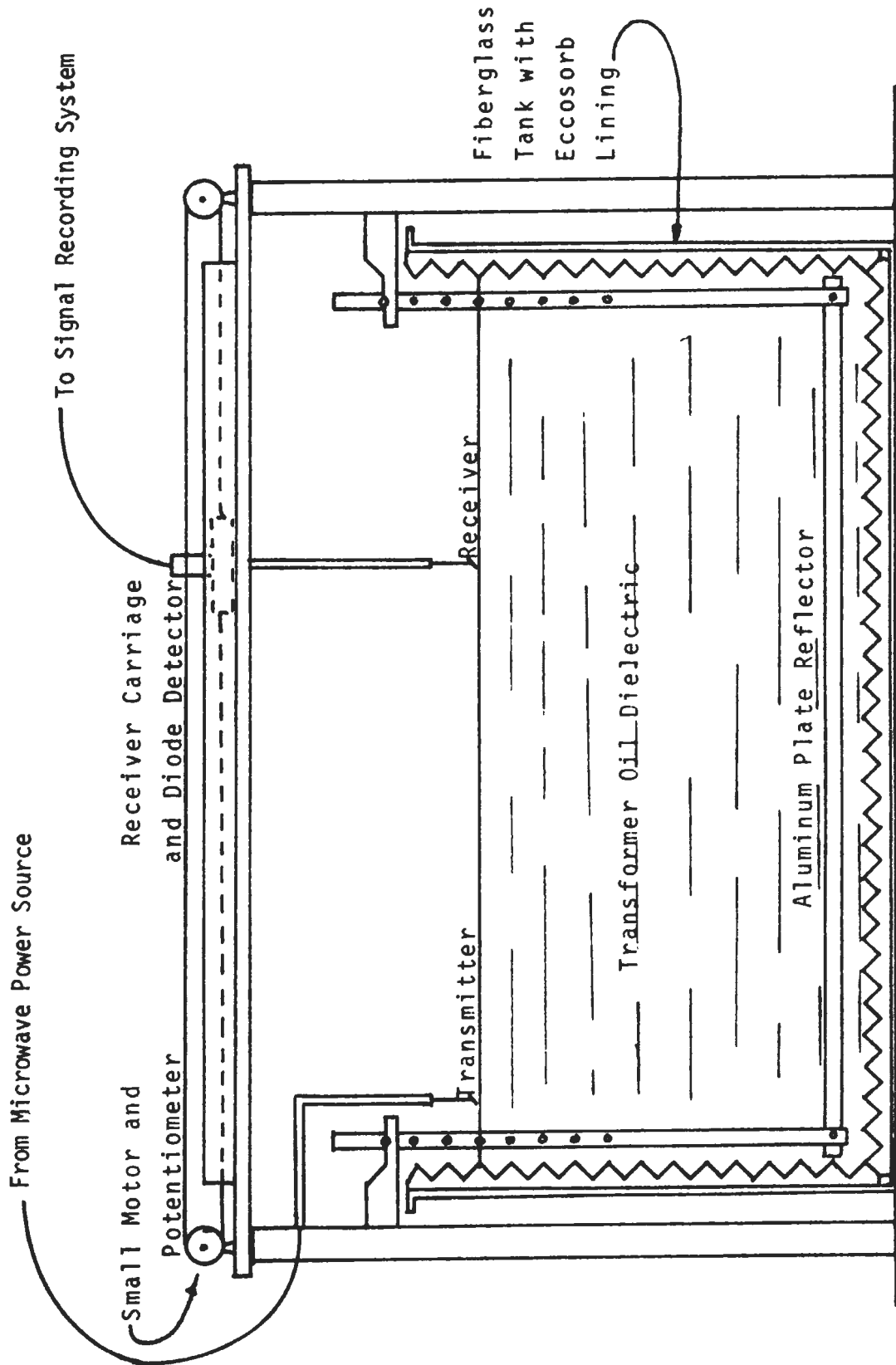


Figure 1-2. — SEP scale model. Side view.

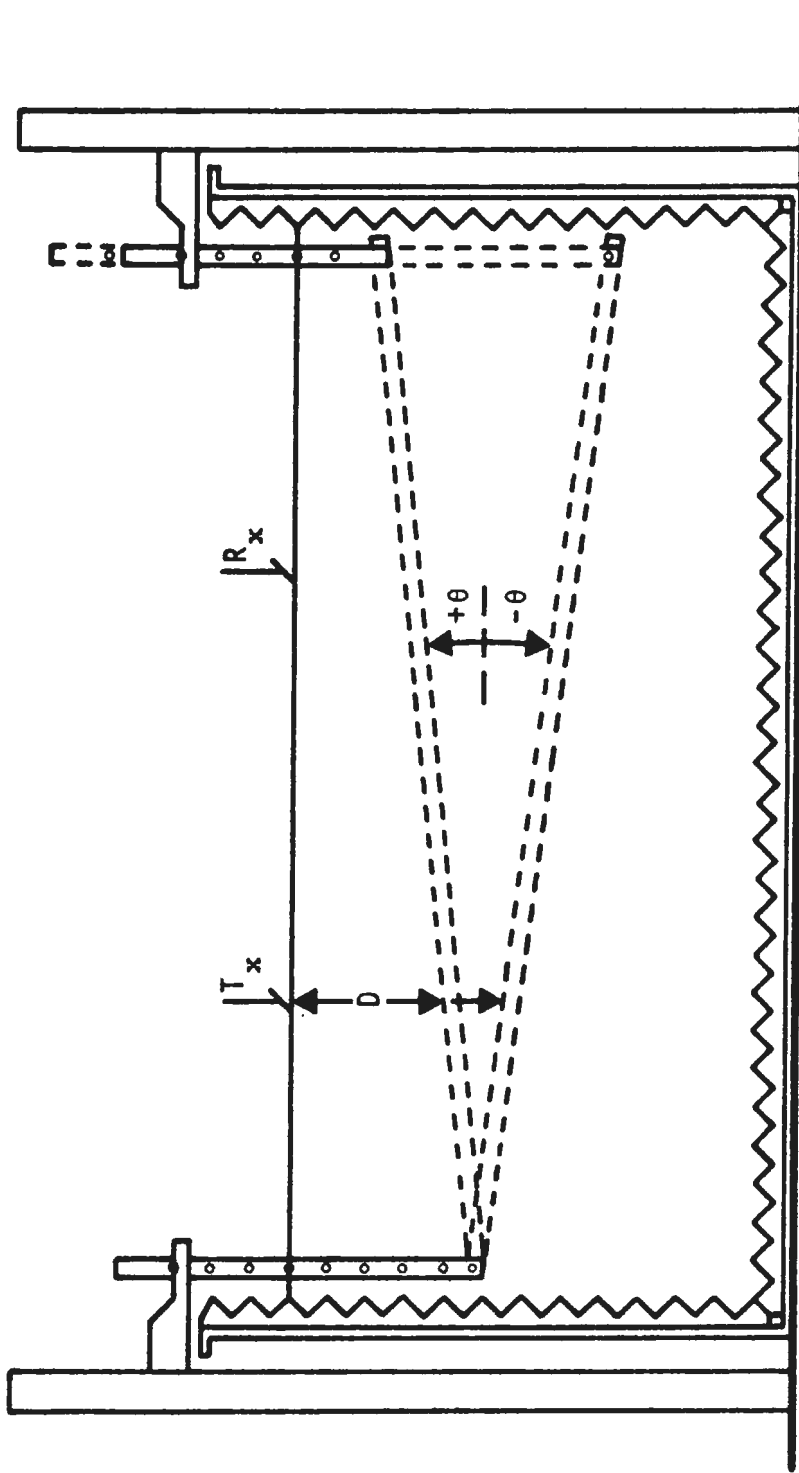


Figure 1-3. — Plate/slab - forward slopes. Side view of tank.

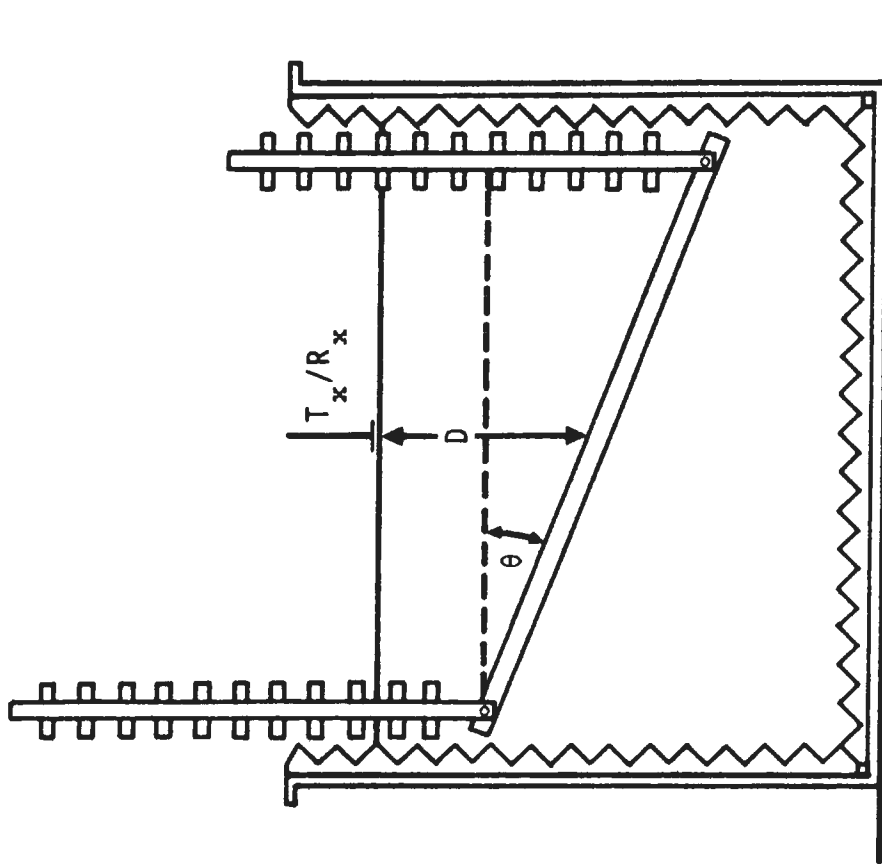


Figure 1-4. - Plate - lateral slopes. End view of tank.

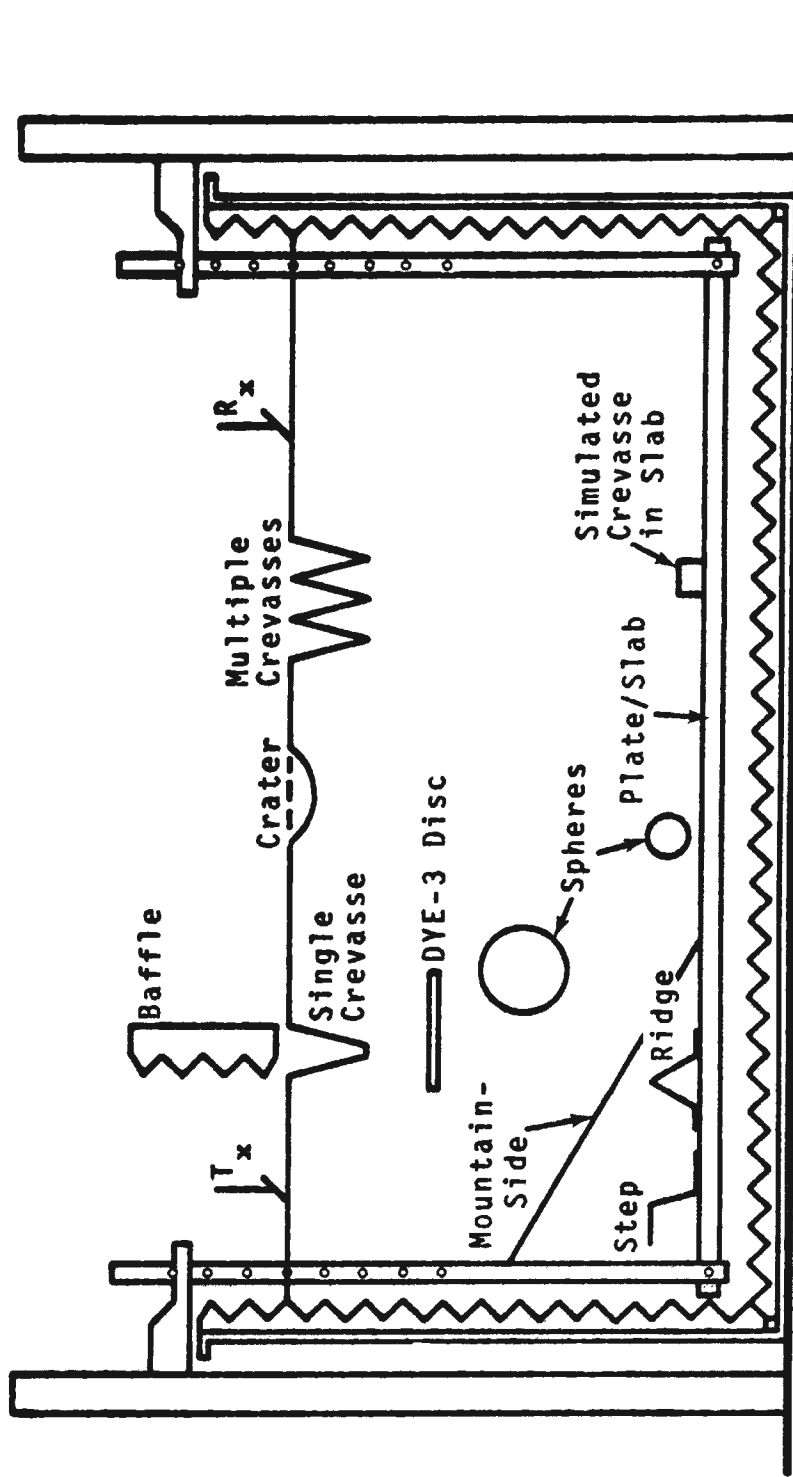


Figure 1-5. — Mélange of structures used. Side view of tank.

2.0 TRAVERSE RECORDINGS

All data discussed in this report were obtained with half-wave dipoles as transmitter and receiver. Transmission power was in the range 1 milliwatt to 1 watt at a fixed frequency of 5.9 GHz (corresponding to a freespace wavelength (w_1) of 5.08 cm). Signal detection was performed with a 1N23 microwave diode.

The receiving antenna was driven at $.127 w_1/\text{sec}$ down the center of a $30 w_1$ long \times $15 w_1$ wide \times $15 w_1$ deep fiberglass tank (see Figure 1-2) lined with microwave absorber (Eccosorb CV-3). The tank was filled with Shell Diala transformer oil having dielectric constant 2.16 and loss tangent .002.

Except for a few curves in Section 2.3 all traverses measure the E-Phi broadside component, i.e. both the transmitter and receiver were horizontal and perpendicular to the traverse direction. Toward the final stages of the model work it was discovered that agreement between model and theory could be greatly improved in the $.6 w_1$ depth-range for a horizontal metal plate by switching from simple half-wave dipole antennas to more sophisticated and better balanced slot-fed half-wave dipoles⁶. These new dipoles were used to collect all data in Sections 2.1 and 2.2 except 2.1.3. All other data were collected with simple dipoles.

In order to minimize unwanted background signal, in some cases in Section 2.1 and 2.2 a sheet of microwave absorber was positioned vertically in front of the transmitter at $1.5 w_1$ range. This "baffle" (see Figure 1-5) extended downward to $.5 w_1$ above the oil's surface. Traverses for which

the baffle was in place can be identified by the fact that the recording begins at approximately 3.25 wl range. Documentation of the small effect of the baffle can be obtained by comparison of the following pairs of redundant traverses: 1, 32; 2, 18; 87, 91; 88, 98; 89, 107; 90, 115.

The traverses included in Section 2.1 through 2.3 are plots of digitally processed data which were originally recorded on magnetic tape. The purpose of the tape is to permit future convenient access to model data for manipulation and interpretation. The digitization process introduced high-frequency noise into the data which was removed by filtering. In some cases additional filtering was used to attenuate undesirable background signal. The digitization process also introduced small range errors which seem to be reflected generally in a shift of the traverses to the right of about .1 wl. In cases where extremely high range resolution is needed the original X-Y recorder plots of the raw data should be referred to. See Sections 4.1, 4.2, and 5 for details on recording and processing and an index to digitized traverses.

Each traverse in Sections 2.1 through 2.3 is labeled to the right with a run number and other special information. In addition each traverse has a reference mark on the vertical axis which corresponds to a fixed received power-level of nominally -25 dBm. Since the transmitter power-level is given for each group of traverses a comparison of absolute signal levels between any two given curves is possible. A convenient way to do this is to adjust each reference mark upwards at the rate of 1" for each 15 dBm of transmitter power; each adjusted reference mark then represents a signal power-level 25 dB below the transmitter power.

The threshold power-level of roughly -62 dBm corresponds to approximately 2.5" below the -25 dBm reference mark.

2.1 TRAVERSES OVER A METAL PLATE

In order to simulate a buried perfectly reflecting layer, an aluminum plate of dimensions $30 w_l \times 15 w_l$ was designed for positioning in the metal tank at various depths and inclinations. The traverses taken accordingly are grouped in Appendix A. Each curve is labeled with plate depth (D) and inclination (θ). All experimental curves in Appendix A were digitally filtered to remove unwanted signal of period approximately $.5 w_l$ apparently associated with undesired reflections off the tank wall at the opposite end from the transmitter. These reflections interfere with the direct transmitter energy to set up a standing wave pattern through which the receiver moves. The filtering has attenuated by roughly 50 percent the close-range oscillations present for the greater plate depths (see Section 4.2).

2.1.1 Horizontal Metal Plate

Figures A-1 – A-3 contain plots of digitized data taken over the full range of metal plate depths used. Figures A-4 – A-10 are similar plots for small depth increments at shallow depths taken using the baffle. The dashed-line curves are theoretical plots of the power associated with the H_z field component calculated using normal-mode theory developed by Dr. A. P. Annan. Where the depth used for theoretical calculations is different from the value given in column "D", the correct depth is indicated near the end of the theory plot.

Generally good agreement between experimental and theoretical data is apparent. Some disagreement at short-range is apparent, especially near .7 w_l and 1.18 w_l depths and at 3 w_l and 4 w_l depths. These disagreements are probably associated with inaccuracies in the mode-theory calculations near certain critical depths. These depths are characterized by a normal mode propagating at or near the critical angle for the oil-air interface and are given by

$$d_m = (2m - 1) [\lambda/4(K' - 1)^{1/2}] \quad m = 1, 2, 3 \dots$$

Where for $K' = 2.16$ the bracketed quantity equals .2321 w_l. Thus .696 w_l, 1.16 w_l, 3.02 w_l, and 3.95 w_l are critical depths possibly connected with the above cited disagreements; indeed recent numerically calculated normal-mode theory (see dotted curves in Figures A2, A6, A7, and A10) disagrees in each of these cases with regular normal-mode theory. While the disagreement between model and theory is in no case completely eliminated by the introduction of this latest improvement in the theory, these discrepancies between the results of different methods of computing the theory at least serve to indicate the difficulty of theoretical calculations near the critical depths. In complete contrast to model results the normal-mode theory shows an absence of oscillations in a range extremely near the critical depths (the dashed lines at .69 and 3 w_l depths give partial evidence of this); the numerically calculated theory at least gives no hint of these nulls. It should be pointed out that these regions of disagreement associated with the critical depths are quite small and are consequently probably more of academic than practical concern.

The apparent poor fits at the shallowest depths are probably due to the low signal-levels being dominated by background signal. A smooth, horizontal line indicates that the total signal is below system response.

Depth accuracy for these horizontal-plate traverses is on the order of .01 wl except for both 1 wl curves where a sharp object with a length of 1 wl was used to locate the oil's surface very precisely. At many of the depths shallower than 1.5 wl the fits could doubtlessly be improved by trying different theory depths near the approximate experimental depth.

2.1.2 Metal Plate-Lateral Slopes

Figures A-11 – A-13 contain traverses in which the metal plate was tilted laterally (see Figure 1-4) at various depths. Each curve is labeled by the approximate plate depth (D) under the traverse path and by the approximate lateral inclination (θ). Analysis of these curves and comparison with corresponding horizontal cases indicate a general rule-of-thumb that lateral inclinations not greater than about 2° per wavelength depth do not substantially affect the traverse pattern. Run 47 for 1 wl depth and Run 44 for 2 wl depth exceed this rough limit and are distorted relative to more nearly horizontal runs.

2.1.3 Metal Plate Forward Slopes

Figures A-14 – A-22 contain traverses in which the metal plate was tilted along the forward direction (see Figure 1-3). Each traverse is labeled with the depth of the plate under the transmitter (D) and the angle of inclination (θ) of the plate. These numbers are both approximate; the depth figures are too

small by about $.02 \times \theta$ and θ is 1-2 percent too large. Positive angles of inclination are those for which the plate is deepest at the transmitter end of the tank. It might be noted that the depth of the far end of the plate is roughly $D - \theta/2$.

A general tendency is apparent for the broad peak associated with the angle of the transmitter pattern lobe to shift to longer range as inclination decreases. The expected range of the peak is given by $2d \cos\theta \sin(\beta-\theta)/\cos(\beta-2\theta)$. These ranges have been plotted in Figures A-14 - A-22 as circles and crosses respectively for β chosen first as the critical angle 42.9° and second as the experimentally measured lobe-angle of 57° . The peak seems to usually lie between these two values.

Associated with the shift of the broad peak to greater range there is a typical increase in the period of the far-field oscillations.

Other than these general observations the traverse recordings are quite sensitive to forward slopes, in contrast to the case for lateral slopes discussed in Section 2.2. Even at a 6 wl depth a change of $\pm 1^\circ$ from the horizontal produces a sizeable effect at far-field. Consequently, it appears that if one wishes to analyze in detail peaks and nulls in field data where even slight slopes are possible, theoretical plots for the non-horizontal case will be an absolute necessity.

2.2 TRAVERSES OVER A DIELECTRIC SLAB

In order to model a dielectric interface, a epoxy slab measured (see Section 4.4) to have dielectric constant 6.75 and loss tangent .11 was poured from a 10 percent carbon blend obtained by mixing the following epoxy materials sold by Hysol (Olean, New York): DP-8-5193 (15 percent carbon concentrate), R9-2039 (resin), and H2-3404 (hardener). The relatively high loss tangent was chosen in order to minimize unwanted reflections off the oil-air interface on the bottom side of the slab. The slab was positioned in the same manner as the metal plate. Its dimensions were 30 w1 long × 6 w1 wide × approximately 2 w1 thick.

It will be noted that the noise level of the dielectric slab traverses (Appendix B) is worse than for the metal plate traverses (Appendix A). This is probably due to the fact that unwanted reflections off the walls and superstructure of the tank remain constant while the amount of desired reflection off the slab is less than for the metal plate. In contrast to the case for the oil-metal interface (100 percent reflection with 180° phase shift), energy incident normally on the oil-slab interface is only 28 percent reflected and is shifted roughly 175° in phase upon reflection. For this case the complex normal reflection coefficient is given in polar coordinates by the approximation:

$$\frac{(K_1')^{1/2} - (K_2')^{1/2}}{(K_1')^{1/2} + (K_2')^{1/2}} \tan^{-1} \left(\frac{\tan \delta}{\left(\frac{K_1'}{K_2'}\right)^{1/2} - \left(\frac{K_2'}{K_1'}\right)^{1/2}} \right) .$$

The traverses discussed in Sections 2.2.1 and 2.2.2 were filtered to remove the half-wavelength background while those in Sections 2.2.3 – 2.2.7 (except Figures B40 and B41) were filtered only enough to remove the noise introduced by digitization (see Section 4.2).

2.2.1 Horizontal Dielectric Slab

Figures B-1 – B-3 and B-4 – B-10 contain large depth increment and small depth increment curves (taken using the baffle), respectively, for the dielectric slab horizontally positioned. Theoretical plots are superimposed as dashed lines; a value of 6.25 rather than 6.75 was used for the lower medium's dielectric constant, but the difference is insignificant. The fits are comparable to those for the metal plate, except for a better consistency probably because of lessening critical-depth theory problems due to the slab being a poorer reflector. Low signal-levels are again apparent at the shallower depths. Some disagreement is possible due to reflections off the bottom side of the slab. In Figure B-1 a fairly good agreement is obtained with a theoretical curve for the case of a 1λ thick slab over oil (dotted line).

2.2.2 Dielectric Slab -- Foward Slopes

Figures B-11 – B-18 contain traverses for which the slab was tilted along the forward direction (see figure 1-3). The curves are analogous to Figures A-14 – A-22 discussed in Section 2.1; the same comments made there apply here and each recording is marked with the identical expected peak positions.

2.2.3 Crater Over Dielectric Slab

Since the crater Camelot was situated adjacent to the Apollo 17 EVA 2 it was decided to use a model simulation of Camelot to briefly investigate its possible effect. Figures B-19 – B-22 contain the results; they strongly indicate that Camelot has no significant effect.

Camelot has approximate dimensions of 600 m diameter × 100 m depth. It was centered approximately 1200 m from the SEP transmitter and its nearest edge was approximately 100 m from the EVA 2 traverse-line. Estimates are that at the Apollo 17 site a $K' = 3.54$ dielectric medium of depth 20 m overlies a $K' = 6$ medium. Our use of the $K' = 2.16$ oil as the upper layer is a significant weakness of our modeling in this case.

Figure 2-1 illustrates with open circles how Camelot would look relative to the model tank at the different SEP frequencies. The corresponding scaled interface depth (20 m) is also given. The cross-hatched circles indicate the positions of the simulated craters (made from polyethylene foam) used in conjunction with the dielectric slab for Figures B-19 – B-22. Actual slab depths used are indicated.

Each run is labeled with the slab depth (D) and range (R) to the center of the simulation craters. The notation "REF." denotes reference traverses without craters.

Runs 143 and 146 for craters centered on the traverse-line for slab depth 1 w1 both show modest deviations from the reference Run 145; however, moving the craters off-center

until their edges are $1/4 w_l$ away from the traverse-line (i.e. just out from under the $1/2 w_l$ receiver) partially removes the deviation in both cases. The same crater centered for slab-depth $.5 w_l$ (Figure B-21) also shows no deviation.

Run 150 was taken with one-quarter (see Figure 2-1) of a $3.5 w_l$ crater positioned with its edge $1 w_l$ distant from the traverse-line for a $3 w_l$ deep slab. The same null results are present as for the other off-center traverses above. Since Camelot itself was decidedly off center we must therefore conclude that Camelot did not affect the Apollo 17 SEP traverses.

2.2.4 Crevasses Over Dielectric Slab

Figures B-23 – B-26 contain traverses taken using polyethylene-foam simulated crevasses over the slab (Figure 1-5). Section 2.3.4 will contain a discussion of a more extensive study done using the metal plate. This brief study with the slab was undertaken to extend the validity of this other study to the case of dielectric interfaces, and indeed the results in both cases are quite similar.

In the present case single crevasses of widths approximately $.3 w_l$, $.15 w_l$, and $.1 w_l$ were positioned across the traverse path. These crevasses had square cross-sections of approximately $3 w_l$, $1.5 w_l$, and $.75 w_l$ dimensions, respectively. Each traverse is labeled with slab depth and range of the crevasses.

Runs 152 – 158 (Run 154 is their common reference) illustrate results for each of the three sizes positioned

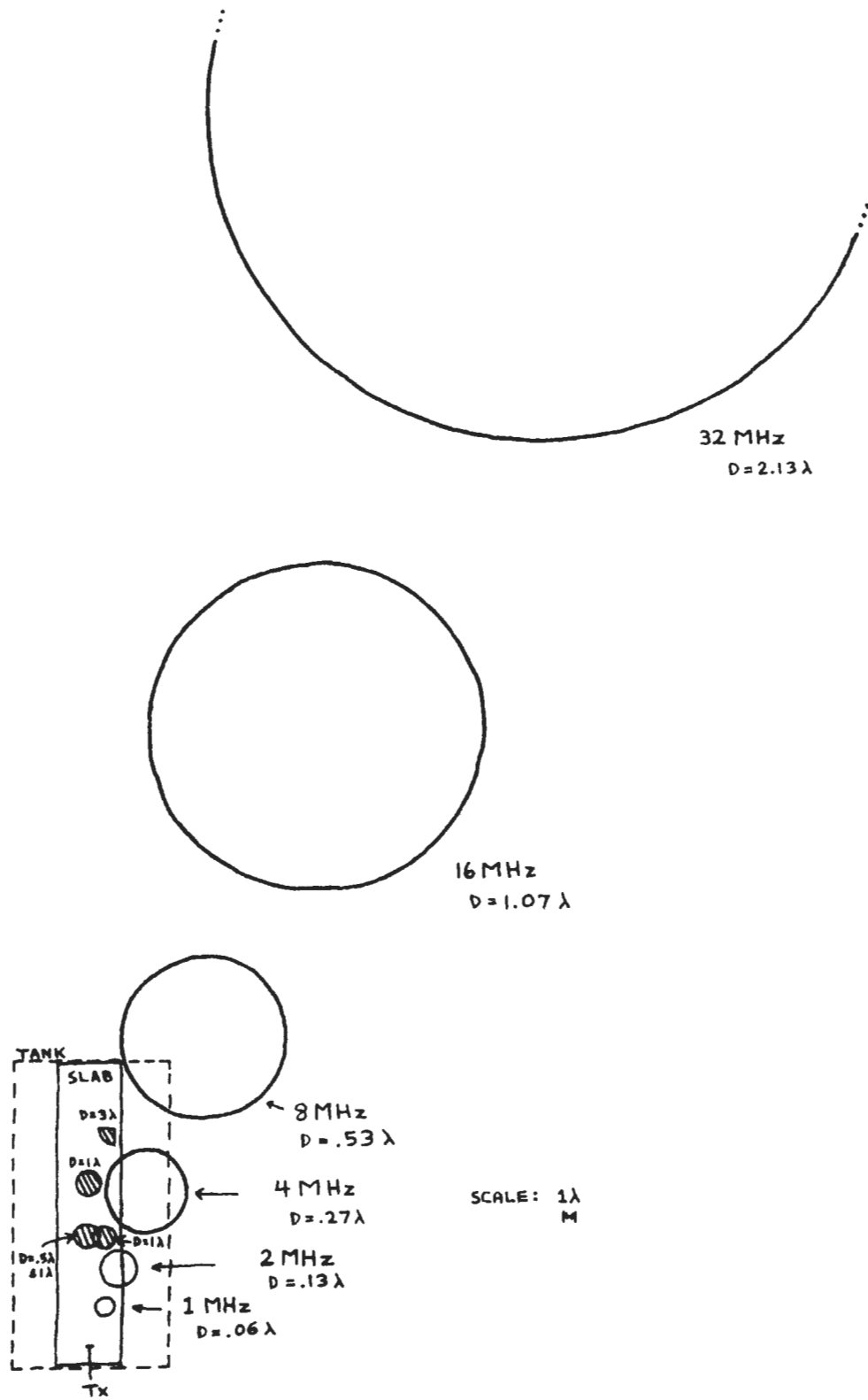


Figure 2-1. - Crater simulation.

at 5 wl and 15 wl range over a 4 wl deep slab. At the longer range all three sizes produced the characteristic .4 wl ripples ending abruptly at the crevasse. At the closer range the crevasses (particularly the largest one) seemed to act to jumble up the near-in oscillations.

The smallest crevasse was used again (Figure B-26) for a 1 wl slab depth and this time the preceding ripples are visible at both near and far range.

Clearly, crevasses may be expected to be as easily visible for dielectric interfaces as for a perfectly reflecting interface.

2.2.5 Spheres Over Dielectric Slab

This is an abbreviated version of a more complete study (see Section 2.4) of the effect of spherical scattering objects. Here again we can conclude that results for the metal plate and dielectric slab are similar.

Figures B-27 – B-29 illustrate the effect of varying sizes and composition (metal and dielectric constant $K' = 6$) of spheres centered 4 wl deep at 5 wl range, with the slab positioned 6 wl deep. The .5 wl diameter spheres seem to produce minimal effects, especially at longer range. At 1 wl diameter the effect of the spheres becomes dominant and at 2 wl diameter the traverse is totally changed from the reference.

Figures B-30 and B-31 illustrate the effect of varying range for the 1 wl diameter, $K' = 6$ sphere positioned 4 wl

deep over the 6 wl deep slab (the reference traverse would still be run 162 in Figure B-27). There is little effect for 0 wl but considerable effect at 5 wl. At 10 wl and greater range there is a characteristic sequence of about three following peaks of period approximately 1 wl which begin directly above the sphere. At 15 wl and greater range small rapid crevasse-type echoes preceding the sphere appear.

Figures B-32 – B-33 feature the same 1 wl diameter, $K' = 6$ sphere now sitting directly atop the dielectric slab positioned at 2 wl depth. Here again, at 0 wl range the sphere has little effect. At 5 wl and especially at 10 wl range the sphere's presence causes large distortions in the traverse recording. Interestingly, for positions greater than 10 wl range the total distortion becomes less, even for the parts of traverses lying beyond the sphere range. For all non-zero sphere ranges the crevasse-echo type ripples are present, especially for the 10 wl range sphere.

Figure B-34 illustrates the lessening of the amplitude of these ripples as the sphere is moved to one side of the traverse path. Moving the 5 wl range sphere 1 wl to the side practically eliminates its effect. However, the 10 wl range sphere had to be moved to 1.5 wl off-center to achieve the same effect, perhaps only because the ripples were much larger to begin with.

2.2.6 Simulated Crevasse in Dielectric Slab

To obtain some sort of idea about the effect of a crevasse located in the buried dielectric layer without actually cutting into the dielectric slab, a rectangular

strip of polyethylene foam was attached to the top of the slab (Figure 1-5). This was done partly under the assumption that the effects of such a crevasse would be associated with reflections off its top rather than off its vertical interfaces. In position the two strips used had a vertical dimension of $.5 w_l$ and were $4 w_l$ long; their dimensions along the range-axis ("width") were $.25 w_l$ and $.5 w_l$.

Figure B-35 illustrates the effect of the $.5 w_l$ wide simulated crevasse at ranges of $5 w_l$ and $15 w_l$ over the $2 w_l$ deep slab. At the $5 w_l$ position, this crevasse produces gross distortions out to $15-20 w_l$ while contributing near-in oscillations of approximately $.75 w_l$. At the $15 w_l$ position, this crevasse contributes gross distortions at ranges beyond its position while also producing preceding echo-type ripples which drop dramatically in frequency as the receiver passes over the crevasse. The $.25 w_l$ wide crevasse in Figure B-36 contributes the same type disturbances substantially reduced.

In Figure B-37 the $.25 w_l$ simulated crevasse is positioned at $5 w_l$ and $15 w_l$ ranges over the $1 w_l$ deep slab. Its effect at both positions is seen to be small.

2.2.7 Random Blocks on Dielectric Slab

To get some idea of the distorting effect of small irregular "blocks", thirteen scraps of the same ($K' = 6.75$, loss tangent = $.11$) material as the slab were arranged on the slab in an area $3 w_l$ wide extending out to $13 w_l$ range. The arrangement is indicated in Figure B-38 to scale. Each block is labeled L ("large" -- approximate cubes of about $.6 w_l$ dimensions), M ("medium"), and S ("small" -- dimensions about $.15 w_l$).

Traverses were recorded at integer horizontal depths from 1 wl - 6 wl. The results (Figures B-38 -- B41) (see Section 4.2 for filtering details) are disappointing. Only at one depth (4 wl) is there even a remote resemblance to corresponding traverses taken without the blocks (Figures B-1 - B-3). Although this is admittedly a small sample, certainly indications are that buried blocks must be a small fraction of a wavelength before their effects can be treated as perturbations and hopefully filtered out. A very crude quantitative estimate can be obtained as follows. A .6 wl block is about .9 "wavelengths-in-the-medium" for the oil. If we arbitrarily choose .5 wavelengths-in-the-medium as our maximum-size standard, then for a $K' = 4$ upper layer, buried blocks would necessarily be .25 free-space wavelengths or under before one could hope to obtain useful SEP data.

2.3 VARIABLE-LOSS DATA

A variety of data was collected both with the pure oil and with the oil doped to various loss-tangent values with benzonitrile obtained from Velsicol Chemical Corporation (Chicago). Unfortunately, the high loss-tangents contributed to low-signal levels and consequently much of this data suffers from high noise levels. The curves discussed below were plotted from digitized data. The traverses included in Sections 2.3.1, 2.3.2, and 2.3.6 were filtered to remove half-wavelength background; all other curves were filtered only to remove digitization noise (see Sections 4.1 and 4.2). The original curves were incorporated in a memo entitled "SEP Simulation Model V"⁷. The approximate measured values of loss tangent/dielectric constant are as follows: .002/2.16, .012/2.17, .025/2.21, .042/2.21, .073/2.30, .142/2.48 (benzonitrile 3 percent by volume).

2.3.1 Half-Space at Various Loss-Tangents

Figures C-1 and C-2 include traverses recorded at each loss-tangent used, with the tank empty of objects. These traverses were intended to simulate half-spaces but obviously they do not, apparently because unwanted reflections off the tank wall and superstructure were too large. Therefore, these traverses can more reasonably be taken as measurements of the background signal level for the oil-tank. Two traverses are recorded at .002 loss-tangent -- Run 199 with the transmitter-receiver pair identically oriented and Run 200 with the receiver rotated 180°. The odometer signal for Run 201 was artificially introduced during digitization, since it was inadvertently left out during recording of the FM data.

2.3.2 Horizontal Metal Plate at Various Loss-Tangents

Figures C-3 -- C-17 contain suites of large-increment depth curves for each of the six loss-tangents used. As loss-tangent increases the effect of the plate diminishes to the point that at longer range the traverse recording is independent of plate depth, i.e. the signal associated with the plate becomes buried in the high background signal level. Insofar as comparisons can be made, the traverse pattern changes little with loss-tangent. The odometer signals for Runs 216-222 were introduced artificially as in Section 2.3.1. Comparison of plots of the digitized and original data showed that no significant error was introduced by this.

2.3.3 Crevasses in Half-Space

Figures C-18 – C-22 contain half-space traverses taken with single crevasses (Figure 1-5) simulated by a wedge of lossless, non-porous polyethylene foam of estimated dielectric constant 1.1. It was desired to simulate a crevasse of length 30 m, depth 30 m, and width 3 m at the top tapering downward to zero width. At 32 MHz this corresponds to a crevasse of dimensions approximately $.3 w_l$ top width \times $3 w_l$ length \times $3 w_l$ depth, at 16 MHz $.15 w_l \times 1.5 w_l \times 1.5 w_l$, and at 8 MHz $.1 w_l \times .75 w_l \times .75 w_l$. The crevasses were oriented at 0° , 45° , and 90° angles (θ in the figures) relative to the traverse path, with 0° corresponding to the width dimension lying along the traverse line. All the single crevasses were centered at $5 w_l$ range (R).

Two field components were measured: broadside E-Phi (both dipoles horizontal and oriented perpendicularly to the traverse-line) and E-Rho (same as E-Phi broadside except the receiver is oriented parallel to the traverse-line). All crevasse recordings have been filtered to remove only high frequency digitization noise. However, this is not true of the reference traverses in Figure C-18 from which most of the half-wavelength signal has been removed. The lowest loss tangent of .002 was used for all curves in this section.

Analyzing Figures C-18 – C-22 it is apparent that only Runs 257 and 263, both E-Phi components with crevasse cutting perpendicularly across the traverse-line, contain even barely visible perturbations due to the single crevasses.

Figures C-23 and C-24 contain traverses taken with a set of six $.15 \text{ wl} \times 1.5 \text{ wl} \times 1.5 \text{ wl}$ (16 MHz) crevasses all parallel and spaced 1.5 wl apart. The crevasse set was rotated about its center, which was positioned at 9 wl range (R). At the 0° position the array extends from 5 wl to 13 wl. As in the single crevasse case, the only significant distortions are for the E-Phi perpendicular-crevasse case.

2.3.4 Crevasses Over Metal Plate

Figures C-25 – C-37 contain traverses taken with simulated crevasses positioned over the metal plate which was held at a constant 4 wl depth. The crevasses were positioned in an identical fashion to that of the previous section and the same terminology is used for labeling the curves. In addition to traverses analogous to the low-loss traverses in the previous section, data was collected at three higher losses for the E-Phi component only. Note here also that the E-Phi reference curve has been filtered to remove .5 wl signal; all other curves have been filtered as in the preceding section.

Figures C-26 – C-29 illustrate the sensitivity of the size of the distortion produced to the size of a single crevasse placed at 5 wl range. The .3 wl wide (32 MHz) crevasse produces sizeable distortions for all components and orientations while the smaller .15 wl wide (16 MHz) crevasse causes significant distortion only for the E-Phi perpendicular crevasse case. Note in Runs 276 and 282 that the period of the disturbances associated with the near-in (5 wl range) position is about .6 wl in contrast to the characteristic .4 wl echo-ripple produced by more distant

crevasses (see below and Section 2.2.4). Figures C-30 and C-31 show again the smallness of the perturbation produced by small crevasses (see Runs 226 and 236 for reference traverses).

Figures C-32 and C-33 illustrate the effect of the set of six 16 MHz crevasses. In contrast to the half-space case, distortions are produced for all components and orientations. Note the shift downward of the period of the oscillations in Run 294 as range increases. Figures C-34 – C-37 contain recordings at higher loss-tangents of the E-Phi component at 0° and 90° orientations of multiple-crevasses. Comparing Figures C-35 and C-36 it seems apparent that there is a sharp drop-off in crevasse visibility between 16 and 8 MHz.

2.3.5 Crater

During the SEP Juneau Ice-Field Expedition a small crater was formed by use of explosives. Rather unsuccessful efforts were made to model this feature. The crater has approximate dimensions of 11-14 m diameter × 3.5 m depth, and was located at a range of 263 m at an offset from the traverse line of 10 m. These dimensions were modeled at 32 and 15 MHz with polyethylene foam objects.

Figures C-38 – C-40 illustrate the effects of the simulated crater at various loss-tangents for the half-space case and for one arrangement over the 4 wl deep plate. Without exception, comparison of these curves with the corresponding reference curves in Figures C-1, C-2, and C-14 reveals only very minor perturbations associated with the

crater simulants. Undoubtedly this is partially due to the high loss-tangents and consequent large background signal. It seems quite likely that for optimum conditions crevasse-like ripples should precede a crater which is placed quite near the traverse-line; however, this study indicates that these ripples would be small in absolute amplitude.

2.3.6 Mountain, Step, and Ridge Simulations

This last group of digitized curves (all E-Phi broad-side) was concerned with studying the possible effect of the Juneau Ice-Field Data of the valley side and of submerged bottom irregularities (Figure 1-5). Since these features would have been most visible at the lower frequencies where the loss-tangent of ice is greatest, modeling was done at high loss-tangents where previously noted high background signal levels existed. The longer range portions of the recordings should be ignored due to high background signal levels, since traverses at the low-frequencies simulated are typically short in terms of wavelengths, and since in some cases the simulated objects did not extend the whole length of the tank.

Figures C-41 – C-45 contain traverses taken using flat metal plates to simulate the presence of a reflective mountain-side which is submerged and inclined at 30° from the horizontal. The actual distance in the model of the transmitter from the base-line of the mountain-side was varied to maintain the scaled distance corresponding to 173 ft. (approximately 1.4 w_l, .7 w_l, and .35 w_l at 8, 4, and 2 MHz, respectively). Traverses were run in three

directions relative to the base-line; θ is the angle between the traverse-line and base-line (e.g., 90° corresponds to a traverse made perpendicularly away from the mountain-side). The modeled frequency in MHz is given for each curve. It can be seen from the effect of orientation changes that the simulated mountain-side has a large effect; comparison of Figures C-42 and C-43 at short range indicates that changes in orientation are dominant over changes in transmitter to base-line distance.

Figures C-46 – C-51 illustrate the effect of an irregularity in a submerged horizontal reflective layer in the shape of a 200 ft. rise or step in the depth of the bottom layer. The connection between the 490 and 290 ft. deep portions was a 45° ramp. This feature was modeled with metal shapes at 8, 4, and 2 MHz at loss-tangents of .042, .073, and .142, respectively. The 490 ft. deep lowest portion of the bottom was 4 w1, 2 w1, and 1 w1 deep at these respective frequencies (see traverses labeled as references).

The transmitter position and traverse direction are indicated for each traverse by a two digit number in the column labeled "TR" ("transmitter-receiver"). The first number (1 equals "top", 2 equals "bottom") indicates whether the transmitter was positioned over the top of the ramp or the bottom. The second number (1 equals "toward", 2 equals "away", 3 equals "along") indicates whether the traverse-path was toward the raised portion of the bottom, away from it, or along the 45° connecting ramp. Figures 50 and 51 contain small sketches indicating the step's position and size relative to the oil-depth at 2 MHz. At the 4 and 8 MHz frequencies the step is twice and four times larger, respectively.

For a given loss tangent, runs having the same second digit differ only in that the step was moved slightly relative to the transmitter. The differences in these recordings are therefore a useful measure of the effect of the ramp itself. Comparisons of the traverses in which the ramp does not lie under the recorded portion of the traverse (those labeled 22, 12, and 23) with the corresponding reference traverses also indicate the visible effect of the ramp. Both these comparisons indicate that the dominant nature of the presence of the steps tends to diminish as the modeled frequency decreases and the loss tangent correspondingly increases. For medium ranges the curves labeled 21 and 11 are almost certainly controlled by the 290 ft. depth, i.e., they would resemble simple horizontal plate traverses modeling a 290 ft. reflector depth.

Figures C-52 — C-54 contain traverses simulating a reflective 200 ft-high ridge having 45° sides and positioned on a horizontal reflecting bottom located at a depth of 490 ft. These traverses are analogous to the step traverses discussed immediately above and are notated similarly. Figure C-54 indicates the ridge size and position at 2 MHz. Reference curves for Figures C-52, C-53, and C-54 are Runs 335, 341, and 347 respectively.

As might be expected, the six ridge traverses labeled "22" and "23" are identical to the corresponding six step traverses similarly labeled. Comparison of the remaining three traverses (labeled "21") to the corresponding reference curves listed above graphically exhibits the effect of the ridge in the case when it is placed just in front of the transmitter.

2.4 SPHERICAL SCATTERING OBJECTS

In order to get a preliminary idea of the effect on traverse data of the presence of buried scattering objects, spherical objects of varying size and composition were positioned in the oil tank both with and without the metal reflecting plate.

Three different sphere compositions were used: solid teflon ($K' = 2.1$), thin-walled hollow fiberglass spheres loaded with low-loss $K' = 6$ material, and aluminum foil covered spheres (at 6 GHz the foil used is 20 penetration depths thick, therefore the spheres are effectively solid metal). Sphere diameters ranged from 3 w1 to .5 w1 (w1 = 2"). For the most part, three basic positions were used, all located in the vertical plane containing the traverse path: (1) 16 w1 out and 2 w1 deep (far out and shallow), (2) 5 w1 out and 4 w1 deep (in the transmitter beam), (3) 4 w1 deep under the transmitter.

Figures D-1 – D-17 contain reduced reproductions of the original recordings. As indicated in small sketches in each Figure, d is the plate depth ($d = \infty$ implies the half-space case without the plate), D is the sphere diameter, and d' and y the depth and range, respectively, at which the sphere is centered. Short horizontal marks to the left of each curve indicate a received power level of approximately -37 dB relative to the transmitter power. The received power scale of 15 dB/inch is indicated in Figure D-1. The deep, almost vertical minimas in Figures D-6, D-10, and D-14-17 are due to an instrumentational problem and should be treated as ordinary minimas.

The data generated can be thought of as providing insight to the following question: "Given a specific location, what is the effect of the presence of a buried object at that location as a function of the object's size and composition?"

In general the effects noted were quite complex but some features did stand out. Understandably, the effect of the scatters was more apparent in the half-space (Figures D-6 - D-17) than in the two-layer case (Figures D-1 - D-5), since power levels are generally larger in the two-layer environment. In all cases the teflon spheres were partially "invisible", which was to be expected due to the low dielectric constant contrast between teflon and our oil (2.1 vs. 2.16). The metal spheres were, somewhat surprisingly, only slightly more "visible" than the $K' = 6$ spheres; however, $K' = 6$ material was in fact used because its K' being approximately 3 times K' for the oil supposedly makes it a good reflector.

Of the three basic scatterer positions listed above, the one at which the most prominent effects were noticed was predictably the position in the transmitter beam (Figures D-3 and D-10 - D-13). Only in this position were the 1 wl and .5 wl diameter metal and $K' = 6$ spheres significant; at the other position even the 2 wl spheres were not especially prominent. Other effects noted for this "beam" position were broad peaks caused by the 3 wl diameter spheres at approximately 15 wl, and sizeable increases in the half-space power levels.

At the "under transmitter" position (Figures D-1 – D-2 and D-6 – D-9) the 2 w_l and larger spheres caused changes in the near-in region and increased half-space power levels. For the "far-out" positions (Figures D-4 – D-5 and D-14 – D-17) two features are apparent: disruption of the usual pattern at ranges beyond the scatterer position (little disruption of near-in signals by retro-reflection from far-out objects was noted), and the addition of small but quite visible short-period oscillations having periods in the .4 w_l – .8 w_l range (the standing wave pattern in the region between a point-source and a plane-reflector is .5 w_l) which disappear beyond the scatterer. In the half-space case these short-period oscillations decrease in period from roughly .8 w_l to .5 w_l as the receiver nears and passes over the scatterer, but in the two-layer case (both for plate depths of 6 w_l and 2 w_l) the oscillations increase somewhat from .5 w_l as the receiver nears and passes over the scatterer. Both features listed above are readily apparent in a suite of two-layer curves with a scattering sphere placed at various ranges (see Figure D-4).

2.5 DYE-3 SIMULATION

Figures E-1 – E-2 contain a single set of traverses simulating the effect of a buried waste water pit at the DYE-3 site in Greenland. The pit for our purposes consists of a discus-shaped region of contaminated snow which supposedly would be reflective. The top of the pit is approximately 100 ft. deep and the pit's diameter is approximately 120 ft. These dimensions were modeled at the six SEP frequencies using a set of thin, flat metal discs (Figure 1-5) having the appropriate diameters and positioned

at the appropriate depth. All six discs were positioned at the same range of 5 wl. One hundred feet corresponds to approximately .1, .2, .41, .81, 1.63, and 3.25 wl for frequencies 1 through 32 MHz, respectively.

The range and diameter of each disc and the corresponding frequency of each traverse are indicated on each curve. Also indicated is the "disc's image" which is the portion of the traverse-line where the receiver receives direct energy reflected specularly from the disc.

The disc's presence begins to affect the pattern at 2 and 4 MHz in very narrow regions just above each disc's position. AT 8 MHz the distortion is evident out to 15 wl range. At 16 and 32 MHz the disc's effect is totally predominant over the full traverse and at 32 MHz there is a very strong peak in the image area. Observationally, it appears that the waste dump would be come noticeable at 8 MHz as a large maxima located just beyond its location. Interestingly, there are half-wavelength ripples preceding the disc at 8 and 16 MHz.

3.0 ANTENNA PATTERNS

3.1 HORIZONTAL ELECTRIC DIPOLE

The antenna patterns in Figure 3-1 were included in previous report⁵. Figure 3-2 illustrates the coordinate system used (all horizontal dipoles were oriented parallel to the x-axis). The substantial difference between the measured and theoretical E_{ϕ}^2 (y-z) dipole patterns⁸ for the oil-air interface was an immediate cause of concern. The patterns in Figure 3-1 were measured at a receiver radius of 3 wl; Figure 3-3 shows that the measured pattern of concern tends to "droop" downward toward the theoretical pattern (with its power maximum at the oil-air critical angle) as the radius is increased to 6 wl. Figure 3-4 illustrates that the 3 wl radius pattern droops as the loss tangent is increased to approximately .142; however, this droop is approximately equal to that expected due to the measured increase in the oil's dielectric constant associated with the addition of the high-loss fluid. A skirt dipole⁶ was also fabricated, but its pattern (top of Figure 3-5) was very similar to that of the conventional dipoles.

Apparently then, the E_{ϕ}^2 (y-z) pattern measured can be made to agree more nearly with theory only by increasing the receiver radius. Since the theoretical pattern is calculated at infinity and since antennas with directional patterns typically have extended near-field distortions, it seems reasonable to conclude that the measured E_{ϕ}^2 (y-z) pattern is valid.

3.2 VERTICAL ELECTRIC DIPOLE

The skirt dipole mentioned previously was also oriented vertically, thus constituting a vertical electric dipole. The patterns measured are given in the bottom part of Figure 3-5 along with theoretical patterns taken from Cooper⁸. Interestingly, the disagreement with theory is about the same for the vertical as for the horizontal electric dipole.

3.3 VERTICAL MAGNETIC DIPOLE

In an attempt to construct a true magnetic dipole for the model a loop of diameter .04" (.02 wl) was fabricated from .02" diameter coax. This loop was of slightly smaller size measured in wavelengths than the Apollo 17 SEP receiver loops were at 32 MHz. Although the loop appeared physically suitable, its antenna patterns (Figure 3-6) were disappointing; quite possibly simply because the loop was not much larger than the feed coax. However, when oriented as receiving antenna in the direction indicated in Figure 3-6 the traverses recorded were essentially identical to standard traverses.

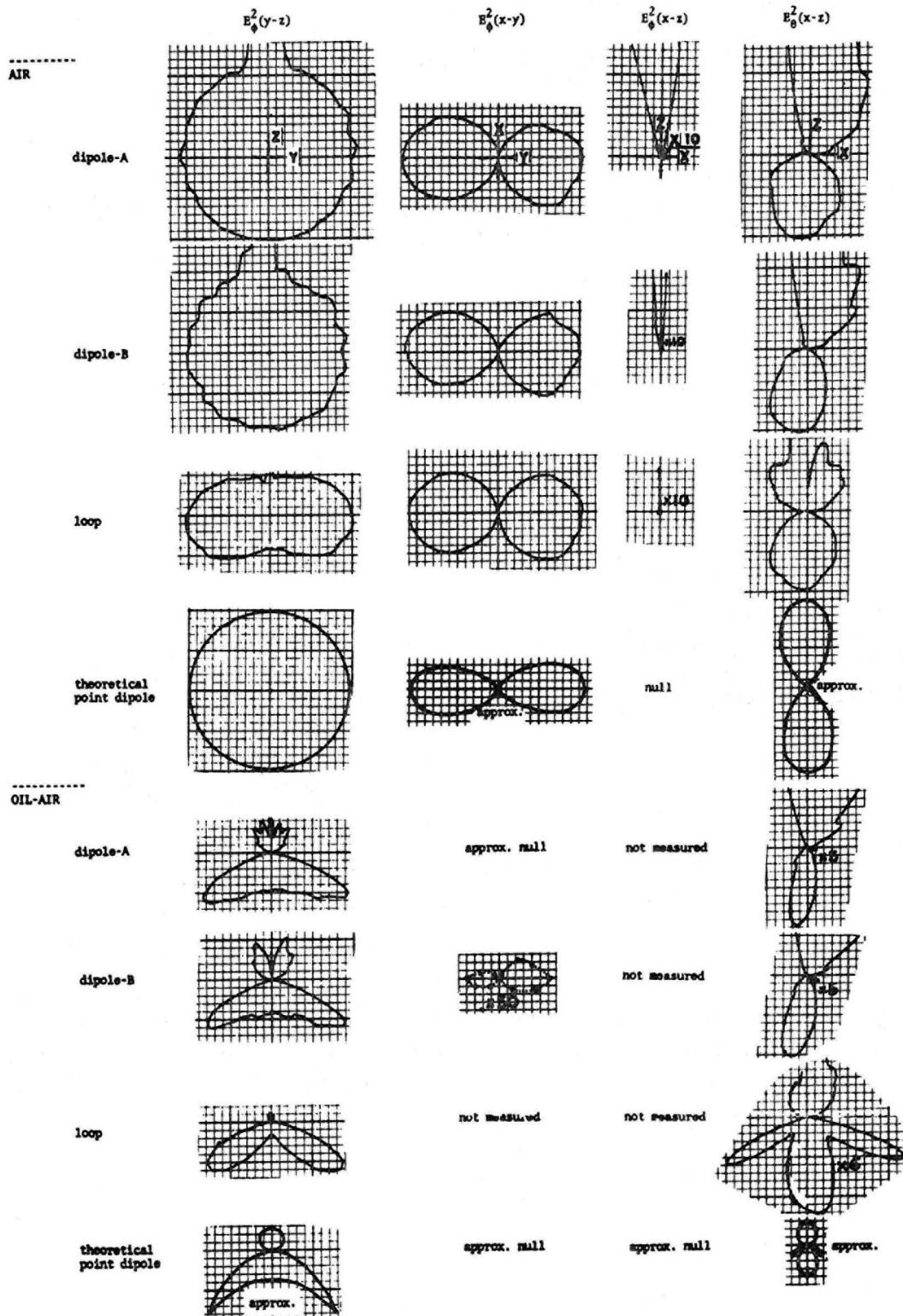


Figure 3-1. - Antenna patterns.

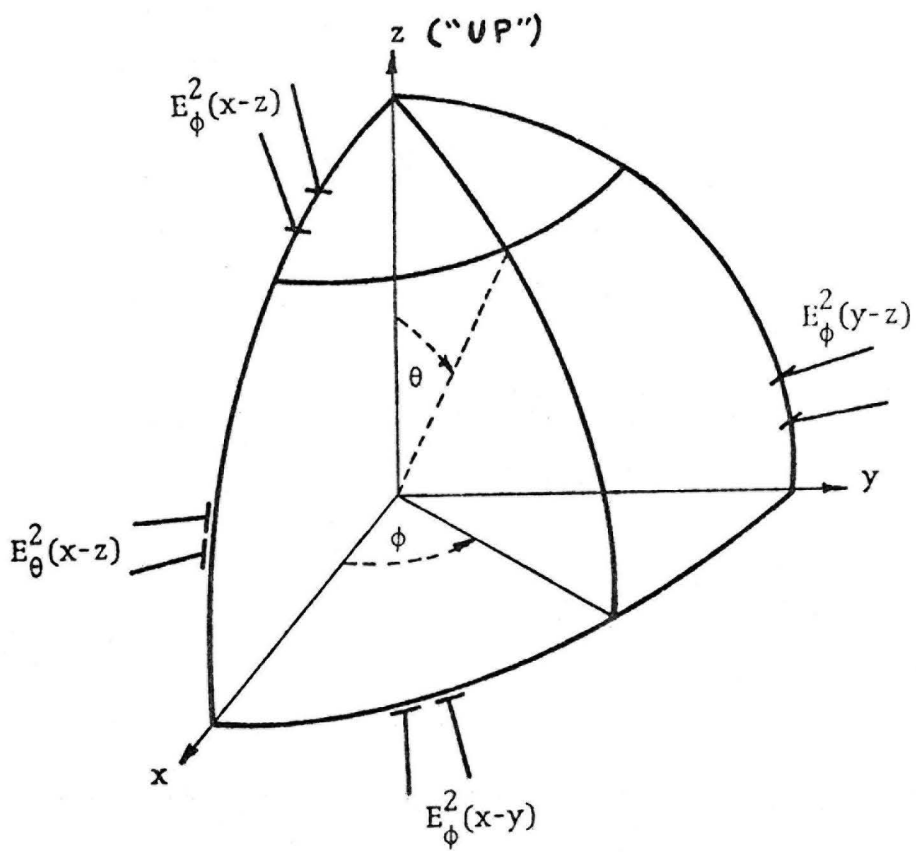


Figure 3-2. — Antenna measurement coordinate system.

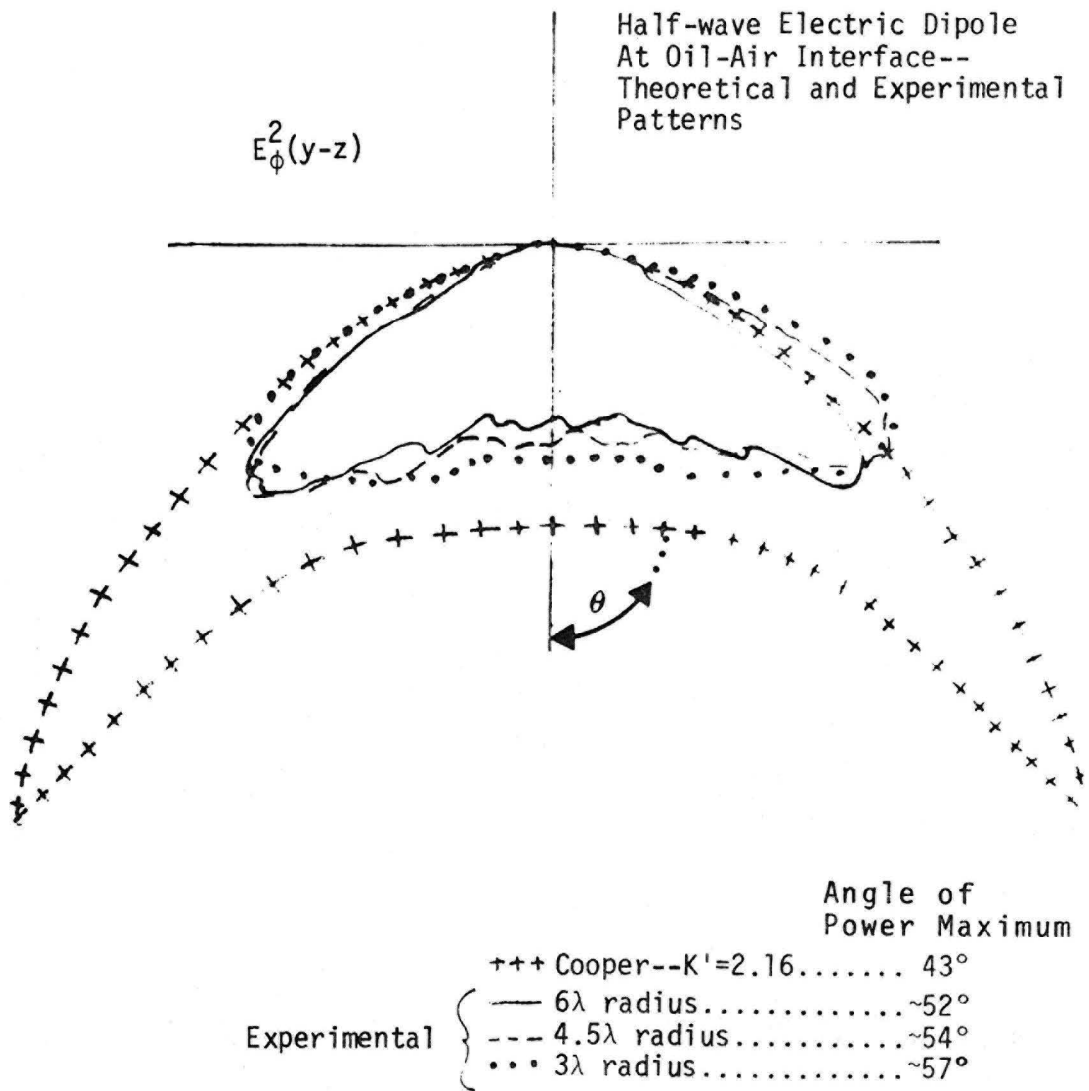
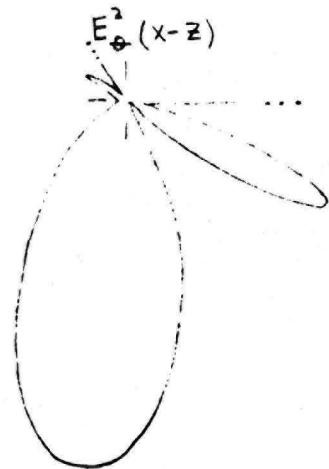
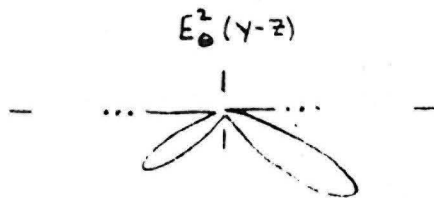
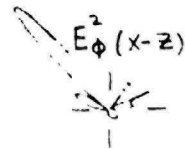
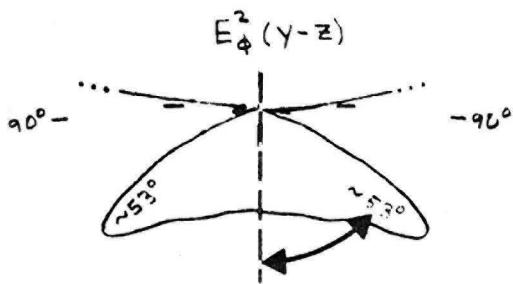


Figure 3-3. — Antenna pattern at various radii.



$\tan \delta \cong .142$

Figure 3-4. — Antenna patterns for high loss-tangent.

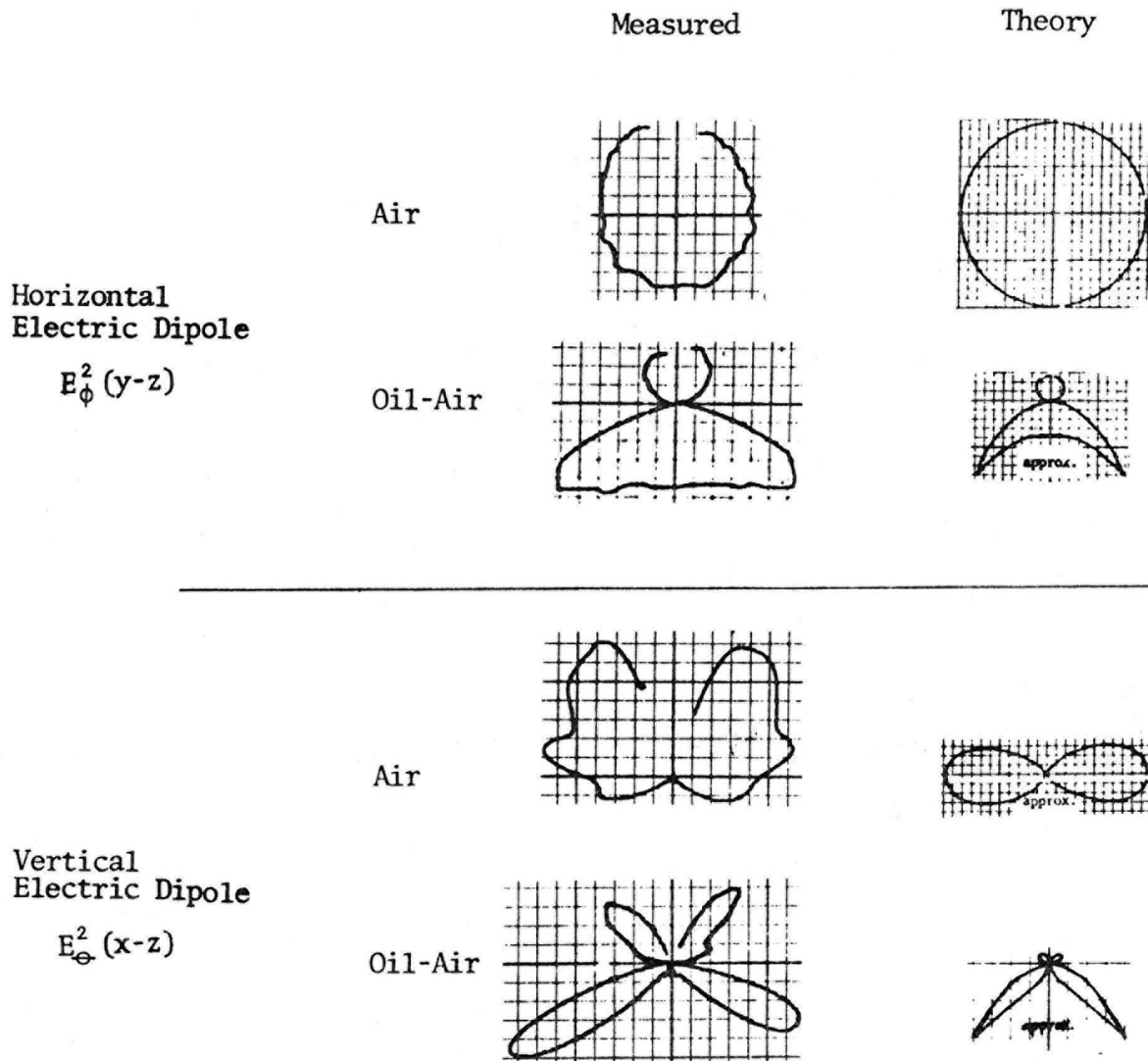


Figure 3-5. — Skirt dipole antenna patterns.

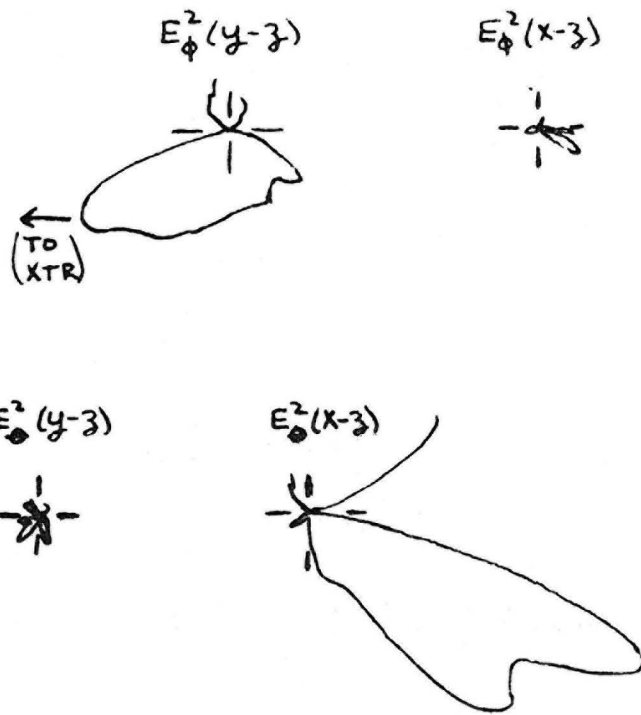
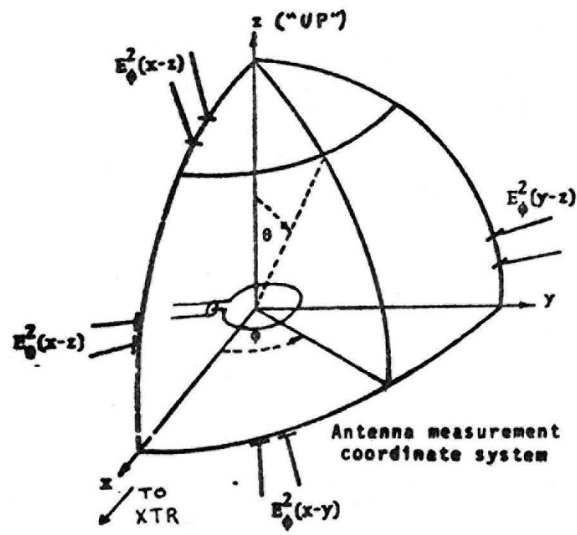


Figure 3-6. - Magnetic dipole antenna patterns.

4.0 EXPERIMENTAL DETAILS

4.1 TAPE RECORDING SYSTEM

The system designed for recording model data is illustrated in Figure 4-1. It essentially consists of a mechanism for conversion of the analog signal strength voltage to a frequency modulated signal suitable for magnetic tape recording. The dependence of frequency on signal (in this case 72.6 Hz/dB) is determined (see Figure 4-1) by the triple product of the log-amplifier output factor (.02 volt/dB), the amplification factor (6.05), and the VCO conversion factor (600 Hz/volt).

The system was initialized so that a 30 mV receiver-diode signal (corresponding to the received power-level of about -25 dBm above which the 1N23 diode began to be noticeably non-linear) was recorded as 3000 Hz signal. In the VCO (left) channel each traverse was begun with a short voice annotation followed by a 3500 Hz start-tone and ended with a 4000 Hz stop-tone.

In the right channel the 5200 Hz reference signal (used to compensate for tape speed irregularities) was superimposed on a pulsed 420 Hz odometer signal. The odometer pulse-rate was nominally .0642 w1/pulse.

4.2 DIGITAL CONVERSION AND PROCESSING

To permit computer processing of the frequency-modulated model data (discussed in the previous section), use was made of the Data Acquisition System (DAS) built to process SEP field and lunar data. The digitized data was recorded on 7-track incremental tape in BCD format.

The frequency modulated-to-digital conversion process basically worked as follows. The frequency modulated tapes were played-back at original speed into the DAS and every 67.5 msec the number of cycles of the VCO signal (containing the signal power information) was counted for a period of approximately 53 msec. During this same period the number of cycles of the 5200 Hz reference signal (electronically separated from the 420 Hz odometer pulses) was also counted.

Each pair of 5200 Hz/VCO readings was then recorded on the incremental tape as one six-digit word with the first three digits for the 5200 Hz reading and the remaining three digits for the VCO reading. One-hundred forty-three words constituted one "record" and the roughly 23 records needed for each traverse constituted a single "file".

To obtain range information, the 420 Hz odometer signal pulses were accumulated by the DAS during the playback. The accumulated number of pulses was read onto the digital tape (substituting for a 5200 Hz/VCO word) every 3.24 sec as the middle four digits of the 46th, 94th, and 142nd words of each record. In addition, words 47, 48, 95, 96, and 143 were occupied by a combination of the run number assigned to each traverse (first three digits) and synchronization pulse intended for a Wang calculator (remaining three digits).

As the digital tape was processed each 5200 Hz/VCO sample was converted back into a power reading by the following formula:

$$\text{power (dB)} = \frac{5200 \text{ Hz} \times \text{number VCO cycles}}{72.6 \text{ Hz/dB} \times \text{number 5200 Hz cycles}}$$

Maximum and minimum power limits were established at approximately -19.5 and -62 dBm received power-levels, corresponding to VCO signals of 3000 and 300 Hz, respectively.

The odometer readings were converted into range readings according to the formula:

$$\text{range (wl)} = .0642 \text{ wl} \times \text{odometer count number.}$$

Next, each power reading was assigned a range value by interpolating between the ranges of the two nearest odometer readings.

For purposes of plotting, the data stream of power readings and assigned ranges was sampled at 0.1 wl increments. For the usual case of no data point having the desired range the two neighboring points were used for interpolation. Since all model recordings started at some non-zero range, the proper starting range was added before plotting.

Figure 4-2 illustrates a particular traverse plotted after the above interpolation without filtering. Also shown is the original X-Y plot of the traverse. It is apparent that somewhere in the recording and digitization process approximately 1 dB of high-frequency noise has been added. At the bottom of Figure 4-2 is the traverse in final form after being filtered with an 11-point filter designed to remove both the high-frequency noise and the unwanted ripples of approximately .5 wl wavelength. This filter operated by replacing the power readings at a given point with a weighted average of the original point plus the five nearest points (spaced at .1 wl increments) on

each side. The weights were .2441 for the central point and .2078, .1239, .0445, .0041 and -.0023 respectively for the receding points. The ideal length of the filter was 1.25 cycles/wavelength.

The filters used were designed using a program written by Mr. James Rossiter following the technique of Gold and Rader⁹. The program generates filter-weights from a given ideal band-pass filter and a given desired number of weights. The program operates by Fourier transforming the ideal band-pass filter, making an approximation to that transform subject to the imposed limitation on number of weights, and Fourier integrating the approximation to generate the final filter and the corresponding desired weights. Figure 4-3 illustrates the ideal and generated filters for a 15-point filter designed and used to reject only high-frequency digitization noise. The weights for this filter are as follows: .5782, .2972, -.0642, -.0546, .0333, .0067, -.0078, and .0003.

The 15-point filter used in Figures B40 and B41 had ideal length .3125 cycles/wavelength and used weights as follows: .1286, .1231, .1081, .0862, .0609, .0365, .0167, .0042.

4.3 POWER MEASUREMENT

To be able to express received signal power relative to transmitter power, it is of course necessary to measure the actual power being transmitted. The most straight forward method would be to place a dual-directional coupler in the transmitter feed line and to simply measure the forward and reflected power levels, the difference between the two being the power dissipated (and assumed transmitted) at the transmitter. Another method would be to use a single

directional coupler to measure the forward power and a slotted-line to measure the ratio between the forward and reflected power, thus yielding by calculation the reflected power and the transmitted power. The actual method used was to calibrate the slotted-line in terms of power and use it to measure the transmitted power. This technique uses the relation that the net power transmitted forward through a slotted-line is equal to the product of the square roots of the minimum and maximum power level of the standing wave pattern in the slotted-line, symbolically

$$P_{TR} = (P_{Min})^{1/2} (P_{Max})^{1/2} .$$

This can be shown as follows. The transmitted power is equal to the difference between the forward power P_o and the reflected power P_r .

$$P_{TR} = P_o - P_r$$

Since power is proportional to the square of the associated electric field,

$$P_{TR} = K(E_o^2 - E_r^2) = K (E_o + E_r)(E_o - E_r) .$$

But $E_o + E_r$ and $E_o - E_r$ are the maximum and minimum fields so

$$P_{TR} = KE_{max}E_{min} = (P_{Max})^{1/2} (P_{Min})^{1/2} .$$

Which was to be shown.

Actually the power levels are measured as a voltage proportioned to power by a detector element so we rewrite P_{TR} as

$$P_{TR} = C (V_{Max})^{1/2} (V_{Min})^{1/2}$$

where C is a factor dependent on the detector sensitivity and insertion depth of the detector probe. Calibration may be accomplished quite easily by substituting a power meter for the transmitter to measure directly the dissipated (in this case absorbed) power. In practice one chooses a desirable power level and detector voltage, say 1 mW and 5 mV, respectively; adjusts the power source for a 1 mW power meter reading; and inserts the detector by trial-and-error until its $(V_{Max})^{1/2} (V_{Min})^{1/2}$ equals 5 mV to within the desired accuracy. For high accuracies, any nonlinearity of the detector can be compensated for by noting the $(V_{Max})^{1/2} (V_{Min})^{1/2}$ detector reading for other desired power levels.

After calibration the transmitter is reconnected and the power source adjusted until $(V_{Max})^{1/2} (V_{Min})^{1/2}$ reaches the desired value.

4.4 DIELECTRIC PROPERTIES TEST-CELL

It was necessary to have the capability to measure the dielectric constant and loss-tangents of various solid and liquid materials used in conjunction with the model. Consequently, a test-cell was assembled from the following General Radio Type 900 precision coaxial components: a reference air-line, a short-circuit termination, and a coaxial adaptor compatible with the slotted-line. The short

and air-line formed a liquid-tight seal, permitting the cell to be operated with its axis vertical for liquids.

Readers are referred elsewhere for the complete theory of standing-wave dielectric measurements¹⁰. In this special case for which samples of a special length are placed flush against the shorted end of a coaxial cell the theory is greatly simplified. The essential point (see Figure 4-4) is as follows: if a sample is adjusted (usually by trial-and-error) in length until the nearest minima in the standing wave pattern is located exactly $1/4 \lambda$ ($1/2 \lambda$) from the sample then the sample itself must "contain" $1/4$ ($1/2$) wavelengths. But of course a wavelength inside the sample is not the same length as in air; it is shorter by a factor $(K'_m)^{1/2}$ equal to the square root of the relative dielectric constant of the sample material. Restating all this mathematically we have:

$\frac{1/4 \lambda_m \text{-case}}{d = \frac{\lambda_m}{4}}$	$\frac{1/2 \lambda_m \text{-case}}{d = \frac{\lambda_m}{2}}$
--	--

where d equals the sample length and λ_m denotes a wavelength in the sample. Above it was stated that $\lambda_m = \lambda / (K'_m)^{1/2}$. Substituting this we get

$d = \frac{\lambda}{4 (K'_m)^{1/2}}$	$d = \frac{\lambda}{2 (K'_m)^{1/2}}$
--------------------------------------	--------------------------------------

Finally, solving for K'_m we see that we have solved for K'_m in terms of the sample length:

$$K'_m = (\lambda/4d)^2 \quad \Bigg| \quad K'_m = (\lambda/2d)^2$$

For these special cases the loss-tangent of the sample material is given by

$$\tan \delta_m = \Delta x / dK'_m \quad \Bigg| \quad \tan \delta_m = \Delta x / d$$

where we have introduced a new experimental quantity Δx , the distance between two points in the slotted-line standing-wave pattern where the power-level is twice that at the minimum-point between them. So we can find both the dielectric constant and loss tangent for a material simply by knowing d and measuring Δx when the above special condition is achieved. We can tell when this special condition occurs by keeping track of the sample length (as the length is adjusted) and noting when the slotted-line standing-wave pattern shifts from its empty-cell position a distance $\lambda/4 - d$ ($\lambda/2 - d$ for a half-wavelength sample) toward the sample.

There are various limitations in the technique. The simple formulae above begin to become significantly inaccurate when the loss tangent of the material exceeds .1. On the other hand there is a minimum loss-tangent (approximately .002) that can be measured since there is a finite Δx (partially nonrepeatable) due to losses in the slotted-line and the various connections. Another difficulty is estimating accurately the length of liquids samples

and allowing for the amount of liquid sample flowing into small voids associated with the center coaxial contact; these difficulties probably contributed about 1.5 percent and 3 percent errors respectively to measurements of loss tangent and dielectric constant of liquid samples.

4.5 ANTENNA-PATTERN MEASUREMENTS

To study the patterns of various antennas both in air and at an oil-air interface, a system (Figure 4-5) was designed to automatically record antenna patterns. To record a pattern the transmitter was first positioned near the center of the tank and a motor-driven fixture which rotated the receiving antenna about the transmitter was mounted on the side of the tank. A potentiometer coupled to the motor-shaft was used to produce a dc voltage proportional to the angular position of the receiver. This analog voltage together with the receiver signal were processed through a polar-to-rectangular coordinate converter which allowed the antenna patterns to be plotted in polar form on an X-Y recorder.

Figure 4-6 diagrams the circuit used. Since the converter had only a 180° coverage it was necessary to do each pattern in two halves, reversing both DPDT switches shown between halves. The potentiometer was initially centered (thus setting the θ -input voltage to zero) for the receiver positioned directly underneath the transmitter. The converter was sufficiently accurate that an essentially perfect circle could be drawn using a constant r-input.

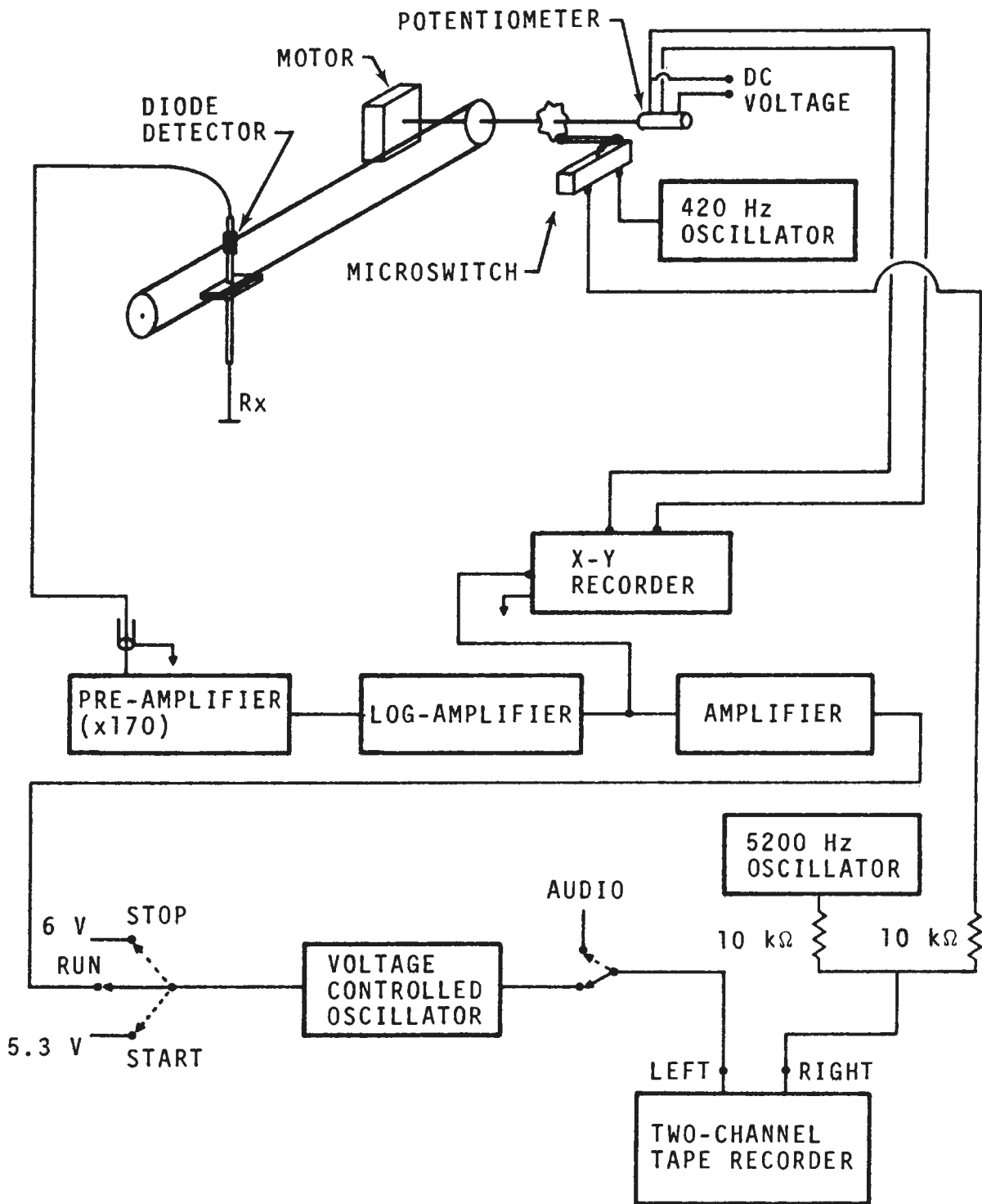


Figure 4-1. — Tape recording system.

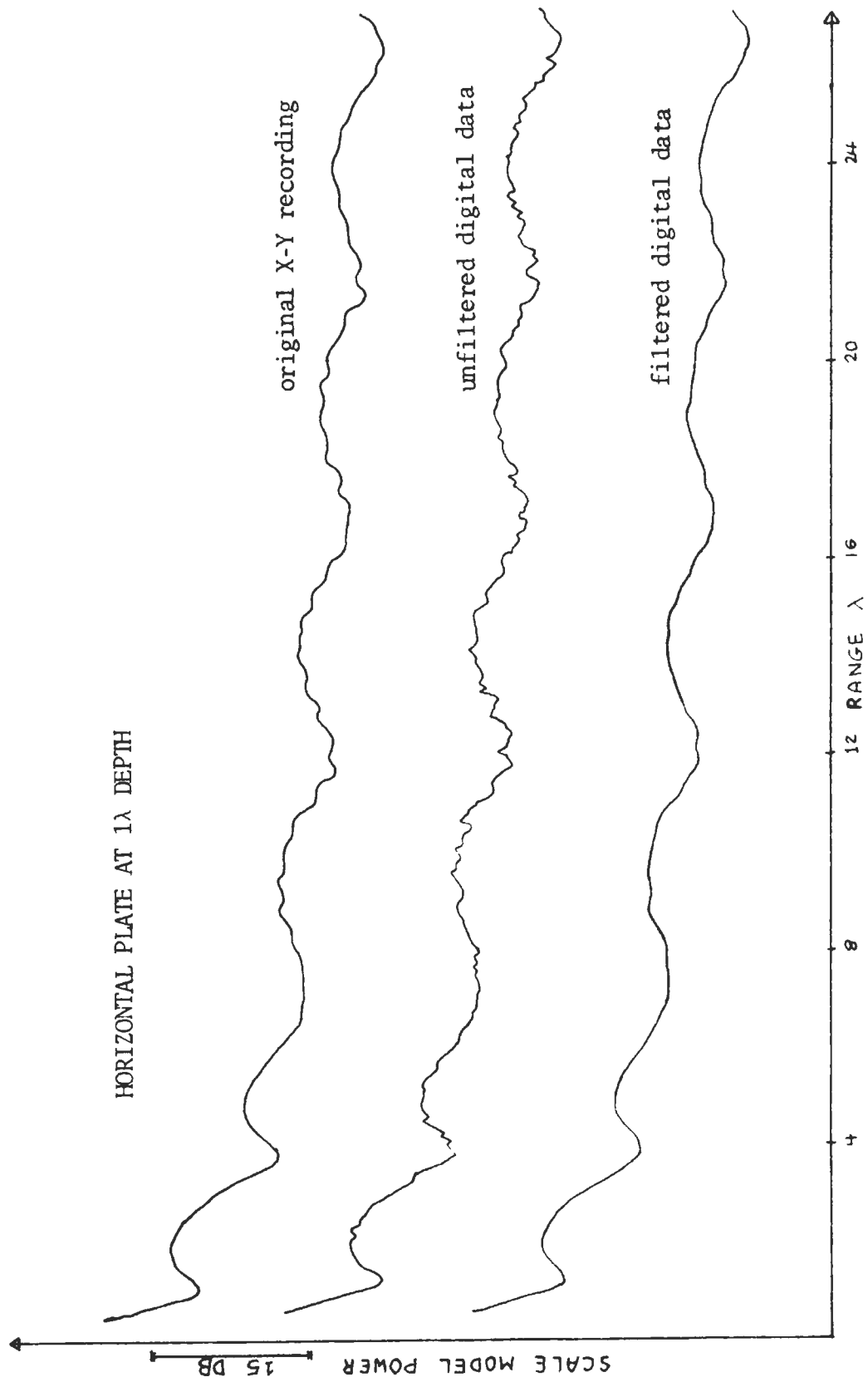


Figure 4-2. — Comparison of filtered and unfiltered data.

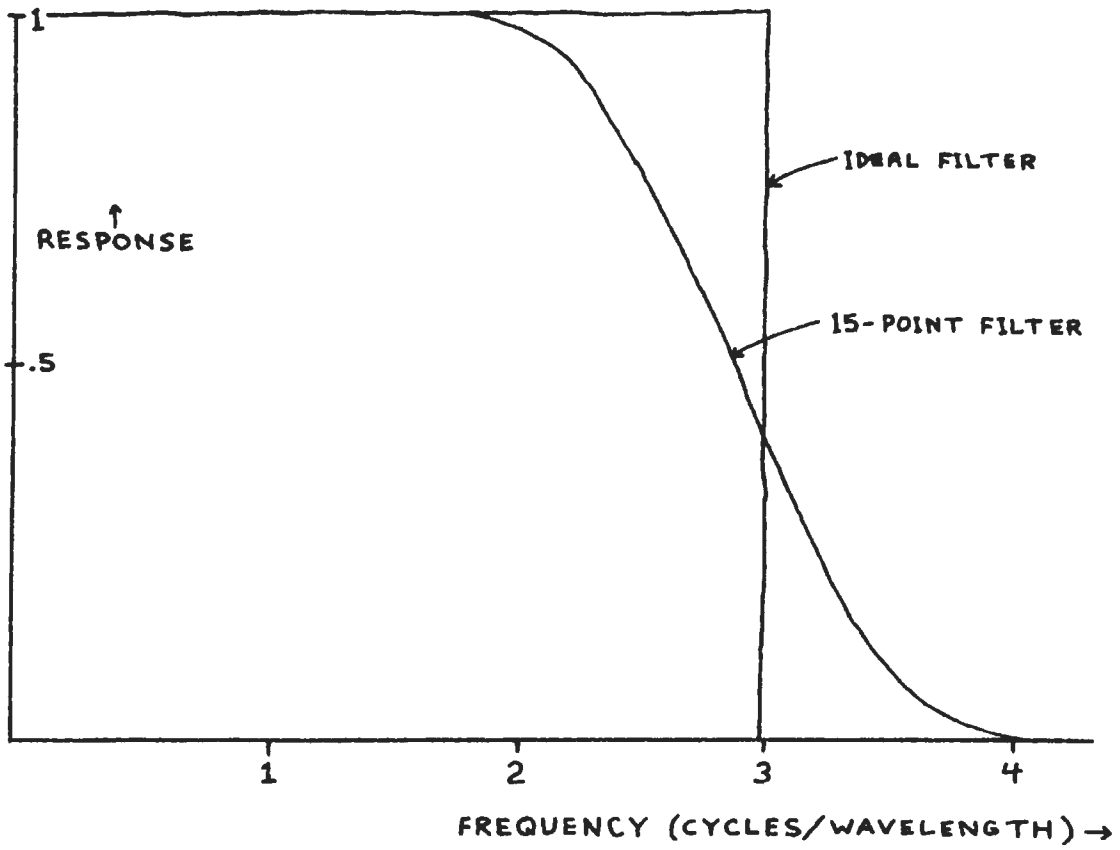


Figure 4-3. - Filter generation.

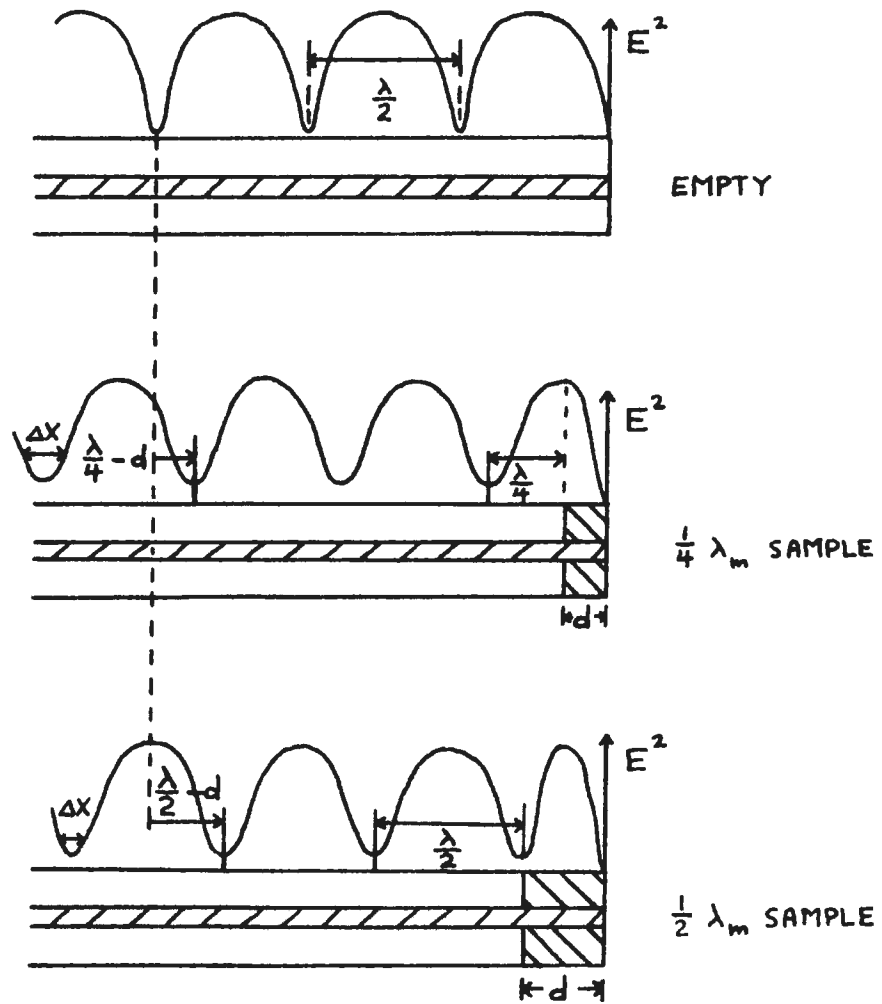


Figure 4-4. - Dielectric properties measurement.

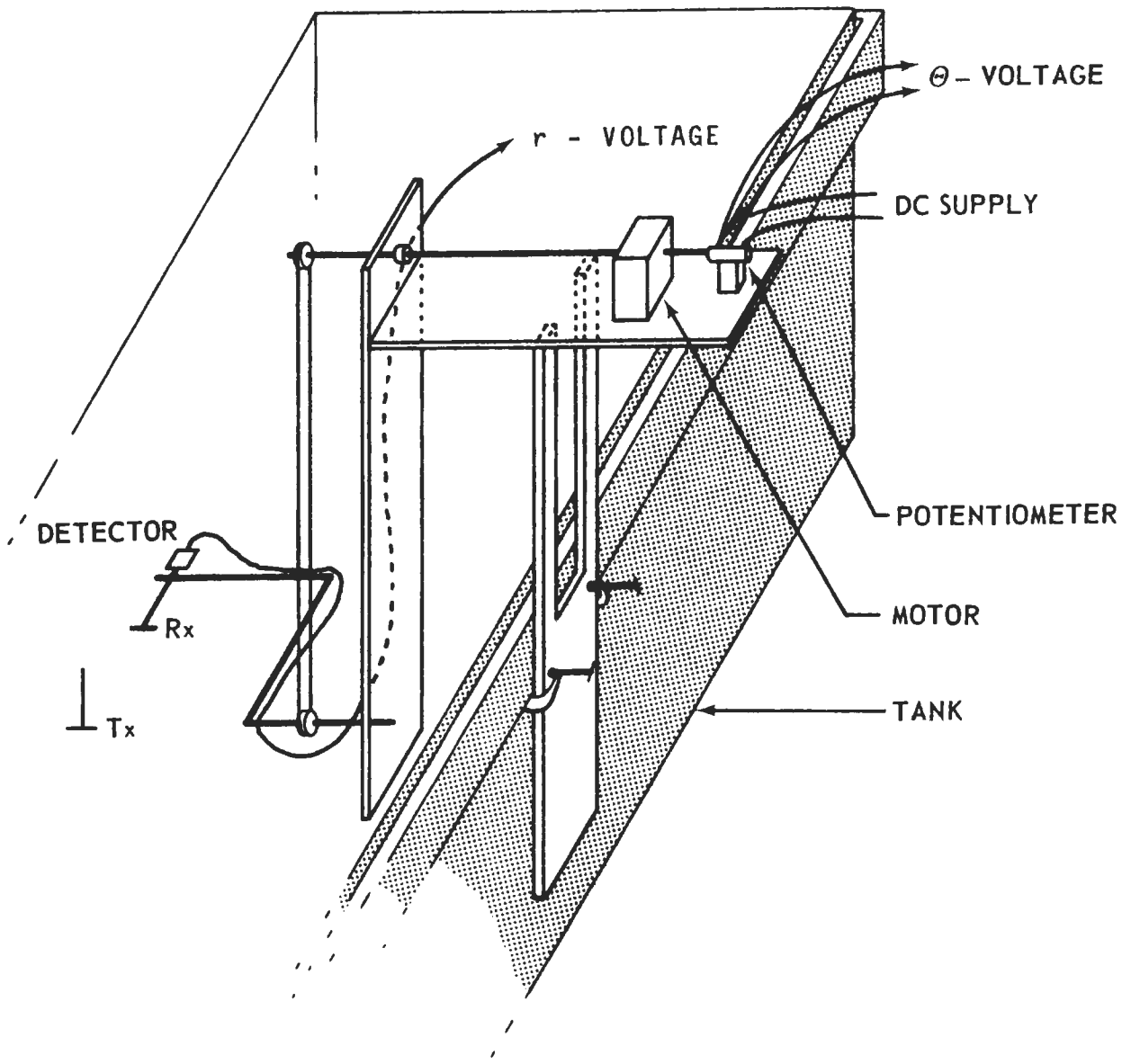


Figure 4-5. — Antenna rotating fixture (simplified).

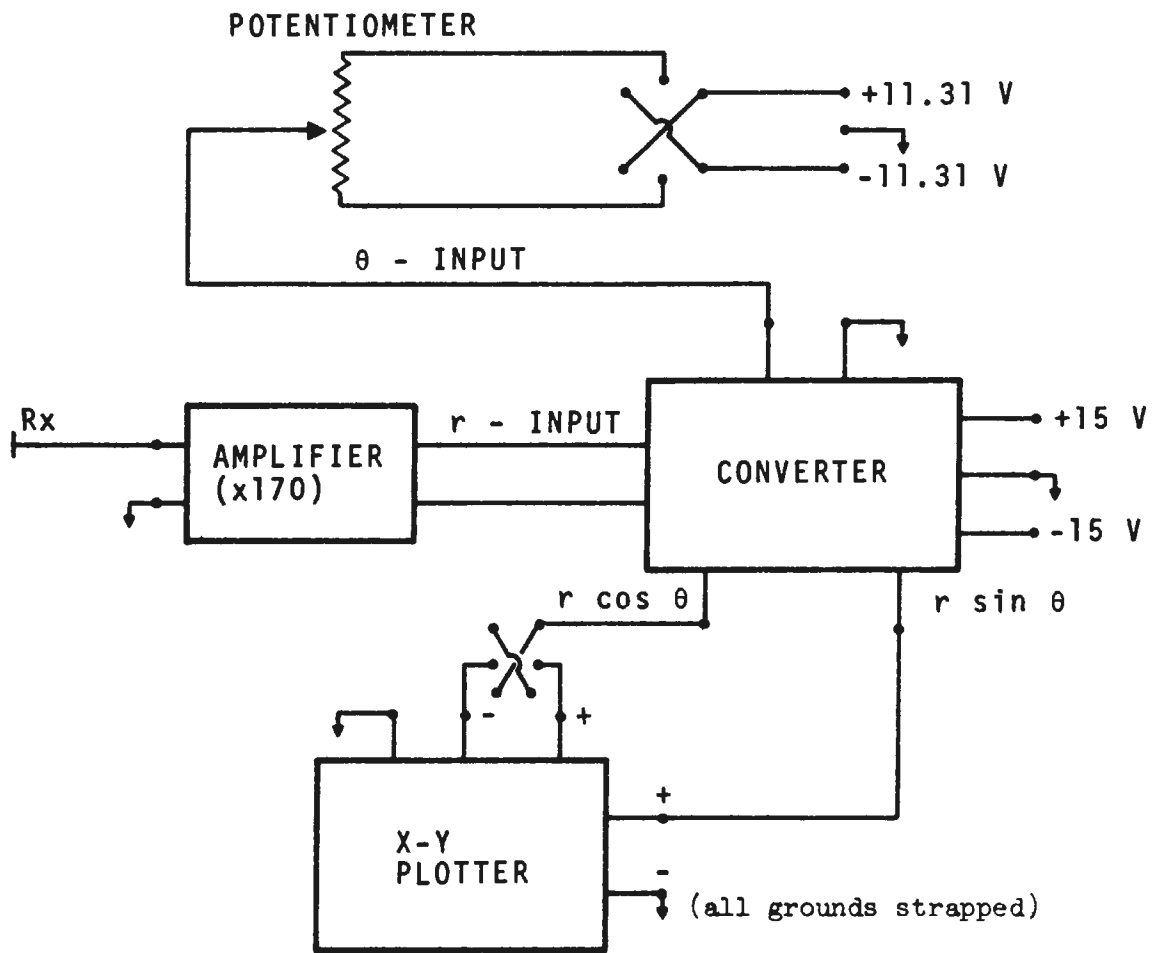


Figure 4-6. — Antenna measurement circuit.

5.0 INDEX TO DIGITIZED TRAVERSES

Following is an index to all traverses recorded and digitized as discussed in Sections 4.1 and 4.2. The first column gives the run number assigned to each traverse and included on the digitized recording at the locations specified in the fourth paragraph of Section 4.2.

The second column gives the file number of each run on both the original digitized tapes (denoted SEPM 1 through SEPM 8). The series of numbers is read "original digital tape number/file number." The third column gives each run's location on the original FM magnetic tapes. Further to the right is given general information about each run. R_o is the starting range.

Thus for example the entry:

"116 3/27 9-012"

means that Run 116 was recorded beginning at position 012 on FM tape number 9; when digitized it was recorded as the 27th file on tape SEPM 3.

Runs marked with an asterisk (*) were digitized twice due to a defect in the original digitization or to some difficulty in plotting a particular run thought possibly to be related to a defect in digitization. If any difficulty is experienced in utilizing the digital recording of a run marked with an asterisk, the supplemental index at the end of the main index should be consulted for the location of a duplicate digitization. Should the difficulty remain the defect is probably in the original FM recording.

Both the original FM tapes and a master digital tape are on file with the Johnson Space Center Records Management Office under the classification: Apollo 17 Surface Electrical Properties Experiment (S-204) Simulation Model.

The master digital tape contains a condensed record of the original digital tapes. On this tape the 356 digitized traverses are ordered consecutively by run number (for duplicate digitizations the last digitization only is used) with one traverse/record and 10 records/file, e.g. run number 13 becomes the third record of the second file and run 348 the eighth record of the thirty-fifth file. Each record (run) contains 300 8-character words (format: xxx.xxxx) giving the power-level in db from 0 - 30 wl range in .1 wl increments. The range corresponding to each word is to be inferred from that word's position. For example, a run for which the power-level was recorded from .5 to 27 wl occupies words 5 through 270. The power-level is set to zero for ranges not actually recorded. In each record the 300 data-words are preceded by the following: four 4-character words giving in order the run number, file number, number of real data-words, and position of first real data-word (starting range multiplied by ten) followed by 16 characters carrying the legend "Scale Model 1973."

INDEX TO DIGITIZED TRAVERSES

HORIZONTAL METAL PLATE

<u>Run No.</u>	<u>Digital Tape Location</u>	<u>FM Tape Location</u>	<u>Plate Depth (wl)</u>	<u>R_o (wl)</u>
001	1/1	4-010	.5	.5
002	1/2	4-095	1	"
003	1/3	4-174	1.5	"
004	1/4	4-234	2	"
005	1/5	4-292	2.5	"
006	1/6	4-345	3	"
007	1/7	4-395	4	"
008	1/8	4-441	5	"
009	1/9	3-156	6	"
010	1/10	3-222	7	"
011	1/11	1-015	1.25	3.25
012	1/12	1-097	1.22	"
013	1/13	1-168	1.18	"
014	1/14	1-233	1.15	"
015	1/15	1-293	1.11	"
016	1/16	1-351	1.08	"
017	1/17	1-404	1.04	"
018	1/18	1-454	1.00	"
019	1/19	1-502	.97	"
020	1/20	1-547	.93	"
021	1/21	1-591	.90	"
022	1/22	1-633	.86	"
023	1/23	1-673	.83	"
024	1/25	2-006	.79	"

INDEX TO DIGITIZED TRAVERSES (Continued)

HORIZONTAL METAL PLATE (Concluded)

<u>Run No.</u>	<u>Digital Tape Location</u>	<u>FM Tape Location</u>	<u>Plate Depth (wl)</u>	<u>R_o (wl)</u>
025	1/26	2-089	.76	3.25
026	1/27	2-161	.72	"
027	1/28	2-226	.69	"
028	1/29	2-286	.65	"
029	1/30	2-343	.62	"
030	1/31	2-396	.58	"
031	1/32	2-447	.55	"
032	1/33	2-496	.48	"
033	1/34	2-541	.41	"
034	1/35	2-584	.34	"
035	1/36	2-625	.27	"
036	1/37	2-665	.20	"
037*	1/38	3-005	.13	"
038*	1/39	3-087	.06	"

INDEX TO DIGITIZED TRAVERSES (Continued)

METAL PLATE - LATERAL SLOPES ($R_o = .5 w_l$)

<u>Run No.</u>	<u>Digital Tape Location</u>	<u>FM Tape Location</u>	<u>Plate Depth (w_l)</u>	<u>Slope Angle</u>
039	1/40	5-015	6	3.8°
040	1/41	5-105	"	7.6°
041	1/42	5-183	4	3.8°
042	1/43	5-254	4	7.6°
043	1/44	5-319	2	3.5°
044	1/45	5-380	2	7.5°
045	1/46	5-437	2	1.4°
046	1/47	5-490	1	1.4°
047	1/48	5-541	1	3.9°
048*	1/49	5-592	.5	1.4°

INDEX TO DIGITIZED TRAVERSES (Continued)

METAL PLATE - FORWARD SLOPES ($R_o = .5 w_l$)

<u>Run No.</u>	<u>Digital Tape Location</u>	<u>FM Tape Location</u>	<u>Plate Depth (wl)</u>	<u>Inclination</u>
049	1/50	5-641	1.04	2°
050	2/1	I-025	1	1°
051	2/2	I-111	"	0°
052*	2/3	I-184	"	-1°
053	2/4	I-247	"	-3°
054	2/5	I-309	"	-5°
055	2/6	I-362	"	-7°
056	2/7	I-411	"	-9°
057*	2/8	II-014	2	3°
058	2/9	II-103	"	1°
059	2/10	II-183	"	0°
060	2/11	II-253	"	-1°
061*	2/12	II-318	"	-3°
062	2/13	II-379	"	-5°
063	2/14	II-436	"	-7°
064	2/15	II-489	"	-9°
065	2/16	III-007	4	7°
066	2/17	III-098	"	5°
067	2/18	III-176	"	3°
068	2/19	III-247	"	1°
069	2/20	III-311	"	0°
070	2/21	III-371	"	-1°
071	2/22	III-428	"	-3°
072	2/23	III-481	"	-5°

INDEX TO DIGITIZED TRAVERSES (Continued)

METAL PLATE — FORWARD SLOPES ($R_o = .5 w_1$) (Concluded)

<u>Run No.</u>	<u>Digital Tape Location</u>	<u>FM Tape Location</u>	<u>Plate Depth (w1)</u>	<u>Inclination</u>
073*	2/24	IV-008	6	9°
074	2/25	IV-095	"	7°
075	2/26	IV-168	"	5°
076	2/27	IV-234	"	3°
077	2/28	IV-293	"	1°
078	2/29	IV-348	"	0°
079	2/30	IV-399	"	-1°
080	2/31	IV-534	"	-2°

INDEX TO DIGITIZED TRAVERSES (Continued)

HORIZONTAL DIELECTRIC SLAB

<u>Run No.</u>	<u>Digital Tape Location</u>	<u>FM Tape Location</u>	<u>Plate Depth (w1)</u>	<u>R_o (w1)</u>
081	2/32	6-009	6	.5
082	2/33	6-098	5	"
083	2/34	6-177	4	"
084	2/35	6-248	3	"
085	2/36	6-314	2.5	"
086*	2/37	6-376	2	"
087	2/38	6-432	1.5	"
088	2/39	6-485	1	"
089	2/40	6-536	.5	"
090	2/41	6-628	0	"
091	3/1	7-012	1.5	3.25
092	3/2	7-092	1.43	"
093	3/3	7-164	1.36	"
094	3/4	7-230	1.29	"
095	3/5	7-290	1.22	"
096	3/6	7-346	1.16	"
097	3/7	7-399	1.09	"
098	3/8	7-450	1.00	"
099	3/10	7-498	.93	"
100	3/11	7-544	.86	"
101	3/12	7-588	.79	"
102	3/13	7-631	.76	"
103	3/14	8-008	.72	"
104*	3/15	8-088	.696	"
105	3/16	8-161	.66	"

INDEX TO DIGITIZED TRAVERSES (Continued)

HORIZONTAL DIELECTRIC SLAB (Concluded)

<u>Run No.</u>	<u>Digital Tape Location</u>	<u>FM Tape Location</u>	<u>Plate Depth (w/l)</u>	<u>R_o (w1)</u>
106*	3/17	8-227	.59	3.25
107	3/18	8-287	.50	"
108	3/19	8-344	.43	"
109	3/20	8-398	.36	"
110*	3/21	8-448	.29	"
111*	3/22	8-496	.22	"
112*	3/23	8-542	.14	"
113	3/24	8-586	.07	"
114	3/25	8-628	.035	"
115	3/26	6-586	0	"

INDEX TO DIGITIZED TRAVERSES (Continued)

DIELECTRIC SLAB - FORWARD SLOPES ($R_o = .5 w_1$)

<u>Run No.</u>	<u>Digital Tape Location</u>	<u>FM Tape Location</u>	<u>Plate Depth (w1)</u>	<u>Inclination</u>
116	3/27	9-012	1	1°
117	3/28	9-101	"	0°
118	3/29	9-179	"	-1°
119	3/30	9-250	"	-3°
120	3/31	9-314	"	-5°
121	3/32	9-375	"	-7°
122	3/33	9-432	"	-9°
123	3/34	10-006	2	-7°
124	3/35	10-096	"	-5°
125	3/36	10-175	"	-3°
126	3/37	10-247	"	-1°
127	3/38	10-312	"	0°
128	3/39	10-373	"	1°
129	3/40	10-431	"	3°
130	3/41	11-009	4	7°
131	3/42	11-099	"	5°
132	3/43	11-177	"	3°
133	3/44	11-248	"	1°
134	3/45	11-314	"	0°
135	3/46	11-374	"	-3°
136	3/47	11-430	"	-3°
137	3/48	12-099	6	0°
138	3/49	12-008	"	1°

INDEX TO DIGITIZED TRAVERSES (Continued)

DIELECTRIC SLAB - FORWARD SLOPES ($R_o = .5 w_1$) (Concluded)

<u>Run No.</u>	<u>Digital Tape Location</u>	<u>FM Tape Location</u>	<u>Plate Depth (w1)</u>	<u>Inclination</u>
139	3/50	12-179	6	3°
140	3/51	12-250	"	5°
141	3/52	12-315	"	7°
142	3/53	12-376	"	9°

INDEX TO DIGITIZED TRAVERSES (Continued)

CRATER OVER DIELECTRIC SLAB ($R_o = 3.25 w_l$)

<u>Run No.</u>	<u>Digital Tape Location</u>	<u>FM Tape Location</u>	<u>Slab Depth (wl)</u>	<u>Crater Diameter (wl)</u>	<u>Crater Range (wl)</u>
143	3/54	13-018	1	2.5	18
144	3/55	13-096	1	"	"
				(off-set .25 wl from traverse-line)	
145	3/56	13-164	1	(reference for runs 143-147)	
146	3/57	13-228	1	2.5	11
147	3/58	13-282	1	"	"
				(off-set .25 wl from traverse-line)	
148	3/59	13-334	.5	2.5	11
149	3/60	13-382	"	(reference for run 148)	
150	3/61	14-017	3	(3.5)	22
				(one-quarter crater, off-set 1 wl)	
151	3/62	14-099	3	(reference for run 150)	

INDEX TO DIGITIZED TRAVERSES (Continued)

CREVASSES OVER DIELECTRIC SLAB

<u>Run No.</u>	<u>Digital Tape Location</u>	<u>FM Tape Location</u>	<u>Slab Depth (w1)</u>	<u>Crevasse Dimensions (w1)</u>	<u>Crevasse Range (w1)</u>	<u>R_o (w1)</u>
152	3/63	15-017	4	.3×3×3	5	.5
153	3/64	15-104	"	"	15	"
154	3/65	15-178	"	(reference for runs 152-158)		
155	3/66	15-245	"	.15×1.5×1.5	5	"
156	3/67	15-305	"	"	15	"
157	3/68	15-361	"	.1×.75×.75	5	"
158	3/69	15-412	"	"	15	"
159*	3/70	16-013	1	"	15	3.25
160	3/71	16-093	"	"	5	"
161	3/72	16-161	"	(reference for runs 159-160)		

INDEX TO DIGITIZED TRAVERSES (Continued)

SPHERES OVER DIELECTRIC SLAB ($R_o = .5 w_1$)

(Slab Depth 6 w_1 . Spheres Centered At 4 w_1 Depth.)

<u>Run No.</u>	<u>Digital Tape Location</u>	<u>FM Tape Location</u>	<u>Sphere Diameter (w_1)</u>	<u>Sphere Material</u>	<u>Sphere Range (w_1)</u>
162	3/73	17-189	(reference for runs 163-174)		
163	3/76	17-018	1	metal	5
164	3/77	17-109	1	$K' = 6$	"
165	3/78	17-258	2	metal	"
166	3/79	17-324	"	$K' = 6$	"
167	3/80	17-386	.5	metal	"
168	3/81	17-444	"	$K' = 6$	"
169	3/82	17-502	1	$K' = 6$	0
170*	3/83	17-553	"	"	5
171	3/84	17-601	"	"	10
172	3/85	17-648	"	"	15
173	3/86	18-006	"	"	20
174	3/87	18-095	"	"	25

INDEX TO DIGITIZED TRAVERSES (Continued)

SPHERES ON DIELECTRIC SLAB ($R_o = .5 w_l$)

(Slab Depth $2 w_l$.)

<u>Run No.</u>	<u>Digital Tape Location</u>	<u>FM Tape Location</u>	<u>Sphere Diameter (w_l)</u>	<u>Sphere Material</u>	<u>Sphere Range (w_l)</u>
175	3/88	18-539	(reference for runs 176-184)		
176	3/89	18-178	1	$K' = 6$	0
177	3/90	18-249	"	"	5
178	3/91	18-315	"	"	10
179	3/92	18-375	"	"	15
180	3/93	18-432	"	"	20
181	3/94	18-487	"	"	25
182	3/95	18-590	"	"	5
			(off-set $1 w_l$ from traverse-line)		
183	3/96	18-639	"	"	10
			(off-set $1 w_l$ from traverse-line)		
184*	3/97	18-682	"	"	10
			(off-set $1.5 w_l$ from traverse-line)		

INDEX TO DIGITIZED TRAVERSES (Continued)

SIMULATED CREVASSE IN DIELECTRIC SLAB ($R_o = .5 w_1$)

<u>Run No.</u>	<u>Digital Tape Location</u>	<u>FM Tape Location</u>	<u>Slab Depth (w1)</u>	<u>Crevasse Dimensions (w1) w×h×l</u>	<u>Crevasse Range (w1)</u>
185	4/1	19-017	2	.5×.5×4	5
186	4/2	19-105	"	.25×.5×4	5
187	4/3	19-178	"	"	15
188	4/4	19-242	"	.5×.5×4	15
189	4/5	19-307	"	(reference for runs 185-189)	
190	4/6	19-361	1	.25×.5×4	5
191	4/7	19-411	"	"	15
192	4/8	19-457	"	(reference for runs 190-191)	

INDEX TO DIGITIZED TRAVERSES (Continued)

BLOCKS ON DIELECTRIC SLAB ($R_0 = .5 w_1$)
(Thirteen Blocks Scattered Inside 15 w_1 Range)

<u>Run No.</u>	<u>Digital Tape Location</u>	<u>FM Tape Location</u>	<u>Slab Depth (w_1)</u>
193	4/9	20-024	1
194	4/10	20-107	2
195	4/11	20-177	3
196	4/12	20-240	4
197	4/13	20-297	5
198	4/14	20-353	6

INDEX TO DIGITIZED TRAVERSES (Continued)

HALF-SPACE AT VARIOUS LOSS-TANGENTS

<u>Run No.</u>	<u>Digital Tape Location</u>	<u>FM Tape Location</u>	<u>Loss-Tangent</u>	<u>R_o (wl)</u>	
199	4/15	A-006	.002	.5	(receiver reversed)
200	4/16	D-442	.002	"	
201	4/18	A-097	.012	"	(odometer artificial)
202	4/19	A-172	.025	1.25	
203	4/20	A-238	.042	"	
204	4/21	A-298	.073	"	
205	4/22	A-353	.142	"	

INDEX TO DIGITIZED TRAVERSES (Continued)

HORIZONTAL METAL PLATE AT VARIOUS LOSS-TANGENTS

<u>Run No.</u>	<u>Digital Tape Location</u>	<u>FM Tape Location</u>	<u>Plate Depth (wl)</u>	<u>Loss-Tangent</u>	<u>R_o (wl)</u>	
206	4/23	M-011	.5	.002	.5	
207	4/24	M-103	1	"	"	
208	4/25	M-181	1.5	"	"	
209	4/26	M-251	2	"	"	
210	4/27	M-316	2.5	"	"	
211	4/28	M-376	3	"	"	
212	4/29	M-433	4	"	"	
213	4/30	M-486	5	"	"	
214	4/31	M-536	6	"	"	
215	4/32	M-586	7	"	"	
216	4/33	N-011	1	.012	"	(odometer artificial)
217	4/34	N-103	2	"	"	"
218	4/35	N-185	3	"	"	"
219	4/36	N-257	4	"	"	"
220	4/37	N-322	5	"	"	"
221	4/38	N-382	6	"	"	"
222	4/39	N-440	7	"	"	"
223	5/1	S-011	1	.025	1.25	
224	5/2	S-100	2	"	"	
225	5/3	S-177	3	"	"	
226	5/4	S-247	4	"	"	
227	5/5	S-311	5	"	"	
228	5/6	S-371	6	"	"	
229	5/8	S-427	7	"	"	
230	5/9	Y-010	.5	.042	1.25	
231	5/10	Y-097	1	"	"	

INDEX TO DIGITIZED TRAVERSES (Continued)

HORIZONTAL METAL PLATE AT VARIOUS LOSS-TANGENTS (Concluded)

<u>Run No.</u>	<u>Digital Tape Location</u>	<u>FM Tape Location</u>	<u>Plate Depth (wl)</u>	<u>Loss-Tangent</u>	<u>R_o (wl)</u>
232	5/11	Y-173	1.5	.042	1.25
233	5/12	Y-243	2	"	"
234	5/13	Y-307	2.5	"	"
235	5/14	Y-366	3	"	"
236	5/15	Y-423	4	"	"
237	5/16	Y-475	5	"	"
238	5/17	Y-525	6	"	"
239*	5/18	Y-574	7	"	"
240	5/19	Z-008	.5	.073	1.25
241	5/20	Z-095	1	"	"
242	5/21	Z-174	1.5	"	"
243	5/22	Z-244	2	"	"
244	5/23	Z-310	2.5	"	"
245	5/24	Z-370	3	"	"
246*	5/25	Z-426	4	"	"
247*	5/26	Z-480	5	"	"
248*	5/27	Z-532	6	"	"
249	5/28	Z-584	7	"	"
250	5/29	CC-009	.5	.142	1.25
251	5/30	CC-097	1	"	"
252	5/31	CC-175	1.5	"	"
253	5/32	CC-246	2	"	"
254	5/33	CC-311	2.5	"	"
255	5/34	CC-371	3	"	"
256	5/35	CC-428	4	"	"

INDEX TO DIGITIZED TRAVERSES (Continued)

SINGLE CREVASSES IN HALF-SPACE ($R_0 = .5 w_1$)

(Crevasse Range 5 w_1 . Loss-Tangent .002.)

<u>Run No.</u>	<u>Digital Tape Location</u>	<u>FM Tape Location</u>	<u>Crevasse Dimensions (w₁) w×l×h</u>	<u>Crevasse Orientation</u>	<u>Field Component</u>
257	5/36	C-006	.3×3×3	0°	E-Phi
258	5/37	C-102	"	0°	E-Rho
259	5/38	C-179	"	45°	E-Rho
260	5/39	C-243	"	45°	E-Phi
261	5/40	C-304	"	90°	E-Phi
262	5/41	C-358	"	90°	E-Rho
263	5/42	D-008	.15×1.5×1.5	0°	E-Phi
264*	5/43	D-097	"	0°	E-Rho
265	5/44	D-271	"	45°	E-Phi
266	5/45	D-237	"	45°	E-Rho
267	5/46	D-296	"	90°	E-Phi
268	5/47	D-348	"	90°	E-Rho
269	5/48	D-397	(reference for runs 257-275, E-Rho component)		
199	4/15	A-006	(reference for run 257)		
200	4/16	D-442	(reference for runs 258-275, E-Phi component)		

INDEX TO DIGITIZED TRAVERSES (Continued)

MULTIPLE CREVASSES IN HALF-SPACE ($R_o = .5 w_1$)

(Set of Six Crevasses Centered at 9 w_1 Range,
Loss-Tangent = .002)

<u>Run No.</u>	<u>Digital Tape Location</u>	<u>FM Tape Location</u>	<u>Crevasse Dimensions (w_1) $w \times l \times h$</u>	<u>Crevasse Orientation</u>	<u>Field Component</u>
270	5/49	E-010	.15×1.5×1.5	0°	E-Phi
271	5/50	E-098	"	0°	E-Rho
272	5/51	E-171	"	90°	E-Rho
273	5/52	E-238	"	90°	E-Phi
274	5/53	E-296	"	45°	E-Phi
275	5/54	E-350	"	45°	E-Rho

INDEX TO DIGITIZED TRAVERSES (Continued)

SINGLE CREVASSE OVER METAL PLATE

(Plate Depth 4 wl. Crevasse Range 5 λ)

<u>Run No.</u>	<u>Location</u>	<u>Location</u>	<u>Crevasse Dimensions (wl) w×l×h</u>	<u>Crevasse Orientation</u>	<u>Field Component</u>	<u>R_o (wl)</u>
276	5/55	I-011	.3×3×3	0°	E-Phi	.5
277	5/56	I-097	"	0°	E-Rho	"
278	5/57	I-172	"	45°	E-Rho	"
279	5/58	I-236	"	45°	E-Phi	"
280	5/59	I-294	"	90°	E-Phi	"
281	5/60	I-349	"	90°	E-Rho	"
282*	8/18	H-011	.15×1.5×1.5	0°	E-Phi	"
283	5/62	H-098	"	0°	E-Rho	"
284	5/63	H-172	"	45°	E-Rho	"
285	5/64	H-239	"	45°	E-Phi	"
286	5/65	H-302	"	90°	E-Phi	"
287	5/66	H-356	"	90°	E-Rho	"
288	5/67	V-014	"	0°	E-Phi	1.25
289	5/68	V-105	"	45°	E-Phi	"
290	5/69	V-184	"	90°	E-Phi	"
291	5/70	V-256	.1×.75×.75	0°	E-Phi	"
292*	5/71	V-321	"	45°	E-Phi	"
293	5/72	V-383	"	90°	E-Phi	"

INDEX TO DIGITIZED TRAVERSES (Continued)

MULTIPLE CREVASSES OVER METAL PLATE

[Plate Depth 4 wl. Set of Six (five for runs 305-308)
 Crevasse Centered at 9 wl Range.]

<u>Run No.</u>	<u>Digital Tape Location</u>	<u>FM Tape Location</u>	<u>Crevasse Dimensions (wl) w×l×h</u>	<u>Crevasse Orientation</u>	<u>Field Component</u>	<u>R₀ (wl)</u>	<u>Loss-Tangent</u>
294*	5/73	G-010	.15×1.5×1.5	0°	E-Phi	.5	.002
295	5/74	G-099	"	0°	E-Rho	"	"
296	5/75	G-174	"	45°	E-Rho	"	"
297	5/76	G-239	"	45°	E-Phi	"	"
298	5/77	G-298	"	90°	E-Phi	"	"
299	5/78	G-353	"	90°	E-Rho	"	"
300	5/79	G-403	(reference for runs 276-299, E-Rho)				
212	4/29	M-433	(reference for runs 276-299, E-Phi)				
301	5/80	U-013	.15×1.5×1.5	0°	E-Phi	1.25	.025
302	5/81	U-107	"	90°	E-Phi	"	"
303	5/82	U-189	"	0°	E-Phi	"	.042
304	5/83	U-258	"	90°	E-Phi	"	"
305	5/84	U-326	.1×.75×.75	0°	E-Phi	"	"
306	5/85	U-387	"	90°	E-Phi	"	"
307	5/86	U-448	"	0°	E-Phi	"	.073
308	5/87	U-501	"	90°	E-Phi	"	"

INDEX TO DIGITIZED TRAVERSES (Continued)

JUNEAU CRATER

(11-14 m Diameter × 3.5 m Deep. Range 263 m.
Off-set 10 m.)

<u>Run No.</u>	<u>Digital Tape Location</u>	<u>FM Tape Location</u>		<u>Frequency Modeled (MHz)</u>	<u>Loss Tangent</u>	<u>R₀ (wl)</u>
309	5/88	U-554	(32 MHz crater at 16 MHz range over metal plate 4 wl deep)		.073	1.25
310	5/89	0-010	Half-space	32	.012	.5
311	5/90	0-101	"	32	.025	1.25
312	5/91	0-180	"	16	.025	1.25
313	5/92	0-254	"	16	.042	1.25
314	5/93	0-320	"	32	.042	1.25

INDEX TO DIGITIZED TRAVERSES (Continued)

30° MOUNTAIN-SIDE ($R_0 = 1.25 w_1$)
(Transmitter 173 ft from Baseline)

<u>Run No.</u>	<u>Digital Tape Location</u>	<u>FM Tape Location</u>	<u>Frequency Modeled (MHz)</u>	<u>Traverse Direction</u>	<u>Loss- Tangent</u>
315	5/95	W-011	8	away	.042
316	5/96	W-112	8	45°	.042
317	5/97	W-182	8	along	.042
318	5/98	W-252	8	away	.073
319	5/99	W-310	4	away	.073
320	5/100	W-364	8	45°	.073
321	5/101	W-416	4	45°	.073
322	5/102	W-467	8	along	.073
323	5/103	W-514	4	along	.073
324	5/104	DD-011	4	away	.142
325	5/105	DD-093	2	away	.142
326*	5/106	DD-166	4	45°	.142
327	5/107	DD-231	2	45°	.142
328	5/108	DD-291	4	along	.142
329	5/109	DD-348	2	along	.142

INDEX TO DIGITIZED TRAVERSES (Continued)

STEP ($R_0 = 1.25 w_1$)
 (45° Ramp Connecting Horizontal Plates 200 and 490 ft deep)

<u>Run No.</u>	<u>Digital Tape Location</u>	<u>FM Tape Location</u>	<u>Frequency Modeled (MHz)</u>	<u>TX Position</u>	<u>RX Position</u>	<u>Loss-Tangent</u>
330	5/110	X-012	8	bottom	away	.042
331	5/111	X-092	"	top	away	"
332	5/112	X-165	"	bottom	along	"
333	5/113	X-232	"	bottom	toward	"
334	5/114	X-292	"	top	toward	"
335	5/115	X-352	(reference for 8 MHz)			
336*	6/1	T-014	4	bottom	away	.073
337	5/2	T-094	"	top	away	"
338	6/3	T-166	"	bottom	along	"
339	6/4	T-232	"	bottom	toward	"
340	6/5	T-293	"	top	toward	"
341	6/6	T-350	(reference for 4 MHz)			
342	6/7	P-012	2	bottom	away	.142
343	6/8	P-094	"	top	away	"
344	6/9	P-166	"	bottom	along	"
345	6/10	P-232	"	bottom	toward	"
346	6/11	P-293	"	top	toward	"
347	6/12	P-351	(reference for 2 MHz)			

INDEX TO DIGITIZED TRAVERSES (Continued)

RIDGE ($R_0 = 1.25 w_1$)
 (45°, 200 ft High Ridge on 490 ft Deep Plate)

<u>Run No.</u>	<u>Digital Tape Location</u>	<u>FM Tape Location</u>	<u>Frequency Modeled (MHz)</u>	<u>TX Position</u>	<u>RX Position</u>	<u>Loss-Tangent</u>
348	6/13	X-406	8	bottom	away	.042
349	6/14	X-456	8	bottom	toward	.042
350	6/15	X-505	8	bottom	along	.042
351	6/17	T-404	4	bottom	away	.073
352	6/18	T-454	4	bottom	toward	.073
353	6/19	T-502	4	bottom	along	.073
354	6/20	P-406	2	bottom	away	.142
355	6/21	P-457	2	bottom	toward	.142
356	6/22	P-506	2	bottom	along	.142

INDEX TO DIGITIZED TRAVERSES (Concluded)

SUPPLEMENTAL INDEX TO DUPLICATED DIGITIZATIONS

<u>Run No.</u>	<u>Indexed Digitization</u>	<u>Duplicate Digitization</u>
037	1/38	7/1
038	1/39	8/1
048	1/49	7/2
052	2/3	6/23
057	2/8	6/24
061	2/12	6/25
073	2/24	8/2
086	2/37	8/3
104	3/15	8/4
106	3/17	8/5
110	3/21	8/6
111	3/22	8/7
112	3/23	8/8
159	3/70	8/9
170	3/83	8/10
184	3/97	8/11
239	5/18	8/12
246	5/25	8/13
247	5/26	8/14
248	5/27	8/15
264	5/43	7/3
282	8/18	5/61
292	5/71	7/4
294	5/73	8/16
326	5/106	8/17
336	6/1	7/5

6.0 REFERENCES

1. Kopal, Z.; and D. Strangway, ed.: Lunar Geophysics, Proceedings of a Conference at the Lunar Science Institute, Houston, Texas, October 18-21, 1971, pp. 258-295. Boston, Reidel, 1972.
2. Annan, A. P.: Radio Interferometry Depth Sounding, Part I - Theoretical Discussion. Geophysics, Vol. 38, No. 3, pp. 557-580.
3. Rossiter, J. R.; *et al*: Radio Interferometry Depth Sounding, Part II - Experimental Results. Geophysics, Vol. 38, No. 3, June 1973, pp. 581-599.
4. Dewan, R. N.: Progress Report I, Surface Electrical Properties Simulation Model. LEC/HASD No. 645D.21.076, July 1971.
5. Hawley, D. E.; and W. M. Waller: Progress Report II, Surface Electrical Properties Simulation Model. LEC/HASD No. 645D.21.077, December 1971.
6. Silver, S., ed.: Microwave Antenna Theory and Design, pp. 239-256. McGraw-Hill, 1949.
7. Waller, W. M.: SEP Simulation Model V. LEC memorandum (ref. 634-526), November 13, 1972.
8. Cooper, W. W.: Patterns of Dipole Antenna on Stratified Medium, Technical Report TR71-3, Massachusetts Institute of Technology Center for Space Research, June 1971.
9. Gold, B.; and C. M. Rader: Digital Processing of Signals. McGraw-Hill, 1969.
10. Von Hippel, A. R., ed.: Dielectric Materials and Applications, pp. 63-122. M.I.T. Press, 1952.

APPENDIX A
TRAVERSES OVER METAL PLATE

FIGURE A1.

HORIZONTAL METAL PLATE.

TX 0 DBM.

0 / e RUN

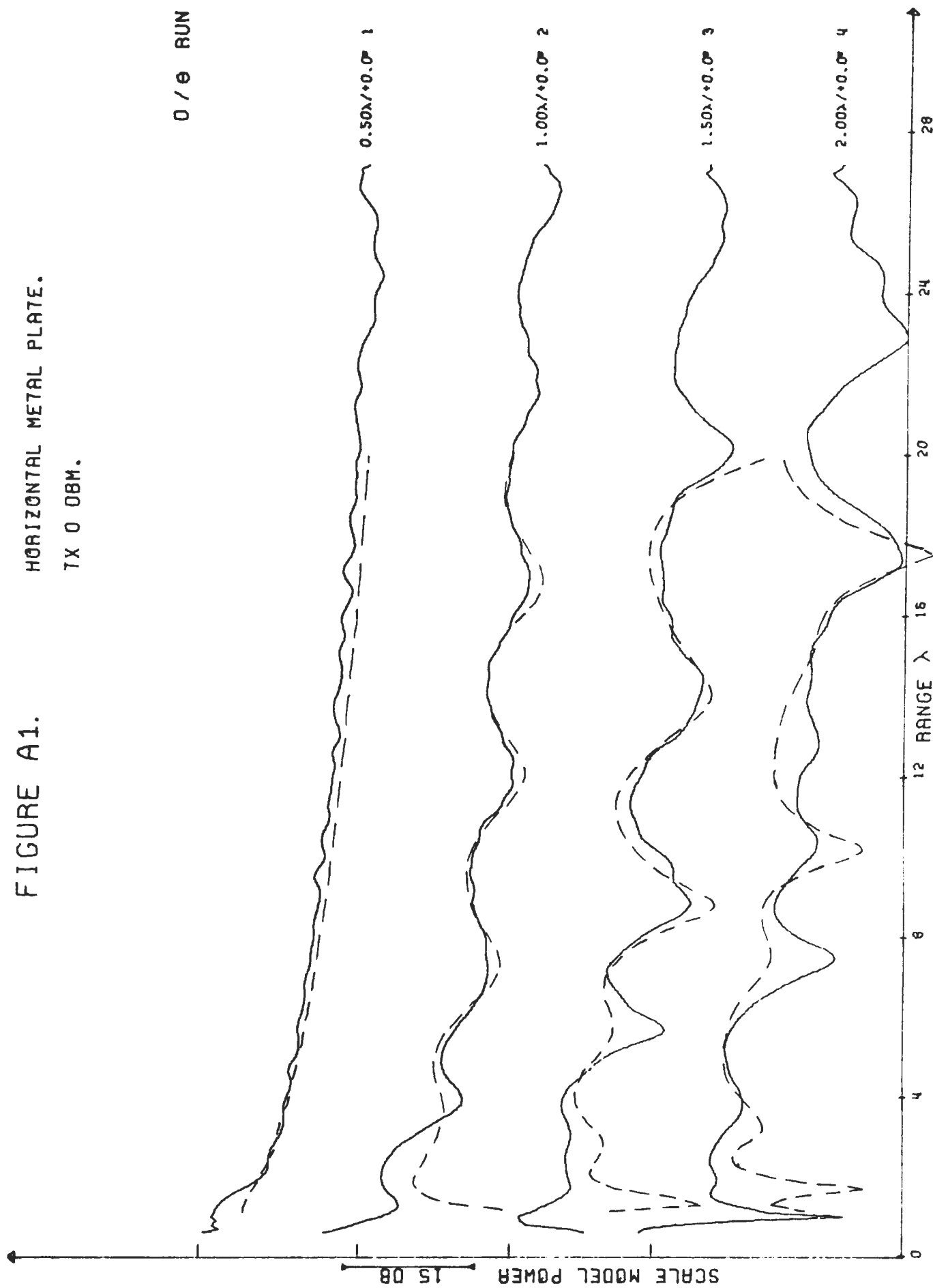


FIGURE A2.

HORIZONTAL METAL PLATE.

TX 0 08M.

0 / θ RUN

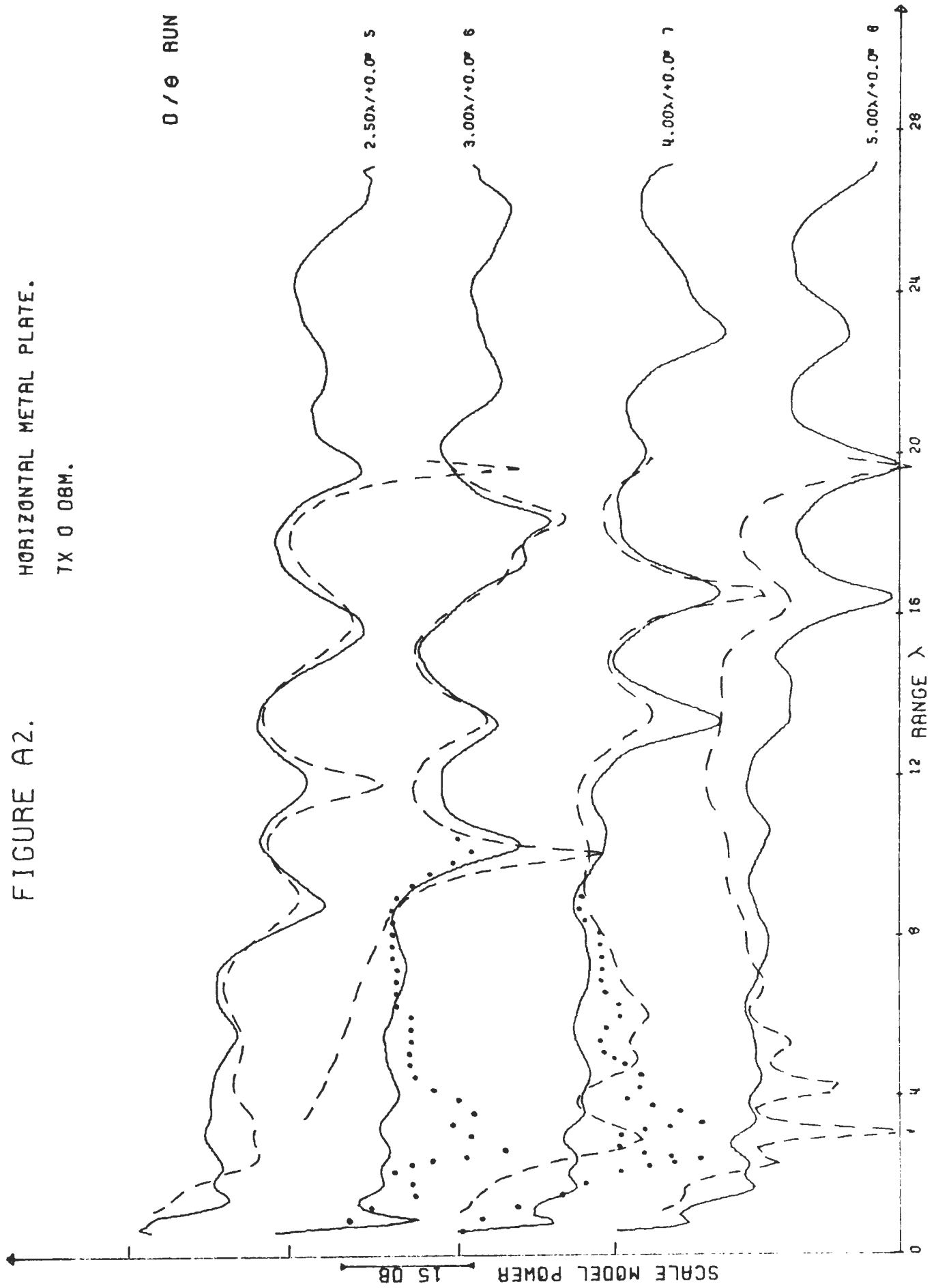


FIGURE A3.

HORIZONTAL METAL PLATE.

TX 0 DBM.

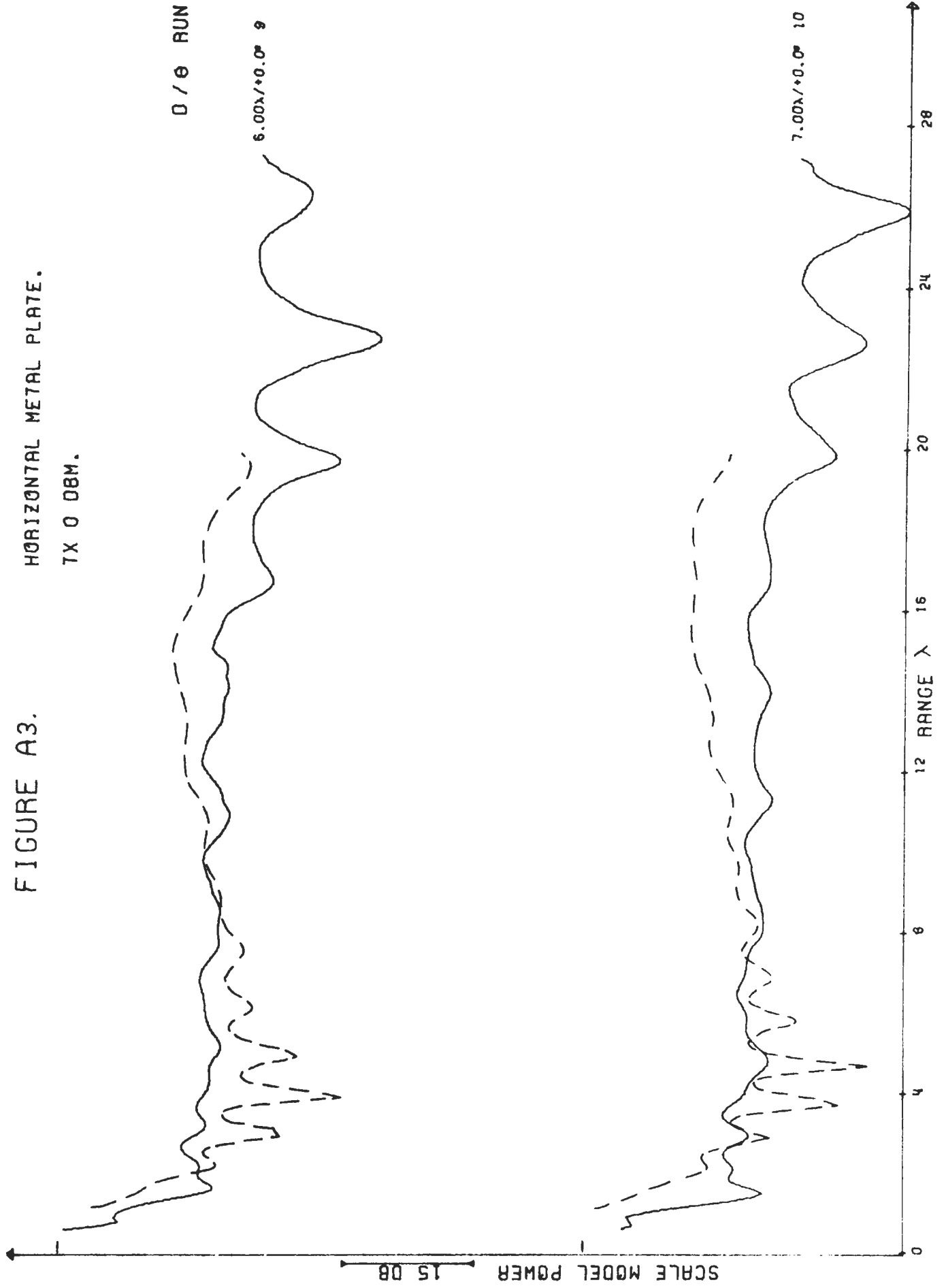


FIGURE A4.

HORIZONTAL METAL PLATE.

7X 0 08M.

0 / 0 RUN

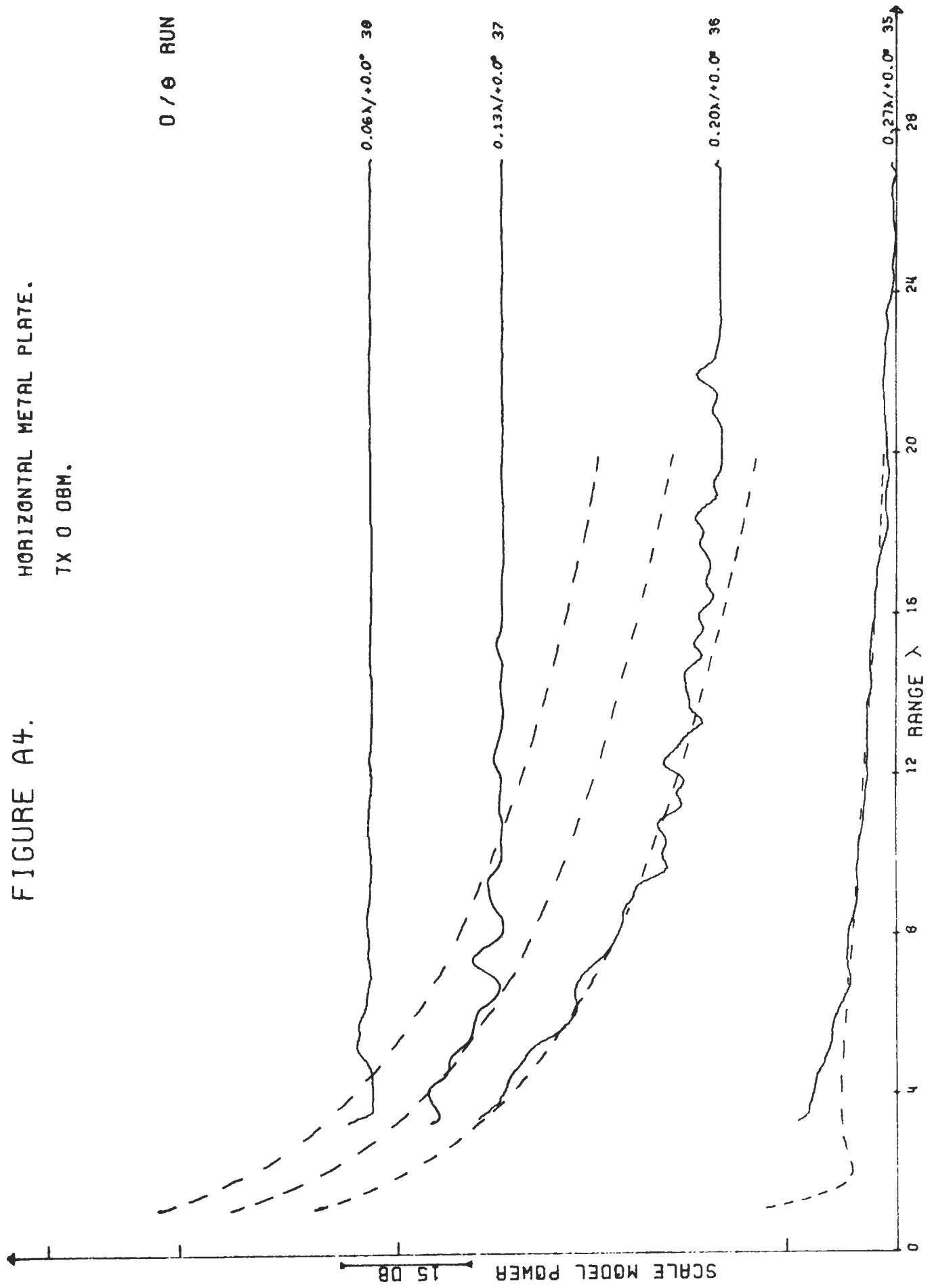


FIGURE A5.

HORIZONTAL METAL PLATE.
TX 0 DBM.

0 / 0 RUN

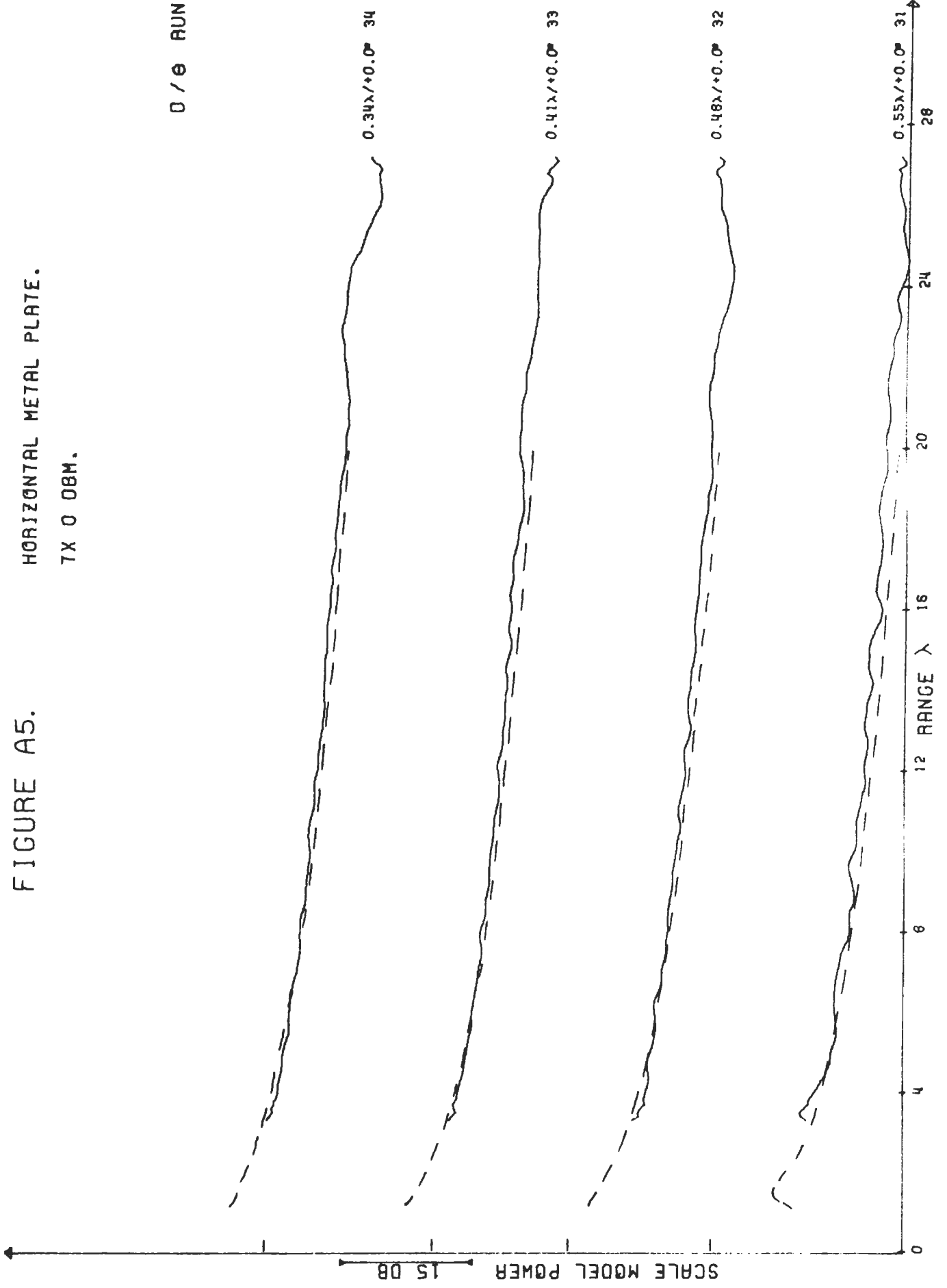


FIGURE A6.
HORIZONTAL METAL PLATE.
TX 0 DBM.

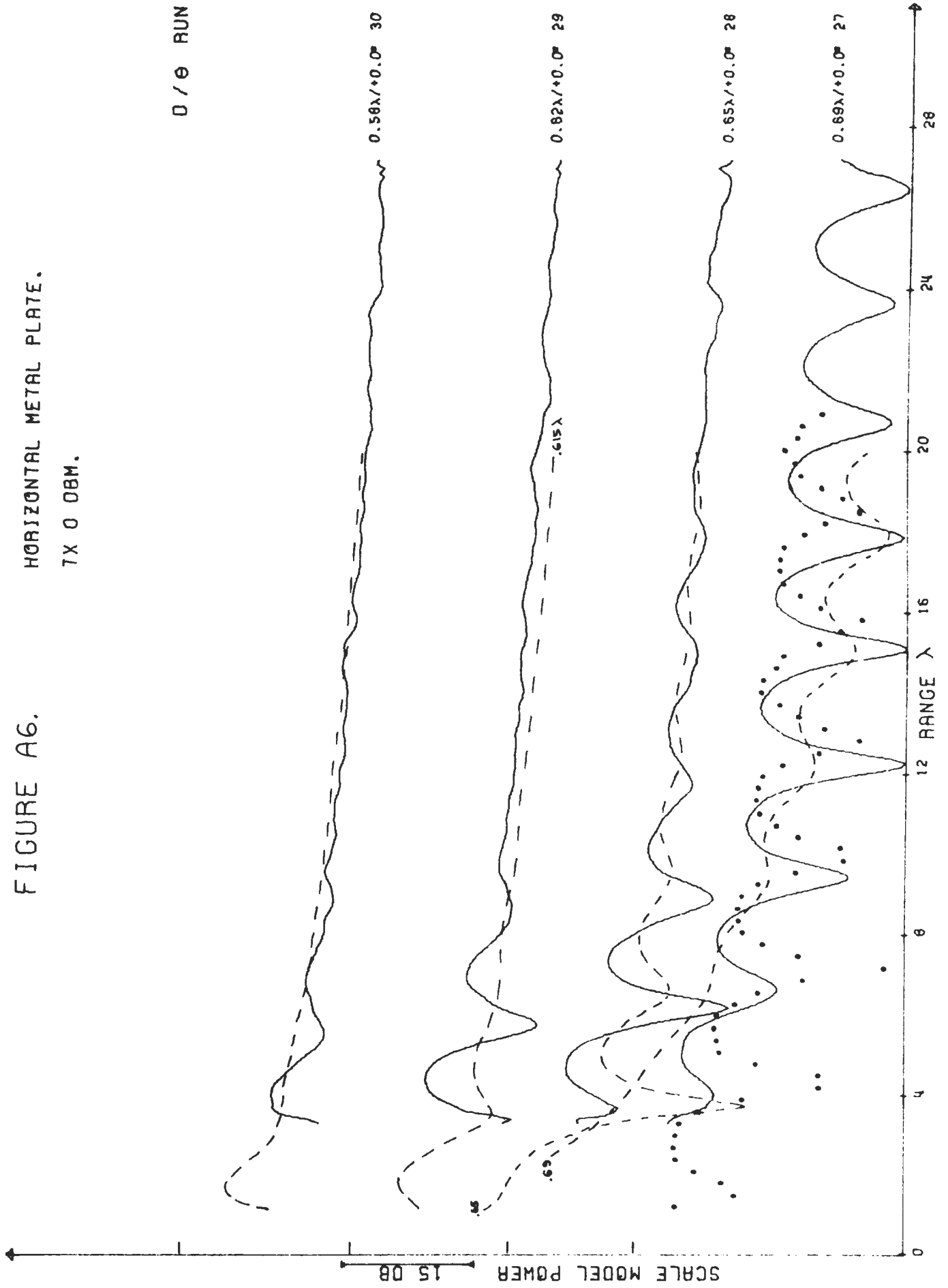


FIGURE A7.

HORIZONTAL METAL PLATE.

TX 0 DBM.

0 / 0 RUN

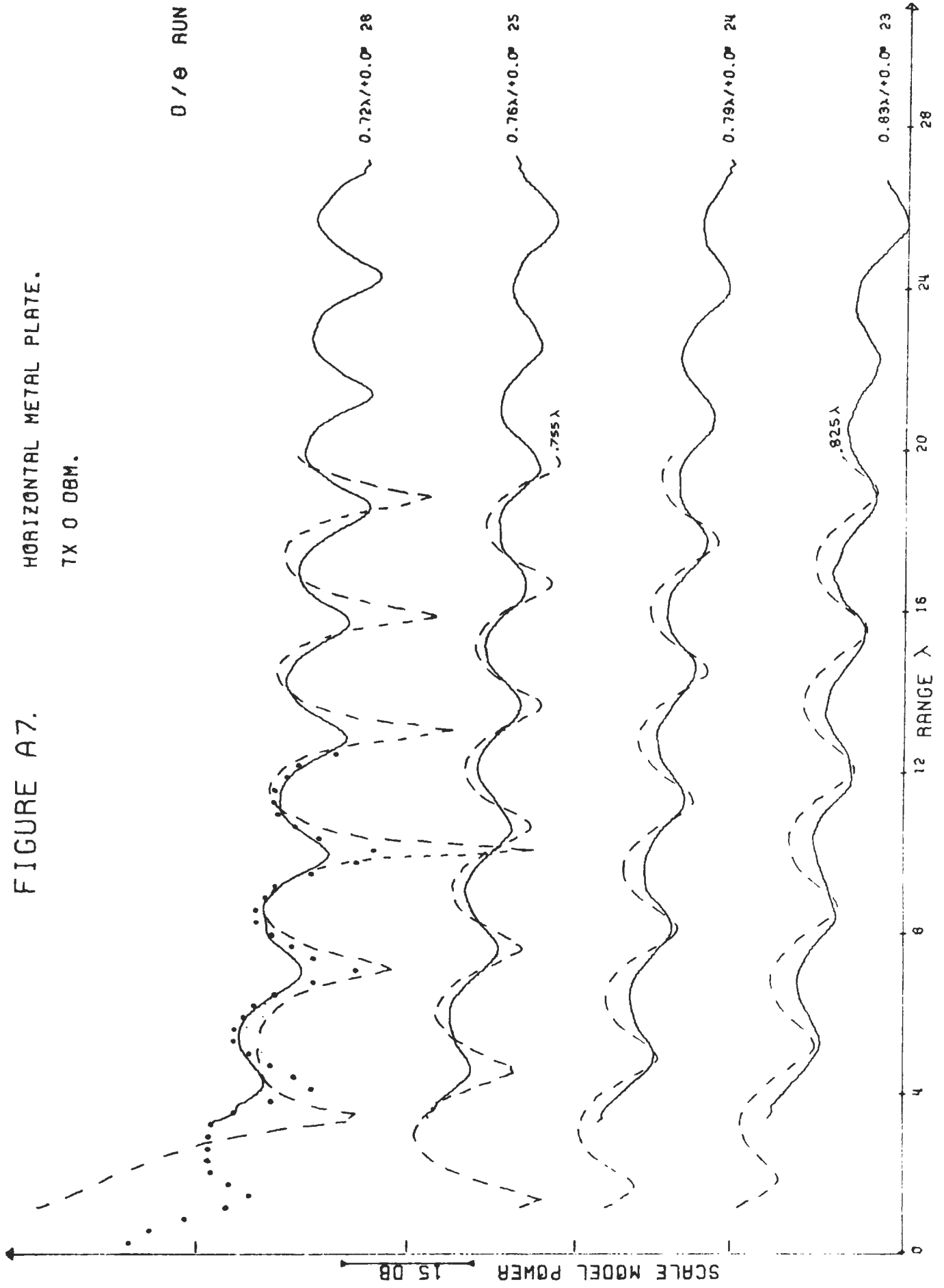


FIGURE A8. HORIZONTAL METAL PLATE.

TX 0 DBM.

θ / θ RUN

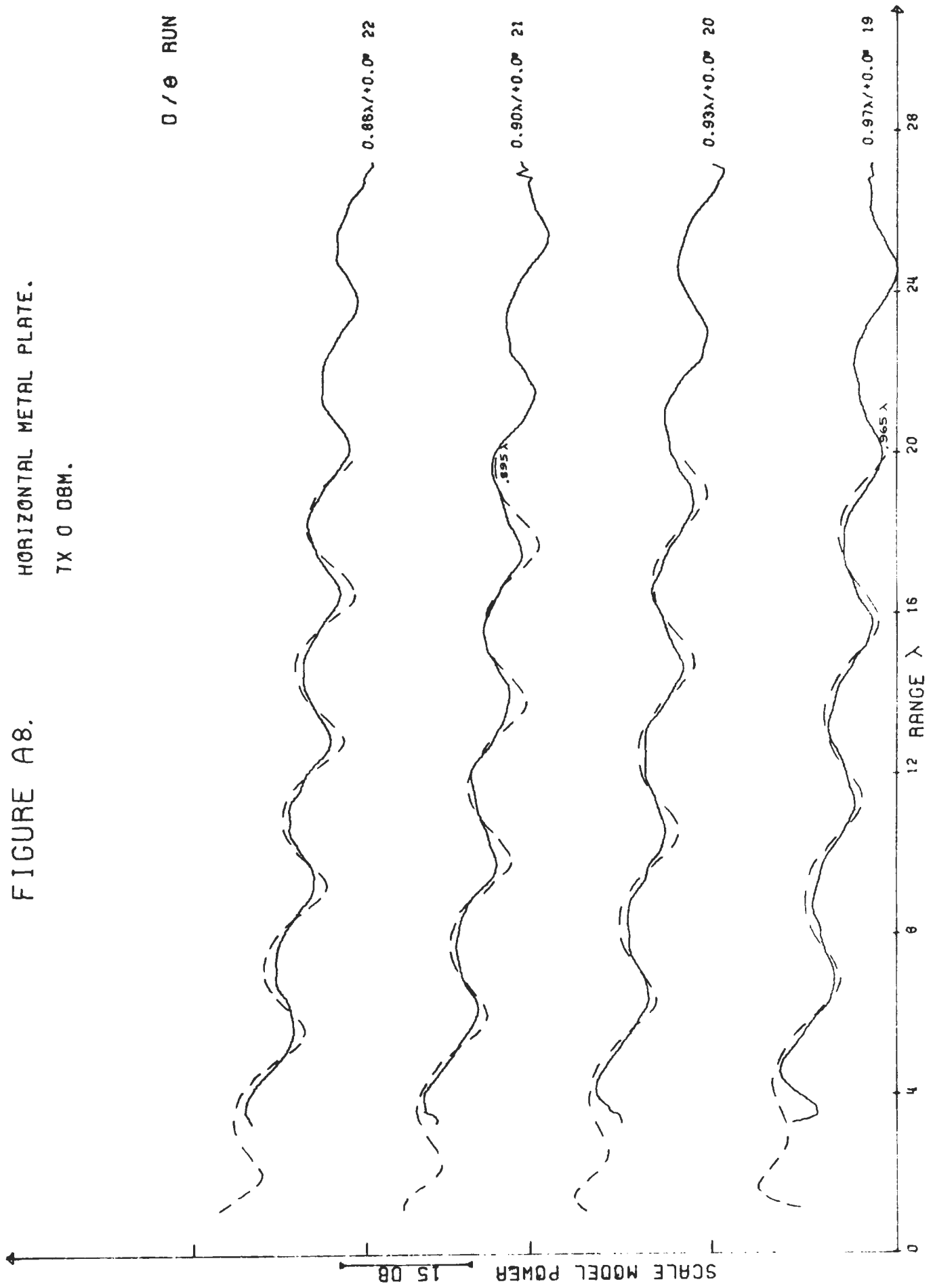


FIGURE A9.

HORIZONTAL METAL PLATE.

TX 0 DBM.

0/0 RUN

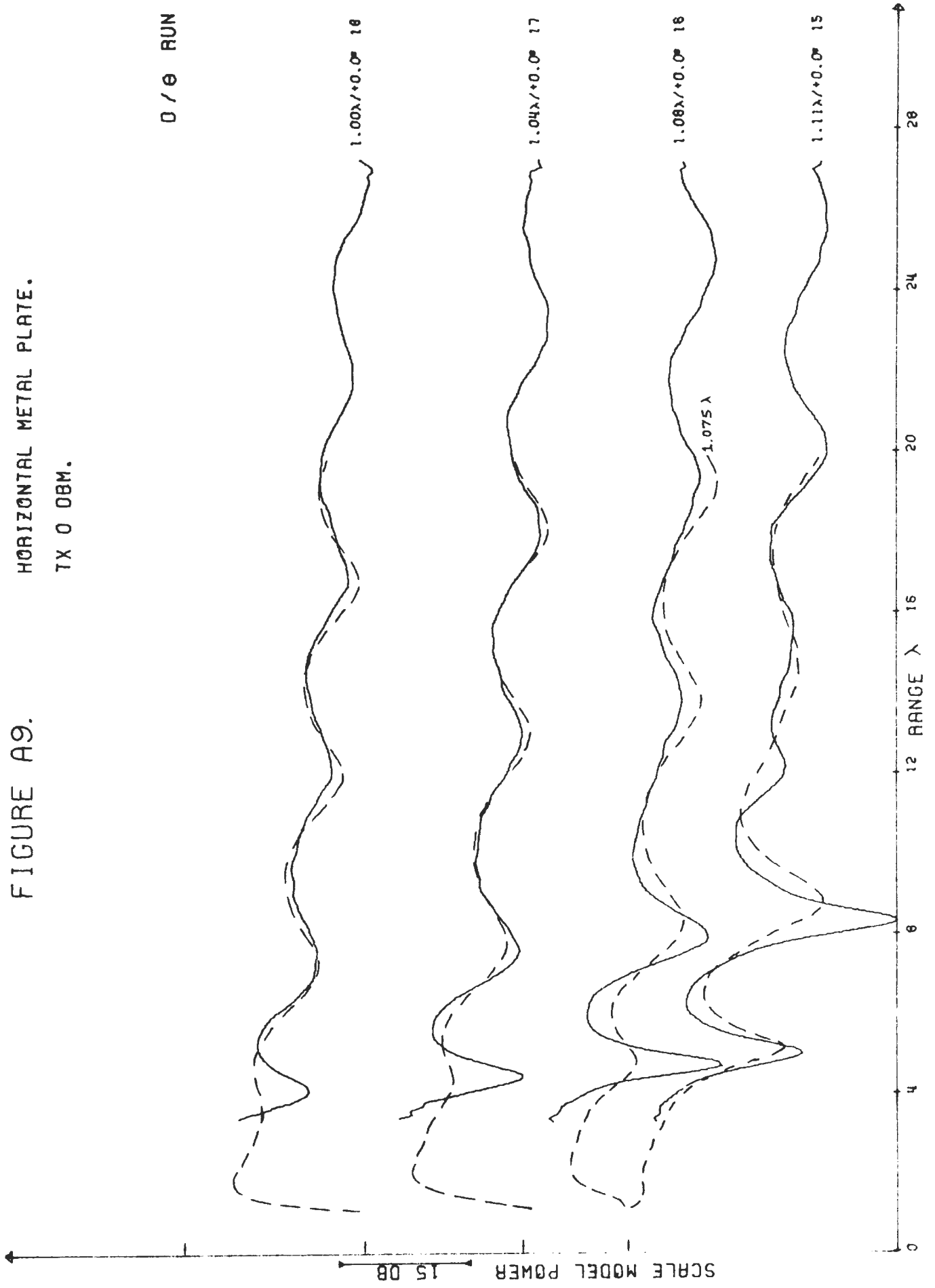


FIGURE A10.
 HORIZONTAL METAL PLATE.
 TX 0 DBM.

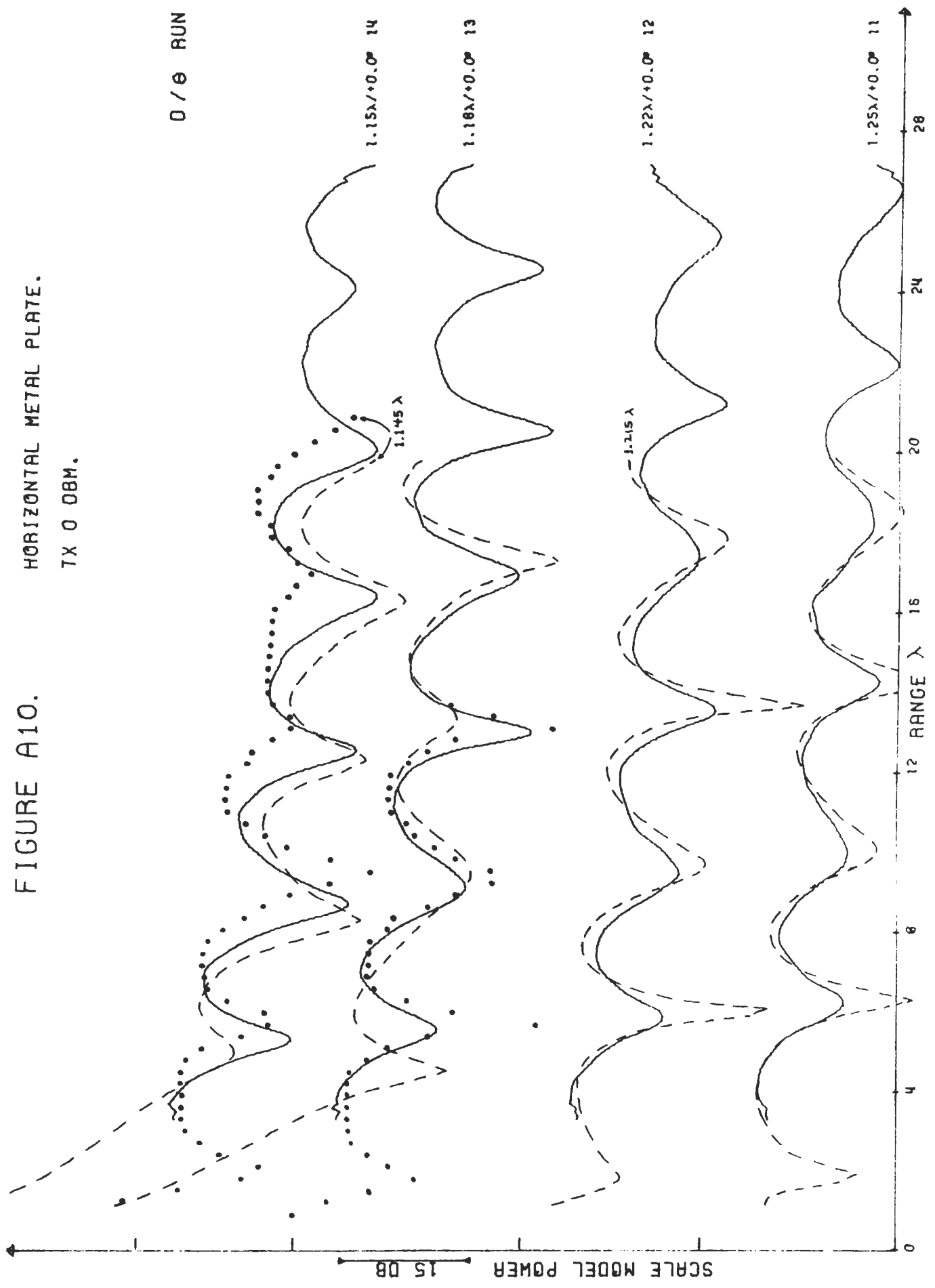


FIGURE A11.

METAL PLATE -- LATERAL SLOPES.
7X 0 DBM.

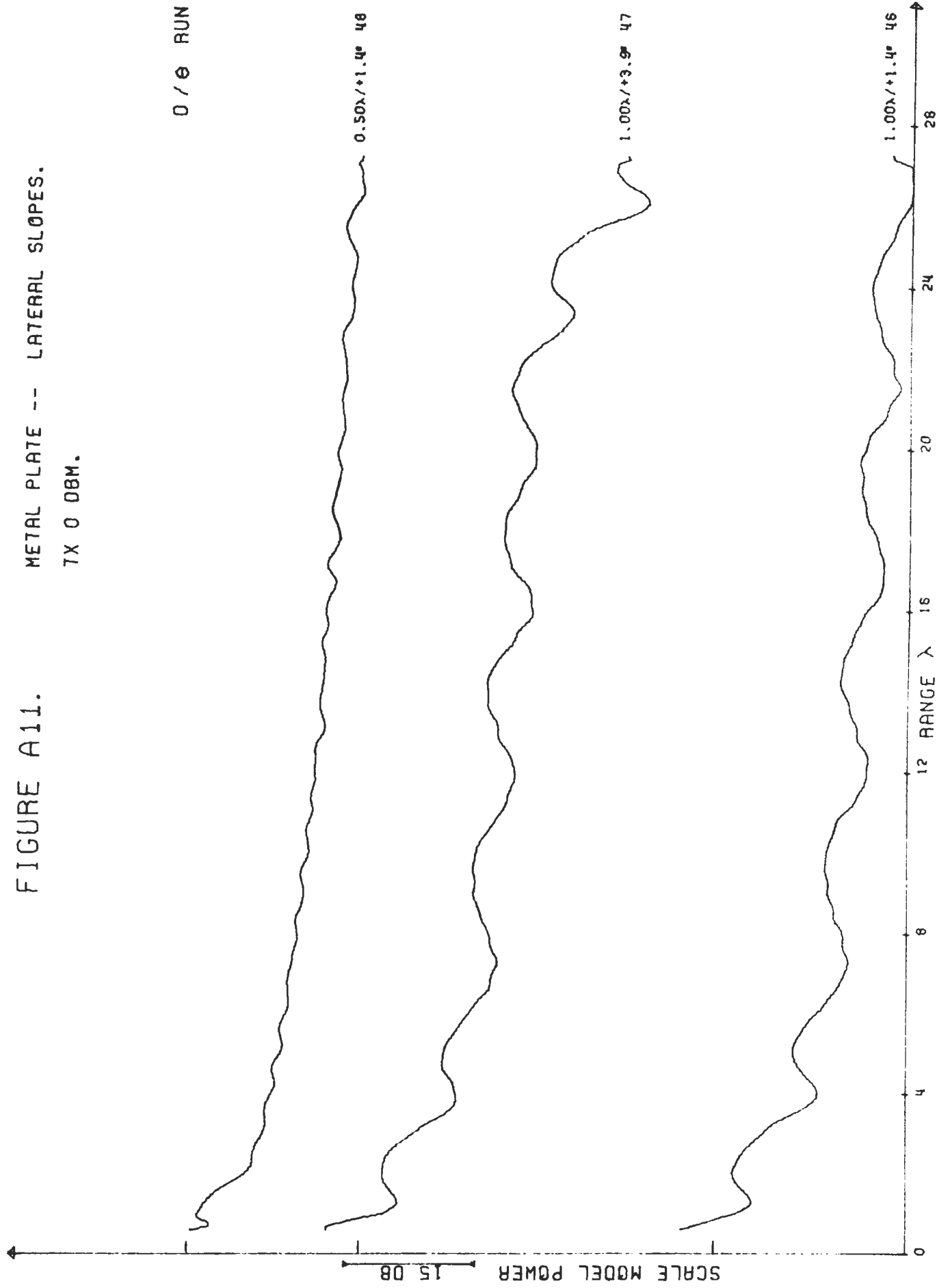


FIGURE A12.

METAL PLATE -- LATERAL SLOPES.

TX 0 DBM.

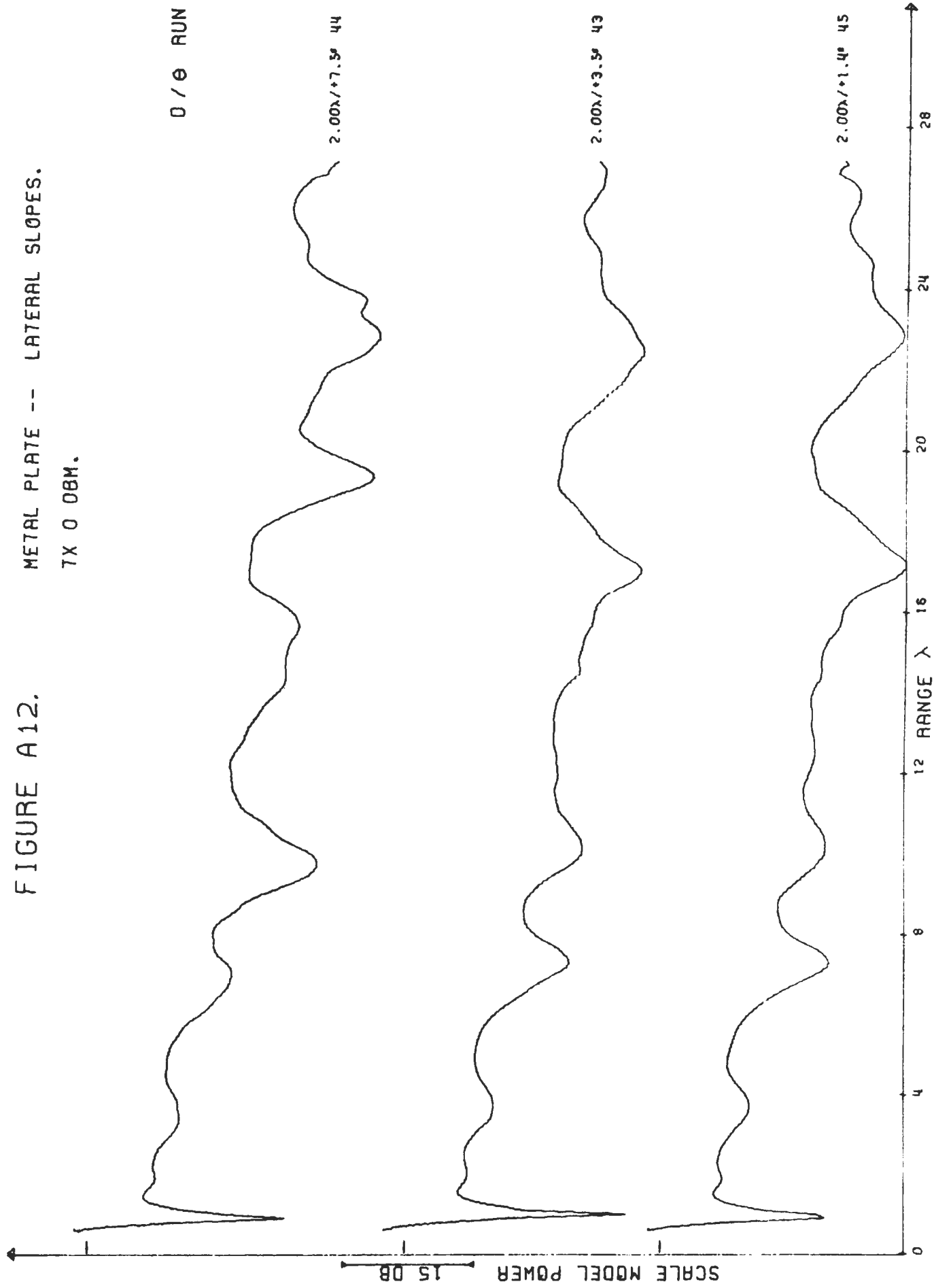


FIGURE A13.

METAL PLATE -- LATERAL SLOPES.
7X 0 DBM.

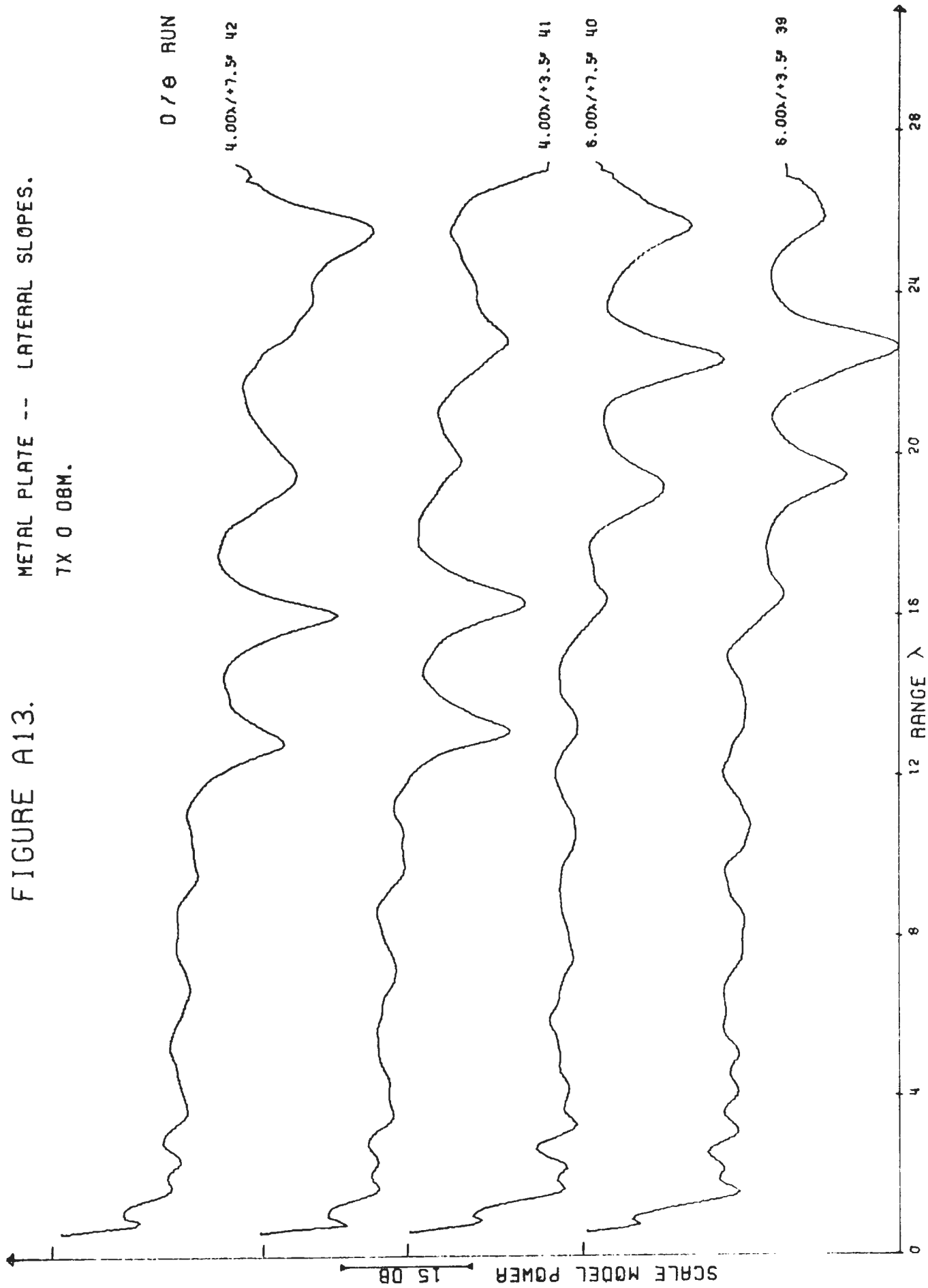


FIGURE A14.

METAL PLATE -- FORWARD SLOPES.

7X 0 DBM.

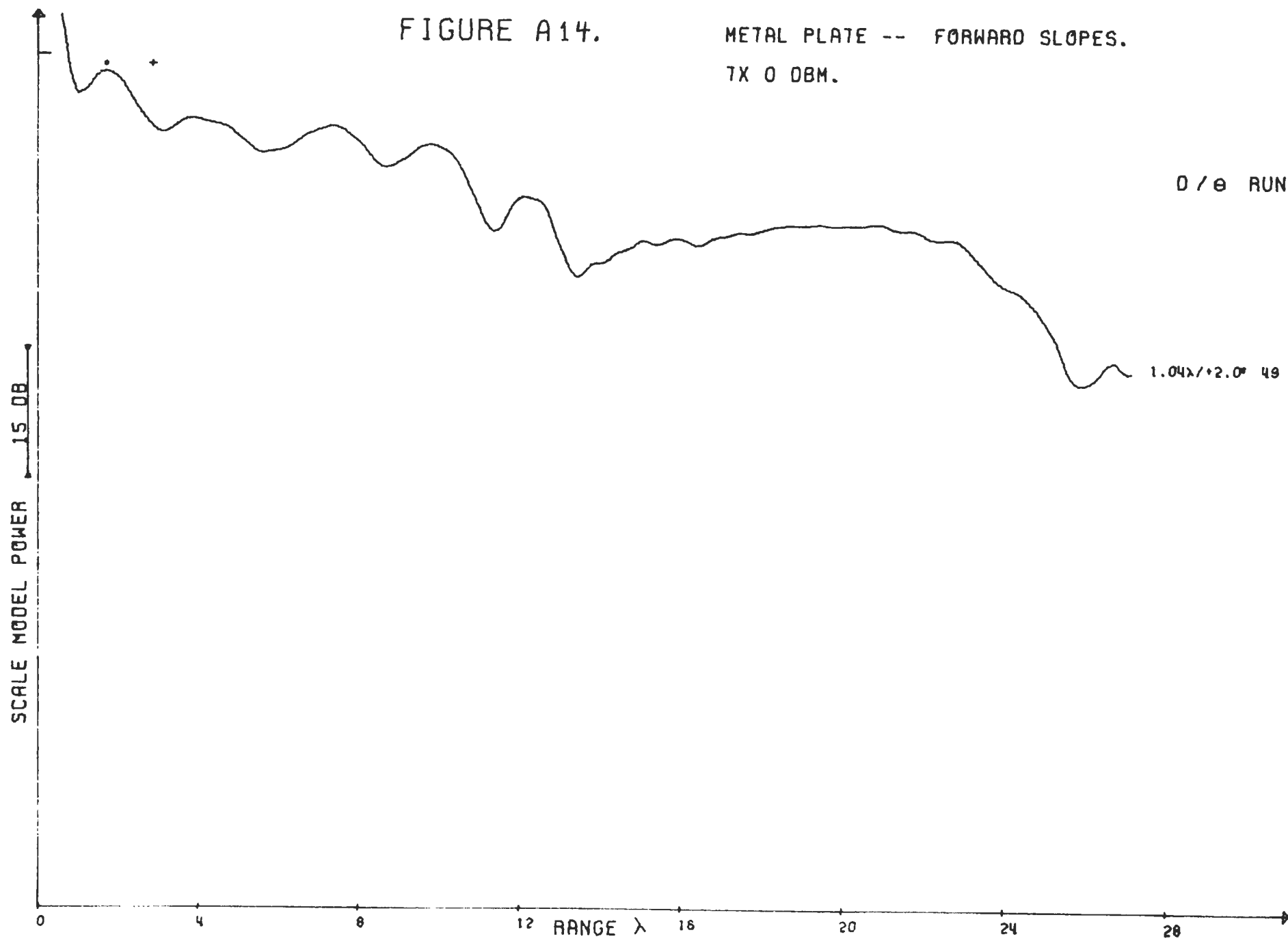


FIGURE A15.

METAL PLATE -- FORWARD SLOPES.

TX 15 08M.

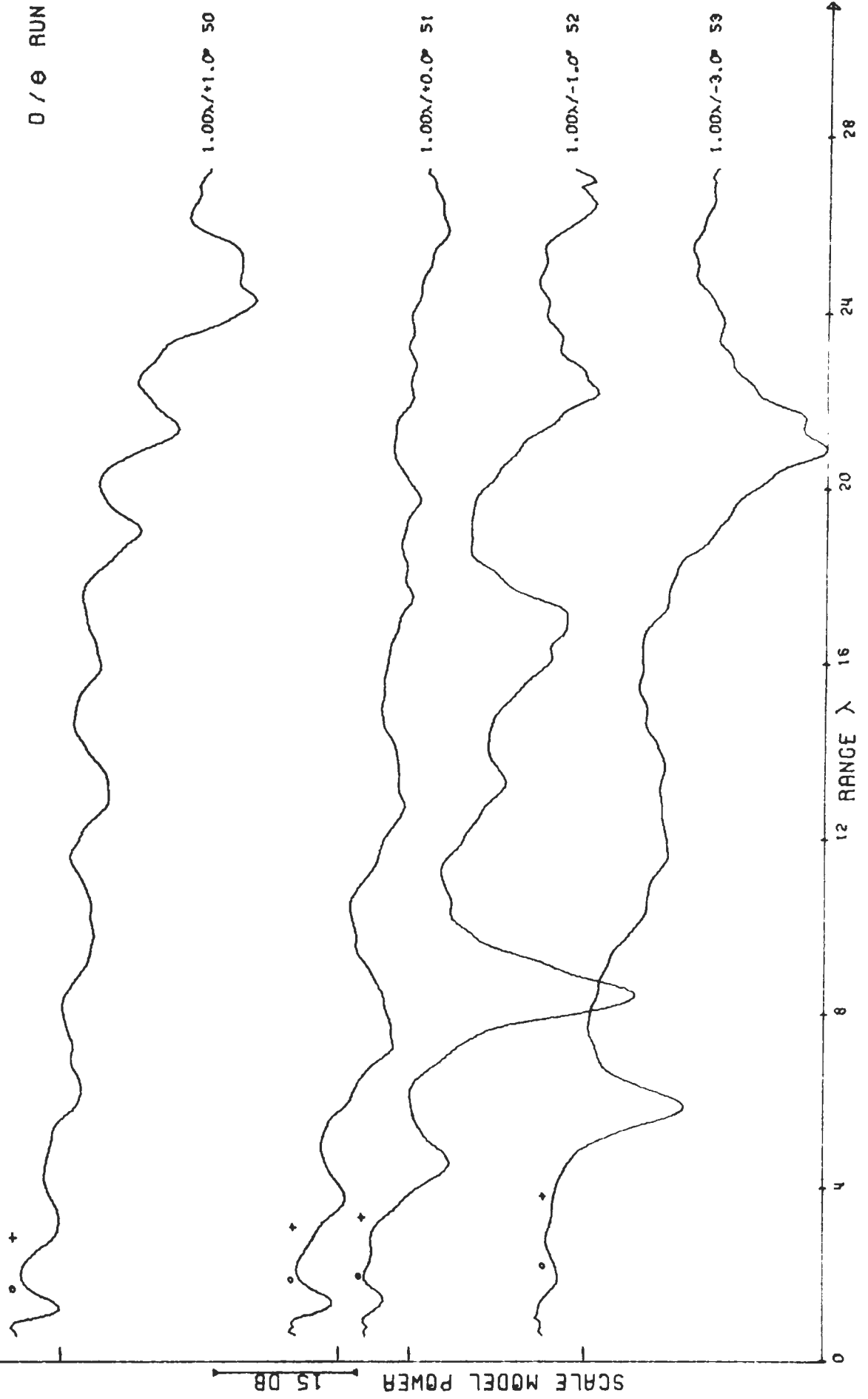


FIGURE A16.

METAL PLATE -- FORWARD SLOPES.
7X 15 DBM.

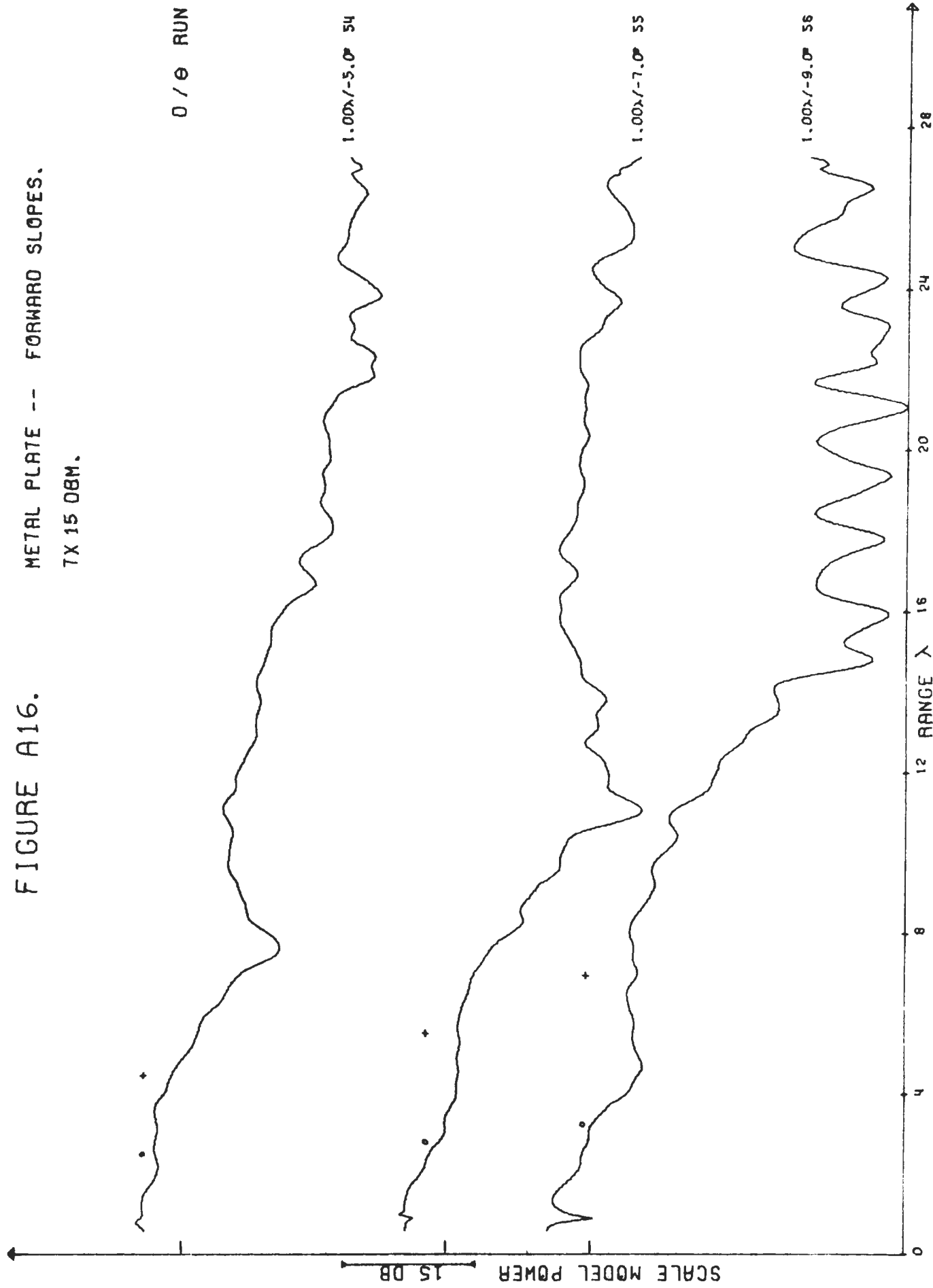


FIGURE A17.

METAL PLATE -- FORWARD SLOPES.

TX 15 DBM.

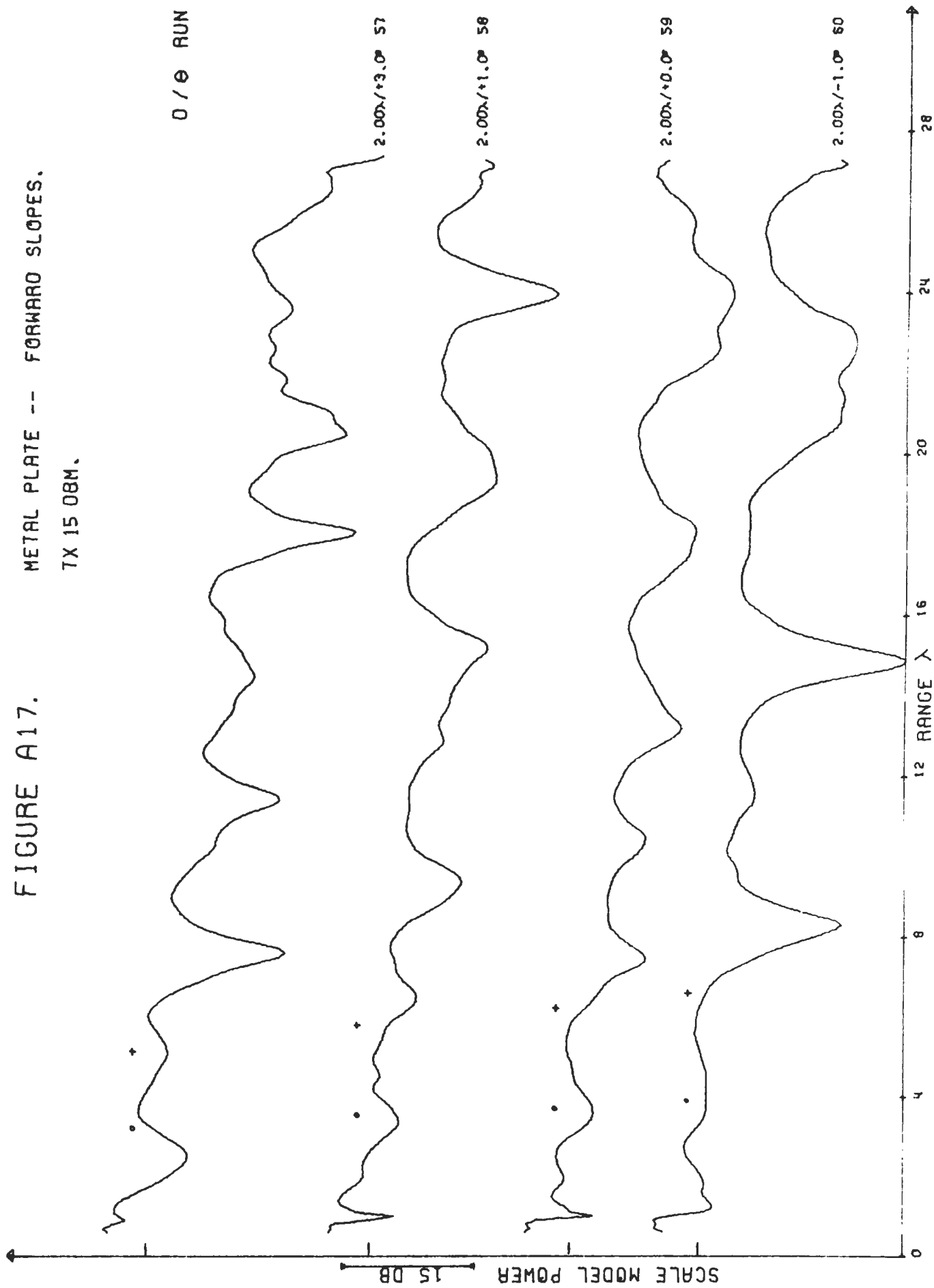


FIGURE A18. METAL PLATE -- FORWARD SLOPES.

TX 15 08M.

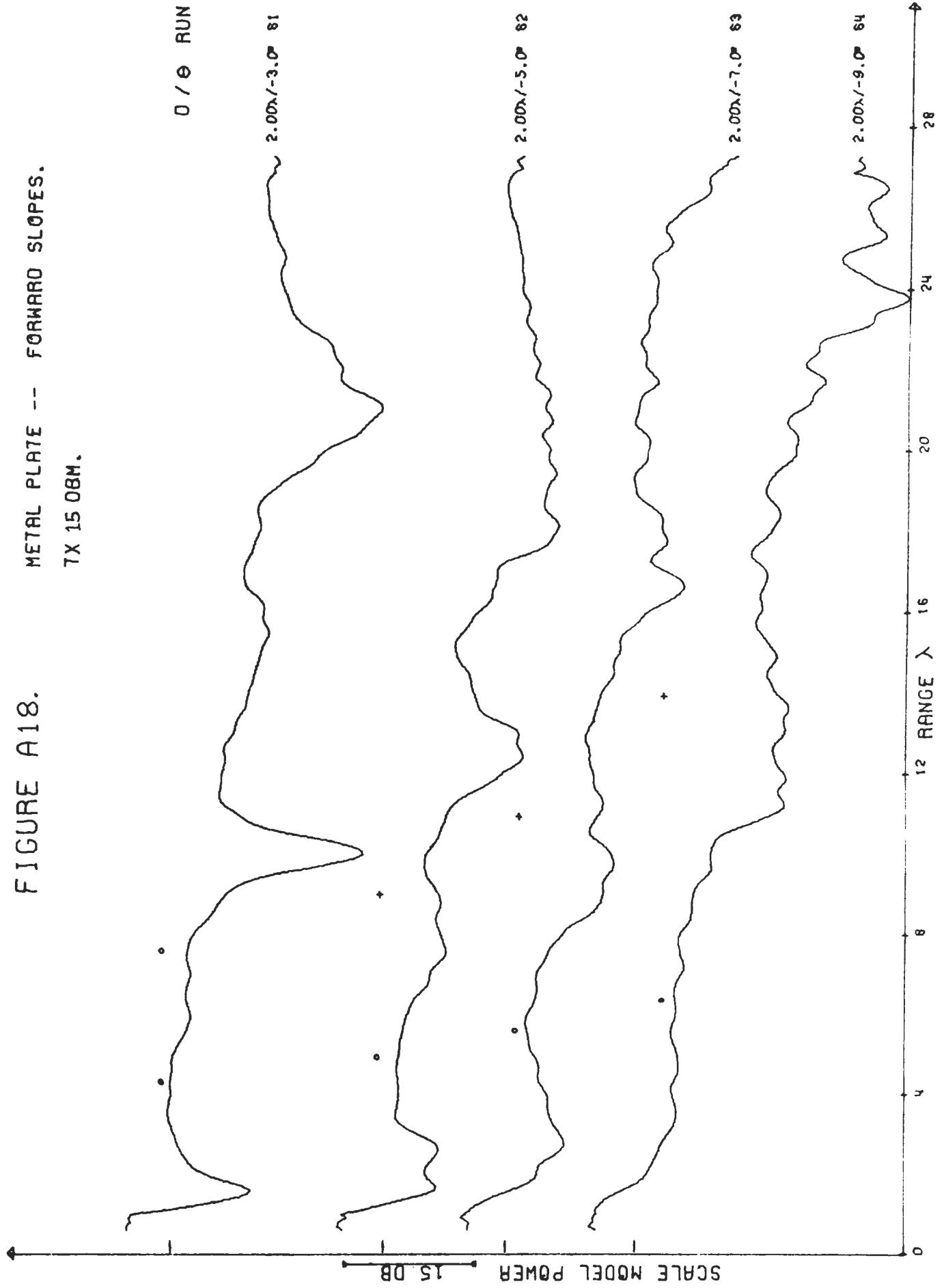


FIGURE A19.

METAL PLATE -- FORWARD SLOPES.
TX 15 DBM.

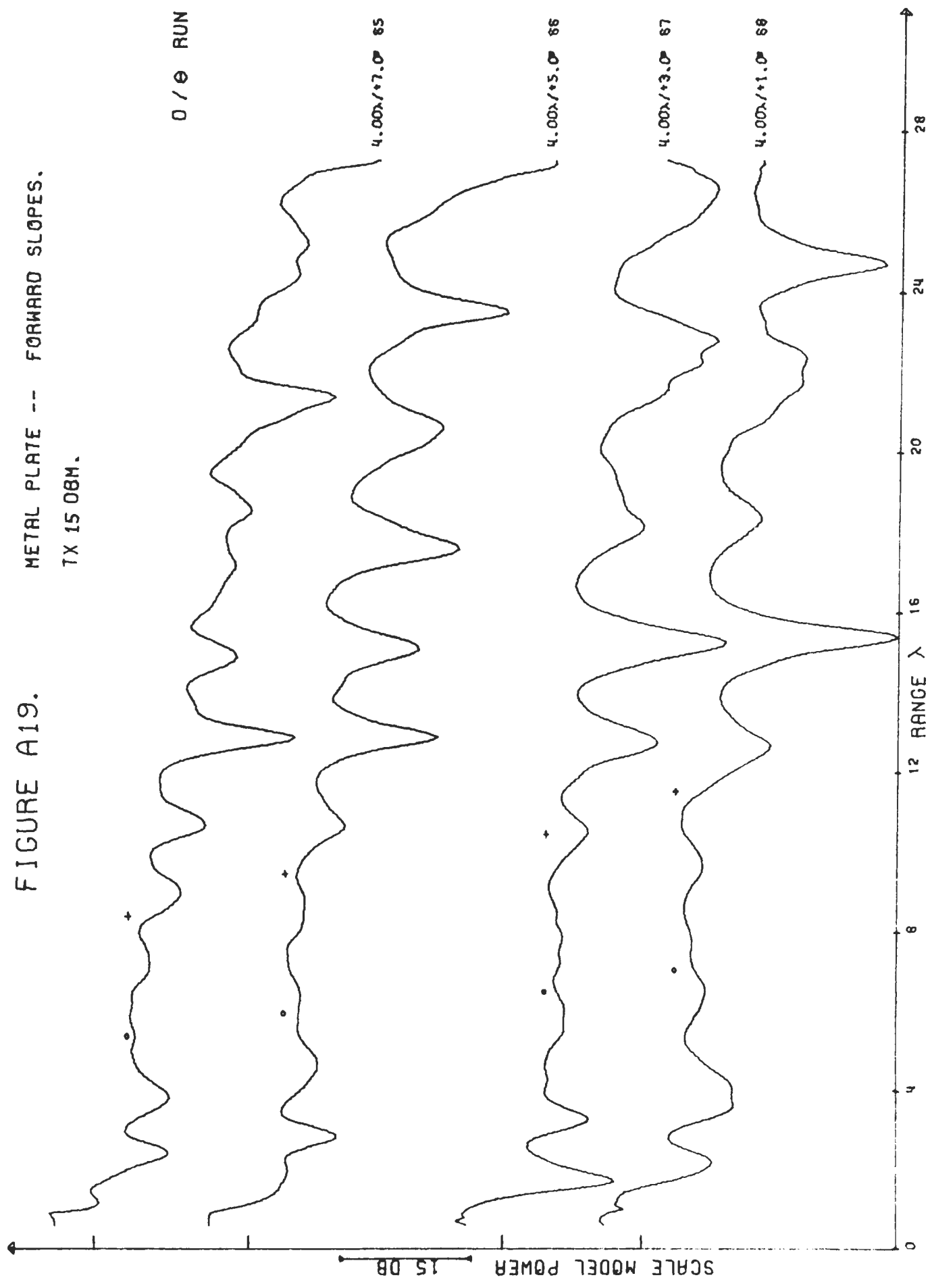


FIGURE A20.

METAL PLATE -- FORWARD SLOPES.
TX 15 08M.

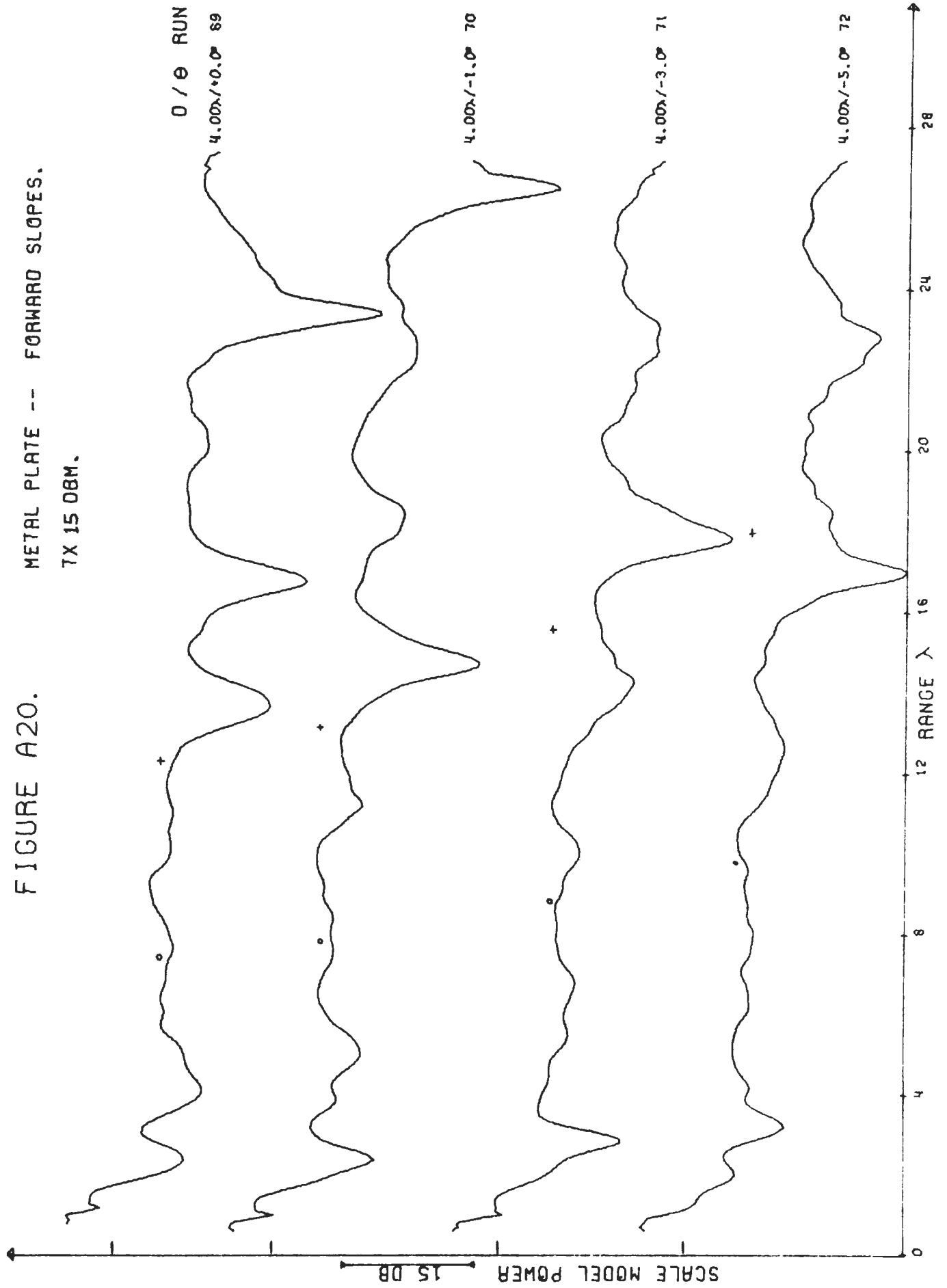


FIGURE A21.

METAL PLATE -- FORWARD SLOPES.

TX 15 DBM.

D / θ RUN

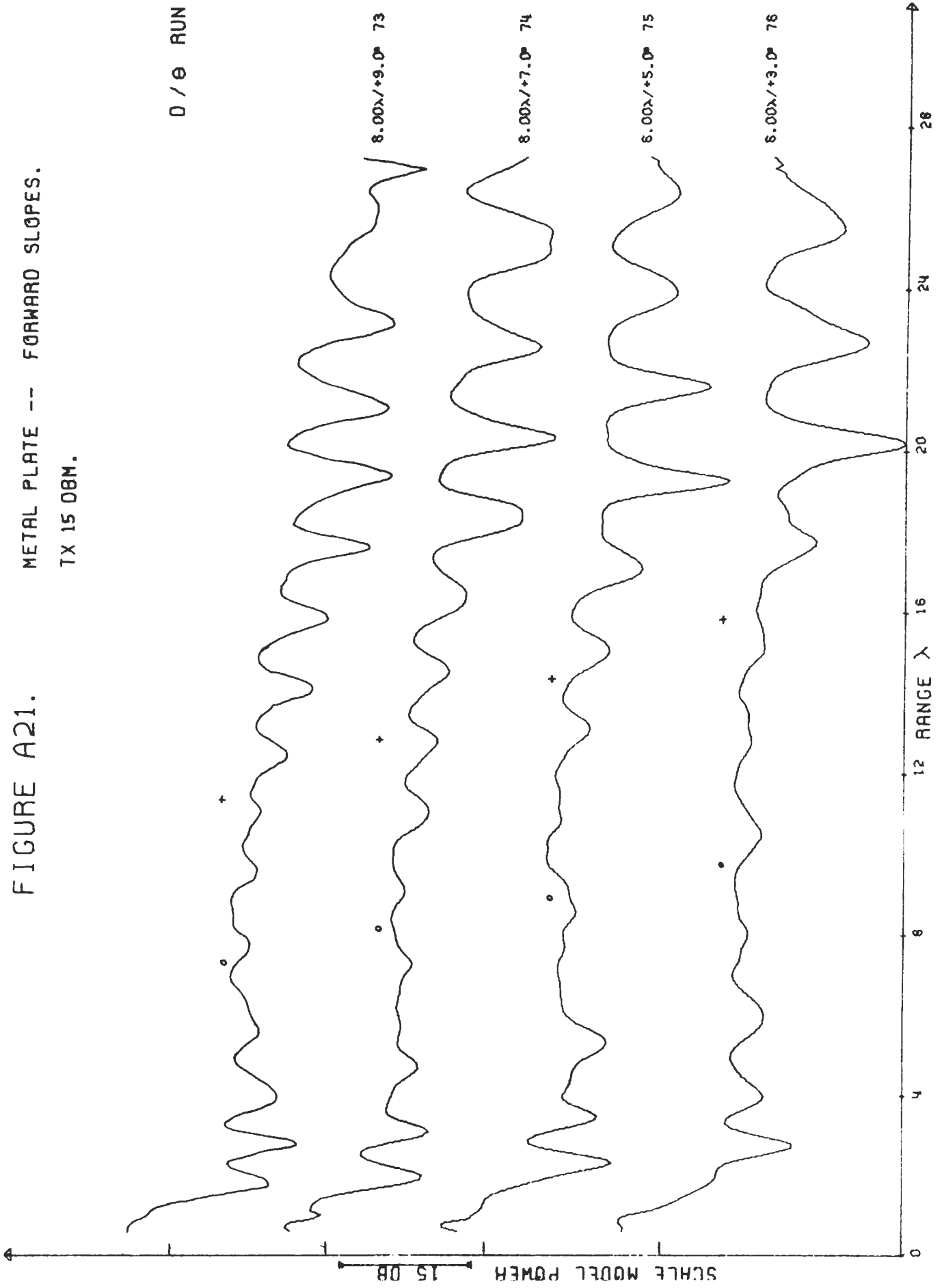
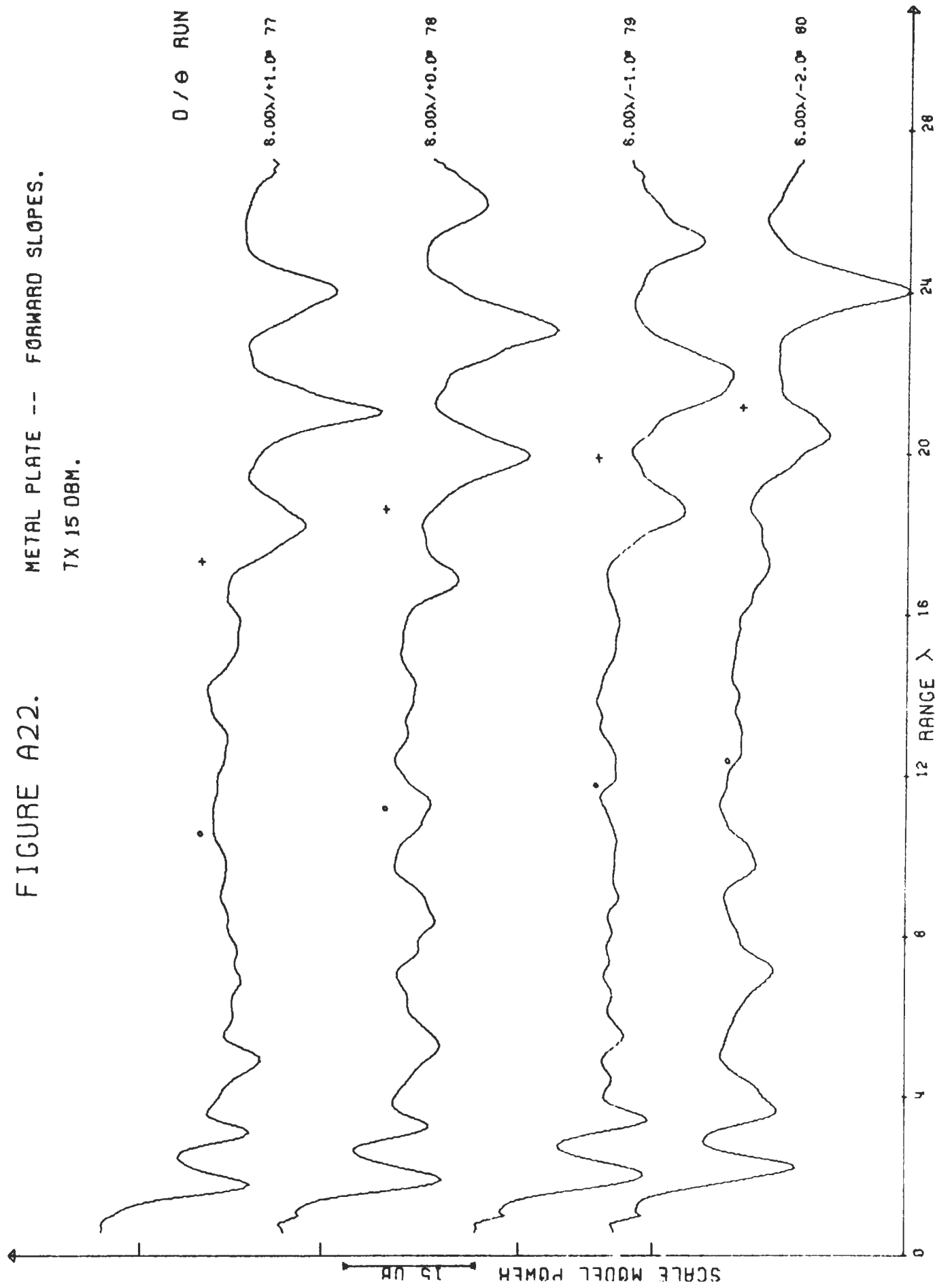


FIGURE A22.

METAL PLATE -- FORWARD SLOPES.

TX 15 DBM.



APPENDIX B
TRAVERSES OVER A DIELECTIC SLAB

FIGURE B1.

HORIZONTAL DIELECTRIC SLAB.

TX 10 DBM.

θ / ϵ RUN

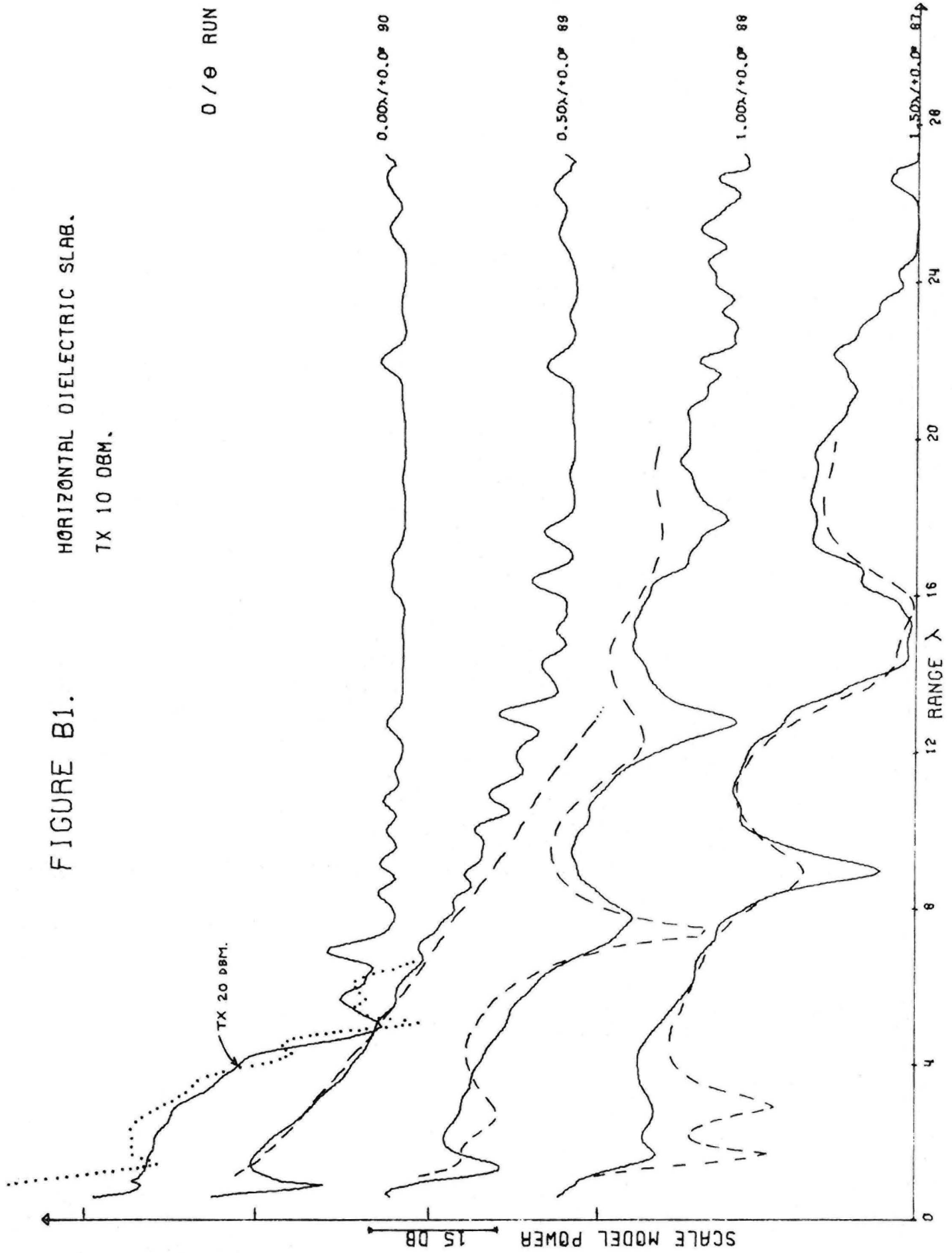


FIGURE B2.

HORIZONTAL DIELECTRIC SLAB.
TX 10 DBM.

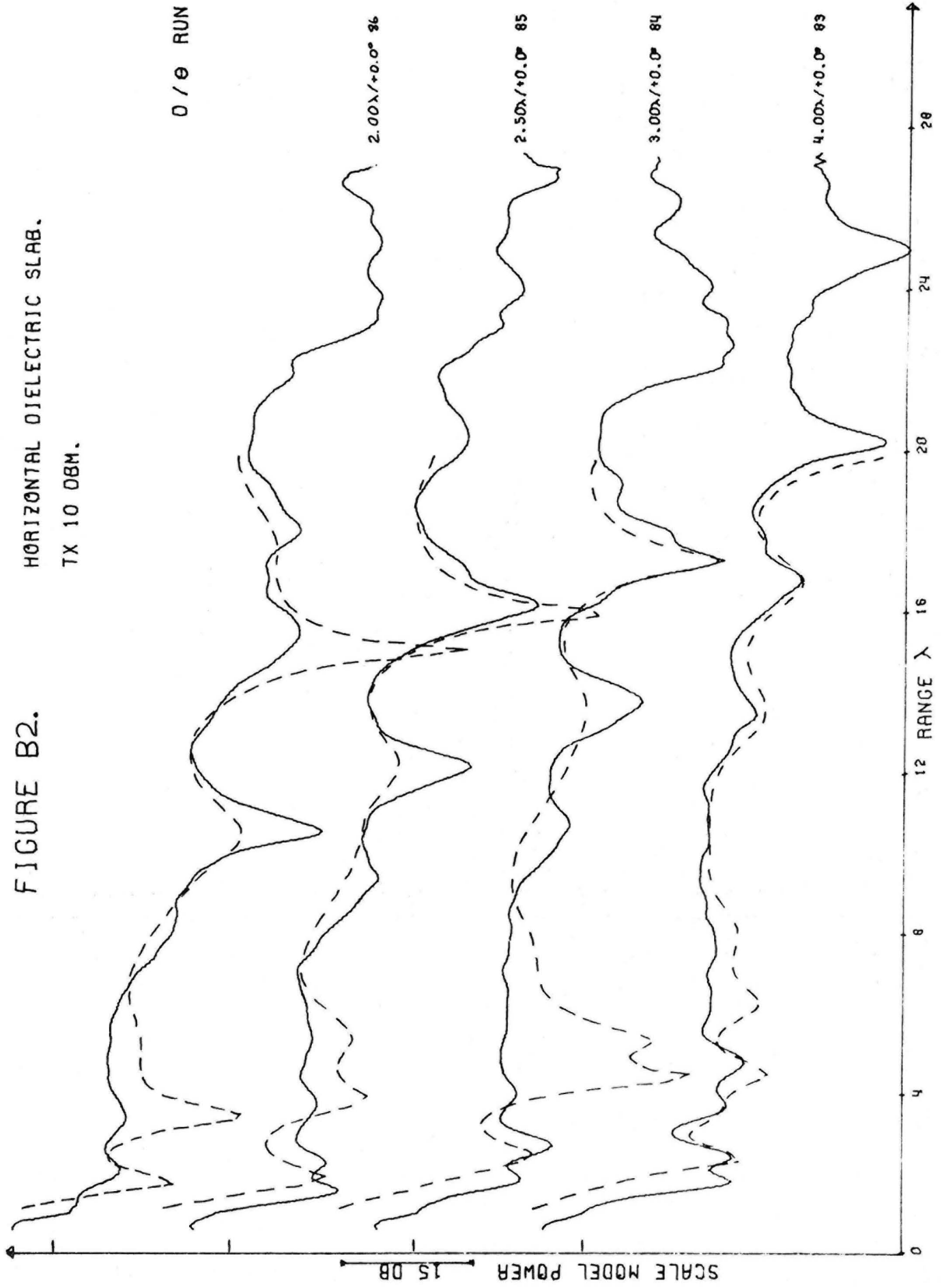


FIGURE B3.

HORIZONTAL DIELECTRIC SLAB.

TX 10 DBM.

0/0 RUN

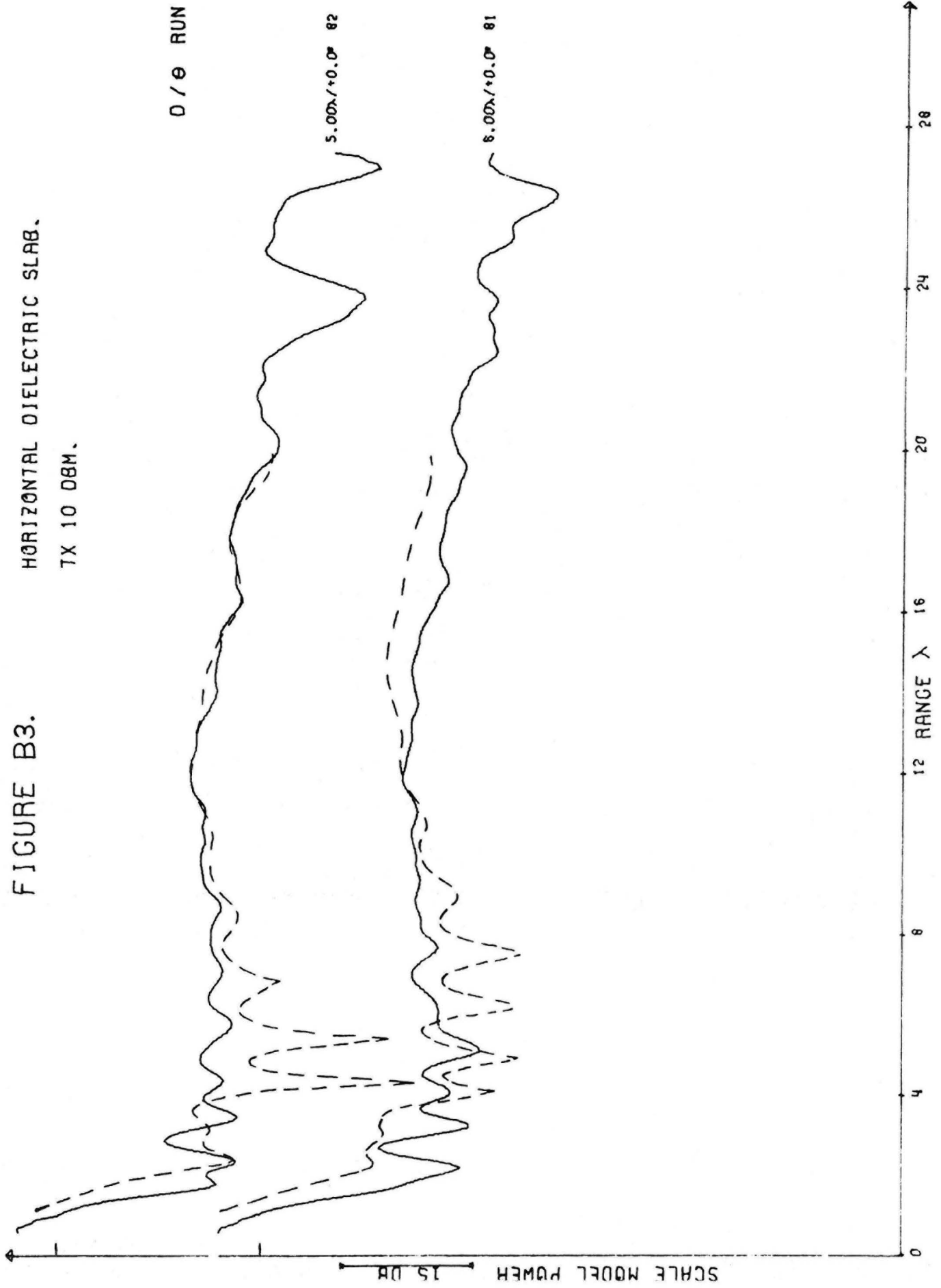


FIGURE B4.

HORIZONTAL DIELECTRIC SLAB.

TX 30 DBM.

0 / θ RUN

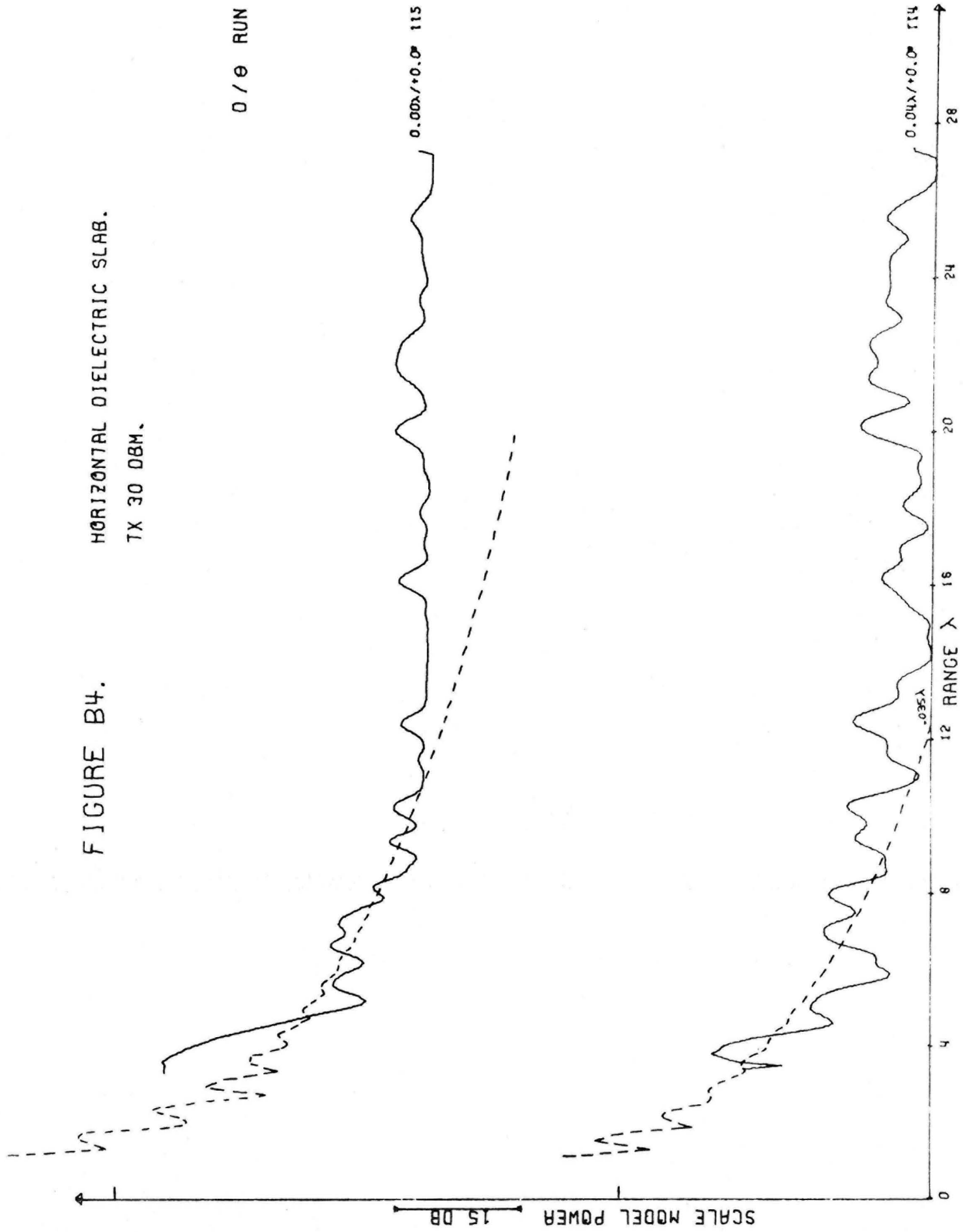


FIGURE B5.

HORIZONTAL DIELECTRIC SLAB.
TX 20 DBM.

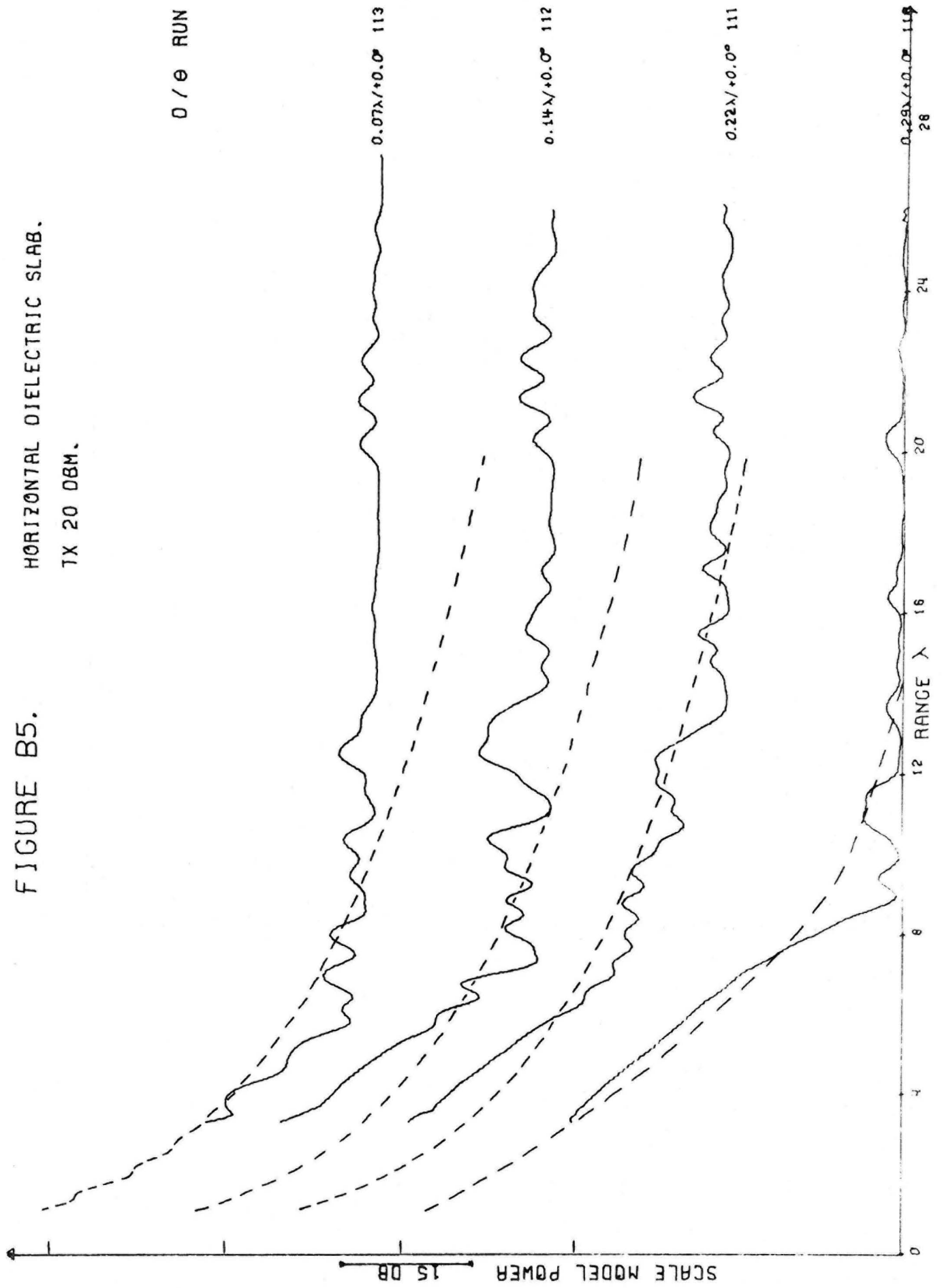


FIGURE B6. HORIZONTAL DIELECTRIC SLAB. 7X 20 DBM.

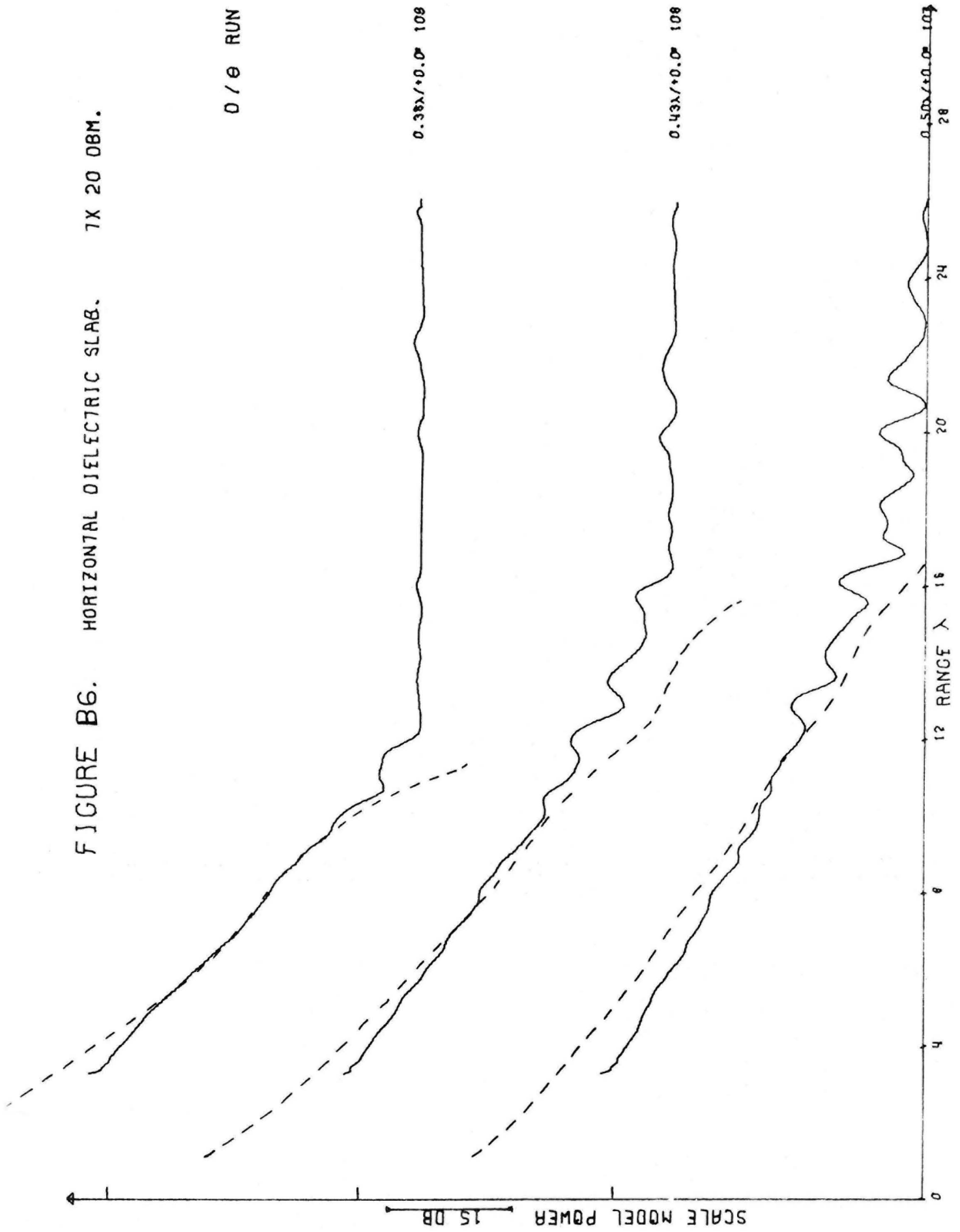


FIGURE B7.

HORIZONTAL DIELECTRIC SLAB.
TX 15 DBM.

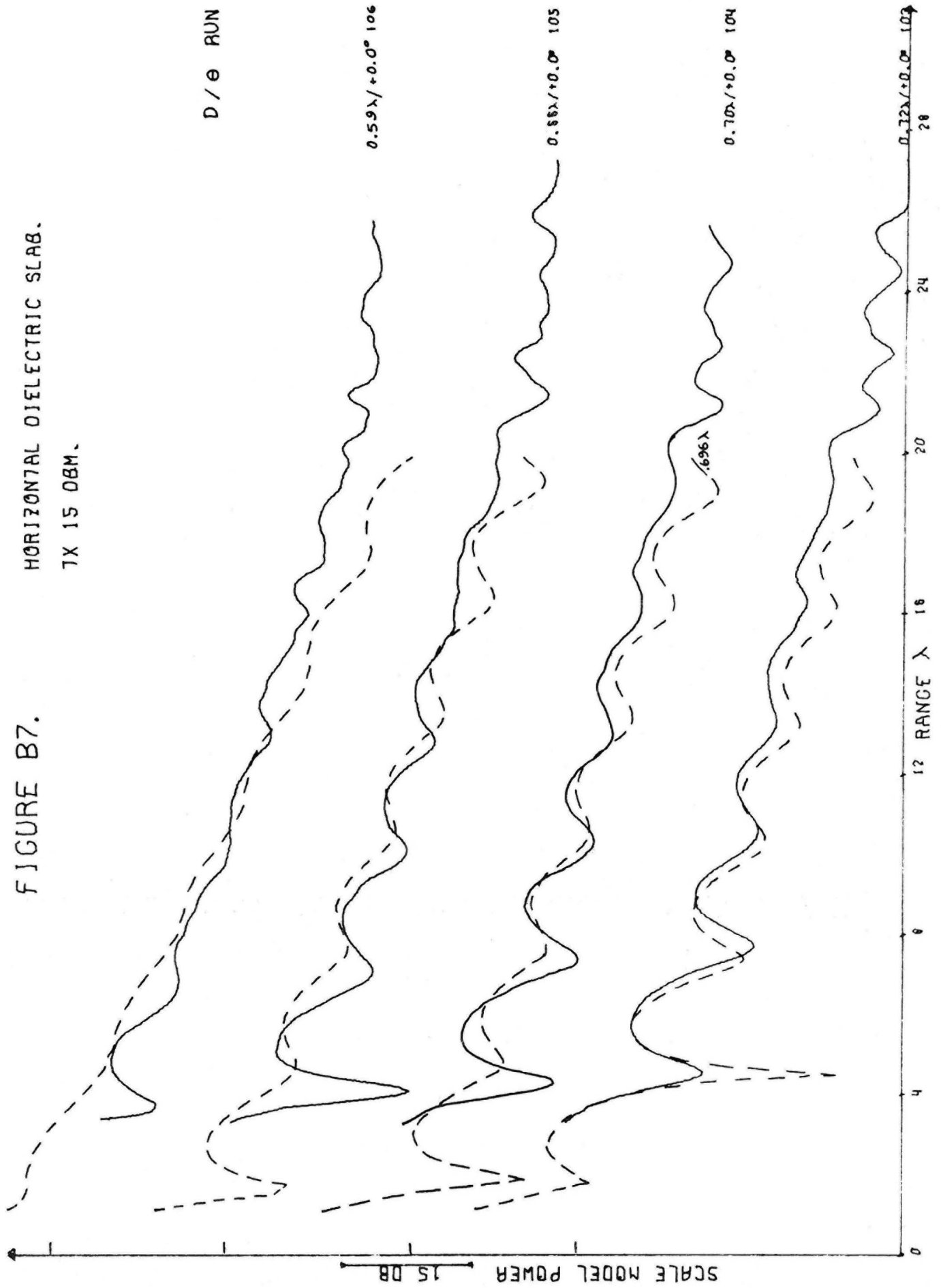


FIGURE B8.

HORIZONTAL DIELECTRIC SLAB.

TX 15 DBM.

0 / θ RUN

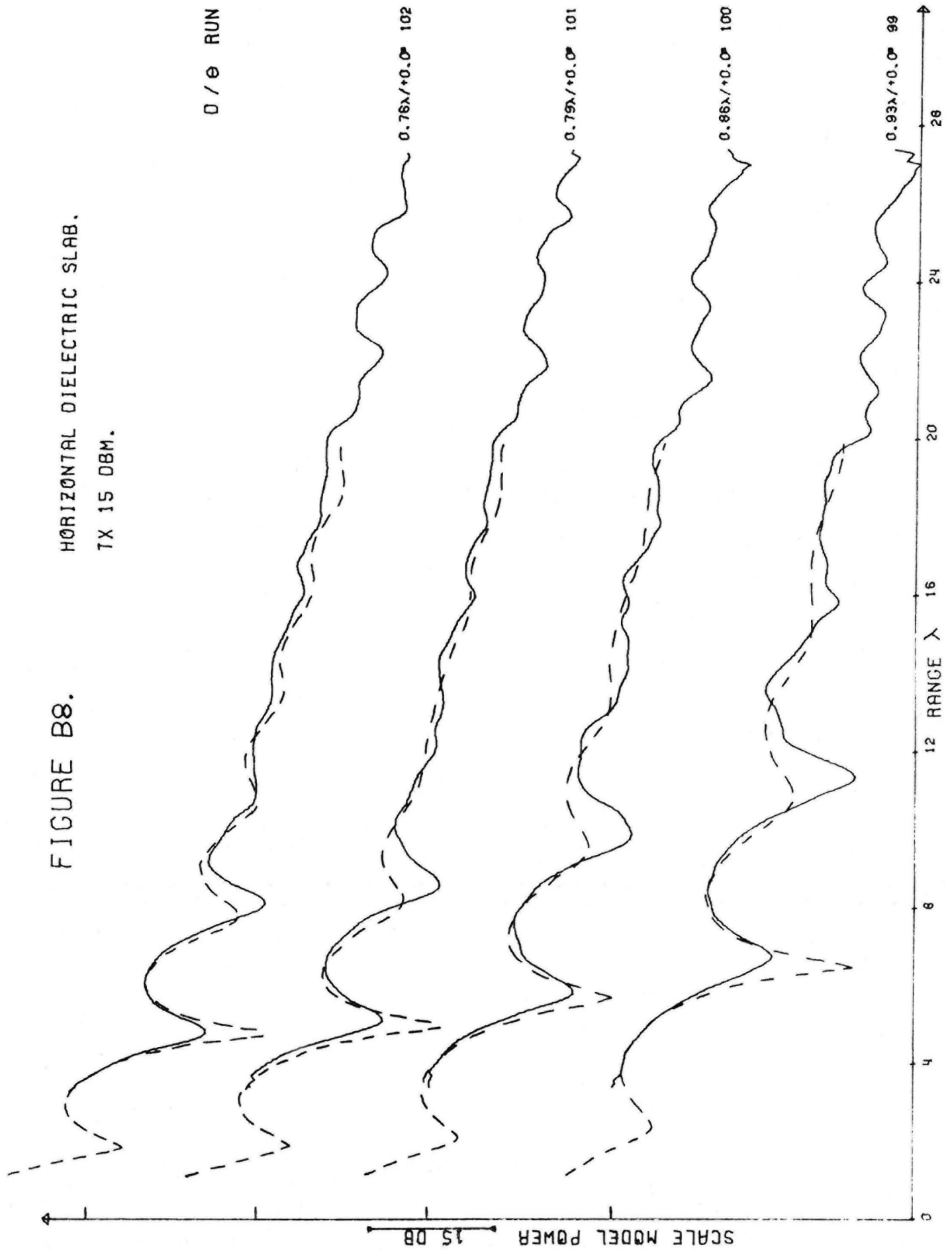


FIGURE B9.

HORIZONTAL DIELECTRIC SLAB.

TX 15 DBM.

D/θ RUN

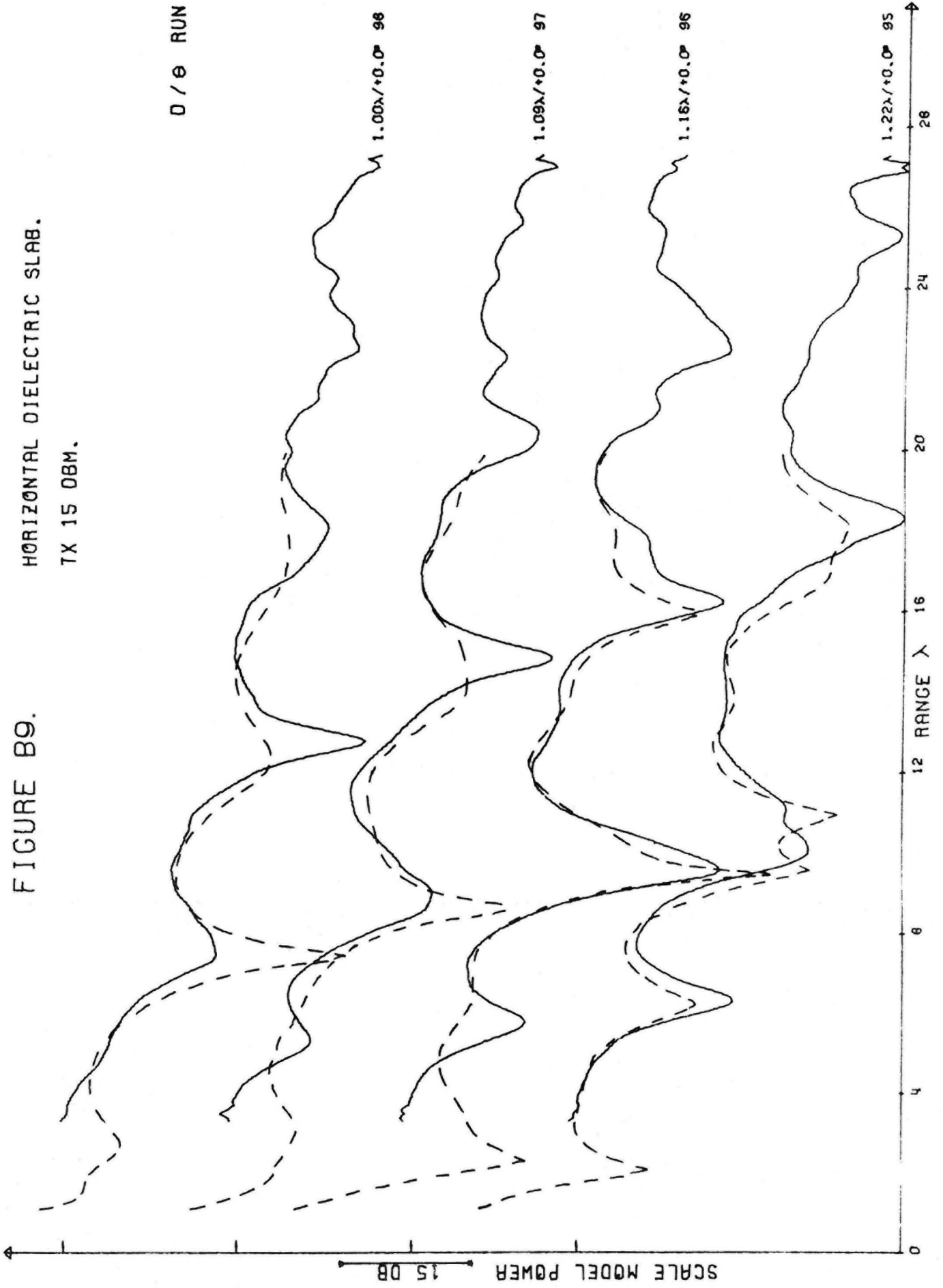


FIGURE B10.

HORIZONTAL DIELECTRIC SLAB.
TX 15 DBM.

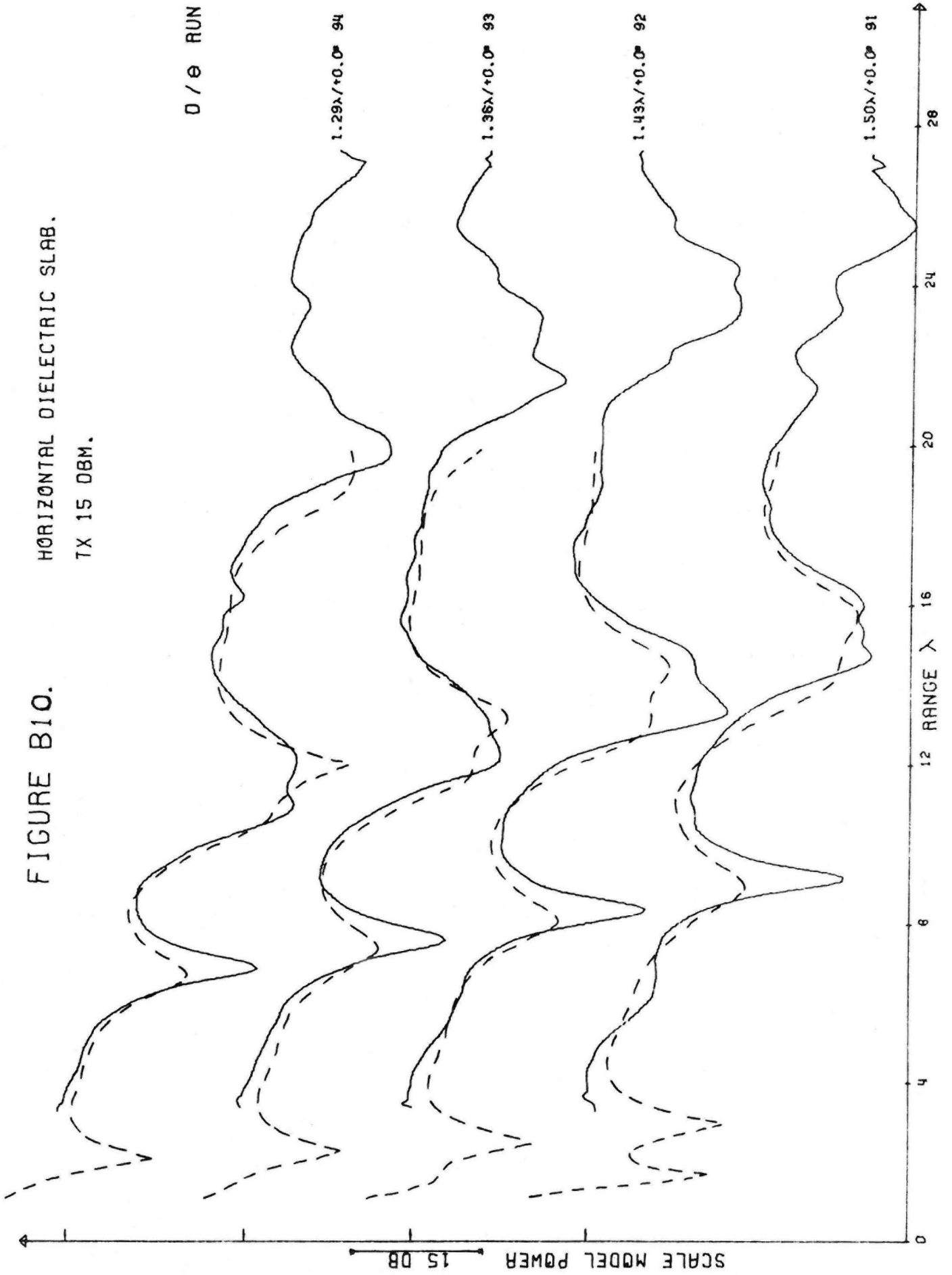


FIGURE B11. DIELECTRIC SLAB FORWARD SLOPES.
TX 15 DBM.

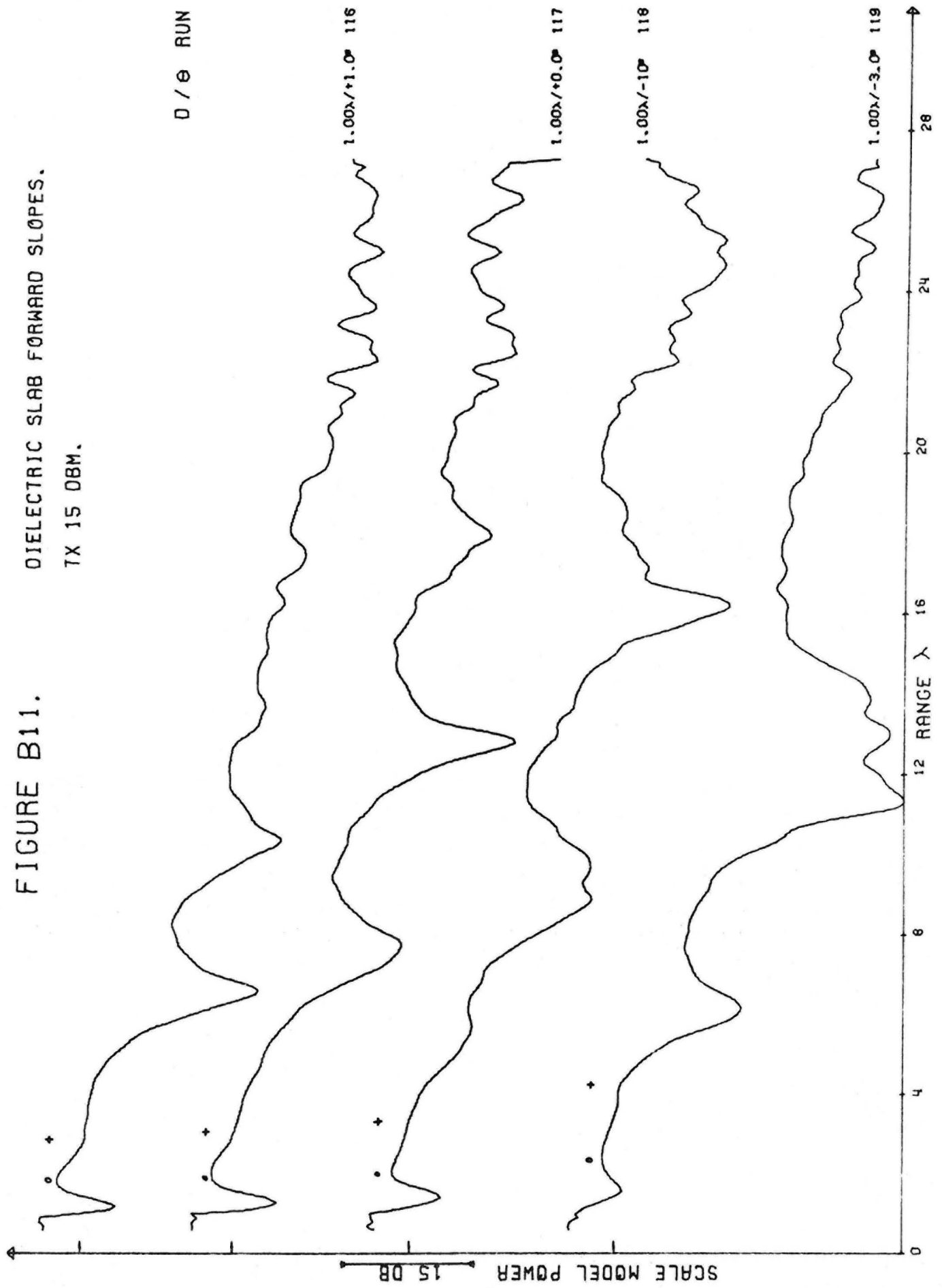


FIGURE B12.

DIELECTRIC SLAB FORWARD SLOPES.

TX 15 DBM.

0 / 0 RUN

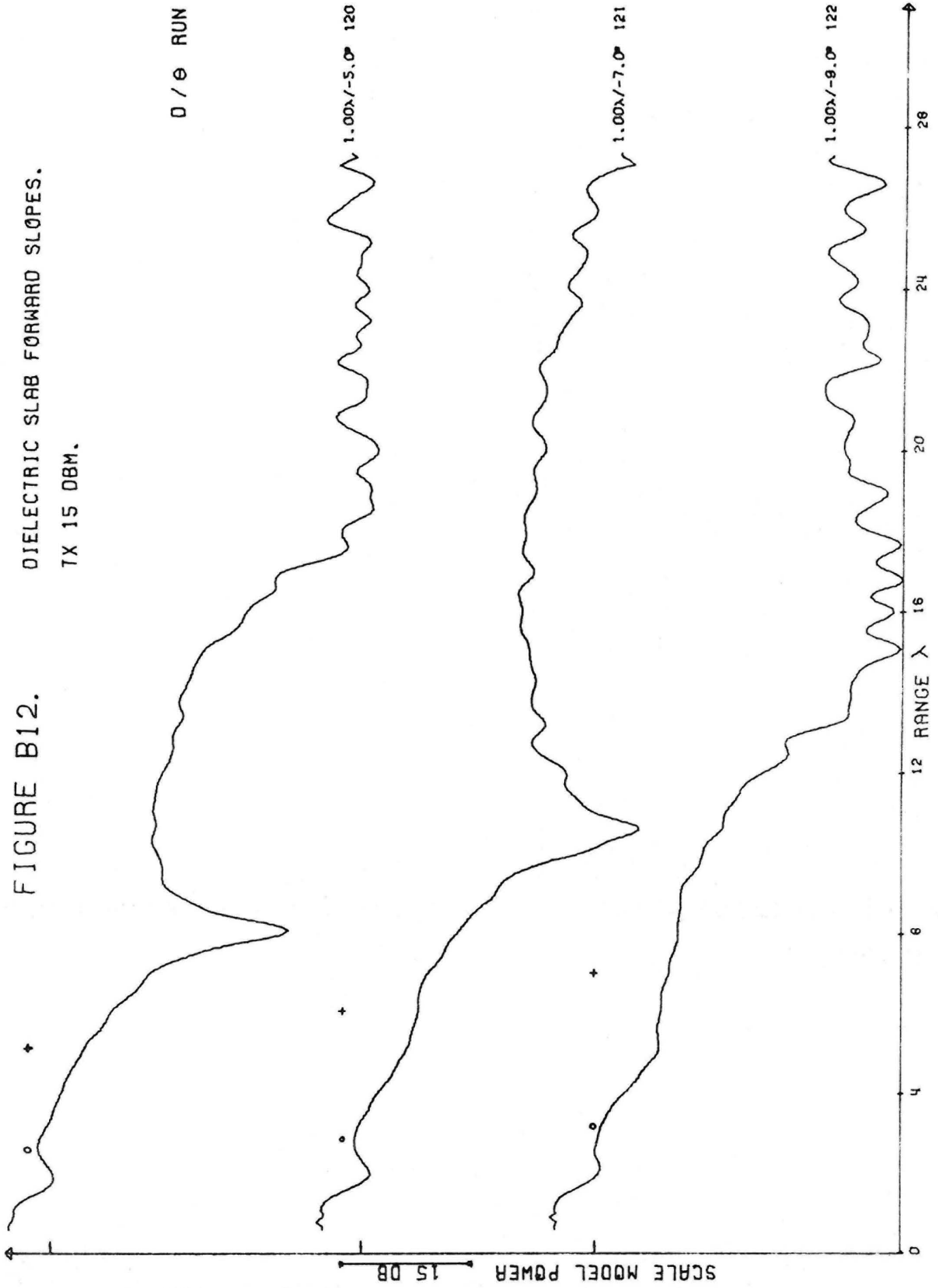


FIGURE B13.

DIELECTRIC SLAB FORWARD SLOPES.
TX 15 DBM.

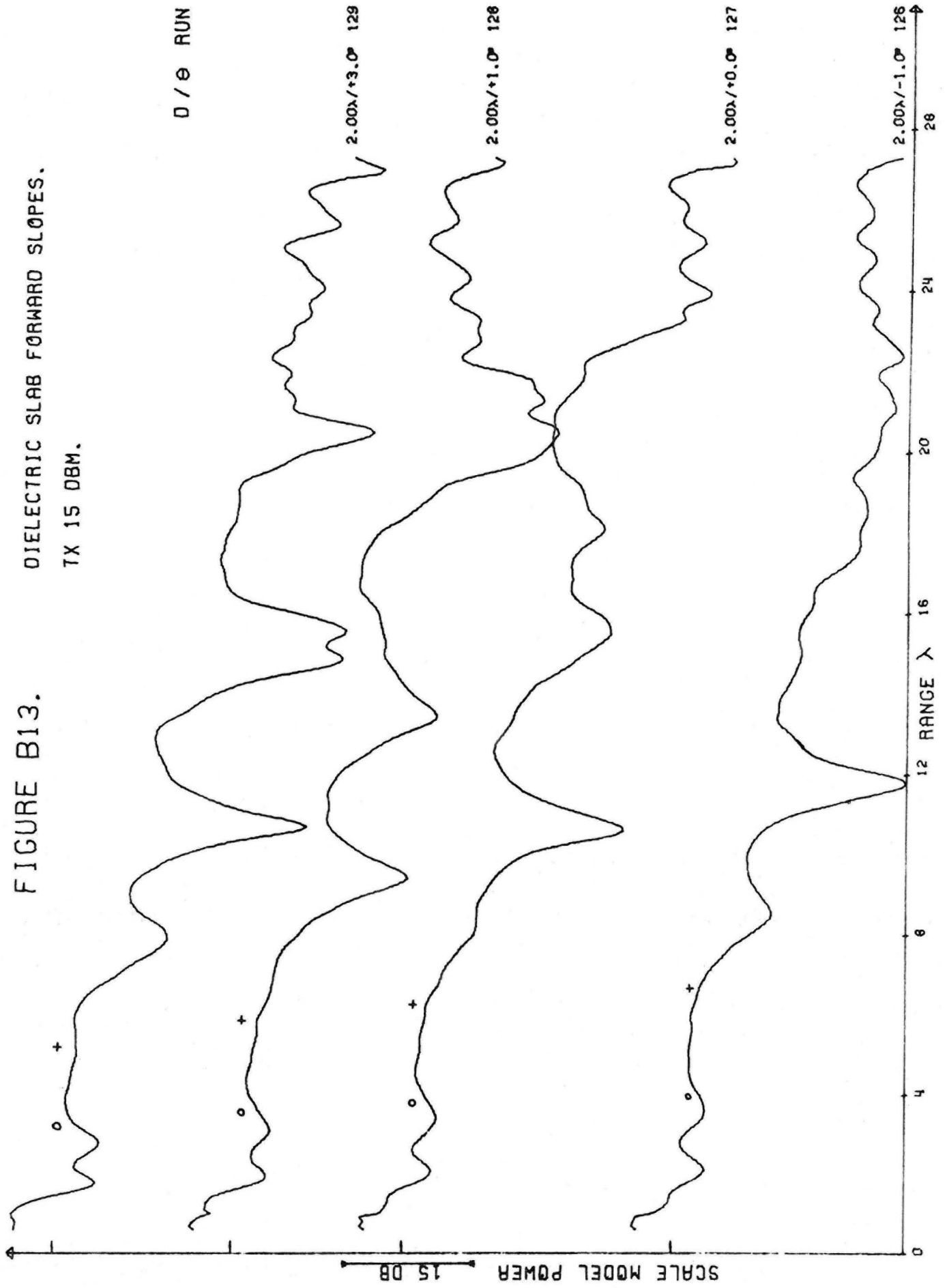


FIGURE B14.

DIELECTRIC SLAB FORWARD SLOPES.
7X 15 DBM.

D/θ RUN

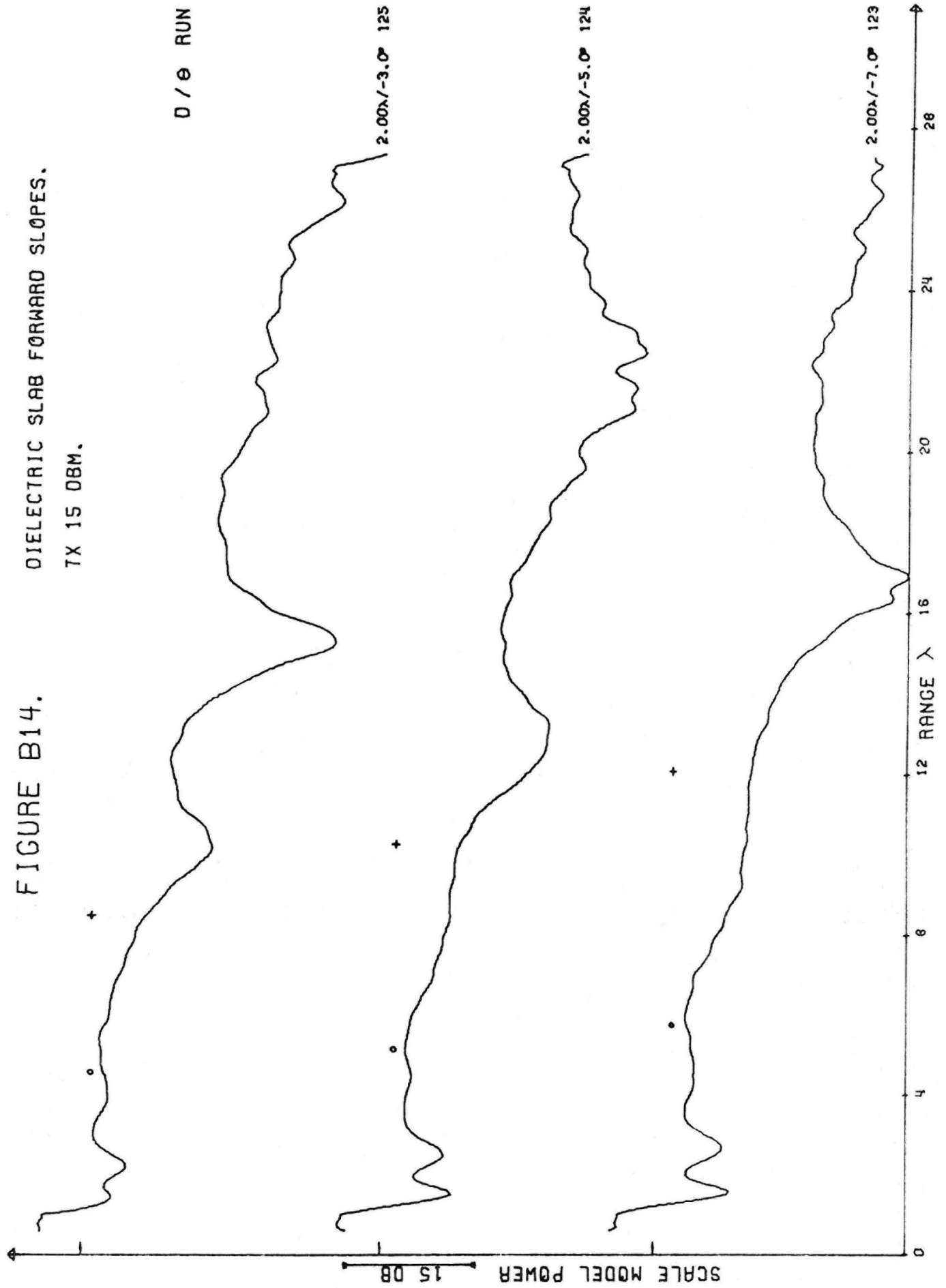


FIGURE B15. DIELECTRIC SLAB FORWARD SLOPES.
TX 15 OBM.

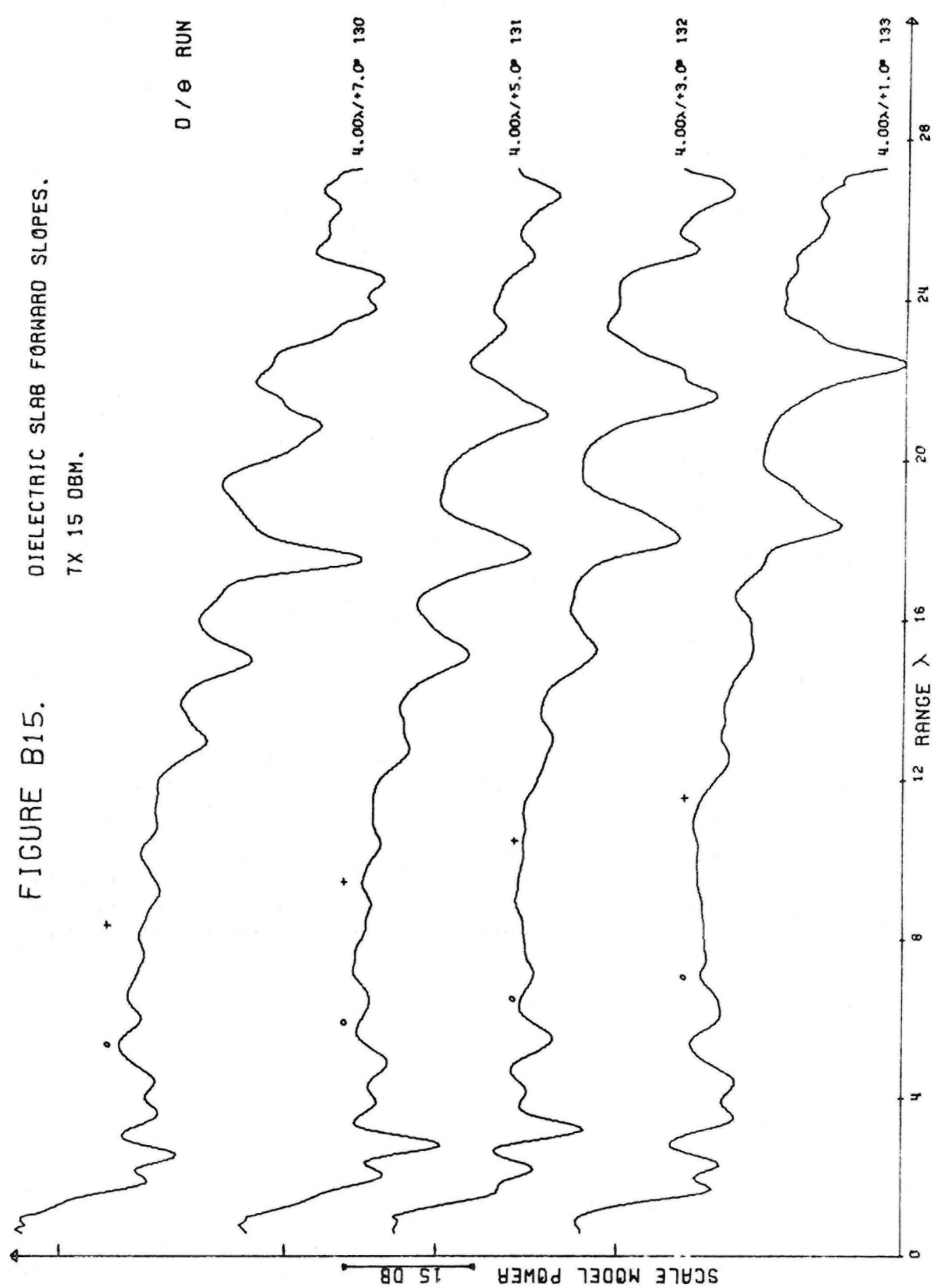


FIGURE B16. DIELECTRIC SLAB FORWARD SLOPES.
TX 15 DBM.

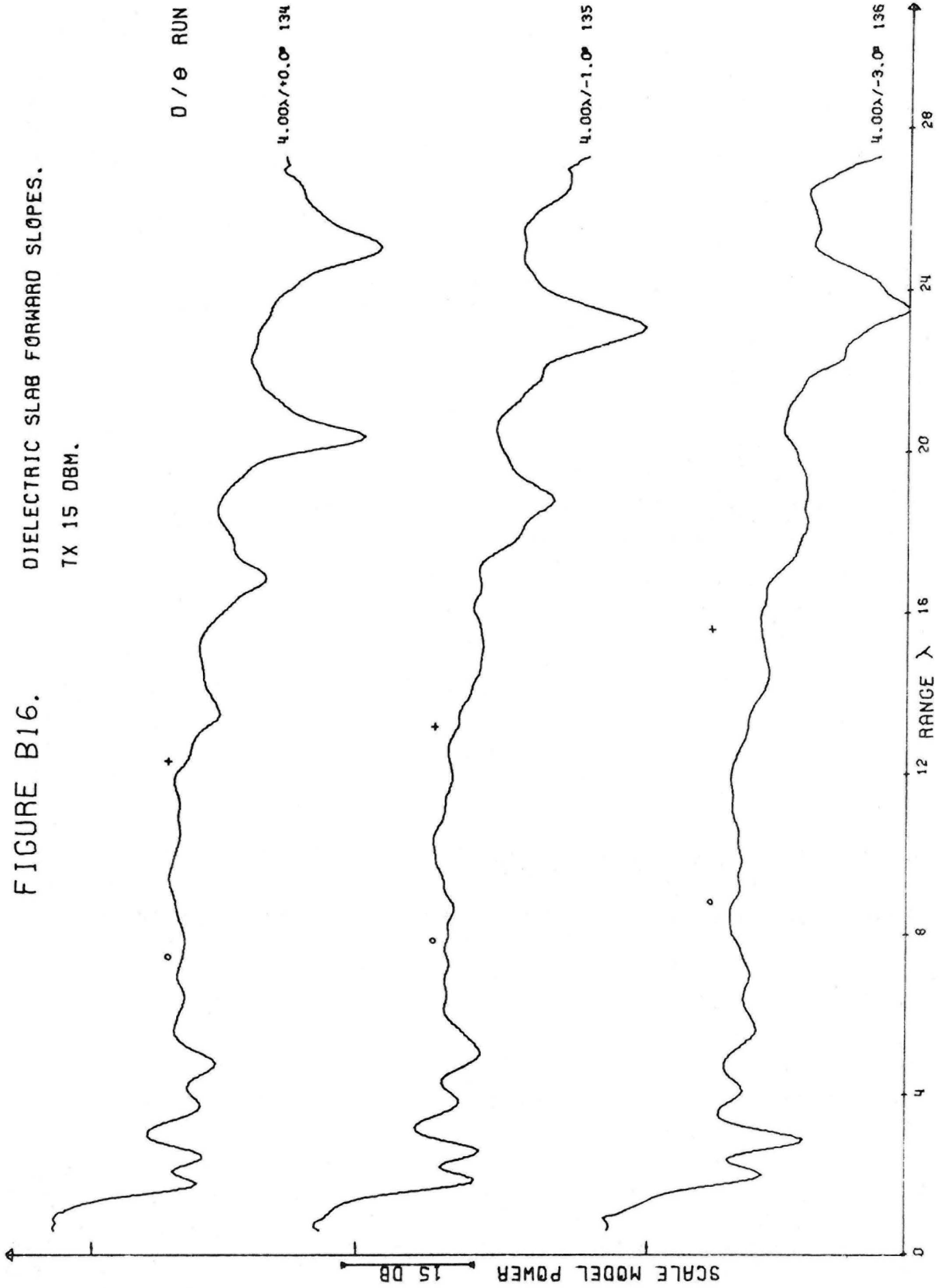


FIGURE B17.

DIELECTRIC SLAB FORWARD SLOPES.

TX 15 DBM.

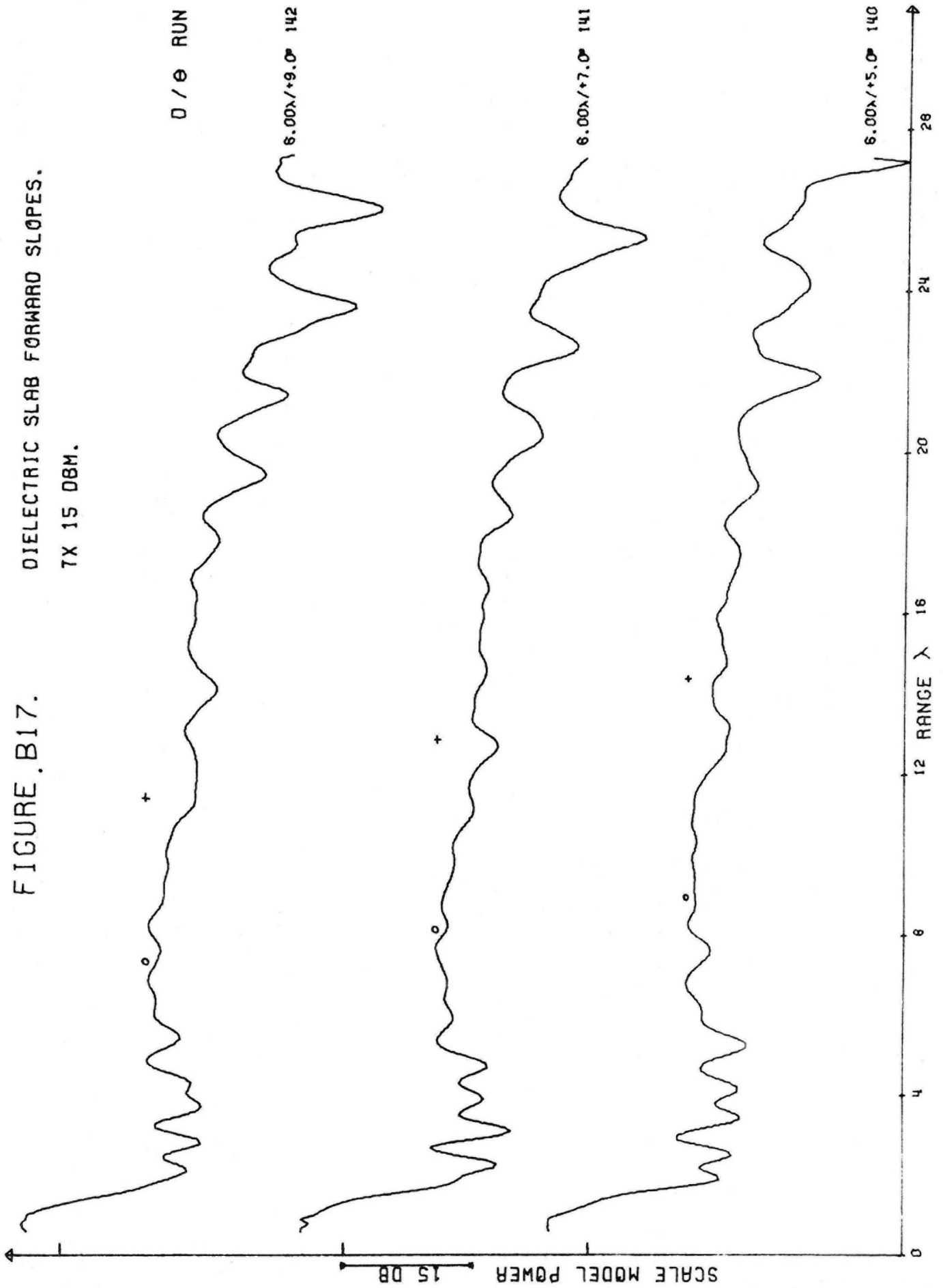


FIGURE B18.

DIELECTRIC SLAB FORWARD SLOPES.
7X 15 DBM.

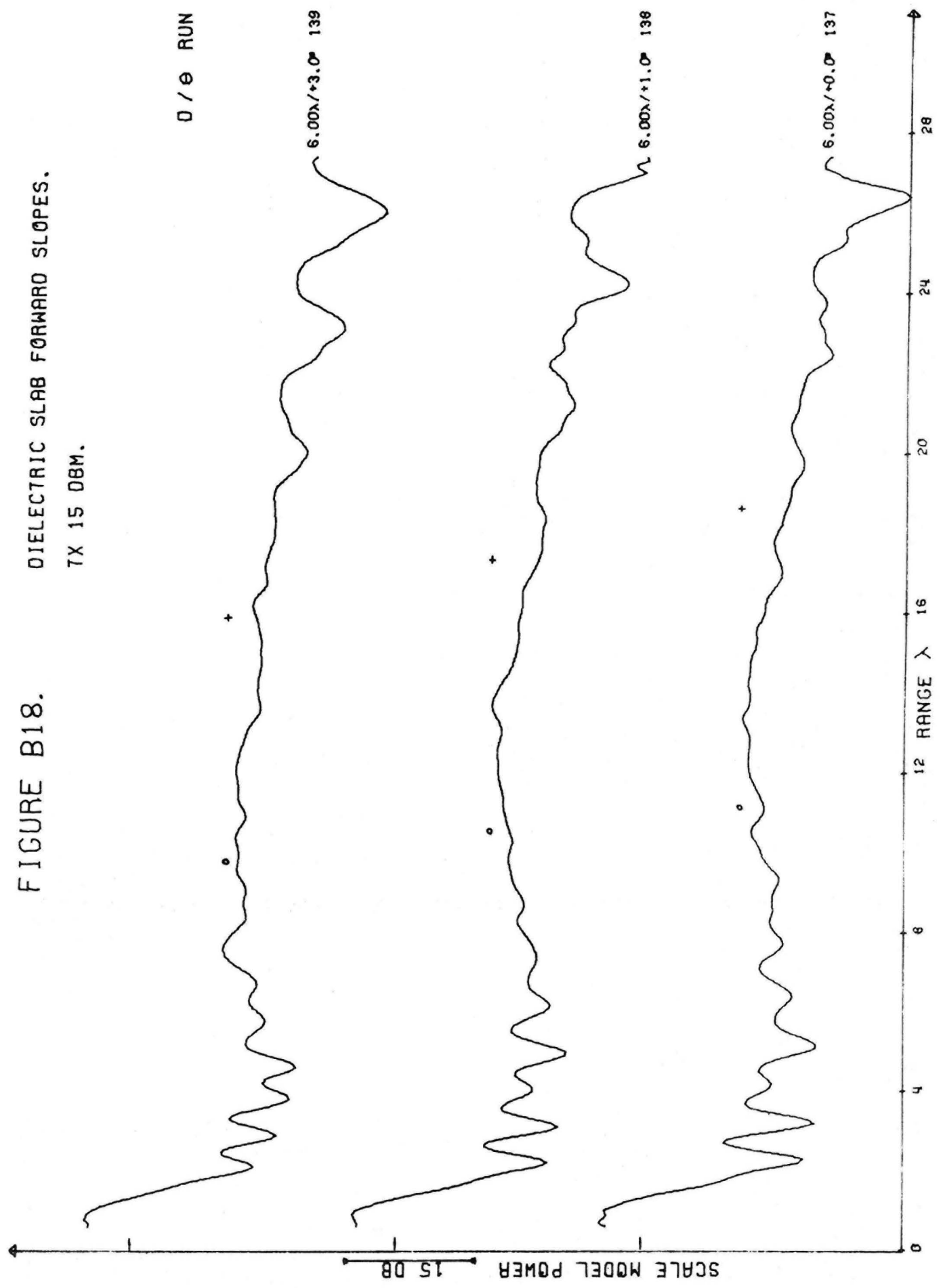


FIGURE B19.

2.5λ DIAMETER CRATER OVER
DIELECTRIC SLAB. TX 20 DBM.

D/R RUN

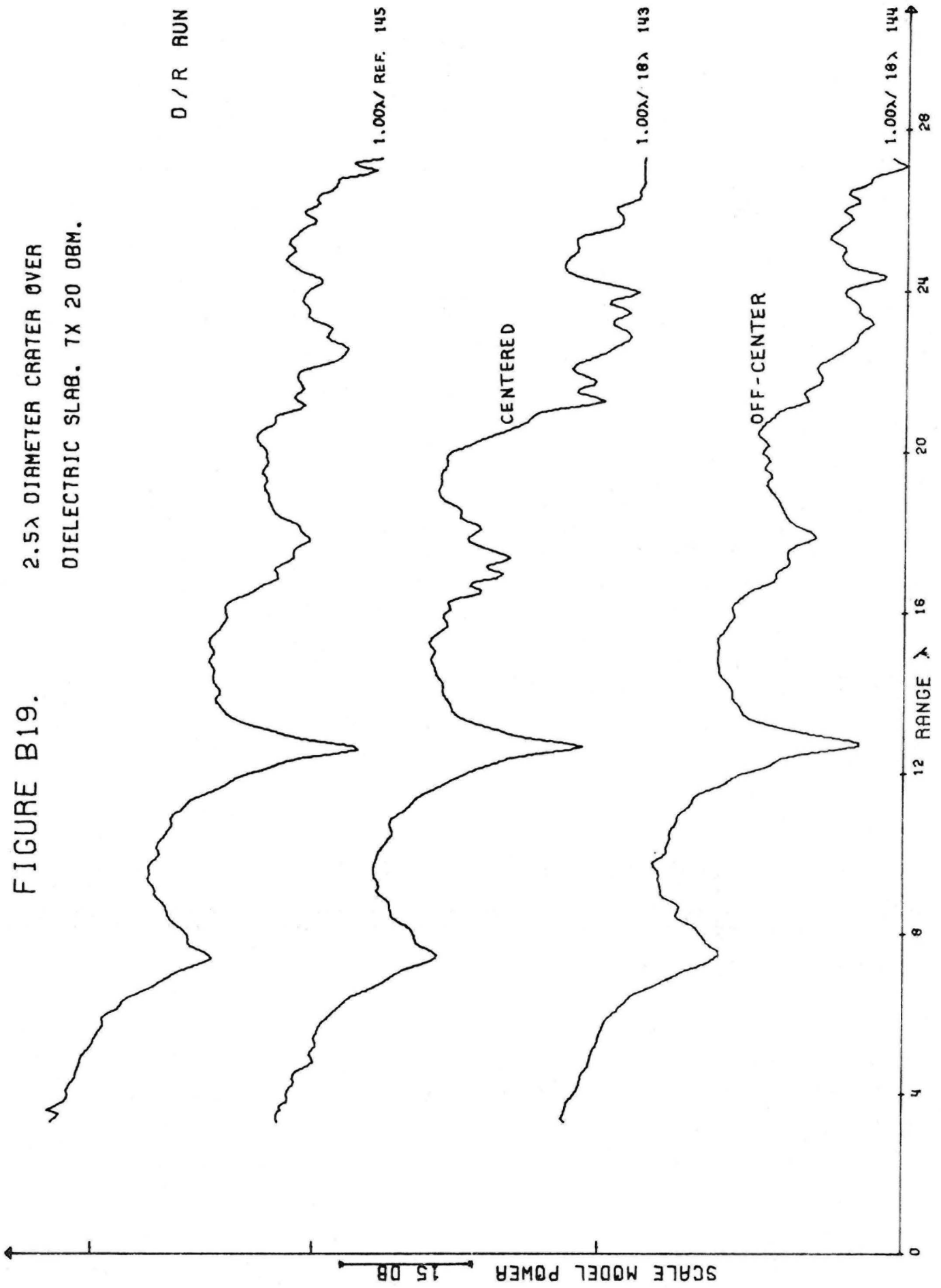
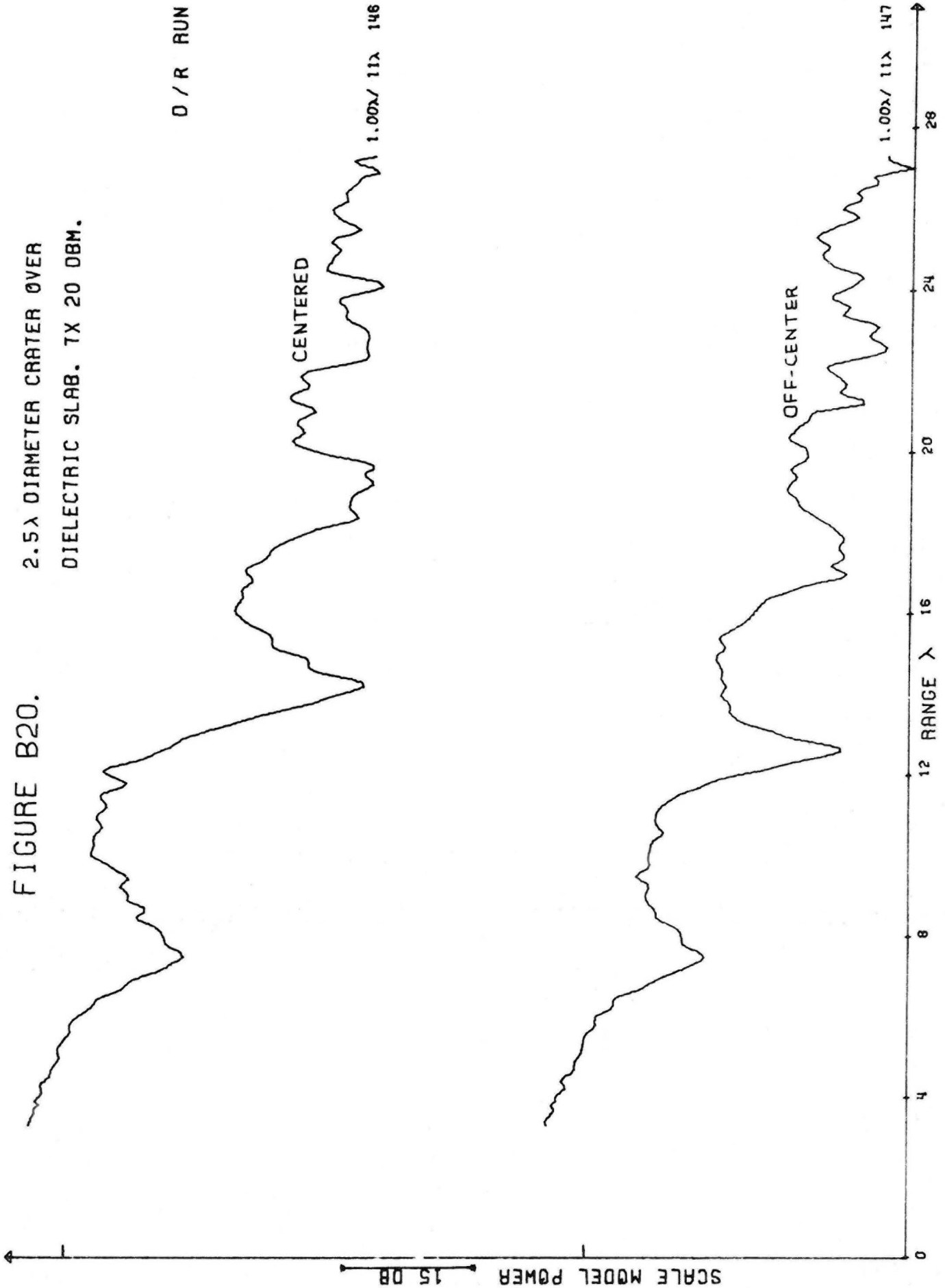


FIGURE B20.

2.5λ DIAMETER CRATER OVER
DIELECTRIC SLAB. TX 20 DBM.

D / R RUN



1.00λ / 11λ 146

1.00λ / 11λ 147

FIGURE B21.

2.5λ DIAMETER CRATER OVER
DIELECTRIC SLAB. TX 20 DBM.

D / R RUN

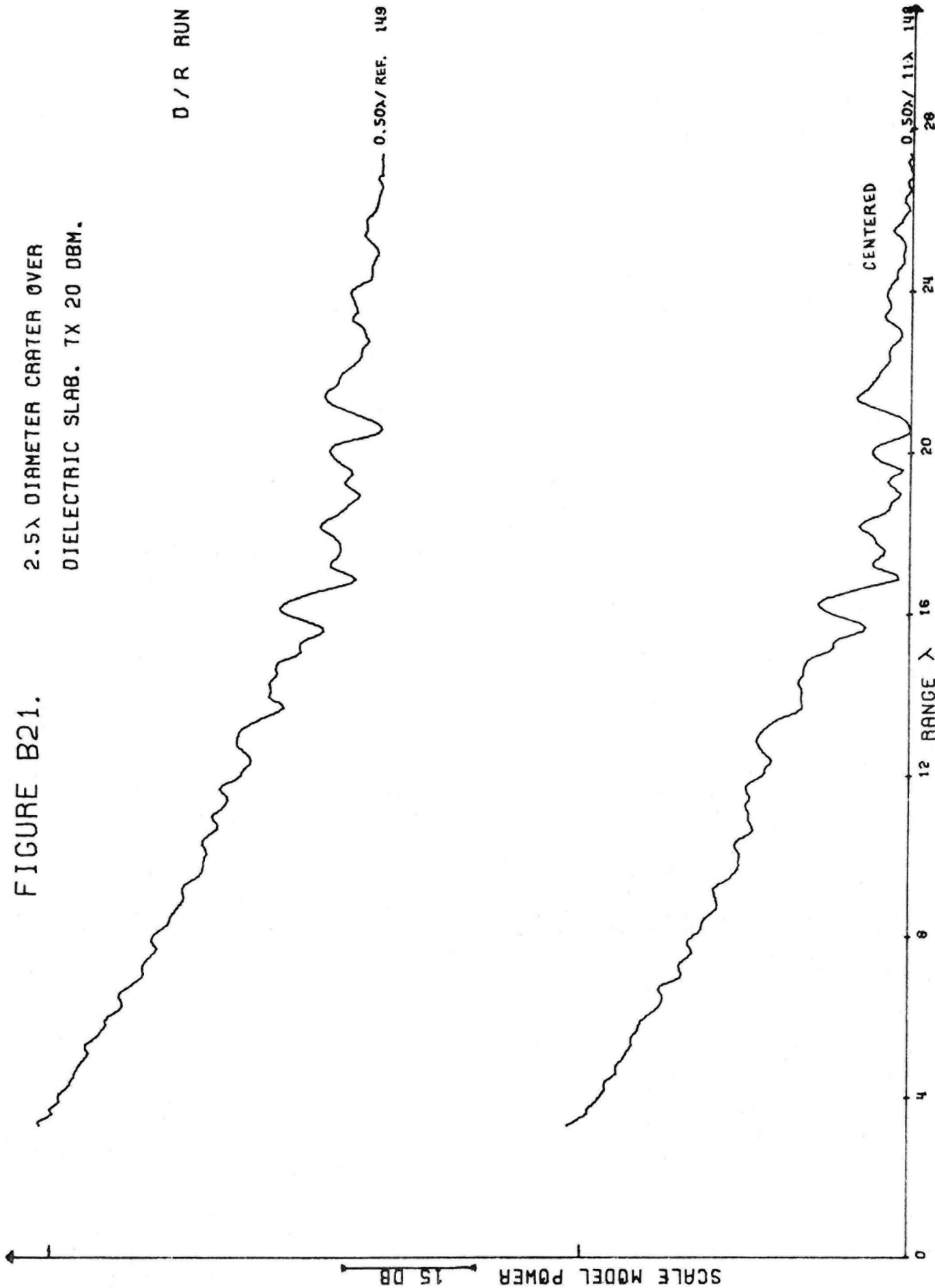


FIGURE B22.

3.5λ DIAMETER CRATER OVER
DIELECTRIC SLAB. TX 20 DBM.

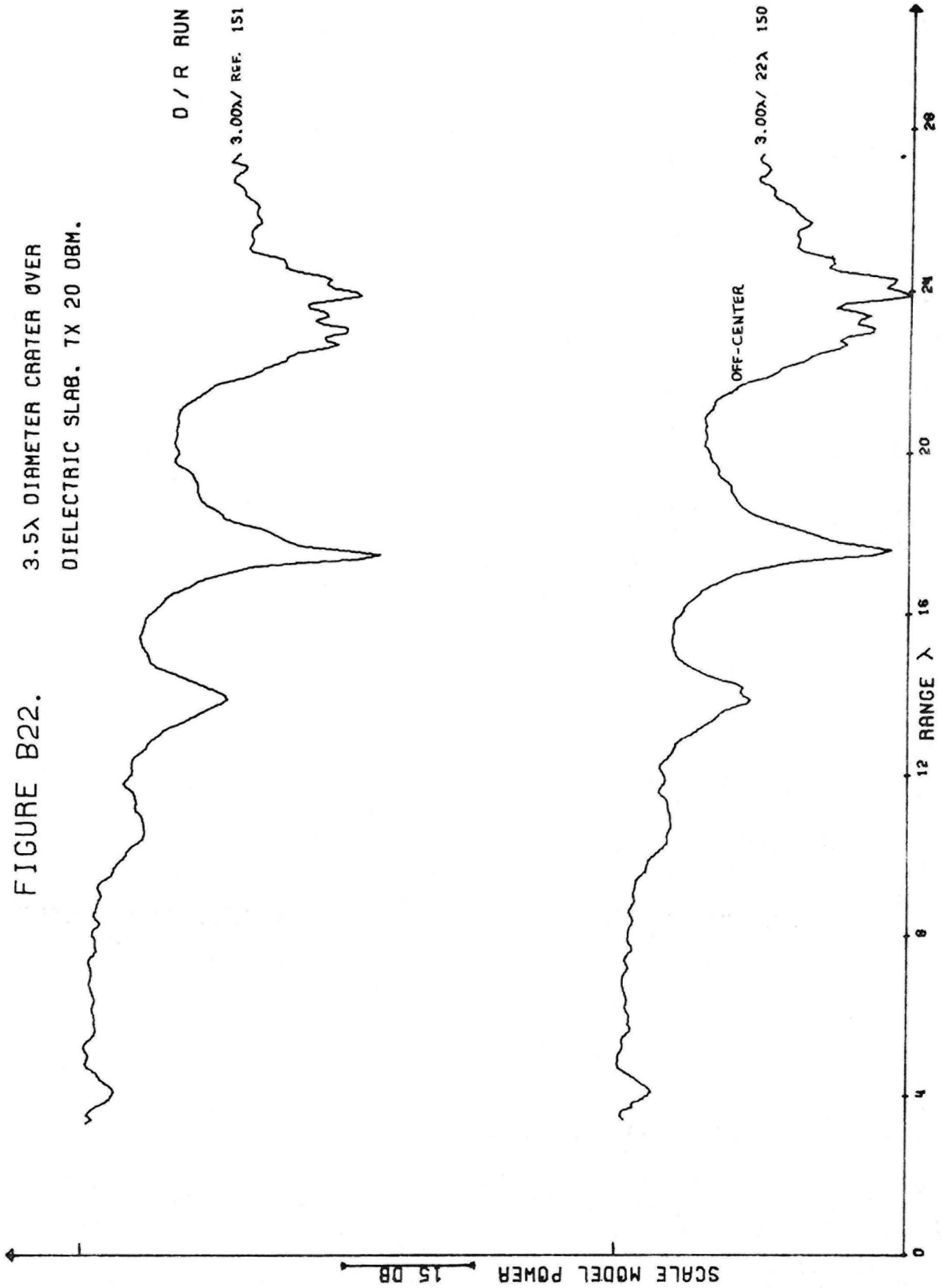


FIGURE B23.

.30λ WIDE CREVASSE OVER
DIELECTRIC SLAB. TX 20 DBM.

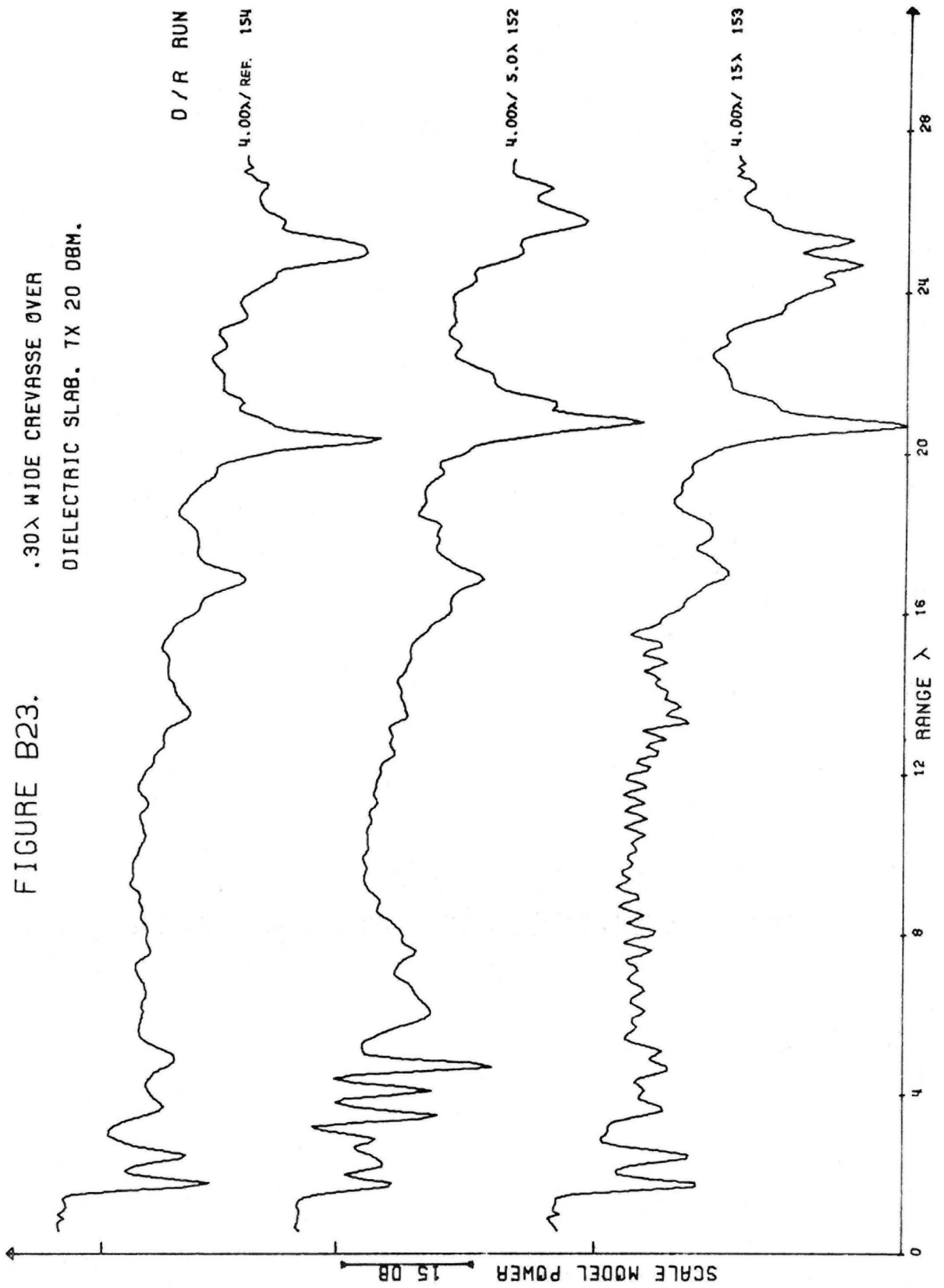


FIGURE B24.

.15λ WIDE CREVASSE OVER
DIELECTRIC SLAB. TX 20 DBM.

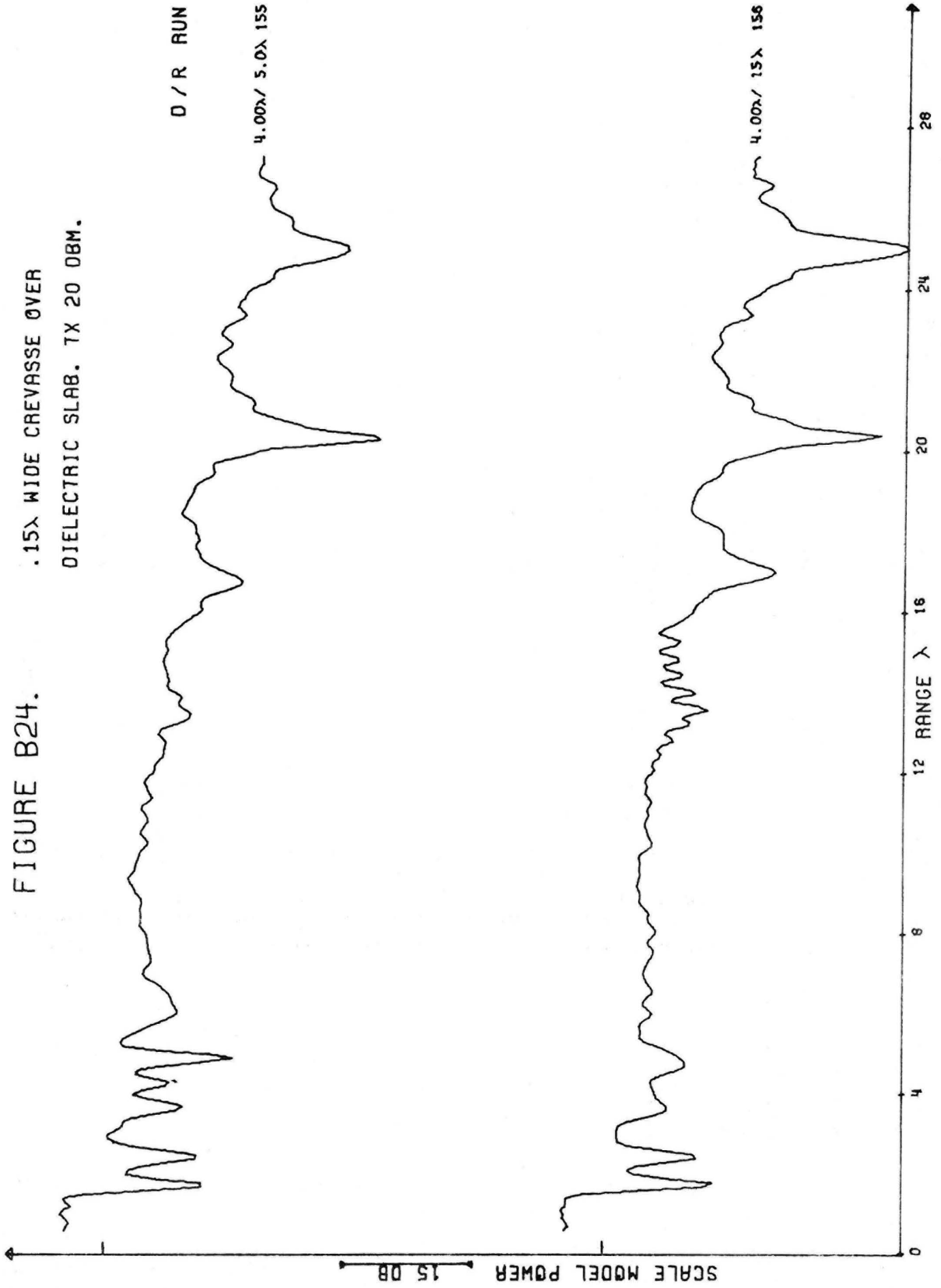


FIGURE B25.

.10λ WIDE CREVASSE OVER
DIELECTRIC SLAB. TX 20 DBM.

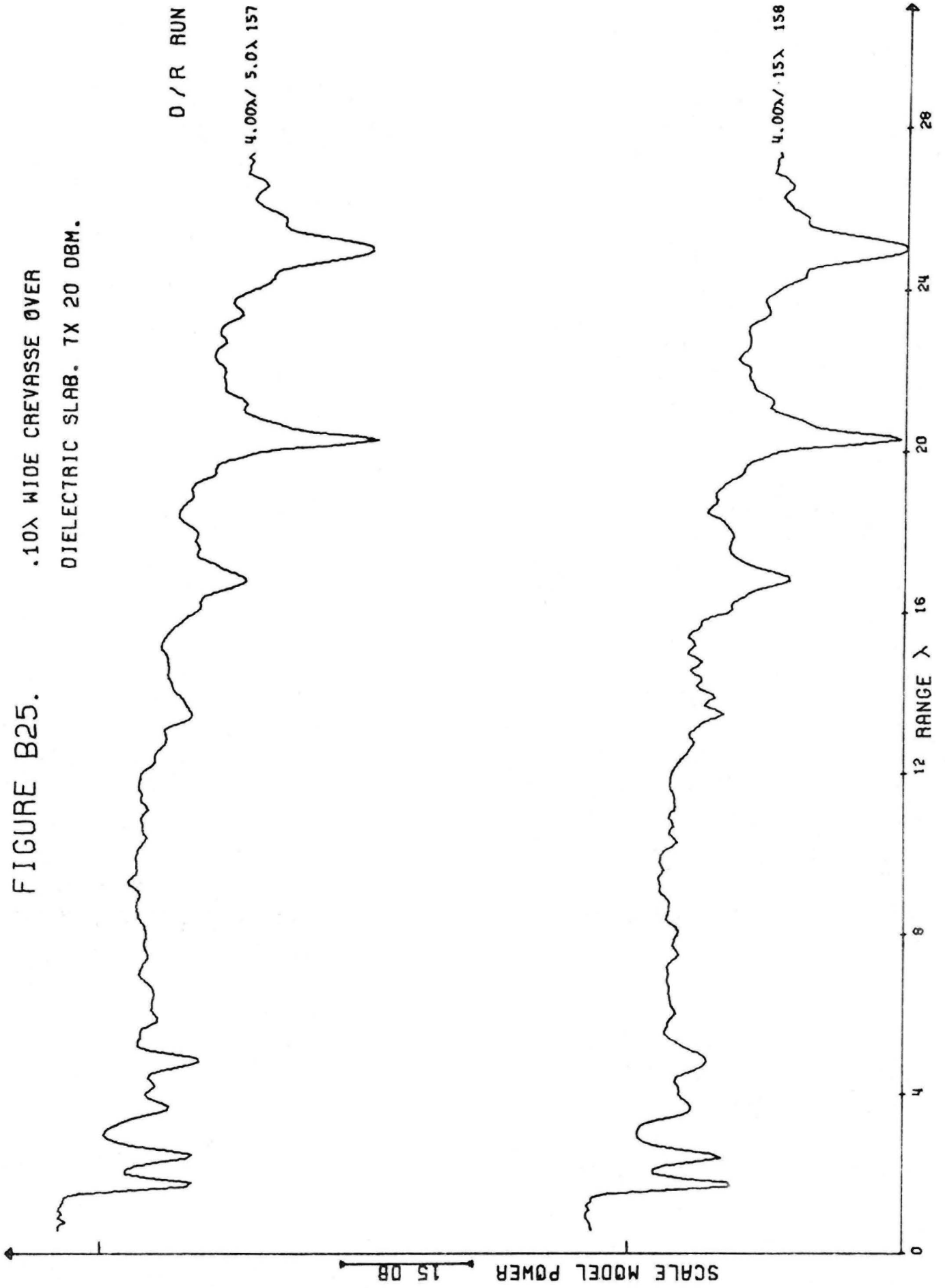


FIGURE B26.

.10λ WIDE CREVASSE OVER
DIELECTRIC SLAB. TX 20 DBM.

D / R RUN

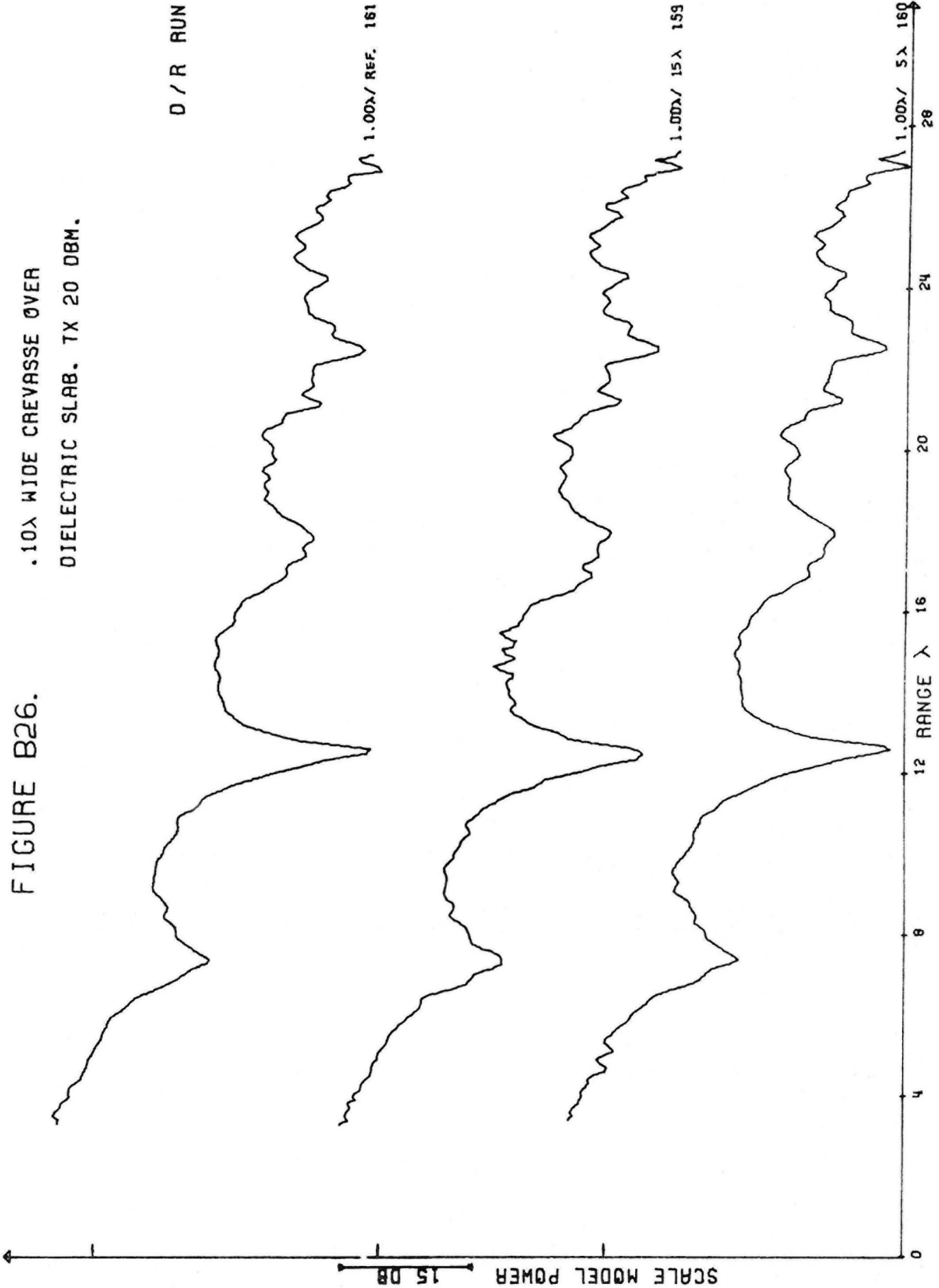


FIGURE B27.

.5λ DIAMETER SPHERE CENTERED 4λ
DEEP OVER SLAB. TX 10 DBM.

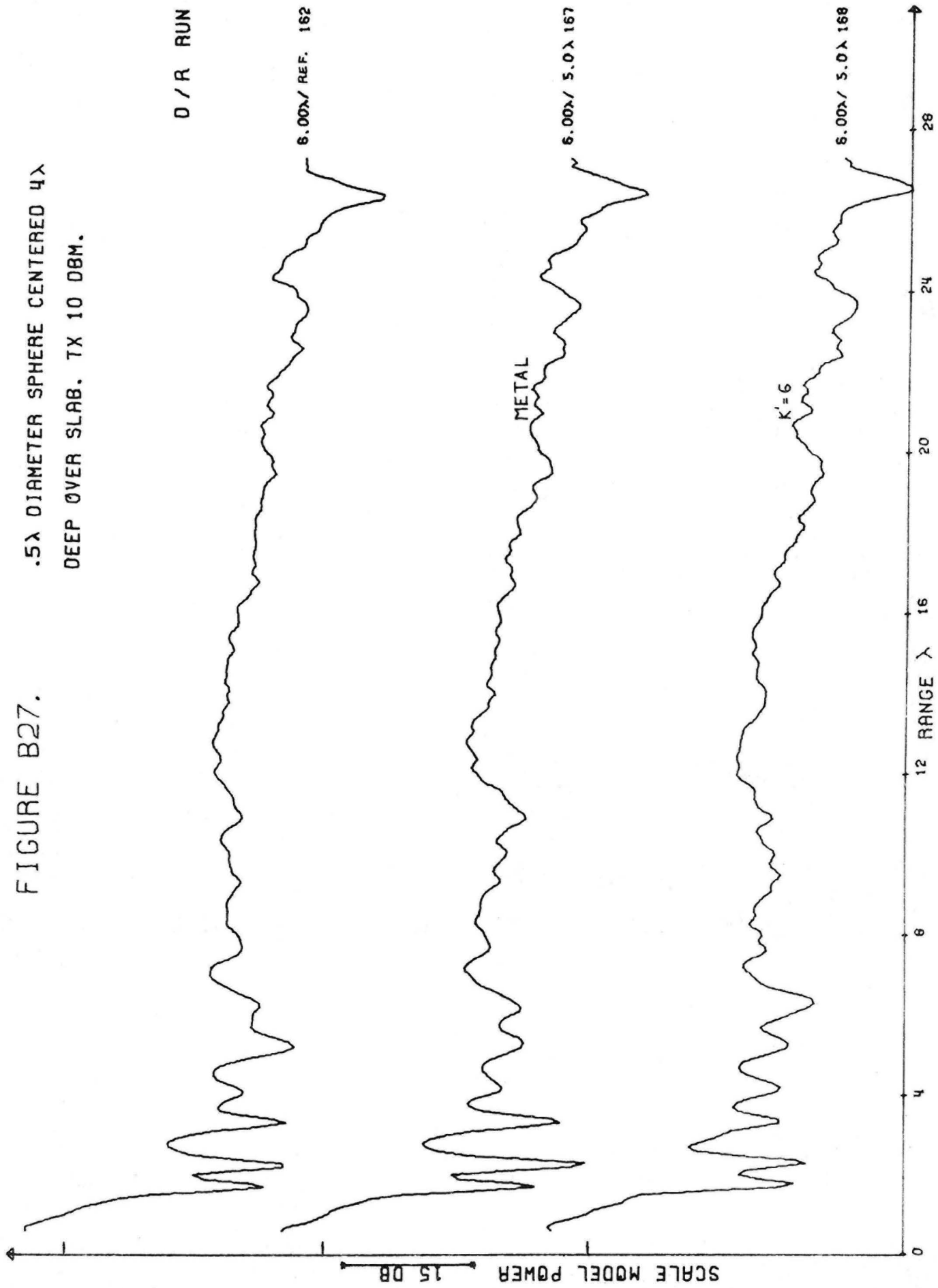


FIGURE B28.

1λ DIAMETER SPHERE CENTERED 4λ
DEEP OVER SLAB. TX 10 OBM .

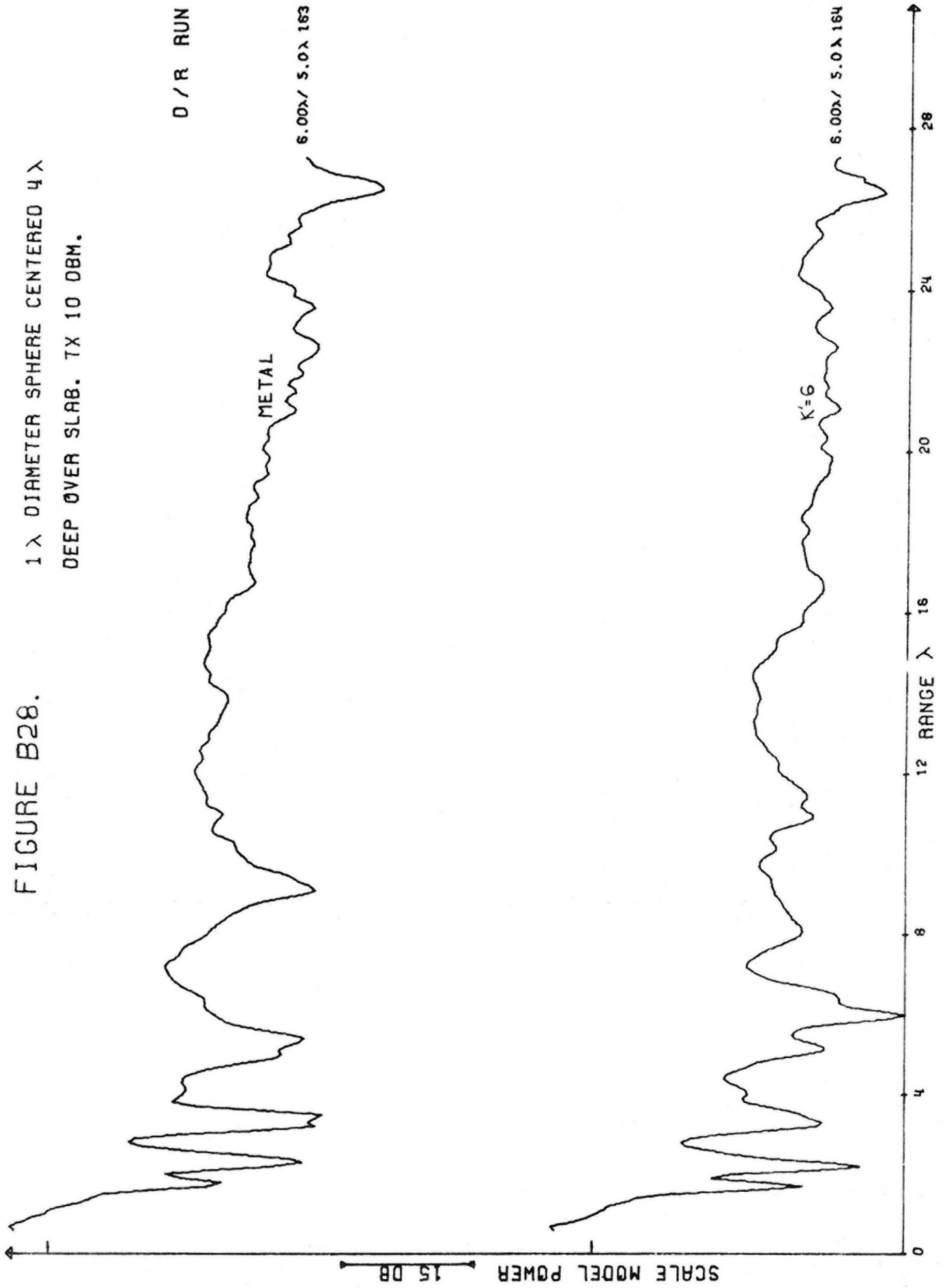


FIGURE B29.

2λ DIAMETER SPHERE CENTERED 4λ
DEEP OVER SLAB. TX 10 DBM.

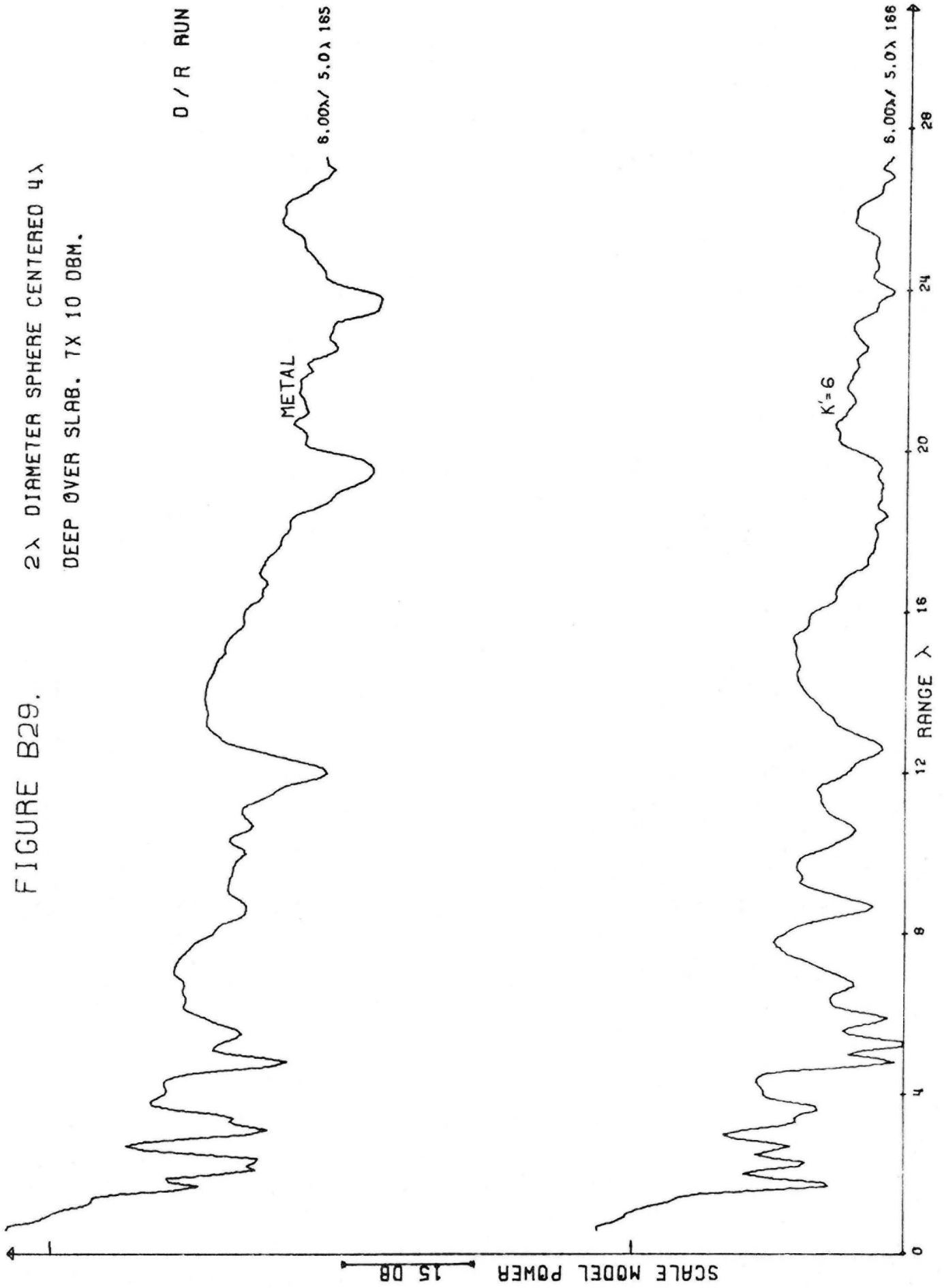


FIGURE B30.

1λ DIAMETER SPHERE CENTERED 4λ
DEEP OVER SLAB. TX 10 DBM.
K=6 FOR SPHERES.

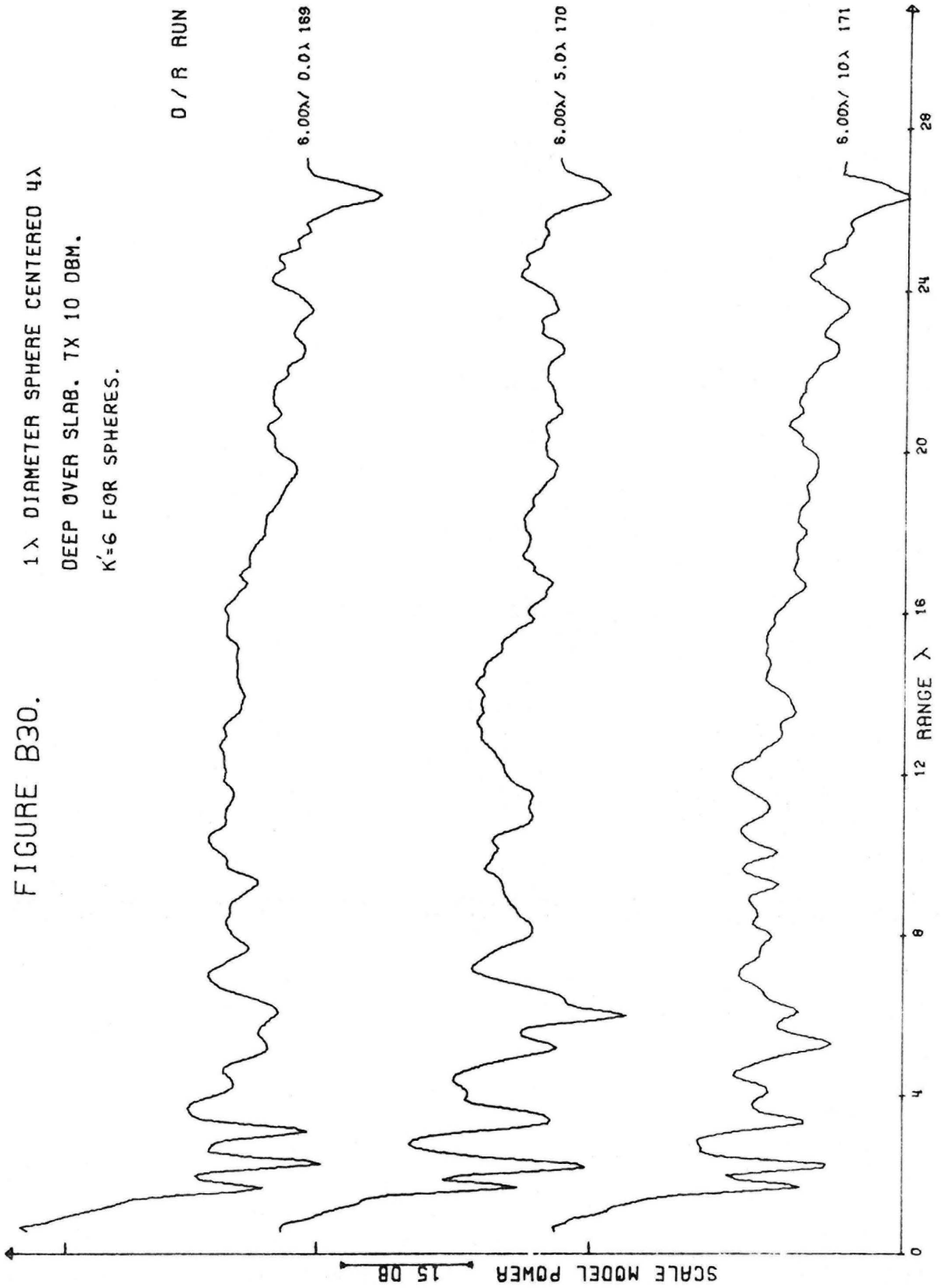


FIGURE B31.

1 λ DIAMETER SPHERE CENTERED 4 λ
DEEP OVER SLAB. TX 10 DBM.
K'=6 FOR SPHERES.

O/R RUN

6.00 λ / 15 λ 172

6.00 λ / 20 λ 173

6.00 λ / 25 λ 174

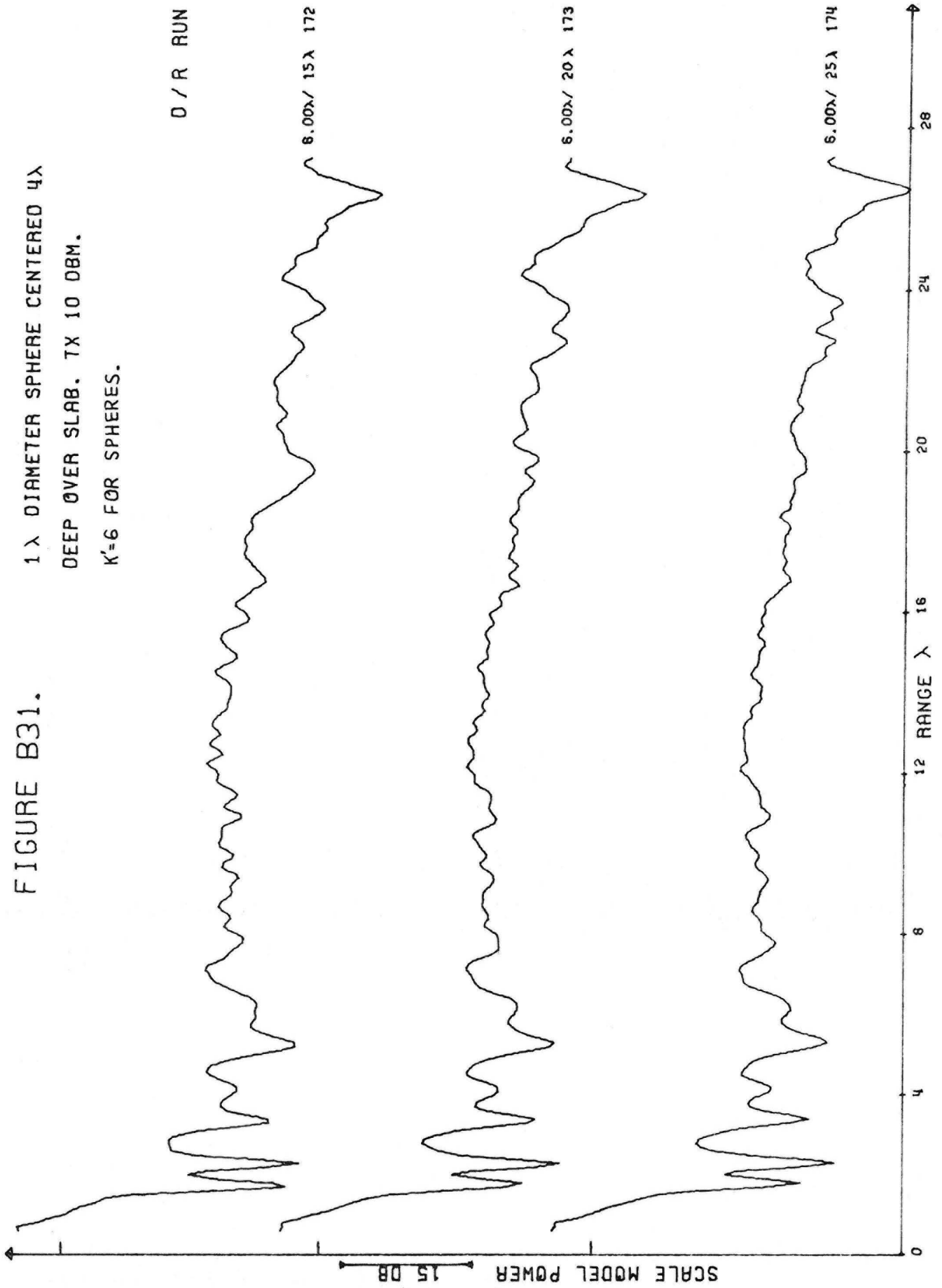


FIGURE B32.

1 λ DIAMETER SPHERE SET ON SLAB.

$K=6$ FOR SPHERES. TX 15 DBM.

D / R RUN

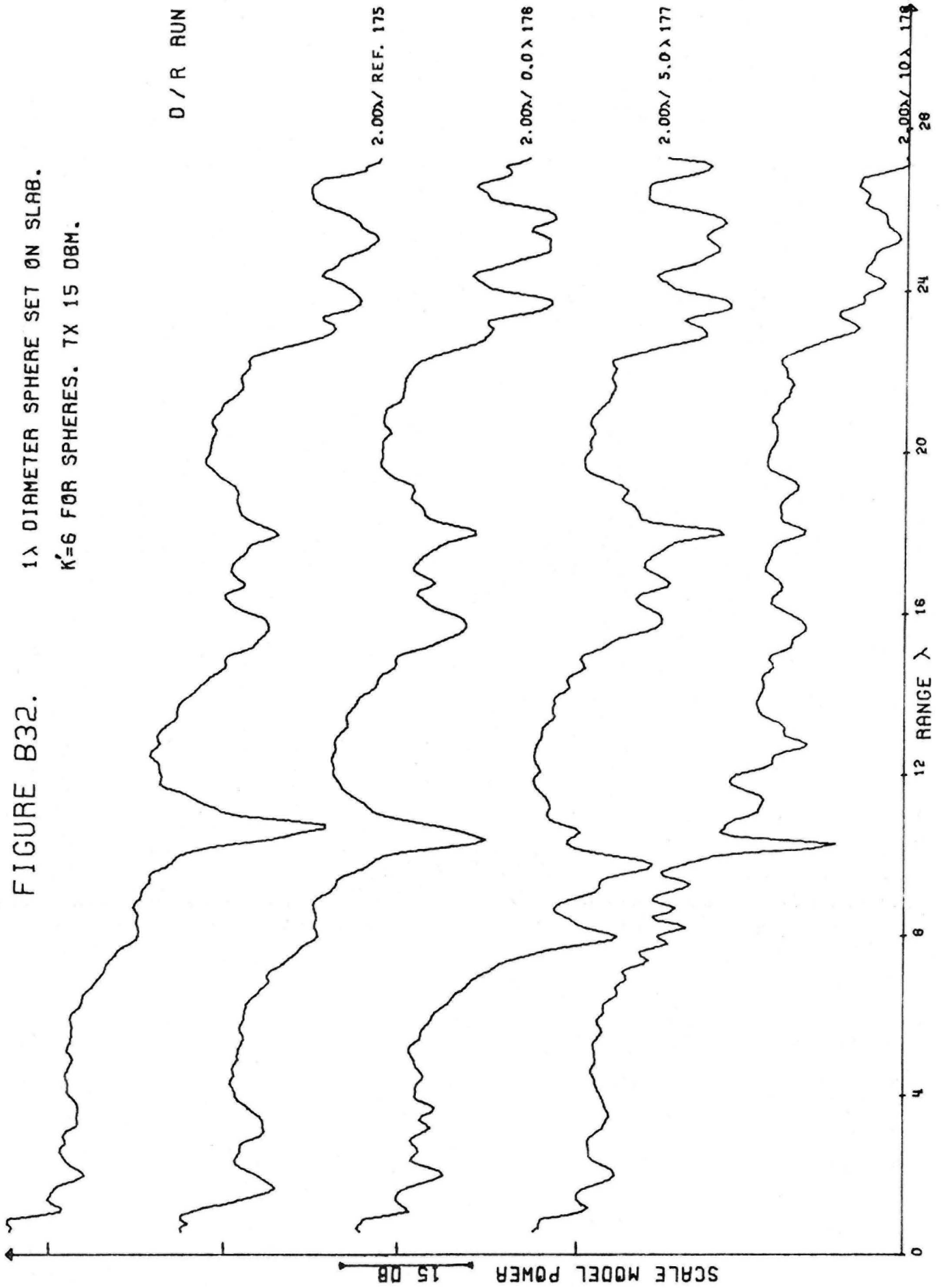


FIGURE B33.

1λ DIAMETER SPHERE SET ON SLAB.

$K=6$ FOR SPHERES. TX 15 DBM.

D / R RUN

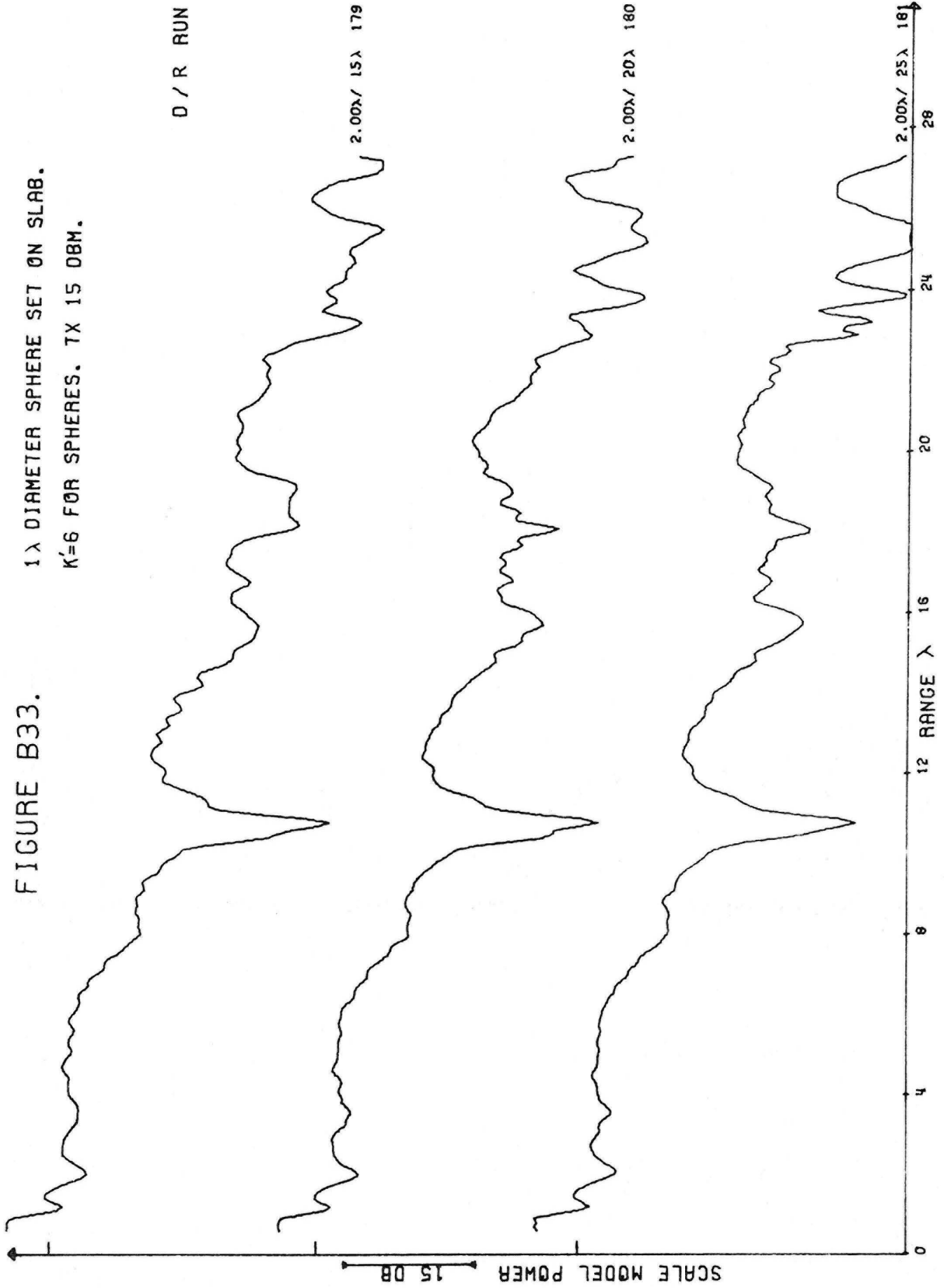


FIGURE B34.

1λ DIAMETER SPHERE SET ON SLAB.
K=6 FOR SPHERES. TX 15 DBM.

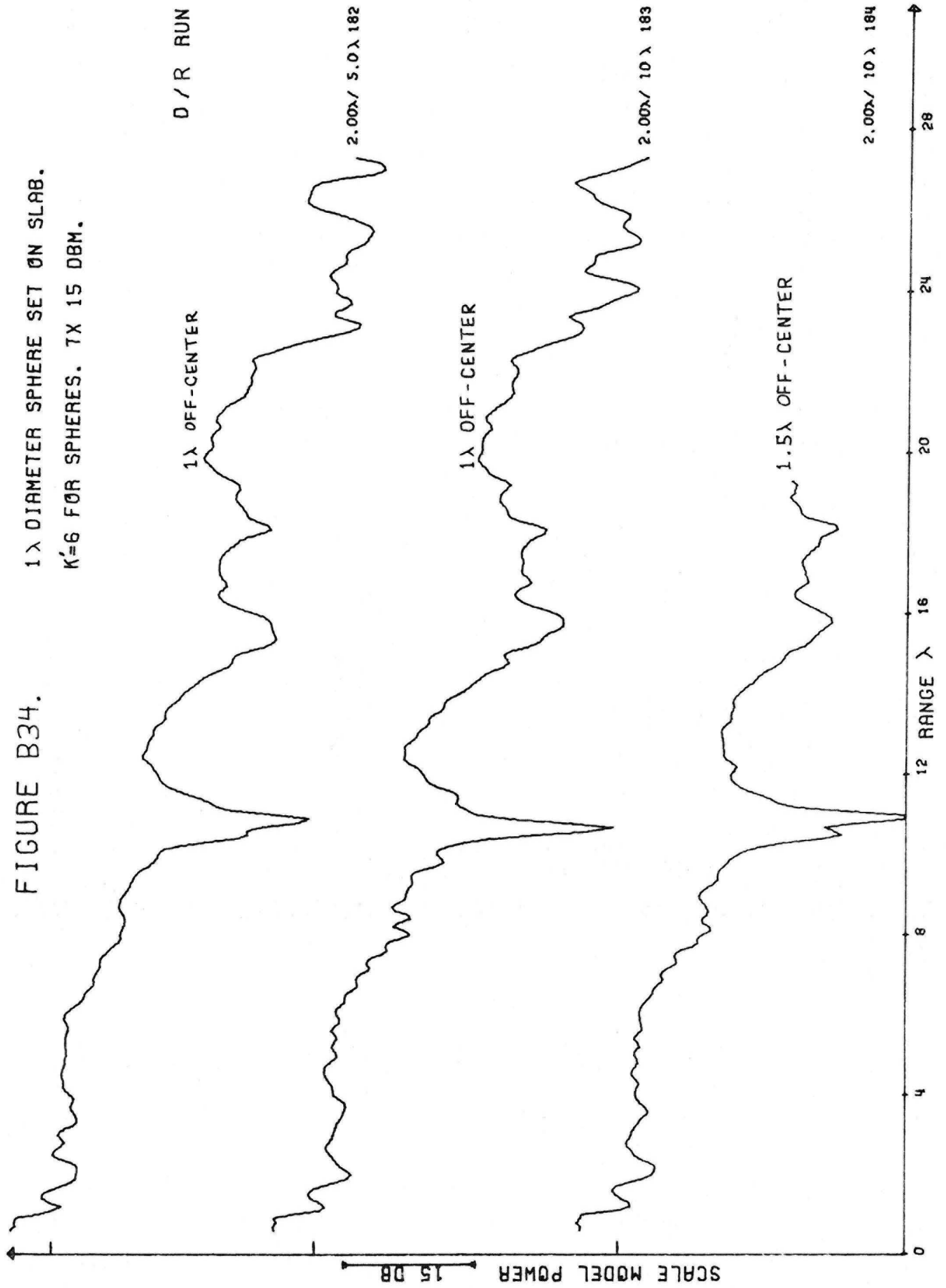


FIGURE B35.
0.5λ WIDE CREVASSE SIMULATED IN
SLAB. TX 15 DBM.

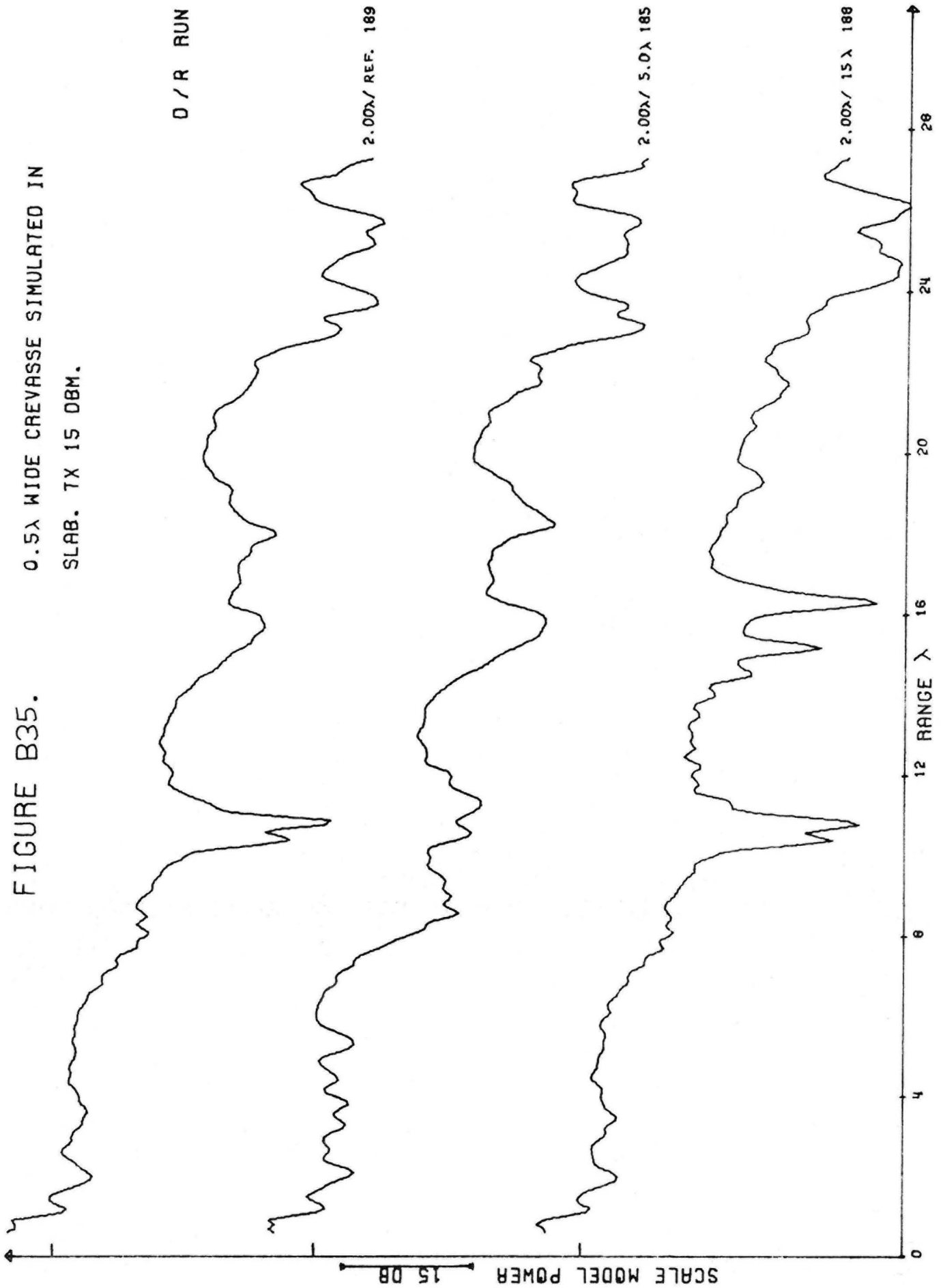


FIGURE B36.

.25λ WIDE CREVASSE SIMULATED IN
SLAB. TX 15 DBM.

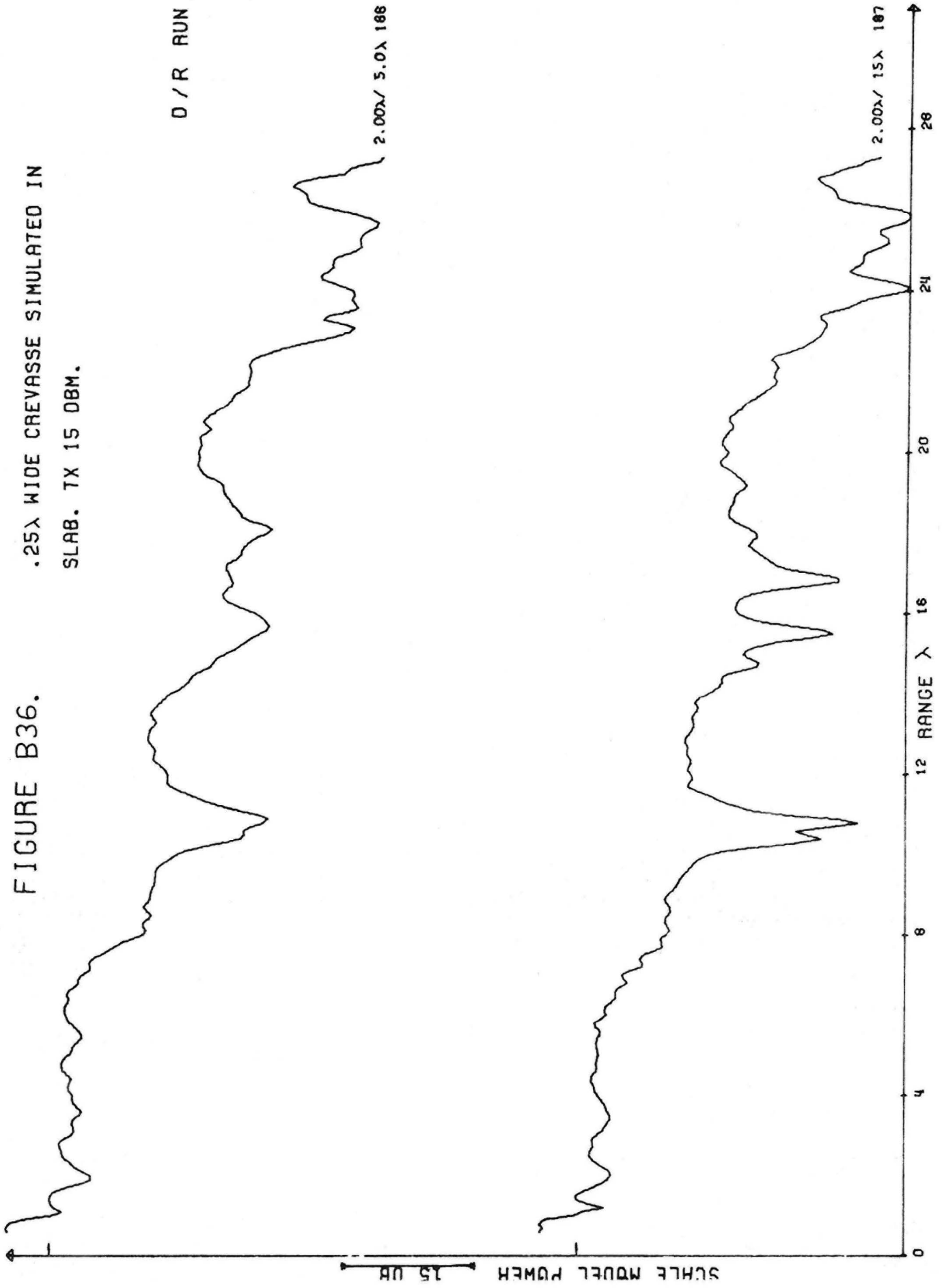


FIGURE B37.

.25λ WIDE CREVASSE SIMULATED IN
SLAB. TX 15 DBM.

D / R RUN

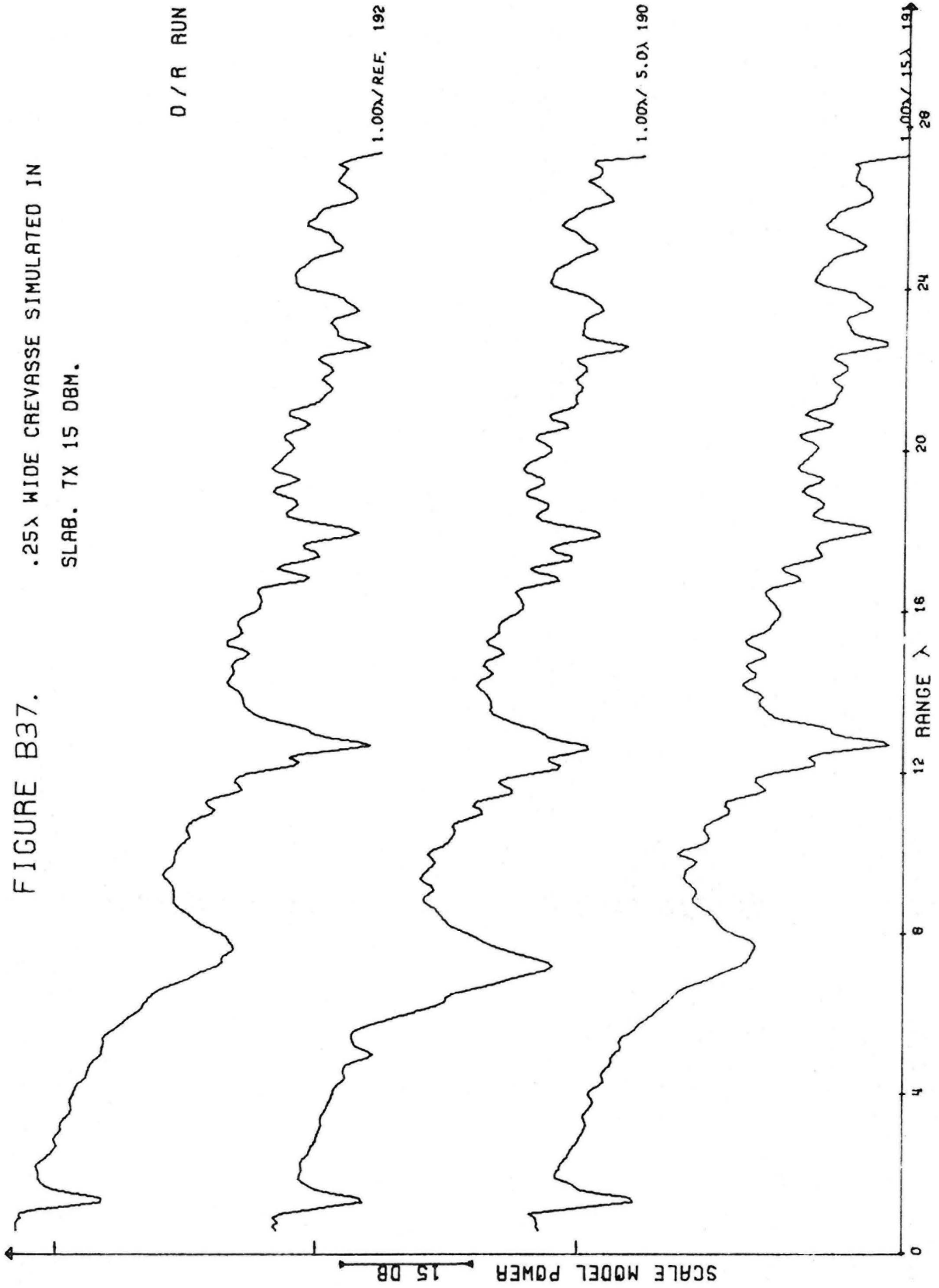


FIGURE B38.

RANDOM BLOCKS ON SLAB. BLOCKS .6λ
SIZE AND UNDER. TX 15 DBM.

D / e RUN

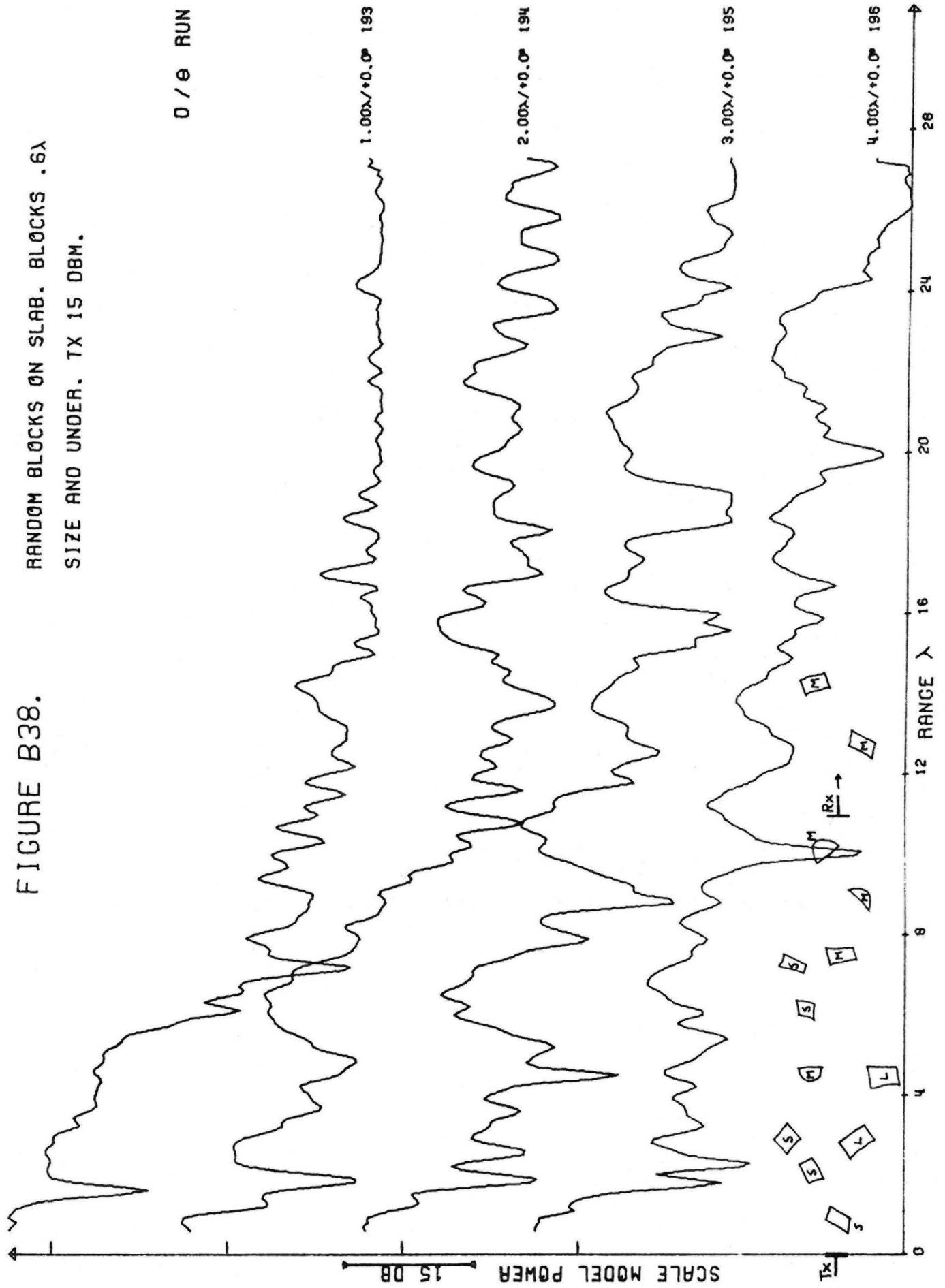


FIGURE B39.

RANDOM BLOCKS ON SLAB. BLOCKS .6λ
SIZE AND UNDER. TX 15 DBM.

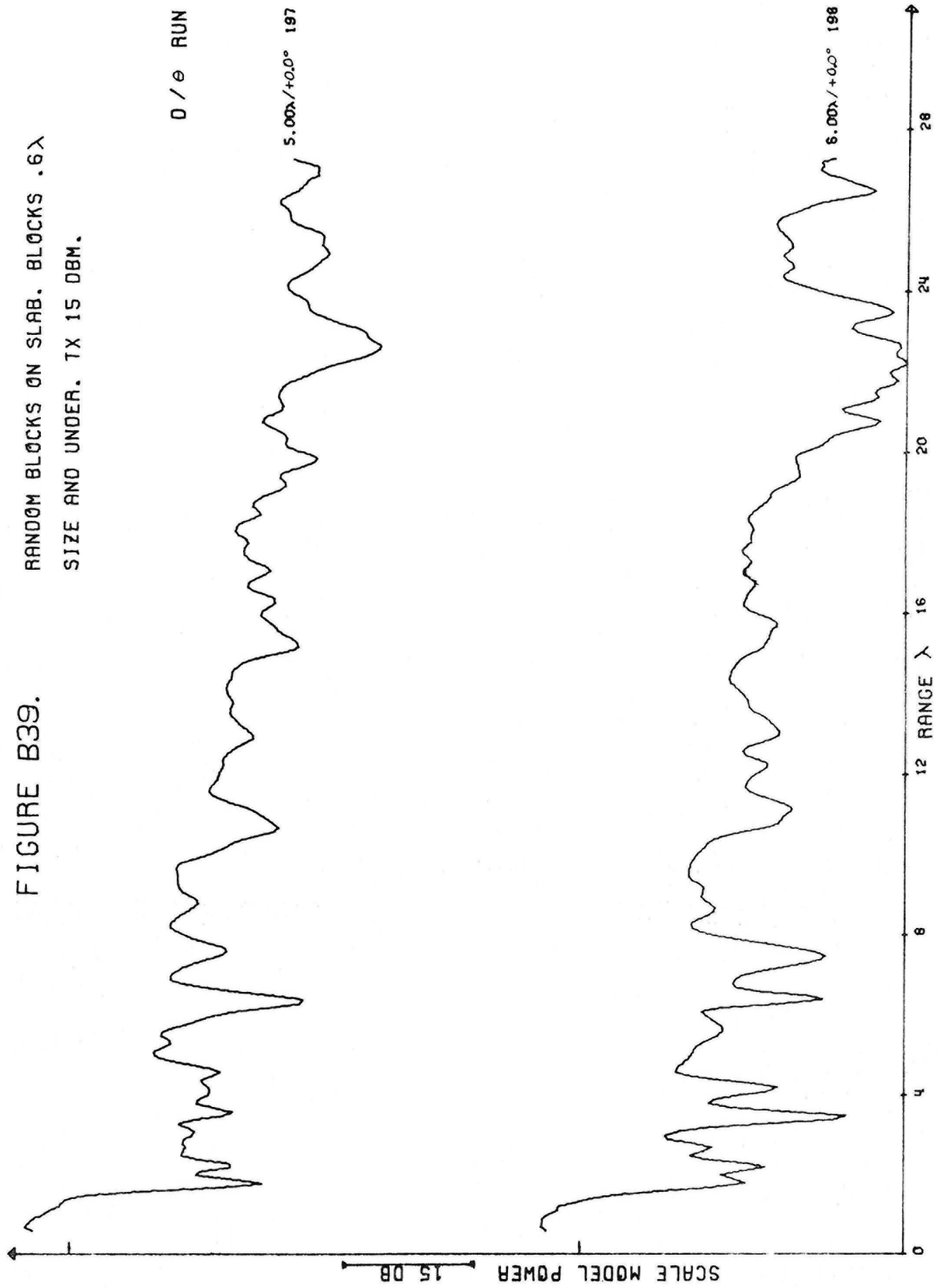


FIGURE B40.

RANDOM BLOCKS ON SLAB. BLOCKS .6
SIZE AND UNDER. TX 15 DBM.
(FIGURE B38, STRONGLY FILTERED.)

0 / 6 RUN

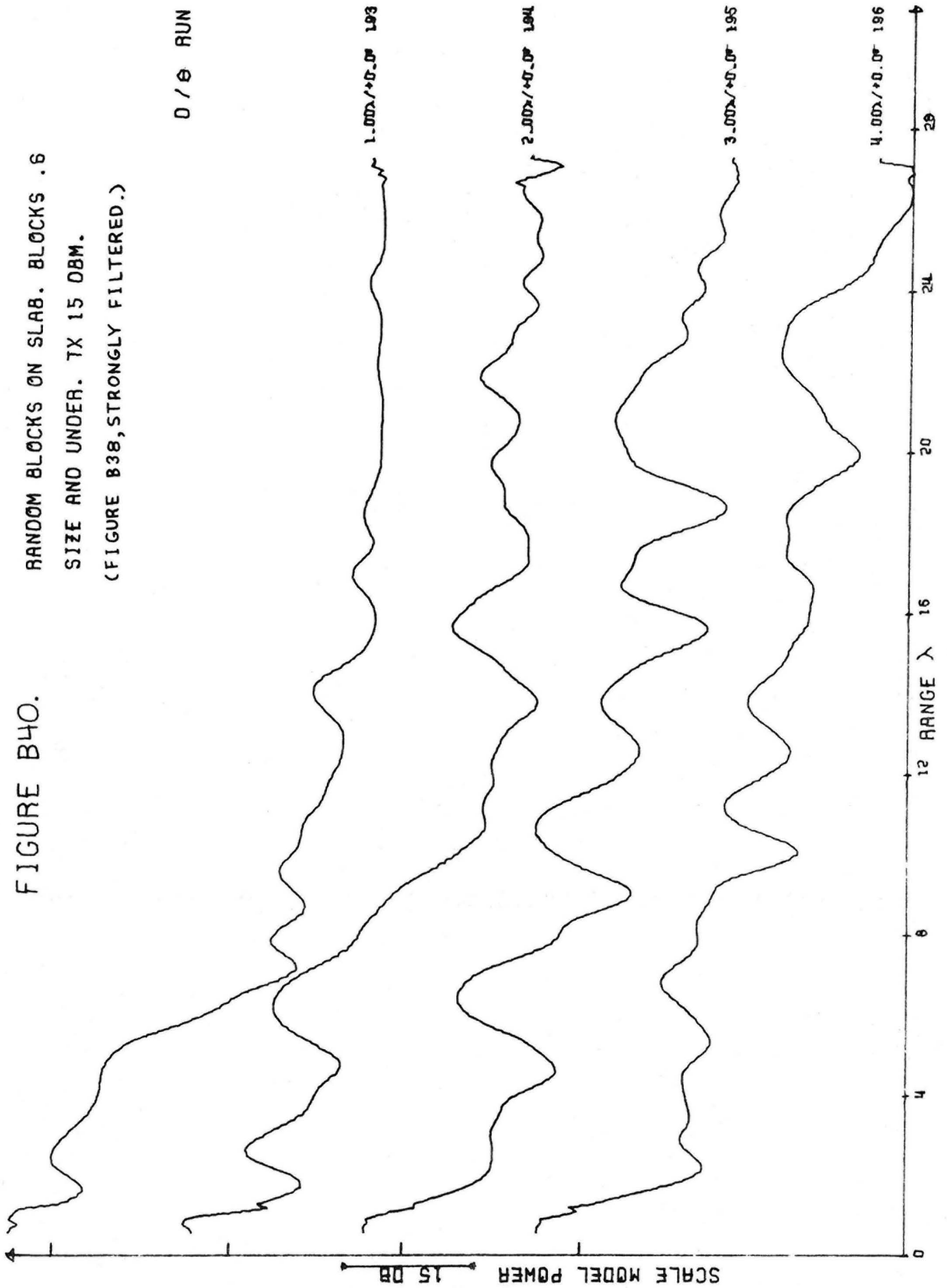
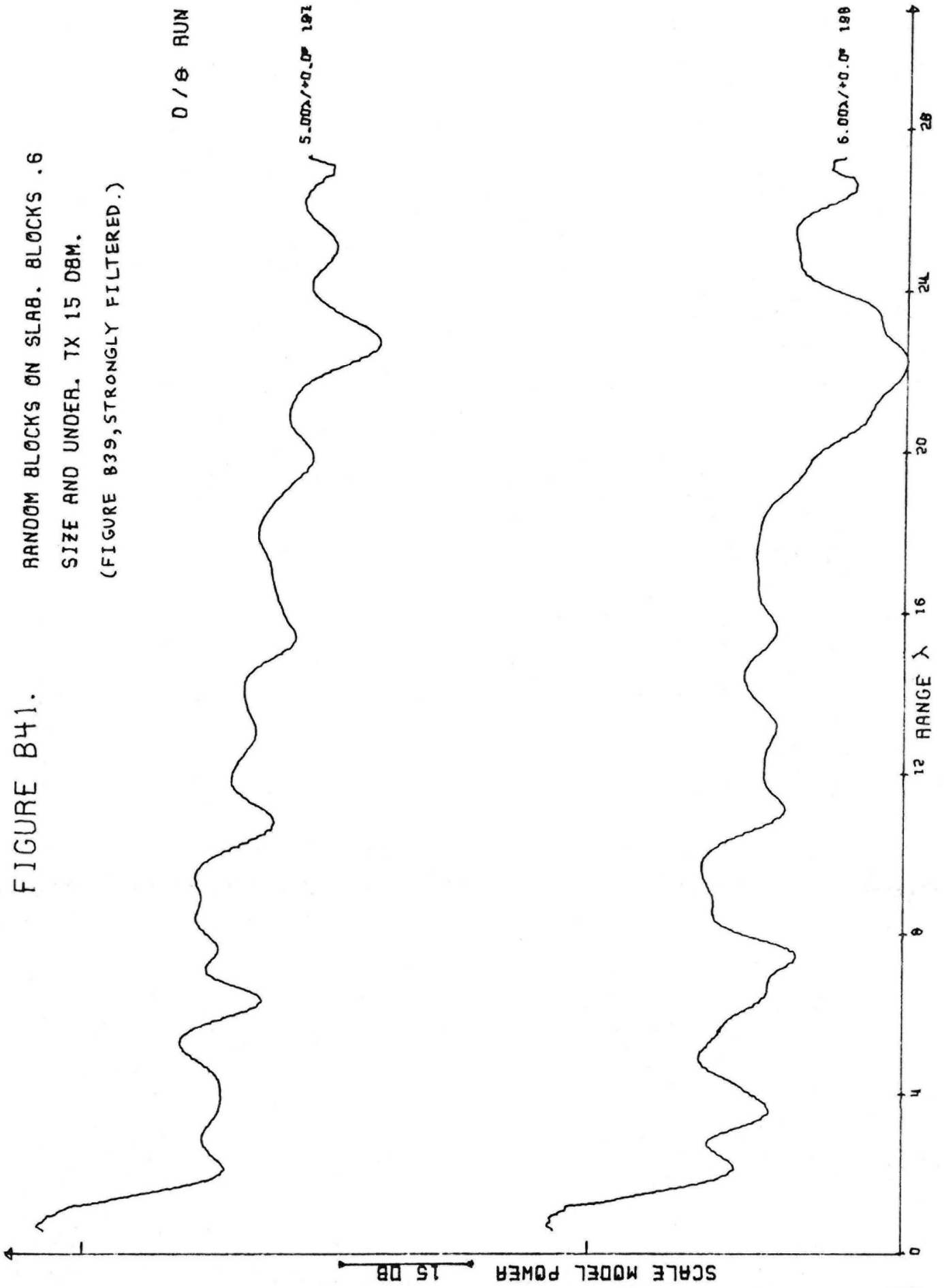


FIGURE B41.

RANDOM BLOCKS ON SLAB. BLOCKS .6
SIZE AND UNDER. TX 15 DBM.

(FIGURE B39, STRONGLY FILTERED.)



APPENDIX C
VARIABLE - LOSS DATA TRAVERSES

FIGURE C1. HALF-SPACE AT VARIOUS LOSS TANGENTS. TX 30 DBM.

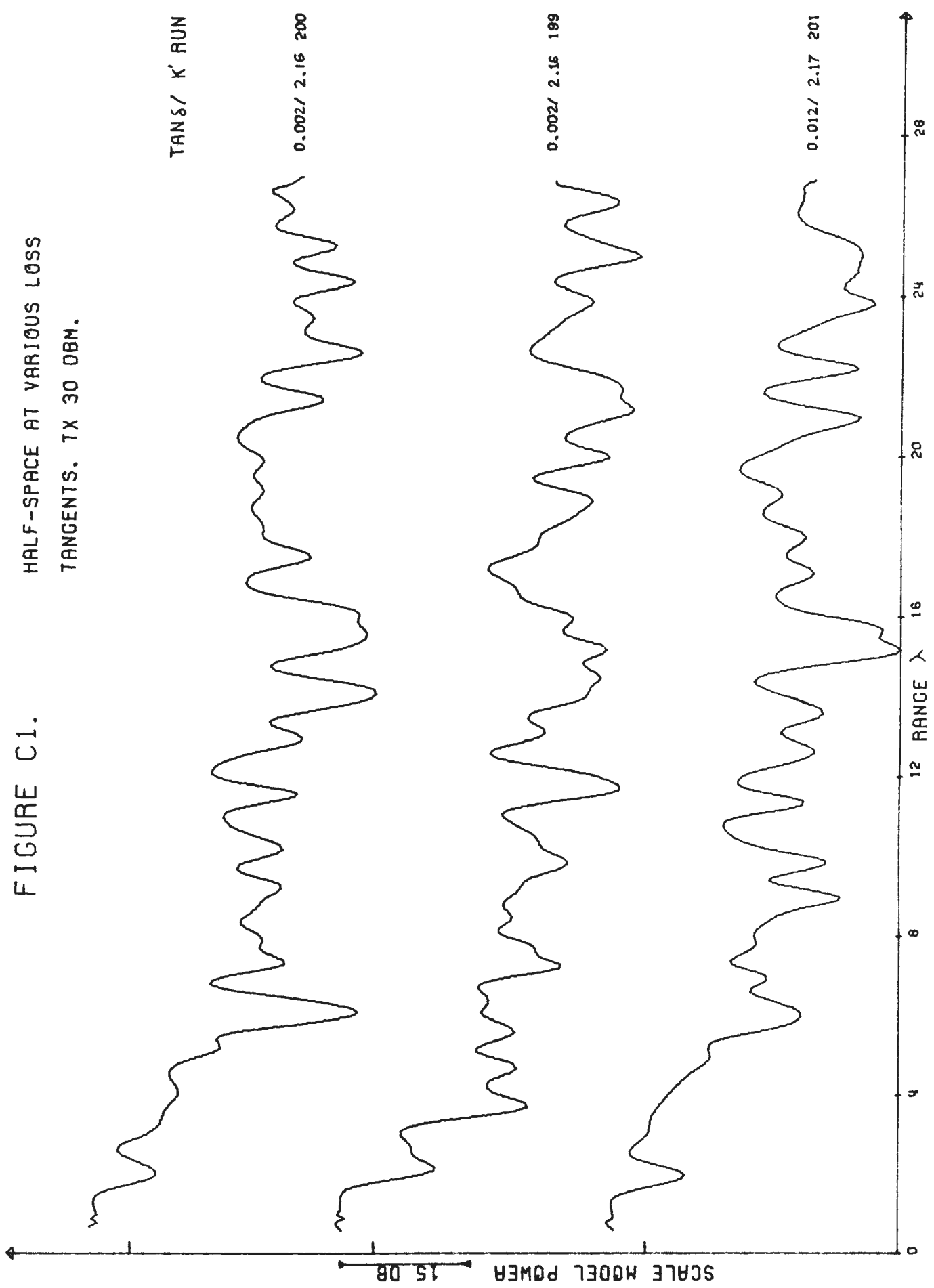


FIGURE C2.
HALF-SPACE AT VARIOUS LOSS
TANGENTS. TX 30 OBM.

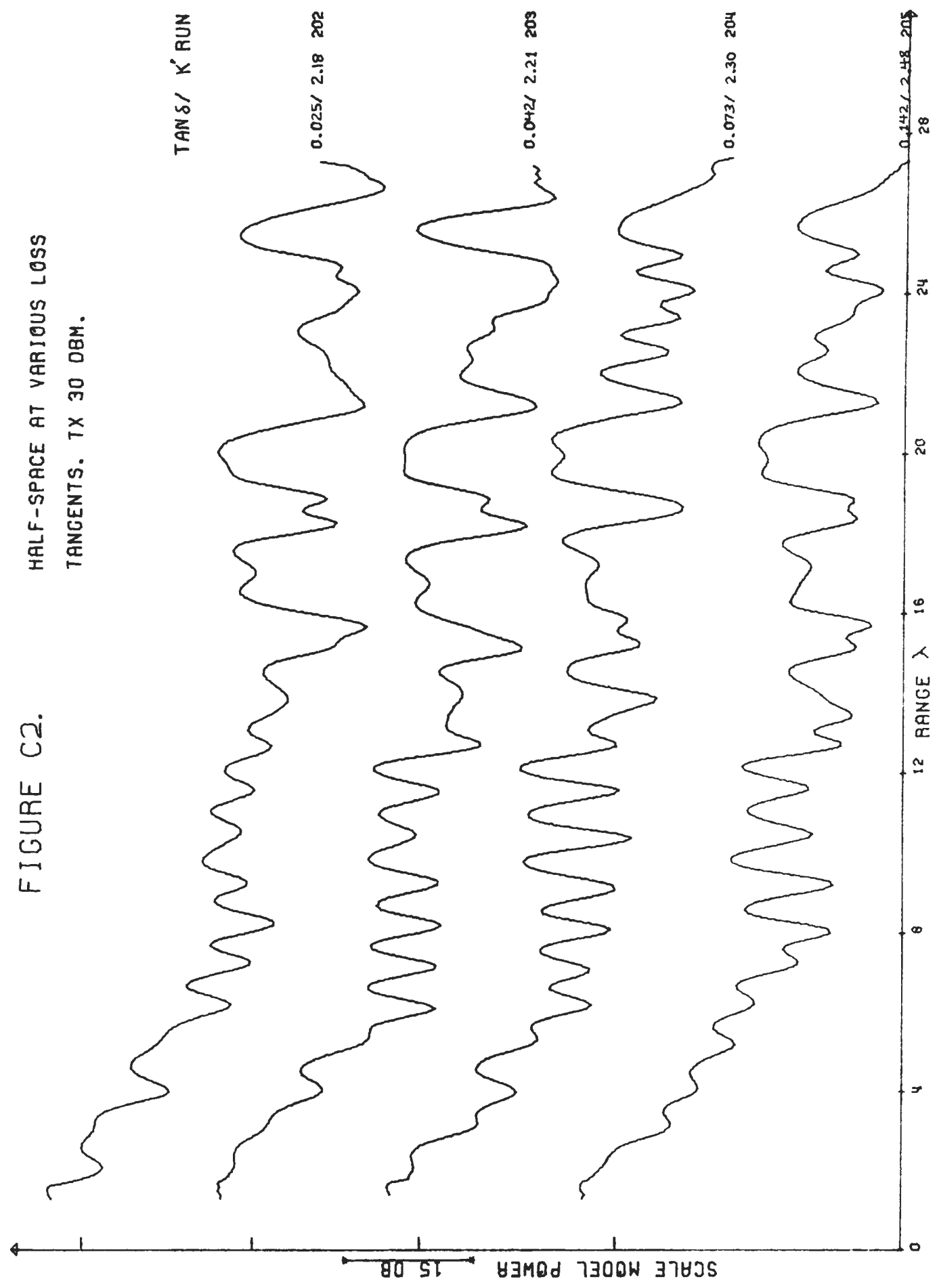


FIGURE C3.

HORIZONTAL METAL PLATE.
LOSS TANGENT .002. TX 15 DBM.

0 / 0 RUN

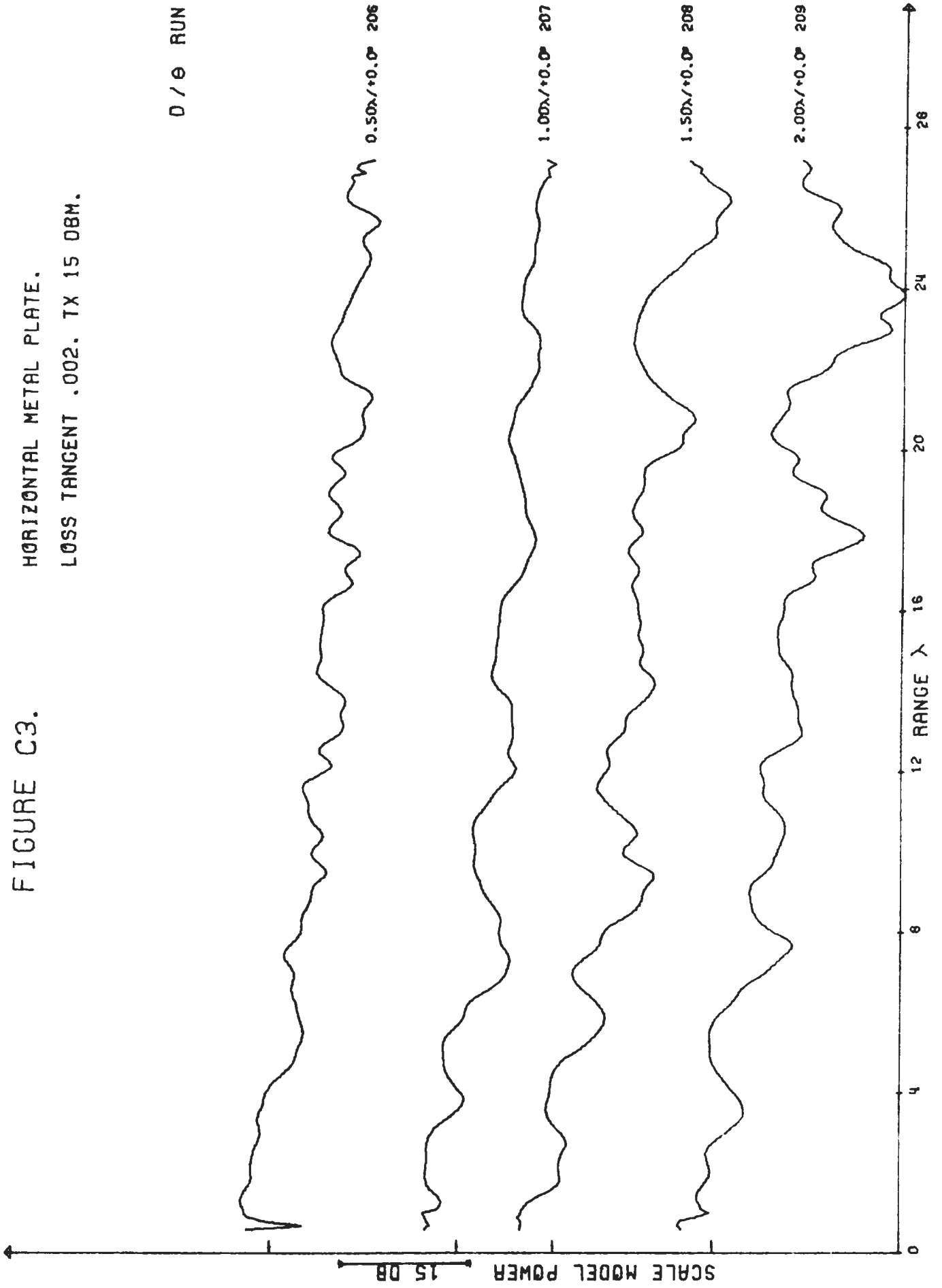


FIGURE C4.

HORIZONTAL METAL PLATE.
LOSS TANGENT .002. TX 15 DBM.

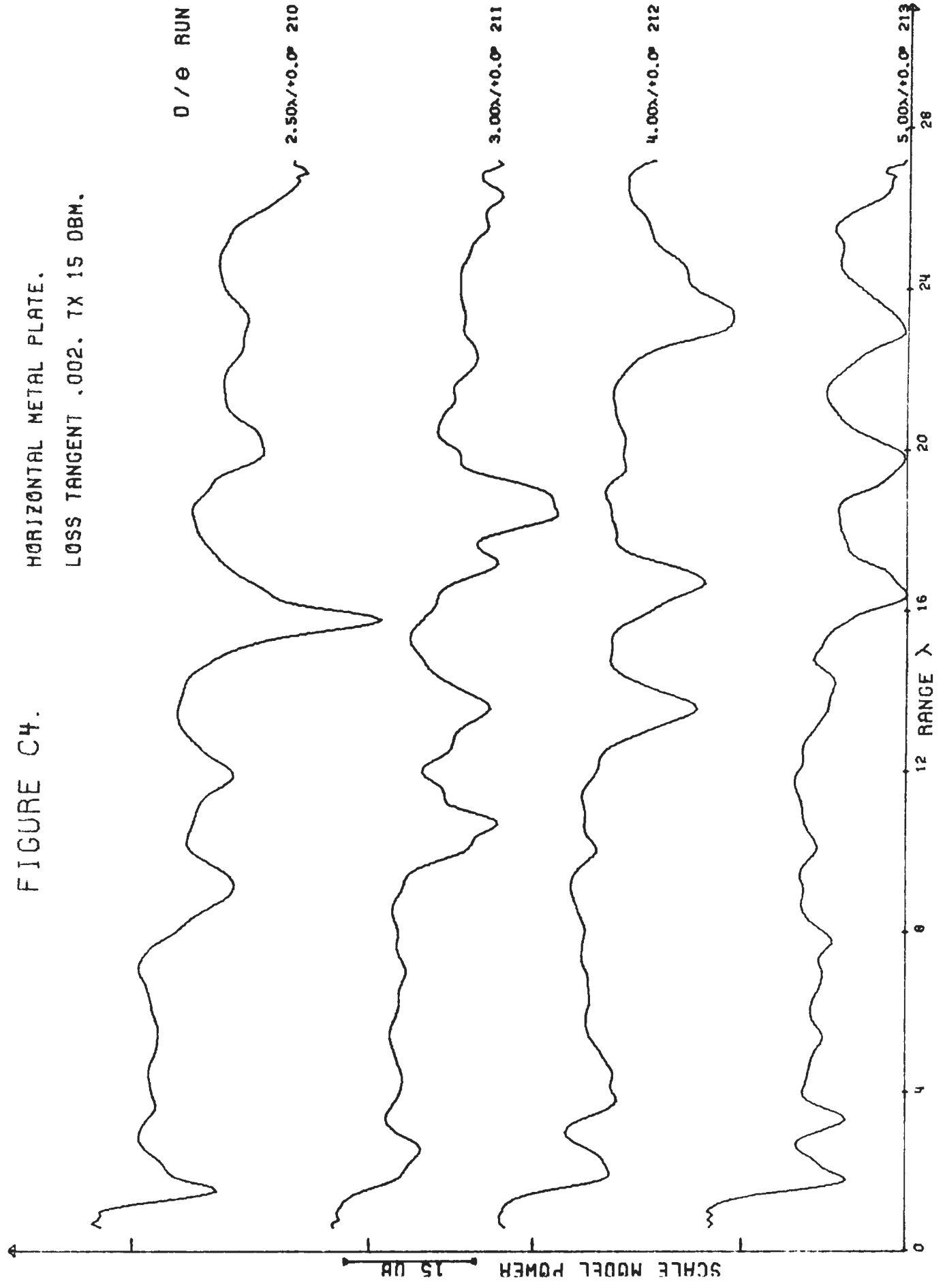


FIGURE C5.

HORIZONTAL METAL PLATE.

LOSS TANGENT .002. TX 15 DBM.

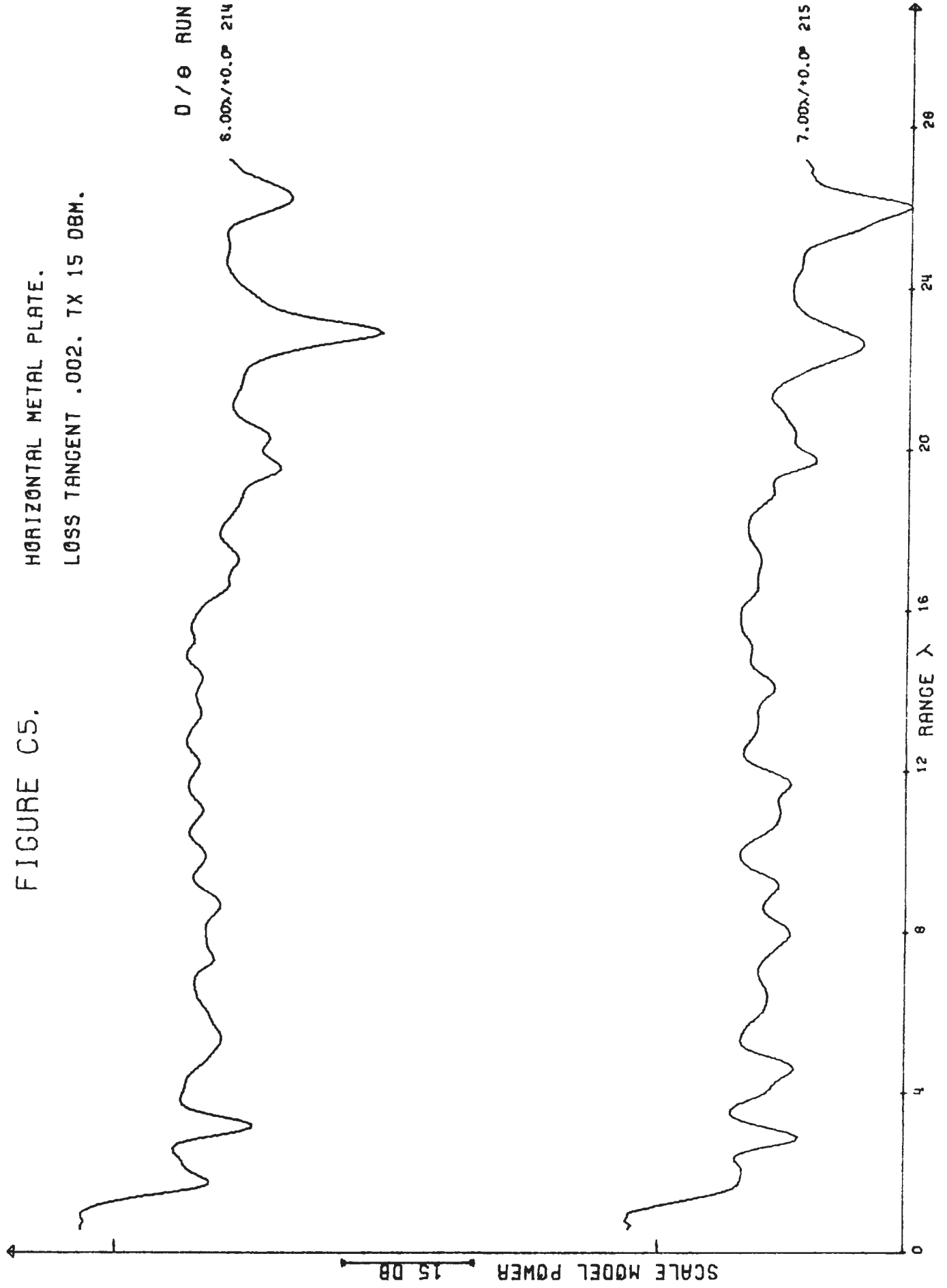


FIGURE C6. HORIZONTAL METAL PLATE.
LOSS TANGENT .012. TX 15 DBM.

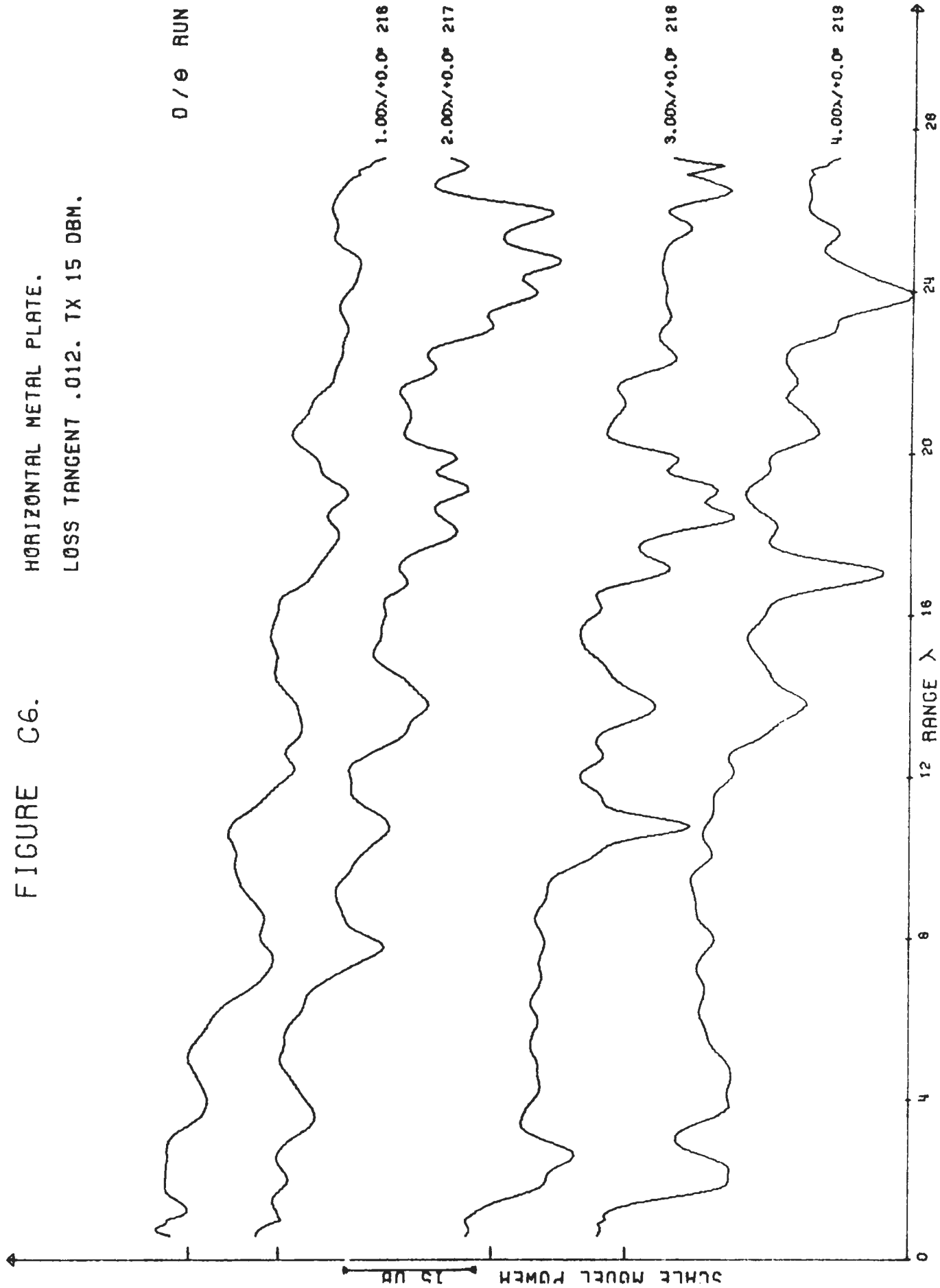


FIGURE C7.

HORIZONTAL METAL PLATE.
LOSS TANGENT .012. TX 15 DBM.

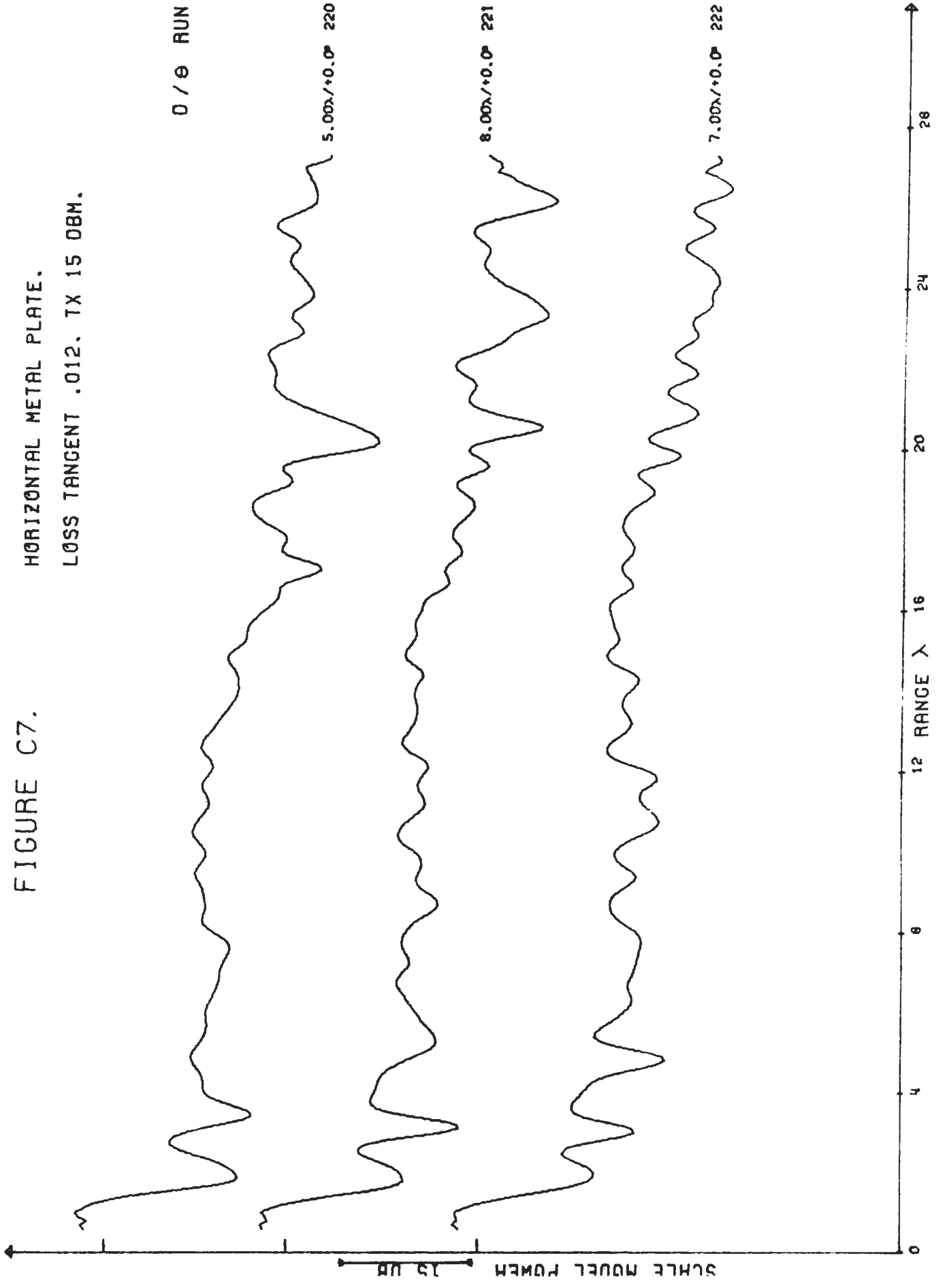


FIGURE C8.

HORIZONTAL METAL PLATE.
LOSS TANGENT .025. TX 15 DBM.

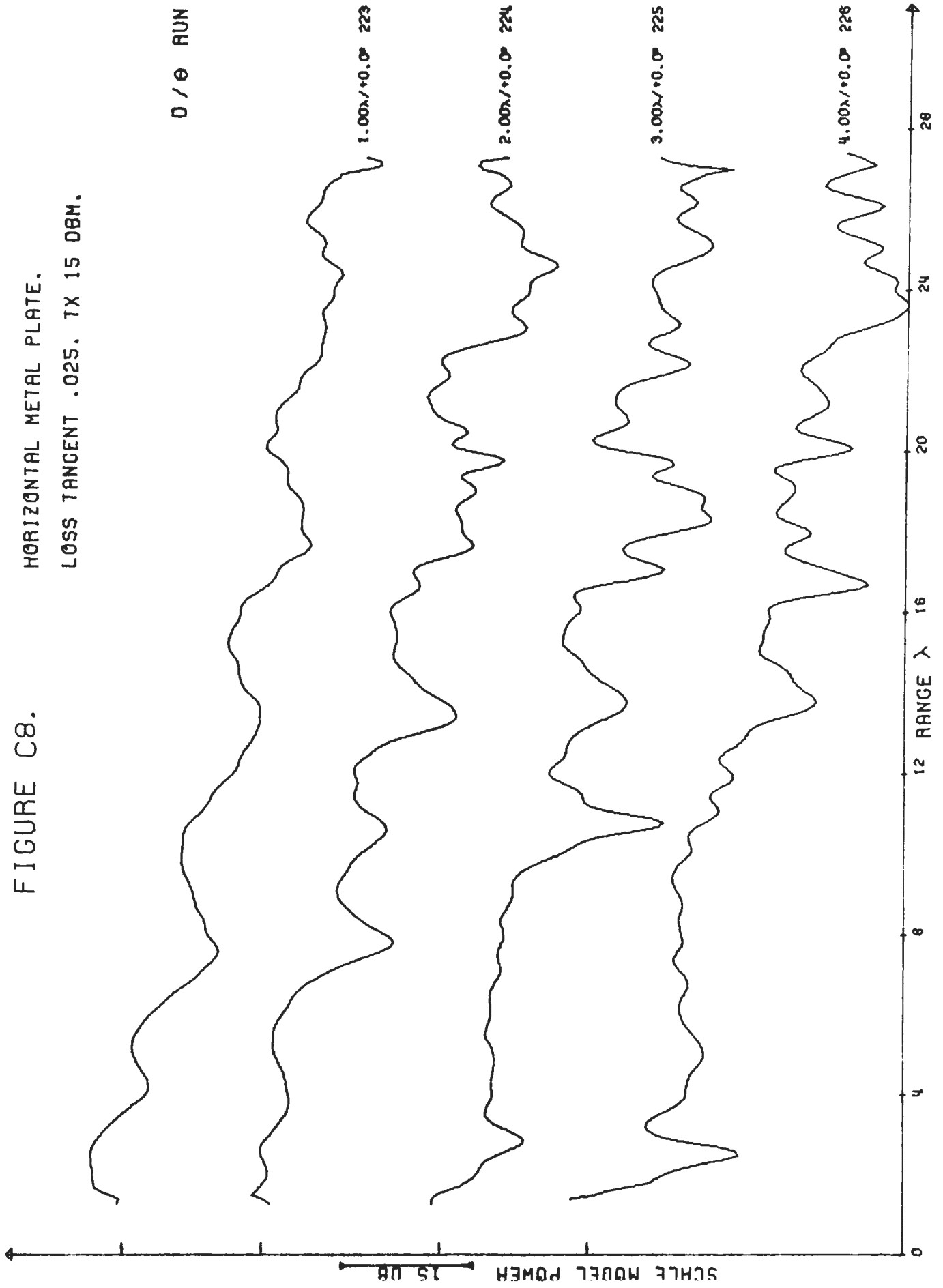


FIGURE C9.

HORIZONTAL METAL PLATE.
LOSS TANGENT .025. TX 15 DBM.

D / e RUN

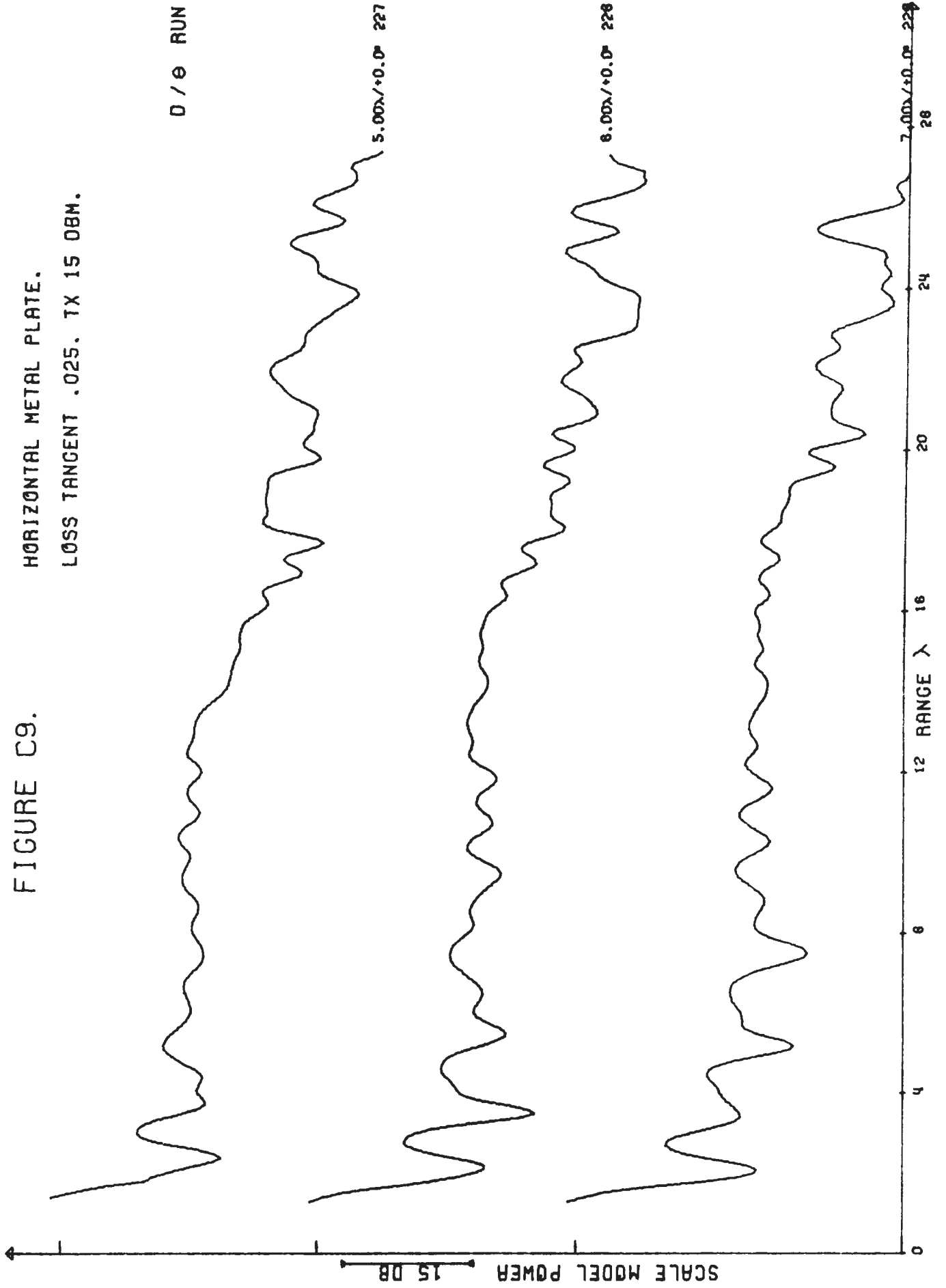


FIGURE C10.

HORIZONTAL METAL PLATE.
LOSS TANGENT .042. TX 20 DBM.

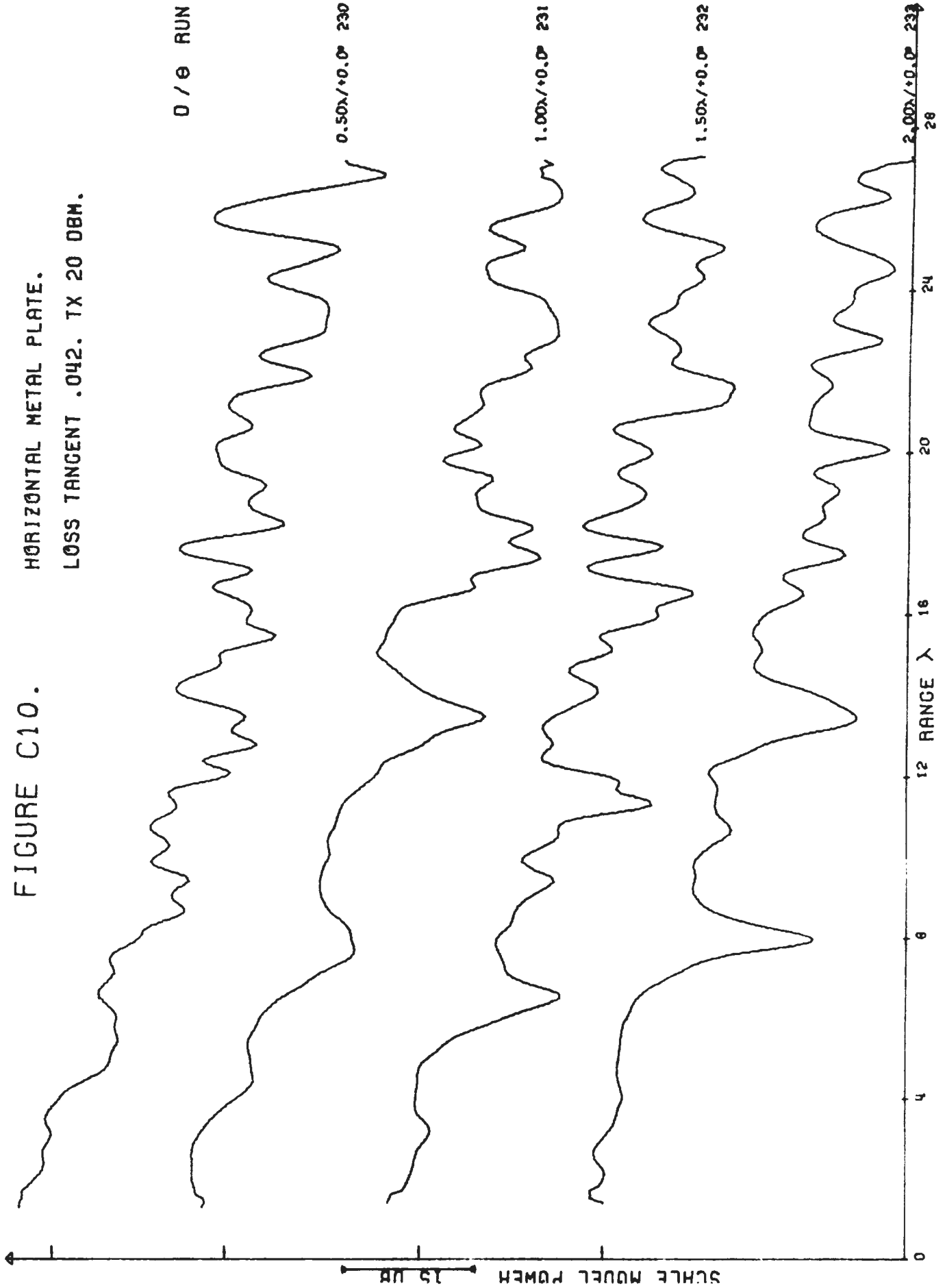


FIGURE C11.

HORIZONTAL METAL PLATE.
LOSS TANGENT .042. TX 20 DBM.

D / e RUN

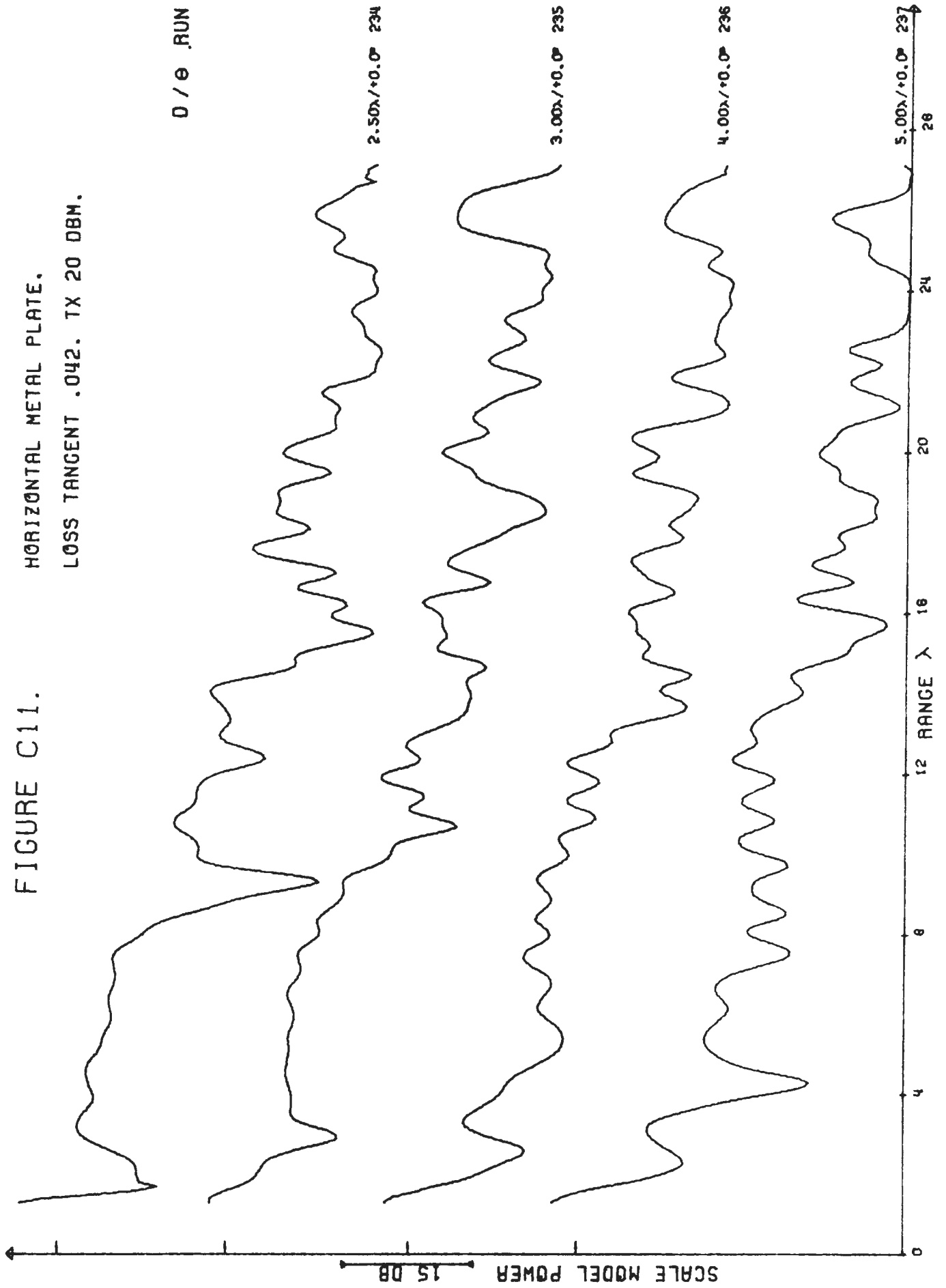


FIGURE C12.

HORIZONTAL METAL PLATE.
LOSS TANGENT .042. TX 20 DBM.

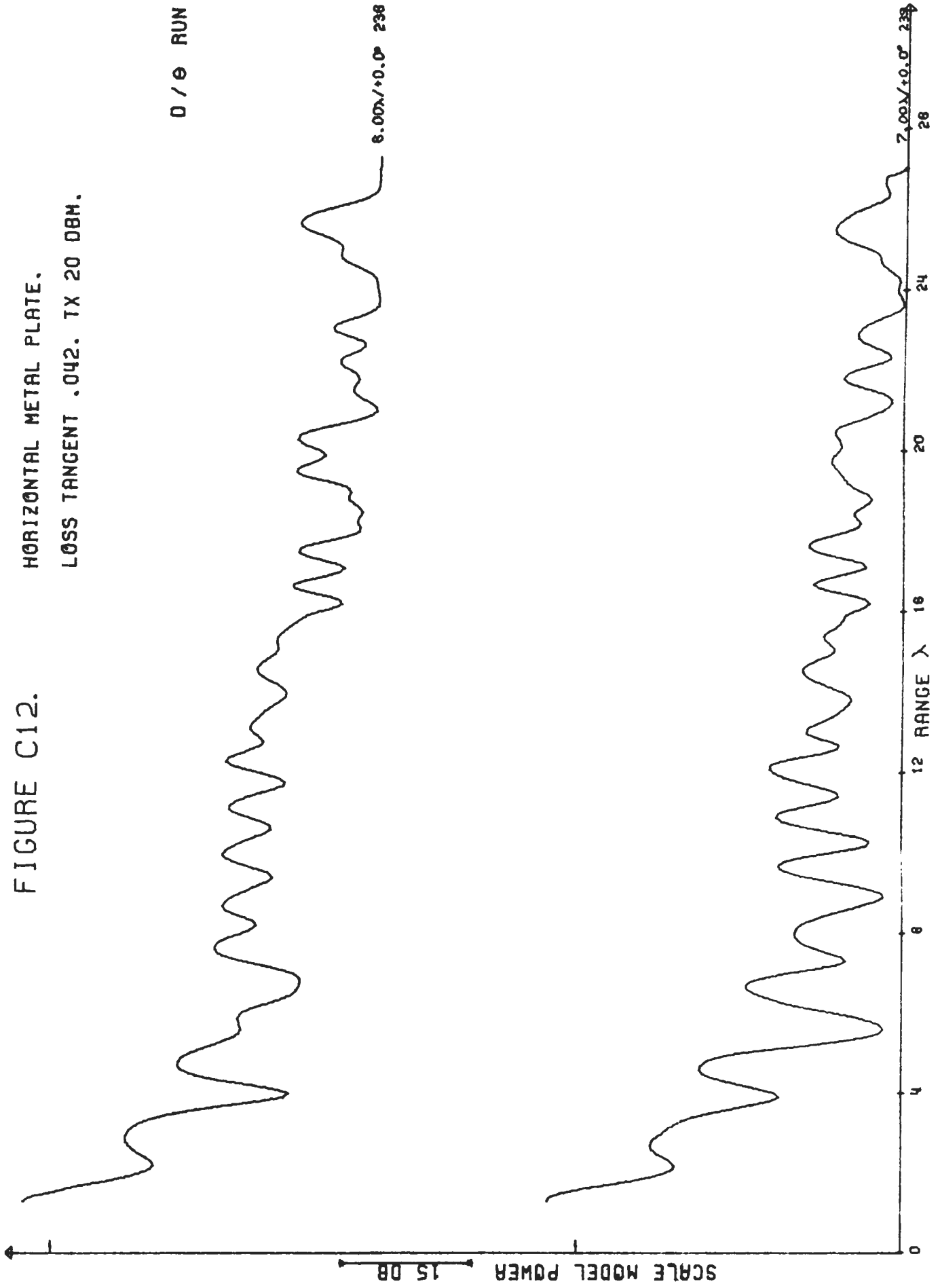


FIGURE C13.

HORIZONTAL METAL PLATE.
LOSS TANGENT .073. TX 20 DBM.

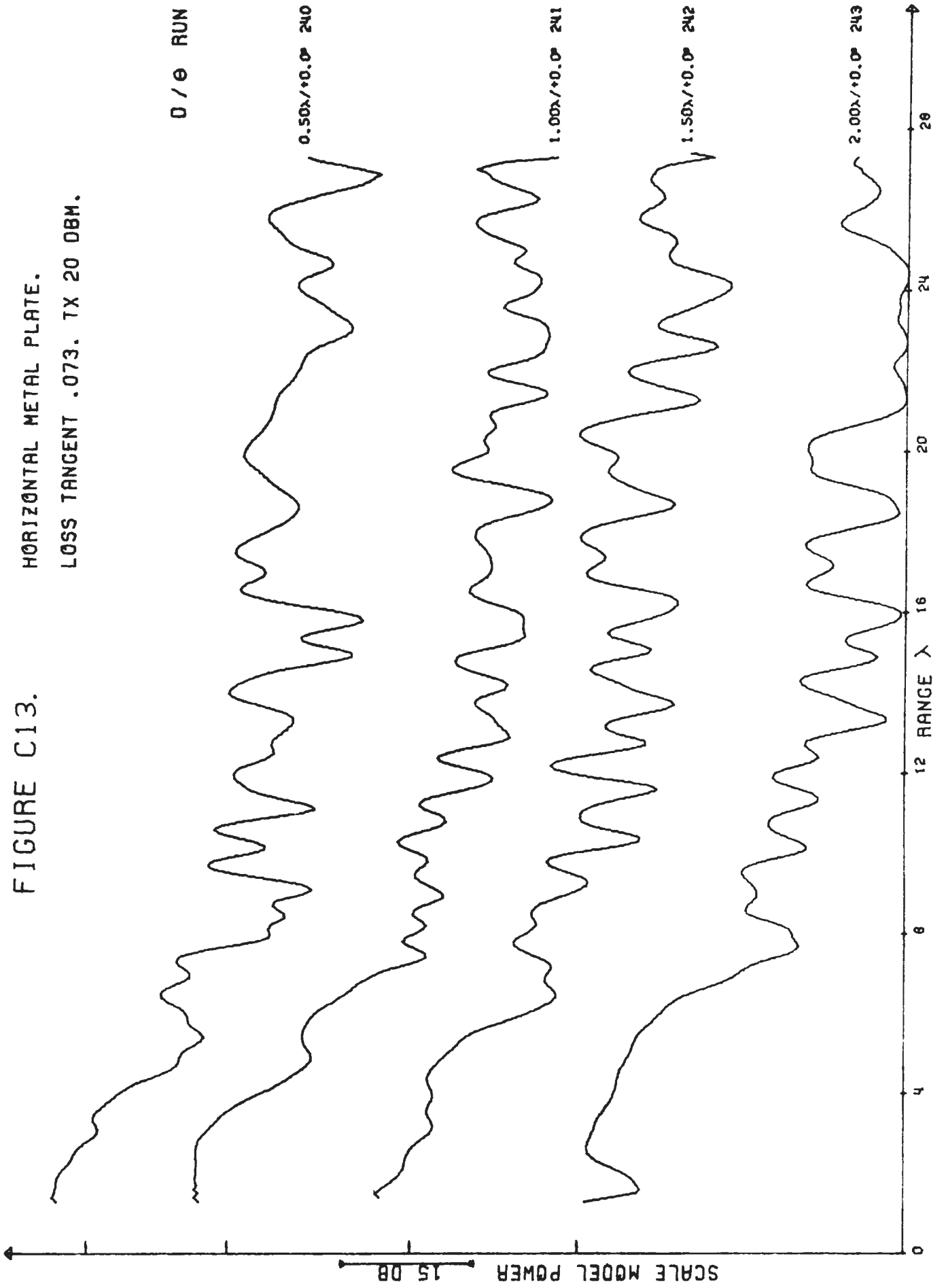


FIGURE C14.

HORIZONTAL METAL PLATE.
LOSS TANGENT .073. TX 20 DBM.

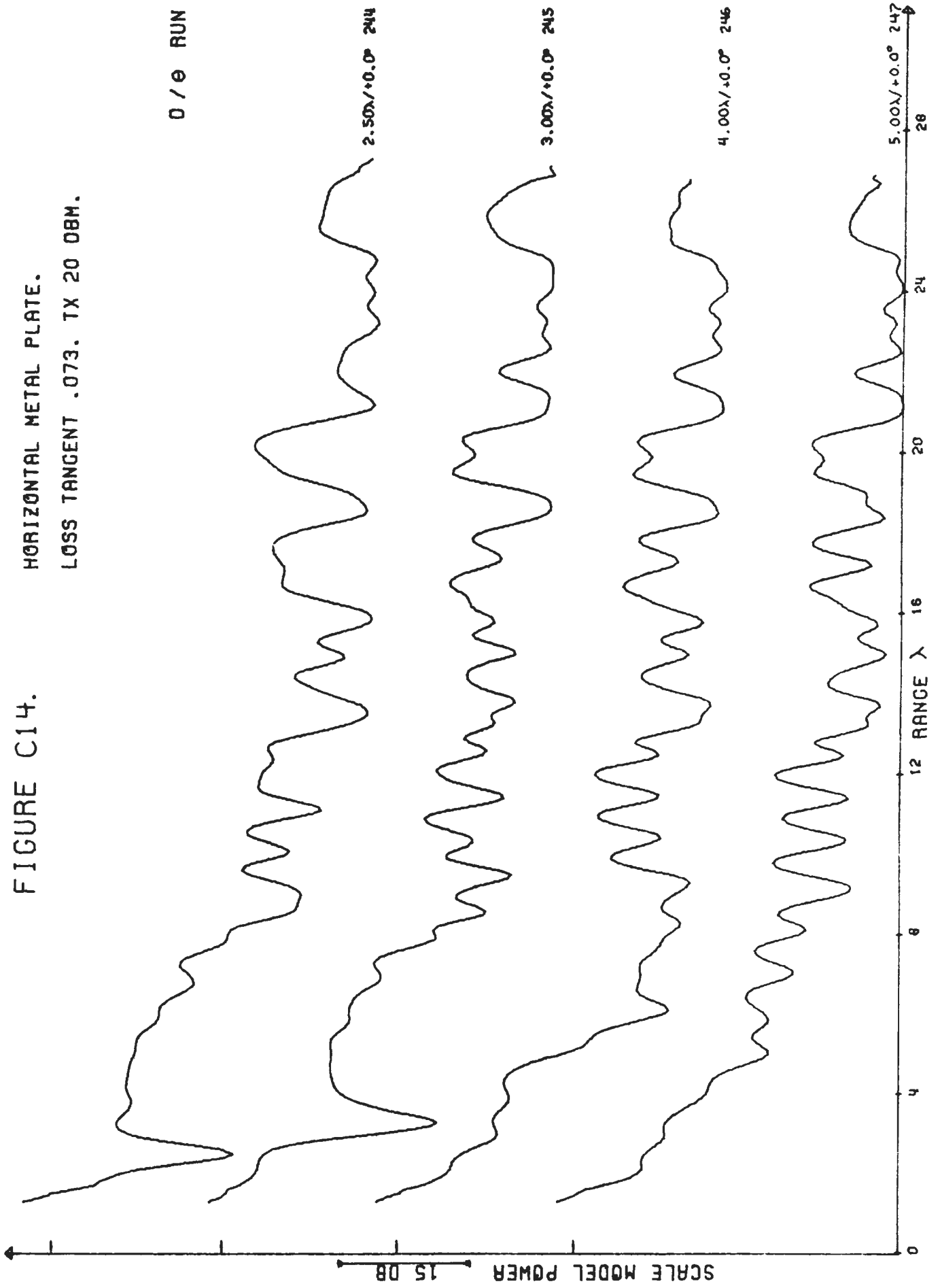


FIGURE C15.

HORIZONTAL METAL PLATE.
LOSS TANGENT .073. TX 20 DBM.

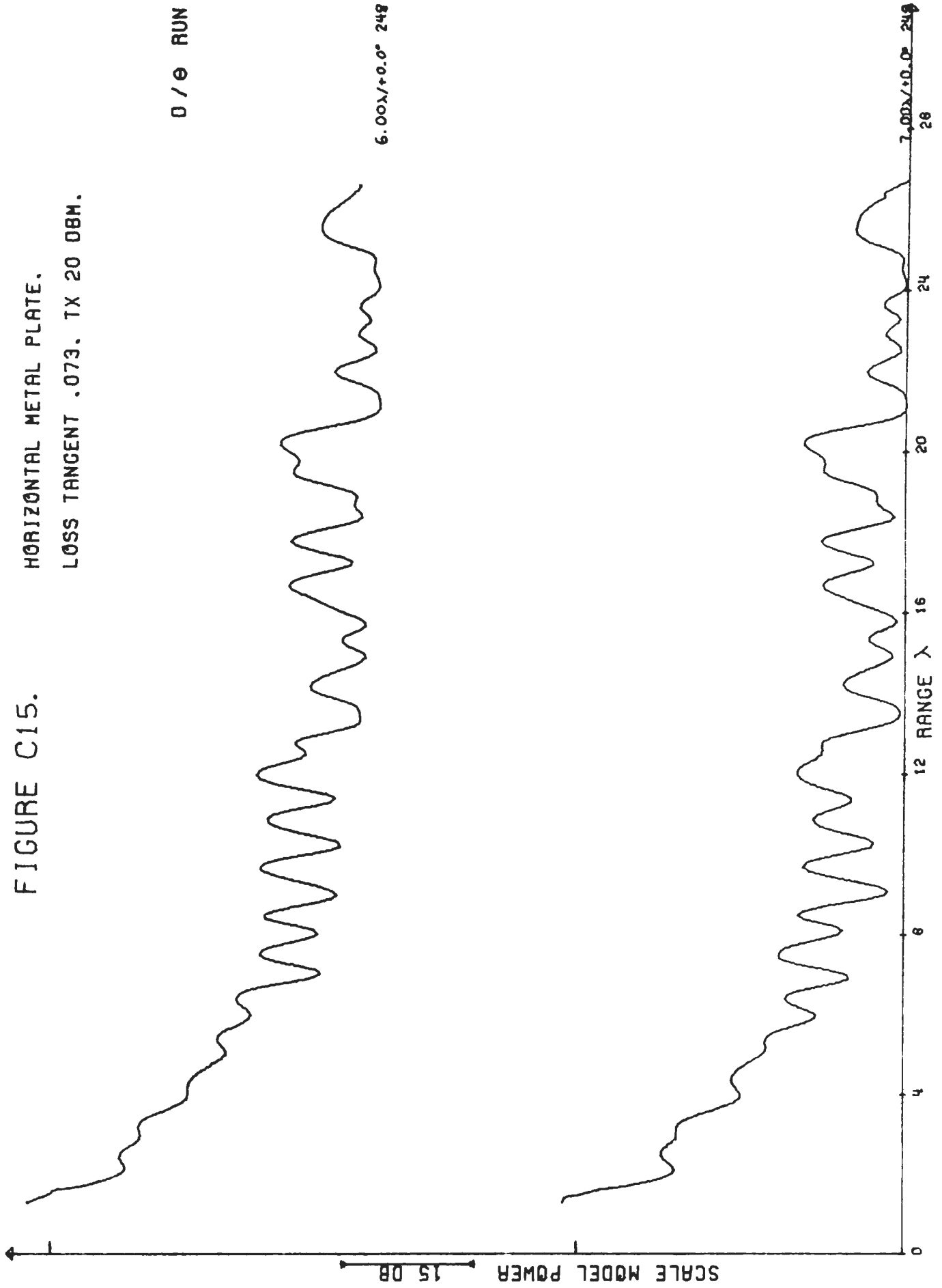


FIGURE C16.

HORIZONTAL METAL PLATE.

LOSS TANGENT .142. TX 20 DBM.

0 / e RUN

0.50λ / ±0.0° 250

1.00λ / ±0.0° 251

1.50λ / ±0.0° 252

2.00λ / ±0.0° 253

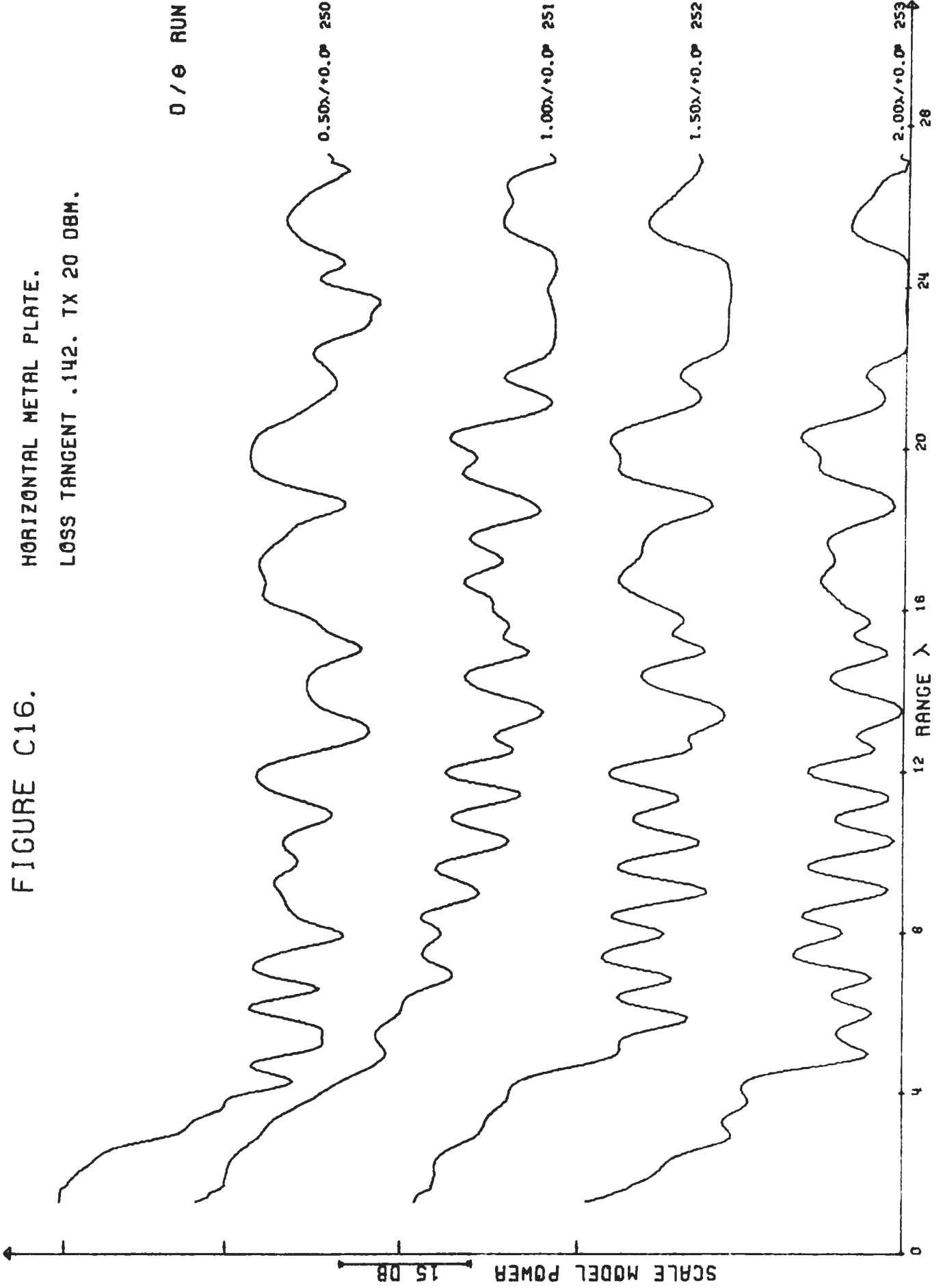


FIGURE C17.

HORIZONTAL METAL PLATE.
LOSS TANGENT .142. TX 20 DBM.

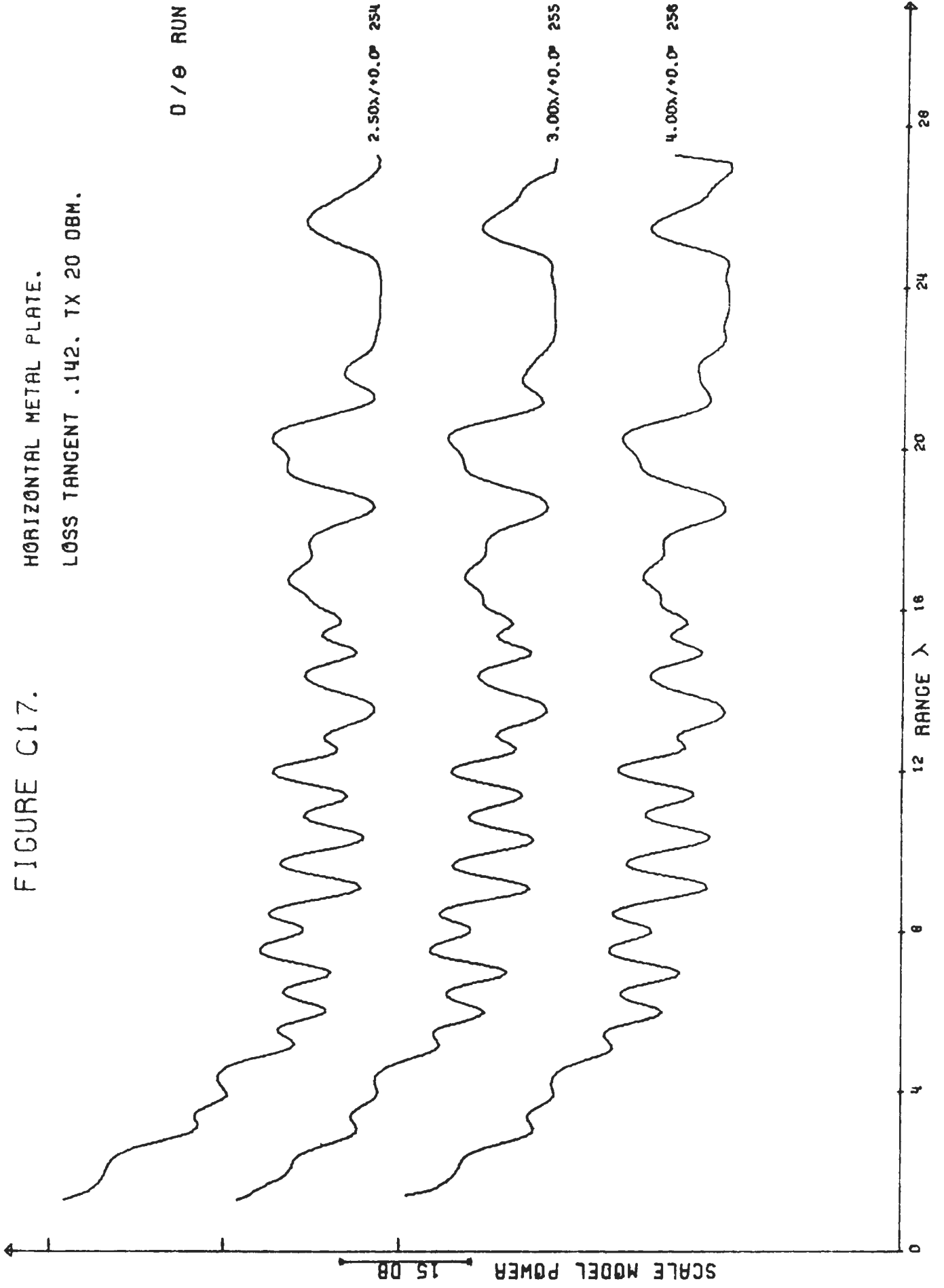


FIGURE C18.

CREVASSE IN HALF-SPACE. LTAN = .002.
REFERENCE TRAVERSES. TX 30DBM.

RUN

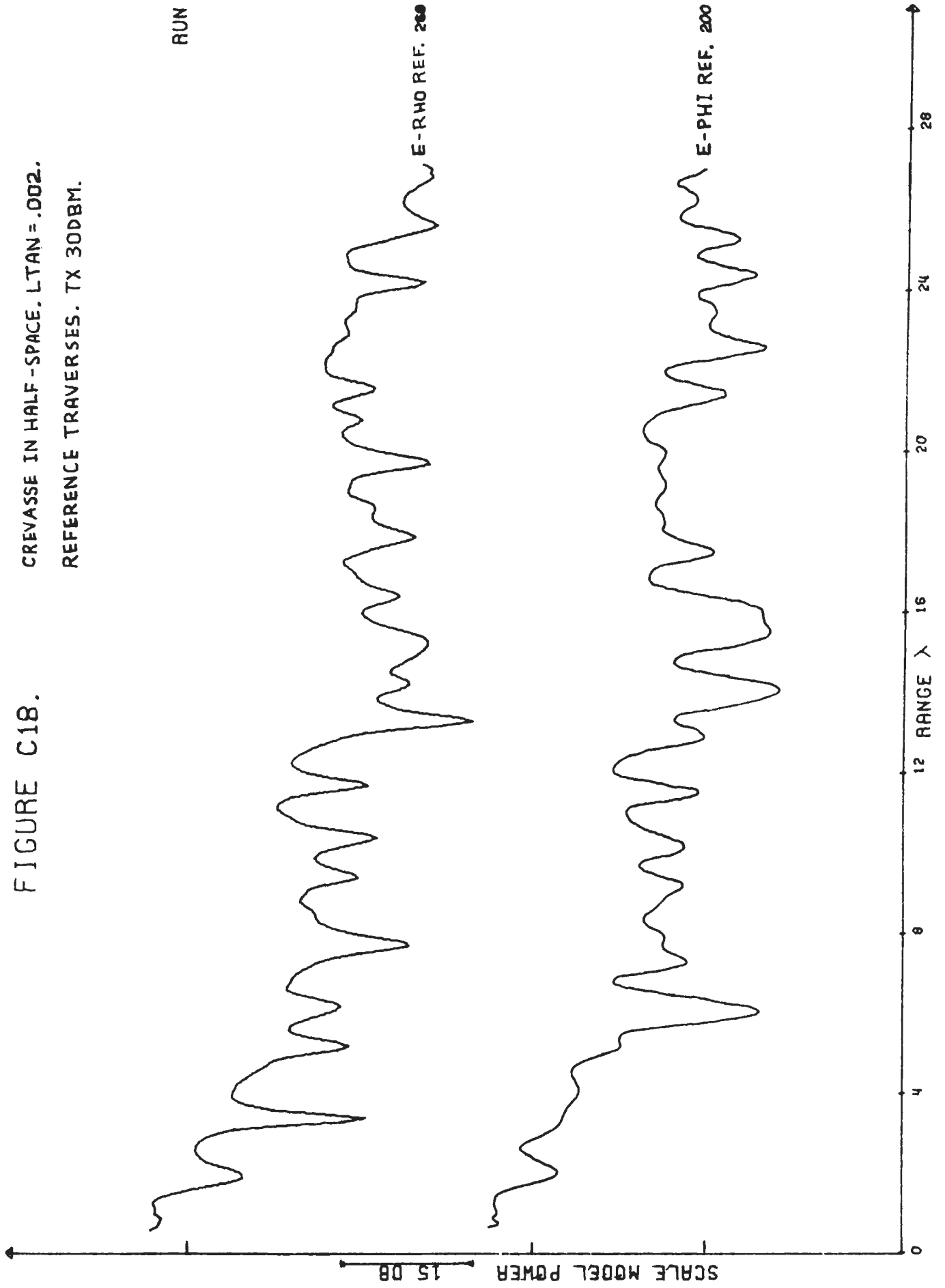


FIGURE C19.

.3λ WIDE CREVASSE IN HALF-SPACE
LTAN=.002. TX 3008M.
E-PHI COMPONENT.

R / θ RUN

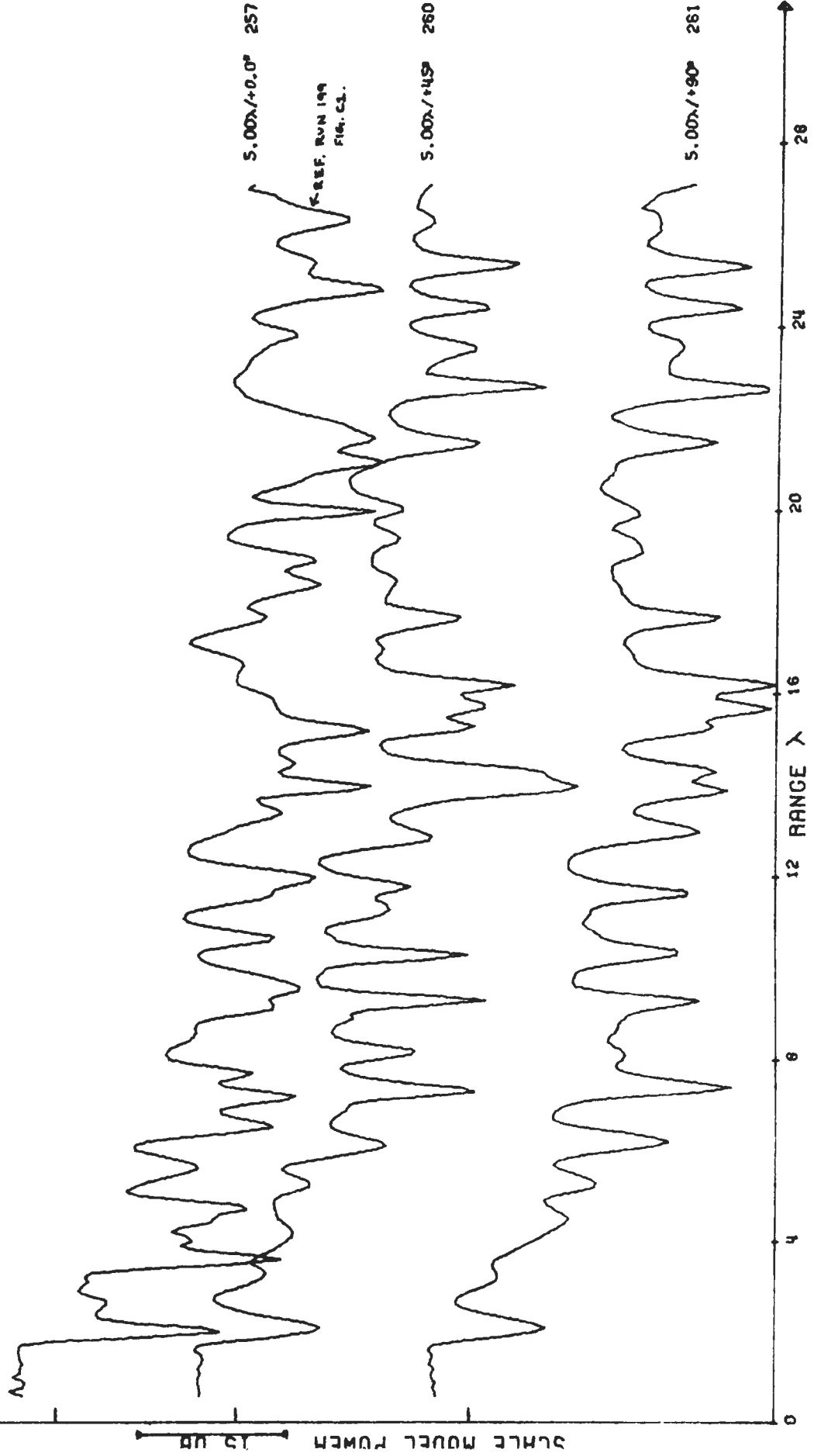


FIGURE C20.

.3λ WIDE CREVASSE IN HALF-SPACE
LTAN=.002. TX 300BM.
E-RHO COMPONENT.

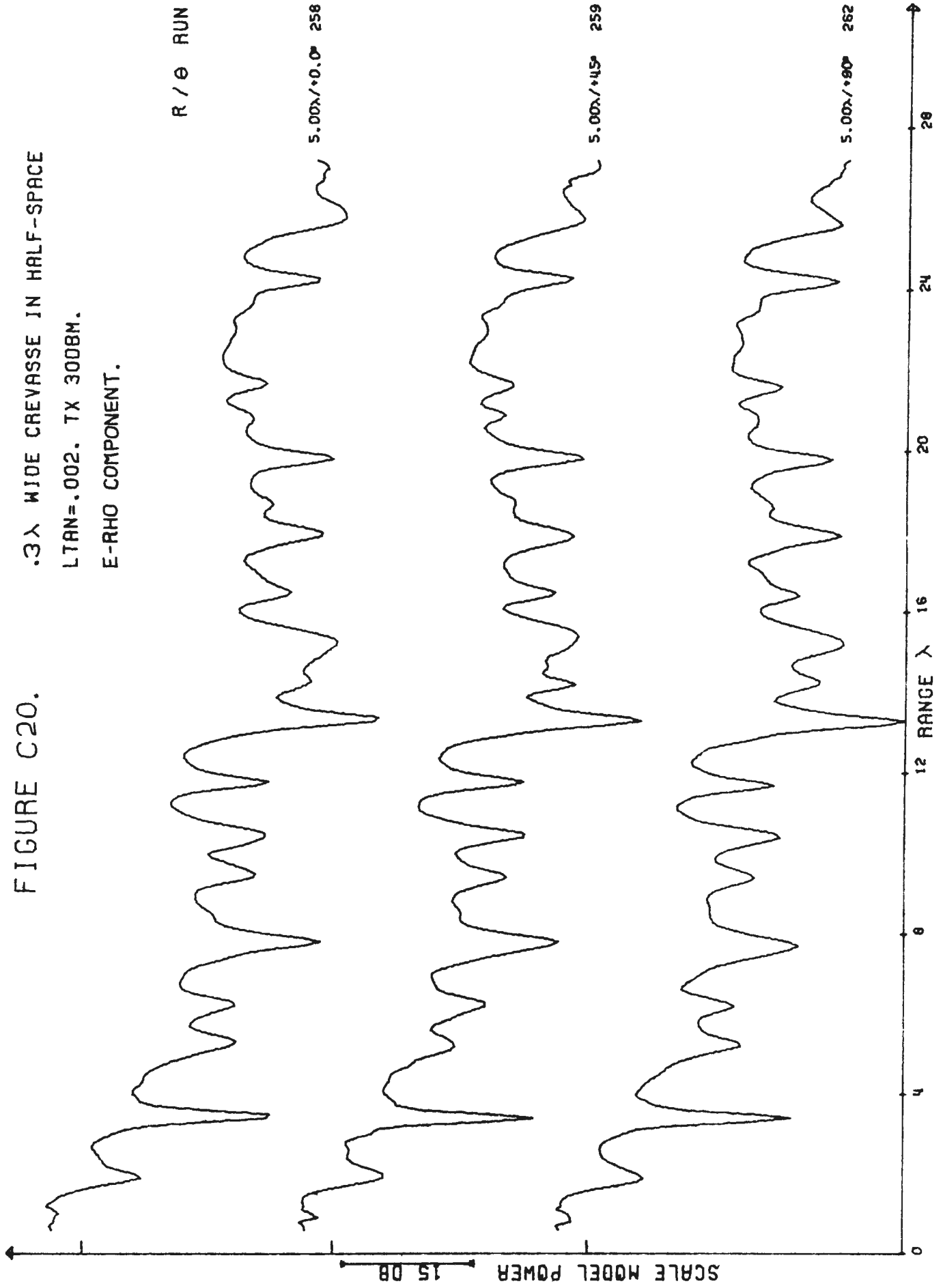


FIGURE C21.

.15λ WIDE CREVASSE IN HALF-SPACE
LTAN=.002. TX 300BM.
E-PHI COMPONENT

R / θ RUN

5.00λ / +0.0° 263

5.00λ / +45° 285

5.00λ / +90° 267

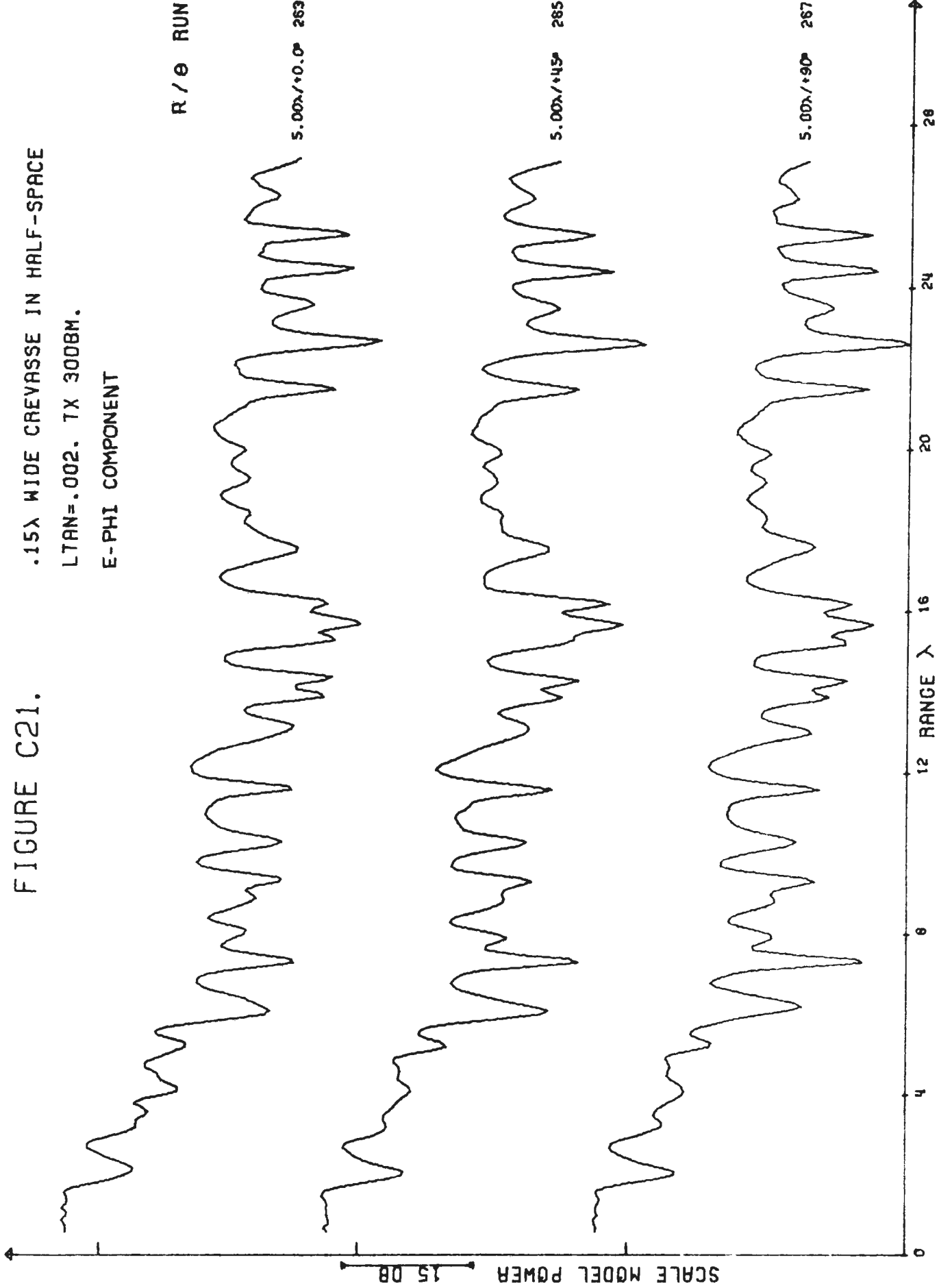


FIGURE C22.

.15λ WIDE CREVASSE IN HALF-SPACE
LTAN=.002. TX 3008M.
E-RHO COMPONENT

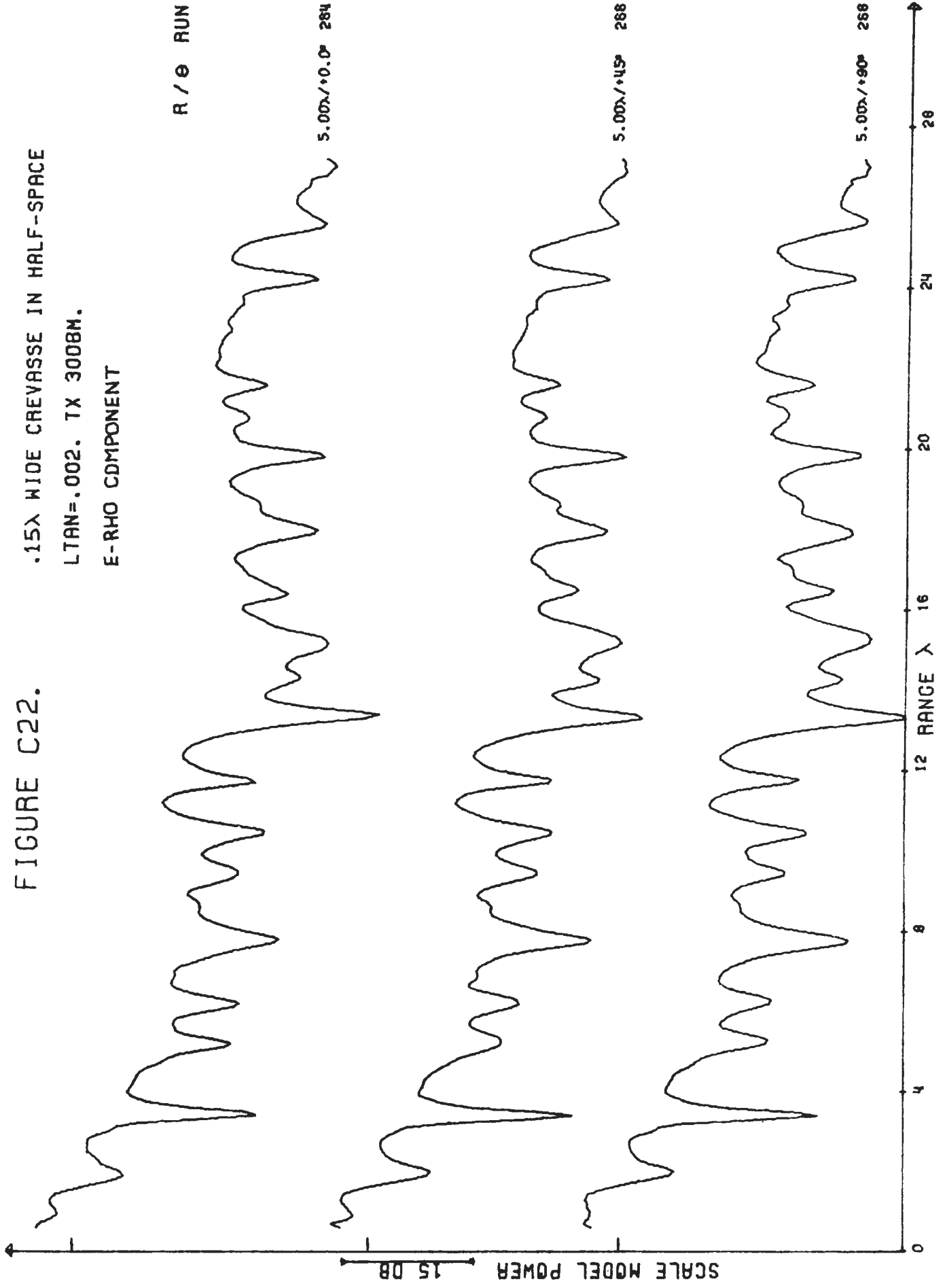


FIGURE C23.

6-.15λ WIDE CREVASSES IN HALF-
SPACE. LTAN=.002. TX 30 DBM.
E-PHI COMPONENT.

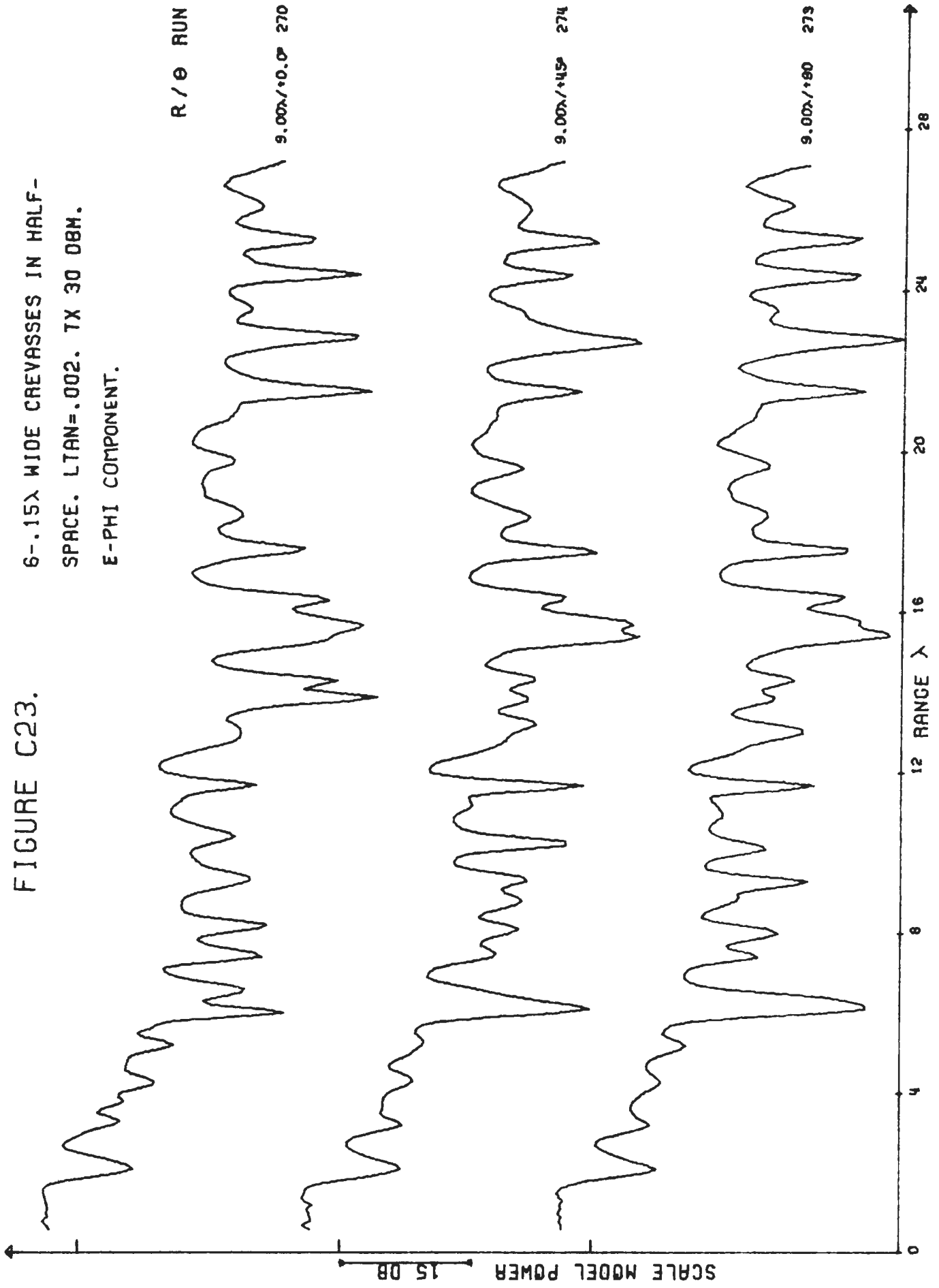


FIGURE C24.

6-.15λ WIDE CREVASSES IN HALF-SPACE. LTAN=.002. TX 30 DBM. E-RHO COMPONENT.

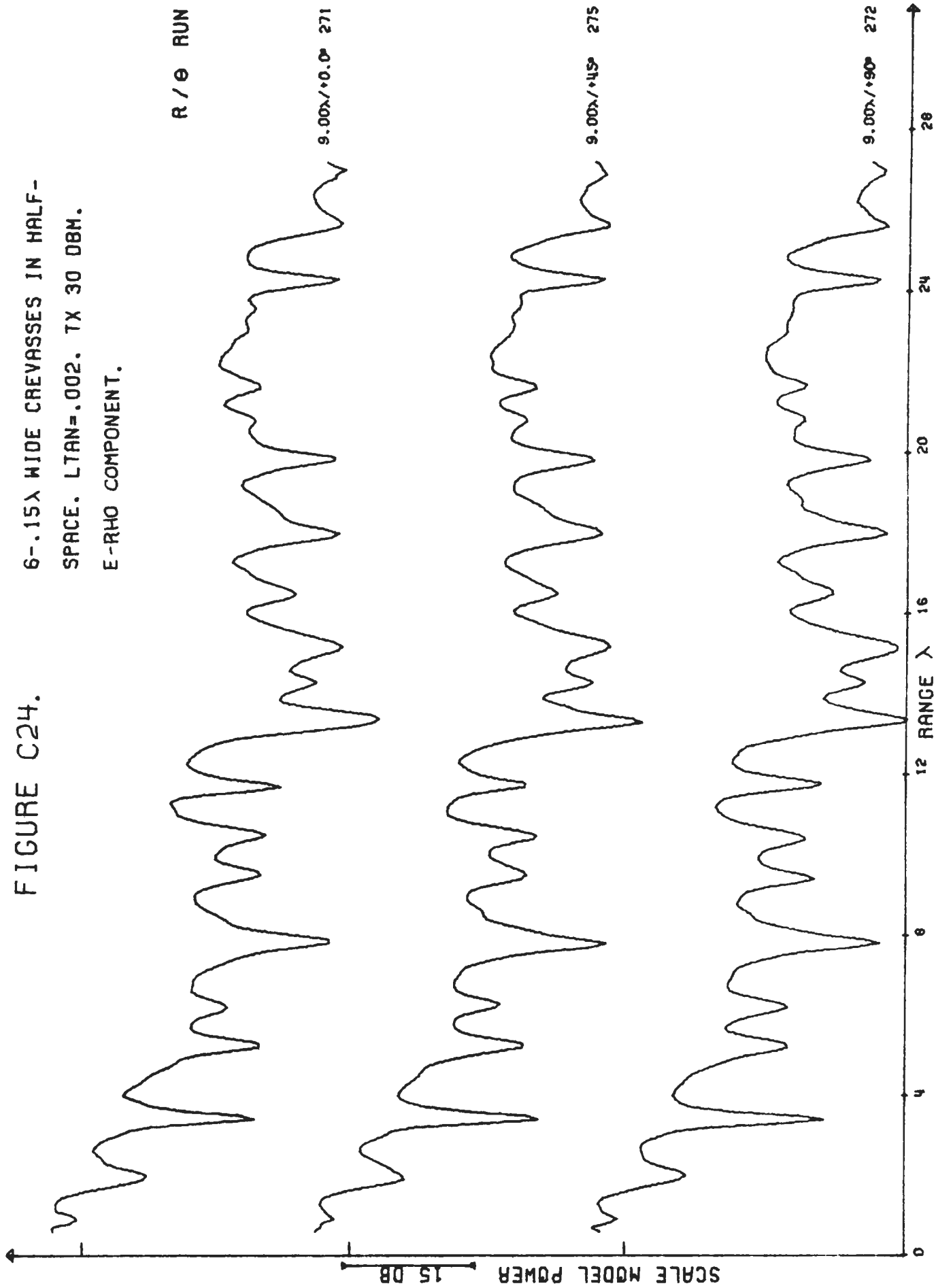


FIGURE C25.

CREVASSES OVER 4λ DEEP
METAL PLATE. LTAN=.002. TX 150BM.
REFERENCE TRAVERSES.

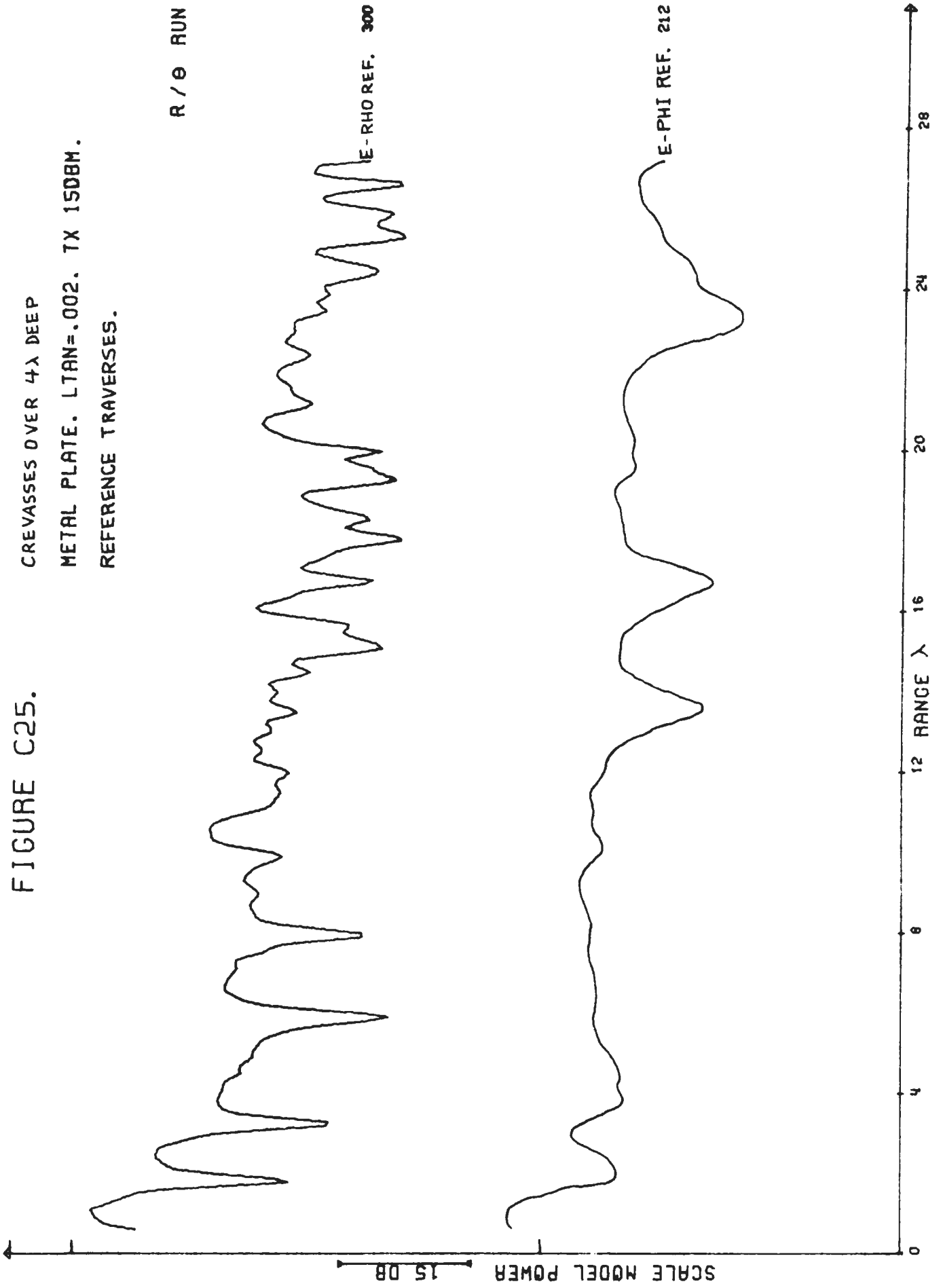


FIGURE C26.

.3λ WIDE CREVASSE OVER 4λ DEEP
METAL PLATE. LTAN=.002. 7X 15DBM.
E-PHI COMPONENT.

R / θ RUN

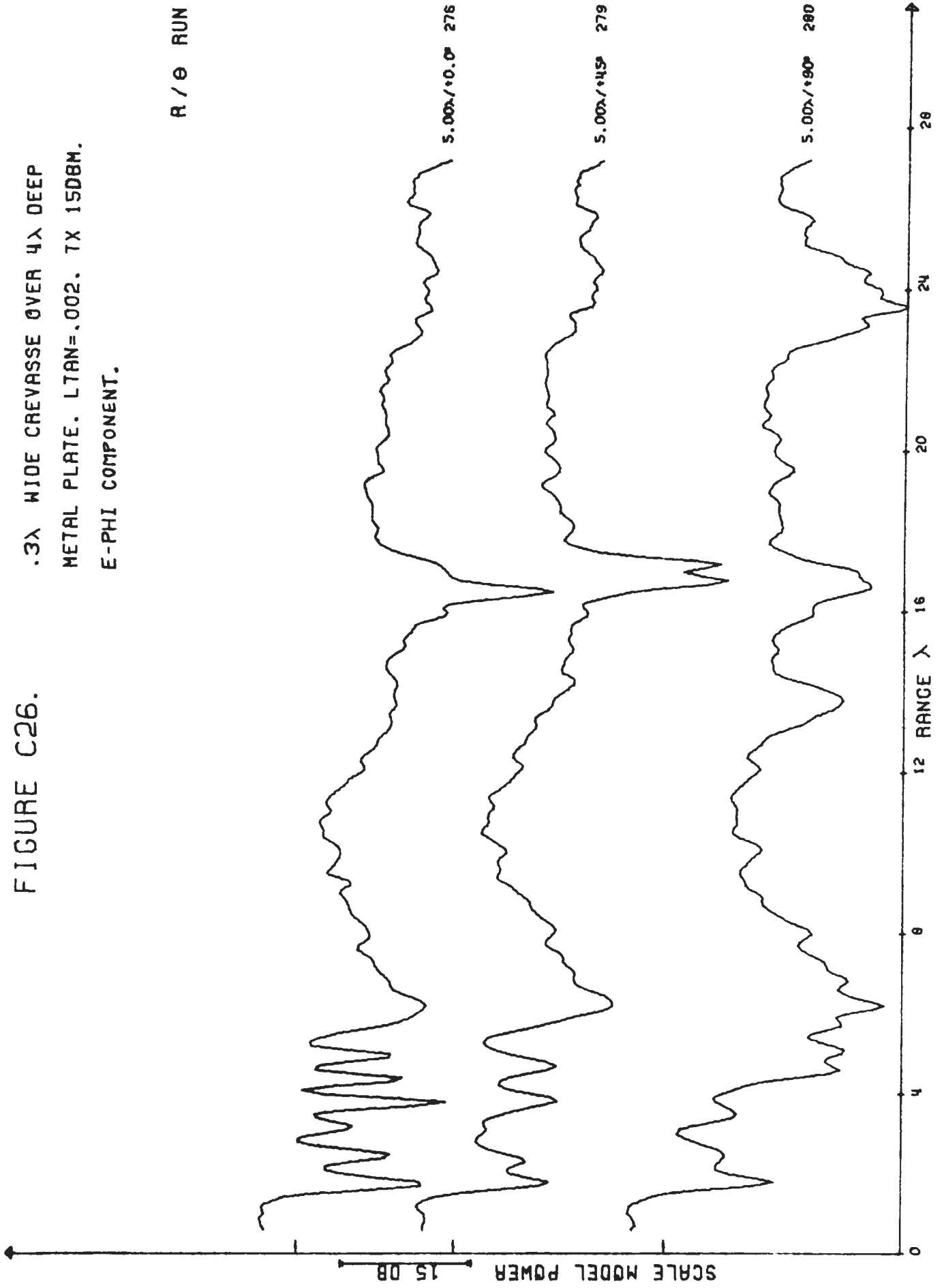


FIGURE C27.

.3λ WIDE CREVASSE OVER 4λ DEEP
METAL PLATE. LTAN=.002. TX 1508M.

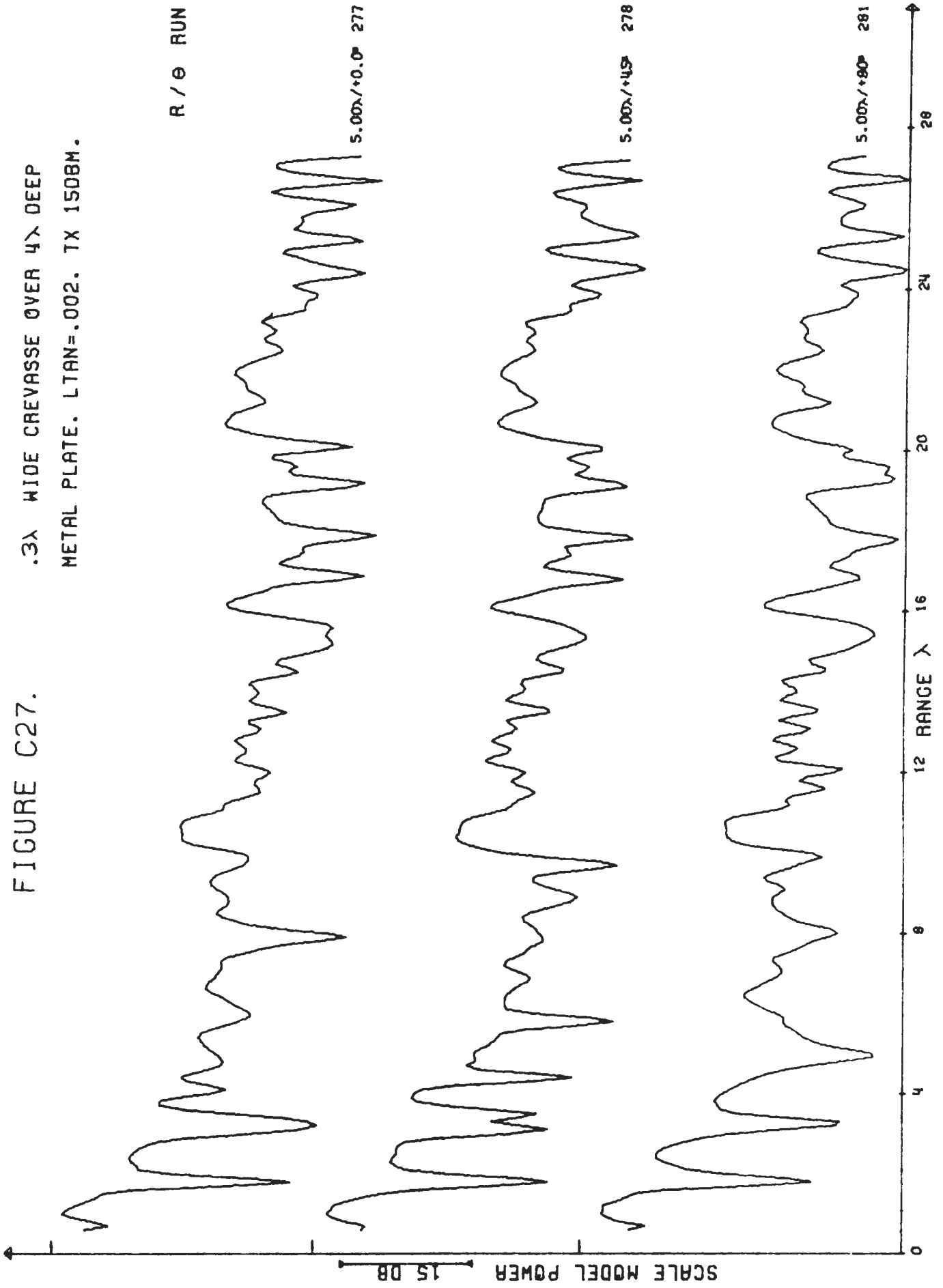


FIGURE C28.

.15λ WIDE CREVASSE OVER 4λ DEEP
METAL PLATE. LTAN=.002. TX 1508M.
E-PHI COMPONENT.

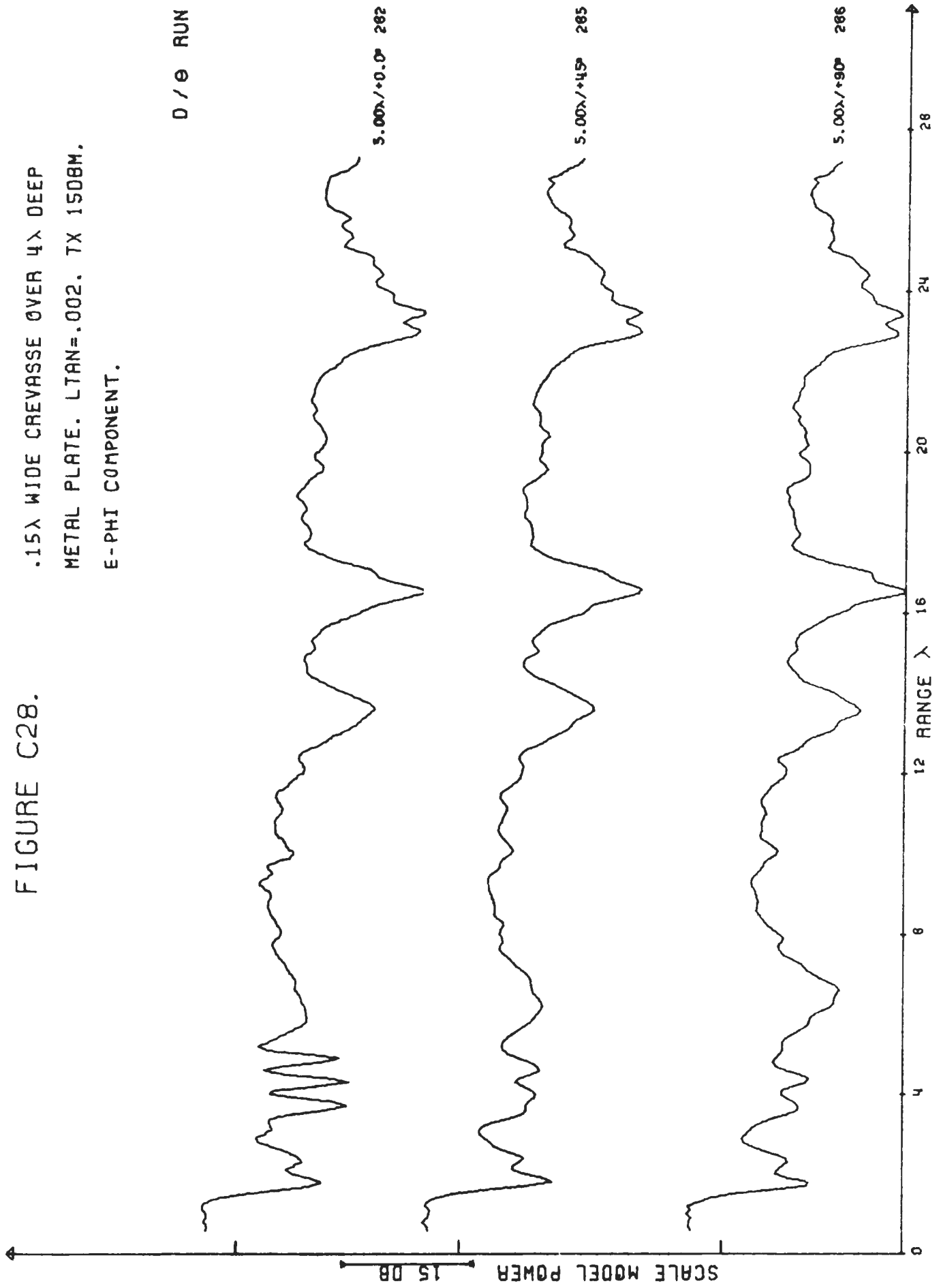


FIGURE C29.

.15λ WIDE CREVASSE OVER 4λ DEEP
METAL PLATE. LTAN=.002. TX 150BM.
E-RHO COMPONENT.

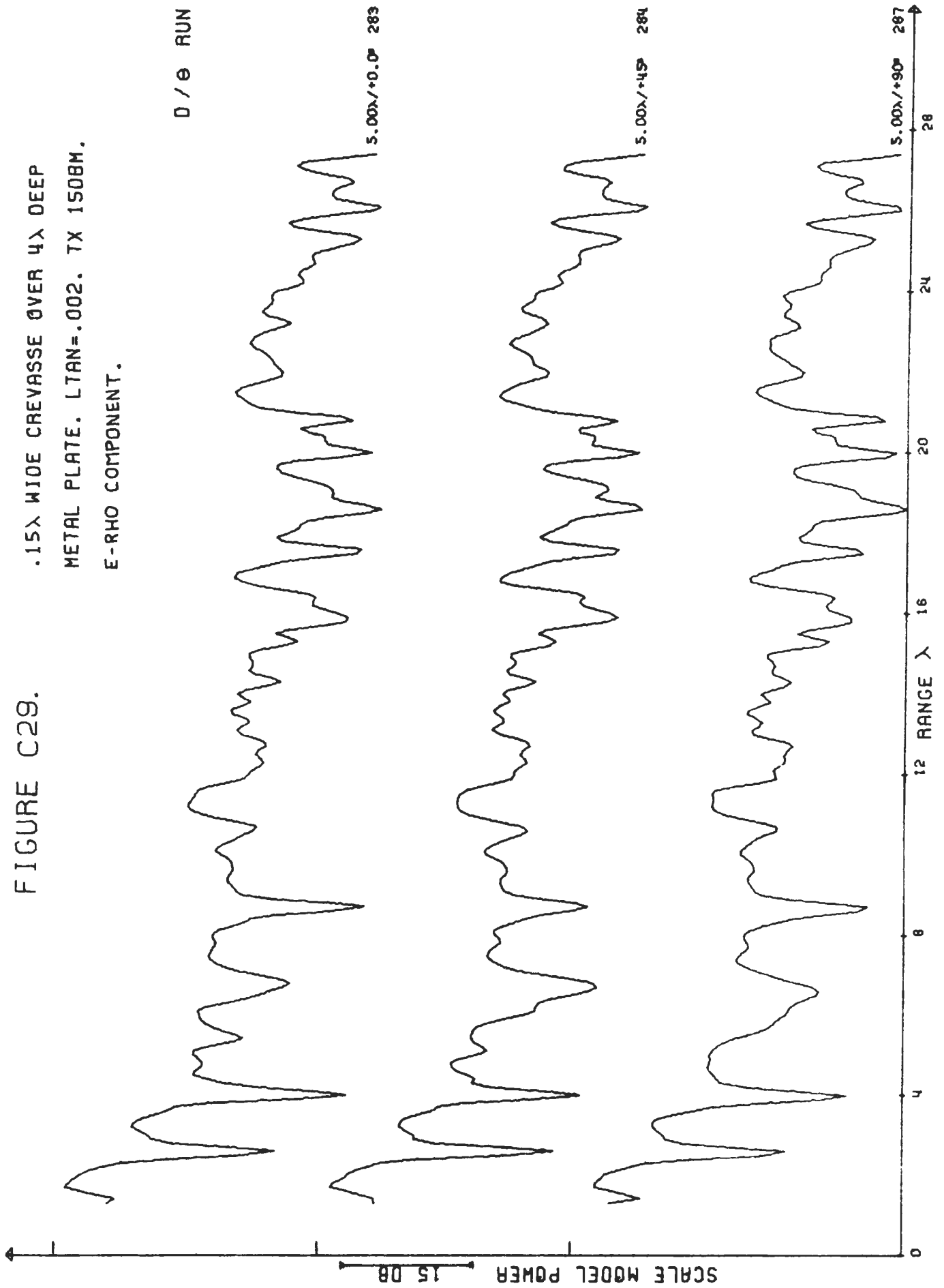


FIGURE C30.

.15λ WIDE CREVASSE OVER 4λ DEEP
METAL PLATE. LTAN=.025. TX 150BM.
E-PHI COMPONENT.

0 / 0 RUN

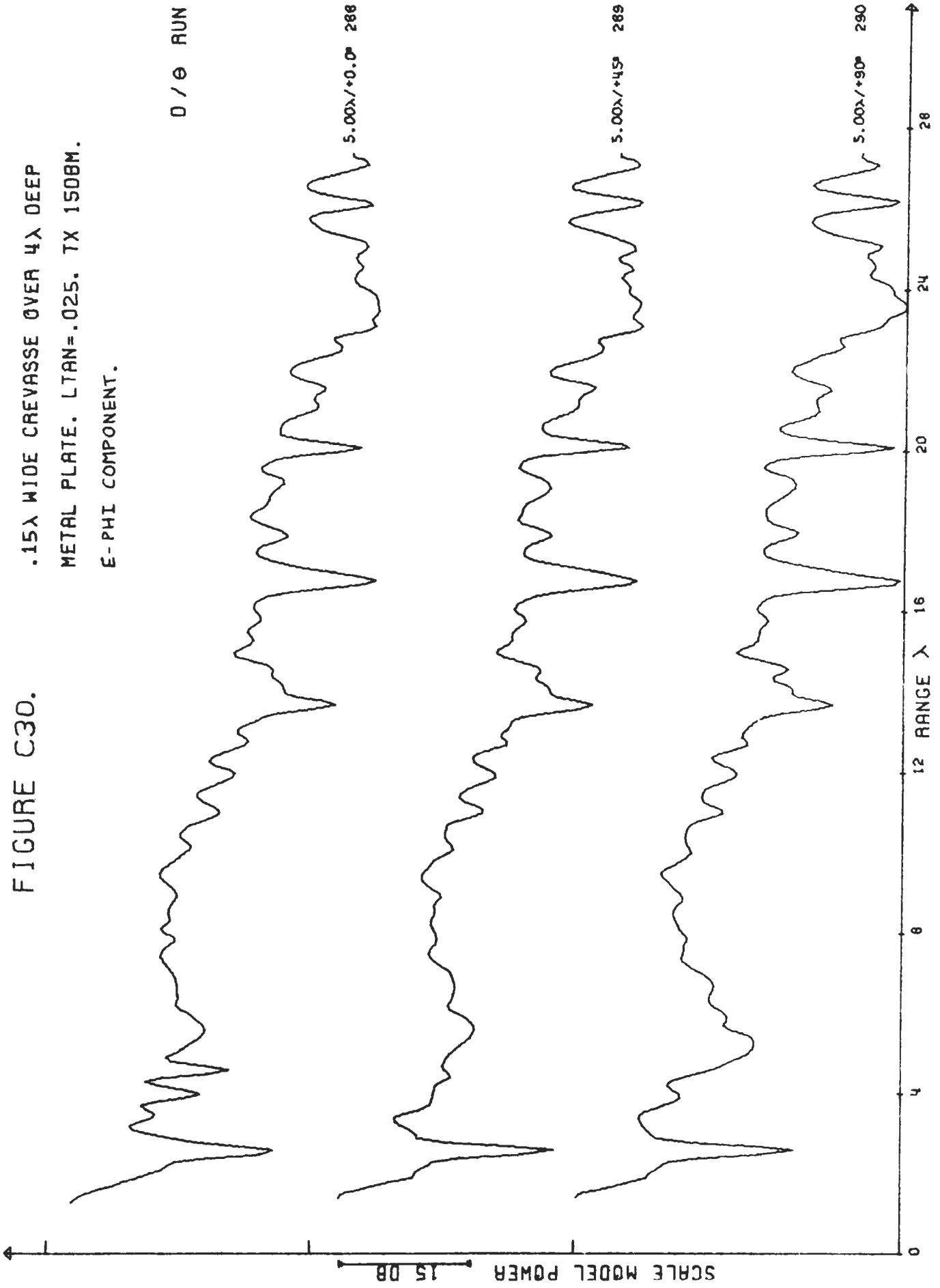


FIGURE C31.

.1λ WIDE CREVASSE OVER 4λ DEEP
METAL PLATE. LTAN=.042. TX 15DBM.
E-PHI COMPONENT.

0 / θ RUN

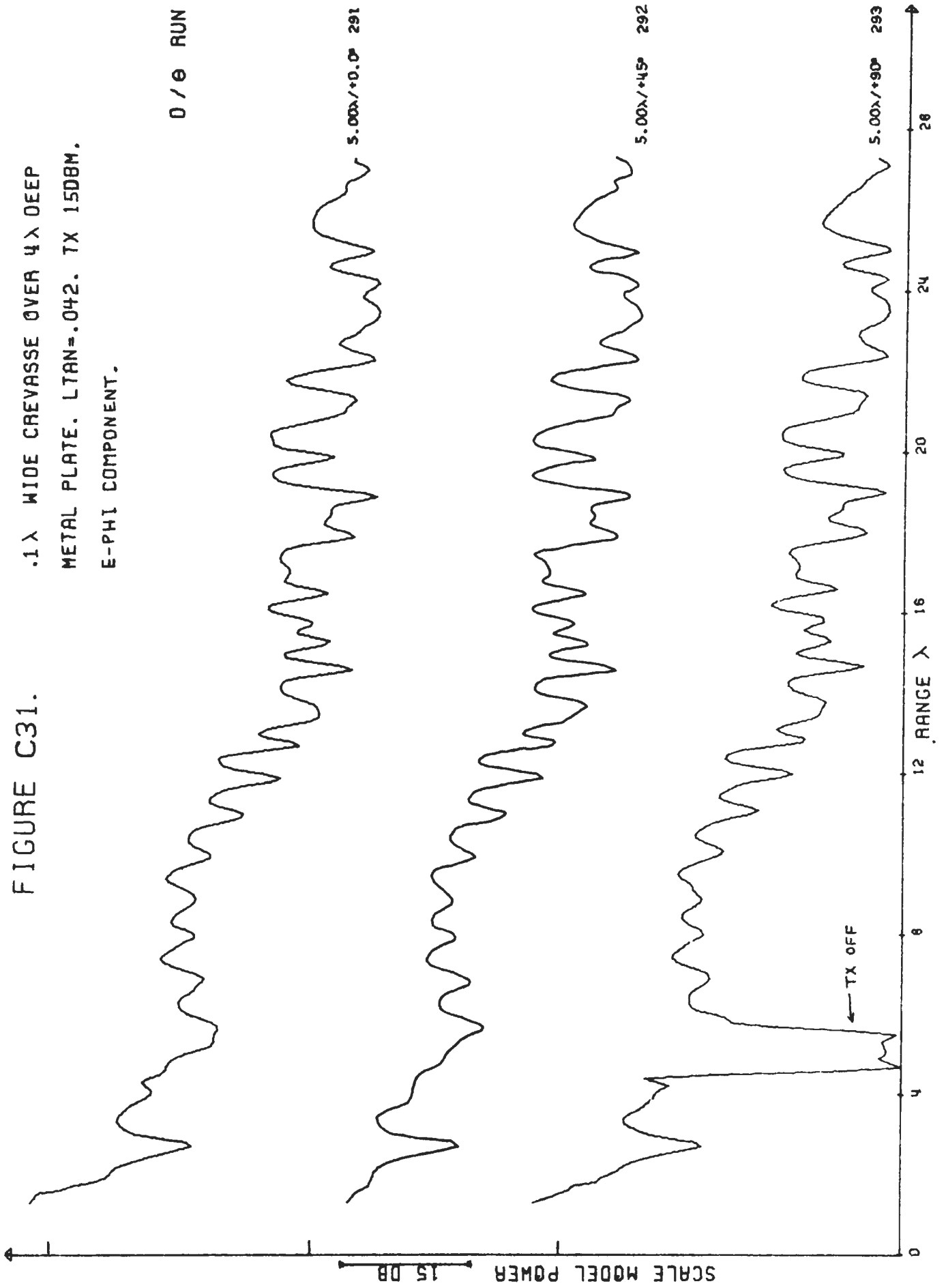


FIGURE C32.

6-.15λ WIDE CREVASSES OVER 4λ DEEP

PLATE. LTAN=.002. TX 15 DBM.

E-PHI COMPONENT.

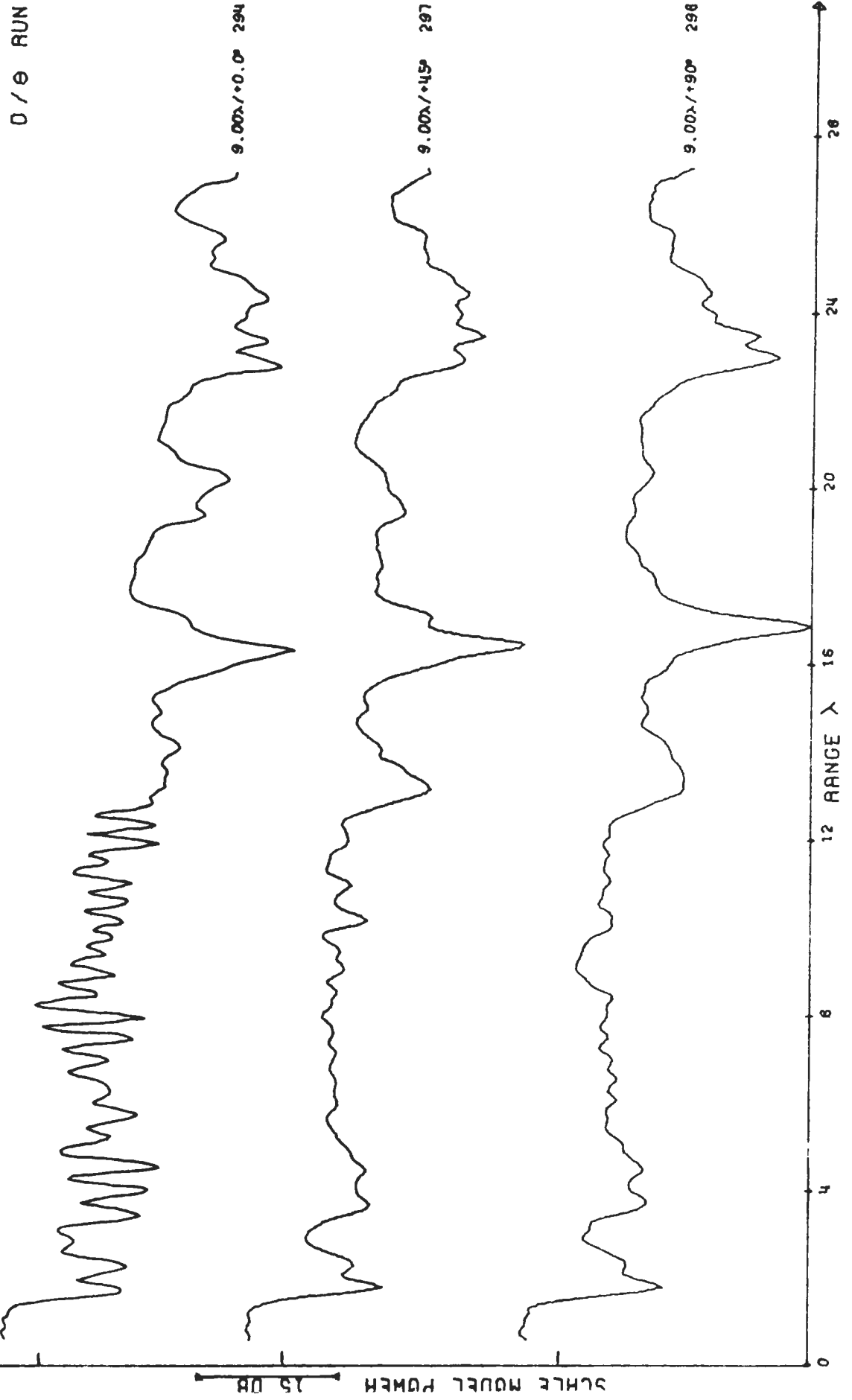


FIGURE C33.

6-.15λ WIDE CREVASSES OVER 4λ DEEP
PLATE. LTAN=.002. TX 15 DBM.
E-RHO COMPONENT.

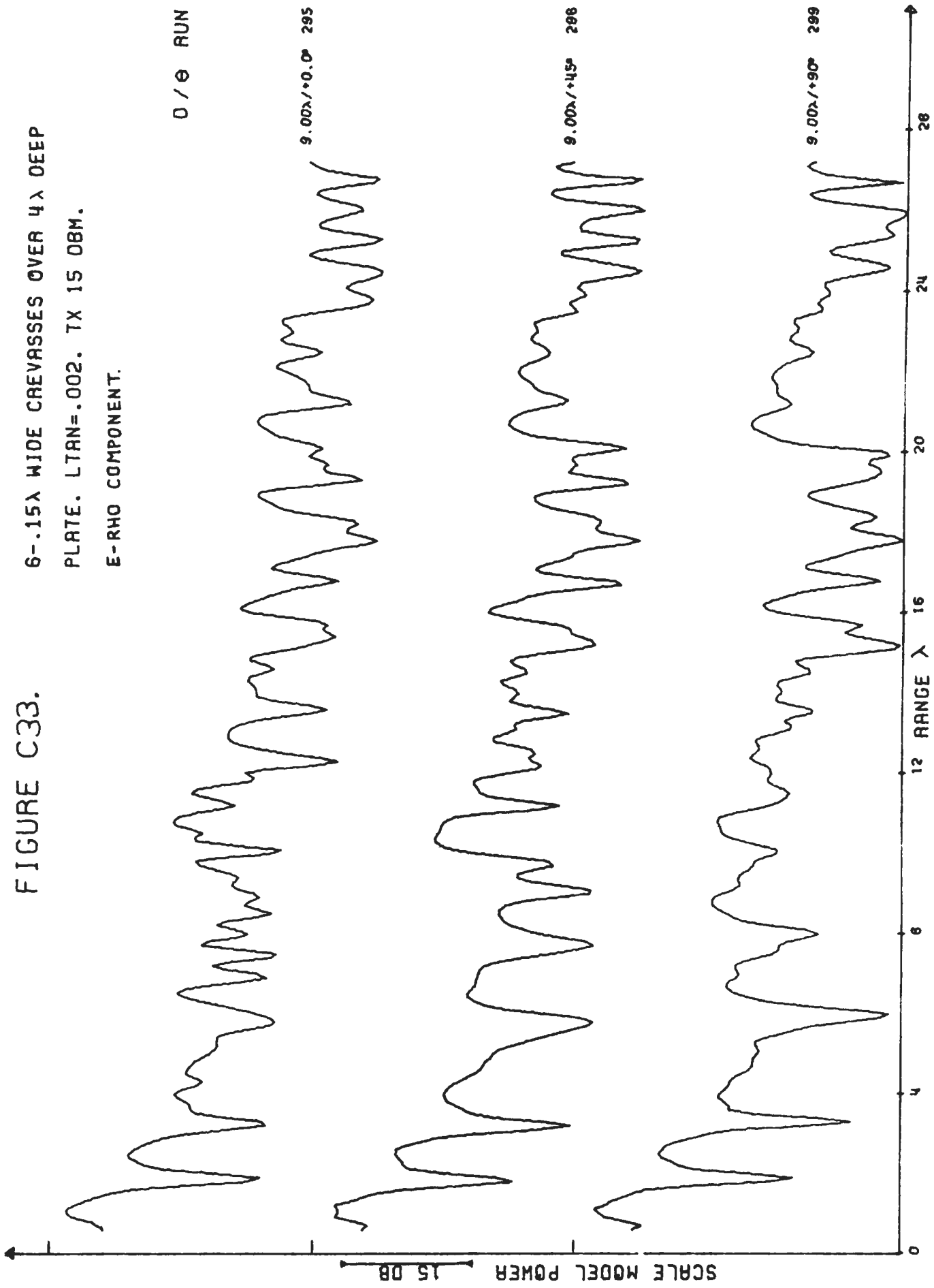


FIGURE C34.

6--.15λ WIDE CREVASSES OVER 4λ DEEP
PLATE. LTAN=.025. TX 15 DBM.
E-PHI COMPONENT.

0 / θ RUN

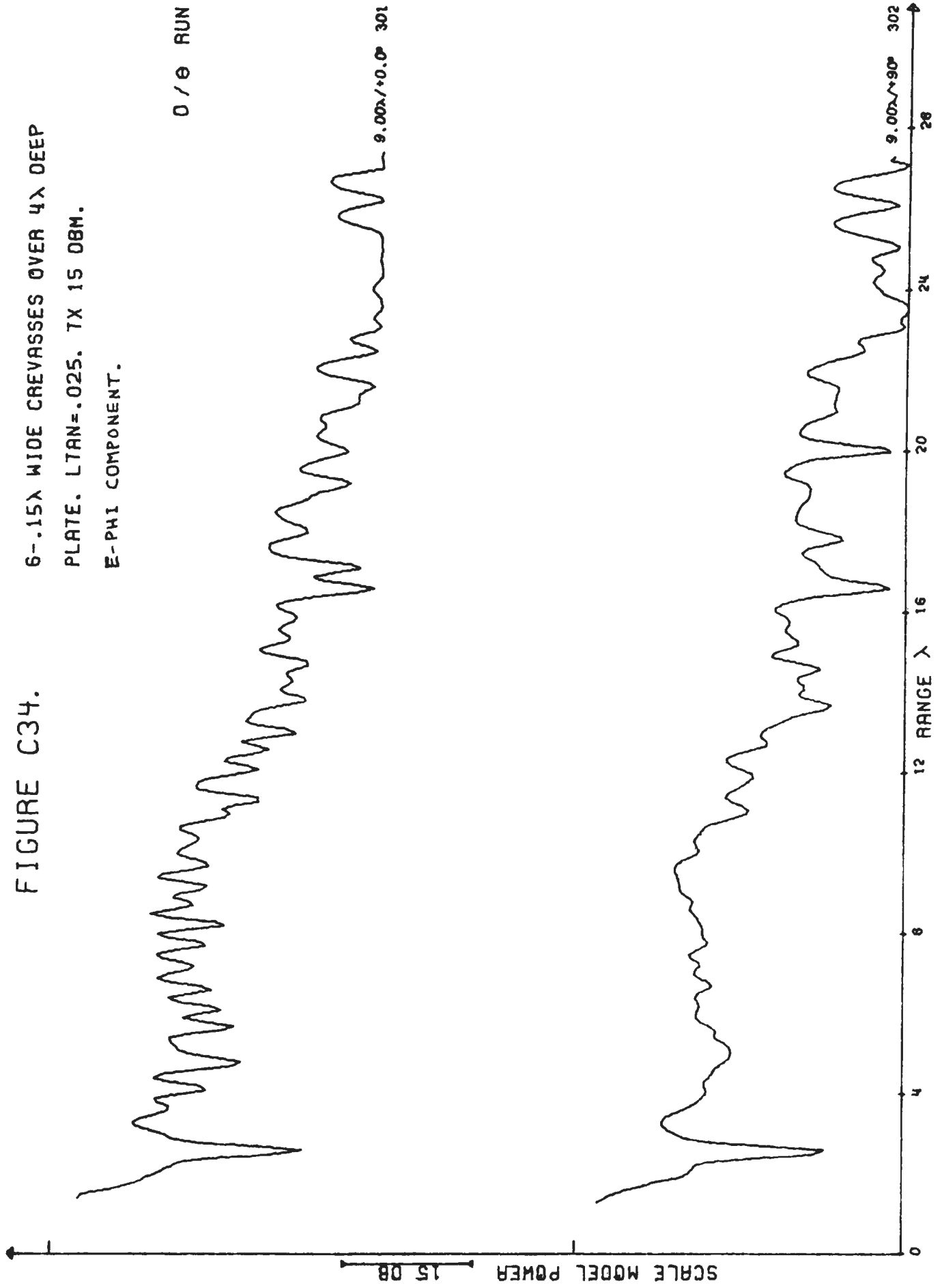


FIGURE C35.

6-.15λ WIDE CREVASSES OVER 4λ DEEP
PLATE. LTAN=.042. TX 20 DBM.
E-PHI COMPONENT.

0 / θ RUN

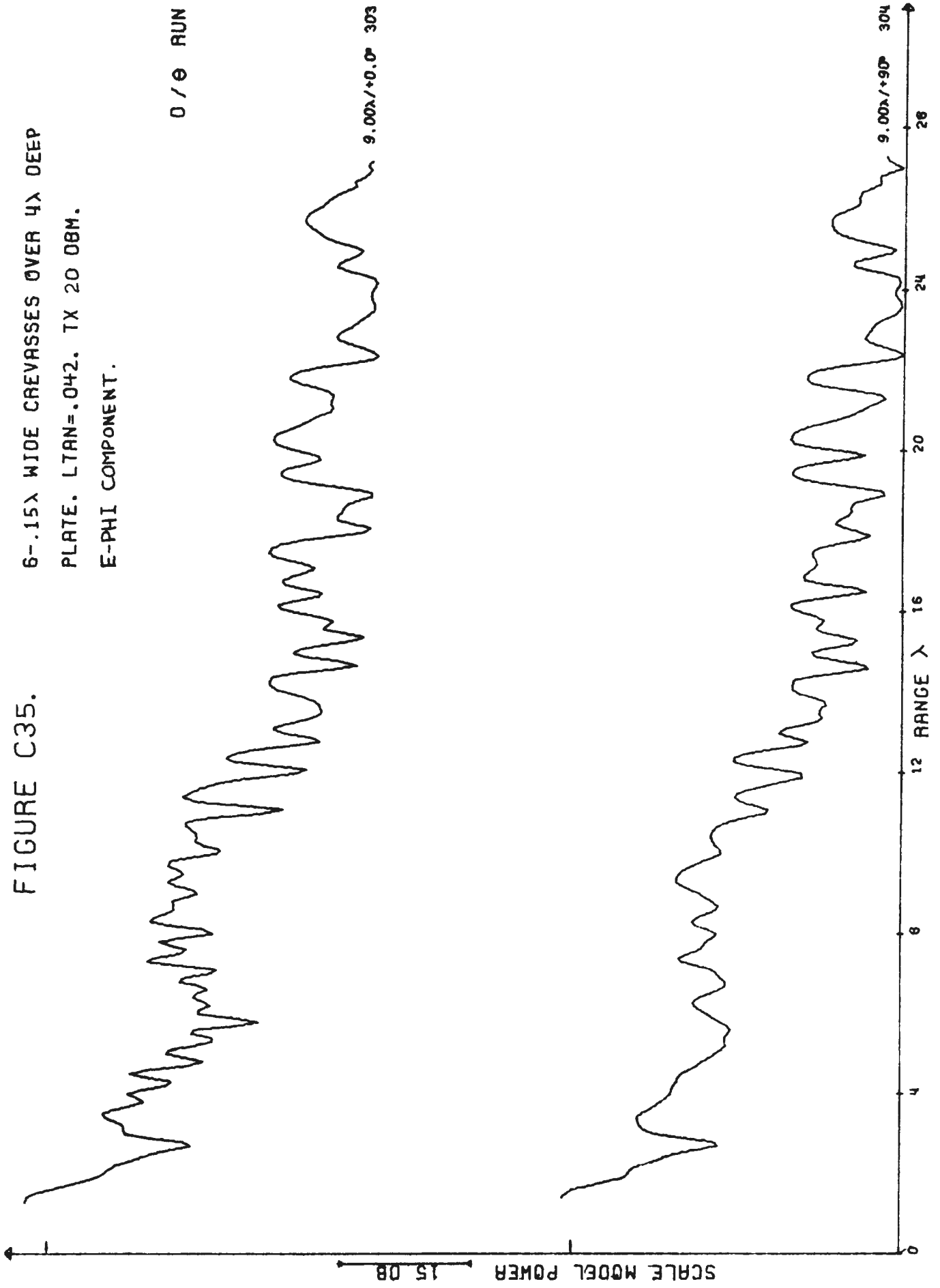


FIGURE C36.

5-.1λ WIDE CREVASSES OVER 4λ DEEP
PLATE. LTAN=.042. TX 20 DBM.
E-PHI COMPONENT.

0 / θ RUN

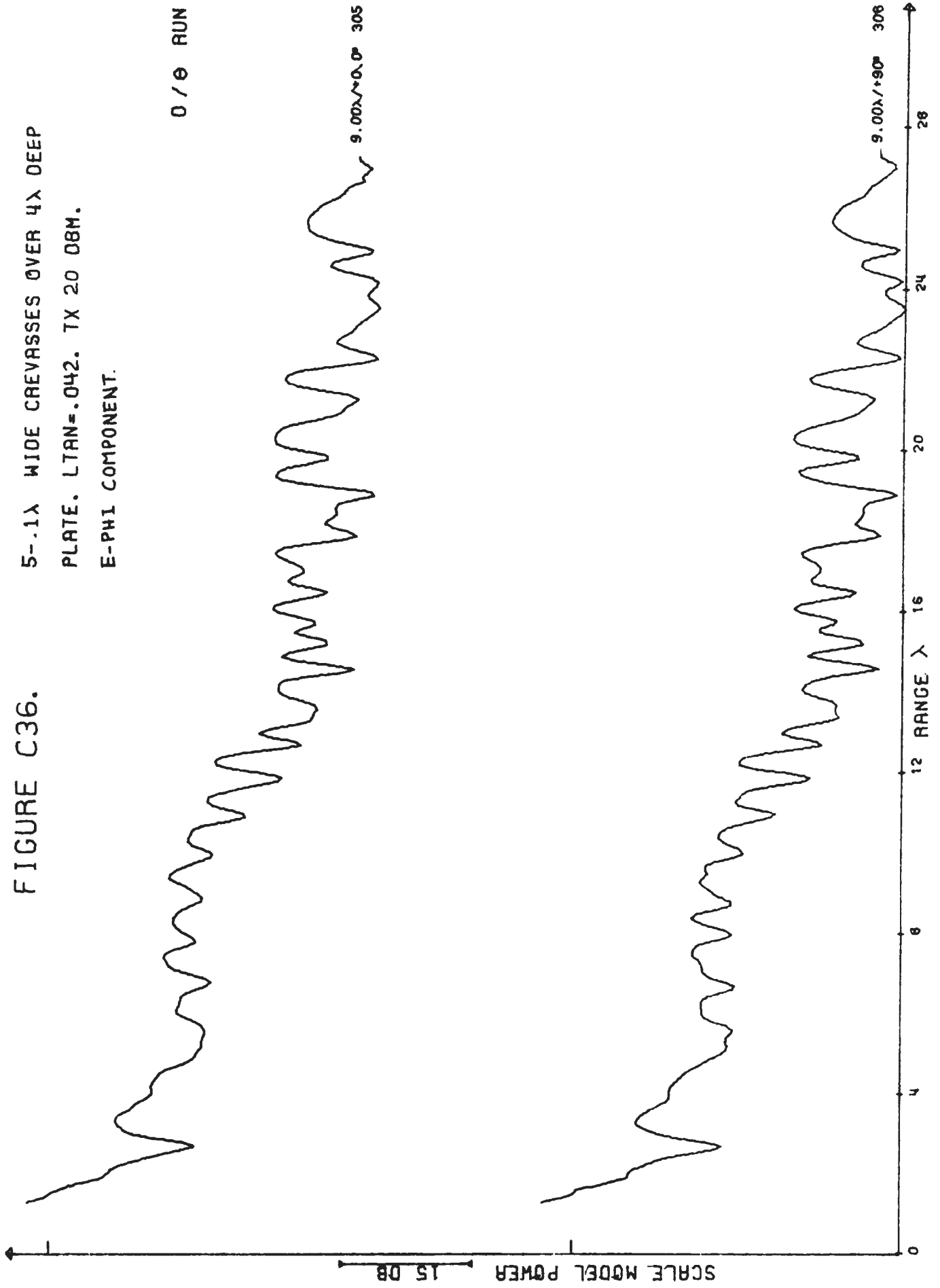


FIGURE C37.

5-.1λ WIDE CREVASSES OVER 4λ DEEP
PLATE. LTAN=.073. TX 20 DBM.
E-PHI COMPONENT.

0 / θ RUN

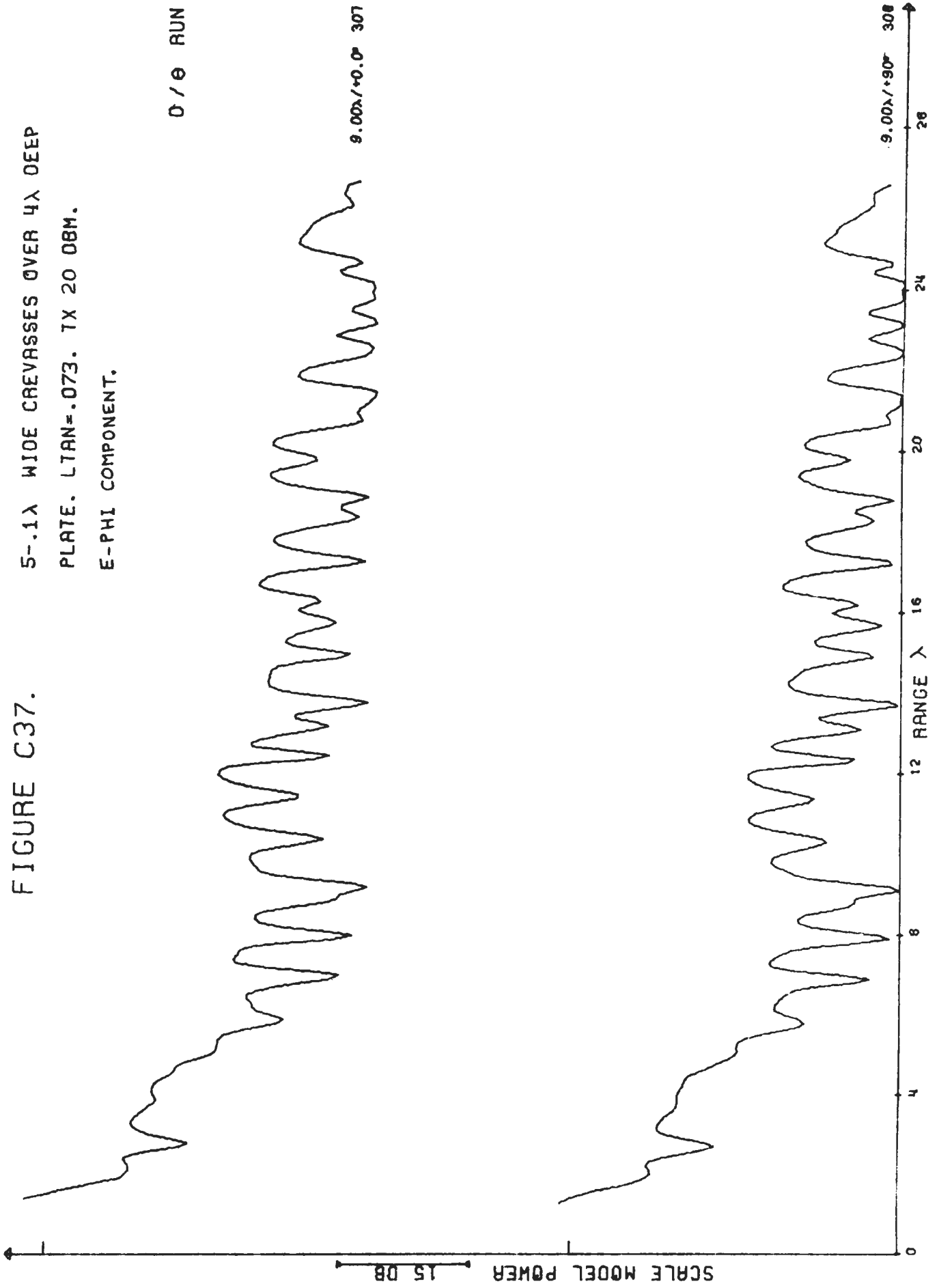


FIGURE C38.

1.5λ DIAMETER CRATER OVER 4λ
DEEP PLATE. LTAN=.073. 7X 200BM.

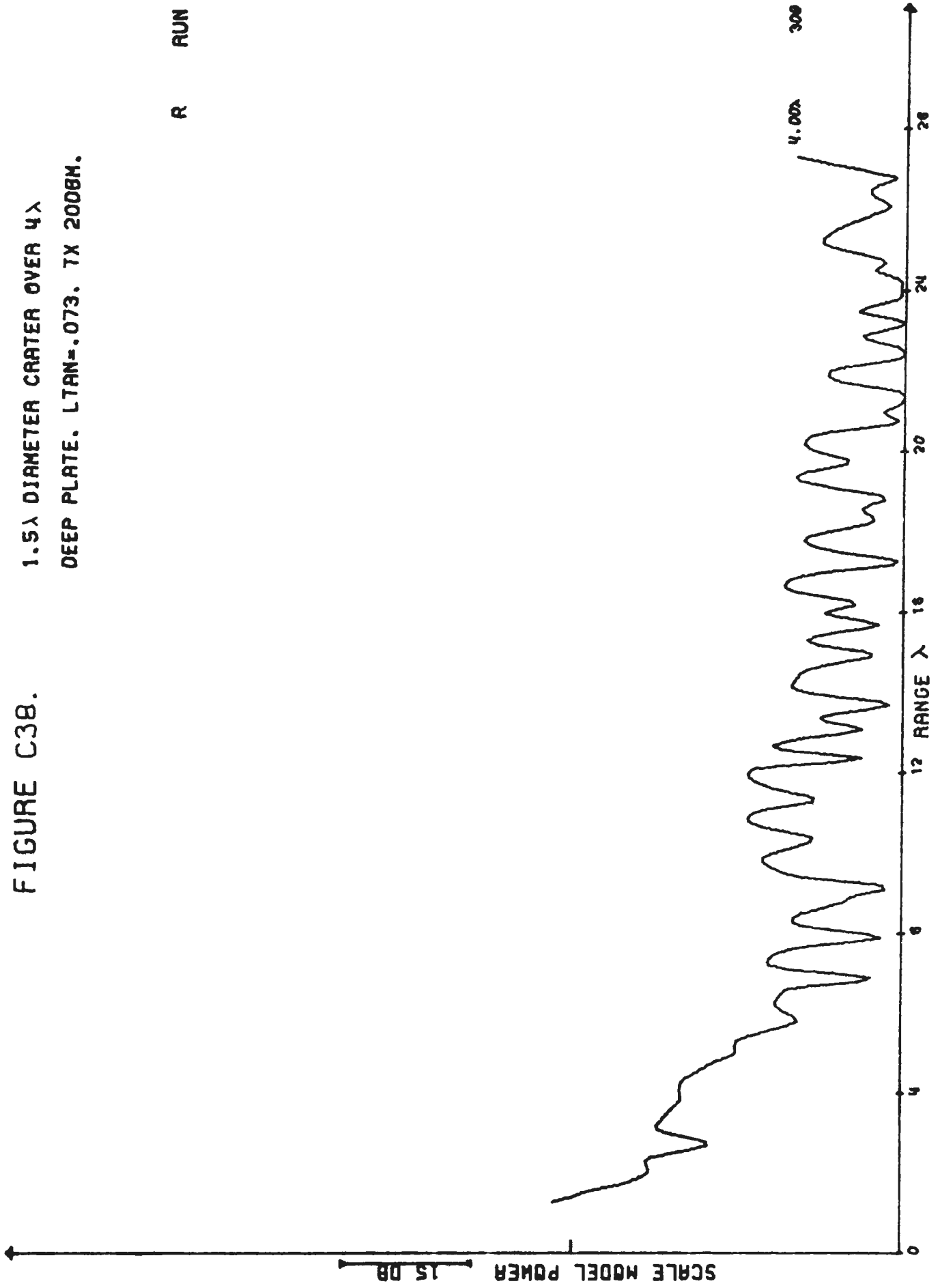


FIGURE C39.

1.5λ DIAMETER CRATER IN HALF-SPACE.
TX 30 DBM.

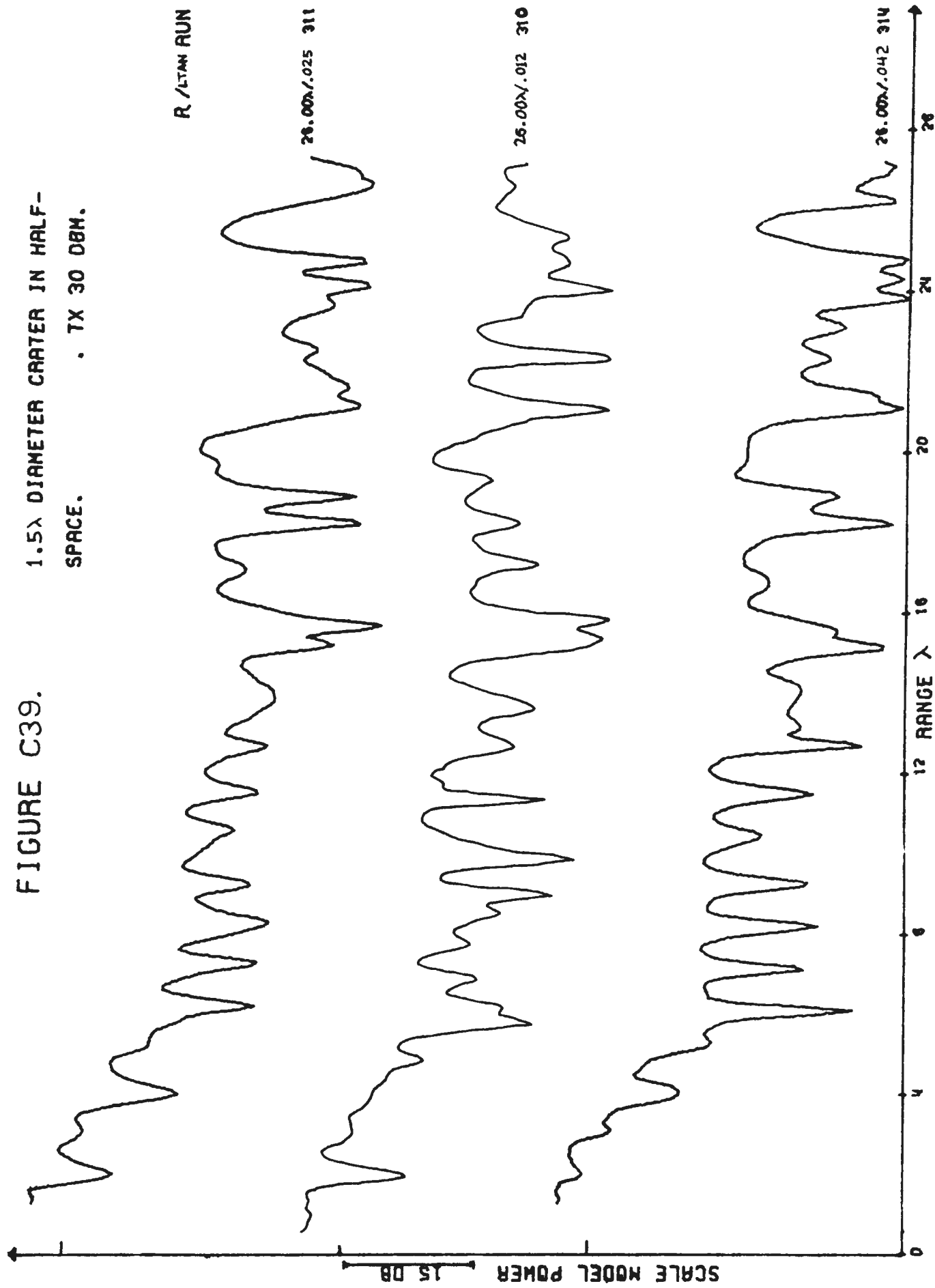


FIGURE C40.

0.6λ DIAMETER CRATER IN HALF-SPACE.
TX 30 DBM.

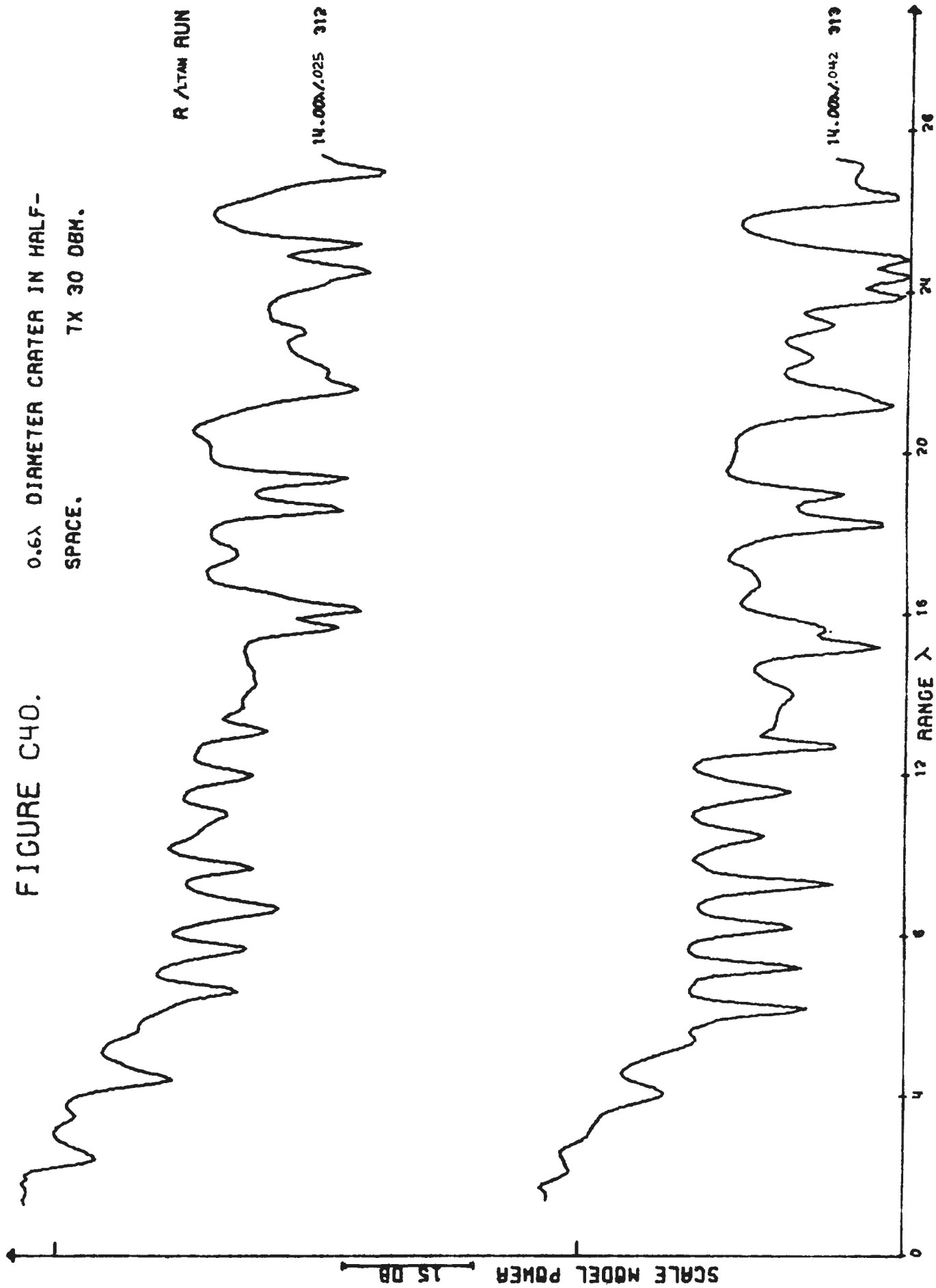


FIGURE C41. 30' MOUNTAIN-SIDE WITH TX 173 FT AWAY. LTAN = .042. TX 200BM.

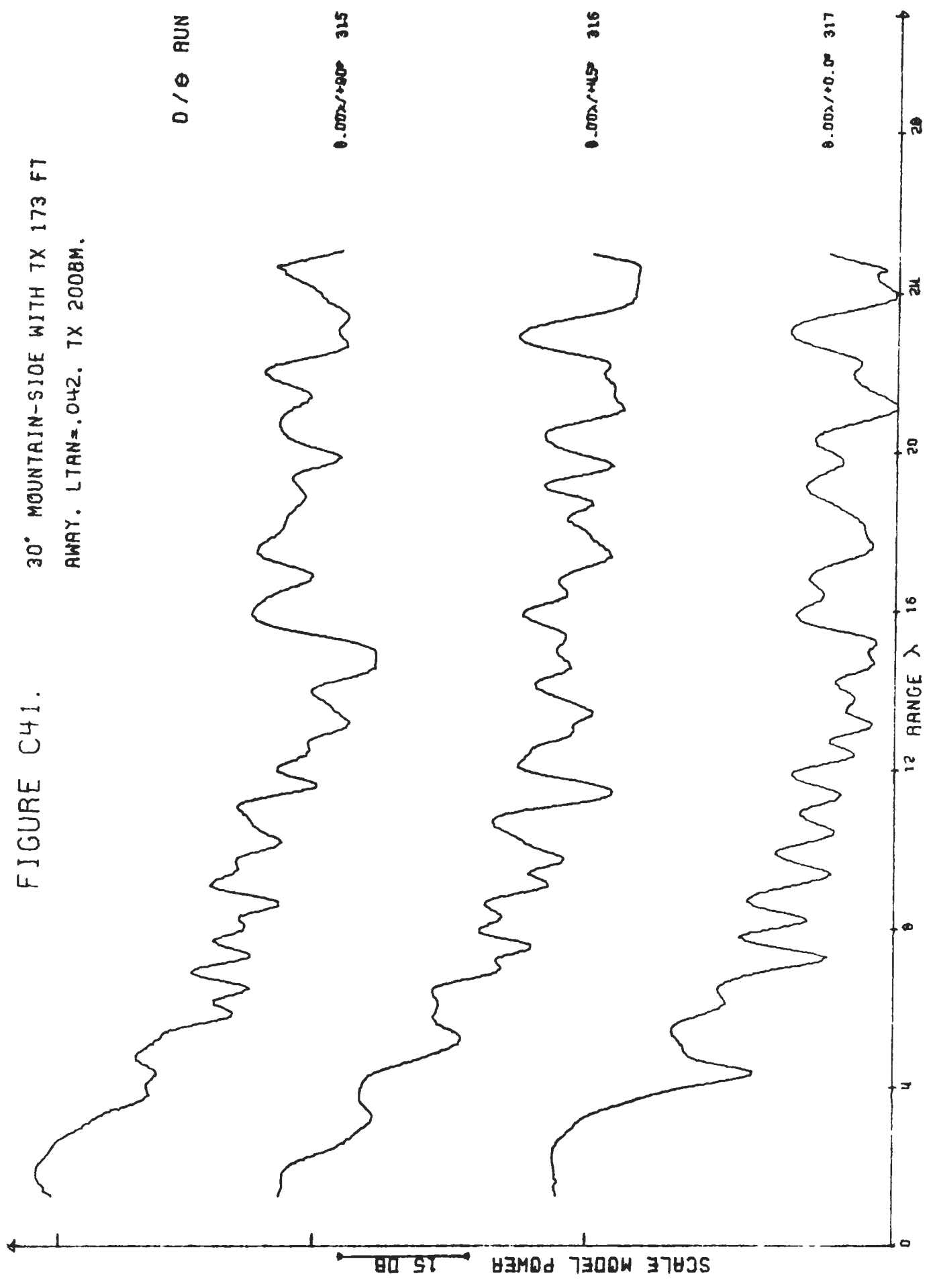


FIGURE C42.
30° MOUNTAIN-SIDE WITH TX 173 FT
AWAY. LTAN=.073. TX 200BM.

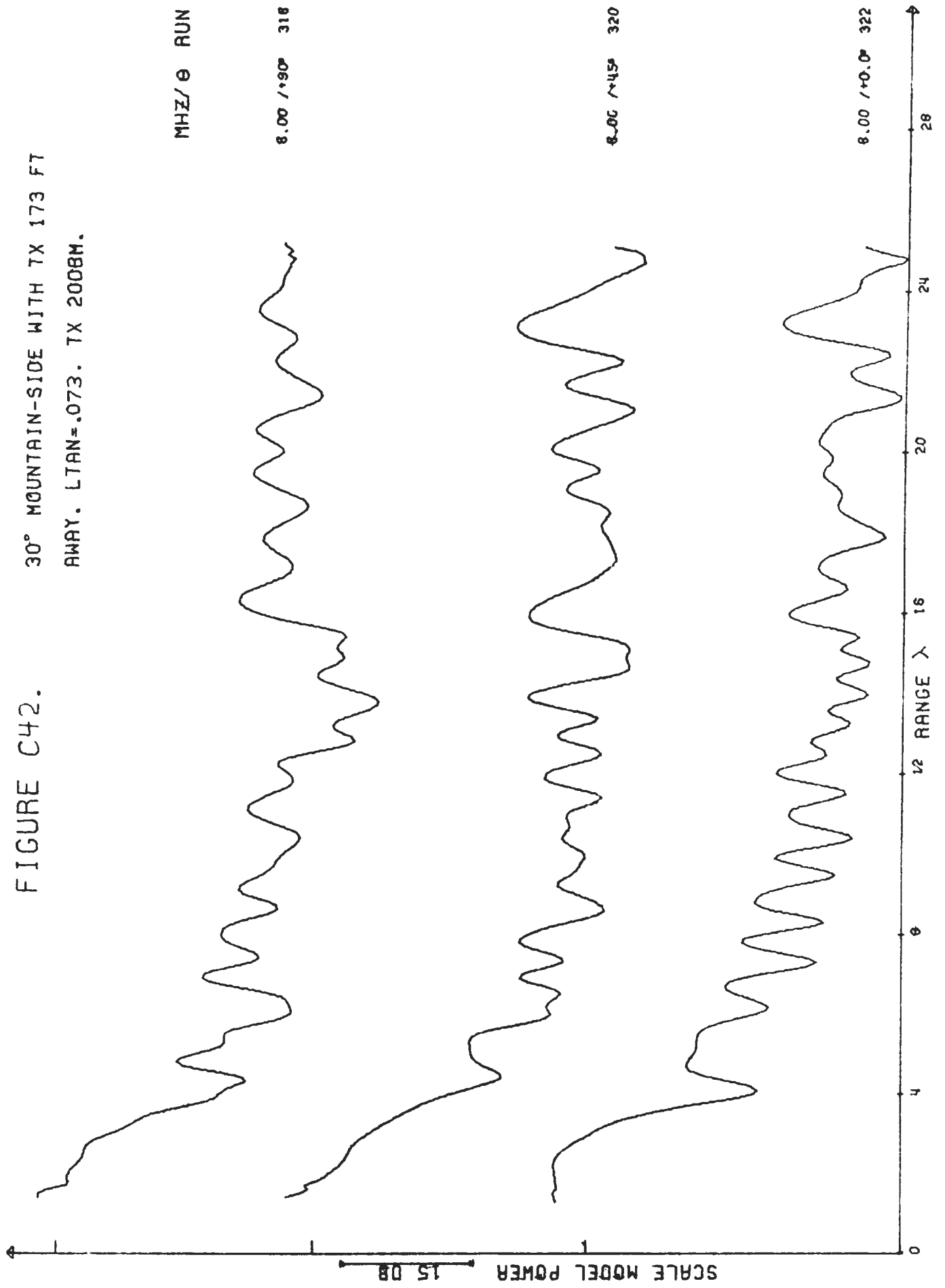


FIGURE C43. 30° MOUNTAIN-SIDE WITH TX 173 FT AWAY. LTAN=.073. TX 200BM.

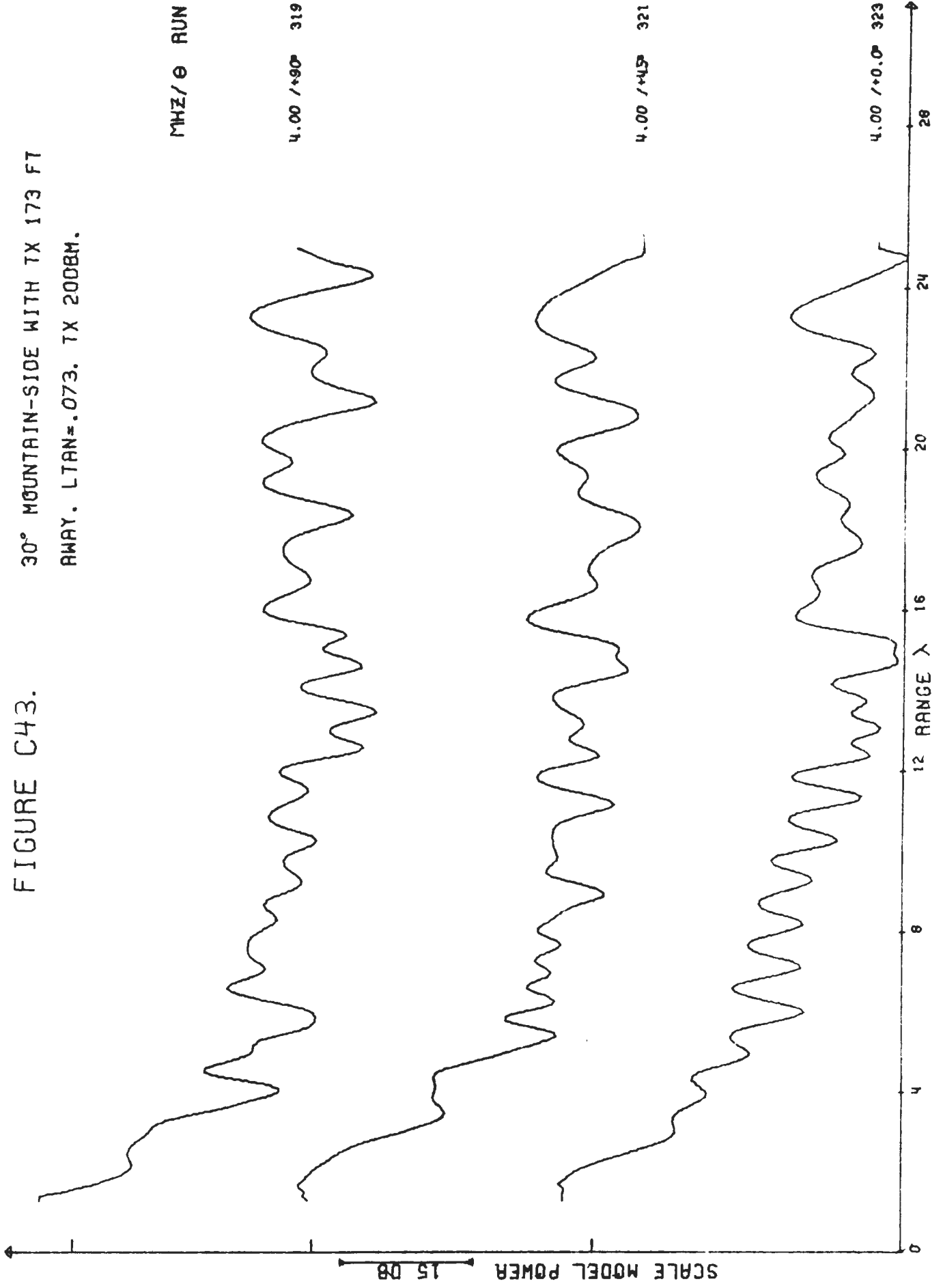


FIGURE C44.

30° MOUNTAIN-SIDE WITH TX 173 FT
AWAY. LTAN=.142. TX 2008M.

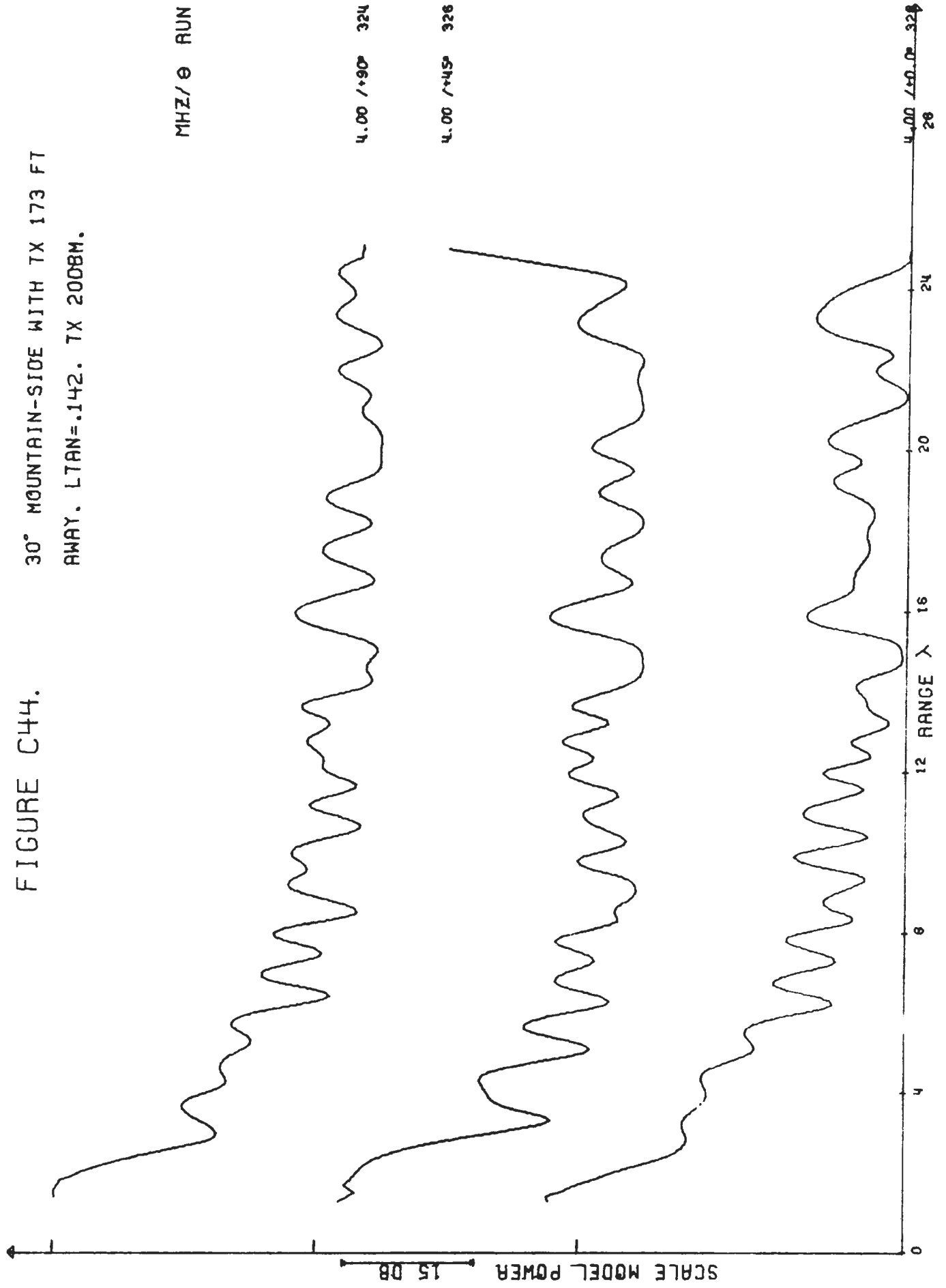


FIGURE C45.

30° MOUNTAIN-SIDE WITH TX 173 FT
AWAY. LTAN=.142. TX 2008M.

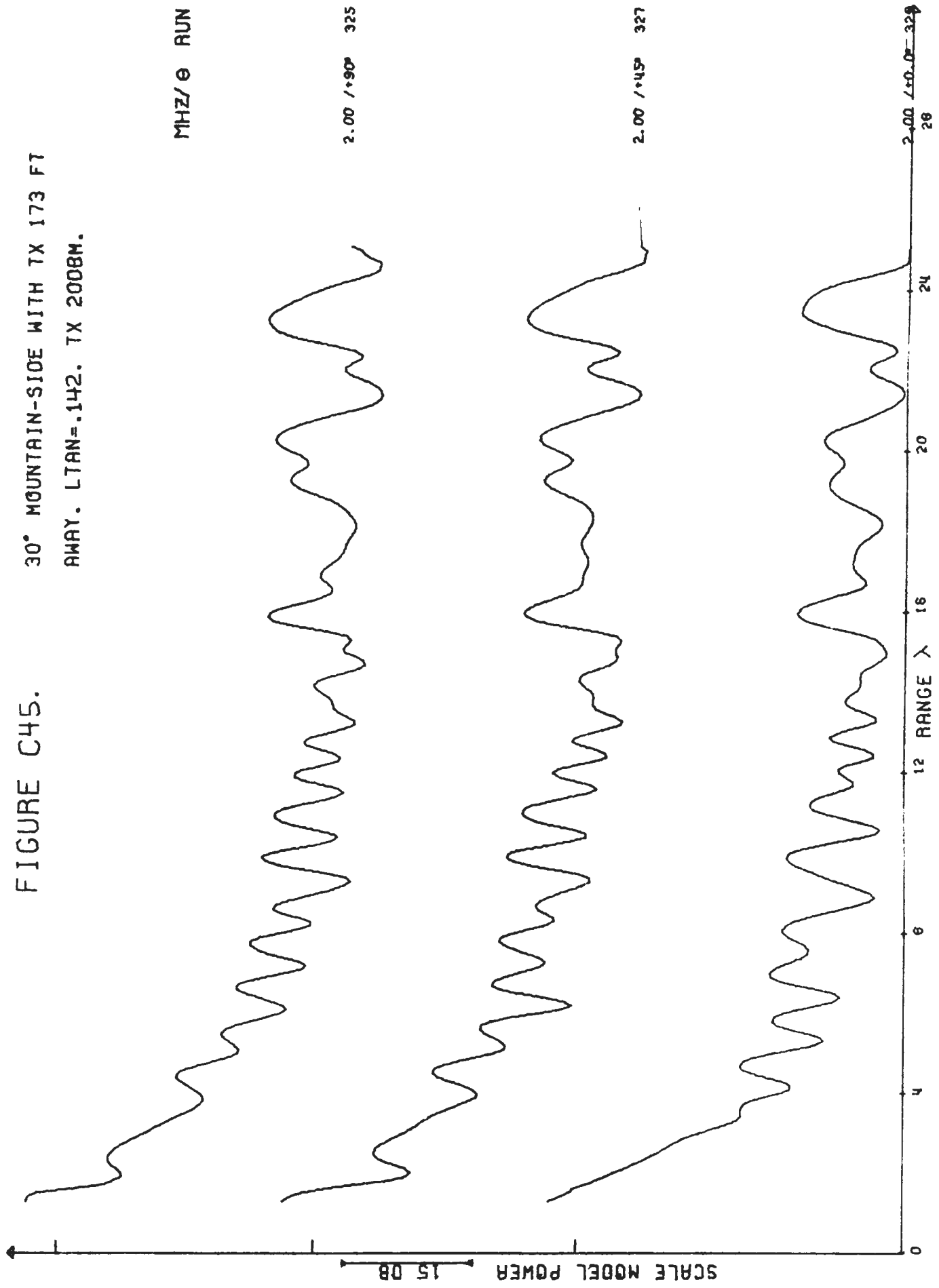


FIGURE C46.

45° STEP BETWEEN PLATES 290&490

FT DEEP. LTAN=.042. TX 2008M.

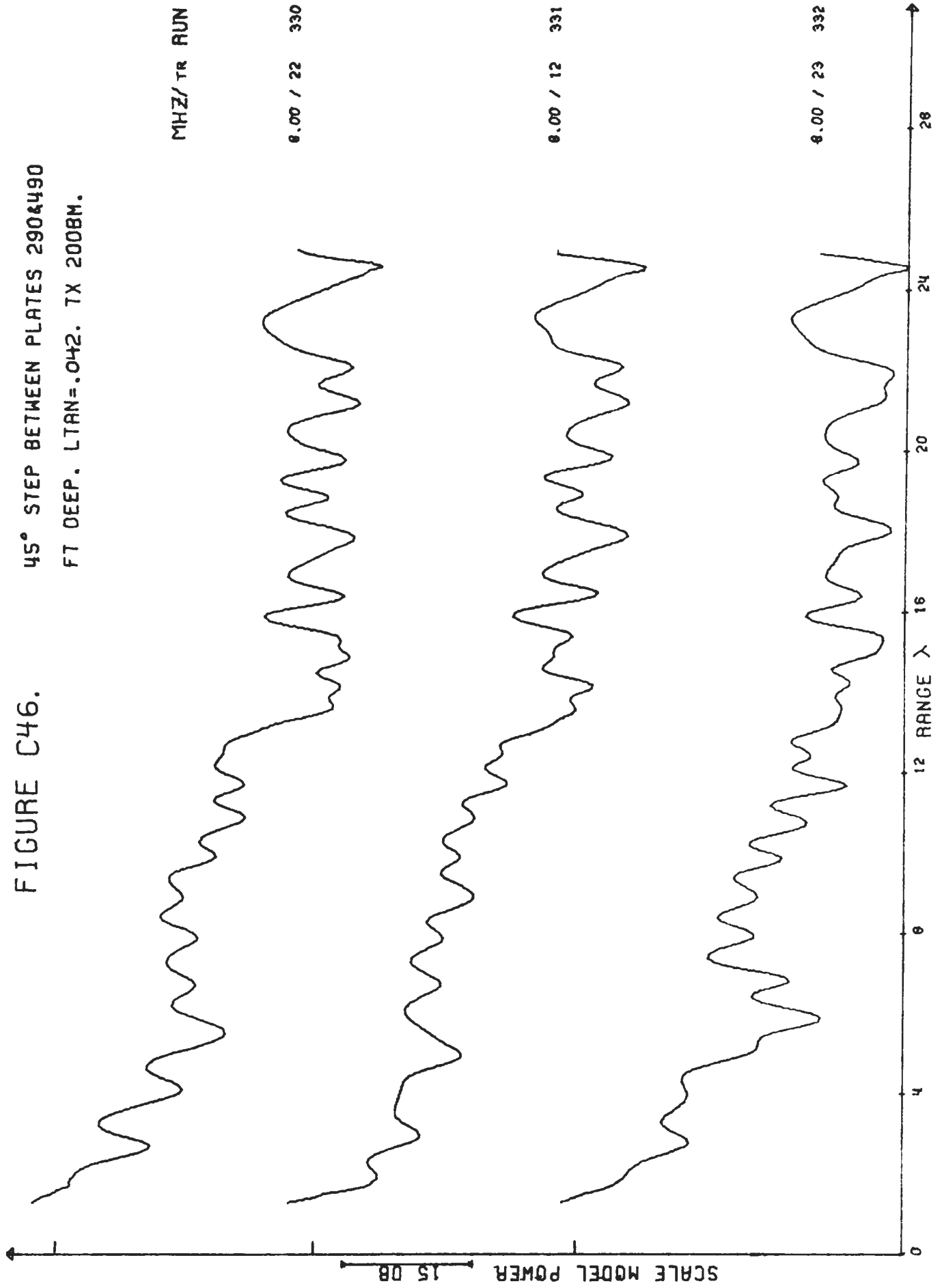


FIGURE C47.

45° STEP BETWEEN PLATES 290&490
FT DEEP. LTAN=.042. TX 2008M.

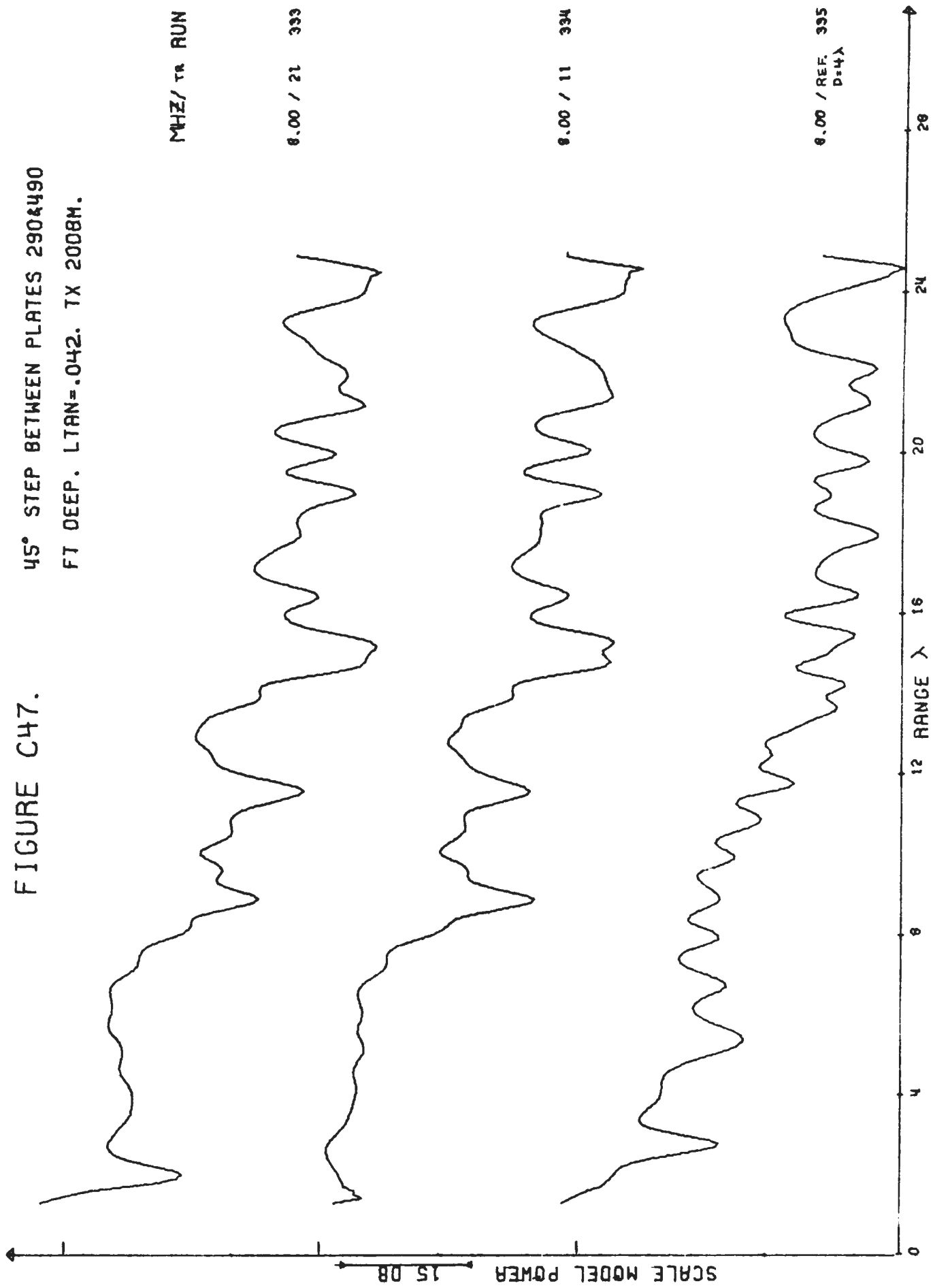


FIGURE C48.

45° STEP BETWEEN PLATES 290&490
FT DEEP. LTAN=.073. TX 20DBM.

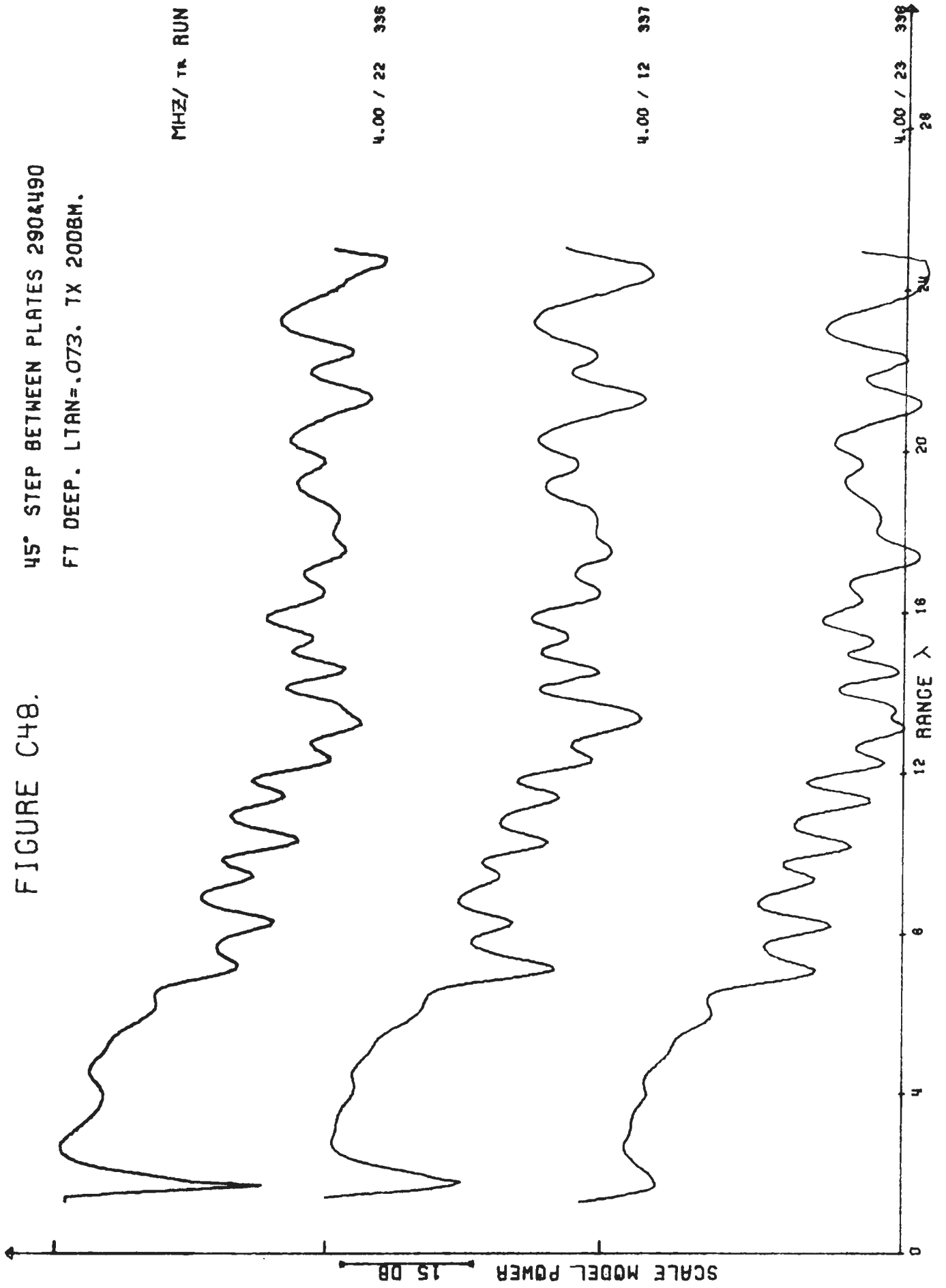


FIGURE C49.

45° STEP BETWEEN PLATES 290&490
FT DEEP. LTAN=.073. TX 200BM.

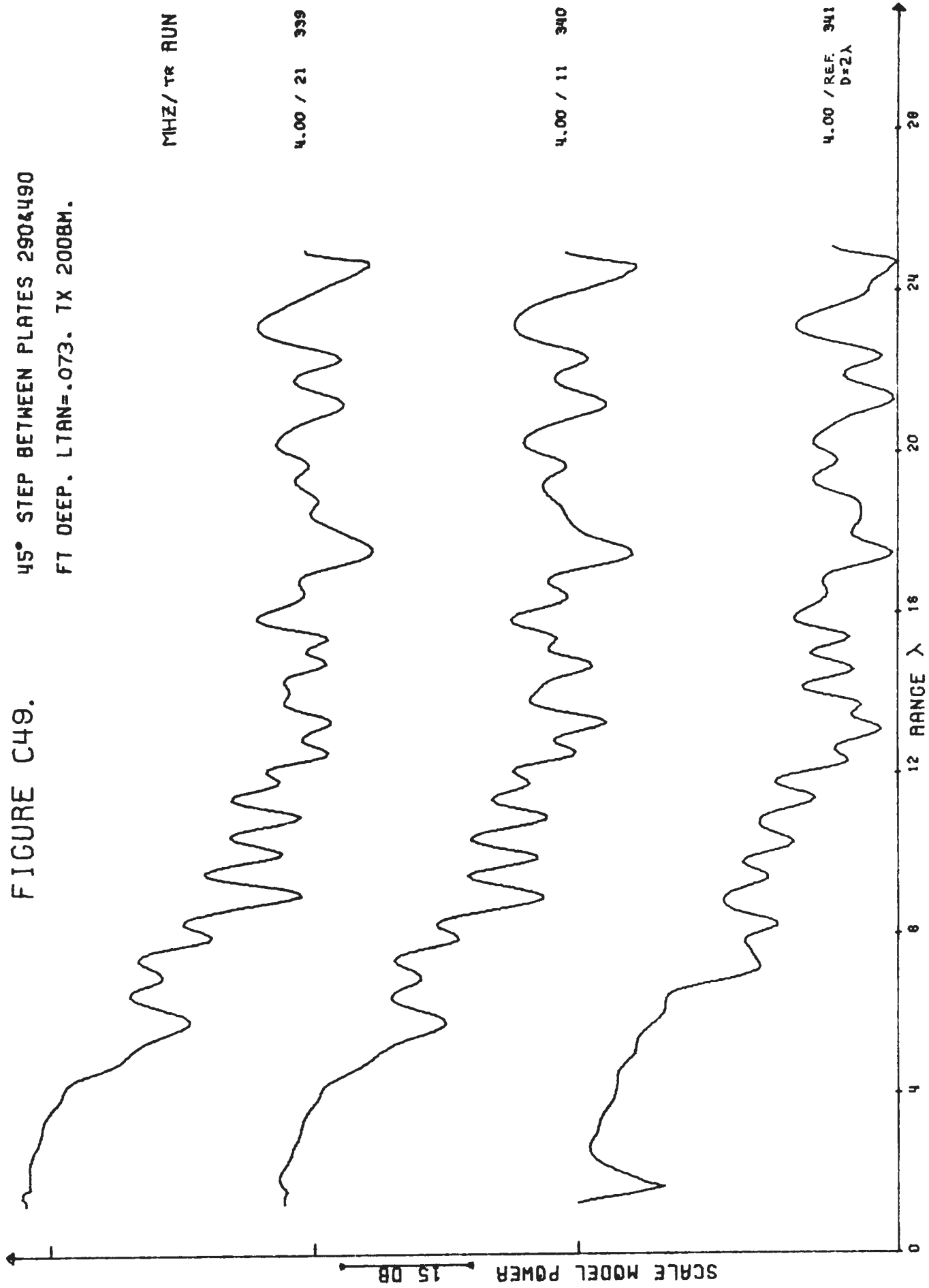


FIGURE C50.

45° STEP BETWEEN PLATES 290&490
FT DEEP. LTAN=.142. TX 2008M.

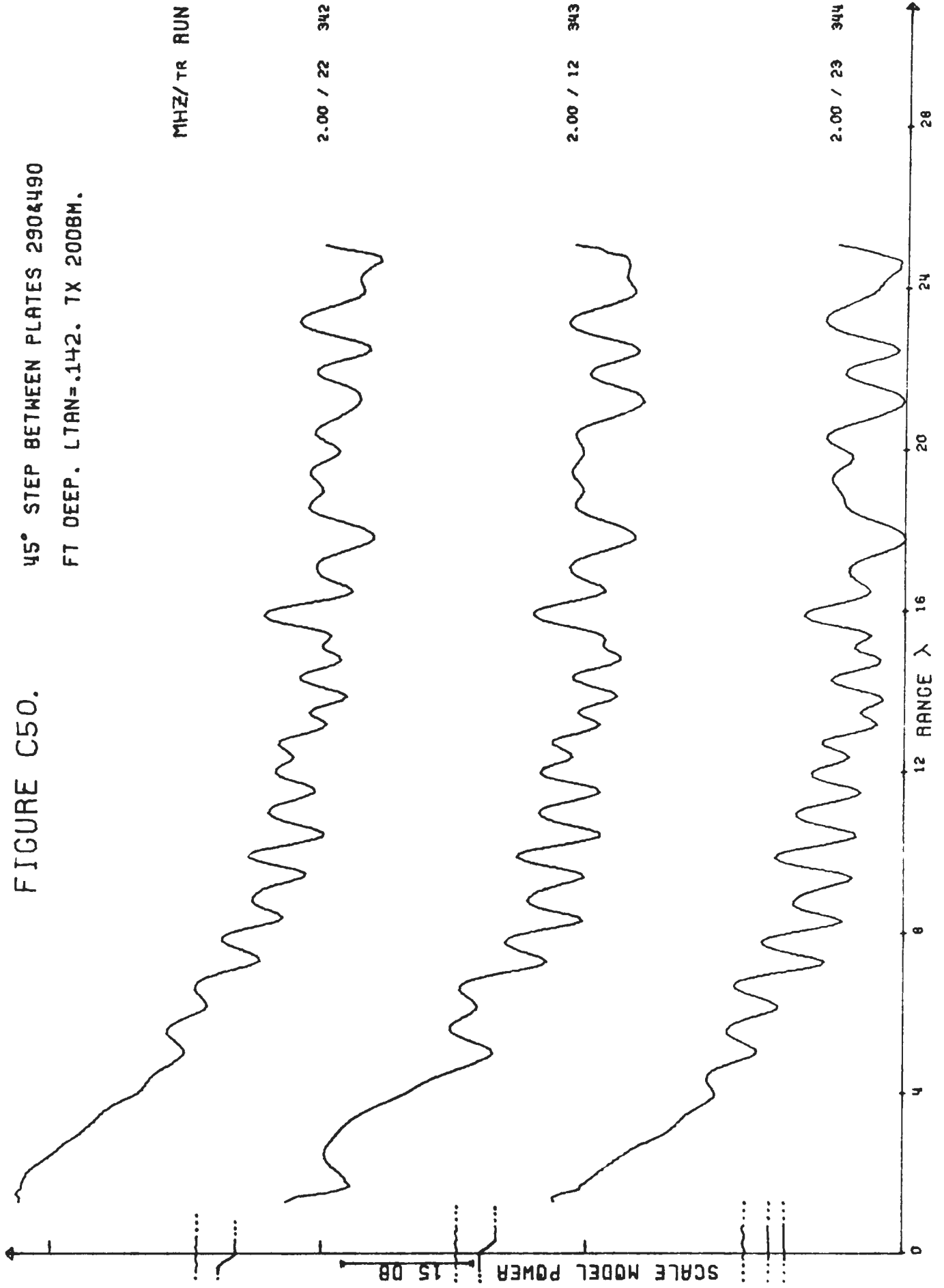


FIGURE C51.

45° STEP BETWEEN PLATES 290&490
FT DEEP. LTAN=.142. TX 2008M.

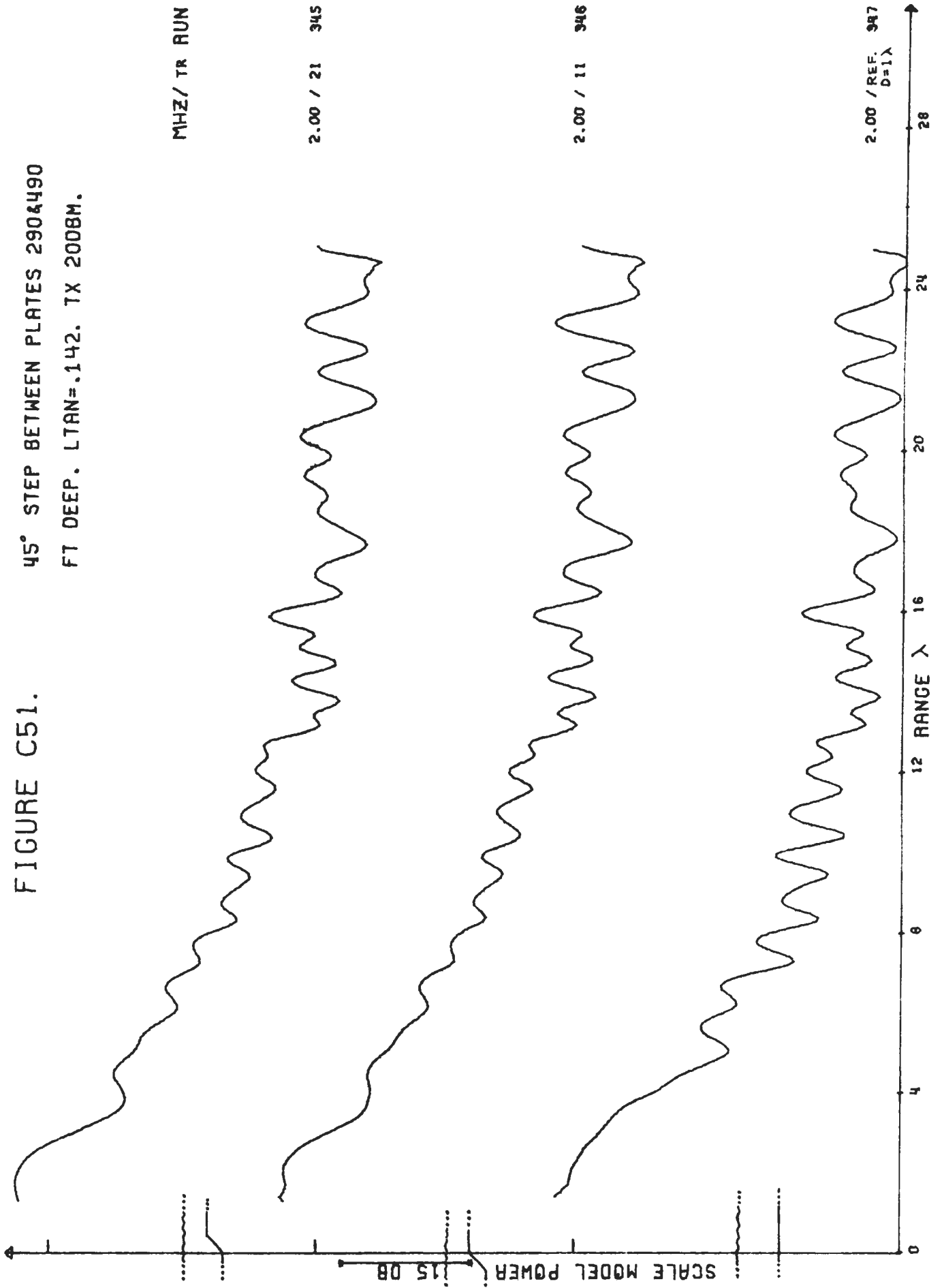


FIGURE C52.

200 FT HIGH 45° RIDGE ON 490 FT
DEEP PLATE. LTAN=.042. TX 200BM.

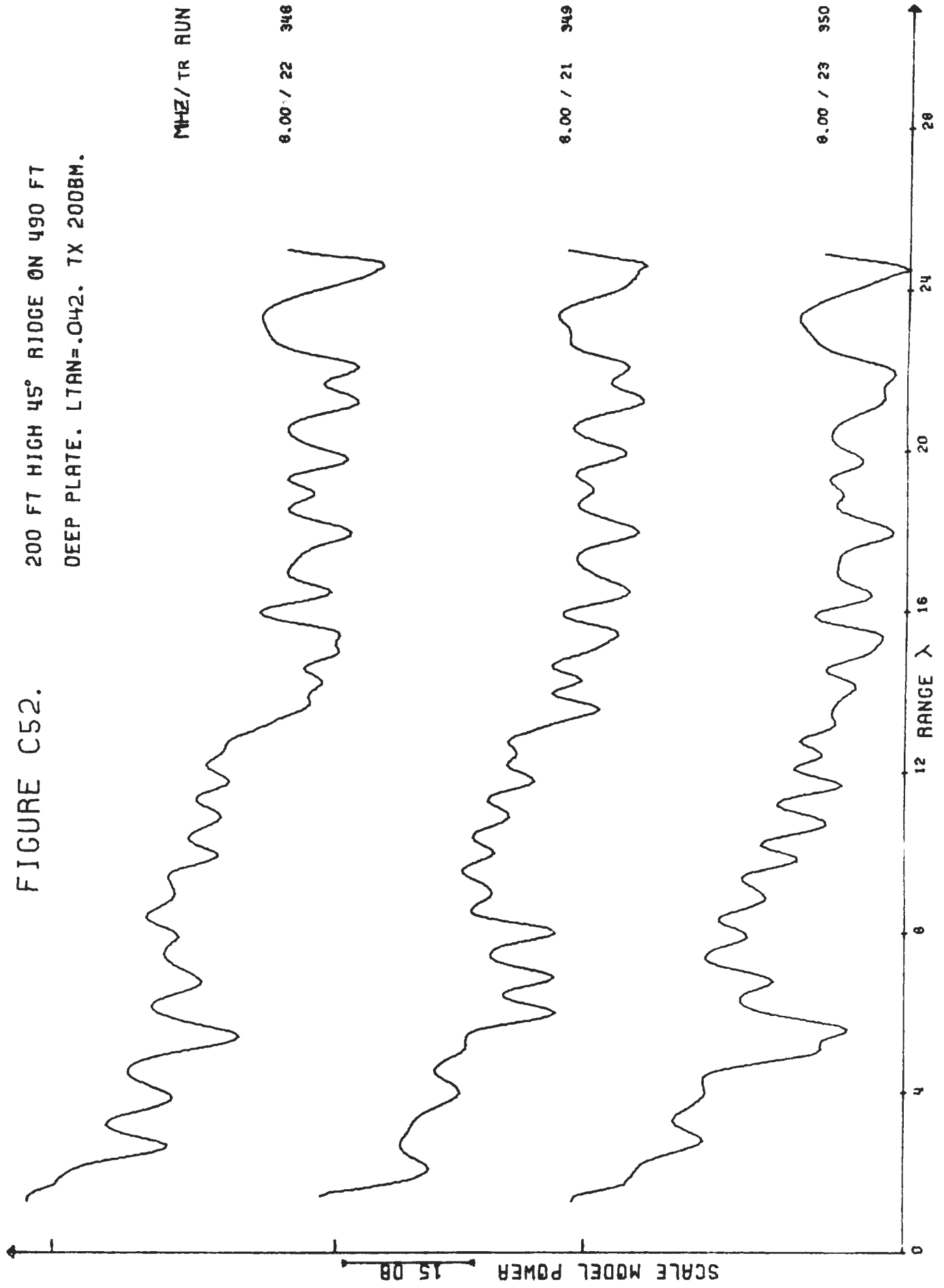


FIGURE C53. 200 FT HIGH 45° RIDGE ON 490 FT DEEP PLATE. LTAN=.073. TX 200BM.

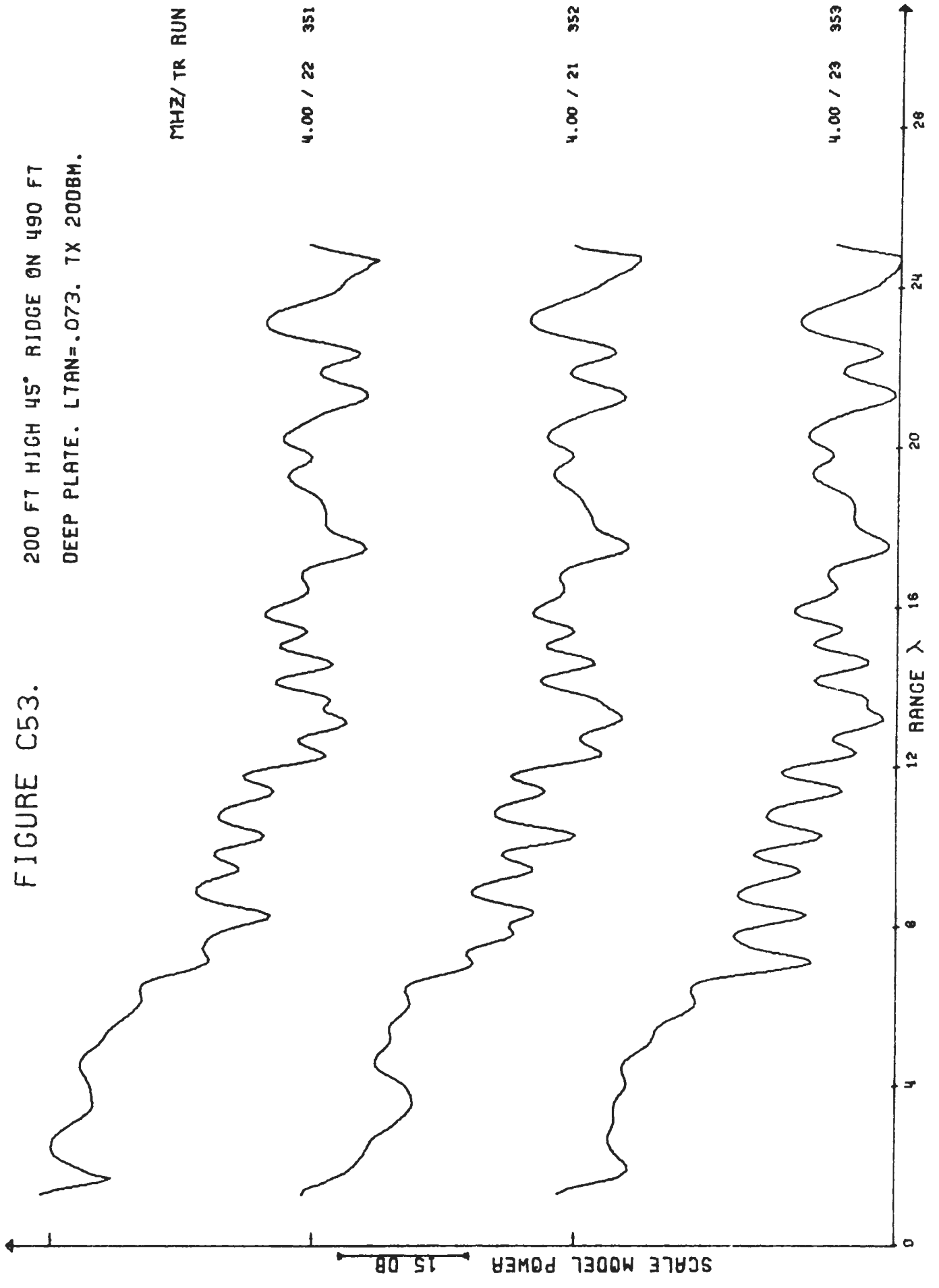
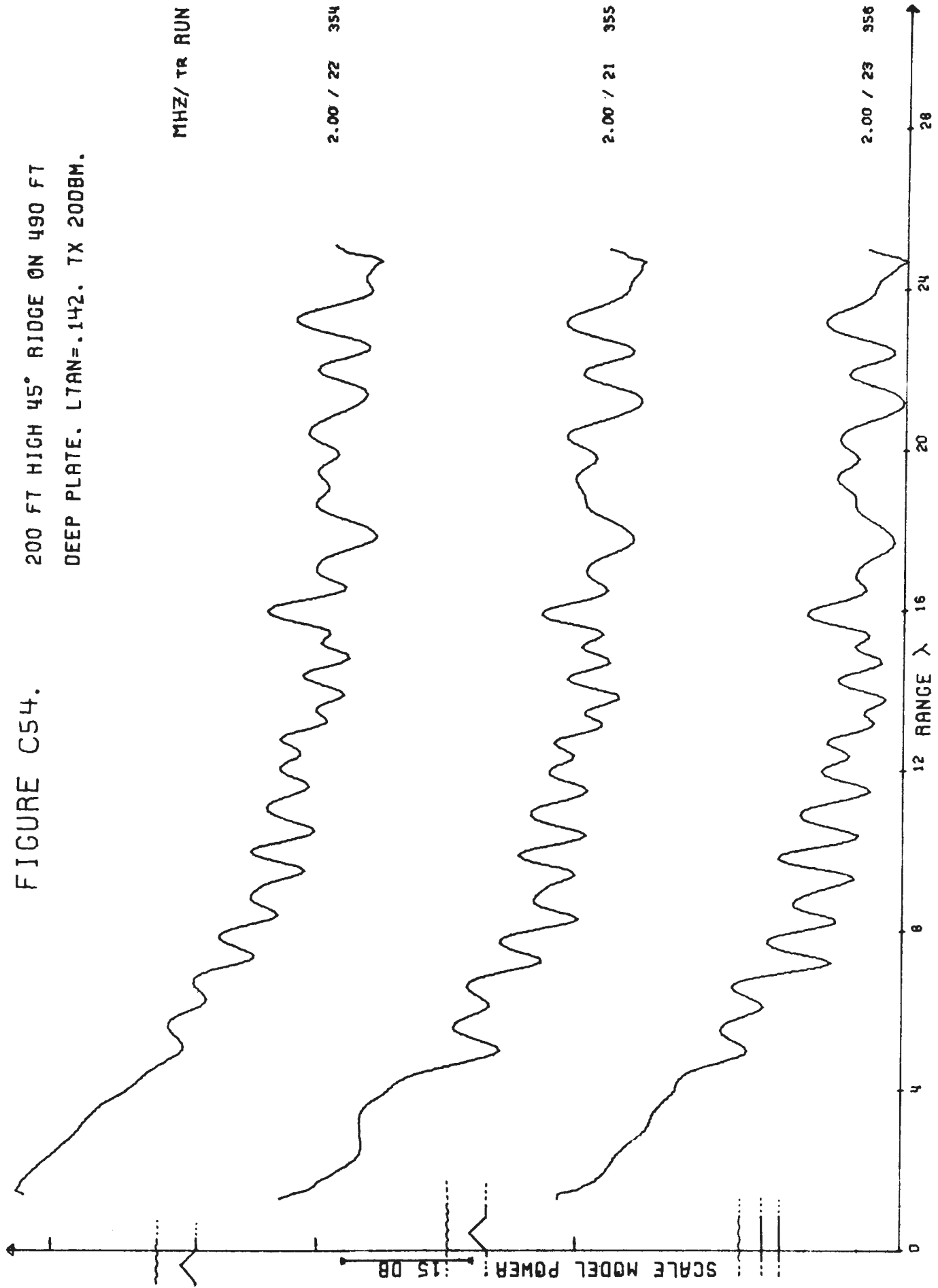
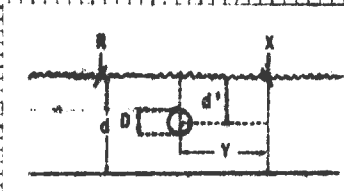


FIGURE C54.

200 FT HIGH 45° RIDGE ON 490 FT
DEEP PLATE. LTAN=.142. TX 20DBM.



APPENDIX D
SPHERICAL SCATTERING OBJECTS TRAVERSES



d D d' y
 6λ 2λ 4λ 0

15 DB

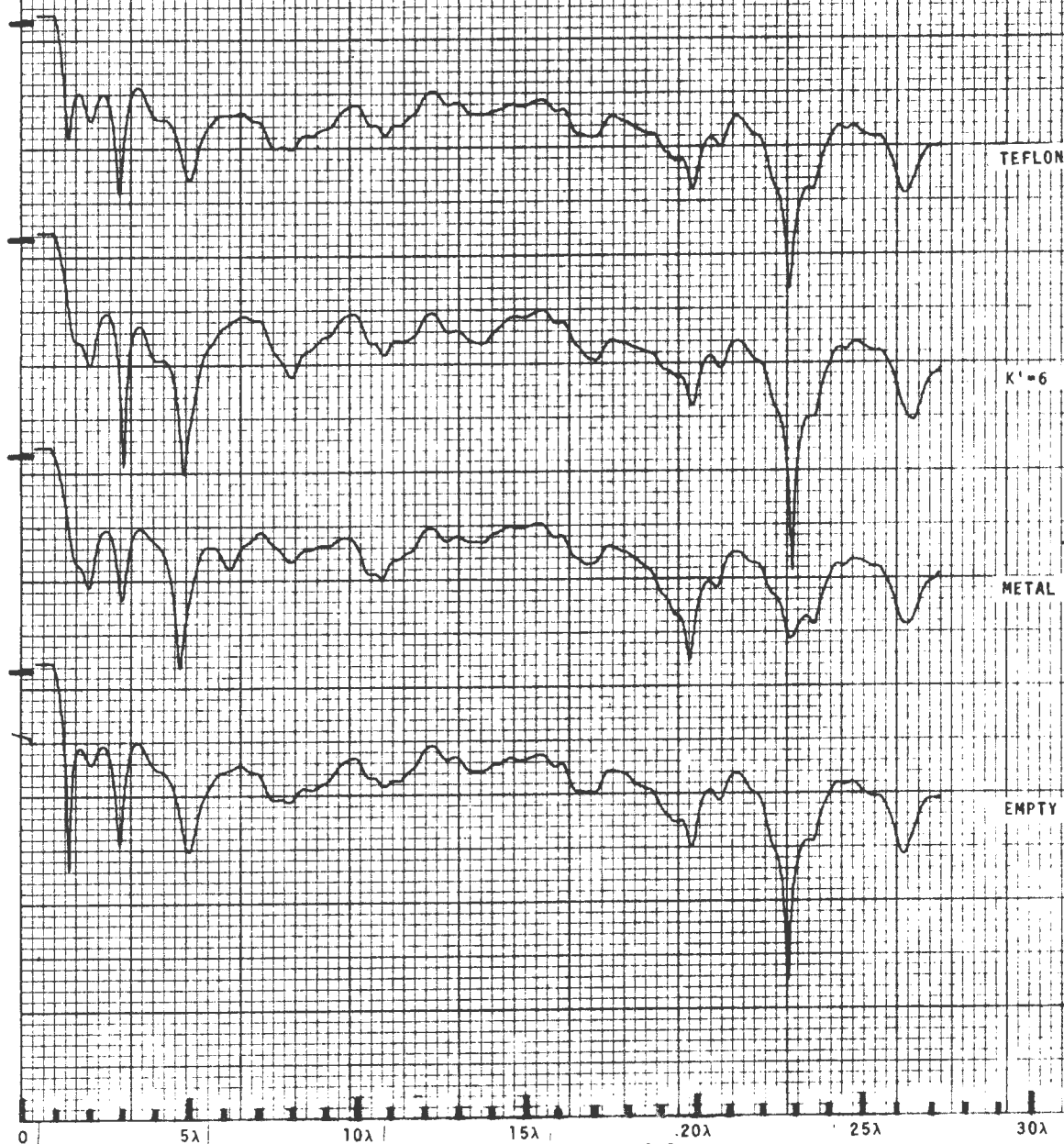
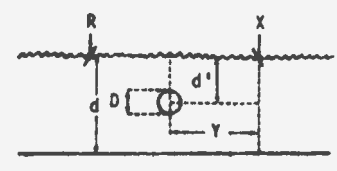
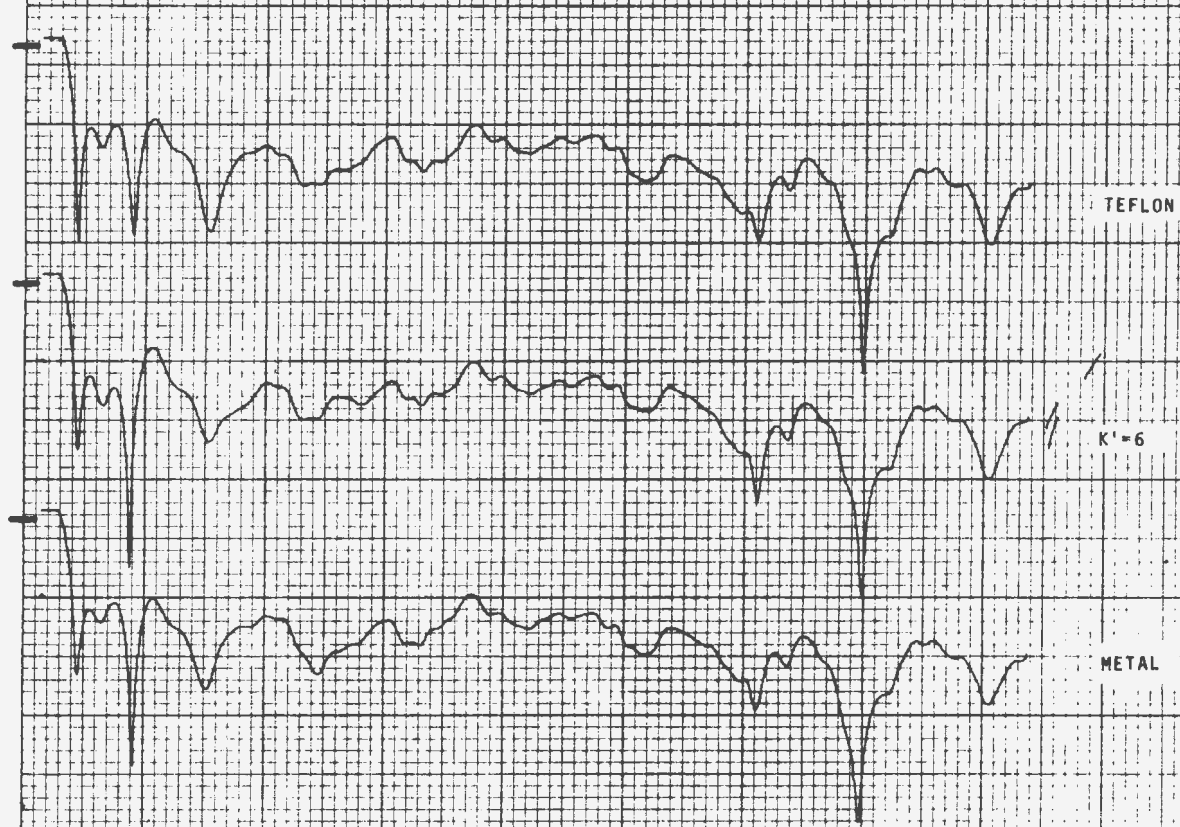


Figure D-1

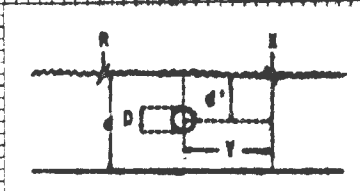
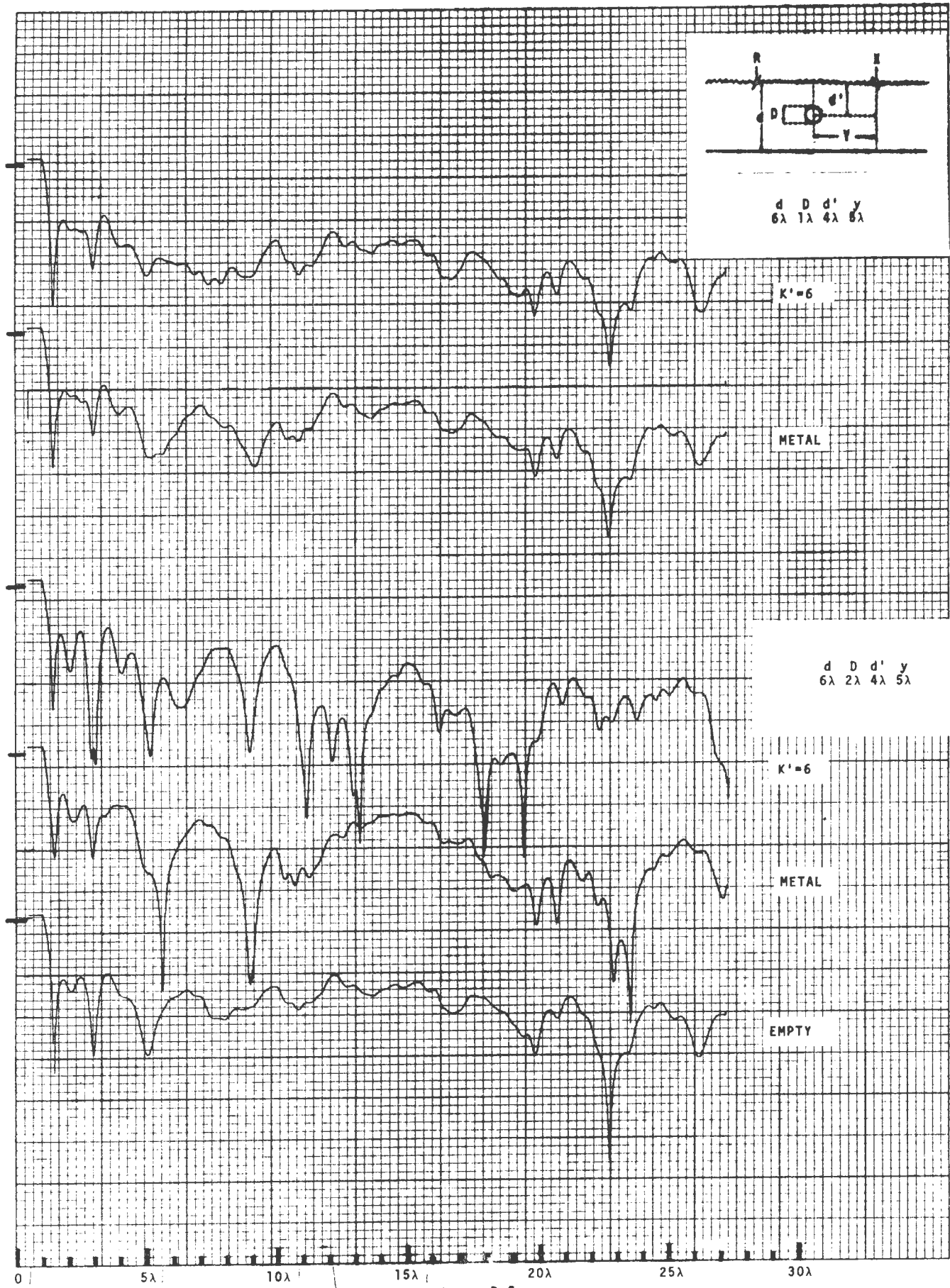


d D d' y
 6λ 1λ 4λ 0



0 | 5λ | 10λ | 15λ | 20λ | 25λ | 30λ

Figure D-2



d D d' y
6λ 1λ 4λ 8λ

K'=6

METAL

d D d' y
6λ 2λ 4λ 5λ

K'=6

METAL

EMPTY

0 5λ 10λ 15λ 20λ 25λ 30λ

Figure D-3

T C

K'-6

d D d' y
6λ 2λ 4λ

25λ

20λ

15λ

10λ

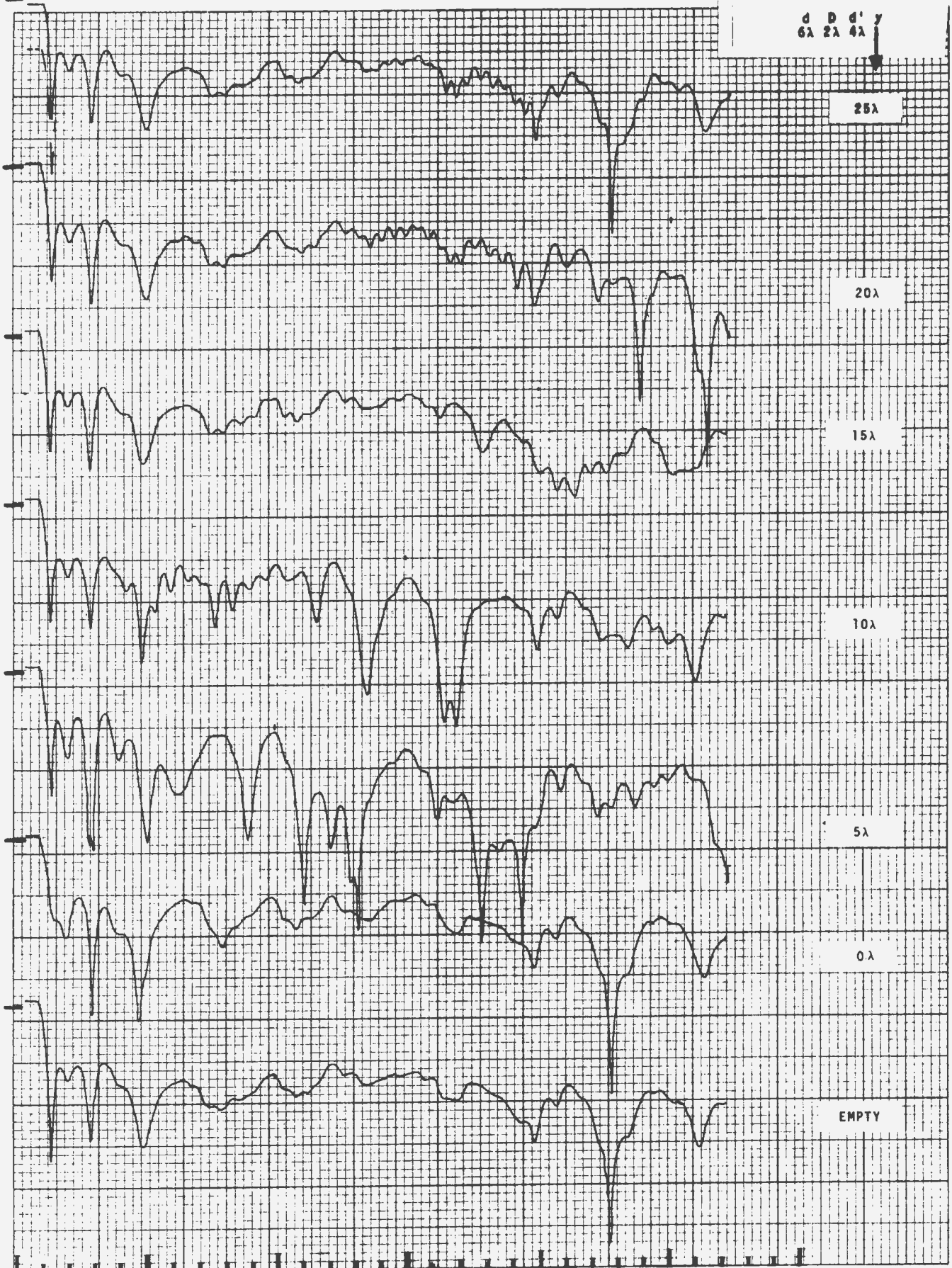
5λ

0λ

EMPTY

0 5λ 10λ 15λ 20λ 25λ 30λ

Figure D-4



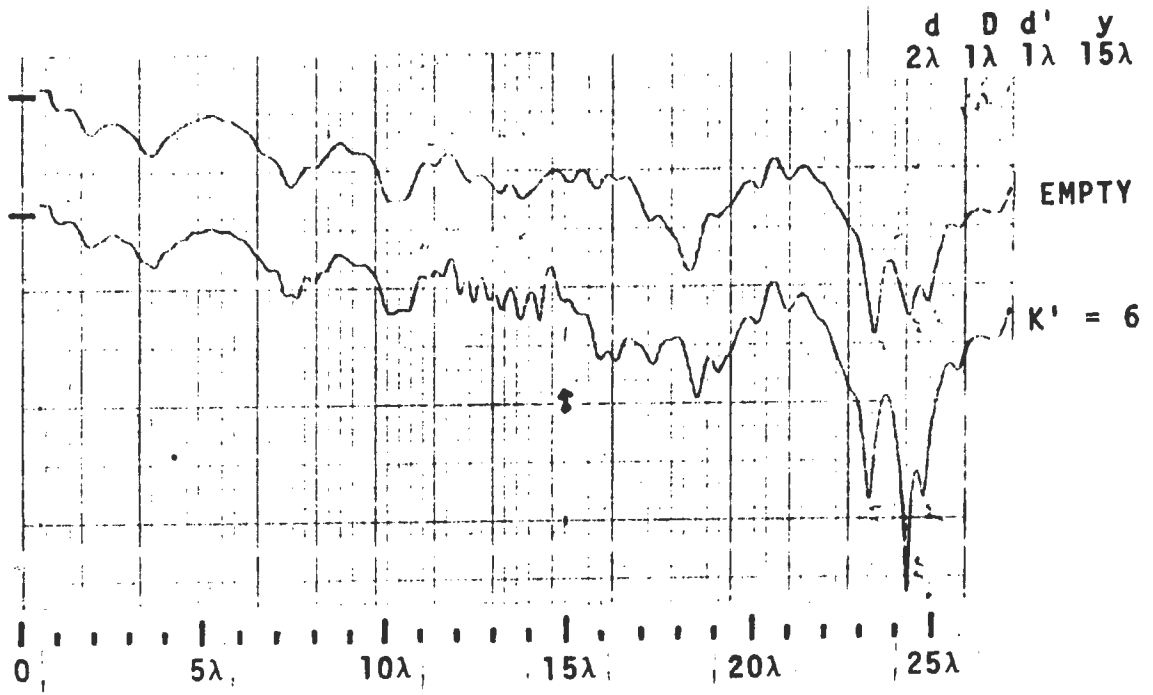
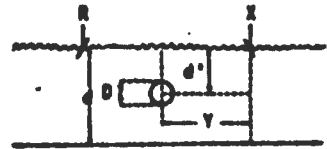
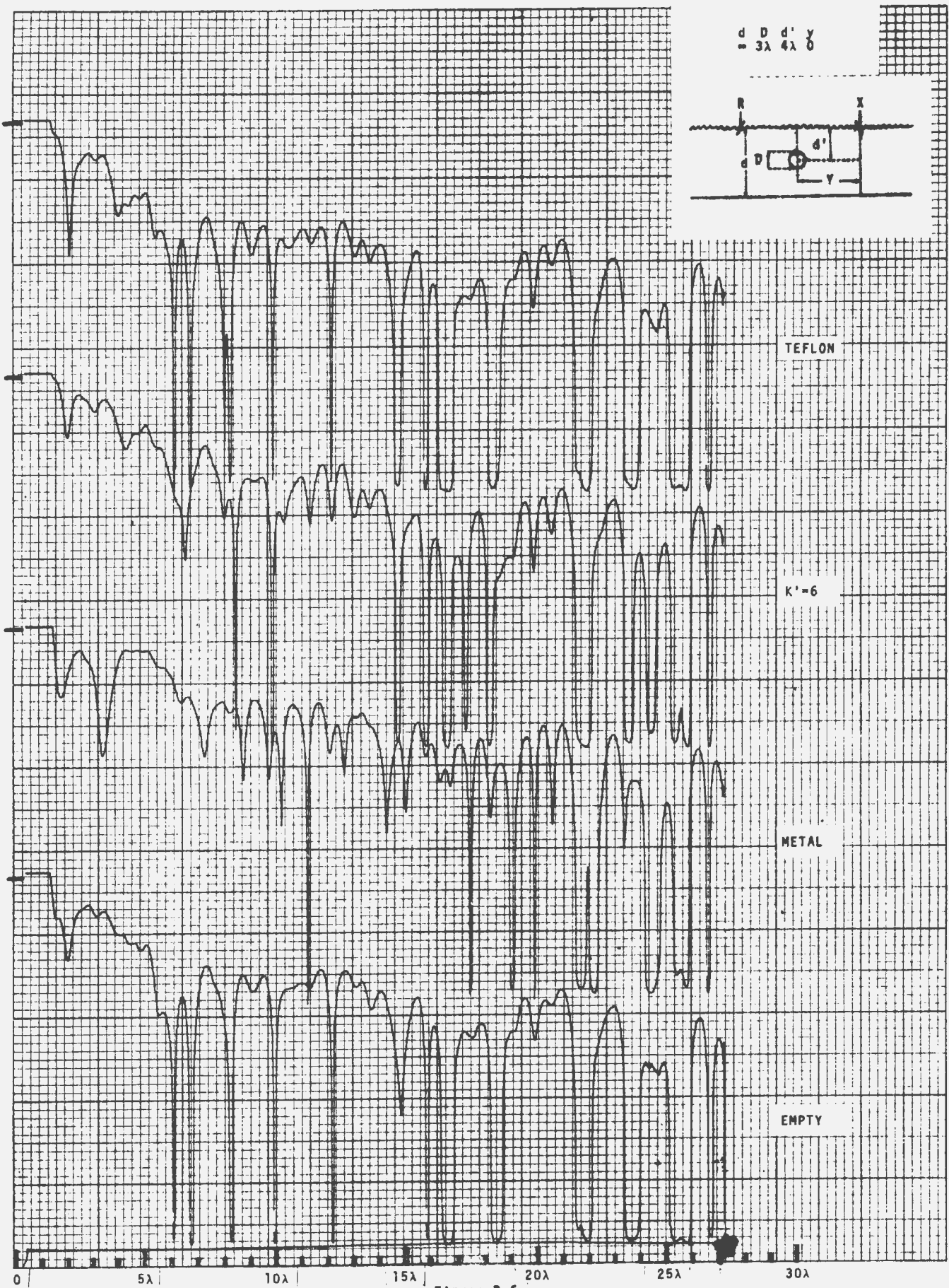
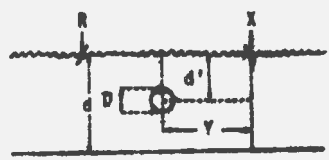


Figure D-5



$$\frac{d}{3\lambda} = \frac{D}{4\lambda} = \frac{d'}{4\lambda} = \frac{y}{\delta}$$



TEFLON

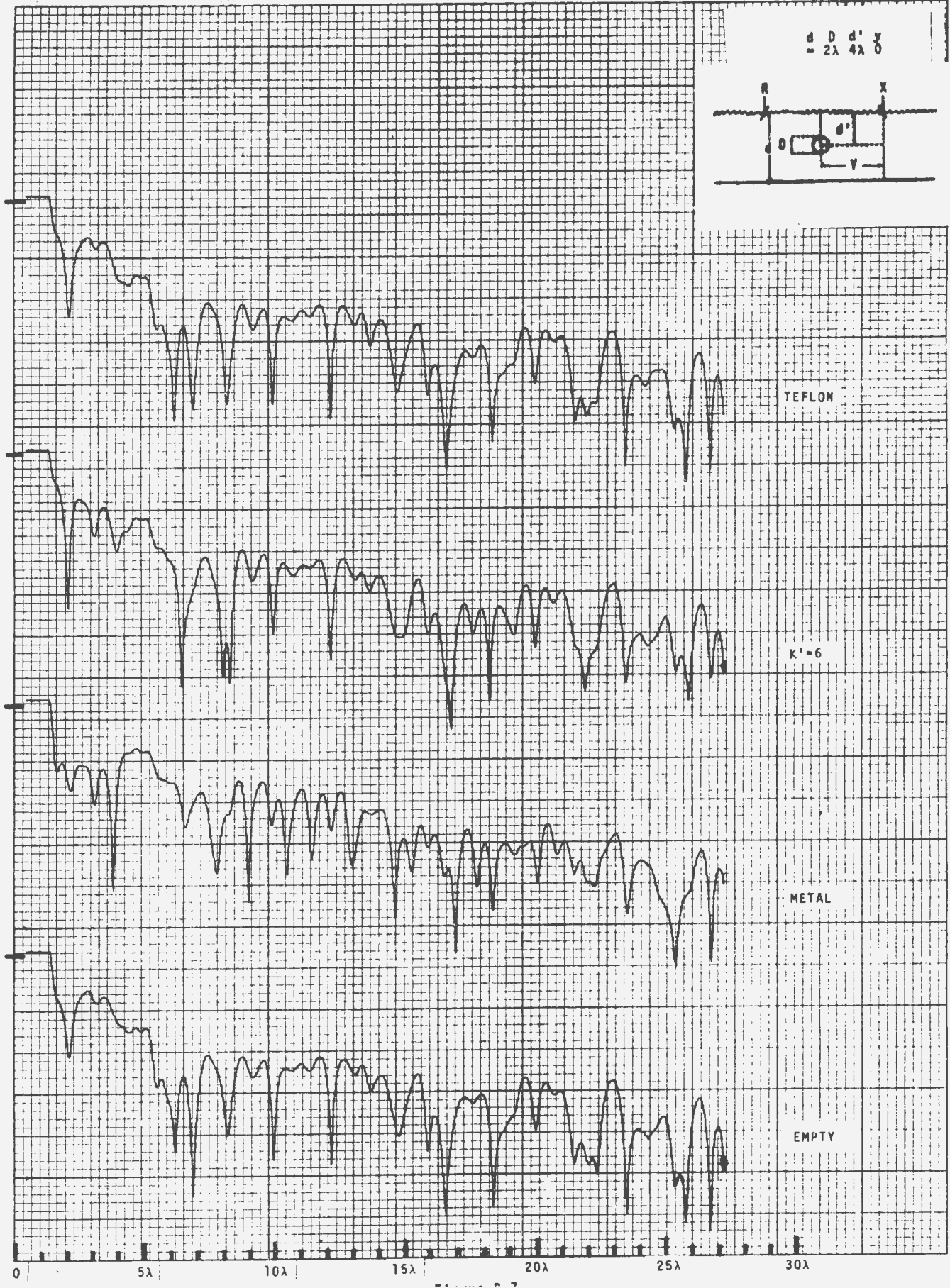
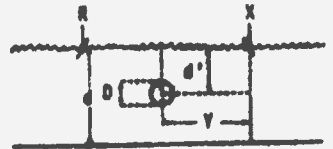
$K' = 6$

METAL

EMPTY

Figure D-6

$$\frac{d}{2\lambda} = \frac{D}{4\lambda} = \frac{d'}{4\lambda} = \frac{y}{0}$$



0 5λ 10λ 15λ 20λ 25λ 30λ

$$\frac{d}{\lambda} = \frac{D}{4\lambda} = \frac{d'}{\lambda} = \frac{y}{\lambda}$$

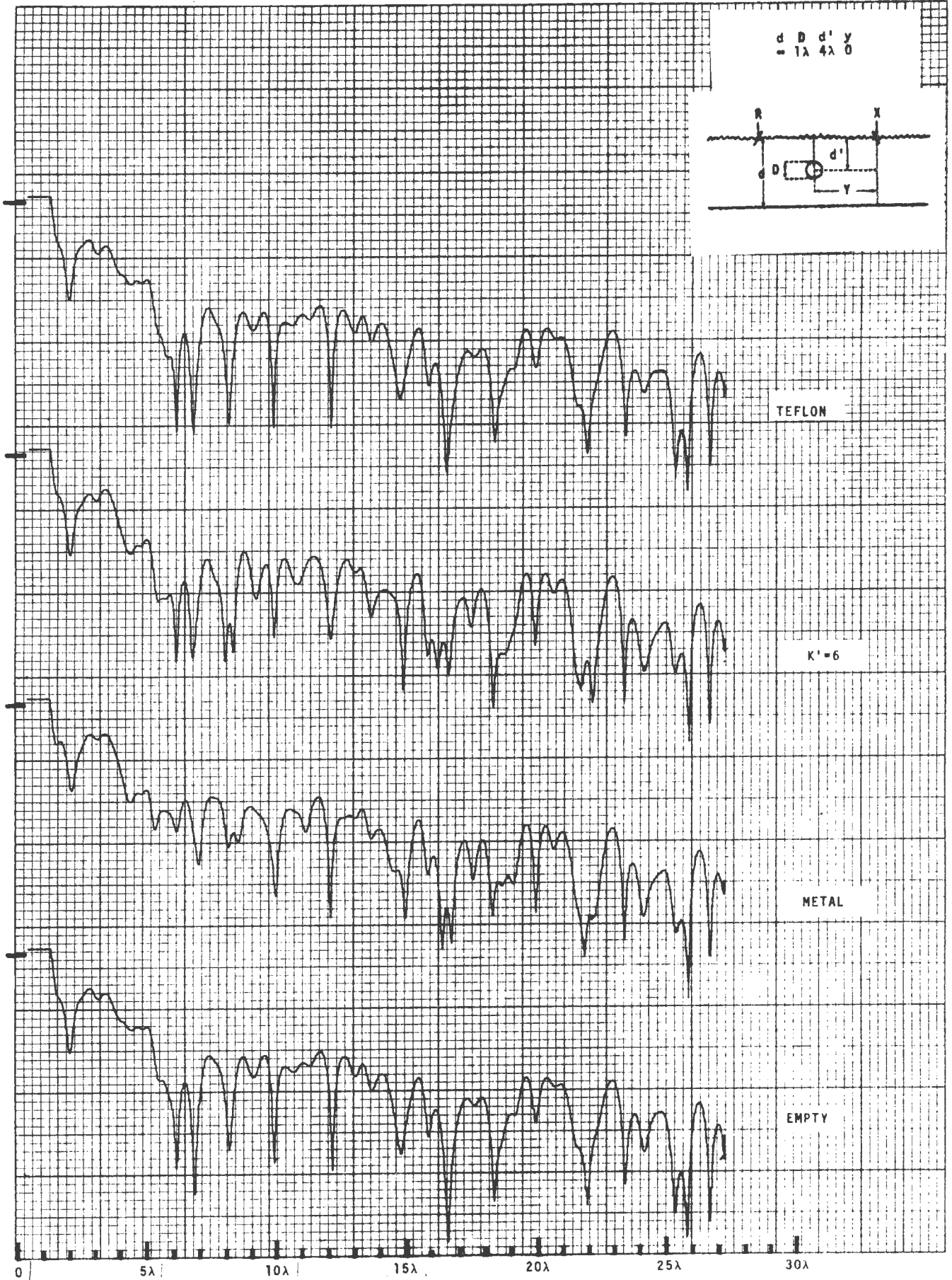
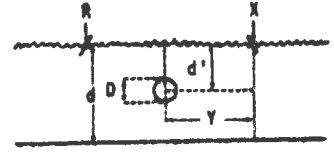
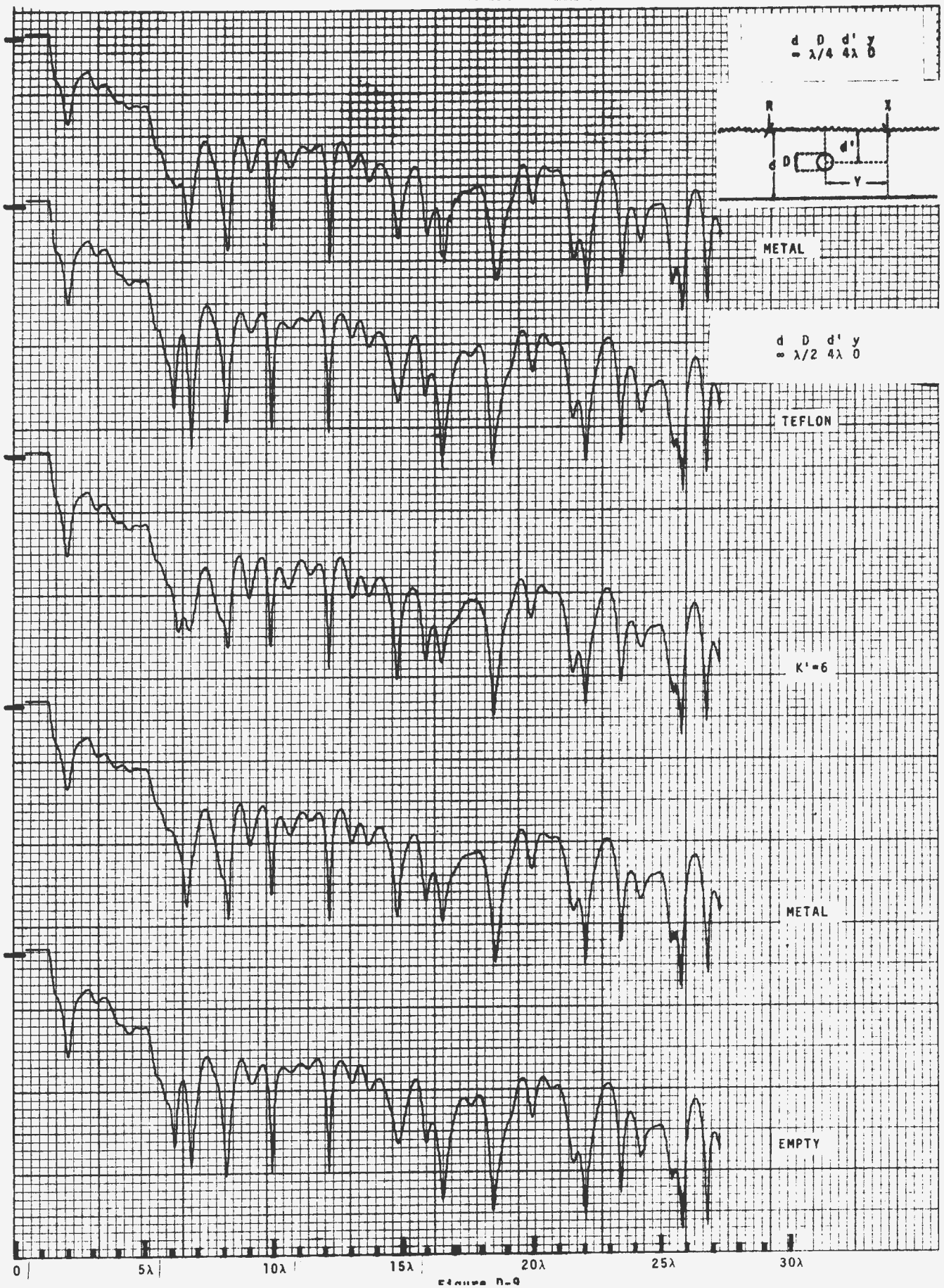
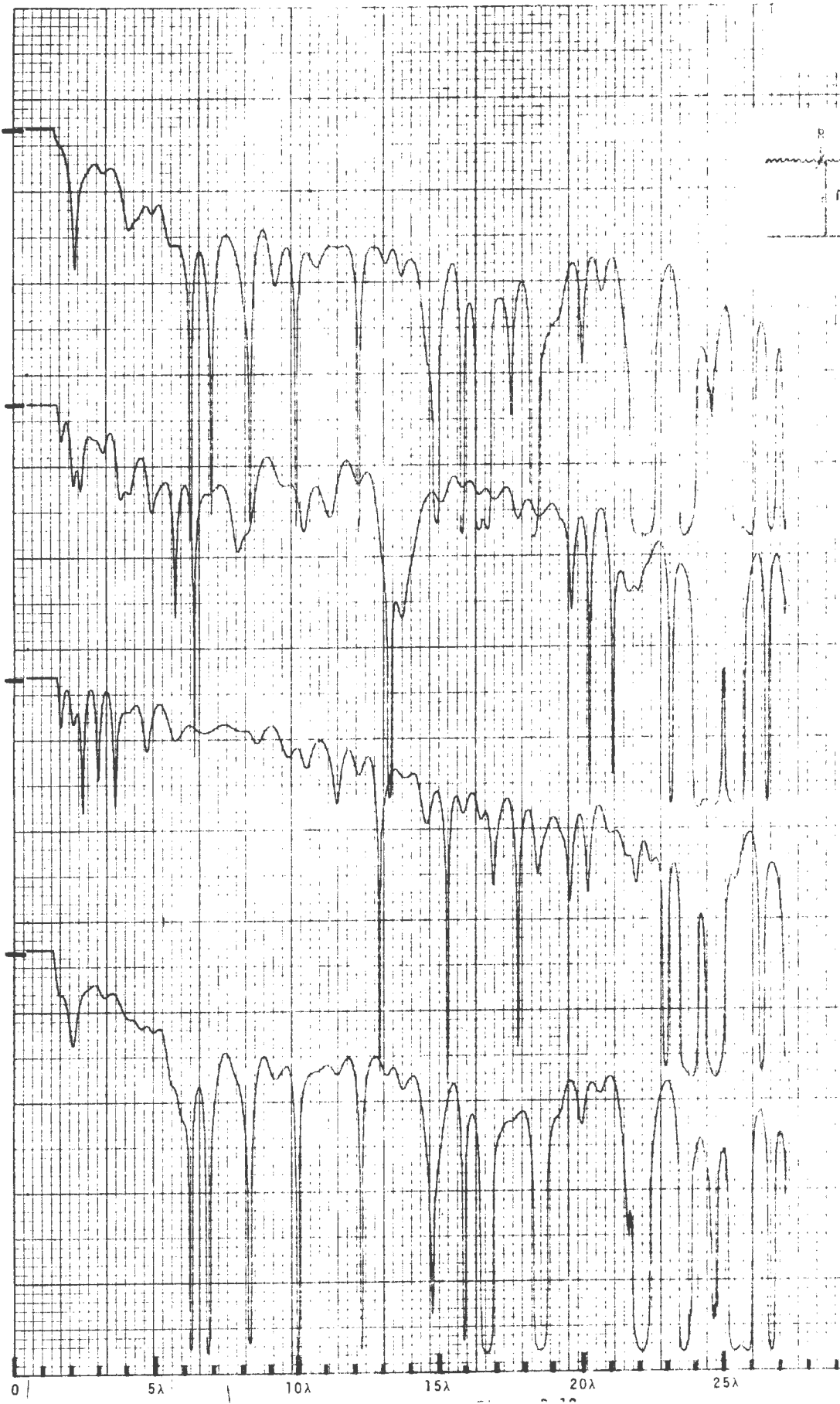
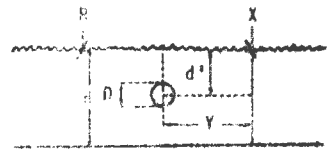


Figure D-2



$d \quad D \quad d' \quad y$
 $\infty \quad 3\lambda \quad 4\lambda \quad 5\lambda$



TEFLON

K¹-6

METAL

EMPTY

0 | 5λ | 10λ | 15λ | 20λ | 25λ | 30λ

$d \quad 0 \quad d' \quad y$
 $= 2\lambda \quad 4\lambda \quad 5\lambda$

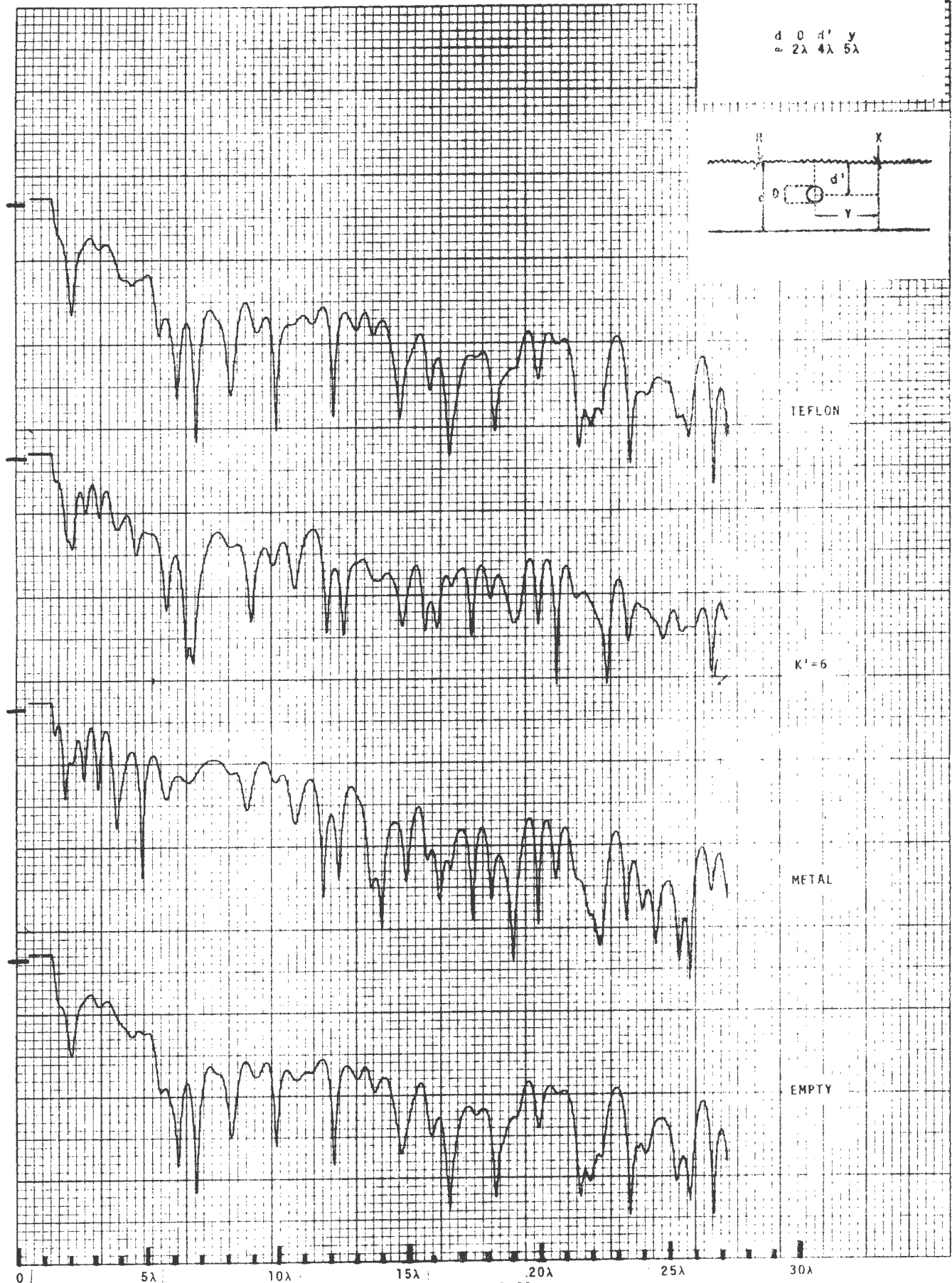
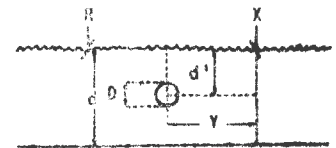


Figure D-11

$d = 1\lambda$ $D = 4\lambda$ $d' = 5\lambda$ $y = 5\lambda$

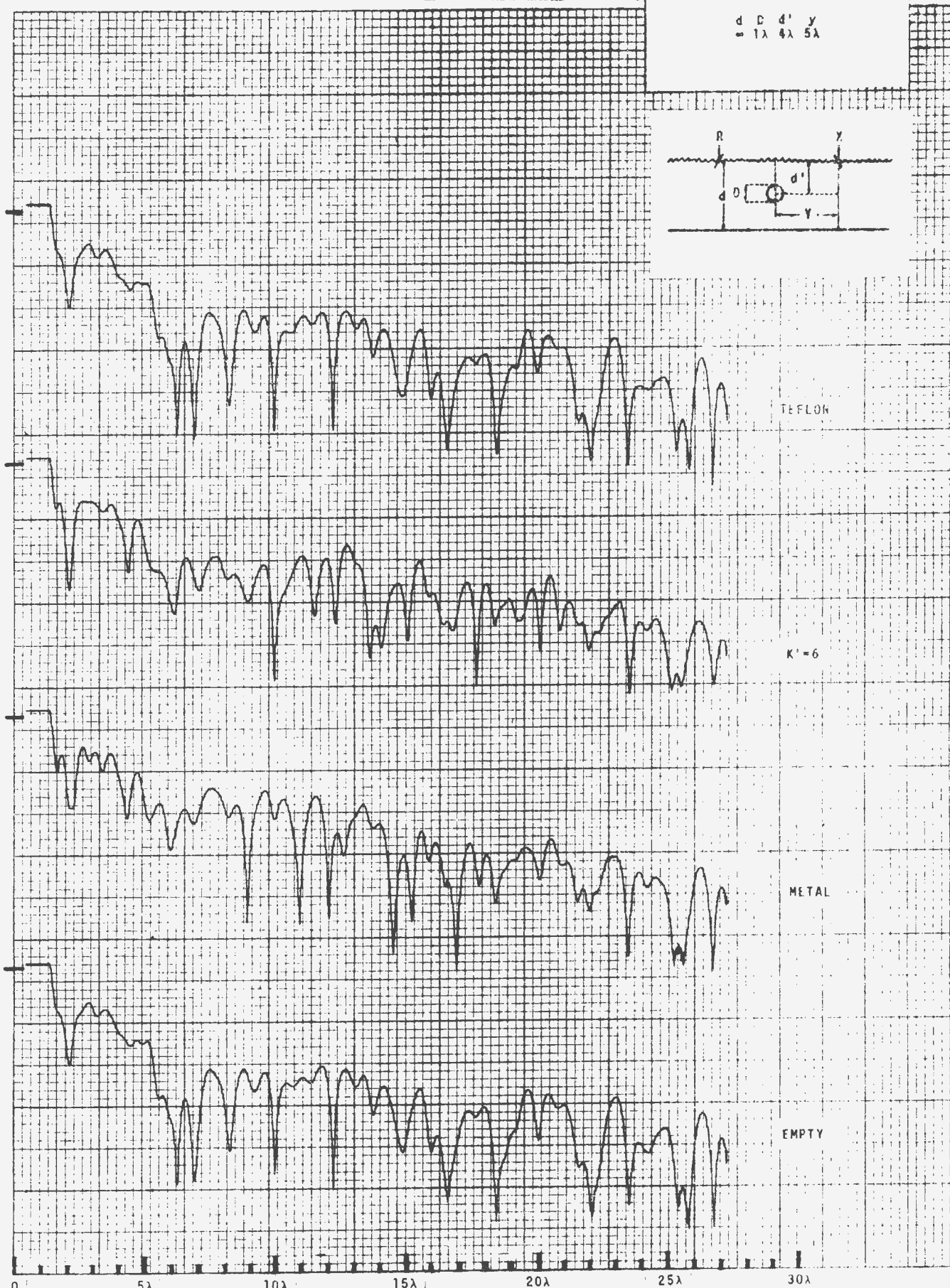
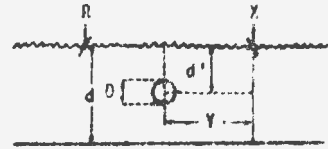


Figure D-12

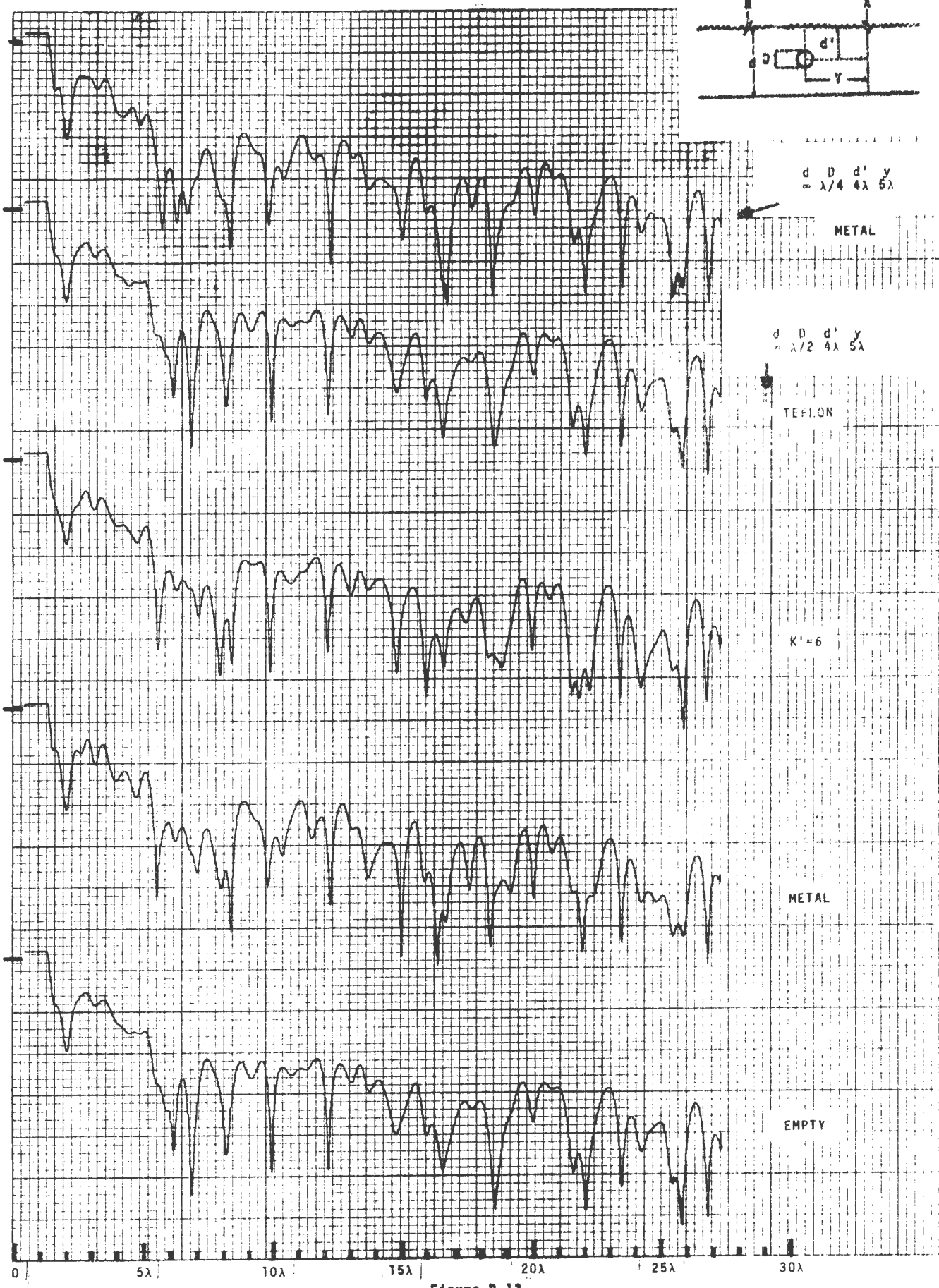
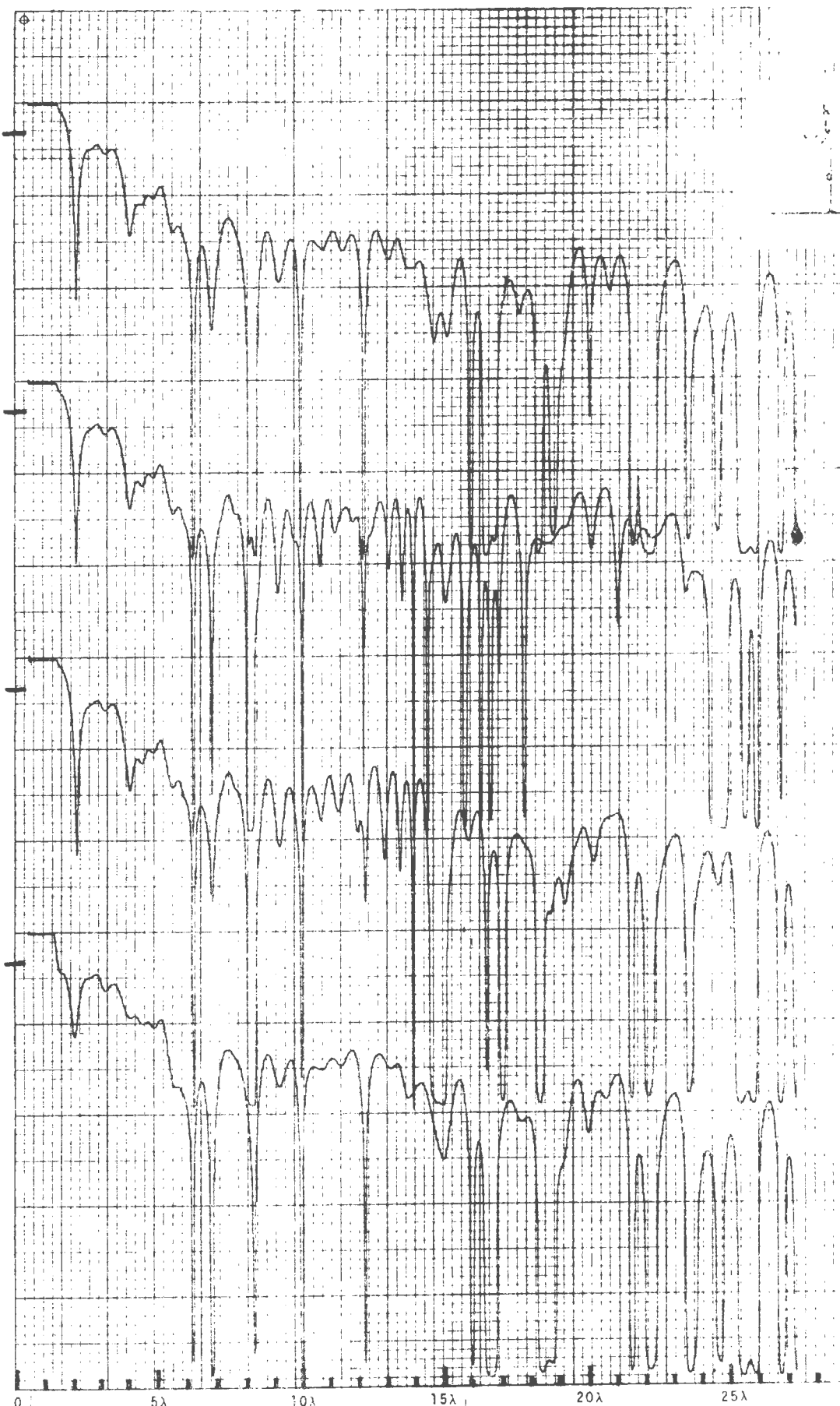
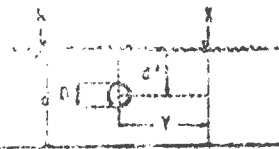


FIGURE 2-19

0 0 d' y
3λ 2λ 10λ



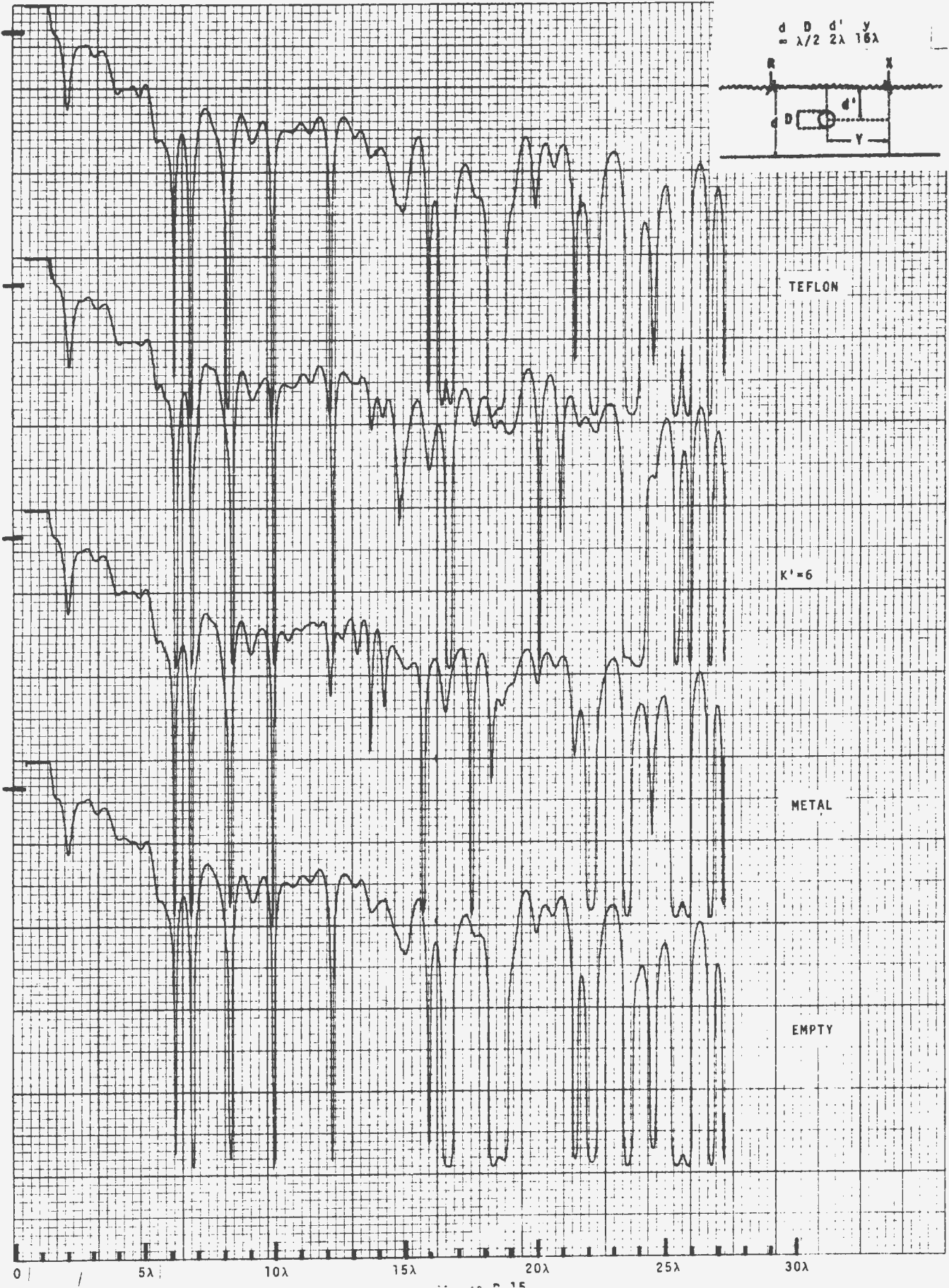
TEFLON

$K' = 6$

MLTAI

EMPTY

0 5λ 10λ 15λ 20λ 25λ 30λ

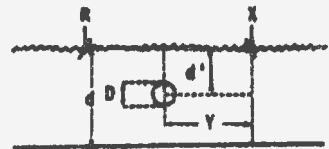


$$d = \lambda/2$$

$$D = 2\lambda$$

$$d' = 1.6\lambda$$

$$y = \lambda$$



TEFLON

$K' = 6$

METAL

EMPTY

0 5λ 10λ 15λ 20λ 25λ 30λ

$$\begin{matrix} d & D & d' & y \\ = & 1\lambda & 2\lambda & 16\lambda \end{matrix}$$

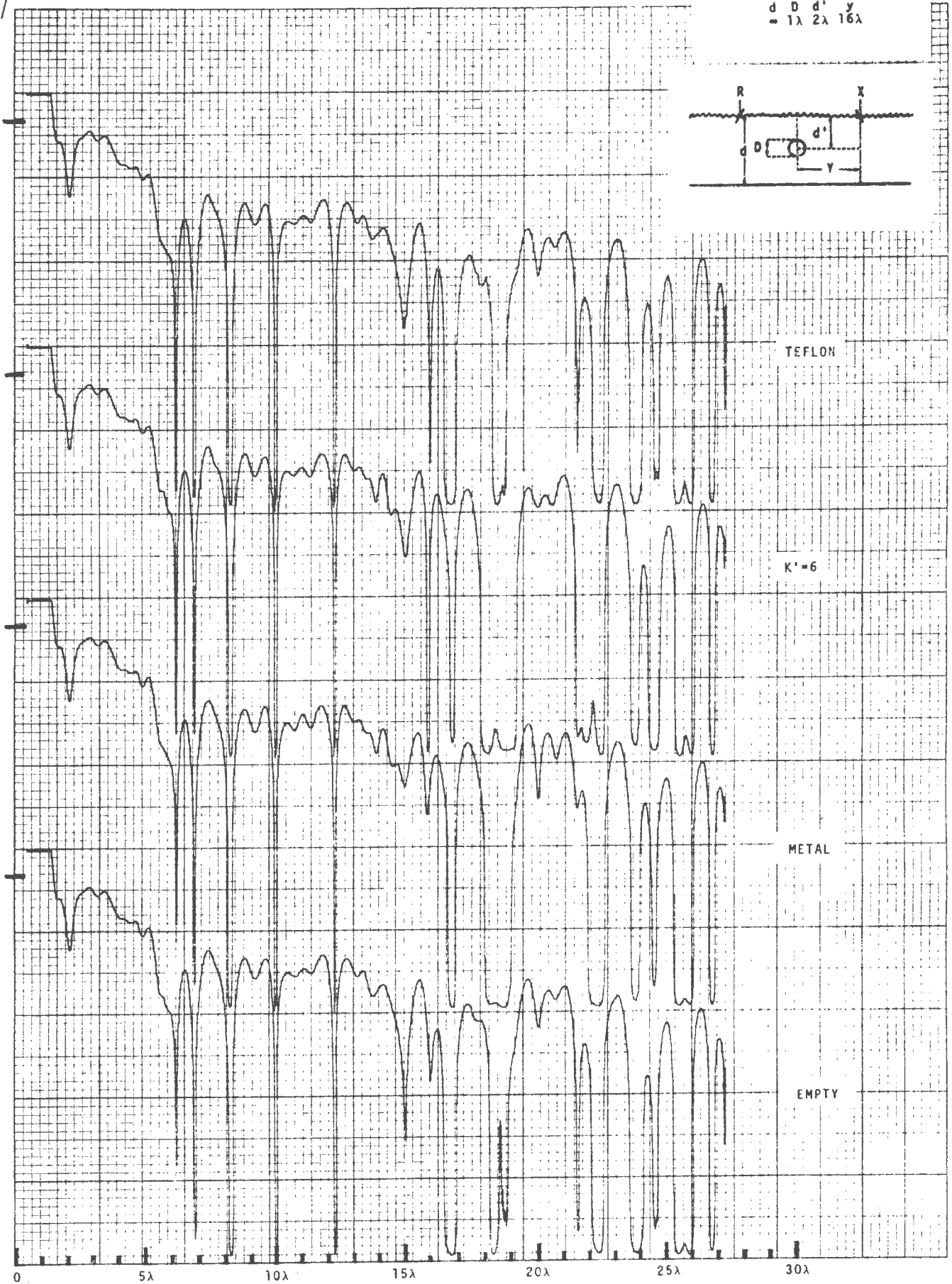
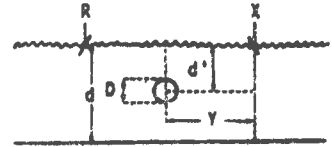
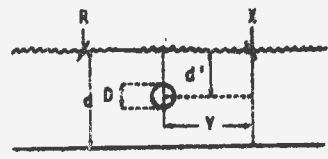
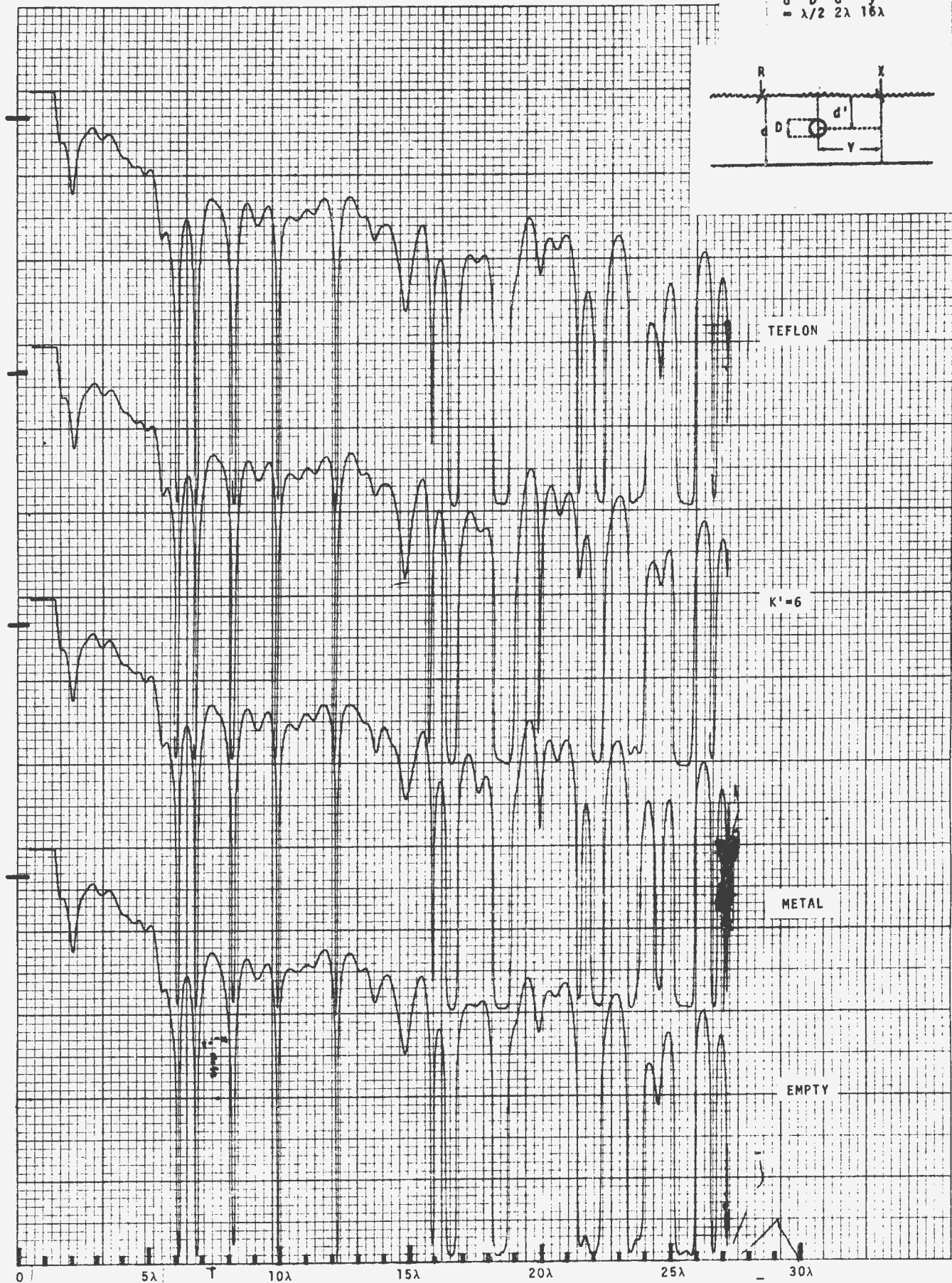


Figure D-16

$$\frac{d}{\lambda} = \frac{D}{2\lambda} = \frac{d'}{16\lambda}$$



Small diameter waveguide - 1/4" 7-26-72



0 5λ 10λ 15λ 20λ 25λ 30λ

Figure D-17

APPENDIX E
DYE-3 TRAVERSES

DYE-3 WASTE DUMP SIMULATION
RCVR DIODE POWER vs RCVR-XTR SEPARATION

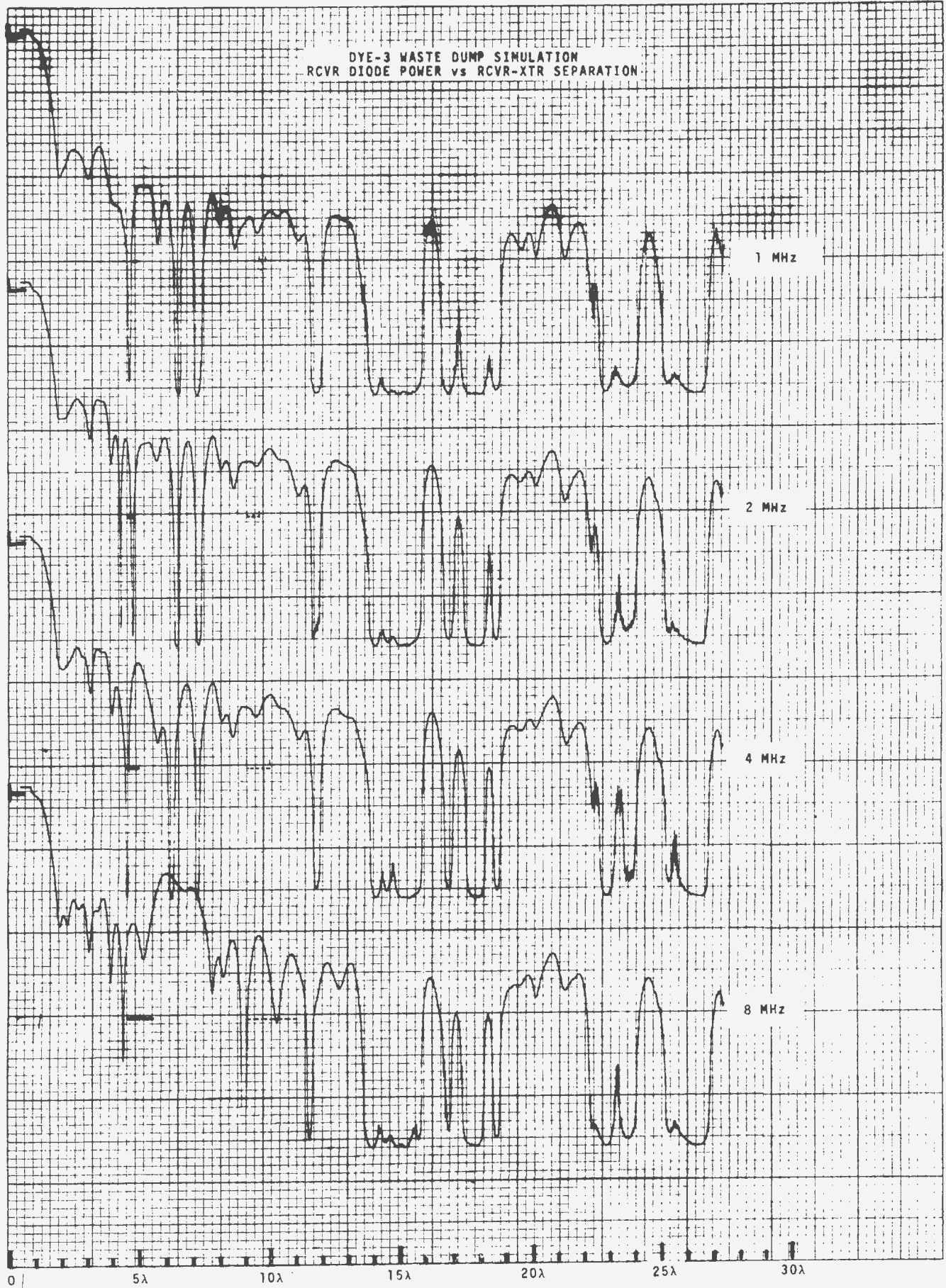


Figure E-1

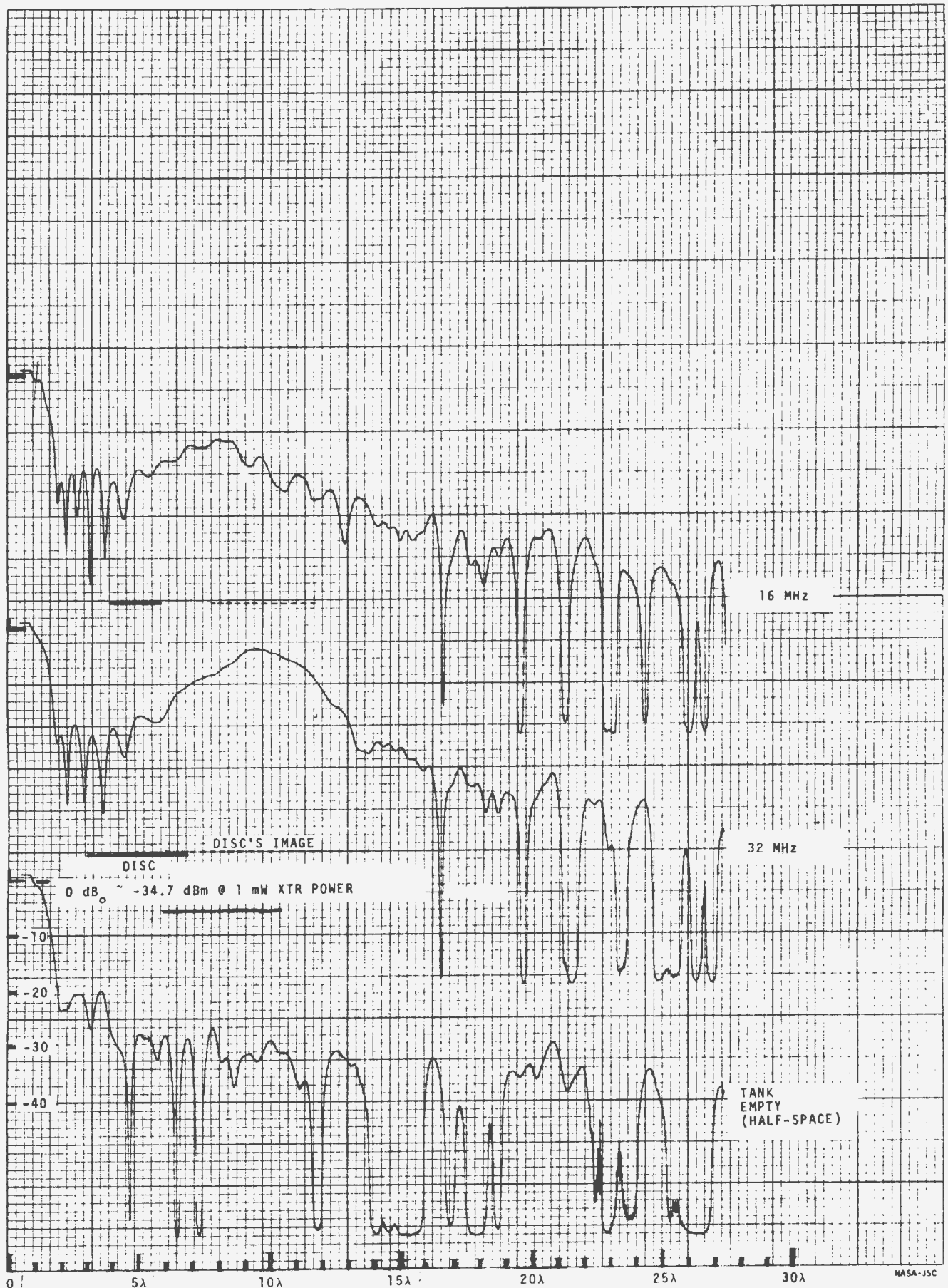


Figure E-2

THE SURFACE ELECTRICAL PROPERTIES EXPERIMENT

GENE SIMMONS

Dept. of Earth and Planetary Sciences, MIT, Cambridge, Mass. 02139, U.S.A.

DAVID W. STRANGWAY

Geophysics Branch, NASA-Manned Spacecraft Center, Houston, Tex. 77058, U.S.A.

L. BANNISTER and R. BAKER

Laboratory for Space Experiments, Center for Space Research, MIT, Cambridge, Mass. 02139, U.S.A.

D. CUBLEY

*Engineering and Development Directorate, NASA-Manned Spacecraft Center,
Houston, Tex. 77058, U.S.A.*

G. LATORRACA

Dept. of Earth and Planetary Sciences, MIT, Cambridge, Mass. 02139, U.S.A.

and

R. WATTS

*Dept. of Physics, University of Toronto, Toronto, Canada, and Lunar Science Institute,
Houston, Tex. 77058, U.S.A.*

Abstract. The surface electrical properties experiment is presently planned for Apollo 17. It uses two orthogonal, electric dipole antennas laid on the surface, each 70 m long (tip-to-tip), to transmit at frequencies of 1, 2.1, 4, 8.1, 16 and 32.1 MHz. The signals are received by three mutually perpendicular coils mounted on the lunar Rover which traverses away from the transmitter. Information from the Rover navigation system is also recorded so that it will be possible to construct profiles at each frequency as a function of distance from the transmitter and for each transmitter and each receiving coil. Interferences between waves propagating just above and just below the surface will give a measure of the dielectric constant and loss tangent of the upper layer. Reflections from either layers or lateral inhomogeneities can also be detected and studied.

One version of the system has been constructed and tested on the Athabasca glacier. Analysis of the results shows that at 32 MHz, 16 MHz and 8 MHz scattering dominates the results suggesting that scattering bodies of 35 m or less in size are numerous. At 4 MHz, the ice was found to have a dielectric constant of about 3.3 and a loss tangent of 0.10, both values typical for ice. The depth of the ice was found to be around 265 m, a value typical for this glacier. At 2 MHz and 1 MHz the losses are much higher but the dielectric constant is still clearly determined as 3.3.

1. Introduction

In this paper we describe the general nature of the Surface Electrical Properties experiment now planned for the Apollo 17 mission. This experiment has been designed specifically to operate in the lunar environment where there is believed to be essentially no moisture present. Electromagnetic experiments on the Earth have a long history in the exploration for minerals, but because of the presence of moisture in the pore spaces in rocks resistivities greater than about $5 \times 10^4 \Omega\text{-m}$ are rare. The net result is that almost all work on the Earth has concentrated on using audio frequencies to get significant depths of penetration. The response parameter for electromagnetic waves is given as $(\epsilon\mu\omega^2 + i\sigma\mu\omega)^{1/2}$ where

ϵ - dielectric constant - farads/m.

μ - magnetic permeability - henries/m.

ω - rotational frequency ($= 2\pi f$ - frequency in Hz)

σ - conductivity - mhos/m.

For most Earth applications $\sigma\mu\omega \gg \epsilon\mu\omega^2$ so that the problem becomes entirely one of diffusion and no propagation takes place. In environments where the resistivity is very high, however, $\epsilon\mu\omega^2 \gg \sigma\mu\omega$ and the problem becomes one of propagation with all the attendant phenomena of diffraction, interference, etc. Early attempts to penetrate the Earth at radio frequencies met with little success simply because the penetration depth (given by $\sqrt{(2/\sigma\mu\omega)}$ for the diffusive case and $(3 \times 10^8)/(\pi f\sqrt{K \tan \delta})$ for the propagation case where K = relative dielectric constant and $\tan \delta$ = loss tangent) was too small. In recent years, experiments on glaciers have shown that it is possible to get radio-frequency reflections from very great depths (Rinker and Mock, 1967; Harrison, 1970) and radar has been used to map the outline of salt domes (Unterberger *et al.*, 1970; Holster *et al.*, 1970). The reason for success in penetrating significant distances in these two media is that they both have very high resistivities, on the order of $10^{+6} \Omega\text{-m}$ or more. Lunar soils and rocks have been shown to have very high values of resistivity and accordingly it would appear that the lunar environment is particularly suited to depth sounding using radio frequencies (Strangway, 1969; St. Amant and Strangway, 1970; Katsube and Collet, 1971; Chung *et al.*, 1971).

The properties of typical dielectrics have been reviewed by many workers but for those of interest to us, the dielectric constant ranges from about 3 for powders to about 10 for solids. Equally important is the general phenomenon that the loss tangent is nearly independent of frequency provided there are no relaxations. This was indeed found to be the case for the lunar samples (Katsube and Collet, 1971; Chung, 1972) so that the lunar materials behave precisely like those earth rocks which have no hydrous minerals (St. Amant and Strangway, 1970). The loss tangent may be converted to a variety of equivalent parameters. Since it is a measure of the imaginary part of the dielectric constant it is also a measure of the real part of the conductivity ($\tan \delta = K\omega \sigma_{app}$). If there is a finite conductivity, however, this can be converted to an equivalent penetration depth ($\sqrt{(2/\sigma_{app} \mu\omega)}$). For a frequency-independent loss tangent this relation is illustrated in Figure 1. Typically, the lunar rocks have values of $\sqrt{(K \tan \delta)}$ of about 0.05 to about 0.2 and the soils have values less by a factor of about 4 or 5 (see Table I). At 1 MHz the penetration depth in lunar materials is typically a few kilometers while at 30 MHz it is typically a few hundred meters.

The experimental results to be discussed in this paper were measured on glaciers which is almost the only environment on Earth in which a suitable analogue experiment can be conducted. The analogy is not perfect, since ice has a relaxation loss that occurs in the audio frequency part of the spectrum. The tail of this relaxation spectrum still affects the loss tangent in the range of frequencies of importance in the Surface Electrical Properties experiment with the result that the loss tangent decreases from 1 MHz to 32 MHz (Evans, 1965) in such a way that the product $f \cdot \tan \delta$ is approximately constant. The precise value is temperature-dependent but typically it has values of around 0.2 to

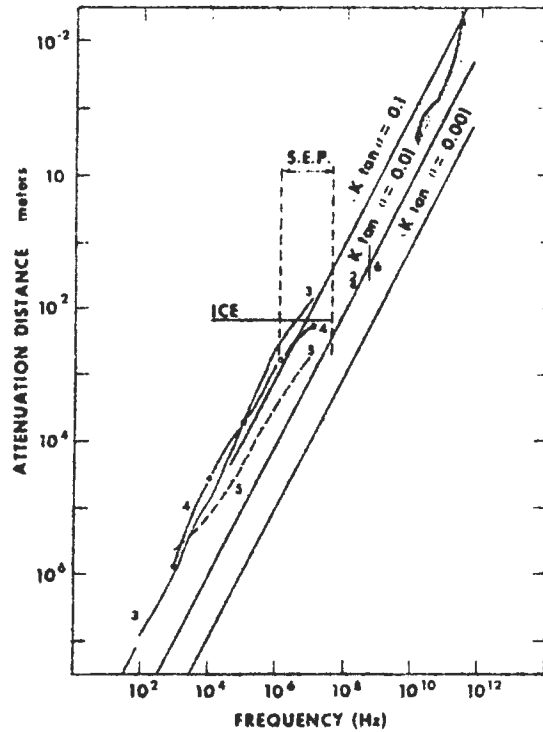


Fig. 1. Attenuation distance as a function of frequency from lunar samples and from remote lunar sensing. Straight lines show theoretical values for typical dielectrics which have a loss tangent which is independent of frequency. (1) Weaver (1965) - thermal emission and radar observations; (2) Tyler (1968) - bistatic radar; (3) Chung *et al.* (1971) - lunar igneous sample 12002; (4) Collett and Katsube (1971) - lunar breccia sample 10065; (5) Collett and Katsube (1971) - lunar fines sample 10084; (6) Gold *et al.* (1971) - lunar fines.

0.5, if the frequency, f , is given in MHz. This effect is illustrated schematically in Figure 1: the attenuation depth in ice is essentially frequency-independent with a value of a few hundred meters. Ice therefore, is not an optimum analogue for what we expect in the lunar case, but at least it is fairly transparent over part of the frequency range.

2. Experiment Concept

The concept of the SEP experiment is illustrated in Figure 2. An electric dipole transmitter is laid on the surface and transmits at six frequencies from 1 MHz to 32 MHz. Energy is propagated in three ways: (a) above the surface with the speed of light in vacuum, (b) below the surface along the interface with the velocity of light in the medium and (c) by reflection from layering or other inhomogeneities in the surface. These various waves interfere with each other as a function of position along the surface. Interference between the surface and subsurface wave gives a measure of the

TABLE I
Dielectric properties of lunar samples and of ice

		Rocks				Soil		Ice (near 0°C)
		10017	10065	12002	12002	10084	12070	
Dielectric constant	1 MHz	8.8	7.3	8.3	7.8	3.8	3.0	3.2
	10 MHz	9.3	7.3	8.3	8.8	3.8	3.0	3.2
	30 MHz	-	-	-	-	-	-	3.2
Loss tangent	1 MHz	0.075	0.063	0.051	0.056	0.0175	0.025	0.3
	10 MHz	0.021	0.019	0.0158	0.0114	0.0089	0.0053	0.03
	30 MHz	-	-	-	-	-	-	0.01

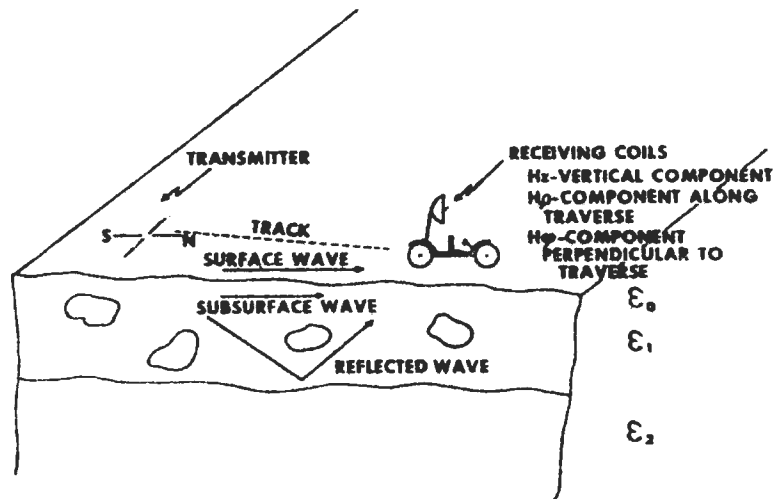


Fig. 2. Sketch illustrating operation of surface electrical properties experiment and various waves expected to be transmitted through and above lunar surface.

dielectric constant according to the formula $\epsilon = (1 + \Delta K)^2$ where ΔK is the interference frequency. The rate of decay of the interferences gives a measure of the loss tangent. The receiver is mounted on the Rover and measures the field strength as a function of range so that the interference frequency can be measured. In addition, reflections from subsurface features can be detected as they interfere with the other waves. Transmission is done sequentially from a pair of orthogonal dipoles and the receiver consists of three orthogonal loops to measure the field strength of three independent components.

3. Instrumentation

Detailed descriptions of the experiment hardware are planned for future papers so we will give only a brief description of the hardware in this section.

The transmitter is powered by solar cells and transmits sequentially at 1, 2.1, 4, 8.1, 16 and 32.1 MHz, each transmission at each frequency from one antenna lasting for 101.25 ms. The pair of orthogonal dipoles, each of which is 70 m long (tip-to-tip), are powered alternately. These dipoles are half-wave dipoles at 2.1, 4, 8.1, 16 and 32.1 MHz. A pair of wires is used for the experiment and a set of traps and suppressors are built into the wires such that the transmitter 'sees' a half-wave resonant dipole at each of the frequencies. At 1 MHz the antenna is not a half-wave dipole but loading is used to compensate this. Precise matching of the antenna impedance with that of the Moon is difficult because of our ignorance of the exact value of the dielectric constant but we have designed the antenna for a value of 3.3 which is consistent with the bistatic radar results of Howard and Tyler (1972). On the ice, the antenna can be adjusted to make the antenna optimum at each frequency. The power radiated is 3.75 W at 1 MHz and 2.0 W at the other frequencies. The transmission sequence is shown in Figure 3 and provides about 10 samples per wavelength per component at 2.1, 4, 8.1, 16 and 32.1 MHz and 20 samples per wavelength per component at 1 MHz at a vehicle speed of 8 km h⁻¹.

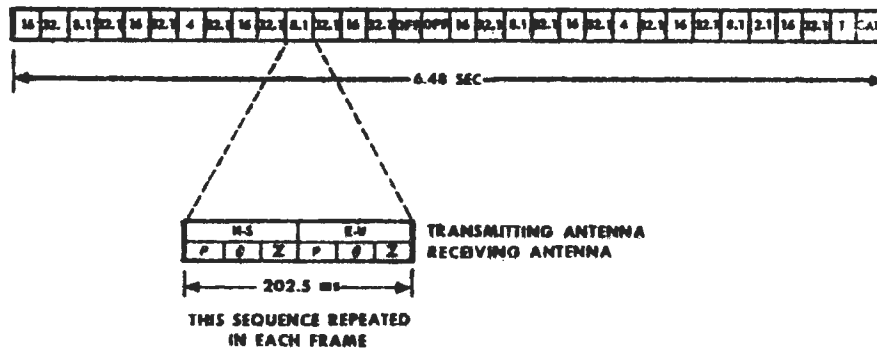


Fig. 3. Format: two frames marked OFF are used to monitor the background external noise at all frequencies and to measure the internal noise. The frame marked cal. is used for synchronizing transmitter and receiver and to record the internal temperature of the receiver.

The receiving antenna consists of three orthogonal coils which are mounted on the Rover. The reception of each coil is examined for 33 ms and in sequence. The signals are demodulated in the receiver and are frequency-coded by a voltage controlled oscillator. This oscillator operates over the frequency range of 300 to 3000 Hz, corresponding to a dynamic range in the instrument of -35 dbm to -135 dbm. This large dynamic range allows accurate field strength recording over a broad distance range from the transmitter. The output of the voltage-controlled oscillator is recorded on a recoverable tape recorder. With six transmission frequencies, two alternate transmitting antennas and three receiving antennas we record a total of 36 separate pieces of information.

In the lunar system, navigation data will be recorded in two different ways. On each

wheel there is a pulse generated every 0.245 m. We will record every second pulse from two separate wheels, for redundancy and as a check on wheel slippage. This means that the traverse can be reconstructed in increments of about 0.5 m. These same wheel pulses and a gyro-stabilized compass provide the basic input to the Rover navigation computer which displays range, bearing, heading, and distance travelled. The bearing and heading are computed in increments of 1° and the range and distance travelled are computed in increments of 100 meters. We will record the bearing every time it changes by $\pm 1^\circ$ (except in the immediate vicinity of the LM) and as a redundant check we will record the range in 100 m increments. The range is computed using the third slowest wheel, so we will have a separate measure of the wheel slip and an internal range check at 100 m increments. Finally, since there may be errors that will accumulate in both the range and bearing measurements we will use the known stop points to correct the traverse. Since these stops are likely to be in increments of one or two kilometers, we will have frequent updates to our traverse map. On the basis of this information we expect to be able to reconstruct the traverse to an accuracy of about 1% of the range and to reconstruct range *differences* over a few hundred meters to about 1 m or better.

For the glacier tests, we have used a simple odometer circuit connected to one of the drive-wheels which generates signals every 1.5 m. These signals are recorded independently on the tape recorder. These pulses have been used to determine the horizontal scale so that all the data discussed in this report have been plotted as field strength versus range.

4. Theoretical Work

We are reporting elsewhere the theory behind this experiment (Annan, 1972; Cooper, 1972; Sinha, 1972a, b, c) and have published a paper on some of the most preliminary glacier results, (Rossiter *et al.*, 1972). We will not, therefore, review all these results in the present paper. Rather we will only summarize a few points which are pertinent to the data analysis.

The transmitting antennas are crossed dipoles; in the simplest case the traverses are run broadside to one dipole and off the end of the other. The geometry is shown in Figure 2. The fields H_x and H_y from the broadside antenna are both maximum-coupled and can be expected to show the interference patterns which are the basis of the experiment. Studies of the antenna patterns for these components show that the power above the surface is comparable to the power just below the surface so that significant interference between these two waves can be expected. In the case of the H_z component off the end of the transmitter, however, power is transmitted above the surface but very little power is transmitted just below the surface. There is little interference, so this component is not as useful for determining the dielectric constant and loss tangent.

The other components (H_y and H_z broadside and H_x endfire) are minimum-coupled to the respective transmitters. These components are consequently useful in looking for energy scattered by either surface irregularities or subsurface inhomogeneities.

The radiation pattern of an electric field dipole at the interface between free space and

a semi-infinite dielectric medium contains a single lobe broadside of the antenna and two lobes endfire of the antenna as shown by Cooper (1972). The broadside or Transverse Electric (TE) radiation pattern and the endfire or Transverse Magnetic (TM) radiation pattern are illustrated in Figure 4 for a dipole over ice. The dipole is colinear with the X -axis in Cartesian coordinates. The angle between the vertical and the peak of the lobe is given by $\sin \beta = \sqrt{(\epsilon_0/\epsilon_1)}$ where ϵ_0 is the dielectric constant of free space

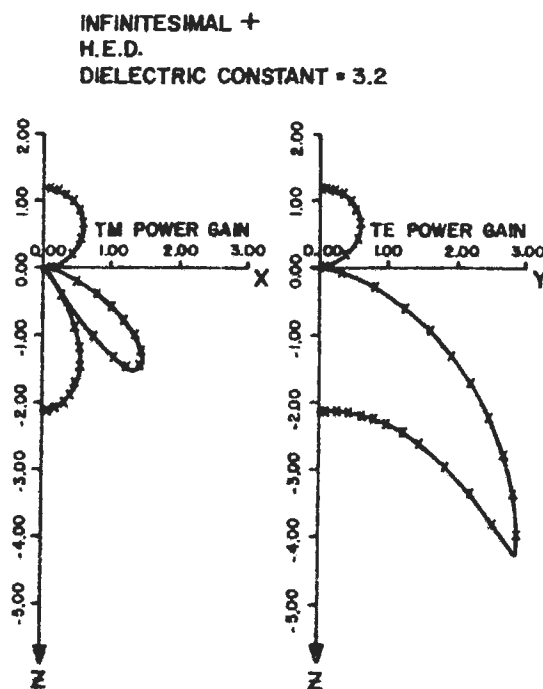


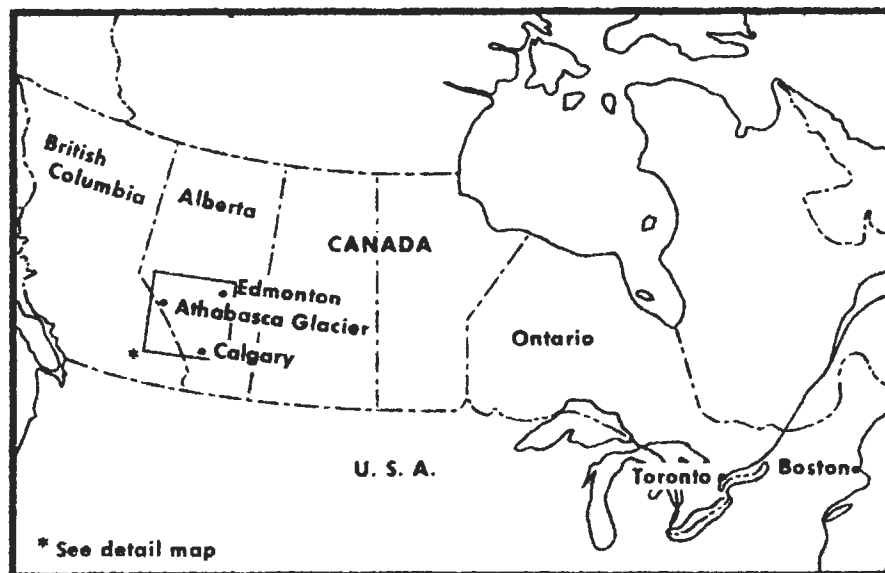
Fig. 4. Radiation pattern of horizontal electric dipole over ice. The dipole extends along the x -axis.

and ϵ_1 is the dielectric constant of the medium. In the case of ice where the ratio ϵ_0/ϵ_1 is given by $1/3.2$ this angle is about 34° . The energy radiated downwards into the medium does not appear at the surface unless there is a reflecting horizon at depth. The presence of a horizontal reflector at depth d causes energy to appear at the surface at a distance $r \approx 2d \tan \beta$. For ice the depth to a reflector is given as $d = 0.8 r$. In principle it is therefore possible to determine the dielectric constant and the loss tangent from the near-field interferences of the H_ϕ and H_x components from the broadside antenna. Reflections can be studied by the H_ϕ and H_x components from the broadside antenna and by the H_ϕ component from the endfire antenna.

5. Athabasca Glacier Data

Most of our work to date has been concentrated on the Athabasca glacier in western

Canada (Figure 5a). It is a well-studied glacier and is very accessible. Previous studies based on gravity (Kanasewich, 1963), seismology and drilling (Paterson and Savage, 1963), and electrical sounding (Keller and Frischknecht, 1961) have been made and a map of approximate ice thickness is shown in Figure 5b. We have reported on earlier preliminary results (Rossiter *et al.*, 1972) and in this paper restrict ourselves to one set of data taken in the summer of 1971 with the evaluation model of the flight equipment which was described in this report. The profile discussed is shown in Figure 5b and is marked by the transmitter at the southern end. The ice thickness is approximately



GENERAL LOCATION MAP

Figs. 5a-b. (a) Location map of the Athabasca glacier. (b) Sketch map of the Athabasca glacier, showing the location of the profile discussed in this report. Contours are the generalized thicknesses as determined from previous drilling and seismic studies.

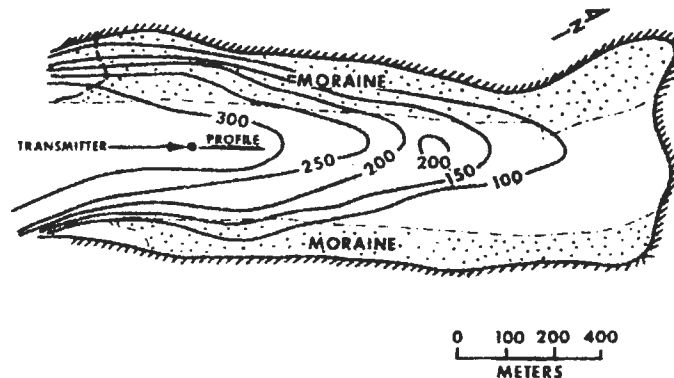


Fig. 5b.

300 m. The line was run from north to south and then repeated south to north with identical results.

The field strength data for all components at 4 MHz are shown in Figure 6 plotted as a logarithm of the power versus the distance in wavelengths. The length of the traverse was about seven wavelengths. Of particular interest and typical of all our runs at 4, 2 and 1 MHz is the fact that H_x and H_y from the broadside antenna and H_ϕ and H_θ from the endfire antenna are large and fairly smooth varying functions. In particular the H_θ endfire component is quite smooth showing no surface and subsurface wave interference. H_x broadside, however, shows sharp nulls at about $1\frac{1}{2}\lambda$, $2\frac{1}{2}\lambda$

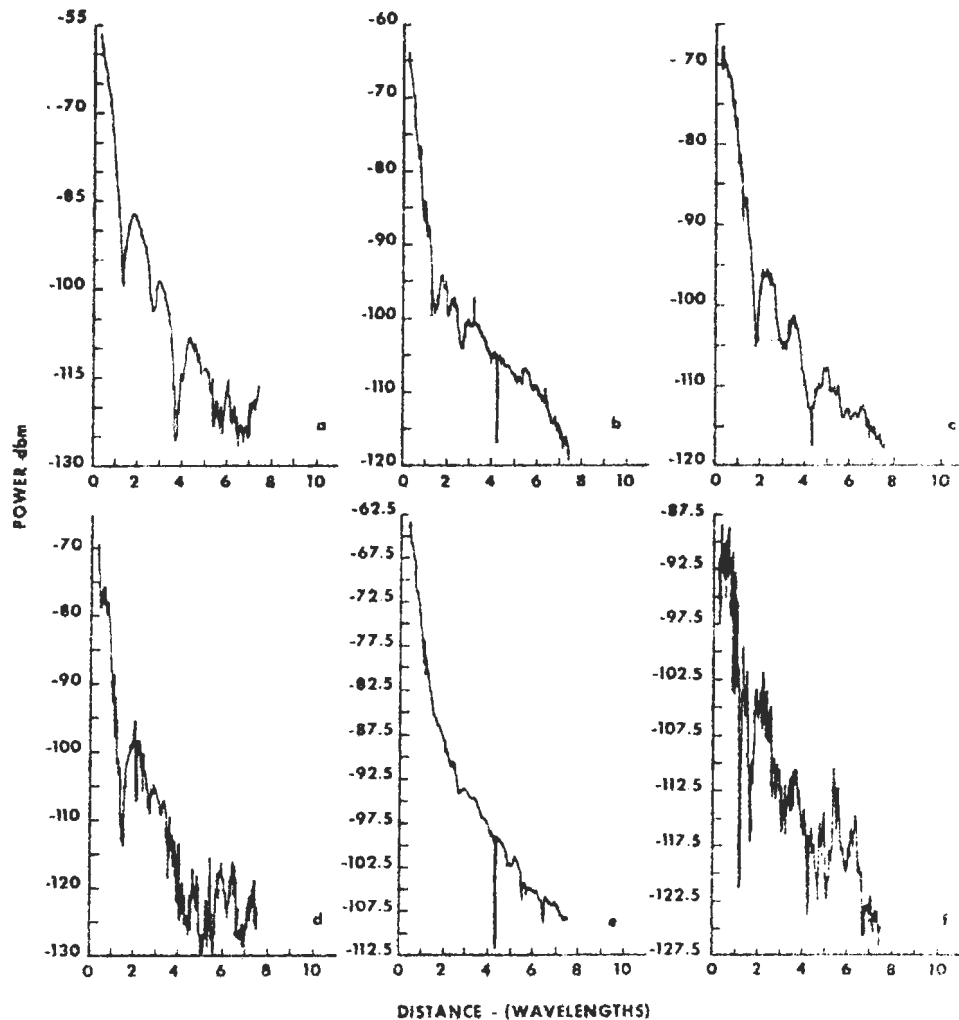
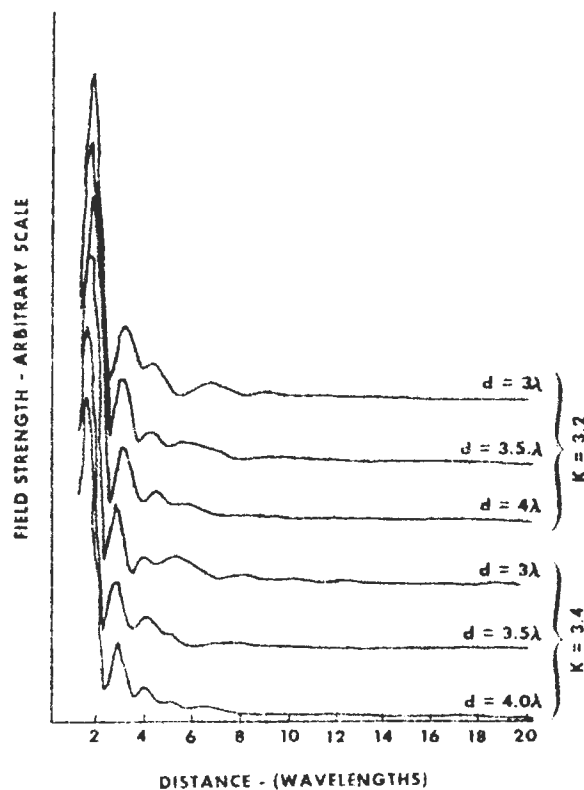


Fig. 6. Complete set of data at 4 MHz showing H_θ , H_ϕ and H_x from both the E-W (broadside) and the N-S (endfire) antenna. (a) E-W transmitter, H_x ; (b) E-W transmitter, H_ϕ ; (c) E-W transmitter, H_θ ; (d) N-S transmitter, H_x ; (e) N-S transmitter, H_ϕ ; (f) N-S transmitter, H_θ .

and $3\frac{1}{2}\lambda$. These nulls are the interferences generated from the surface and sub-surface waves as shown in Figure 7. Using the 4 MHz data, comparison with theoretical curves leads to a dielectric constant of about 3.3 and a loss tangent of 0.10.

Evidence in this particular subset of the data for reflected energy is not very strong but the simple curve is clearly disturbed at a distance of about 5 wavelengths from the source. We have compared this curve to a variety of theoretical curves and it appears that a depth of about 3.5 wavelengths for a reflector is indicated as shown in Figure 7b. This fact suggests a depth to the bottom of the ice of around 265 m. This depth is somewhat less than the predicted depth of about 300 m but the agreement is relatively good and it is possible that the ice thickness varies locally.

The other components are generally weaker and show very little character. This relation is to be expected for the minimum-coupled components and suggests that scattering at 4MHz (75 m) is minimal. At higher frequencies scattering becomes more significant and at 32 MHz and at 16 MHz the main structure is that due to scattering.



Figs. 7a-b. H_z component from E-W antenna. (a) theoretical curves showing effect of varying depth to the reflector and dielectric constant with a constant loss tangent of 0.10. (b) field data and theoretical curves showing effect of varying loss tangent and dielectric constant for a constant depth of 3.5 wavelengths.

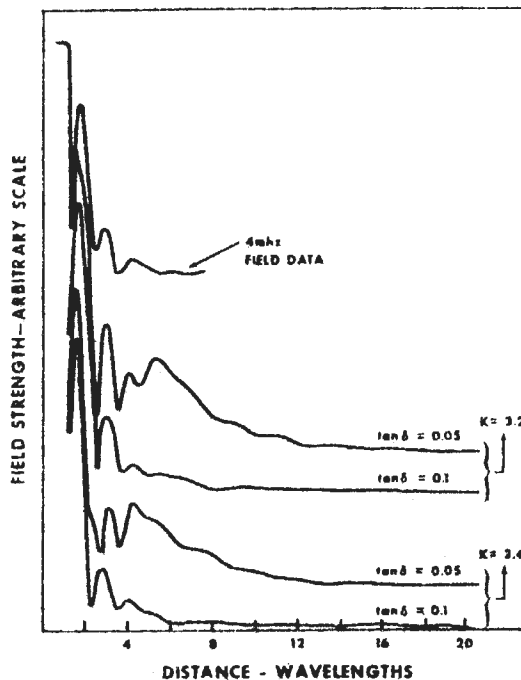


Fig. 7b.

In Figure 8 a set of data for all three components from the E-W transmitting antenna at 16 MHz is shown. The features to note in this plot are twofold. First, all components are about equal suggesting that as much energy is scattered into the minimum-coupled H_y component as is present in the maximum-coupled H_x and H_z components. Second is the erratic behaviour of the field components, which show a wide range of rapid variations on a scale that is smaller than a wavelength. We conclude therefore that scattering is a dominant process at 16 MHz, important at 8 MHz and relatively unimportant at 4 MHz. This observation suggests that the size of scatterers is typically about equal to the wavelength at 8 MHz which is about 35 m.

This result seems reasonable because this valley glacier is heavily crevassed and the typical size for the vertical and lateral extent of crevasses could be typically 30 m. These results are comparable to those of Gudmandsen and Christensen (1968) who had trouble doing airborne radio sounding at 35 MHz over valley glaciers in West Greenland. They attribute at least part of their difficulties to the presence of crevasses in the valley glaciers.

6. Conclusions

The radio frequency interference technique developed for the Apollo lunar program will be useful for measuring the dielectric constant and loss tangent of the upper layers of the moon in the frequency range from 1 MHz to 32 MHz. It will also be useful for

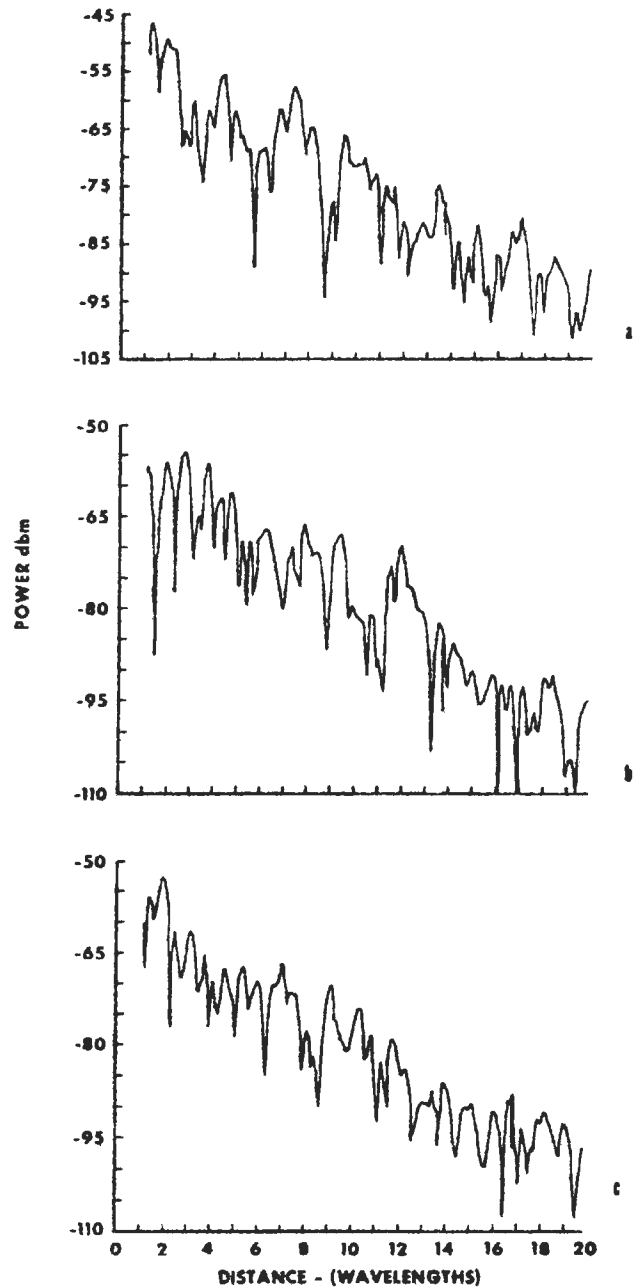


Fig. 8. Typical set of data taken at 16 MHz to illustrate scattering effect of glacier. All components H_x , H_y and H_z from the E-W transmitter are about equal.

detecting layering in the range from a few tens of meters to a few kilometers depending on the nature of the layers and of the electrical properties. In addition, it is likely to yield information on the presence of scattering bodies. This experiment has been tested on the Athabasca glacier. Here it was possible to measure the dielectric constant of ice as 3.3 and the loss tangent at 4 MHz as 0.10 giving a value of 0.4 for $f \cdot \tan \delta$. The depth of the ice was estimated to be about 265 m, a value in rough agreement with other determinations.

Acknowledgements

We would like to acknowledge permission from the Jasper National Park authorities to work on the Athabasca glacier.

This work was conducted under NASA Contract No. NAS 9-11540 at MIT and under a subcontract at the University of Toronto.

References

- Annan, A. P.: 1970, Master of Science thesis, Department of Physics, University of Toronto.
- Annan, A. P.: 1972, *Geophysics*, submitted for publication.
- Chung, D. H.: 1972, this volume, p. 276.
- Chung, D. H., Westphal, W. B., and Simmons, Gene: 1971, *Proceedings of the Second Lunar Science Conference 3*, pp. 2381-90, MIT Press, Cambridge, Mass.
- Cooper, William W.: 1972, 'TE/TM Patterns of Hertzian Dipole in Two- or Three-Layered Medium', submitted for publication.
- Evans, S.: 1965, *J. Glaciol.* **5**, 773-92.
- Gudmandsen, P. and Lintz Christensen, E.: 1968, 'Radioglaciology', interim report for EGIG of measurements in Greenland, May 1968, Laboratory of Electromagnetic Theory, The Technical University of Denmark, Lyngby, D 77.
- Harrison, C. H.: 1970, *Geophysics* **35**, 1099-1115.
- Holser, W. T., Brown, R. J. S., Roberts, F. A., Fredriksson, O. A., and Unterberger, R. R.: 1970, 'Radio Frequency Propagation in Salt Domes 2. Pulse Reflections from Salt Flanks', presented at SEG 40th Annual International Meeting, New Orleans.
- Howard, H. L. and Tyler, G. L.: 'Bastatic-Radar Investigation', Apollo 15 Preliminary Science Report, NASA SP 289, 1972.
- Kanasewich, E. R.: 1963, *J. Glaciol.* **4**, 617-31.
- Katsube, T. J. and Collett, L. S.: 1971, *Proceedings of the Second Lunar Science Conference*, Vol. 3, pp. 2367-79, MIT Press, Cambridge, Mass.
- Keller, G. V. and Frischknecht, F. C.: 1961, in G. O. Raasch (ed.), *Geology of the Arctic 2* (International Symposium), Toronto, University of Toronto, pp. 809-32.
- Paterson, W. S. B. and Savage, J. C.: 1963, *J. Geophys. Res.* **68**, 4513-20.
- Rinker, J. N. and Mock, S. J.: 1967, 'Radar Ice Thickness Profiles, Northwest Greenland', Special Report 103, U.S. Army Materiel Command, Cold Regions Research & Engineering Lab., Hanover, New Hampshire.
- Rossiter, J. R., Annan, A. P., LaTorraca, G. A., Strangway, D. W. and Simmons, G.: 1972, 'Radio Interferometry Depth Sounding, Part II - Experimental Results', submitted for publication.
- Saint-Amant, M. and Strangway, David W.: 1970, *Geophysics* **35**, 624-45.
- Sinha, Ajit K.: 1972a, 'Fields from a Horizontal Electric Dipole over a Lossy Dielectric Medium and Its Applications in the Radio-Interferometry Method, Part I - The Half-Space,' submitted for publication.
- Sinha, Ajit K.: 1972b, 'Fields from a Horizontal Electric Dipole over a Lossy Dielectric Medium and Its Application in the Radio-Interferometry Method, Part II - Layer over a Perfect Reflector', submitted for publication.

C-2

RADIO INTERFEROMETRY DEPTH SOUNDING: PART I—THEORETICAL DISCUSSION†

A. P. ANNAN*

Radio interferometry is a technique for measuring in-situ electrical properties and for detecting subsurface changes in electrical properties of geologic regions with very low electrical conductivity. Ice-covered terrestrial regions and the lunar surface are typical environments where this method can be applied. The field strengths about a transmitting antenna placed on the surface of such an environment exhibit interference maxima and minima which are characteristic of the subsurface electrical properties.

This paper (Part I) examines the theoretical wave nature of the electromagnetic fields about various types of dipole sources placed on the surface of a low-loss dielectric half-space and two-

layer earth. Approximate expressions for the fields have been found using both normal mode analysis and the saddle-point method of integration. The solutions yield a number of important results for the radio interferometry depth-sounding method. The half-space solutions show that the interface modifies the directionality of the antenna. In addition, a regular interference pattern is present in the surface fields about the source. The introduction of a subsurface boundary modifies the surface fields with the interference pattern showing a wide range of possible behaviors. These theoretical results provide a basis for interpreting the experimental results described in Part II.

INTRODUCTION

The stimulus for this work was the interest in the measurement of lunar electrical properties in situ and the detection of subsurface layering, if any, by electromagnetic methods. Unlike most regions of the earth's surface, which are conductive largely due to the presence of water, the lunar surface is believed to be very dry and, therefore, to have a very low electrical conductivity (Strangway, 1969; Ward and Dey, 1971). Extensive experimental work on the electrical properties of dry geologic materials by Saint-Amant and Strangway (1970) indicates that these materials are low-loss dielectrics having dielectric constants in the range 3 to 15 and loss tangents considerably less than 1, in the Mhz frequency range. Analysis of the electrical properties of lunar samples by Katsube and Collett (1971) indicates that the

lunar surface material has similar electrical properties.

Since electromagnetic methods commonly used in geophysics are designed for conductive earth problems, a method of depth sounding in a dominantly dielectric earth presented a very different problem. One possible method of detecting the presence of a boundary at depth in a dielectric is the radio interferometry technique, first suggested by Stern in 1927 (reported by Evans, 1963) as a method to measure the thickness of glaciers. The only reported application of the technique is the work of El-Said (1956), who attempted to sound the depth of the water table in the Egyptian desert. Although he successfully measured some interference maxima and minima, his method of interpretation of the data is open to question in light of the present work.

† Presented at the 39th Annual SEG International Meeting, September 18, 1969. Manuscript received by the Editor April 6, 1972; revised manuscript received September 22, 1972.

* University of Toronto, Toronto 181, Ontario, Canada.

© 1973 Society of Exploration Geophysicists. All right reserved.

The radio interferometry technique is conceptually quite simple. The essential features of the method are illustrated in Figure 1. A radio-frequency source placed on the surface of a dielectric earth radiates energy both into the air (or free space) above the earth and downward into the earth. Any subsurface contrast in electrical properties at depth will result in some energy being reflected back to the surface. As a result, there will be interference maxima and minima in the field strengths about the source due to waves traveling different paths. The spatial positions of the maxima and minima are characteristic of the

electrical properties of the earth and can be used as a method of inferring the earth's electrical properties at depth.

The problem chosen for study in the theoretical work was that of the wave nature of the fields about various point-dipole sources placed on the surface of a two-layer earth. The mathematical solution to this type of boundary-value problem is found in numerous references. The general problem of electromagnetic waves in stratified media is extensively covered by Wait (1970), Brekhovskikh (1960), Budden (1961), Norton (1937), and Ott (1941, 1943). Although the solu-

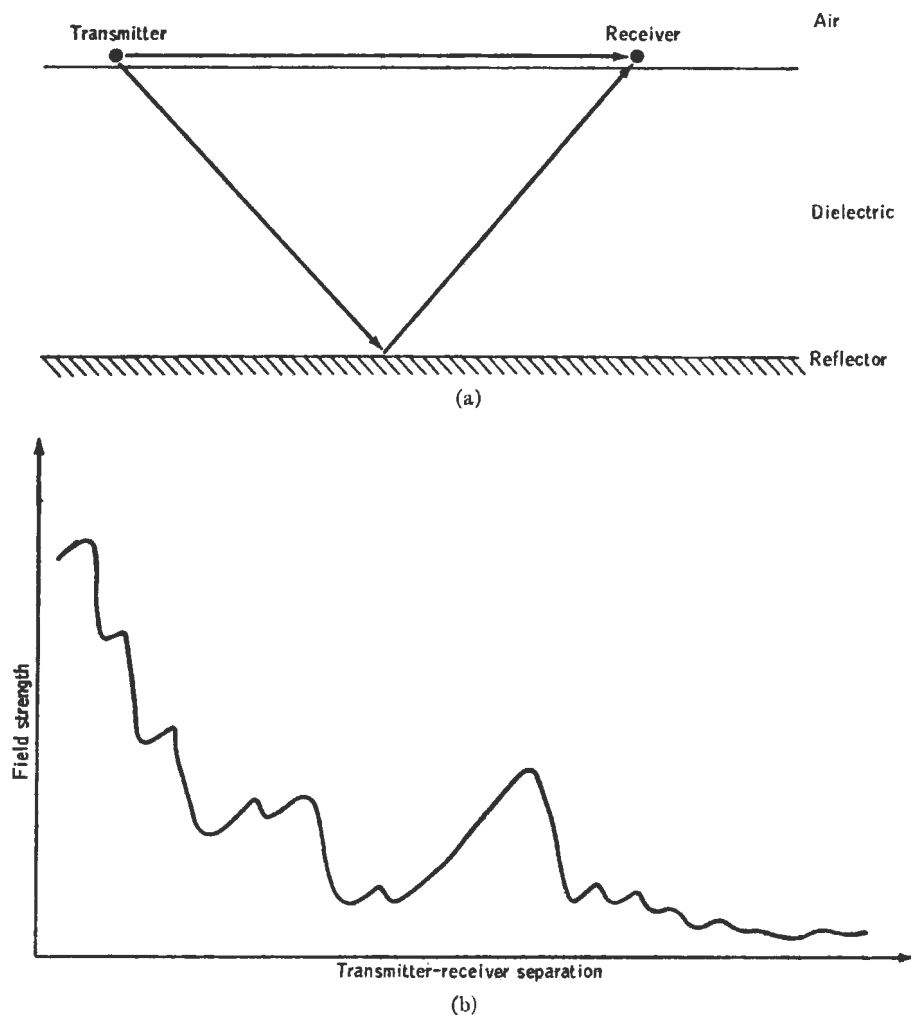


FIG. 1. (a) Transmitter-receiver configuration for radio interferometry, showing a direct wave and a reflected wave. (b) Schematic sketch of typical field-strength maxima and minima as the transmitter-receiver separation increases.

tion to the boundary-value problem can be found analytically, the integral expressions for fields cannot be evaluated exactly. In the radiation zone, approximate solutions to the integrals can be obtained by use of the theory of complex variables and special methods of contour integration. The preceding references, plus numerous others, discuss these techniques in detail. Since much of the detailed work in the mathematical development of these solutions is contained in the above references, the discussion of the solutions that follow will be primarily aimed at the radio interferometry application rather than the mathematical manipulations required to obtain them.

THEORETICAL BOUNDARY-VALUE PROBLEM

Although the various solutions of the boundary-value problem for horizontal and vertical electric and magnetic dipole sources over a two-layer earth appear in the literature, a complete and consistent tabulation of the solutions does not. Therefore, the boundary-value problem is outlined here, and a unified notation is used to express the solutions. This consistent notation is of considerable help in later discussions of the solutions.

The geometry and coordinate systems used in the boundary-value problem are shown in Figure 2. A point-dipole source is located at a height h on the z -axis above a two-layer earth, where the earth's surface is in the x - y -plane at $z=0$, and the subsurface boundary is at $z=-d$. The region $z \geq 0$ is taken as air or free space. The region $-d \leq z < 0$ is a low-loss dielectric slab, and the region $z < -d$ is a half-space of arbitrary electrical properties. These regions are denoted 0, 1, and 2, respectively. K_i and M_i are the complex dielectric constant and relative permeability of each region, respectively. For consideration of vertical dipole sources, the dipole moments are taken aligned with the z -axis; for the horizontal dipole sources, the dipole moments are taken aligned parallel to the x -axis.

The solutions are most conveniently written and discussed using the electric and magnetic Hertz vector potential notation. On the assumption of a time dependence $e^{-i\omega t}$ and linear constitutive equations in Maxwell's equations, one obtains the following expressions for the electric and magnetic fields in terms of the Hertz vectors. For electric dipole sources, the electric Hertz vector satisfies the Helmholtz equation,

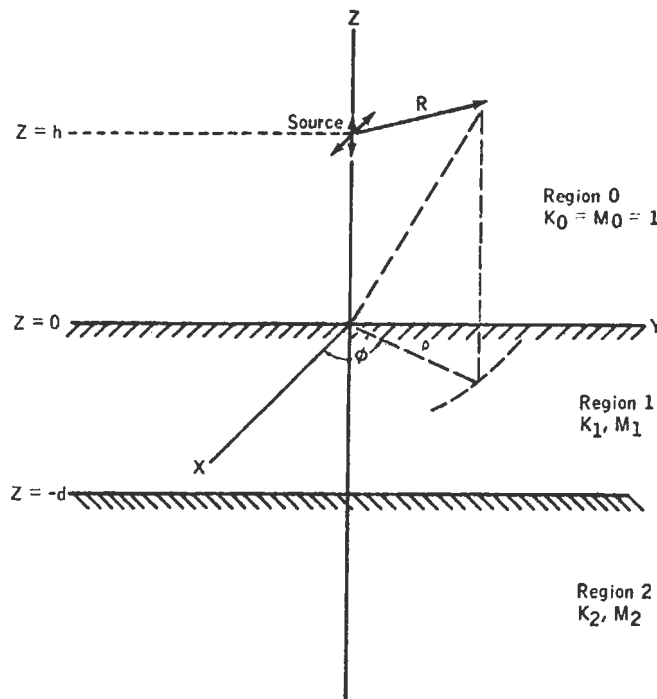


FIG. 2. Geometry of the boundary-value problem for a two-layer earth, showing notation used.

$$\nabla^2 \mathbf{\Pi} + k^2 \mathbf{\Pi} = - \frac{\mathbf{P}}{K \epsilon_0}, \tag{1}$$

with the electric and magnetic fields defined by

$$\mathbf{E} = k^2 \mathbf{\Pi} + \nabla \nabla \cdot \mathbf{\Pi}, \tag{2}$$

and

$$\mathbf{H} = - i \omega K \epsilon_0 \nabla \times \mathbf{\Pi} \tag{3}$$

where k is the propagation constant. $\omega \sqrt{KM \epsilon_0 \mu_0}$ and ϵ_0, μ_0 denote the permittivity and permeability of free space throughout. \mathbf{P} is the electric dipole moment density distribution. Similarly, for magnetic dipole sources, the results for the magnetic Hertz vector are

$$\nabla^2 \mathbf{\Pi} + k^2 \mathbf{\Pi} = - \mathbf{M}, \tag{4}$$

and

$$\mathbf{H} = k^2 \mathbf{\Pi} + \nabla \nabla \cdot \mathbf{\Pi}, \tag{5}$$

$$\mathbf{E} = i \omega M \mu_0 \nabla \times \mathbf{\Pi}, \tag{6}$$

where \mathbf{M} is the magnetic dipole moment density distribution.

The dipole sources are taken as "unit" point dipole sources located in the region $z \geq 0$. The electric dipole moment density distribution is

$$\mathbf{P} = 4\pi \epsilon_0 \delta(R) \mathbf{e}_j, \tag{7}$$

where \mathbf{e}_j is a unit vector in the z -direction for a vertical electric dipole source and in the x -direction for the horizontal dipole source. $\delta(R)$ is the three-dimensional delta function, and $R = [x^2 + y^2 + (z-h)^2]^{1/2}$. Similarly for the magnetic dipole sources,

$$\mathbf{M} = 4\pi \delta(R) \mathbf{e}_j. \tag{8}$$

In the following discussions, no distinction between the electric and magnetic Hertz vectors is made. When we refer to electric dipole sources, the electric Hertz vector is implied; for magnetic dipole sources, the magnetic Hertz vector is implied. In addition, the free-space wavelength is taken as the scaling parameter for all length measurements. In other words, a distance, denoted ρ , is in free-space wavelengths, and the true length is $W\rho$, where W is the free-space wavelength:

$$W = \frac{2\pi}{\omega(\epsilon_0 \mu_0)^{1/2}}. \tag{9}$$

This choice of scaling parameter makes all the following integral solutions dimensionless.

As shown by Sommerfeld (1909) for a half-space earth, and extended to a multilayered earth by Wait (1970), the Hertz vectors for the vertical dipole sources have only a z -component, while for the horizontal dipole sources, the Hertz vectors have both x - and z -components. The vertical dipole sources have solutions of the form

$$\Pi_z^0 = \frac{e^{ik_0 R}}{R} + \frac{1}{2W} \int_{-\infty}^{\infty} \frac{\lambda}{P_0} a_0(\lambda) e^{-P_0(Z+h)} H_0^1(\lambda \rho) d\lambda, \tag{10}$$

$$\Pi_z^1 = \frac{1}{2W} \int_{-\infty}^{\infty} \frac{\lambda}{P_0} [a_1(\lambda) e^{P_1 Z} + a_2(\lambda) e^{-P_1 Z}] \cdot e^{-P_0 h} H_0^1(\lambda \rho) d\lambda, \tag{11}$$

and

$$\Pi_z^2 = \frac{1}{2W} \int_{-\infty}^{\infty} \frac{\lambda}{P_0} a_3(\lambda) \cdot e^{P_2 Z + (P_2 - P_1)d - P_0 h} H_0^1(\lambda \rho) d\lambda. \tag{12}$$

λ is the separation constant of the differential equation, and $p_j = (\lambda^2 - k_j^2)^{1/2}$, with the sign of the root being chosen such that the solution satisfies the radiation condition. In the above form, after scaling by W , λ is a dimensionless parameter, and $k_j = 2\pi(K_j M_j)^{1/2}$ is the relative propagation constant of each region. The $a_j(\lambda)$ are unknown functions of λ which are found by satisfying the boundary conditions that tangential \mathbf{E} and \mathbf{H} be continuous at $z=0$ and $z=-d$.

For horizontal dipole sources, the solutions for the Hertz vector take the form

$$\Pi_x^0 = \frac{e^{ik_0 R}}{WR} + \frac{1}{2W} \int_{-\infty}^{\infty} \frac{\lambda}{P_0} b_0(\lambda) e^{-P_0(Z+h)} H_0^1(\lambda \rho) d\lambda, \tag{13}$$

and

$$\Pi_z^0 = \frac{\cos \phi}{2W} \int_{-\infty}^{\infty} \frac{\lambda^2}{P_0} c_0(\lambda) \cdot e^{-P_0(Z+h)} H_1^1(\lambda \rho) d\lambda, \tag{14}$$

for region 0;

$$\Pi_x^1 = \frac{1}{2W} \int_{-\infty}^{\infty} \frac{\lambda}{P_0} [b_1(\lambda)e^{\rho_1 z} + b_2(\lambda)e^{-\rho_1 z}] \cdot e^{-\rho_0 h} H_0^1(\lambda \rho) d\lambda, \quad (15)$$

and

$$\Pi_z^1 = \frac{\cos \phi}{2W} \int_{-\infty}^{\infty} \frac{\lambda^2}{P_0} [c_1(\lambda)e^{\rho_1 z} + c_2(\lambda)e^{-\rho_1 z}] \cdot e^{-\rho_0 h} H_1^1(\lambda \rho) d\lambda \quad (16)$$

for region 1; and

$$\Pi_x^2 = \frac{1}{2W} \int_{-\infty}^{\infty} \frac{\lambda}{P_0} b_3(\lambda) \cdot e^{\rho_2 z + (\rho_2 - \rho_1)d - \rho_0 h} H_0^1(\lambda \rho) d\lambda, \quad (17)$$

and

$$\Pi_z^2 = \frac{\cos \phi}{2W} \int_{-\infty}^{\infty} \frac{\lambda^2}{P_0} c_3(\lambda) \cdot e^{\rho_2 z + (\rho_2 - \rho_1)d - \rho_0 h} H_1^1(\lambda \rho) d\lambda \quad (18)$$

for region 2.

The parameters λ and P_j are the same as for the vertical dipole solutions, and the coefficients $b_j(\lambda)$ and $c_j(\lambda)$ are found by satisfying the condition that tangential \mathbf{E} and \mathbf{H} be continuous at the boundaries.

The boundary conditions for the Hertz vectors and the resulting expressions for $a_j(\lambda)$, $b_j(\lambda)$, and $c_j(\lambda)$ are tabulated in Appendix A. The expressions for $a_j(\lambda)$, $b_j(\lambda)$, and $c_j(\lambda)$ are written in terms of the *TE* and *TM* Fresnel plane-wave reflection and transmission coefficients. Using this notation, the similarity of all the solutions is clearly emphasized and makes general discussion of the solutions possible rather than dealing with each source separately.

In discussing the approximate evaluation of the above integral expressions, extensive use is made of the plane-wave spectrum concept, since the wave nature of the problem is most clearly understood using this approach. A brief outline of the plane-wave spectrum notation used and approximate evaluation of integrals by the saddle-point method is given in Appendix B.

For radio interferometry applications, the fields at the earth's surface for the source placed at the earth's surface are of primary interest; this

corresponds to setting both z and h equal to 0 in the preceding expressions for the Hertz vectors. In the following discussions, h is always set equal to 0, and, in most instances, z is assumed to be close to 0. The solutions are discussed in two parts; the half-space solutions and the two-layer earth solutions. The half-space solutions for the Hertz vectors are obtained by setting $K_1 = K_2$ and $M_1 = M_2$ in expressions (10) through (18). The half-space solution is of considerable interest since the fields about the source show interference maxima and minima without a subsurface reflector present. It also provides a base level for detection of reflections from depth.

APPROXIMATE SOLUTIONS

Half-space earth

The solution of the half-space problem is treated by numerous authors, and the wave nature of the fields is well defined. In the following discussions, the results of Ott (1941) and Brekhovskikh (1960) are followed quite closely, and detailed discussions of various aspects of the solutions can be found in these references. The wave nature of the fields about the source is illustrated in Figure 3. The wavefronts denoted *A* and *B* are spherical waves in the air and earth regions; wave *C* in the air is an inhomogeneous wave, and wave *D* in the earth has numerous names, the most common being head, flank, or lateral wave. Waves *C* and *D* exist only in a limited spatial region, which is defined as those points whose position vectors make an angle greater than α_c with the z -axis. The angle α_c is related to the critical angle of the boundary and is defined in Appendix B.

All the dipole sources exhibit the same wave nature. To demonstrate how the waves are derived from the integral expressions, the vertical magnetic dipole source is used for illustration. In the air, the Hertz vector is given by

$$\Pi_z^0 = \frac{e^{ik_0 R}}{WR} + \frac{ik_0}{2W} \int_c \sin \theta_0 R_{01}(\theta_0) \cdot e^{-ik_0 z} \cos \theta_0 H_0^1(k_0 \rho \sin \theta_0) d\theta_0, \quad (19)$$

and in the earth by

$$\Pi_z^1 = \frac{ik_1}{2W} \int_c \sin \theta_1 T_{10}(\theta_1) \cdot e^{-ik_1 z} \cos \theta_1 H_0^1(k_1 \rho \sin \theta_1) d\theta_1. \quad (20)$$

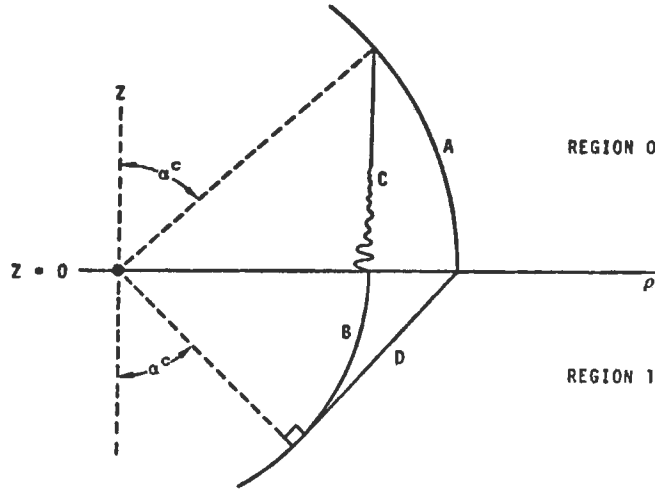


FIG. 3. Wavefronts about a dipole source on the surface of a half-space earth. *A* and *B* are spherical waves in the air and earth, respectively, wave *C* is an inhomogeneous wave in air, and *D* is the head wave in the earth.

With the aid of the Hankel transform identity and (Sommerfeld, 1949),

$$\frac{e^{ik_0R}}{WR} = \frac{ik_0}{2W} \int_c \sin \theta_0 \cdot e^{ik_0|Z| \cos \theta_0} H_0^1(k_0\rho \sin \theta_0) d\theta_0, \quad (21)$$

and the relation $R_{ij} = T_{ij} - 1$ for the Fresnel coefficients, equation (19) becomes

$$\Pi_Z^0 = \frac{ik_0}{2W} \int_c \sin \theta_0 T_{01}(\theta_0) \cdot e^{ik_0|Z| \cos \theta_0} H_0^1(k_0\rho \sin \theta_0) d\theta_0. \quad (22)$$

Using the saddle-point method as discussed in Appendix B, the approximate solutions of the integral expressions (20) and (22) are

$$\Pi_Z^0 = \frac{e^{ik_0R}}{WR} \left\{ T_{01}(\alpha) - \frac{i}{2k_0R} (T_{01}''(\alpha) + \cot \alpha T_{01}'(\alpha)) \right\}, \quad (23)$$

$$\Pi_Z^1 = \frac{e^{ik_1R}}{WR} \left\{ T_{10}(\alpha) - \frac{i}{2k_1R} [T_{10}''(\alpha) + \cot \alpha T_{10}'(\alpha)] \right\}, \quad (24)$$

where $R = (\rho^2 + Z^2)^{1/2}$, and $\alpha = \tan^{-1} \rho/|Z|$. Expressions (23) and (24) correspond to the spherical waves *A* and *B* in Figure 3. The bracketed terms on the right may be interpreted as the modification to the directionality of the source due to the presence of the boundary.

The waves *C* and *D* are generated by crossing the branch points of T_{01} and T_{10} to obtain the saddle-point solutions (23) and (24) for angles $\alpha > \alpha^c$. As outlined in Appendix B, the contribution of the branch point can be approximately evaluated by the method of steepest descent as long as α is not close to the branch point. For $\alpha > \alpha^c$ the expressions

$$I_B^0 = \frac{2ik_1\eta_{01}(1 - \cot \alpha \tan \theta_{01}^c)^{-3/2} e^{ik_1\rho - (k_1^2 - k_0^2)^{1/2}Z}}{(k_1^2 - k_0^2)W\rho^2}, \quad (25)$$

and

$$I_B^1 = \frac{2ik_0\eta_{10}(1 - \cot \alpha \tan \theta_{10}^c)^{-3/2} e^{ik_0\rho - i(k_1^2 - k_0^2)z}}{(k_1^2 - k_0^2)W\rho^2} \quad (26)$$

must be added to (23) and (24) in order that the solutions be correct. Expression (25) is readily identified as the inhomogeneous wave *C*, and (26) corresponds to the lateral wave *D*.

The asymptotic solutions have the form of the geometrical optics solution plus second-order correction terms. For a perfectly dielectric earth, expressions (24) and (26) become infinite as α approaches α^c . The singular behavior arises from the second-order terms which depend on the derivatives of $T_{10}(\theta_1)$. The first-order term which is the geometrical optics solution remains bounded. In this particular case, the angle α^c is the critical angle of $T_{10}(\theta_1)$. As a result, the saddle point and branch point coincide at $\alpha = \alpha^c$, and the approximate methods used to evaluate the integrals are no longer valid. The conical surface about the *z*-axis, defined by $\alpha = \alpha^c$, is the region where the lateral and spherical waves merge together. In this region the two waves cannot be considered separately; the combined effect of the saddle point and branch point must be evaluated. Detailed analysis of this region for integrals similar to expression (20) is given by Brekhovskikh (1960), who obtains an asymptotic solution with the geometrical optics solution, as the leading term plus a connection term which falls off as $(k_1R)^{-5/4}$ instead of $(k_1R)^{-2}$. This result indicates that the geometrical optics solution still describes the fields adequately for $\alpha \sim \alpha^c$ when $(k_1R)^{-1/4} \ll 1$. The correction terms given in (24) and (26), however, are not valid when α is close to α^c .

The fields at the earth's surface are of primary interest and are obtained by setting $z=0$ and $\alpha = \pi/2$ in (23), (24), (25), and (26). The solutions given are valid for this region provided the contrast in material properties is not extremely large. In the case of large contrasts, as occur in conductive earth problems, the transmission and reflection coefficients have a pole near $\theta_0 = \pi/2$. The pole is located at $\theta_0 = \pi - \theta_B$, where θ_B is the Brewster angle. The role of this pole in radio wave propagation over a conductive earth has been the subject of a tremendous amount of discussion since Sommerfeld (1909, 1949) equated the contribution of this pole to the Zenneck surface wave. Numerous people (Norton, 1937; Ott, 1943; Van

der Waerden, 1951; Brekhovskikh, 1960; and Wait, 1970) have considered the problem since then using the modified saddle-point technique to evaluate the integrals for $\alpha \sim \pi/2$. While a true surface wave is not excited, the pole enhances the fields near the source in such a manner that they fall off approximately as $(kR)^{-1}$. At large distances from the source, the fields are those determined by the normal saddle-point method which have a $(kR)^{-2}$ fall off. The transition between the ranges is determined by the proximity of θ_B to $\pi/2$. In the radio interferometry application, the earth properties of interest are those of a low-loss dielectric which is assumed to have only moderate contrasts with the free-space properties. The pole in this case is well away from $\pi/2$ and does not affect the preceding solutions.

In the particular situation of an earth where $M_0 = M_1$, the Hertz vector for a vertical magnetic dipole can be evaluated exactly for $z = h = 0$. The result is

$$\Pi_Z^0 = \Pi_Z^1 = \frac{2}{(k_1^2 - k_0^2)W\rho^2} \left[e^{ik_0\rho} \left(ik_0 - \frac{1}{\rho} \right) - e^{ik_1\rho} \left(ik_1 - \frac{1}{\rho} \right) \right], \quad (27)$$

as shown by Wait (1951). This provides a check on the approximate solution. The approximate solution, obtained by adding (23) and (25) or (24) and (26) for $\alpha = \pi/2$, is

$$\Pi_Z^0 = \Pi_Z^1 = \frac{2i}{(k_1^2 - k_0^2)W\rho^2} [k_0 e^{ik_0\rho} - k_1 e^{ik_1\rho}], \quad (28)$$

which is the same as (27) if third-order terms are neglected.

The integral expressions for the Hertz vectors for the other dipole sources can be treated in the same manner as for the vertical magnetic dipole. For $z \sim 0$, in the air, they have the form

$$\begin{aligned} & (-ik_0 \cos \phi \sin \alpha)^n \frac{e^{ik_0 R}}{WR} \left[G_1(\alpha) + \frac{G_2(\alpha)}{2k_0 R} \right] \\ & + (\cos \phi)^n (1 - \cot \alpha \tan \theta_{10}^c)^{-3/2} \quad (29) \end{aligned}$$

$$G_3(\alpha) = \frac{e^{ik_1\rho - (k_1^2 - k_0^2)^{1/2}Z}}{W\rho^2}$$

The $G_i(\alpha)$ for the various sources are tabulated in Table 1. The electric and magnetic fields can be obtained by differentiation of the preceding solutions; the particular form of the integrals encountered permits interchange of the integration and differentiation steps.

The half-space solutions demonstrated that interference patterns will be observed in the field strengths even when there is no subsurface reflector. This is readily seen from equation (28). The fields at the earth's surface are composed of two propagating components with one having the phase velocity of the air, and the other the velocity of the earth. Another important feature of the half-space solutions is that the fields near the boundary fall off as the inverse square of the radial distance from the source at distances greater than two or three wavelengths from the source.

A convenient method of interpreting the solu-

tions is to equate the radiation pattern of the source on the boundary to the first-order term in the preceding solutions. This technique demonstrates how the boundary modifies the directionality of the source. The radiation pattern is sharply peaked in the direction of the critical angle into the earth. A sketch of the radiation pattern for a vertical dipole source is shown in Figure 4. This directionality of the source is important when reflections from a subsurface boundary are considered.

Two-layer earth

The analysis of the integral expressions for the two-layer earth problem is carried out in two different ways. The depth of the subsurface boundary and the electromagnetic losses of the first layer determine which approach is more useful. The primary method of analysis is to treat the first layer of the earth as a leaky waveguide and use normal mode analysis. In certain cases the mode analysis is cumbersome, and these cases

Table 1. Coefficients $G_i(\alpha)$ for half-space earth solutions for various dipole sources.

Source	Hertz Vector	n	G_1	G_2	G_3
Vertical Magnetic Dipole	Magnetic H_z^0	0	$T_{01}(\alpha)$	$-i(G_1''(\alpha) + G_1'(\alpha) \cot \alpha)$	$-\frac{2ik_1\eta_{01}}{k_1^2 - k_0^2}$
Vertical Electric Dipole	Electric H_z^0	0	$S_{01}(\alpha)$	$-i(G_1''(\alpha) + G_1'(\alpha) \cot \alpha)$	$-\frac{2ik_1\xi_{01}}{k_1^2 - k_0^2}$
Horizontal Magnetic Dipole	Magnetic H_x^0	0	$S_{01}(\alpha)$	$-i(G_1''(\alpha) + G_1'(\alpha) \cot \alpha)$	$-\frac{2ik_1\xi_{01}}{k_1^2 - k_0^2}$
	Magnetic H_z^0	1	$\frac{(\gamma_{01} - 1)T_{01}(\alpha)S_{01}(\alpha)}{2P_0(\alpha)}$	$-i(G_1''(\alpha) + 3G_1'(\alpha) \cot \alpha - 2G_1(\alpha))$	$\frac{2ik_0^2(\xi_{10} + \eta_{10})}{k_1^2(k_0^2 - k_1^2)^{1/2}}$
Horizontal Electric Dipole	Electric H_x^0	0	$T_{01}(\alpha)$	$-i(G_1''(\alpha) + G_1'(\alpha) \cot \alpha)$	$\frac{2ik_1\eta_{01}}{k_1^2 - k_0^2}$
	Electric H_z^0	1	$\frac{(\gamma_{01} - 1)T_{01}(\alpha)S_{01}(\alpha)}{2P_0(\alpha)}$	$-i(G_1''(\alpha) + 3G_1'(\alpha) \cot \alpha - 2G_1(\alpha))$	$\frac{2ik_0^2(\eta_{10} + \xi_{10})}{k_1^2(k_0^2 - k_1^2)^{1/2}}$
Definition:			$G_1'(\alpha) = \left. \frac{dG_1(\theta_0)}{d\theta_0} \right _{\theta_0=\alpha}$	$G_1'' = \left. \frac{d^2G_1(\theta_0)}{d\theta_0^2} \right _{\theta_0=\alpha}$	

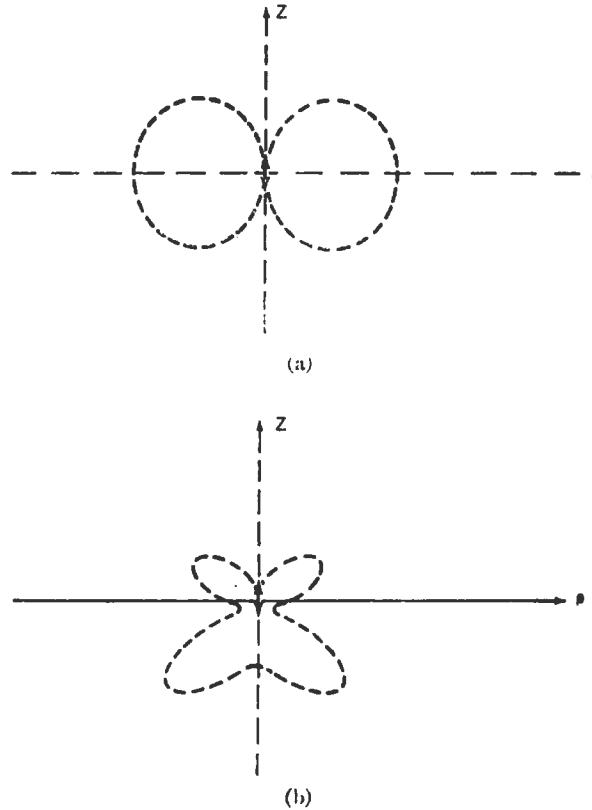


FIG. 4. Sketch showing how a dielectric boundary modifies the directionality of a vertical dipole source placed on the boundary. (a) No boundary present. (b) Boundary at $Z=0$.

yield more useful results when the integrals are solved approximately using the saddle-point method of integration.

The various dipole sources may all be treated in the same manner. For the purpose of illustrating the method of analysis, the horizontal electric dipole source solutions are used as an example. The x - and z -components of the electric Hertz vector in the air for this source are given by equations (13) and (14) where the coefficients b_0 and c_0 are listed in Table A-2.

For normal mode analysis, equation (13) is rewritten using the integral identity [equation (21)]. The components of the Hertz vector are given by

$$\Pi_z^0 = \frac{ik_1}{2W} \int_c \sin \theta_1 m_{10}(\theta_1) [1 + b_0(\theta_1)] \cdot e^{ik_0 Z \cos \theta_0} H_0^1(k_1 \rho \sin \theta_1) d\theta_1, \quad (30)$$

and

$$\Pi_z^0 = \cos \phi \frac{ik_1^2}{2W} \int_c \sin^2 \theta_1 m_{10}(\theta_1) c_0(\theta_1) \cdot e^{ik_0 \cos \theta_0 Z} H_1^1(k_1 \rho \sin \theta_1) d\theta_1, \quad (31)$$

where the integration variable is θ_1 , as defined in Appendix B. The singularities of the coefficients b_0 and c_0 determine the nature of the solutions to equations (30) and (31).

The expressions

$$m_{10}(1 + b_0) = \frac{\eta_0 T_{10}(1 + R_{12}\beta)}{1 - R_{10}R_{12}\beta}, \quad (32)$$

and

$$m_{10}c_0 = \frac{1}{2\rho_0} \left[\frac{(\gamma_{01} - 1)\eta_{10}T_{10}(1 + R_{12}\beta)S_{01}(1 + X_{12}\beta)}{(1 - X_{10}X_{12}\beta)(1 - R_{10}R_{12}\beta)} \right]$$

$$\frac{(\gamma_{21} - 1)\xi_{10}S_{10}S_{12}\gamma_{01}T_{01}\gamma_{12}T_{12}\beta}{(1 - X_{10}X_{12}\beta)(1 - R_{10}R_{12}\beta)} \quad (33)$$

$$(1 - R_{10}R_{12}\beta) = \sum_{n=0}^{\infty} (R_{10}R_{12}\beta)^n \quad (36)$$

have branch points at the two critical angles of the two boundaries in question. In addition, equation (32) has an infinite set of simple poles, and (33) has a doubly infinite set of poles on each Riemann surface. These poles are determined by the normal mode equations,

$$1 - R_{10}R_{12}\beta = 0, \quad (34)$$

and

$$1 - X_{10}X_{12}\beta = 0. \quad (35)$$

Equations (34) and (35) are the *TE* and *TM* normal mode equations, respectively. Both are transcendental equations with infinite sets of roots. The relation between the normal modes and multiple reflections is readily obtained by expanding the denominators of equations (32) and (33) into infinite geometric series. For example,

The positions of the poles and branch points in the complex plane determine the wave nature of the solutions to equations (30) and (31). The normal mode solutions are obtained by deforming the contour of integration C to C' , as schematically illustrated in Figure 5. The integral from $-\pi/2 + i\infty$ to $\pi/2 + i\infty$, and from $\pi/2 - i\infty$ to $-\pi/2 - i\infty$ is identically zero. Along the first part of C' the integral is zero since the integrand is zero. Along the second part of the contour C' the integral is zero due to the asymmetry of the integrand about $\theta_1 = \pi/2$. This result is common in mode analysis and has a wide range of applications as discussed in detail by Brekhovskikh (1960). The integral along C is equal to the residues of the poles crossed in deforming the contour to C' , plus the integrals along contours C_1 and C_2 which run from $-i\infty$ around the branch points and back to $+i\infty$. The components of the Hertz vector are given by

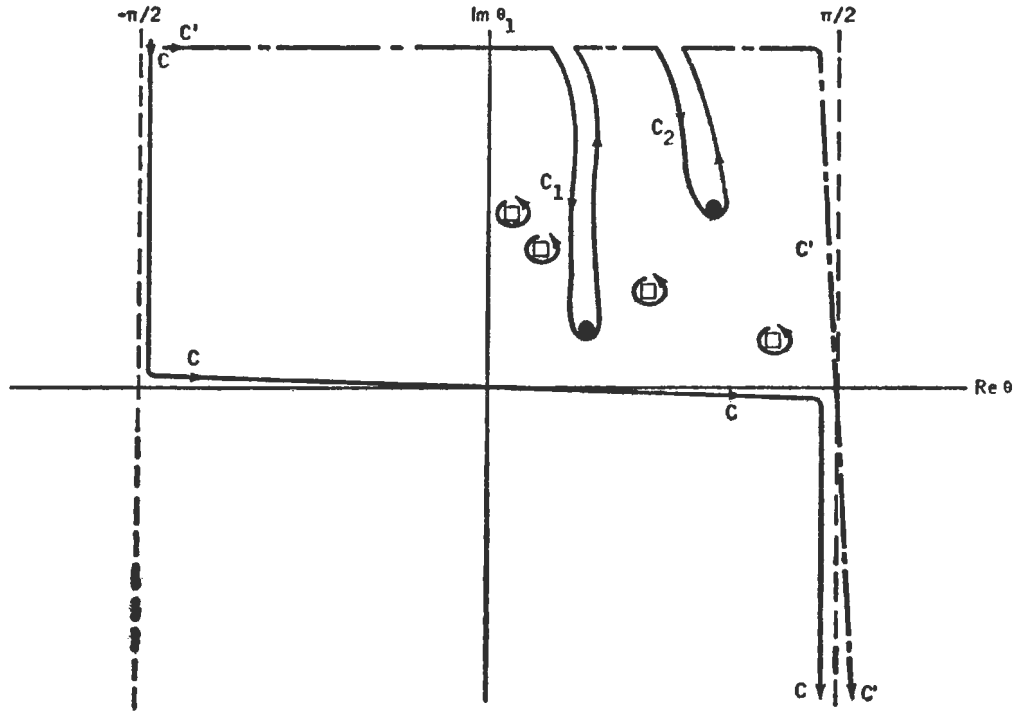


FIG. 5. Complex θ_1 plane showing how integration contour C is modified to C' in order to obtain normal mode solutions. Branch points denoted by solid circles and the poles by squares.

Table 2. Residues of poles for normal mode analysis for horizontal electric dipole.

Π_x^0 TE Mode Residue	$ik_1 \sin \theta_1' \eta_{10} T_{10}(\theta_1') [1 + R_{12}(\theta_1') \beta(\theta_1')] e^{ik_0(1-\gamma_{10} \sin^2 \theta_1')^{1/2} z}$ $2W \left(i2k_1 d \cos \theta_1' - \frac{\partial \ln R_{10}(\theta_1) R_{12}(\theta_1)}{\partial \theta_1} \right) \Big _{\theta_1 = \theta_1'} H_0^1(k_1 \rho \sin \theta_1')$
Π_z^0 TE Mode Residue	$\cos \phi ik_1^2 \sin^2 \theta_1' t(\theta_1') e^{ik_0(1-\gamma_{10} \sin^2 \theta_1')^{1/2} z}$ $2W [1 - X_{10}(\theta_1') X_{12}(\theta_1') \beta(\theta_1')] \left(i2k_1 d \cos \theta_1' - \frac{\partial \ln R_{10}(\theta_1) R_{12}(\theta_1)}{\partial \theta_1} \right) \Big _{\theta_1 = \theta_1'} H_1^1(k_1 \rho \sin \theta_1')$
Π_z^0 TM Mode Residue	$\cos \phi ik_1^2 \sin^2 \theta_1' t(\theta_1') e^{ik_0(1-\gamma_{10} \sin^2 \theta_1')^{1/2} z}$ $2W [1 - R_{10}(\theta_1') R_{12}(\theta_1') \beta(\theta_1')] \left(i2k_1 d \cos \theta_1' - \frac{\partial \ln X_{10}(\theta_1) X_{12}(\theta_1)}{\partial \theta_1} \right) \Big _{\theta_1 = \theta_1'} H_1^1(k_1 \rho \sin \theta_1')$

where $t(\theta_1') = \frac{(\gamma_{01} - 1)}{2P_0(\theta_1')} [\eta_{10} T_{10}(\theta_1')] [1 + R_{12}(\theta_1') \beta(\theta_1')] S_{01} (1 + X_{12}(\theta_1') \beta(\theta_1'))$
 $- \frac{(\gamma_{21} - 1)}{2P_0(\theta_1')} [\xi_{10} S_{10}(\theta_1') S_{12}(\theta_1') \gamma_{01} T_{01}(\theta_1') \gamma_{12} T_{12}(\theta_1') \beta(\theta_1')]$

$$\Pi_z^0 = 2\pi i \sum (TE \text{ pole residues}) + I_1 + I_2, \tag{37}$$

and

$$\Pi_z^0 = 2\pi i \sum (TE \text{ pole residues}) + 2\pi i \sum (TM \text{ pole residues}) + I_3 + I_4, \tag{38}$$

where

$$I_1 = \frac{ik_1}{2W} \int_{c_1} \sin \theta_1 m_{10}(\theta_1) [1 + b_0(\theta_1)] e^{ik_0 z \cos \theta_0} H_0^1(k_1 \rho \sin \theta_1) d\theta_1, \tag{39}$$

$$I_2 = \frac{ik_1}{2W} \int_{c_2} \sin \theta_1 m_{10}(\theta_1) [1 + b_0(\theta_1)] e^{ik_0 z \cos \theta_0} H_0^1(k_1 \rho \sin \theta_1) d\theta_1, \tag{40}$$

$$I_3 = \cos \phi \frac{ik_1^2}{2W} \int_{c_1} \sin^2 \theta_1 m_{10}(\theta_1) c_0(\theta_1) e^{ik_0 z \cos \theta_0} H_1^1(k_1 \rho \sin \theta_1) d\theta_1, \tag{41}$$

$$I_4 = \cos \phi \frac{ik_1^2}{2W} \int_{c_2} \sin^2 \theta_1 m_{10}(\theta_1) c_0(\theta_1) e^{ik_0 z \cos \theta_0} H_1^1(k_1 \rho \sin \theta_1) d\theta_1. \tag{42}$$

The solutions (37) and (38) are completely general and valid provided a branch point and a pole, or a TE and TM pole, do not coincide. In the first situation, the pole and branch-point contributions must be considered together rather than separately, as indicated. In the other situation, (38) must include the residue of a second-order pole rather than the residues of two simple poles, as indicated. Since these situations rarely occur, they are not discussed further here.

The expressions for the residues in (37) and (38) are tabulated in Table 2. Approximate solutions to the branch cut integrals may be obtained by steepest-descent integration as discussed in Appendix B. The solutions are the second-order lateral and inhomogeneous waves generated at the boundaries. The approximate solutions are listed in Table 3.

The behavior of the fields at the earth's surface is very dependent on the position of the singular points in the complex θ_1 plane, which points are, in turn, determined by the material properties of the earth and the layer thickness d . The important features of the solutions are the radial dependences and the initial amplitudes of the various terms in the solutions. All the residues contain Hankel functions, which, for radial distances greater than one or two wavelengths, have the form

Table 3. Approximate steepest-descent solutions to branch-cut integrals for normal mode analysis of the horizontal electric dipole.

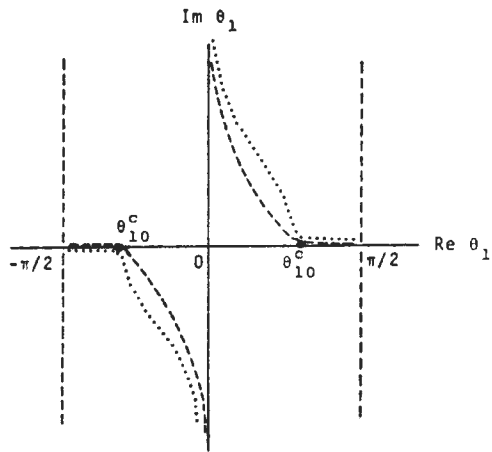
I_1	$\frac{2ik_0\eta_{10}^2(1 + R_{12}(\theta_{10}^c)\beta(\theta_{10}^c))^2 e^{ik_0\rho}}{(k_1^2 - k_0^2)(1 - R_{12}(\theta_{10}^c)\beta(\theta_{10}^c))^2 W\rho^2}$
I_2	$\frac{2ik_1^2\eta_{20}T_{10}^2(\theta_{12}^c)(1 - \cot\alpha_d \tan\theta_{12}^c)^{-3/2} e^{ik_2\rho - 2d(k_2^2 - k_1^2)^{1/2}} (k_2^2 - k_0^2)^{1/2} Z}{k_2(k_1^2 - k_0^2)(1 - R_{10}(\theta_{12}^c)\beta(\theta_{12}^c))^2 W\rho^2}$
I_3	$-\frac{\cos\phi k_0}{2(k_1^2 - k_0^2)^{1/2}} \left[\frac{C_1(\theta_{10}^c) e^{ik_0\rho}}{W\rho^2} + \frac{(1 - \cot\alpha_d \tan\theta_{10}^c)^{-3/2} C_2(\theta_{10}^c) e^{ik_0\rho + 2d(k_1^2 - k_0^2)^{1/2}}}{W\rho^2} \right]$
I_4	$-\frac{\cos\phi k_2(1 - \cot\alpha_d \tan\theta_{12}^c)^{-3/2} C_3(\theta_{12}^c) e^{ik_2\rho - (k_2^2 - k_1^2)^{1/2} 2d} (k_2^2 - k_0^2)^{1/2} Z}{2(k_1^2 - k_0^2)^{1/2} W\rho^2}$
$C_1(\theta_{10}^c)$	$\frac{4i\gamma_{10}}{k_0} \left[\frac{\eta_{01}(1 - R_{12}^2\beta^2)(1 + X_{12}\beta)^2 + \xi_{01}(1 - X_{12}^2\beta^2)(1 + R_{12}\beta)^2}{(1 - X_{12}\beta)^2(1 - R_{12}\beta)^2} \right]$
$C_2(\theta_{10}^c)$	$\frac{4i\gamma_{10}(1 - \gamma_{12})\gamma_{01}S_{12}T_{12}[\eta_{01}(1 + X_{12}\beta)(1 - R_{12}\beta) + \xi_{01}(1 - X_{12}\beta)(1 + R_{12}\beta)]}{k_0(1 - \gamma_{01})(1 - X_{12}\beta)^2(1 - R_{12}\beta)^2}$
$C_3(\theta_{12}^c)$	$\frac{2i\eta_{10}T_{10}S_{01}\sqrt{\gamma_{21}}\{(\gamma_{01} - 1)[\xi_{12}S_{10}(1 + T_{01}\beta - R_{10}\beta^2) + \eta_{12}T_{10}(1 + S_{01}\beta - X_{10}\beta^2)] - 2(1 - \gamma_{12})\gamma_{01}\gamma_{12}[\xi_{21}(1 + X_{10}\beta)(1 - R_{10}\beta) + \eta_{21}(1 - X_{10}\beta)(1 + R_{10}\beta)]\}}{k_0(1 - \gamma_{20})^{1/2}(1 - \gamma_{21})^{1/2}(1 - X_{10}\beta)^2(1 - R_{12}\beta)^2}$
	$\sin\theta_{10}^c = \frac{k_0}{k_1} \quad \sin\theta_{12}^c = \frac{k_2}{k_1} \quad \alpha_d = \tan^{-1} \left \frac{2d}{\rho} \right $

$$\rho^{-1/2} e^{ik_{10}\rho \sin\theta_{10}^c}, \quad (4.3)$$

where θ_{10}^c is a pole defined by equations (34) and (35). The branch cut contributions, I_1 and I_3 , fall off as ρ^{-2} with no exponential attenuation, while I_2 and I_4 fall off as ρ^{-2} and are exponentially attenuated when the earth is lossy. The amplitudes of the modes are largest for those poles in the vicinity of θ_{10}^c . This effect is related to the modified directionality of the source as discussed for the half-space fields. When the earth has a finite loss all terms in the solution except I_1 and the first term of I_3 have amplitudes which decay exponentially with increasing loss or increasing d .

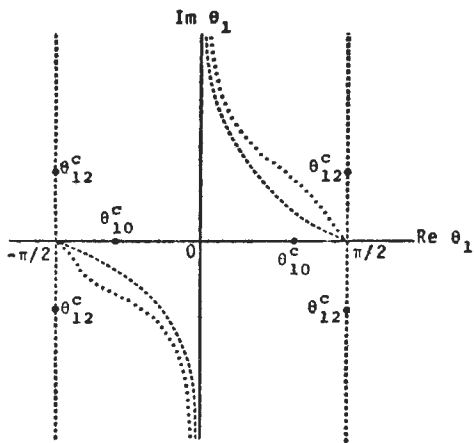
The positions of the poles in the complex θ_1 plane for three idealized models are illustrated schematically in Figure 6. The earth consists of a perfect dielectric slab over a half-space, which is a perfect conductor in case (a), a perfect dielectric with $K_2 > K_1$ in case (b), and a perfect dielectric

with $K_2 < K_1$ in case (c). In all cases $M_0 = M_1 = M_2$ is assumed since permeabilities of bulk earth materials vary little from the free-space value. The poles lie on the lines $|R_{10}R_{12}\beta| = 1$ and $|X_{10}X_{12}\beta| = 1$, with the density of distribution of the poles on these lines controlled by the slab thickness d . For d small, the poles are widely spaced with most of them lying high up the lines near the imaginary θ_1 axis. For increasing d , the poles move down the lines toward $\theta_1 = \pi/2$ and are more closely packed. Unattenuated modes occur only when the θ_1^c lie on or close to the real θ_1 axis. In case (a), the pole contours lie on the real axis for $\theta_{10}^c \leq \theta_1 \leq \pi/2$; unattenuated modes can be excited when θ_1 exceeds the critical angle of the free-space-earth interface. In case (c), the slab forms a dielectric waveguide when θ_1 is greater than the critical angles of both boundaries. For both (a) and (c), the modes with real θ_1^c less than the largest critical angle are highly damped due to energy leaking out of the slab. In



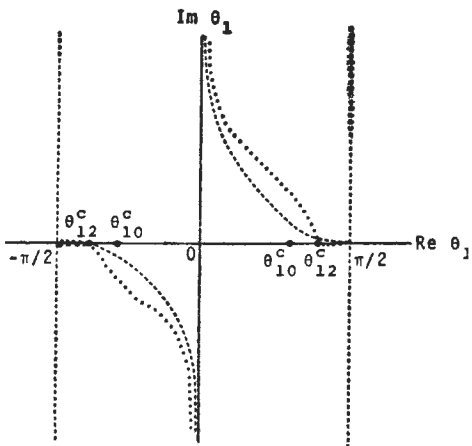
$K_0 = 1$	FREE SPACE
K_2	PERFECT DIELECTRIC
	PERFECT CONDUCTOR

(a)



$K_0 = 1$	FREE SPACE
K_1	PERFECT DIELECTRIC
$K_2 > K_1$	PERFECT DIELECTRIC

(b)



$K_0 = 1$	FREE SPACE
K_1	PERFECT DIELECTRIC
$K_2 < K_1$	PERFECT DIELECTRIC

(c)

FIG. 6. Sketches of complex θ_1 -plane showing positions of branch points and pole lines for 3 simple two layer earth cases; case (a), dielectric slab over a perfect conductor; case (b), dielectric slab over dielectric half space with $K_2 > K_1$; case (c) dielectric slab over a dielectric half-space with $K_2 < K_1$. The dashed lines are contours where $|R_{10} R_{12} \beta| = 1$; the dotted lines are contours where $|X_{10} X_{12} \beta| = 1$; the branch points are denoted by solid circles.

case (b), no unattenuated mode can exist, since energy is continually flowing out of the slab into the lower half-space. The effect of a finite loss in the slab moves the pole contours up away from the real axis, and all modes have a finite attenuation. These models demonstrate the general position and behavior of the singular points in the complex plane. More detailed studies are given by Wait (1970), Brekhovskikh (1960), and Buden (1961).

The normal mode approach is most useful when the distance from the source is greater than the depth of the boundary d and when the earth has a very low loss. In a lossy dielectric, the complex dielectric constant is $K'(1+i \tan \delta)$, where K' is the real dielectric constant and $\tan \delta$ is the loss tangent; and the attenuation distance in free-space wavelengths for a plane wave is

$$D = \frac{1}{\pi \sqrt{K' \tan \delta}}, \tag{44}$$

when $\tan \delta \ll 1$. When d approaches the attenuation distance, the solutions begin to approach those of a lossy dielectric half-space. An alternate approach to evaluating the fields when the distance from the source is less than d , or when $d \geq D$, is desirable, since the normal mode approach is cumbersome in these cases.

The integrals can be approximately evaluated by the saddle-point method of integration when multiple reflections are not strong. The fields can then be expressed as the half-space solution plus a contribution from the subsurface boundary. By regrouping the coefficients b_0 and c_0 in the form

$$b_0 = R_{01} + b_0^1 \beta, \tag{45}$$

$$c_0 = \frac{1}{2} (\gamma_{01} - 1) \frac{S_{01} T_{01}}{P_0} + c_0^1 \beta, \tag{46}$$

$$b_0^1 = \frac{T_{01} T_{10} R_{12}}{(1 - R_{10} R_{12} \beta)}, \tag{47}$$

and

$$c_0^1 = \frac{1}{2P_0} \left[\frac{(\gamma_{01} - 1) S_{01} T_{01} [T_{10} R_{12} + S_{10} X_{12} + (S_{01} + T_{01} - S_{21} T_{01}) X_{12} R_{12} \beta]}{(1 - R_{10} R_{12} \beta)(1 - X_{10} X_{12} \beta)} - \frac{(\gamma_{21} - 1) \xi_{10} S_{10} S_{12} m_{01} T_{01} \gamma_{12} T_{12}}{(1 - R_{10} R_{12} \beta)(1 - X_{10} X_{12} \beta)} \right]. \tag{48}$$

The Hertz vector components can then be written as

$$\Pi_x^0 = L_1 + L_2, \tag{49}$$

and

$$\Pi_z^0 = L_3 + L_4, \tag{50}$$

where L_1 and L_2 are the half-space earth solutions discussed earlier, and L_3 and L_4 , given by

$$L_2 = \frac{ik_1}{2W} \int_c \sin \theta_1 m_{10} b_0^1(\theta_1) \cdot e^{ik_0 z \cos \theta_0} \beta H_0^1(k_{1\rho} \sin \theta_1) d\theta_1, \tag{51}$$

and

$$L_4 = \cos \phi \frac{ik_1^2}{2W} \int_c \sin^2 \theta_1 m_{10} c_0^1(\theta_1) \cdot e^{ik_0 z \cos \theta_0} \beta H_1^1(k_{1\rho} \sin \theta_1) d\theta_1 \tag{52}$$

describe the effect of the subsurface boundary.

L_2 and L_4 can be approximately evaluated by the saddle-point method, which results in the geometric optics solution. Since \mathbf{z} is assumed close to zero throughout, the expression

$$\beta H_n^1(k_{1\rho} \sin \theta_1) \tag{53}$$

in the integrands may be regrouped using the asymptotic expansion of the Hankel function in the manner discussed in Appendix B. L_2 and L_4 then contain the expression

$$e^{i2k_{1d} \cos \theta_1 + ik_{1\rho} \sin \theta_1} = e^{ik_1 R_d \cos(\theta_1 - \alpha_d)} \tag{54}$$

in the integrand, where $R_d = (\rho^2 + 4d^2)^{1/2}$ and $\alpha_d = \tan^{-1}(\rho/2d)$. In this form α_d is the saddle point of the integrand and is the geometric optics direction of a ray reflected from the subsurface boundary. The saddle-point solutions of L_2 and L_4 , outlined in Appendix B, are

$$L_2 \approx \frac{e^{ik_1 R_d}}{WR_d} \left[P(\alpha_d) - \frac{i}{2k_1 R_d} (P''(\alpha_d) + P'(\alpha_d) \cot \alpha_d) \right], \quad (55)$$

and

$$L_4 = \cos \phi \sin \alpha_d \frac{e^{ik_1 R_d}}{WR_d} \cdot \left[Q(\alpha_d) - \frac{i}{2k_1 R_d} (Q''(\alpha_d) + 3 \cot \alpha_d Q'(\alpha_d) - 2Q(\alpha_d)) \right], \quad (56)$$

where

$$P = m_{10}(\alpha_d) b_0^1(\alpha_d) e^{ik_0 Z (1 - \gamma_{10} \sin^2 \alpha_d)^{1/2}}, \quad (57)$$

and

$$Q = m_{10}(\alpha_d) \ell_0^1(\alpha_d) e^{ik_0 Z (1 - \gamma_{10} \sin^2 \alpha_d)^{1/2}}. \quad (58)$$

Expressions (55) and (56) can be interpreted as having replaced the subsurface boundary by an image source at twice the depth. The image source has a radiation pattern which depends on the reflection and transmission coefficients of the boundaries and the layer thickness.

In obtaining the saddle-point solution, the effect of the poles and branch points has been neglected; such neglect is justified when the boundary is deep and the earth has a significant loss. This is illustrated in Figure 7. To obtain the saddle-point contribution, the integration contour C must be deformed into the saddle-point contour Γ . The position of Γ in the complex θ_1 plane is determined by α_d , which, in turn, is determined by the ratio of the radial distance to the depth of the boundary, $\rho/2d$. In order that a given pole or branch point be crossed when C is deformed to Γ , α_d must exceed a certain value which is determined by equation (B-11), which defines the contour Γ . Since $\rho = 2d \tan \alpha_d$, the radial distance from the source at which the singular point is

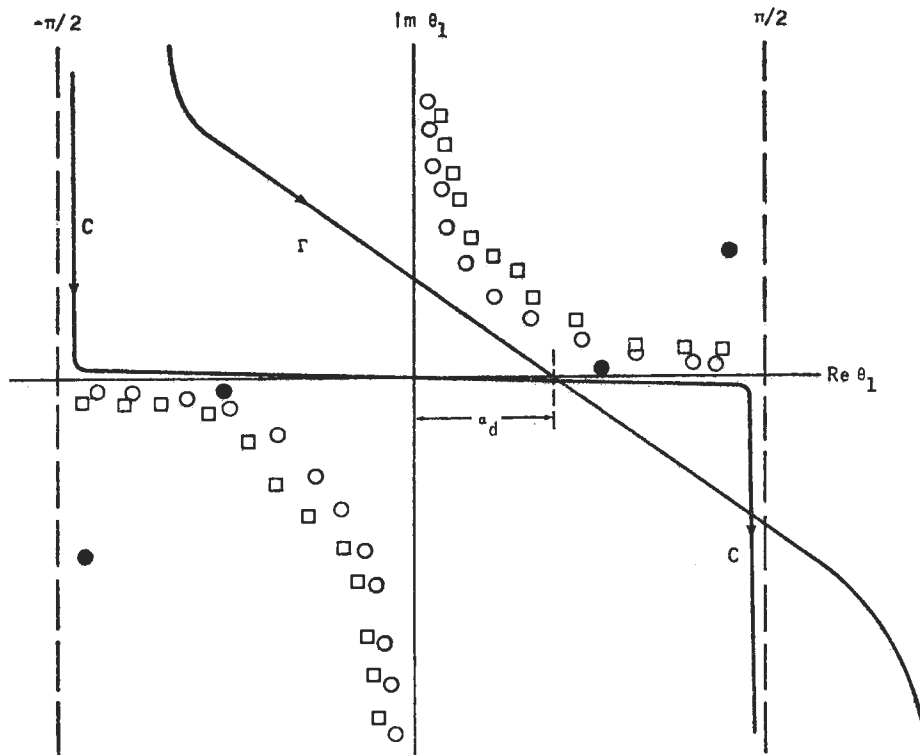


FIG. 7. Complex θ_1 -plane showing deformation of contour C to saddle-point contour Γ . Solid circles = branch points; squares = TE poles, and open circles = TM poles.

crossed in obtaining Γ is defined. When the singular point is a pole, the contribution to the integral after crossing the pole is a residue of a form similar to those in Table 2. When the pole is not on the real θ_1 axis, the residue is exponentially attenuated with increasing radial distance. The value of ρ at which the pole must be considered in determining the integral is also defined, and is usually much greater than the attenuation distance of the mode. As a result, the residue of the pole is extremely small and is negligible compared to the saddle-point contribution. For cases when some poles lie on or near the real θ_1 axis, a fixed radial distance from the source must be exceeded before their effect needs to be considered. Beyond this distance, the normal mode approach is more convenient for expressing the solutions.

The branch-point contributions yield inhomogeneous and lateral waves generated at or reflected from the subsurface boundary. As in the case of the poles, a finite distance from the source must be exceeded before these contributions need to be considered. For the earth models where the saddle-point method is useful, these contributions, which are second-order effects, are negligible. When these second-order waves are significant in the determination of the field strengths at the earth's surface, the normal mode approach is the better method for computing the fields.

The two-layer earth solutions cover a wide range of possible responses. The important results are as follows:

1. When the first layer of the earth is very thin and the second layer is a low-loss medium, the first layer is undetectable. The response of the earth is the same as that of a half-space composed of the second layer of the earth.

2. When the first layer of the earth is on the order of one wavelength thick, the surface fields become extremely complex. The fields exhibit a $\rho^{-1/2}$ fall-off out to the attenuation distance of the least attenuated mode which is strongly excited. Beyond this distance, the contribution of the modes becomes negligible and the second-order lateral and inhomogeneous waves, with no radial exponential attenuation, determine the field strengths which then fall off as ρ^{-2} . When modes with low attenuation are excited, they

are generally few in number. Since each propagates radially with a different phase velocity, the fields will show a regular periodic beating as the various modes move in and out-of-phase.

3. When the first layer of the earth is lossy and several wavelengths deep, the geometric optics solution is more useful than the normal mode approach. The expression for the fields is the half-space solution plus a contribution from the reflecting boundary. This is the type of solution used by El-Said (1956). In El-Said's analysis, the waves propagating along the surface were not correctly expressed, and the modification in directionality of the source due to the air-earth interface was not considered. This form of solution is particularly useful for a quick computation of the strength of reflections from subsurface boundaries and of the effect on surface fields of changes in electrical properties.

4. The saddle-point solution is useful for determining the radial distance from the source at which the various contributions of the singularities of the integrand become important. Since the saddle-point contour is positioned in the complex plane by the ratio $\rho/2d$, a ratio $\rho/2d$ can be defined for each singularity. For normal modes, the radial distance defined by this ratio may be interpreted as the distance from the source required for a given mode to develop. For the branch points, this ratio defines the critical distances from the source, where lateral waves and inhomogeneous waves from the subsurface boundary reach the surface.

DISCUSSION

The radio interferometry technique provides a method of determining electrical properties in situ and of detecting subsurface stratification of the electrical properties in environments which are moderately transparent to electromagnetic waves. The theoretical analysis of the two-layer earth problem defines the behavior of the fields at the earth's surface and provides a basis for understanding experimental results reported by Rossiter et al (1973) in Part II. The various solutions derived here are also useful for computing rough estimates of the interference patterns in the fields at the earth's surface, provided the asymptotic

nature of the expressions is given due respect. Examples of these are given in Part II.

The half-space solutions provide a method of determining the electrical properties for a half-space. Any strong departures from the half-space wave nature (i.e., a regular interference pattern and a ρ^{-2} distance dependence) indicate that reflections from depth are important. When the reflections from depth are due to a horizontal boundary in electrical properties, the behavior of the fields varies considerably. For example, when normal modes are excited, the fields fall off as $\rho^{-1/2}$ with regular beating in the field strengths with distance from the source.

The treatment of a two-layer earth with plane boundaries, homogeneous media, and point sources is a considerable simplification of most real environments. These simple models and the approximate solutions obtained do, however, provide insight into the field behavior in the radio interferometry application. Methods to accurately compute field strengths for these models are currently under investigation. The effect of rough and dipping boundaries on the solutions is extremely important. Also, the presence of scattering by inhomogeneities in the earth can drastically alter the fields at the earth's surface. These problems are virtually impossible to treat in a general manner theoretically. Scale model experiments seem to be the most feasible method of studying these problems. This work is presently in progress.

The free-space wavelength provides the most

useful unit of length when discussing and plotting radio interferometry data. Scale model construction is based on keeping all dimensions the same on the wavelength scale and having the same loss tangent. In the analysis of field data, plotting distances on a wavelength scale makes comparison of data taken at different frequencies straightforward. If the electrical properties are not frequency dependent, running the experiment using several different frequencies can effectively vary the depth of a subsurface interface from a fraction of a wavelength to many wavelengths.

APPENDIX A: COEFFICIENTS AND PARAMETERS

The coefficients in the integral expressions for the Hertz vectors for the various dipole sources are obtained by satisfying the boundary conditions at $z=0$ and $z=-d$. Without a consistent notation, the coefficients are extremely complicated expressions, which lose the symmetry of equations (1) through (6) and are difficult to interpret physically. In this section, the solutions for the coefficients are tabulated, and the notation used throughout the body of the text is defined.

In Table A-1, the boundary conditions for the Hertz vectors are listed. In Table A-2, the expressions for the $a_j(\lambda)$, $b_j(\lambda)$, and $c_j(\lambda)$ are listed for each dipole source. Examination of these solutions shows the symmetry between the electric and magnetic dipole sources. Interchanging the roles of K_i and M_i , one can readily obtain the solution for a magnetic dipole source from that of an equivalent electric dipole source, and vice versa

Table A-1. Boundary conditions for Hertz vectors for various dipole sources.

Vertical Magnetic Dipole (VMD)	Magnetic	$M_i \Pi_z = M_{i+1} \Pi_z^{i+1}$	$\frac{\partial \Pi_z^i}{\partial Z} = \frac{\partial \Pi_z^{i+1}}{\partial Z}$
Vertical Electric Dipole (VED)	Electric	$K_i \Pi_z^i = K_{i+1} \Pi_z^{i+1}$	$\frac{\partial \Pi_z^i}{\partial Z} = \frac{\partial \Pi_z^{i+1}}{\partial Z}$
Horizontal Magnetic Dipole (HMD)	Magnetic	$k_i^2 \Pi_x^i = k_{i+1}^2 \Pi_x^{i+1}$ $\nabla \cdot \Pi^i = \nabla \cdot \Pi^{i+1}$	$M_i \Pi_z^i = M_{i+1} \Pi_z^{i+1}$ $M_i \frac{\partial \Pi_x^i}{\partial Z} = M_{i+1} \frac{\partial \Pi_x^{i+1}}{\partial Z}$
Horizontal Electric Dipole (HED)	Electric	$k_i^2 \Pi_x^i = k_{i+1}^2 \Pi_x^{i+1}$ $\nabla \cdot \Pi^i = \nabla \cdot \Pi^{i+1}$	$K_i \Pi_z^i = K_{i+1} \Pi_z^{i+1}$ $K_i \frac{\partial \Pi_x^i}{\partial Z} = K_{i+1} \frac{\partial \Pi_x^{i+1}}{\partial Z}$

Table A-2(a). Coefficients $a_i(\lambda)$, $b_i(\lambda)$, and $c_i(\lambda)$ for vertical dipole source.

		Two-layer earth	Half-space
	a_0	$\frac{R_{01} + R_{12}\beta}{1 - R_{10}R_{12}\beta}$	R_{01}
Vertical	a_1	$\frac{\eta_{01}T_{01}}{1 - R_{10}R_{12}\beta}$	$\eta_{01}T_{01}$
Magnetic			
Dipole	a_2	$\frac{\eta_{01}T_{01}R_{12}\beta}{1 - R_{10}R_{12}\beta}$	0
	a_3	$\frac{\eta_{01}T_{01}\eta_{12}T_{12}}{1 - R_{10}R_{12}\beta}$	$\eta_{01}T_{01}$
	b_0	$\frac{X_{01} + X_{12}\beta}{1 - X_{10}X_{12}\beta}$	X_{01}
Vertical	b_1	$\frac{\xi_{01}S_{01}}{1 - X_{10}X_{12}\beta}$	$\xi_{01}S_{01}$
Electric			
Dipole	b_2	$\frac{\xi_{01}S_{01}X_{12}\beta}{1 - X_{10}X_{12}\beta}$	0
	b_3	$\frac{\xi_{01}S_{01}\xi_{12}S_{12}}{1 - X_{10}X_{12}\beta}$	$\xi_{01}S_{01}$

The various parameters used in the solutions are listed in Table A-3.

The expressions X_{ij} , S_{ij} , R_{ij} , and T_{ij} are the Fresnel plane-wave reflection and transmission coefficients. The subscript notation ij has the following meaning: subscript i denotes the medium from which the plane wave is incident on the plane boundary between media i and j . For example, the subscripts 01 mean a plane-wave incident from the air on the boundary between the air and the first layer of the earth. The X_{ij} and S_{ij} are the reflection and transmission coefficients respectively for a TM plane wave; the R_{ij} and T_{ij} are the reflection and transmission coefficients for a TE plane wave.

APPENDIX B: PLANE-WAVE SPECTRUM AND EVALUATION OF INTEGRALS

The physical meaning of the integral expressions for the various Hertz vector solutions is

much more apparent when the plane-wave spectrum notation is used. The form of the plane-wave spectrum used throughout is obtained by defining three complex angles, $\theta_0, \theta_1, \theta_2$, and transforming the integration variable by setting

$$\lambda = k_0 \sin \theta_0 = k_1 \sin \theta_1 = k_2 \sin \theta_2. \quad (B-1)$$

The angle θ_0 is used in the region $Z > 0$, θ_1 in the region $-d \leq Z \leq 0$, and θ_2 in the region $Z \leq -d$. The above transformation is just an expression of Snell's law. A plane-wave incident from the region $Z > 0$ on the earth's surface at an angle θ_0 to the z -axis is refracted into medium 1 at an angle θ_1 , and to the z -axis and into medium 2 at an angle θ_2 , as illustrated in Figure B-1. The reader is referred to Clemmow (1966) for details.

The expressions for the Hertz vectors in equations (10) through (18) transform as follows, where the Π_Z^0 for a vertical dipole has been chosen as an example:

$$\Pi_Z^0 = \frac{e^{ik_0 Z}}{WR} + \frac{ik_0}{2W} \int_C \sin \theta_0 a_0(\theta_0) \cdot e^{ik_0 \cos \theta_0 (Z+h)} H_0^1(k_0 \rho \sin \theta_0) d\theta_0. \quad (B-2)$$

The integration contour C runs from $-\pi/2 - i\infty$ to $-\pi/2$ along the real θ_0 axis to $\pi/2$ and then to $\pi/2 - i\infty$, as illustrated in Figure B-2. For the angles θ_i , the contour C is obtained from equation (B-1). The P_i transform to $-ik_i \cos \theta_i$, where the negative sign is chosen in order to satisfy the radiation condition. Substituting for P_i in the Fresnel coefficients of Table A-3 results in the more familiar form

$$X_{ij} = \frac{\left(\frac{K_j}{K_i}\right)^{1/2} \cos \theta_i - \left(\frac{M_j}{M_i}\right)^{1/2} \cos \theta_j}{\left(\frac{K_j}{K_i}\right)^{1/2} \cos \theta_i + \left(\frac{M_j}{M_i}\right)^{1/2} \cos \theta_j}, \quad (B-3)$$

where the TM reflection coefficient is shown as an example.

The integral expressions can be approximately evaluated by manipulating the integration contour C in the complex θ plane. The approach is to replace the Hankel function by its asymptotic expansion, which is valid when the argument is considerably greater than unity.

Table A-2(b). Coefficients $a_i(\lambda)$, $b_i(\lambda)$, and $c_i(\lambda)$ for horizontal dipole sources.

	Two layer earth	Half space	
HMD	b_0	$\frac{X_{01} + X_{12}\beta}{1 - X_{10}X_{12}\beta}$	X_{01}
	b_1	$\frac{\gamma_{01}S_{01}}{1 - X_{10}X_{12}\beta}$	$\gamma_{01}S_{01}$
	b_2	$\frac{\gamma_{01}S_{01}X_{12}\beta}{1 - X_{10}X_{12}\beta}$	0
	b_3	$\frac{\gamma_{01}S_{01}\gamma_{12}S_{12}}{1 - X_{10}X_{12}\beta}$	$\gamma_{01}S_{01}$
	c_0	$\frac{1}{2P_0} \frac{(\gamma_{01}-1)T_{01}(1+R_{12}\beta)S_{01}(1+X_{12}\beta) - (\gamma_{21}-1)\eta_{01}T_{10}T_{12}m_{01}\gamma_{01}S_{01}\gamma_{12}S_{12}\beta}{(1-R_{10}R_{12}\beta)(1-X_{10}X_{12}\beta)}$	$\frac{1}{2P_0} (\gamma_{01}-1)T_{01}S_{01}$
	c_1	$\frac{1}{2P_0} \frac{(\gamma_{01}-1)\eta_{01}T_{01}S_{01}(1+X_{12}\beta) - (\gamma_{21}-1)R_{10}T_{12}m_{01}S_{01}\gamma_{12}S_{12}\beta}{(1-R_{10}R_{12}\beta)(1-X_{10}X_{12}\beta)}$	$\frac{1}{2P_0} (\gamma_{01}-1)\eta_{01}T_{01}$
c_2	$\frac{1}{2P_0} \frac{(\gamma_{01}-1)\eta_{01}T_{01}R_{12}\beta S_{01}(1+\gamma_{12}\beta) - (\gamma_{21}-1)T_{12}m_{01}\gamma_{01}S_{01}\gamma_{12}S_{12}\beta}{(1-R_{10}R_{12}\beta)(1-X_{10}X_{12}\beta)}$	0	
c_3	$\frac{1}{2P_0} \frac{(\gamma_{01}-1)\eta_{01}T_{01}\eta_{12}T_{12}S_{01}(1+X_{12}\beta) - (\gamma_{21}-1)\eta_{12}T_{12}(1+R_{10}R_{12}\beta)m_{01}\gamma_{01}S_{01}\gamma_{12}S_{12}}{(1-R_{10}R_{12}\beta)(1-X_{10}X_{12}\beta)}$	$\frac{1}{2P_0} (\gamma_{01}-1)\eta_{01}T_{01}$	
HED	b_0	$\frac{R_{01} + R_{12}\beta}{1 - R_{10}R_{12}\beta}$	R_{01}
	b_1	$\frac{\gamma_{01}T_{01}}{1 - R_{10}R_{12}\beta}$	$\gamma_{01}T_{01}$
	b_2	$\frac{\gamma_{01}T_{01}R_{12}\beta}{1 - R_{10}R_{12}\beta}$	0
	b_3	$\frac{\gamma_{01}T_{01}\gamma_{12}T_{12}}{1 - R_{10}R_{12}\beta}$	$\gamma_{01}T_{01}$
	c_0	$\frac{1}{2P_0} \frac{(\gamma_{01}-1)S_{01}(1+X_{12}\beta)T_{01}(1+R_{12}\beta) - (\gamma_{21}-1)\xi_{12}S_{12}m_{01}\gamma_{01}T_{01}\gamma_{12}T_{12}\beta}{(1-R_{10}R_{12}\beta)(1-X_{10}X_{12}\beta)}$	$\frac{1}{2P_0} (\gamma_{01}-1)S_{01}T_{01}$
	c_1	$\frac{1}{2P_0} \frac{(\gamma_{01}-1)\xi_{01}S_{01}T_{01}(1+R_{12}\beta) - (\gamma_{21}-1)S_{12}X_{10}m_{01}\gamma_{01}T_{01}\gamma_{12}T_{12}\beta}{(1-R_{10}R_{12}\beta)(1-X_{10}X_{12}\beta)}$	$\frac{1}{2P_0} (\gamma_{01}-1)\xi_{01}S_{01}$
c_2	$\frac{1}{2P_0} \frac{(\gamma_{01}-1)\xi_{01}S_{01}X_{12}\beta(1+R_{12}\beta)T_{01} - (\gamma_{21}-1)S_{12}m_{01}\gamma_{01}T_{01}\gamma_{12}T_{12}\beta}{(1-R_{10}R_{12}\beta)(1-X_{10}X_{12}\beta)}$	0	
c_3	$\frac{1}{2P_0} \frac{(\gamma_{01}-1)\xi_{01}S_{01}\xi_{12}S_{12}T_{01}(1+R_{12}\beta) - (\gamma_{21}-1)\xi_{12}S_{12}(1+\gamma_{01}\beta)m_{01}\gamma_{01}T_{01}\gamma_{12}T_{12}}{(1-R_{10}R_{12}\beta)(1-X_{10}X_{12}\beta)}$	$\frac{1}{2P_0} (\gamma_{01}-1)\xi_{01}S_{01}$	

Table A-3. Parameters used and Fresnel coefficients.

Parameters	
$\gamma_{ij} = \frac{k_i^2}{k_j^2}$	$\xi_{ij} = \frac{K_i}{K_j}$
$m_{ij} = \frac{P_i}{P_j}$	$\beta = e^{-2P_i t}$
$\eta_{ij} = \frac{M_i}{M_j}$	$k_i^2 = K_i M_i (2\pi)^2$

TM Fresnel Coefficients	
Reflection:	$X_{ij} = \frac{K_j P_i - K_i P_j}{K_j P_i + K_i P_j}$
Transmission:	$S_{ij} = \frac{2K_j P_i}{K_j P_i + K_i P_j}$
Relations:	$X_{ij} = -X_{ji} \quad X_{ij} = S_{ij} - 1$ $X_{ij} = 1 - S_{ji} \quad S_{ij} = \frac{\xi_{ji}}{m_{ji}} S_{ji}$

TE Fresnel Coefficients	
Reflection:	$R_{ij} = \frac{M_j P_i - M_i P_j}{M_j P_i + M_i P_j}$
Transmission:	$T_{ij} = \frac{2M_j P_i}{M_j P_i + M_i P_j}$
Relations:	$R_{ij} = -R_{ji} \quad R_{ij} = T_{ij} - 1$ $R_{ij} = 1 - T_{ji} \quad T_{ij} = \frac{\eta_{ji}}{m_{ji}} T_{ji}$

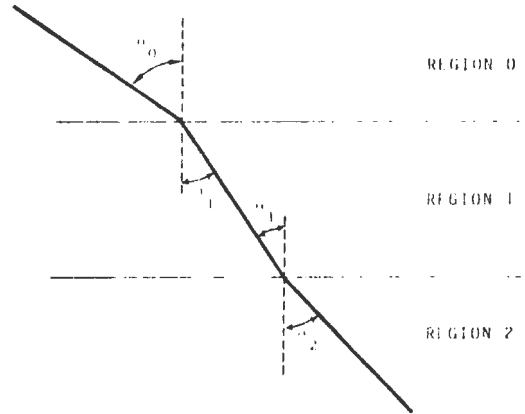


FIG. B-1. Illustration of integration variables θ_0 , θ_1 , and θ_2 and Snell's law.

$$H_0^1(t) = e^{i(t - (\pi/4))} \left(\frac{2}{\pi t}\right)^{1/2} \cdot \left(1 + \frac{1}{i8t} + \dots\right), \tag{B-4}$$

and

$$H_1^1(t) = e^{i(t - (3\pi/4))} \left(\frac{2}{\pi t}\right)^{1/2} \cdot \left(1 - \frac{3}{i8t} + \dots\right). \tag{B-5}$$

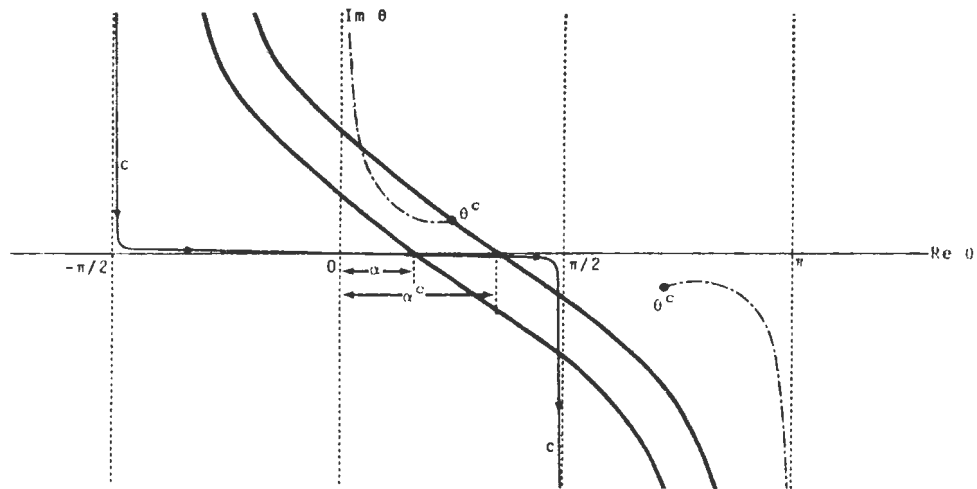


FIG. B 2. Complex θ plane showing contour C , saddle point contours Γ and Γ' , and the positions of the branch point θ^c and branch cut (chain line).

Substitution into the integrals, such as that in equation (B-2), results in an expression of the form

$$e^{iZk \cos \theta + ik\rho \sin \theta} \quad (\text{B-6})$$

in the integrand, which can be written as

$$e^{ikR \cos (\theta - \alpha)}, \quad (\text{B-7})$$

where $R = (\rho^2 + Z^2)^{1/2}$, and R and α are just the length and direction of the geometric-optics ray-path. An integral with exponential of the form (B-7) is amenable to the saddle-point method integration, where $\theta = \alpha$ is the saddle point. By deforming C to the contour of most rapid descent away from the saddle point Γ one obtains an asymptotic series in the parameter $(kR)^{-1}$ for the integral. The leading term in the series is the geometric-optics solution to the problem.

The saddle-point contour Γ is defined from the argument of the exponential in expression (B-7). Along the contour Γ ,

$$ikR \cos (\theta - \alpha) = ikR - kRs^2, \quad (\text{B-8})$$

where

$$s^2 = -\sin (\theta' - \alpha) \sinh \theta'', \quad (\text{B-9})$$

and

$$\theta = \theta' + i\theta'', \quad (\text{B-10})$$

The contour Γ is then given by the equation

$$\cos (\theta' - \alpha) \sinh \theta'' = 1 \quad (\text{B-11})$$

and is illustrated in Figure B-2.

An excellent evaluation of the particular types of integrals that appear in the text is given by Brekhovskikh (1960), and the reader is referred to this reference for more detailed discussion. In the rest of the discussion, solutions to the integrals valid to the second order in kR^{-1} are used. This involves using the second-order terms in the Hankel-function expansion and then taking the asymptotic solution to the integrals to the second order. The integrals in the text have two forms:

$$I_1 = \frac{ik}{2W} \int_C \sin \theta A(\theta) \cdot e^{ikZ \cos \theta} H_0^1(k\rho \sin \theta) d\theta, \quad (\text{B-12})$$

and

$$I_2 = \frac{ik^2}{2W'} \int_C \sin^2 \theta A(\theta) \cdot e^{ikZ \cos \theta} H_1^1(k\rho \sin \theta) d\theta. \quad (\text{B-13})$$

The solutions to the second order are given by

$$I_1 \sim \frac{e^{ikR}}{WR} \left\{ A(\alpha) - \frac{i}{2kR} \left[A''(\alpha) + A'(\alpha) \cot \alpha \right] \right\}, \quad (\text{B-14})$$

and

$$I_2 \sim -ik \sin \alpha \frac{e^{ikR}}{WR} \left\{ A(\alpha) - \frac{i}{2kR} \left[A''(\alpha) + 3 \cot \alpha A'(\alpha) - 2A(\alpha) \right] \right\}. \quad (\text{B-15})$$

Solutions (B-14) and (B-15) are valid as long as $A(\theta)$ is a slowly varying function of θ near the saddle point α . This assumption is valid provided $A(\theta)$ does not have a singular point near α . In the expressions for the various $A(\theta)$ appearing in the text, branch points and poles of $A(\theta)$ are of the utmost importance in the solutions. The branch points of $A(\theta)$ are the critical angles of the boundaries in the problem. The critical angles enter all the $A(\theta)$ through the relation

$$\cos \theta_j = \pm [1 - \gamma_{ij} \sin^2 \theta_i]^{1/2} \quad (\text{B-16})$$

in all the Fresnel coefficients subscripted ij .

The radical splits the complex θ -plane into two Riemann sheets with branch points at

$$\sin \theta_{ij}^* = \pm \frac{k_j}{k_i}. \quad (\text{B-17})$$

For the two-layer earth there are two boundaries which give two critical angles and result in a four-sheeted θ -plane. In the half-space earth problem, the complex θ -plane is two-sheeted. The convention followed throughout is that of taking the positive square root. The surface defined in this manner is referred to as the upper Riemann surface. For one to evaluate the integrals, the branch cuts from the branch points must be defined. The convention used here is the same as that of Ott and Brekhovskikh, who define the branch lines as those contours along which the imaginary part of

equation (B-16) is zero. The branch line is the chain line in Figure B-2.

The branch points must be taken into account for saddle-point angles greater than α^c . As illustrated in Figure B-2, for $\alpha > \alpha^c$, in order to deform contour C into Γ , the branch point θ^c must be crossed. A modified integration contour to take θ^c into account is shown in Figure B-3. As long as α and θ^c are well separated, the saddle-point and branch-point contributions can be evaluated separately. The contribution of the branch point is a second-order effect (Ott, 1941) as long as $\alpha \neq \theta^c$ and an approximate evaluation of the branch-point contribution can be obtained using the method of steepest descent. In general, α^c is obtained by substituting $\theta = \theta^c$ in equation (B-11). In the particular case of two perfect dielectric materials, i and j , forming the boundary,

$$\alpha_{ij}^c = \sin^{-1} \left(\frac{k_i}{k_j} \right), \quad k_i < k_j, \quad (\text{B-18})$$

and

$$\alpha_{ij}^c = \sin^{-1} \left(\frac{k_j}{k_i} \right), \quad k_j < k_i. \quad (\text{B-19})$$

The steepest-descent evaluation of the branch-point contribution is summarized as follows: The branch cut integral has the form

$$I_B = \frac{ik_i^{(n+1)}}{2W'} \int_B \sin^{n+1} \theta_i A(\theta_i) \cdot e^{ik_i R \cos \theta_i} H_n^1(k_i \rho \sin \theta_i) d\theta_i, \quad (\text{B-20})$$

where the contour B runs from $i\infty$ to θ^c on the left of the branch cut and from θ^c back to $i\infty$ along the right of the branch cut. For approximate evaluation, I_B is rewritten

$$I_B \sim - \frac{ik_i^{n+1}}{2W'} e^{-i(2n+1)\pi/4} \left(\frac{2}{\pi k_i \rho} \right)^{1/2} \int_{B'} \sin^{n+1(1/2)} \theta_i [A^+(\theta_i) - A^-(\theta_i)] \cdot e^{ik_i R \cos(\theta_i - \alpha)} d\theta_i, \quad (\text{B-21})$$

where the Hankel function has been replaced by the first term of its asymptotic expansion. The superscripts $+$ and $-$ on $A(\theta_i)$ denote the sign of the radical in equation (B-16) taken in $A(\theta_i)$, and the contour B' runs from θ_{ij}^c to $i\infty$. The contour B' is deformed into the steepest-descent contour, B'' , away from θ_{ij}^c . The path of steepest descent is defined by

$$\text{Im } ik_i R \cos(\theta_i - \alpha) = \text{constant} \quad (\text{B-22})$$

and is illustrated by the dotted line in Figure B-3. On the assumption that $k_i R \gg 1$, so that only

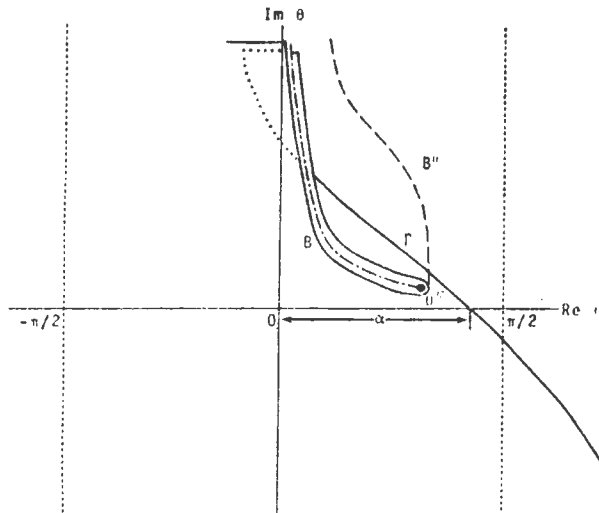


FIG. B-3. Complex θ plane showing modification of saddle point contour Γ to contour B in order to account for branch point contribution, and path of steepest descent (dotted line).

angles very close to θ_{ij}^c contribute significantly to the integral, θ_i can be set equal to θ_{ij}^c in all expressions in the integrand except for the radical. In general,

$$A^+(\theta_i) - A^-(\theta_i) = F(\theta_i) \cos \theta_j, \quad (B-23)$$

and the integral is approximately

$$I_B = \frac{-ik_i^{n+1}}{2W} e^{-i(2n+1)\pi/4} \cdot \left(\frac{2}{\pi k_i \rho}\right)^{1/2} \sin^{n+(1/2)} \theta_{ij}^c F(\theta_{ij}^c) \cdot \int_{B'} \cos \theta_j e^{ik_i R \cos(\theta_i - \alpha)} d\theta_i. \quad (B-24)$$

For low-loss media, θ_{ij}^c is close to the real axis for $k_j < k_i$ or close to the $\pi/2$ line for $k_i < k_j$ in the complex θ plane. The method of solution of the integral in equation (B-24) is slightly different in the two situations, but the results are identical. Here, the θ_{ij}^c will be assumed close to the real axis. The approximate solution is valid for θ_{ij}^c near the $\pi/2$ line.

Along the steepest-descent contour near θ_{ij}^c ,

$$\theta_i \approx \theta_{ij}^c + iu, \quad (B-25)$$

where u is much less than unity. Then,

$$\cos \theta_j \approx -e^{-i\pi/4} \sqrt{2u} \left(\frac{k_i^2 - k_j^2}{k_j^2}\right)^{1/4}, \quad (B-26)$$

and

$$ik_i R \cos(\theta_i - \alpha) \approx ik_i R \cos(\theta_{ij}^c - \alpha) - k_i R \sin(\alpha - \theta_{ij}^c)u. \quad (B-27)$$

The integral in equation (B-24) becomes

$$-ie^{-i\pi/4} \sqrt{2} \left(\frac{k_i^2 - k_j^2}{k_j^2}\right)^{1/4} e^{ik_i R \cos(\theta_{ij}^c - \alpha)} \cdot \int_{B''} \sqrt{u} e^{-k_i R \sin(\alpha - \theta_{ij}^c)u} du. \quad (B-28)$$

Now, the integral

$$\int_{B''} \sqrt{u} e^{-ku} du \sim \int_0^\infty x^2 e^{-x^2} dx = \frac{1}{2} \sqrt{\frac{\pi}{\delta^3}} \quad (B-29)$$

Rearranging equations (B-24) and (B-28), one finally obtains

$$I_B = \frac{ik_j^n}{2W\rho^2} e^{in(\pi/2)} F(\theta_{ij}^c) \cdot (k_i^2 - k_j^2)^{1/2} \cdot (1 - \cot \alpha \tan \theta_{ij}^c) \cdot e^{ik_i \rho \sin \theta_{ij}^c + ik_i \cos \theta_{ij}^c Z}, \quad (B-30)$$

which must be added to equations (B-14) and (B-15) when $\alpha > \alpha^c$.

The assumption in the saddle-point and steepest-descent techniques that $kR \gg 1$ is reasonably valid when R is greater than two wavelengths, since $k > 2\pi$ and $kR > 10$ when $R > 2$.

The poles of the integrands are also of importance in the solutions. Discussion of their role in the solutions is given in the text.

ACKNOWLEDGMENTS

The author is grateful to the National Research Council of Canada for a fellowship which supported this work.

This work is the first paper in a series providing the background for the Surface Electrical Properties Experiment planned for the Apollo 17 lunar mission.

REFERENCES

Brekhovskikh, L. M., 1960, Waves in layered media: New York, Academic Press.
 Budden, K. G., 1961, The wave-guide mode theory of wave propagation: Englewood Cliffs, Prentice-Hall, Inc.
 Clemmow, P. C., 1966, The plane wave spectrum representation of electromagnetic fields: New York, Pergamon Press.
 El-Said, M. A. H., 1956, Geophysical prospection of underground water in the desert by means of electromagnetic interference fringes: Proc. I.R.E., v. 44, p. 24-30 and 940.
 Evans, S., 1963, Radio techniques for the measurement of ice thickness: The Polar Record, v. 11, p. 406-410 and 795.
 Katsube, T. J., and Collett, L. S., 1971, Electrical properties of Apollo 11 and 12 lunar samples, in Proceedings of the Second Lunar Science Conference, Houston, Texas, edited by A. A. Levinson: Cambridge, Mass. Inst. Tech. (in press).
 Norton, K. A., 1937, The propagation of radio waves over the surface of the earth and in the upper atmosphere.

- sphere, Part I: Proc. I.R.E., v. 24, p. 1367-1387; Part II: Proc. I.R.E., v. 25, p. 1203-1236.
- Ott, H., 1941, Reflexion und Brechung von Kugeln: Effekte Q. Ordnung: Ann. Physik, v. 41, p. 443-466.
- 1943, Die Sattelpunktmethode in der Umgebung eines Pols mit Anwendungen auf die Wellenoptik und Akustik: Ann. Physik, v. 43, p. 393.
- Rossiter, J. R., LaTorraca, G. A., Annan, A. P., Strangway, D. W., and Simmons, G., 1973, Radio interferometry depth sounding: part II--experimental results: Geophysics, this issue.
- Saint-Amant, M., and Strangway, David W., 1970, Dielectric properties of dry, geologic materials: Geophysics, v. 35, p. 624-645.
- Sommerfeld, A., 1909, Über die Ausbreitung der Wellen in der Drahtlosen telegraphie: Ann. Physik, v. 28, p. 665-737.
- 1949, Partial differential equations in physics: New York, Academic Press.
- Strangway, D. W., 1969, Moon: Electrical properties of the uppermost layers: Science, v. 165, p. 1012-1013.
- Van der Waerden, B. L., 1951, On the method of saddle points: Appl. Sci. Res., B2, p. 33-45.
- Wait, J. R., 1951, The magnetic dipole over the horizontally stratified earth: Can. J. Phys., v. 29, p. 577-592.
- Wait, J. R., 1970, Electromagnetic waves in stratified media, 2nd edition: New York, The Macmillan Co.
- Ward, S. H., and Dey, A., 1971, Lunar surface electromagnetic sounding: A theoretical analysis, I.E.E.E. Trans. GE-9, no. 1, p. 63-71.

RADIO INTERFEROMETRY DEPTH SOUNDING: PART II—EXPERIMENTAL RESULTS†

JAMES R. ROSSITER*, GERALD A. LATORRACA‡, A. PETER ANNAN*,
DAVID W. STRANGWAY*§, AND GENE SIMMONS†

In such highly resistive geologic environments as ice sheets, salt layers, and the moon's surface, radio waves penetrate with little attenuation. The field strengths about a transmitting antenna placed on the surface of such an environment exhibit interference maxima and minima which are indicative of the in-situ electrical properties and the presence of subsurface layering.

Experimental results from an analog scale

model and from field tests on two glaciers are interpreted on the basis of the theoretical results of Part I. If the upper layer is thick, the pattern is very simple and the dielectric constant of the layer can be easily determined. An upper bound on the loss tangent can be estimated. For thin layers, the depth can be determined if the loss tangent is less than about 0.10, and a crude estimate of scattering can be made.

INTRODUCTION

The attenuation of electromagnetic waves propagating through terrestrial rocks is extremely high due to the moisture content; as a result, EM methods in the radio-frequency range have not found general use in exploring the earth. A few highly resistive geologic environments, such as ice sheets (Evans, 1963, 1965, 1967; Jiracek, 1967) and dry salt layers (Unterberger et al, 1970; Holser et al, 1972), are sufficiently dry to be transparent to radio waves. The uppermost layers of the moon are also very resistive (Strangway, 1969; Saint-Amant and Strangway, 1970), and typical attenuation distances (or skin depths) for lunar material are shown in Figure 1.

In these materials, EM waves propagate with little attenuation and are useful, in theory, for depth sounding. The Surface Electrical Properties Experiment, which was developed for Apollo 17, uses such a method to measure the electrical properties of the moon and to search for layering. The method is based on the interference pattern generated between various radio waves.

Theoretical background to the method and a general introduction to this series of papers is presented in Part I by Annan (1973, p. 557). In preparation for interpretation of lunar data, we have tested the method both in the laboratory with analog scale models using wavelengths in the centimeter range and in the field on glaciers using wavelengths about the same as will be used on the moon. These results are presented here.

INTERFEROMETRY TECHNIQUE

Radio-frequency interferometry (RFI) is described simply as follows: A transmitter and associated antenna on the dielectric surface generate RF waves which are received and amplified at some distance. Several waves reach the receiver—e.g., A, B, and C shown in Figure 2. Because the various waves travel different distances and/or at different velocities, they interfere with each other. The interference pattern can be generated in one of two different ways. Either frequency or distance can be varied, holding the other constant. Frequencies of 500 khz to 50 Mhz and distances

† Presented at the 40th Annual International SEG Meeting, November 9, 1970, New Orleans, Louisiana. Manuscript received by the Editor April 6, 1972; revised manuscript received November 22, 1972.

* University of Toronto, Toronto 181, Ontario, Canada.

‡ Massachusetts Institute of Technology, Cambridge, Massachusetts 02139.

§ Presently on leave to NASA Manned Spacecraft Center, Houston, Texas 77058.

© 1973 Society of Exploration Geophysicists. All rights reserved.

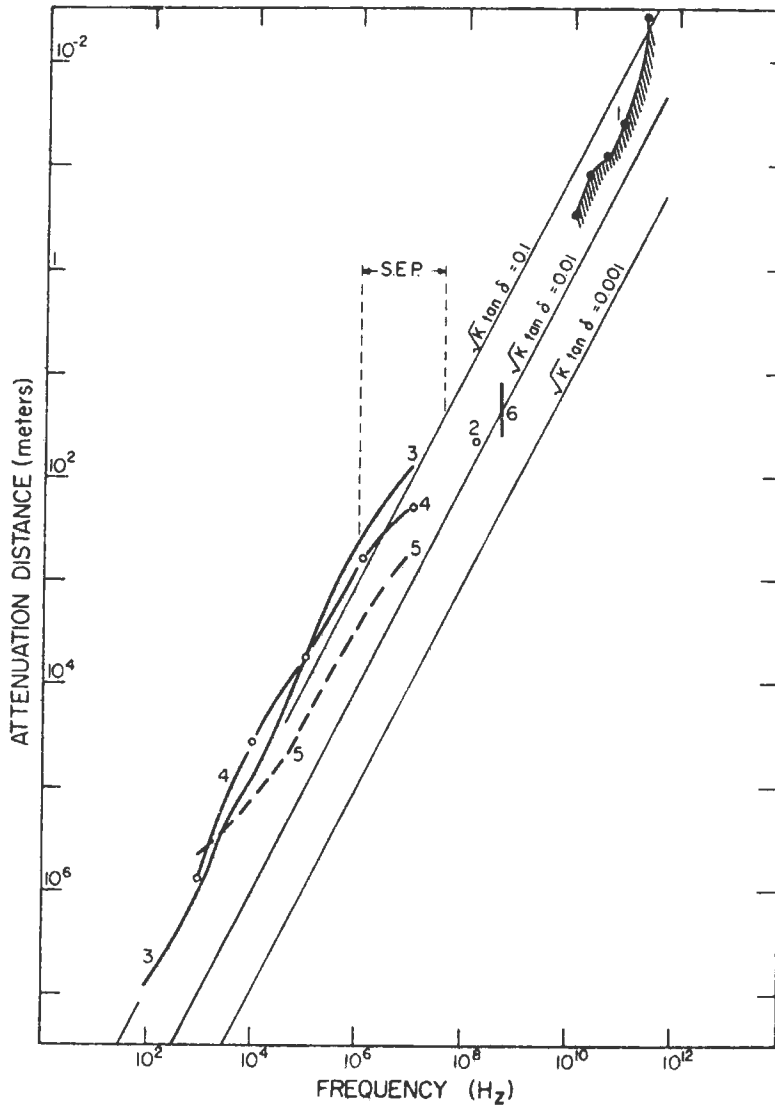


FIG. 1. Attenuation distance in lunar surface material: 1. Weaver (1965) —thermal emission; 2. Tyler (1968) — bistatic radar; 3. Chung et al (1971)—igneous sample 12002,58; 4. Katsube and Collett (1971) —breccia sample 10065; 5. Katsube and Collett (1971) — fines sample 10084; 6. Gold et al (1971) — fines, various densities. The frequency range to be used in the Surface Electrical Properties Experiment on Apollo 17 is marked 'S.E.P.'

of a few meters to a few kilometers are characteristic. However, it is not feasible now to build a tuned sweep-frequency antenna that gives interpretable results over our frequency band of interest; thus, we restrict ourselves to the variation of distance of a few fixed frequencies.

Two criteria must be met for the RFI method to effectively detect and determine depth of a subsurface boundary. First, the dielectric medium

must have a loss tangent less than about 0.1, or the amplitude of the waves that travel in the medium will be too low to interfere well with the direct wave—i.e., the medium probed must be transparent at the frequency used. Second, there must exist a contrast in electrical or magnetic properties below the surface in order to reflect energy.

Several waves are generated which are im-

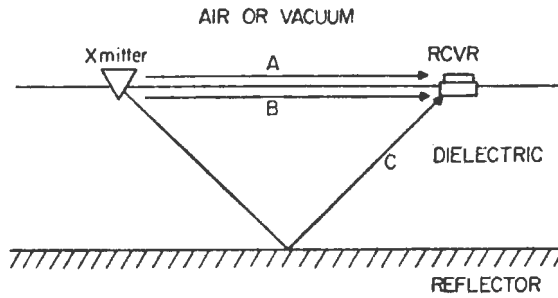


FIG. 2. The basic interferometry concept. The interference of the direct waves A and B and the reflected waves C is measured at the receiver.

portant near the source. Their geometric relations are illustrated in Figure 3. Two spherical waves, A and C, travel directly between the transmitter and the receiver. Wave C travels in the upper medium (air or vacuum), and wave A, in the earth. Since these waves have different velocities, they will interfere with each other. This interference gives a measure of the dielectric constant of the lower medium, since the greater the difference in the velocities of these two waves, the greater will be the interference frequency.

The flank, head, or lateral wave B and the spherical wave A give the transmitting antenna a highly directional radiation pattern. The lateral wave satisfies the boundary conditions imposed by wave C at the interface, since the horizontal phase velocity of B in the earth is the same as that

of wave C in the upper medium. To have the same horizontal phase velocity, wave B propagates downward at an angle β as shown in Figure 3. This angle is the angle of total internal reflection between the two media familiar to seismologists, defined by

$$\sin \beta = \sqrt{\frac{\epsilon_0}{\epsilon_1}}, \quad (1)$$

where the critical angle β is the angle between the negative z -axis and the direction of propagation of wave B, and ϵ_0 and ϵ_1 are the dielectric constants of the upper and lower media, respectively (assuming nonmagnetic media). The amplitudes of A and B are largest in the direction β . This feature is important in RFI depth sounding since energy is preferentially transmitted downward at an angle β .

The spherical wave A, traveling in the lower medium, also has a complementary wave which matches the boundary conditions. An inhomogeneous wave D is produced at the surface; this wave propagates radially from the source with the velocity of A, but decays exponentially with height above the surface. This wave is significant near the boundary, but its effect decreases as the receiver moves away from the surface.

A "critical distance" r_c is defined as

$$r_c = 2d \tan \beta, \quad (2)$$

where d is the depth to a plane horizontal reflector. Three general regions exist: the near-field, where the transmitter-receiver distance is much less than r_c ; the region near the critical distance, where the bulk of the reflected energy arrives; and the far-field, well beyond r_c . In the near-field

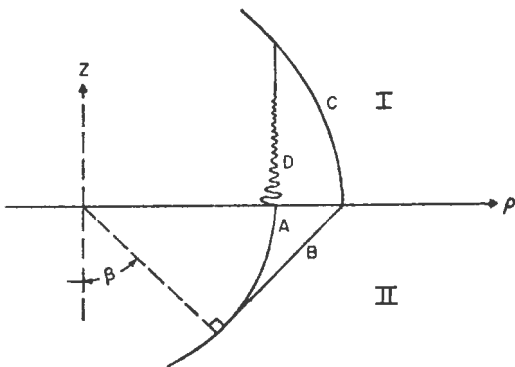


FIG. 3. Wavefronts at the air dielectric ($\epsilon_1=0$) boundary. ρ is the radial direction from the source. Medium I is air or vacuum (ϵ_0, μ_0), and medium II is a dielectric (ϵ_1, μ_1). A is a spherical wave propagating radially in medium II; B is a head wave propagating downward at the critical angle; C is a spherical wave propagating radially in medium I; and D is an inhomogeneous wave propagating radially in medium I, but attenuating exponentially with height.

the interaction between the two spherical waves A and C dominates and can be used to measure the dielectric constant of the upper layer. As the transmitter-receiver distance approaches r_c , several different waves with roughly comparable magnitudes arrive and produce a very confusing interference pattern. In the far field, multiple reflections are important, and only the normal modes of the system propagate with low attenuation.

From data obtained in the three regions, three pieces of information can be determined. The *dielectric constant* is related simply to the spatial frequency in the near-field. The *depth* to an interface can be roughly estimated from the dielectric constant and the critical distance. Third the shape of the curve and the number of far-field peaks are indicative of the *loss tangent* of the upper layer.

Two different configurations of equipment have been used in our tests; namely, horizontal electric dipole sources with magnetic dipole receivers for field work, and a vertical magnetic dipole source with an electric dipole receiver for early analog scale-model studies. Both horizontal electric and vertical magnetic dipoles produce horizontally polarized waves. Since the E-field polarization is then perpendicular to the plane of incidence, the reflection coefficient does not go through the Brewster angle null, which is associated only with waves polarized in the plane of incidence on the assumption of nonmagnetic materials.

The general configuration and notation used are shown in Figure 4 for the electric dipole. The dipole is on the surface, extends along the x -axis, and traverses are run orthogonal to it. For this configuration, approximate theoretical solutions for components H_z (vertical magnetic field), H_ρ (radial magnetic field), and E_ϕ (tangential electric field) have been found. The other components are negligible for the case of infinite horizontal plane boundaries. Nonmagnetic materials have been assumed throughout so that $\mu_0 = \mu_1 = \mu_2$.

Three cases involving infinite plane horizontal layers have been studied theoretically:

(a) the half-space;

(b) the two-layer earth with a perfect reflector at some depth; i.e., either $\epsilon_2 \rightarrow \infty$ or $\tan \delta_2 \rightarrow \infty$ so that the reflection coefficient of the lower boundary is always unity;

(c) the general two-layer earth in which $\epsilon_1 \neq \epsilon_2$ and $\tan \delta_1 \cong \tan \delta_2$. For the experimental results,

the material properties are such that only cases (a) and (b) need to be considered. Theoretical computations are compared with both scale model and glacier field data. First, however, a brief description of the scale model and the field tests will be given.

ANALOG SCALE MODEL

Scaling of an electromagnetic model is particularly simple when the conductivity is negligible. The wavelength is inversely proportional to the frequency used, and all other relations remain invariant. In our scale model, we used microwave frequencies with free-space wavelengths of 3 to 5 cm. By scaling all data in terms of wavelengths, model, field, and theoretical results can readily be compared.

The first scale model consisted of a klystron source at 10 Ghz feeding a vertical magnetic slot antenna, a small diode receiver, a traversing system, and an automatic recording arrangement. The dielectric used was dry, pure quartz sand (160 mesh), and the reflector was an aluminum plate. The plate and sand were contained in a plywood box with sides that sloped out at about 45 degrees. The box was approximately 30 wavelengths long and 15 wavelengths wide, at the bottom. The setup is shown schematically in Figure

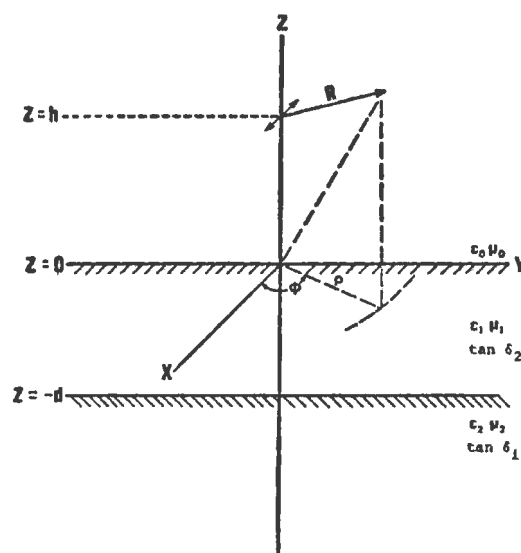


FIG. 4. General configuration of a horizontal electric dipole over a two-layer earth. ϵ_i is the real dielectric constant, μ_i is the permeability, and $\tan \delta_i$ is the loss tangent of the i th layer.

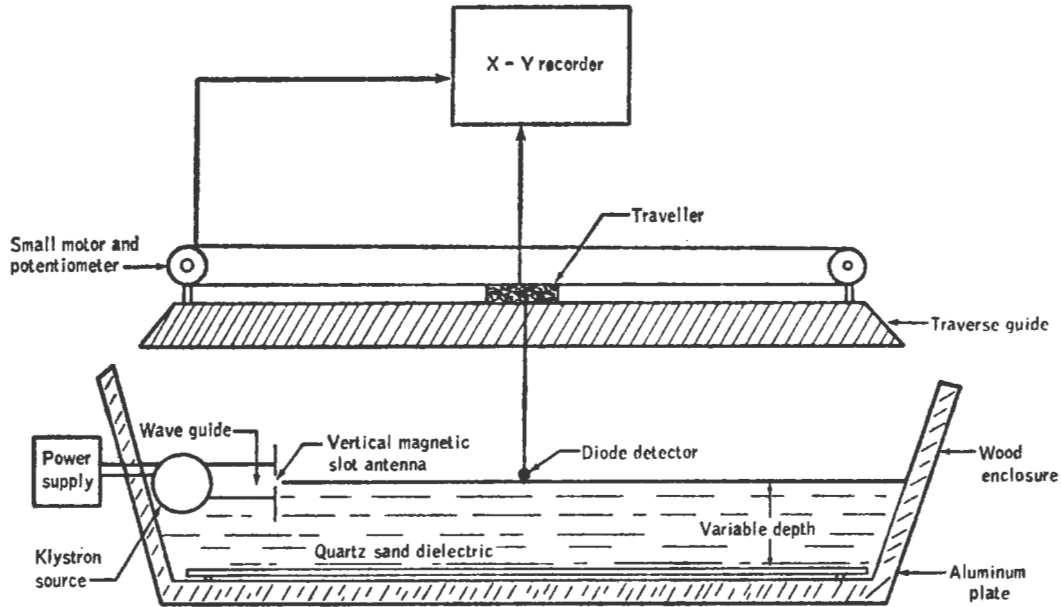


FIG. 5. The analog scale model. The transmitter was composed of a klystron tube radiating at 10 GHz into a rectangular waveguide. A vertical magnetic slot antenna was formed by a slit at the end of the waveguide. The transmitter could be raised or lowered. Signals were received by a small diode which could traverse for about 20 wavelengths at any height. The dielectric used was quartz sand and the reflector was a flat aluminum plate. Received signal strength versus receiver position was recorded directly on an X-Y recorder.

5. A later version of the scale model using transformer oil as a liquid dielectric has also proved very successful. The transmitter and receiver were small electric dipoles, operated at 6 GHz, and the model was contained in a tank lined with microwave absorbing material.

The validity of our experimental arrangement was initially tested by comparing model results with theoretical predictions for a very simple case. The transmitter and receiver were both placed at height h above the aluminum plate without the sand.

From Part I, the EM radiation from a vertical magnetic dipole at height h over a magnetically uniform half-space is described completely by the vertical magnetic Hertz vector, given by

$$\pi_z = \frac{e^{ik_0 R}}{R} + R_{01} \frac{e^{ik_0 R'}}{R'}, \quad z \geq 0, \quad (3)$$

where k_0 is the wavenumber, R_{01} is the reflection coefficient at the boundary ($z=0$), R is the direct distance to the receiver, and R' is the distance traveled by the reflected wave. If the boundary is a perfect reflector, $R_{01} = -1$. For the receiver at height h :

$$R = [r^2 + (z - h)^2]^{1/2} = r, \quad (4)$$

and

$$R' = [r^2 + (z + h)^2]^{1/2} = [r^2 + 4h^2]^{1/2}. \quad (5)$$

The tangential electric field E_ϕ is then

$$\begin{aligned} E_\phi &= -i\omega\mu \frac{\partial \pi_z}{\partial r} \\ &= -i\omega\mu \left[\frac{e^{ik_0 r}}{r} \left(ik_0 - \frac{1}{r} \right) \right. \\ &\quad \left. - \frac{e^{ik_0 [r^2 + 4h^2]^{1/2}}}{\sqrt{r^2 + 4h^2}} \left(ik_0 - \frac{1}{\sqrt{r^2 + 4h^2}} \right) \right. \\ &\quad \left. \left(\frac{r}{\sqrt{r^2 + 4h^2}} \right) \right]. \end{aligned} \quad (6)$$

Then,

$$\begin{aligned} E(r, h) &= -i\omega\mu \left[\frac{e^{ik_0 r}}{r} \left(i - \frac{1}{r} \right) - \frac{e^{ik_0 [r^2 + 4h^2]^{1/2}}}{\sqrt{r^2 + 4h^2}} \right. \\ &\quad \left. \frac{r}{\sqrt{r^2 + 4h^2}} \left(i - \frac{1}{\sqrt{r^2 + 4h^2}} \right) \right]. \end{aligned} \quad (7)$$

where $A = -i\omega\mu(4\pi^2/\lambda^2)$ and is an arbitrary scaling factor for a unit magnetic dipole, r is the transmitter-receiver separation in wavelengths, h is the transmitter-receiver height above the reflecting plate in wavelengths, and λ is the wavelength in free-space.

Typical comparisons between theory and experiment are shown in Figure 6. The agreement in the position of the peaks is very good. Although the amplitudes are on an arbitrary scale and are therefore not directly comparable, the ratio between each theoretical and experimental peak is approximately constant. Experimental deviations from theoretical solutions are not large and are primarily due to reflections between the transmitter and either the receiver or the sides of the box. The good agreement between calculated and measured curves was taken as the main proof that the experimental arrangement was satisfactory to measure interference between various waves.

GLACIER FIELD TESTS

Introduction

Ice is one of the few terrestrial rocks with uniformly high resistivity. Resistivities of 10^5 to 10^7

ohm-m have been measured consistently (e.g., R othlisberger, 1967; Keller and Frischknecht, 1961). A few glaciers have been carefully mapped and are accessible for field tests. We selected two on which to test the RFI technique.

The dielectric properties of ice and snow have been reviewed by Evans (1965). The dielectric properties of glacial ice and snow have been studied in situ by Watt and Maxwell (1960) and by Walford (1968). Two parameters are important—the dielectric constant and the loss tangent. Ice has a relaxation in the audio-frequency range, but unlike many dielectric materials has none near the radio frequencies. Hence, while the value of its dielectric constant is frequency independent in the radio frequencies, the value of its loss tangent is roughly inversely proportional to frequency and is strongly temperature dependent.

From 1 to 30 Mhz, the value of the dielectric constant is 3.20 ± 0.05 and is fairly independent of frequency, impurities, or temperature. Over the same frequencies, $f \cdot \tan \delta \cong 0.25$ at 0°C , but $f \cdot \tan \delta \cong 0.10$ at -10°C , where f is the frequency in Mhz. Although the effects of impurities, cracks, air bubbles, and free water on the loss tangent are not well understood, the values for losses in gla-

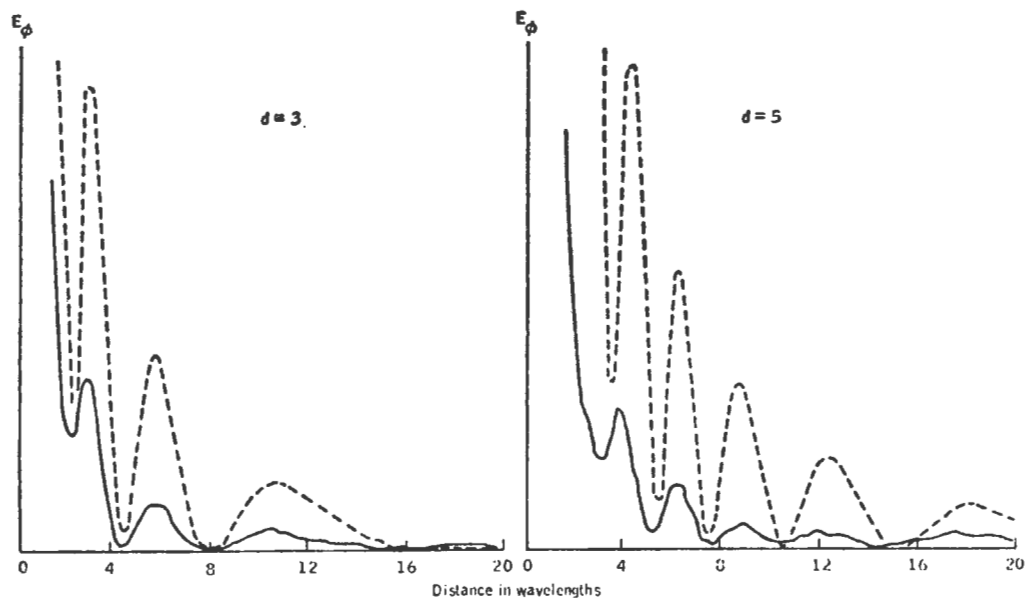


FIG. 6. Typical theoretical and experimental curves for calibration of the scale model. Dashed line is theoretical and solid line is scale model. Curves for a depth of 3 wavelengths are on the left, and for 5 wavelengths, on the right. No dielectric is present. Scaling is different for each of the four curves.

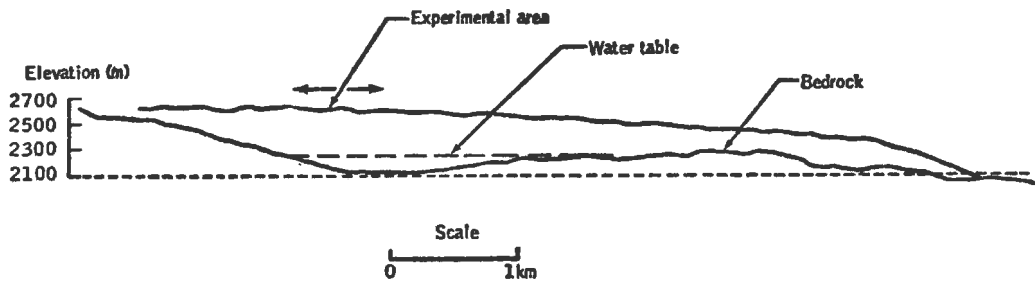


FIG. 7. Cross-section of the Gorner Glacier, from Swiss seismic data.

cier ice are not appreciably different from those in pure ice.

The inverse-frequency dependence of the loss tangent in ice implies that the attenuation of an EM wave in ice is directly proportional to the absolute distance, not to the number of wavelengths that the wave travels. Therefore, the maximum sounding depth in ice free of scattering bodies is virtually independent of the frequency used by any radio or radar technique in the frequency range from 0.1 to nearly 1000 Mhz.

The Gorner Glacier

The Gorner Glacier, located in southern Switzerland, has been extensively drilled and mapped seismically for the Swiss Hydroelectric System, and a longitudinal section of the glacier is shown in Figure 7. It is a deep glacier; the depth in the test area to the postulated water-table is about 400 m and the depth to bedrock is 500 m. It is effectively a half-space for the interferometry technique.

Equipment used on the tests, run in September, 1969, was both simple and portable. The transmitter was a General Radio 1330A bridge oscillator, which fed the transmitting antenna through a ferrite core 1 to 1 balun. Two types of transmitting antennas were used: an untuned horizontal electric dipole and a small ($\lambda/10$ diameter) loop as a vertical magnetic dipole. Output power was less than $\frac{1}{2}$ watt. The receiver was fed by either a 5-m electric dipole or a Singer single-turn 1-m diameter loop, with simple broad-band matching to the 50-ohm input impedance of a Galaxy R530 communications receiver. The receiver output was read from a Hewlett-Packard 427A portable voltmeter and recorded manually.

Field procedure consisted of recording field strength about every $\frac{1}{4}$ wavelength along tra-

verses away from the transmitter. Frequencies of 1, 2, 4, 7, and 10 Mhz were used. E_ϕ , H_z , and H_ρ components were measured for both horizontal electric and vertical magnetic transmitting antennas.

The Athabasca Glacier

The Athabasca Glacier, located in Alberta, Canada, has also been studied extensively: a gravity survey has been conducted by Kanasewich (1963), seismic and drilling studies have been made by Paterson and Savage (1963), and EM and resistivity soundings have been run by Keller and Frischknecht (1961). A depth contour map, reconstructed from Paterson and Savage and showing our traverse line, is given in Figure 8. The thickness of the ice along the traverse varies from about 130 m to 280 m.

The Athabasca Glacier tests, run in March, 1970 used a crystal-controlled transmitter that was operated at frequencies of 2, 4, 8, 16, and 24 Mhz. Output power was about one watt. It fed a ribbon-wire tuned horizontal electric dipole antenna through a balun feed network. The antenna consisted of several number-22 wires, each cut to the resonant length for a single frequency, lying beside each other on the ice surface. Each wire was cut to the resonant length of one of the frequencies in free space and connected in parallel to the balun feed. Each wire had to then be cut to between 75 and 90 percent of its length in order to reflect minimum power back to the transmitter.

This antenna was experimental, and several problems may have been associated with its use. The amount of clipping needed to retune the wires after they had been placed on the ice was insufficient to account for the dielectric contrast between ice and air. We feel that each wire was

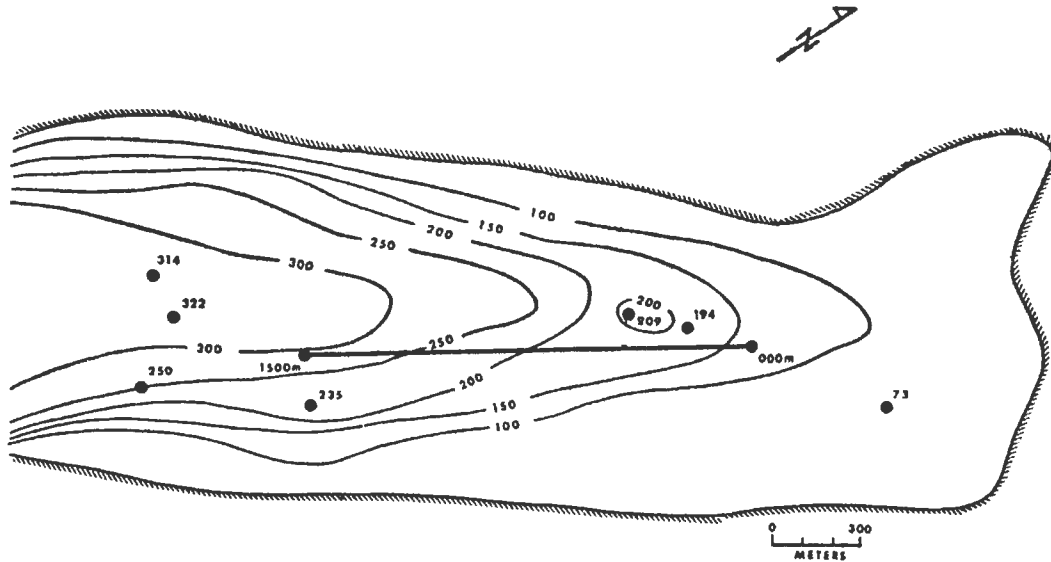


FIG. 8. Contour map of the Athabasca Glacier, drawn from the seismic and drilling data of Paterson and Savage (1963). Boreholes, with depths in meters, are shown. Our interferometry traverse line is marked 000 m to 1500 m.

reactively coupled to the other wires, which then radiated energy. Therefore, the longer wires were effectively long antennas (greater than a half wavelength) for the higher frequencies and could have radiated significantly off the orthogonal direction. The antenna was probably not well coupled either to the subsurface or to the traverse direction, and spurious reflections could have been received from the sides of the glacier.

The receiver and the field procedure were similar to those used on the Gorner Glacier with the following differences: A smaller $\frac{1}{3}$ -m-diameter loop was used for 16 and 32 Mhz. Readings were taken every $\frac{1}{8}$ wavelength, to a distance of 20 wavelengths or until the signal was too low to detect. Most traverses were run from NE to SW, although a few were run from SW to NE with the transmitter displaced to the SW end of the traverse line. Both H_z and H_p components were taken, as well as one E_ϕ traverse.

RESULTS

The half-space

If the boundary between the first and second layers is not important, the only waves which reach the receiver are the direct waves through the air (or vacuum) and the dielectric. This case

is simple to solve theoretically, and suites of curves have been compiled for the E_ϕ , H_p , and H_z components (see, for example, Figure 9). There is very good agreement between theory and experimental results from the Gorner Glacier. Figure 10 shows a typical experimental curve and a series of theoretical curves for various dielectric constants. The interference peaks and troughs align best with those calculated for $\epsilon_1 = 3.2$. By comparison with curves like those in Figure 9, we have estimated the loss tangent to be less than 0.07 at 10 Mhz.

One interesting feature of both the theoretical and experimental half-space curves is that results for the H_z and E_ϕ components are identical, but the peaks and troughs of the H_p component are shifted $\frac{1}{2} \lambda$ away from the transmitter (see Figure 11). This relation between the interference patterns in H_z , E_ϕ , and H_p provides a basis on which to detect departures of the fields from the half-space response which could be due to subsurface reflections or scattering from surface or subsurface irregularities.

Therefore, in a half-space, RFI can easily be used to determine the dielectric constant of the upper layer if we know the positions of the peaks and troughs. Theoretical results indicate that the

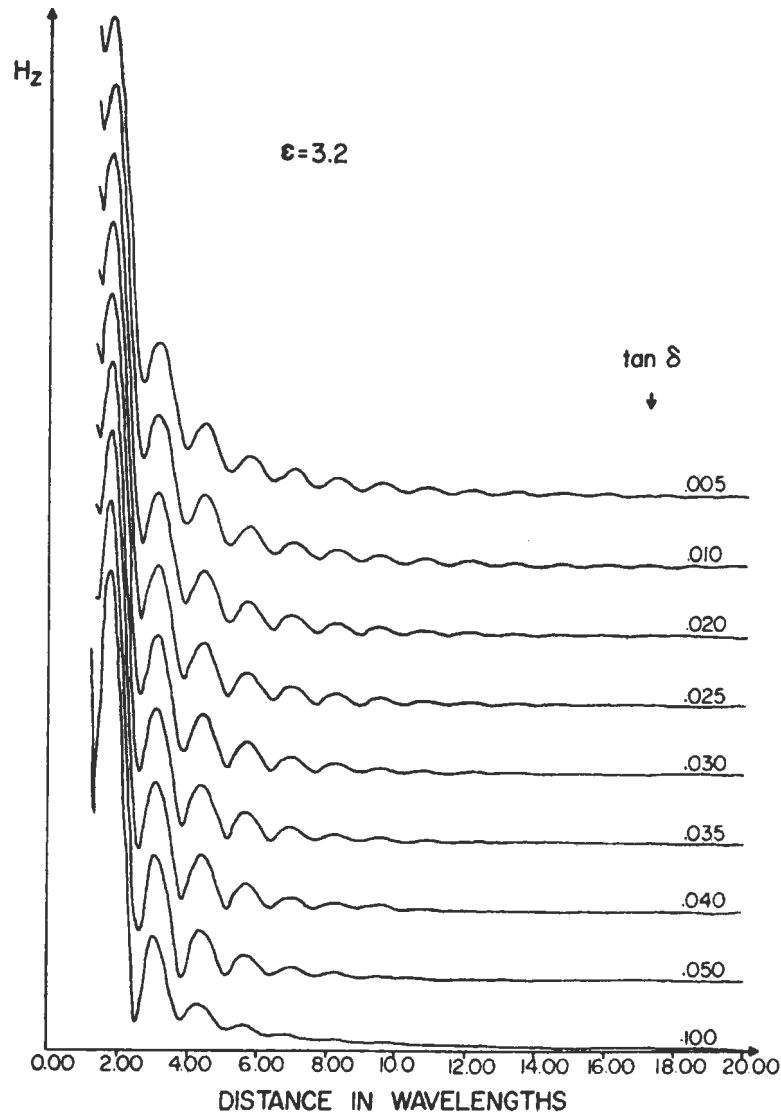


FIG. 9. Theoretical half-space curves for a dielectric constant of 3.2 and various loss tangents. Peaks and nulls, are less distinct for higher loss tangents, but their positions do not change.

loss of the layer does not change the position of the peaks, but as the loss decreases, both the sharpness of the nulls and the number of observable peaks increases. By measuring several components it may be possible to determine if the measurements have been affected by random scattering.

Two-layer earth: Perfect reflector

Calculations for the two-layer model are more

complex. Exact theoretical solutions have not been obtained, but after performing the mathematical manipulations discussed in Part I, approximate numerical solutions have been compiled and plotted. Typical suites of curves are shown in Figure 12 to illustrate the effect of changes in dielectric constant, thickness, and loss tangent, of the first layer. Although the effects of these parameters are not fully separable, in general, the frequency of the initial peaks and troughs is indi-

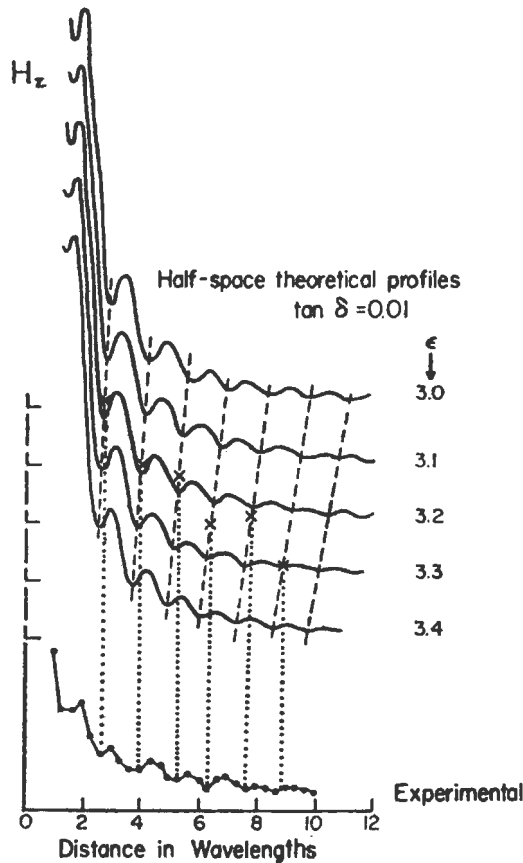


FIG. 10. Several theoretical half space curves and an experimental curve from the Gorner Glacier at 10 Mhz (H_z component). The experimental curve has peaks and troughs that correspond to the theoretical curve for a dielectric constant of 3.2.

cative of the dielectric constant; the position of the main energy peak is determined by the thickness and the dielectric constant; and the sharpness of the pattern changes with the loss tangent. For this example, the dependence on loss tangent is particularly noticeable for loss tangents in the range .01 to .05.

A suite of analog scale-model patterns and the corresponding theoretical curves are shown in Figure 13. The dielectric oil had a measured dielectric constant of 2.16 and a loss tangent of 0.0022. In general, for thicknesses greater than 2 or 3 wavelengths the agreement in both position and amplitude of the peaks and nulls is good. For thinner layers the agreement is poorer, probably because the theoretical solutions become less ac-

curate (see Part I). Differences between experimental and theoretical results in the near-field may also be caused by the theoretical approximations. They might also be caused by spurious reflections in the experimental tank from wires connecting the transmitting antenna to its source. The other major discrepancy between the two solutions is at the critical angle where the approximations made in the theory are most significant. However, the good agreement between the theoretical and scale-model results has given us confidence in both.

The results from the Athabasca Glacier are complicated by the fact that the thickness of the glacier increases along the traverse with a slope of approximately 1:10. Since the general theory for this geometry is extremely difficult, and has not been worked out in detail, we used theoretical curves for several thicknesses near the mean traverse thickness for comparison. Such a comparison is not altogether accurate, since the effects of a thickening layer depend on both the thickness and the rate of change of thickness.

Comparisons were made between data measured on the Athabasca Glacier and many suites of theoretical curves. It was found that the family of theoretical curves for the known parameters of the glacier, when compared with the experimental data as a whole, fitted better than any other set, although there was some ambiguity. Several examples are shown in Figure 14. The experimental data were run through a simple 1, 1, 1 running average filter before plotting. This filtering enhanced the main features of the curves by reducing small random variations. The agreement between theoretical and experimental data is far from perfect. However, if it is recognized that because the thickness of the ice is increasing along the traverse, some moveout of the measured peaks is to be expected, and a consistent picture emerges.

Figure 14 shows data obtained at 2, 4, 8, and 24 Mhz on the Athabasca Glacier, along with three theoretical curves with depths bracketing those along the traverse. As the frequency increases, the thickness of the ice, measured in wavelengths, also increases, so that quite different curves are found for each frequency. At 2 Mhz the curves are smooth and regular and the agreement between theory and experiment is quite good. At 4 Mhz the patterns are more complex, and although these are similar features, the the-

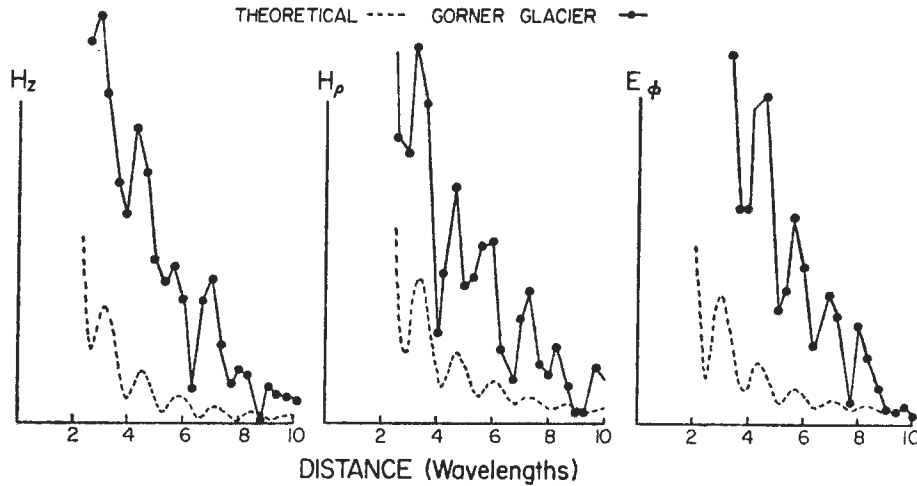


FIG. 11. Theoretical half-space curves and results from the Gorner Glacier. Source is a horizontal electric dipole at 10 Mhz. Theoretical curves are for dielectric constant of 3.2 and a loss tangent of 0.03. Peaks and troughs for the H_ρ component are shifted away from the transmitter one-half wavelength.

oretical curves do not correspond exactly to the experimental. At 8 Mhz the curves are complex, but the agreement is better, especially the large peak at about 7 wavelengths distance. At 24 Mhz there are many peaks and troughs in both curves. We feel the lack of correlation between theory and experiment is largely due to many randomly scattered reflections in the experimental curve. At 24 Mhz the wavelength of 12.5 m is the same size as many crevasses and surface roughness features.

In summary, as the thickness of the dielectric layer increases, the interference patterns change from curves with a few well-defined peaks to curves with high spatial frequencies and no large peaks. These features are seen in both theoretical and experimental results. The fact that both H_ρ and H_z components are basically similar, although they differ in their fine structure, increases our confidence in the match between theory and experiment.

INTERPRETATION

Dielectric constant

This parameter is easy to obtain directly from the data, since, as shown above, the direct air and subsurface waves interact near the source to give a pattern dependent only on this parameter. If the air wave has a wavenumber k_0 ,

$$k_0 = \frac{2\pi}{\lambda_0}, \tag{8}$$

where λ_0 is the free-space wavelength; and if the subsurface wave has wavenumber k_1 ,

$$k_1 = \frac{2\pi}{\lambda_1} = \frac{2\pi\sqrt{\epsilon_1}}{\lambda_0} = \sqrt{\epsilon_1} k_0, \tag{9}$$

then the beat frequency wavenumber k is

$$\Delta k = k_1 - k_0 = \frac{2\pi}{\lambda_0} (\sqrt{\epsilon_1} - 1). \tag{10}$$

The spatial interference wavelength λ_b is then

$$\lambda_b = \frac{2\pi}{\Delta k} = \frac{\lambda_0}{\sqrt{\epsilon_1} - 1}. \tag{11}$$

Therefore,

$$\epsilon_1 = \left(\frac{\lambda_0}{\lambda_b} + 1 \right)^2 \tag{12}$$

and can be obtained directly from the data. For ice, $\lambda_b \cong 1.27\lambda_0$.

Loss tangent

The loss tangent can be estimated in a qualitative way from the sharpness of the patterns in the

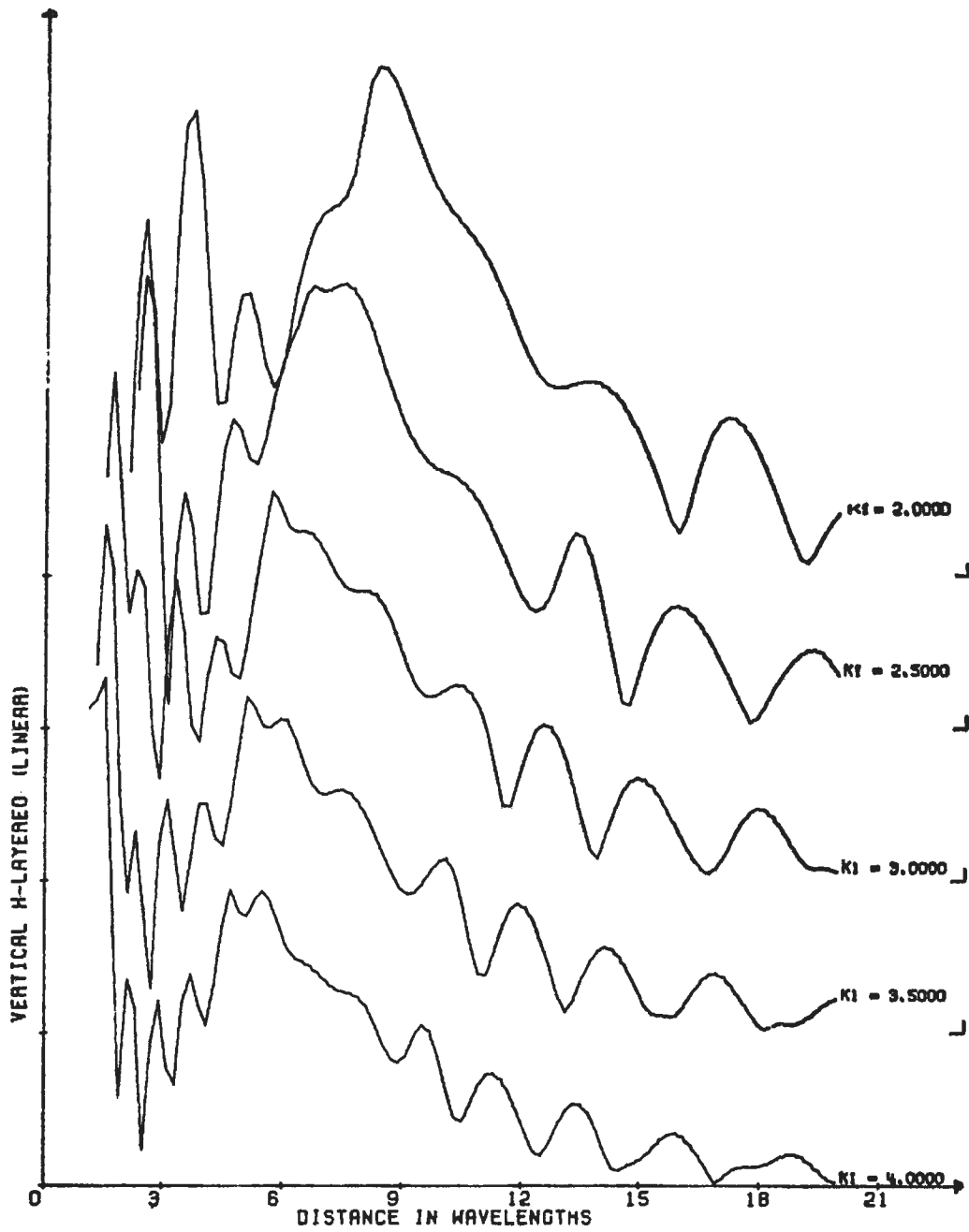


Fig. 12a. Theoretical interference curves for H_z component over a two-layer earth. Dependence on dielectric constant is shown. Depth = 4.000λ , $L/T_1 = 0.0200$, $K_1 =$ varying.

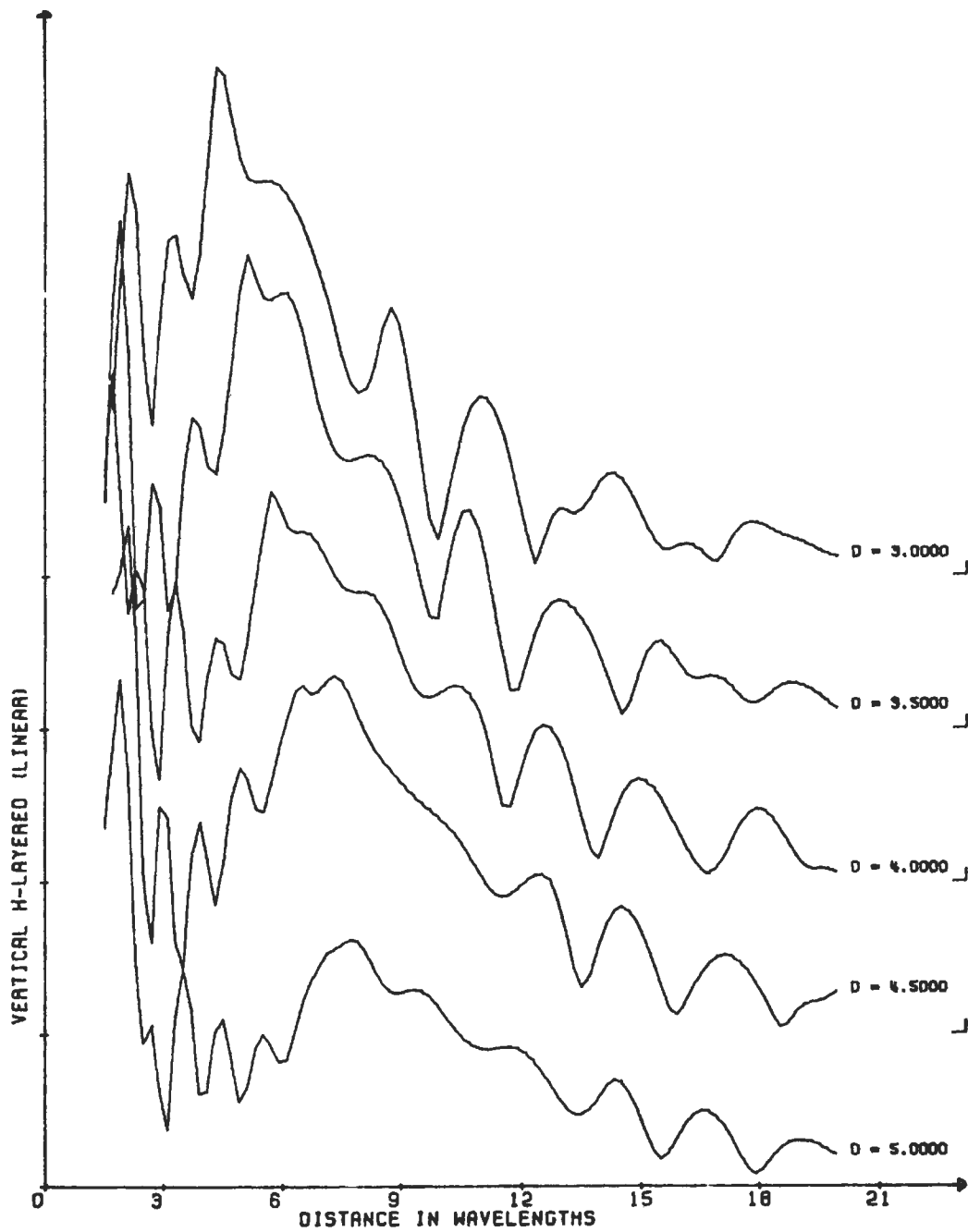


Fig. 12b. Theoretical interference curves for H_z component over a two-layer earth. Dependence on thickness is shown. Depth = varying, $L/T1 = 0.0200$, $K1 = 3.000$.

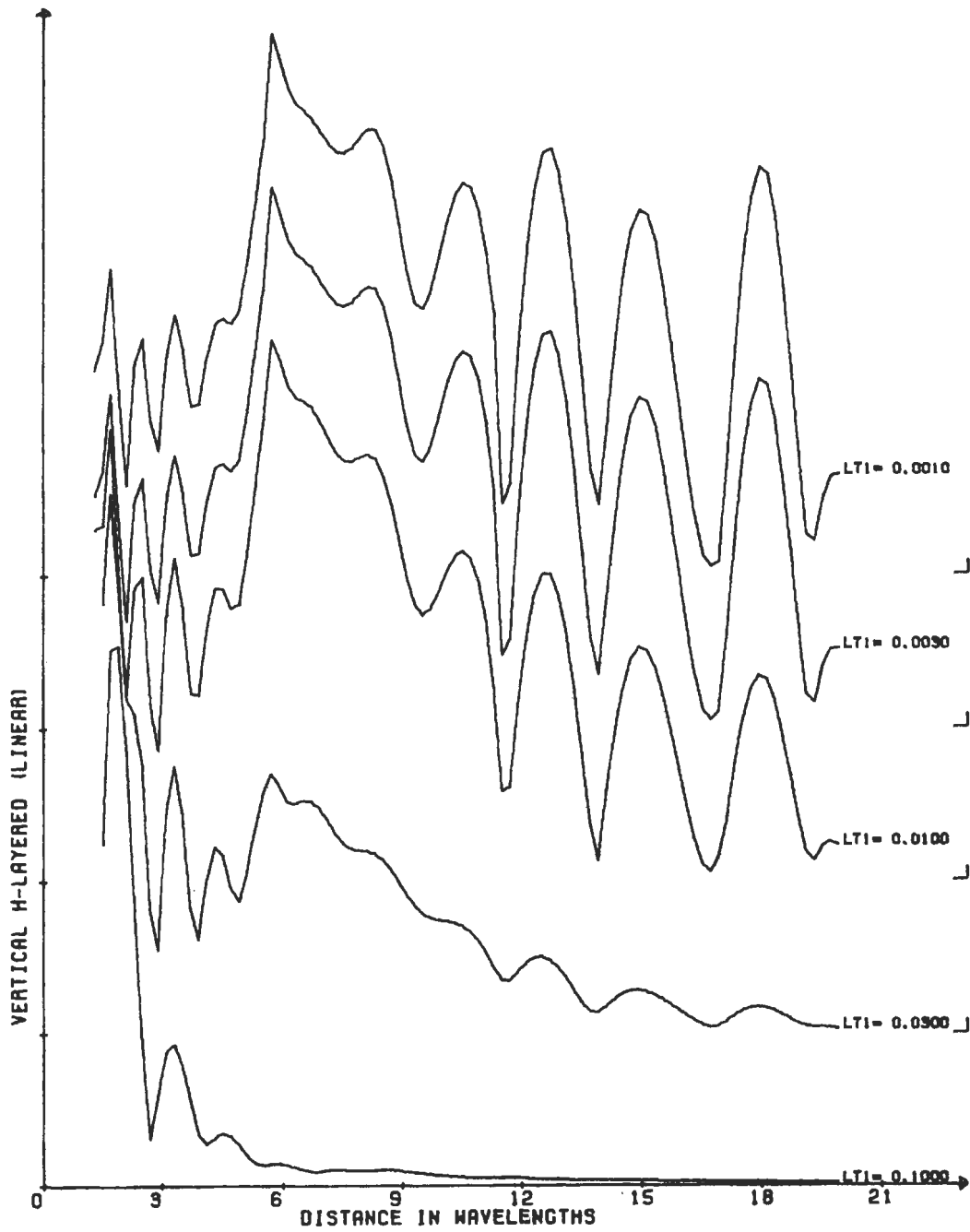


FIG. 12c. Theoretical interference curves for H_z component over a two-layer earth. Dependence on loss tangent is shown. Depth = 4.000λ , $LT1 =$ varying, $K1 = 3.000$.

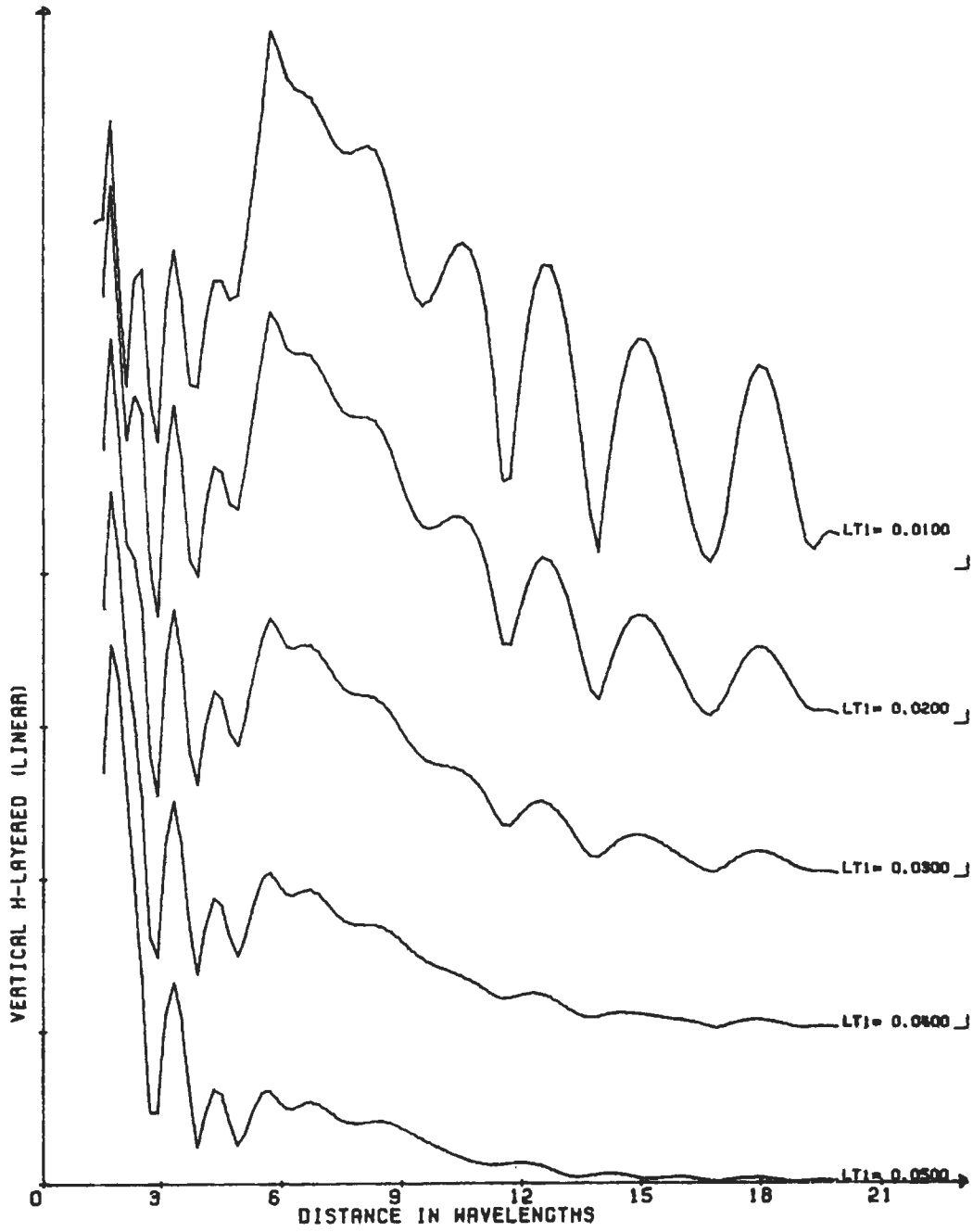


FIG. 12d. Theoretical interference curves for H_z component over a two layer earth. Dependence on loss tangent is shown. Depth = 4.000λ , $LT_1 =$ varying, $K_1 = 3.000$.

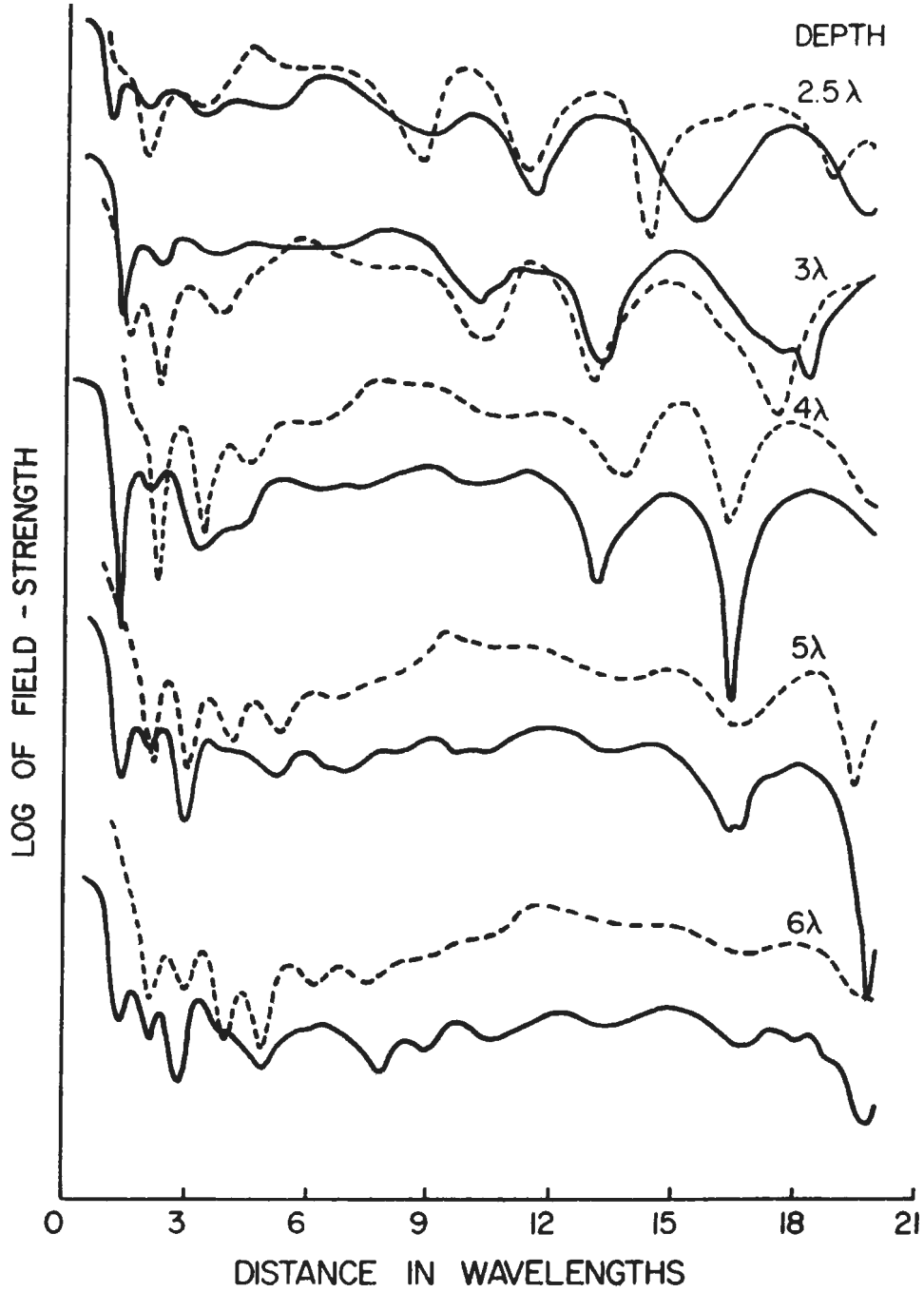


FIG. 13. Analog scale-model curves (solid line, E_θ) and corresponding theoretical curves (dashed line, H_x , $K = 2.16$, $\tan \delta = .0022$) for various thicknesses of the upper layer. E_θ and H_x are identical in this configuration. Dielectric constant (K) and loss tangent ($\tan \delta$) were measured independently.

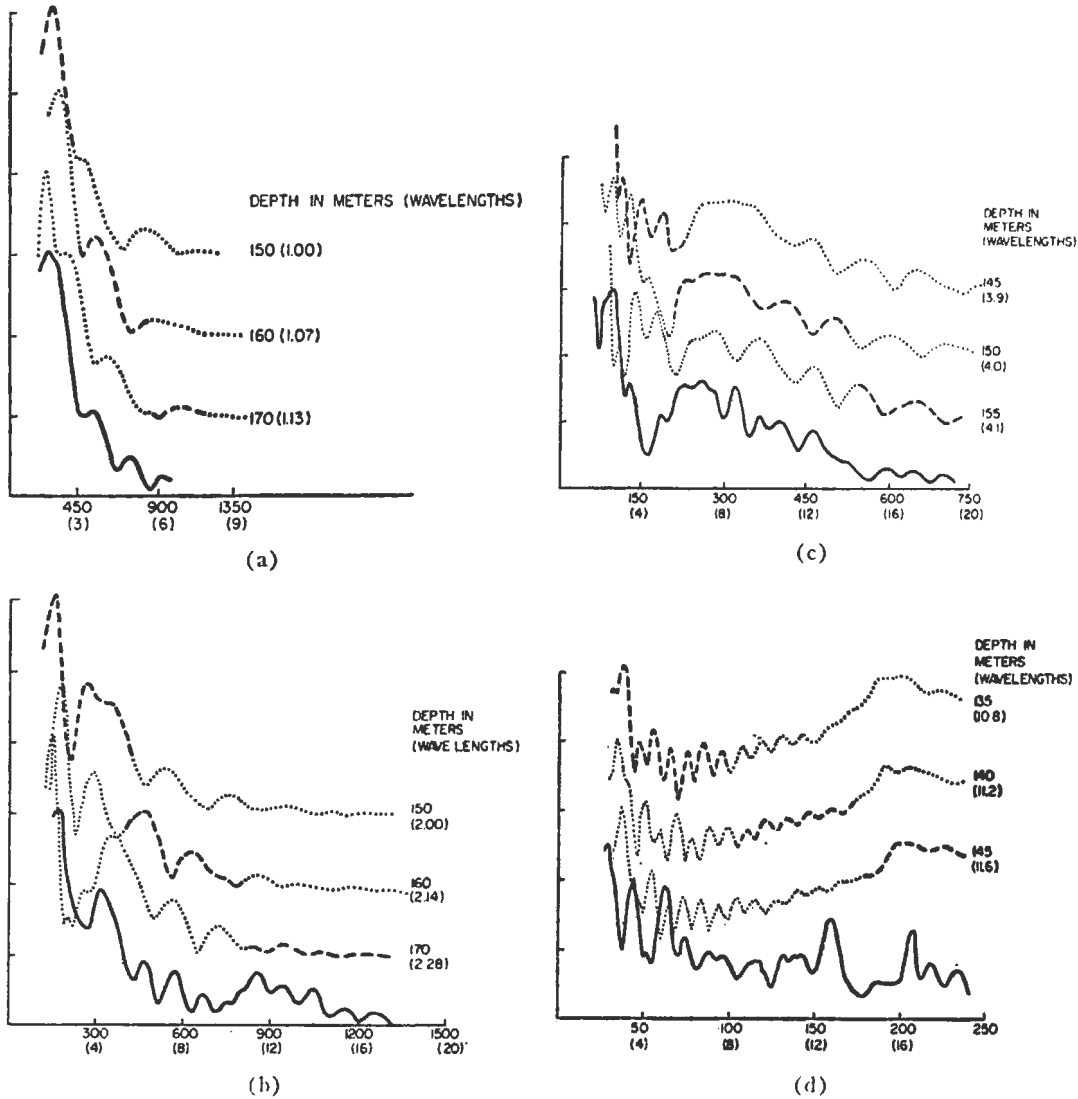


FIG. 14. Theoretical curves and Athabasca Glacier results at (a) 2, (b) 4, (c) 8, and (d) 24 Mhz. (a) dashed/dotted line, theoretical H_z , $K=3.2$, $\tan \delta=0.08$; solid line, experimental Athabasca Glacier, H_z , 2 Mhz. (b) dashed/dotted line, theoretical H_ρ , $K=3.2$, $\tan \delta=0.04$; solid line, experimental Athabasca Glacier, H_ρ , 4 Mhz. (c) dashed/dotted line, theoretical H_ρ , $K=3.2$, $\tan \delta=0.02$; solid line, experimental Athabasca Glacier, H_ρ , 8 Mhz. (d) dashed/dotted line, theoretical H_z , $K=3.2$, $\tan \delta=0.007$; solid line, experimental Athabasca Glacier, H_ρ , 24 Mhz. Distance in meters (wavelengths).

near field. In the near field the two direct waves add to form peaks and subtract to form nulls. If the waves are about the same size, the peaks and nulls will be sharp, but if one wave is much larger than the other, there will be little interference.

As the amplitude of the subsurface wave decreases below the amplitude of the air wave, the

pattern becomes less sharp. An envelope formed by joining the peaks and by joining the nulls of the interference pattern becomes thinner at a rate determined by the loss tangent of the medium.

In the Gornier Glacier data, the loss tangent was estimated to be less than $0.7/f$ (Mhz), well

within the published value for ice. In the Athabasca data, reflections appear to disturb the two direct waves too greatly to be able to use this simplified approach.

Depth

An estimate of the dielectric constant and the critical distance from the field data can be used to estimate the depth. However, an assumption about the dip of the reflector must be made. The method fails if either the dielectric constant or the critical distance cannot be estimated accurately.

Scattering

One of the major unknowns in the application of the RFI technique is the effect of irregularities in the medium. It is reasonable to believe that the effects of irregular surfaces, inhomogeneities within the dielectric, and objects near the antennas could all perturb the measured data. One possible way to remove small random effects is to appropriately filter the data, and a simple running-average filter was used to enhance the pertinent features of the Athabasca Glacier data.

An estimate of scattering is important to understand geologic structure. During the Athabasca trials the H_ϕ component, which should theoretically be null for plane horizontal layers, was observed to be significant (though weaker than the other components). Therefore, H_ϕ provided a measurement of the scattering, which was considerable at the higher frequencies. The similarity of all the components measured on the Gorner Glacier on the other hand implied that scattering was not significant up to 10 Mhz.

CONCLUSIONS

1. The RFI technique is a practical method with which to study layering in low-loss dielectrics ($\tan \delta < 0.1$).

2. Three parameters of the upper layer can be estimated from the data: the dielectric constant, the loss tangent, and an estimate of the thickness to a reflector. Measurements of $\epsilon = 3.2$ and $f \cdot \tan \delta = 0.7$ (f in Mhz) for ice are in agreement with known results.

3. The method is an inexpensive way to sound ice sheets less than a few hundred meters thick, and could be used to study low-loss layers on the moon.

4. Further work is required to refine and quantify the interpretational procedure, to extend it to

more complex geometries, and to understand better the effects of random scatterers.

ACKNOWLEDGMENTS

We would like to acknowledge the assistance of the following: Mr. E. A. Johnston of MIT's Center for Space Research, who built the transmitter used on the Athabasca Glacier and participated in the expedition; Dr. H. Röthlisberger, Mr. P. Fohn, and Mr. M. Aellen, who provided advice on the logistics of the Gorner Glacier; The Department of National and Historic Parks Branch, Calgary, who gave us permission to work on the Athabasca Glacier, and, along with Brewster Transport Company and the Administration of Jasper National Park, provided much useful support; and Dr. A. K. Sinha, who allowed us to use some of his preliminary theoretical curves. We would also like to thank Mr. L. Tsang and Dr. J. A. Kong for pointing out a sign error in programming the theoretical equations.

Financial support was provided by NASA grant no. NGL 22-009-257 and contract NAS9-11540 at MIT with subcontracts at the University of Toronto; Rossiter thanks The Lunar Science Institute, Houston, Texas for support under contract no. NSR 09-051-001.

This work is the second paper in a series providing the background for the Surface Electrical Properties Experiment, planned for the Apollo 17 lunar mission.

REFERENCES

- Annan, A. P., 1973, Radio interferometry depth sounding: Part I—Theoretical discussion: *Geophysics*, this issue.
- Chung, D. H., Westphal, W. B., and Simmons, G., 1971, Dielectric behavior of lunar samples: Electromagnetic probing of the lunar interior, *in* *Proceedings of the Second Lunar Science Conference: MIT Press, Cambridge*, v. 3, p. 2381-2390.
- Evans, S., 1963, Radio techniques for the measurement of ice thickness: *The Polar Record*, v. 11, p. 406-410 and 795.
- 1965, Dielectric properties of ice and snow—a review: *J. Glaciol.*, v. 5, p. 773-792.
- 1967, Progress report on echo sounding: *The Polar Record*, v. 13, p. 413-420.
- Gold, T., O'Leary, B. T., and Campbell, M., 1971, Some physical properties of Apollo 12 lunar samples, *in* *Proceedings of the Second Lunar Science Conference: MIT Press, Cambridge*, v. 3, p. 2173-2181.
- Holser, W. T., Brown, R. J. S., Roberts, F. A., Fredriksson, O. A., and Unterberger, R. R., 1972, Radar logging of a salt dome: *Geophysics*, v. 37, p. 889-906.
- Jiracek, G. R., 1967, Radio sounding of Antarctic ice: Res. Rep. No. 67-1, *Geophys. and Polar Res. Center, University of Wisconsin*.
- Kanasevich, E. R., 1963, Gravity measurements on the

- Athabasca Glacier, Alberta, Canada: *J. Glaciol.*, v. 4, p. 617-631.
- Katsube, T. J., and Collett, L. S., 1971, Electrical properties of Apollo 11 and 12 lunar samples, *in* Proceedings of the Second Lunar Science Conference: MIT Press, Cambridge, v. 3, p. 2367-2379.
- Keller, G. V., and Frischknecht, F. C., 1961, Induction and galvanic resistivity studies on the Athabasca Glacier, Alberta, Canada, *in* Geology of the Arctic (International Symposium): edited by G. O. Raasch, Toronto, University of Toronto, v. 2, p. 809-832.
- Paterson, W. S. B., and Savage, J. C., 1963, Geometry and movement of the Athabasca glacier: *J. Geophys. Res.*, v. 68, p. 4513-4520.
- Röthlisberger, Hans, 1967, Electrical resistivity measurements and soundings on glaciers: Introductory remarks: *J. Glaciol.*, v. 6, p. 599-606.
- Saint-Amant, M., and Strangway, David W., 1970, Dielectric properties of dry, geologic materials: *Geophysics*, v. 35, p. 624-645.
- Strangway, D. W., 1969, Moon: electrical properties of the uppermost layers: *Sci.*, v. 165, p. 1012-1013.
- Tyler, G. L., 1968, Oblique scattering radar reflectivity of the lunar surface: Preliminary results from Explorer 35: *J. Geophys. Res.*, v. 73, p. 7609-7620.
- Unterberger, R. R., Holser, W. T., and Brown, R. J. S., 1970, Radio frequency propagation in salt domes I. Theory, laboratory and field measurements of attenuation: Presented at SEG 40th Annual International Meeting, New Orleans.
- Walford, M. E. R., 1968, Field measurements of dielectric absorption in Antarctic ice and snow at very high frequencies: *J. Glaciol.*, v. 7, p. 89-94.
- Watt, A. D., and Maxwell, E. L., 1960, Measured electrical properties of snow and glacial ice: *J. Res. U. S. Nat. Bur. Stan.*, v. 64D, p. 357-363.
- Weaver, Harold, 1965, The interpretation of thermal emissivity from the moon, *in* Solar system radio astronomy: edited by J. Aarons, New York, Plenum Press, p. 295-354.

C-4

INSTRUMENTS AND METHODS

RADIO-FREQUENCY INTERFEROMETRY—A NEW TECHNIQUE FOR STUDYING GLACIERS

By D. W. STRANGWAY,*

(Geophysics Branch, Lyndon B. Johnson Space Center, Houston, Texas 77058, U.S.A.)

GENE SIMMONS, G. LATORRACA,

(Department of Earth and Planetary Sciences, Massachusetts Institute of Technology,
Cambridge, Massachusetts 02139, U.S.A.)

R. WATTS,

(Department of Physics, University of Toronto, Toronto, Ontario, Canada and Lunar Science
Institute, Houston, Texas 77058, U.S.A.)

L. BANNISTER, R. BAKER,

(Laboratory of Space Experiments, Center for Space Research, Massachusetts Institute of
Technology, Cambridge, Massachusetts 02139, U.S.A.)

J. D. REDMAN and J. R. ROSSITER

(Department of Physics, University of Toronto, Toronto, Ontario, Canada)

ABSTRACT. A new method of electromagnetic sounding in resistive electrical environments has been developed for use in lunar exploration. It is applicable to the study of terrestrial glaciers and ice sheets. A horizontal electric dipole antenna on the ground is used to transmit power at frequencies of 1, 2, 4, 8, 16 and 32 MHz. A set of orthogonal receiving coils is mounted on a vehicle which traverses away from the transmitter. Field strength is recorded as a function of distance. Waves which travel above the surface interfere with waves from the subsurface, generating interference patterns which can be used to determine the dielectric constant, the loss tangent, and depth to reflecting horizons.

The technique was tested on the Athabasca Glacier in western Canada. At 1, 2 and 4 MHz the ice was found to have a dielectric constant of about 3.3, a loss tangent ($\tan \delta$) which is roughly inversely proportional to frequency giving values of $f \tan \delta$ in the range of 0.25 to 0.35 (where f is in MHz). These values correspond well with the known properties of ice near 0° C, which is a temperature typical of temperate glaciers. It has been possible to determine the depth of the ice but results are not always consistent with previous seismic and gravity surveys and with drilling. At frequencies of 16 and 32 MHz, scattering is the dominant feature of the results. At 8 MHz there is a transition from clear-cut interference patterns to the scattering patterns. From these findings, we suggest that the Athabasca Glacier has a large number of dielectric scatterers with dimensions less than about 35 m, probably due in large part to crevasses.

RÉSUMÉ. *Interferometrie de fréquences radio — une nouvelle technique pour l'étude des glaciers.* Une nouvelle méthode de sondages électromagnétique à travers des milieux électriques résistants, a été imaginé à l'usage des explorations lunaires. Elle présente des possibilités d'application dans l'étude des glaciers terrestres et des calottes glaciaires. Une antenne électrique dipolaire horizontale sur le sol est utilisée pour transmettre de l'énergie sur des fréquences de 1, 2, 4, 8, 16 et 32 MHz. Un ensemble de bobines réceptrices disposées orthogonalement est monté sur un véhicule qui circule à distance de l'émetteur. L'intensité du champ est mesurée en fonction de la distance. Les ondes qui se propagent au-dessus de la surface se combinent avec celles venues de dessous la surface, engendrant des interférences dont on peut se servir pour calculer la constante diélectrique, la perte en tangente et la profondeur des horizons réflecteurs.

On a essayé cette technique dans le glacier de l'Athabasca dans l'Ouest Canadien. A 1, 2 et 4 MHz, on a trouvé pour la glace une constante diélectrique de 3,3, une perte de tangente ($\tan \delta$) qui est grossièrement inversement proportionnelle à la fréquence, donnant des valeurs de $f \tan \delta$ de l'ordre de 0,25 à 0,35 (où f est en MHz). Ces valeurs correspondent bien avec les propriétés connues de la glace au voisinage de 0° C, température typique des glaciers tempérés. On a pu déterminer l'épaisseur de la glace mais les résultats ne concordent pas toujours avec les anciennes mesures sismiques et gravitaires, ni avec les forages. Pour les fréquences de 16 et 32 MHz, la dispersion est le trait dominant des résultats. A 8 MHz, il y a une transition entre un net phénomène d'interférence et la dispersion. A partir de ces constatations, nous suggérons que le glacier l'Athabasca possède un grand nombre de dispersants diélectriques mesurant moins d'environ 35 m, probablement en raison, pour une large part, de la présence de crevasses.

* Present address: Department of Geology, University of Toronto, Toronto, Ontario, Canada.

ZUSAMMENFASSUNG. *Hochfrequenz-Interferenzmessung — eine neue Methode für Gletscheruntersuchungen.* Für den Gebrauch bei der Erforschung des Mondes wurde eine neue Methode der elektromagnetischen Lotung durch widerstandsfähige Oberflächenschichten entwickelt. Es besteht die Möglichkeit, damit terrestrische Gletscher und Eisschilde zu untersuchen. Eine horizontale elektrische Dipolantenne am Boden wird dazu benutzt, um Energie in den Frequenzen von 1, 2, 4, 8, 16 und 32 MHz auszusenden. Ein Satz von orthogonalen Empfangsspulen ist auf einem sich vom Sender wegbewegenden Fahrzeug befestigt. Die Feldstärke wird als Funktion der Entfernung aufgezeichnet. Die Wellen, die sich auf der Oberfläche und in den darunter liegenden Schichten ausbreiten, erzeugt Interferenzmuster, die zur Bestimmung der Dielektrizitätskonstante, der Verlusttangente und der Tiefe beliebiger Reflexionshorizonte verwendet werden können.

Die Methode wurde am Athabasca Glacier in Westkanada erprobt. Bei 1, 2 und 4 MHz wurde für das Eis eine Dielektrizitätskonstante von $\epsilon \approx 3,3$ und eine Verlusttangente gefunden, die annähernd umgekehrt proportional zur Frequenz ist und Werte von $f \tan \delta$ im Bereich von 0,25 bis 0,35 (wobei f in MHz angegeben ist) ergibt. Diese Werte stimmen gut mit den bekannten Eigenschaften von Eis nahe 0° C, der charakteristischen Temperatur temperierter Gletscher, überein. Es ist möglich, die Eisdicke zu bestimmen, aber die Ergebnisse stehen nicht immer in Einklang mit früheren Bohrungen sowie seismischen und gravimetrischen Messungen. Bei Frequenzen von 16 und 32 MHz sind Streuungen das Hauptcharakteristikum der Ergebnisse; bei 8 MHz liegt ein Übergang von wohldefinierten Interferenzmustern zu Streumustern. Auf Grund dieser Ergebnisse schliessen wir darauf, dass im Athabasca Glacier eine grosse Anzahl von Streuobjekten vorhanden ist, deren Dimensionen unter $\epsilon \approx 35$ m liegen und die vermutlich zum grossen Teil Gletscherspalten zuzuschreiben sind.

INTRODUCTION

The physical basis of the radio interferometry technique was described in detail by Annan (1973). The practical application was discussed by Rossiter and others (1973). The planned use of the technique in the exploration of the moon was described by Simmons and others (1972). Only a brief introduction to the experiment is given here; the reader interested in further description should consult the references above.

A horizontal electric dipole is laid on the surface and used to transmit electromagnetic energy at frequencies of 1, 2, 4, 6, 18 and 32 MHz in sequence. A coil mounted on a vehicle is used with the receiver. The vehicle is moved away from the transmitting antenna and the field strength at each frequency is detected and recorded on magnetic tape and on a strip chart recorder. One axis on the chart recorder is driven by an odometer, producing plots of field strength as a function of distance from the transmitter.

Energy is propagated from the transmitter to the receiver in three important waves (Fig. 1a). The first is the wave above the surface of the ice. Its velocity is the speed of light in vacuum. The second wave travels just below the surface of the ice. Its velocity is controlled by the dielectric constant of the ice. The interference between these two waves is used to determine the dielectric constant. The third wave travels through the body of the ice and is reflected from the glacier bottom. Its interference with the other waves causes modifications to the interference pattern which are indicative of the glacier depth. It should be noted that this wave is reflected from the bottom at different places depending on the separation between source and receiver. Since interpretation depends on characteristics of the whole curve, and since glacier depth may not be constant over the whole traverse, the measurement represents some sort of mean depth along the traverse line.

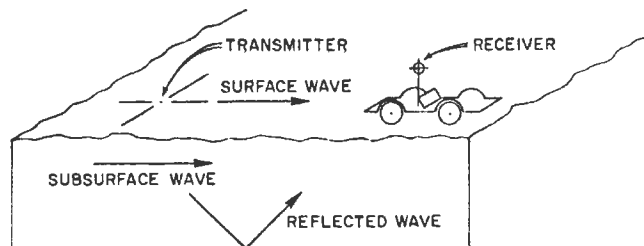


Fig. 1. (a) The three waves used in radio-frequency interferometry. The surface wave travels above the surface of the dielectric, the subsurface wave travels immediately below the surface in the dielectric. These two waves travel at different velocities and their beat frequency is a function of the dielectric constant. The third wave, designated reflected wave here, travels downward and into the dielectric and is reflected from some horizon at depth.

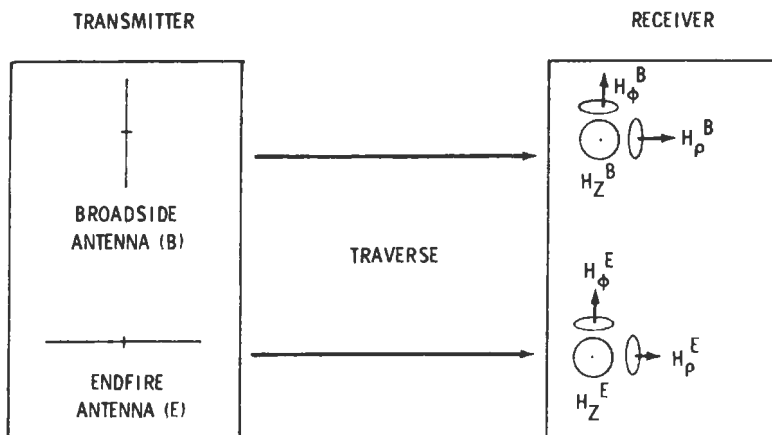


Fig. 1. (b) Relation of receiver components to transmitting antenna. The superscript B on the field components designates that measurements are taken broadside to the dipole. The superscript E indicates that the field components are measured with respect to the endfire antenna. The subscripts ρ , ϕ and z are those used in a right-handed cylindrical coordinate system. The transmitting antennas are actually coincident and there is only one set of receiving antennas. Each antenna is activated by the transmitter/receiver in the sequence shown in Figure 2.

In the present instrumentation, two orthogonal transmitting antennas are employed. Three orthogonal receiving coils are mounted on the traverse vehicle. By transmitting and receiving each of the possible combinations in sequence, six separate pieces of information are recorded at each frequency (Fig. 2). With six frequencies, 36 separate records are obtained as a function of distance from the transmitter. If the traverse is run orthogonal to one of the transmitting antennas, then three of the six components are maximum coupled and carry the interference patterns. The other three components are minimum-coupled. Ideally these components show near-zero amplitudes; in practice their amplitudes prove to be useful indicators of scattering from the subsurface or of reflections from lateral inhomogeneities such as valley walls.

One way of interpreting a set of field data is by matching theoretical curves with the observations (Annan, 1973). Families of theoretical curves for various dielectric constants, loss tangents and depths to reflector have been computed. To date our theory is adequate only for a single horizontal reflector in the subsurface. It may be a dielectric interface or a perfect (conducting) reflector.

We chose glaciers as the test area for our lunar experiment because the high electrical resistivity of ice is nearly unparalleled in other geological materials on earth. Because lunar rocks are exposed to a vacuum and are exceedingly dry, their resistivity should be similar to that of glacier ice, and quite unlike that of terrestrial rocks.

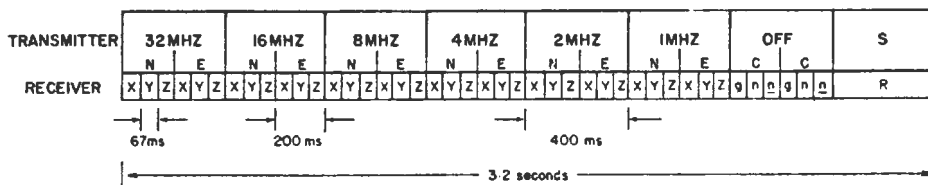


Fig. 2. Timing diagram showing sequence of transmitted signals and calibration data. N and E refer to alternate transmitting antennas; x, y, z refer to alternate receiving antennas; C refers to calibration with g referring to noise background with no transmitter on, and n and \bar{n} referring to noise from two known diode sources at the receiver input; S refers to transmitted synchronization signal and R to received synchronization signal.

THE GLACIER

There have been several previous studies of the Athabasca Glacier. Most important from our viewpoint are the results reported by Paterson and Savage (1963), Keller and Frischknecht (1961), and Kanasewich (1963). These studies include the results of drilling, seismic and electrical soundings, and gravity surveys. Their results are illustrated in Figure 3, which specifically shows the depths determined by drilling. There are uncertainties in the precise values of the thickness, except in the immediate vicinity of drill holes and seismic sounding points. In particular, note that Keller and Frischknecht (1961), on the basis of an electrical sounding in the south-eastern part of the glacier, suggested a fairly shallow depth. This sounding is in the general vicinity of our sites 2, 3, 4 and 5. Paterson and Savage (1963) point out "that there is some evidence that a bedrock shelf may exist on the right (southeast) edge of the glacier . . . ; the seismic evidence, however, is not sufficient to establish its existence. Such a shelf has been indicated by the resistivity surveys of Keller and Frischknecht (1961) but not by the gravity surveys of Kanasewich (1963)". We will assume therefore that the drilling, seismic and gravity results are the most definitive.

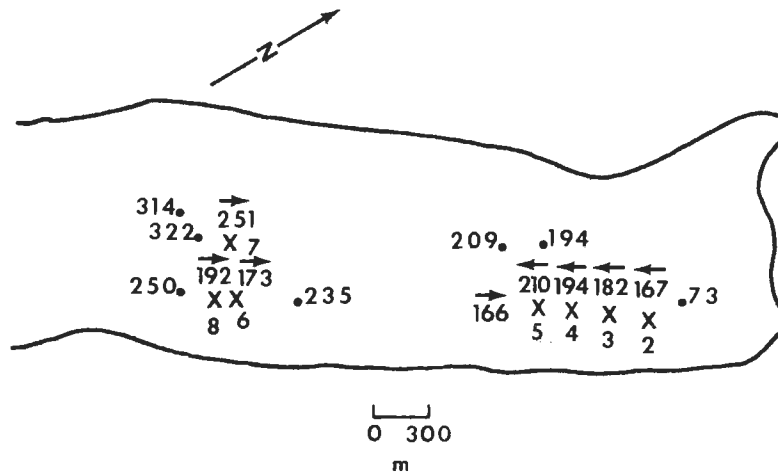


Fig. 3. Map of Athabasca Glacier showing locations of drill holes and radio-interferometry transmitter sites.

- 252 Station 9, depth 252 m, traversing down-glacier (north).
- x 9 Drill-hole, depth 112 m.
-

Watt and Maxwell (1960) measured the electrical properties of the glacier ice *in situ* on the Athabasca Glacier using frequencies from 20 Hz to 100 kHz. At the high-frequency limit they showed that the ice had a dielectric constant of about 3.2. This value is typical for pure ice, and in general the value is frequency and temperature independent from 100 kHz to 1 000 MHz (Evans, 1965; Gudmandsen, 1971). Also the depths of glacier ice as measured by radar-sounding field studies agree well with drilling results, if a dielectric constant of 3.2 is assumed (Gudmandsen, 1971).

The loss tangent of ice is controlled in this frequency range by the tail of the well-known relaxation which occurs in the audio-frequency range. In the range of our experiment (1–32 MHz) the loss tangent is inversely proportional to frequency f , so that $(f \tan \delta)$ is nearly a

constant (Evans, 1965; Gudmandsen, 1971). However, this constant is strongly dependent on temperature; its value is about 0.30 at 0° C, a typical temperature for a temperate glacier, and about 0.10 at -20° C, a typical temperature for polar ice sheets (where f is in MHz). These values correspond to attenuation rates of 0.048 dB/m at 0° C and 0.016 dB/m at -20° C. This latter value is similar to the values estimated by Gudmandsen for the Greenland ice sheet.

The attenuation distance of electromagnetic energy in a dielectric is:

$$\frac{c}{\pi f \epsilon^{\frac{1}{2}} \tan \delta}$$

where ϵ is the dielectric constant and c the velocity of light in vacuum.

The interferometry technique requires waves which are of similar amplitude. If a wave reflected from the glacier bottom is minute in comparison to the other waves, then it is unobservable. Increasing the power of the transmitter is of no benefit, for the relative power of the waves remains unaltered. The attenuation of waves in the ice consequently limits the detection of the bottom reflector to depths of a few hundred meters in temperate glaciers and a kilometer or two in polar ice sheets. Because $f \tan \delta$ is nearly constant, the depth penetration is not frequency-dependent; rather it is temperature dependent.

GLACIER DATA

Data were collected at seven major sites on the glacier (stations 2-8 on Fig. 3). Interpretation was based on data from the transmitting antenna normal to the traverse line. Both radial (H_{ρ}^B) and vertical (H_z^B) components were examined (Fig. 1b). The tangential component (H_{ϕ}^B) would be zero if no lateral reflections were received. The true amplitude of this component is indicative of departures from these ideal conditions. The components from the antenna parallel to the traverse line (H_{ρ}^E , H_{ϕ}^E , H_z^E , Fig. 1b) were also recorded but were not specifically used in the interpretation. More sophisticated future interpretations will probably use all the data.

Figure 4 shows the H_{ρ}^B and H_z^B components from one traverse (Run 26). Figure 5 illustrates the process of interpreting a profile for one component. A set of theoretical master curves is compared with the data. Our best fit in this case is for the dielectric constant of 3.3, loss tangent of 0.09, and depth of 2.425 wavelengths (182 m); a perfectly reflecting bottom is assumed.

Such an interpretation is not always unambiguous. There may be several different combinations of parameters which appear to fit the data equally well. In such cases the redundancy of several components and several frequencies comes into play. The criterion of consistency is applied to select the correct determination from the various possibilities.

The most consistent set of interpretations for Run 26 is tabulated in Table I. There is somewhat greater error in the interpreted depths for the low frequencies (1 and 2 MHz) because the curves have fewer features and generally less definitive character. It should be noted that the depth estimate discrepancy between curves exceeds the error of the individual depth estimates (Table II). This is probably because of the non-ideal glacier geometry; the non-planar and non-parallel bottom affects the various profiles in different ways.

If there is a single great difficulty in the interpretation of interferometry data, it is the sensitivity of curve shape to small changes in geometrical and electrical parameters. It is this sensitivity which causes the error estimate for the interpretation of a single profile to be small, while the inconsistency between curves may indicate considerably higher error. Present studies are aimed at finding ways to pre-process the data to reduce their sensitivity to small parameter changes.

At 8 MHz the field curves contain many more fluctuations than the theoretical curves. This is an indication of the influence of inhomogeneities within the glacier or of the surface roughness. Scatterers considerably smaller than a wavelength will influence wave propagation very little, while those exceeding a wavelength in size will modify the fields considerably. The appearance of wavelength-size disturbances at 8 MHz ($\lambda = 37.5$ m) indicates that internal inhomogeneities in the Athabasca Glacier are seldom larger than several tens of meters. The strong disturbance in all Athabasca data at 16 and 32 MHz ($\lambda = 18.7$ m and 9.4 m) indicates that scatterers of this size or less are common throughout the glacier.

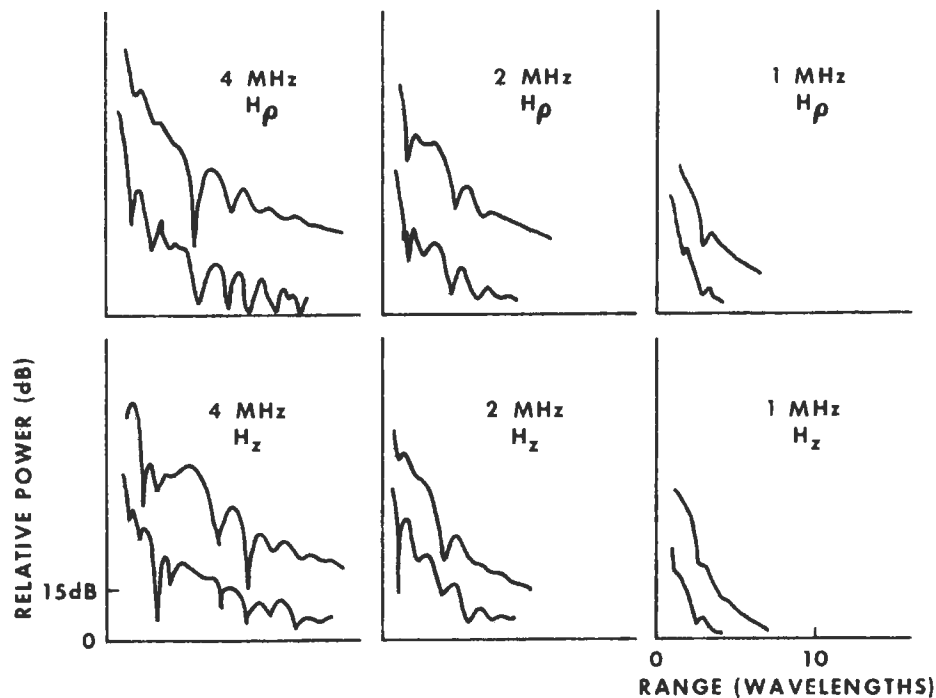


Fig. 4. Typical set of data for maximum-amplitude components H_{ρ}^B and H_z^B from the broadside antenna. Frequencies 1, 2 and 4 MHz are shown. Upper curves are theoretical curves for the parameters given in Table I [Run 26].

TABLE I. INTERPRETATION OF H_{ρ}^B AND H_z^B DATA. SITE 3S: RUN 26
Dielectric constant for all fits = 3.3

Frequency MHz	Component	Loss tangent	Depth λ	Depth m
1	H_{ρ}	0.26	0.65	195
1	H_z	0.26	0.55	165
2	H_{ρ}	0.14	1.3	195
2	H_z	0.15	1.175	176
4	H_{ρ}	0.09	2.425	182
4	H_z	0.09	2.425	182
			Average	182 m

TABLE II. PRECISION OF INDIVIDUAL FIT

	1 MHz	2 MHz	4 MHz
Dielectric constant	± 0.02	± 0.1	± 0.1
Loss tangent	± 0.01	± 0.01	± 0.005
Depth m	± 8	± 8	± 4

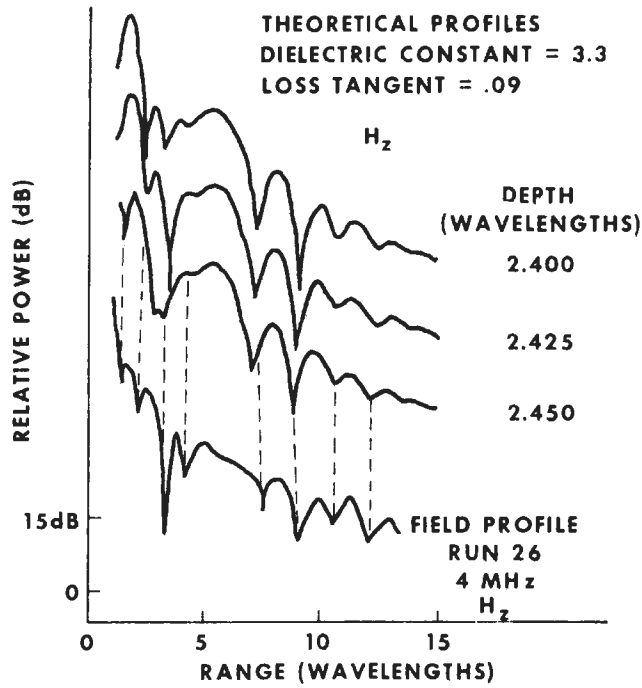


Fig. 5. Typical set of data at 4 MHz for the H_z component, with theoretical curves for three different depths. The theoretical curves are offset for clarity of presentation. The best fit is at 2.425 wavelengths (182 m) [Run 26].

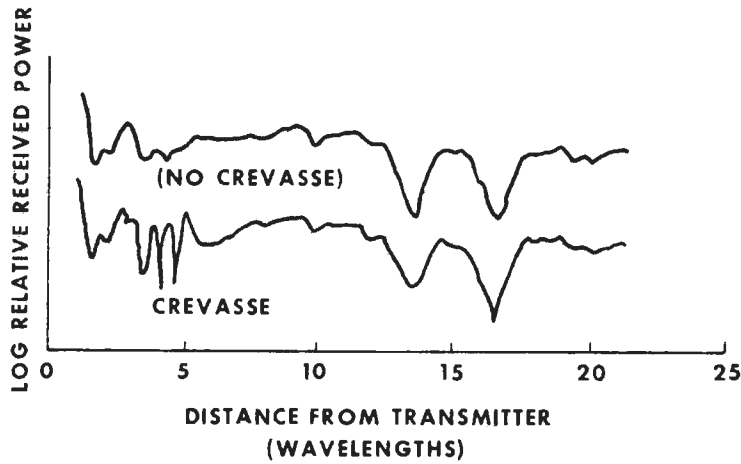


Fig. 6. Interference curve from crevasse in scale model. When scaled to 8 MHz, crevasse is $30\text{ m} \times 30\text{ m} \times 3\text{ m}$ in size, 5 wavelengths from the transmitter. High interference frequency is apparent on the transmitter side of the crevasse and slight field-strength diminution on the opposite side.

MODEL RESULTS

One particular type of scatterer has been investigated using a high-frequency analog scale model. The modeling medium was dielectric oil with a dielectric constant of 2.2 and loss tangent of 0.002. Because these properties differ somewhat from those of ice, the results must be taken as qualitative indications only. The modeling wavelength was ≈ 5 cm.

A crevasse was simulated with a styrofoam wedge (Fig. 6) (the dielectric constant of low-density styrofoam is approximately 1). The field-strength profile shows a high-frequency interference on the side of the crevasse nearer to the transmitter, and a minor diminution of field strength on the far side. Similar features are present on the curve from field data shown in Figure 7, although positive identification of the particular crevasse responsible for this pattern was not made in the field.

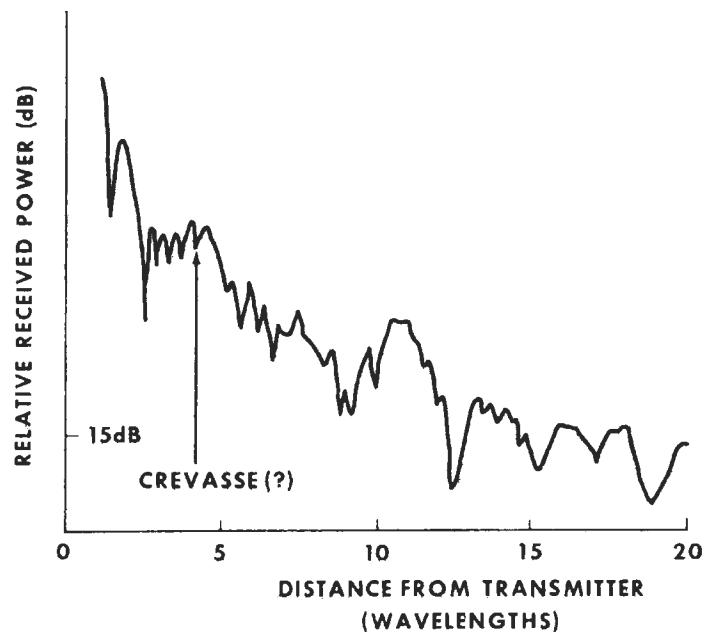


Fig. 7. Possible location of crevasse in field data.

DISCUSSION

The best fits to all data were obtained for dielectric constant values of 3.3 ± 0.1 . The loss tangents for the best-fit curves were from 0.18 to 0.26 at 1 MHz, 0.11 to 0.18 at 2 MHz, and 0.06 to 0.12 at 4 MHz. The mean value for $f \tan \delta$ is approximately 0.3.

Depth determinations have been made using the average values of the most consistent set of fits at the various stations. These are tabulated in Table III and are located on the map of Figure 3. Except for stations 6 and 8, deeper depth determinations are obtained at stations higher on the glacier. Stations 3, 4 and 5 show particularly consistent results in comparison to drilling information. The apparently high depth gradient between station 2 and a nearby drill hole (depth 73 m) may be real, a result of extensions of the bedrock topography currently being exposed at the retreating terminus.

TABLE III. DEPTH DETERMINATIONS
(AVERAGE 1, 2, 4 MHz. H_p AND H_z)

Site	Direction of traverse	Depth m
2	S	167
3	S	182
4	S	194
5	S	210
5	N	166
6	N	173
7	N	251
8	N	192

The interferometric depth determination at station 7 is not entirely inconsistent with drilling results, although the indicated depth is probably too shallow. This determination was fairly ambiguous because reflections from the bottom are weak in such deep ice. A further complication was the short traverse length imposed by rough surface conditions.

The most inconsistent results occurred at stations 6 and 8. These stations were near the side of the glacier, so observed reflections might not have come from directly below the traverse line. A hanging tributary glacier enters Athabasca Glacier a short distance above these stations; morainal material within the glacier may therefore have adversely affected the observations.

CONCLUSIONS

Radio interferometry appears to give reasonable estimates of glacier depth under favorable conditions. Erroneous estimates can be obtained when internal structure affects the observations and possibly when the bottom slopes too much relative to the surface. The limit of detectability of the bottom is about 300 m in temperate glaciers.

At the same time, the radio interferometry method gives an *in situ* measurement of both the dielectric constant and the loss tangent of the glacier ice. Hence there is no need to assume a dielectric constant in order to obtain a depth estimate, as is required by radar reflection techniques.

Scattering signatures in the curves may indicate the position (and possibly the orientation, if profiles are made in several directions) of crevasses or other near-surface scatterers. This detection is probably possible through many meters of snow cover, although it was only tested on bare ice in the ablation zone of the Athabasca Glacier.

As a field technique, radio interferometry is fast and simple. It requires an instrumented vehicle, but data collection is rapid if the glacier surface allows for easy driving. Operation on snow-covered portions of a glacier is probably easier than on the rough ice surface of the ablation zone.

Interpretation is fairly rapid. Collections of theoretical curves with appropriate parameters can be made up before the field trip. Daily comparison of the field data with these curves allows constant monitoring of results. Sophisticated analysis and processing must, of course, wait until a computer is available.

Methods are being investigated for making the data less sensitive to small variations of parameters. This will require computer processing of the data. Current theory is being extended to investigate the effects of sloping bottoms and other more complex geometries. The ultimate aim of the data analysis program is to use the full complement of redundant data to minimize the ambiguity of interpretation.

ACKNOWLEDGEMENTS

We appreciate permission from the Canadian National Park Service to work in Jasper National Park. Financial support was provided by NASA under Contract NAS9-11540. Partial support of R. Watts and J. Rossiter was provided by the Lunar Science Institute, Houston, Texas. J. Proctor calculated the theoretical curves used in making the fits. J. Kong and L. Tsang, of the Department of Electrical Engineering, M.I.T., pointed out a sign error in our theoretical curves which would have invalidated our results.

MS. received 5 February 1973 and in revised form 23 August 1973

REFERENCES

- Annan, A. P. 1973. Radio interferometry depth sounding: part I—theoretical discussion. *Geophysics*, Vol. 38, No. 3, p. 557–80.
- Evans, S. 1965. Dielectric properties of ice and snow—a review. *Journal of Glaciology*, Vol. 5, No. 42, p. 773–92.
- Gudmandsen, P. 1971. Electromagnetic probing of ice. (In Bahar, E., and others. *Electromagnetic probing in geophysics*. Boulder, Golem Press, p. 321–48.)
- Kanasevich, E. R. 1963. Gravity measurements on the Athabasca Glacier, Alberta, Canada. *Journal of Glaciology*, Vol. 4, No. 35, p. 617–31.
- Keller, G. V., and Frischknecht, F. C. 1961. Induction and galvanic resistivity studies on the Athabasca Glacier, Alberta, Canada. (In Raasch, G. O., ed. *Geology of the Arctic. Proceedings of the first international symposium on Arctic geology, held in Calgary, Alberta, January 11–13, 1960*. Toronto, University of Toronto Press, Vol. 2, p. 809–32.)
- Paterson, W. S. B., and Savage, J. C. 1963. Geometry and movement of the Athabasca Glacier. *Journal of Geophysical Research*, Vol. 68, No. 15, p. 4513–20.
- Rossiter, J. R., and others. 1973. Radio interferometry depth sounding: part II—experimental results, by J. R. Rossiter, G. A. LaTorraca, A. P. Annan, D. W. Strangway and G. Simmons. *Geophysics*, Vol. 38, No. 3, p. 581–99.
- Simmons, G., and others. 1972. The Surface Electrical Properties Experiment, by G. Simmons, D. W. Strangway, L. Bannister, R. Baker, D. Cubley, G. LaTorraca and R. Watts. (In Kopal, Z., and Strangway, D. W., ed. *Lunar geophysics. Proceedings of a conference at the Lunar Science Institute, Houston, Texas, 18–21 October 1971*. Dordrecht, D. Reidel, p. 258–71.)
- Watt, A. D., and Maxwell, E. L. 1960. Measured electrical properties of snow and glacial ice. *Journal of Research of the National Bureau of Standards* (Washington, D.C.), Sect. D, Vol. 64, No. 4, p. 357–63.

The Electromagnetic Response of a Low-loss,
2-Layer, Dielectric Earth for Horizontal
Electric Dipole Excitation

A.P. Annan¹, W.M. Waller², D.W. Strangway³
J.R. Rossiter¹, J.D. Redman³, R.D. Watts⁴

1. Department of Physics
University of Toronto
Toronto, Ontario
Canada
2. Lockheed Electronics Company
NASA - JSC, Houston,
Texas, U.S.A.
3. Department of Geology
University of Toronto
Toronto, Ontario
Canada
4. NAS/NRC Post-doctoral Fellow,
Johnson Spacecraft Centre,
Houston, Texas, 77058, U.S.A.
(Presently at USGS, Denver, Colorado)

Abstract

The use of the radio interferometry method requires a detailed understanding of the nature of electromagnetic wave propagation in structures composed of materials with low electrical loss. This paper presents the results of a detailed experimental and theoretical study into the response of a 2-layer, plane-stratified, low-loss dielectric earth. The technique used to construct a scale model with microwave equipment to experimentally simulate the 2-layer structure response is discussed. The wave nature of the response derived from the theoretical investigations is used to interpret the features of the experimental results. The experimental results in turn are useful in demonstrating the reliability of approximate theoretical solutions for the electromagnetic fields about the dipole obtained by the normal mode and geometrical optic methods. Such features as the modification of the dipole radiation pattern when the antenna is placed at the interface between media of differing electrical properties and development of guided and leaky modes in the layered structure are examined in detail.

Introduction

The radio interferometry method, previously summarized by Annan (1973) and Rossiter et al. (1973), is a useful geophysical method in geologic regions exhibiting extremely high electrical resistivities. In this context, high resistivity implies that displacement currents in the media

must be considerably greater than the conduction currents. In terrestrial materials, this situation is encountered in ice-covered regions (glaciers, polar ice caps) for radio frequencies of the order of 1 Mhz and higher. Lunar materials also behave as low-loss dielectric materials in the Mhz frequency range (Olhoeft et al., (1973). Katsube and Collett, (1971).

The original papers, mentioned above, presented much of the preliminary work conducted to study the feasibility of the radio interferometry method. Subsequent to this work, a lunar experiment was designed, constructed and carried on Apollo 17 (Simmons et al., (1972). In order to be able to make a coherent interpretation of data from glaciers and the Moon, a much more detailed understanding of the basic features of the radio interferometry method was required. An in-depth computational analysis of the theoretical response of idealized models was made and these responses were simulated with a scale model experiment to check their validity. In addition, full scale experiments were conducted on glaciers in Alberta (Strangway et al, (1974) and in Alaska (Rossiter et al., see companion paper).

In this paper, a subset of the theoretical and scale model studies are analysed. The purpose is to present a detailed, documented study of the response of a 2-layer, low-loss dielectric earth for excitation by an electric dipole antenna laid on the surface. Some preliminary results of the scale model and theoretical analysis are given by

Rossiter et al, (1973). In the course of this study, the theoretical and experimental work were carried out together in order that each could be used to confirm the other. The end product was an in-depth understanding of the intuitively simple, but complex in detail, physical phenomena involved.

Idealized 2-Layer Earth

The idealized model studied is shown in Figure 1. The 2-layer earth is characterized by the dielectric constants K_i and the loss tangents δ_i . Variations in magnetic properties are not considered; all regions have free space permeability. The cartesian coordinates (x_1, x_2, x_3) , the associated unit vectors $(\hat{e}_1, \hat{e}_2, \hat{e}_3)$ and the cylindrical coordinates (ρ, φ, z) are shown in the diagram. For the computational analysis, the earth is excited by a point electric dipole located at the origin of the coordinate system with its moment aligned with the \hat{e}_1 axis. In actual experiments, the source is a half wavelength electric dipole antenna. The time variation of the dipole moment is of the form $e^{-j\omega t}$ and in all subsequent mathematical expressions the time dependence is suppressed.

In applying the radio interferometry method, the field strength about the transmitter primarily along profiles which run radially outward from the dipole. The profiles commonly used are denoted the broadside, (B), and the endfire, (E), profiles. The B profile is run radially out from the dipole normal to the direction of the dipole moment. In Figure 1,

the B profile is along the \hat{e}_2 axis while the E profile is along the \hat{e}_1 axis. In field applications, the 3 components of magnetic field are measured. In the scale model measurements, electric fields, primarily E_p and E_ϕ are measured due to the difficulty in constructing satisfactory magnetic field antennas. The field strength along these profiles exhibits maxima and minima at various spatial positions due to interference of waves propagating with different horizontal phase velocities. The position of these maxima and minima and the rate of decay of the fields with distance are indicators which can be used to infer the electrical properties of the earth and layer thickness.

In the following discussions, all spatial dimensions are normalized in terms of the free space wavelength W . All propagation constants and wavenumbers are normalized in terms of the free space propagation constant $k_0 = 2\pi/W$.

Mathematical Formalism

The mathematical formulation of the electromagnetic response of a plane layered earth is well known since it is a standard boundary value problem (Wait (1970), Brekhovskikh (1960)). The difficult part of the analysis occurs when actual numerical computations of the response are required. The fields are expressed as Hankel transforms (or 2 dimensional Fourier transforms) which cannot be evaluated analytically. In all but the simplest case of a whole-space, approximate methods of integration must be used to extract useable

results. The most straight forward method of obtaining numerical results is to numerically integrate the Hankel transforms. Other methods involve limiting material properties to special values in order to reduce the integrand to a sufficiently simple form that an analytical evaluation can be made. The other alternative is to look at the physical nature of the response by use of approximate solutions which can be obtained by manipulation of the integration countour in the complex plane. Two solutions in this class are known as the geometrical optics and the normal mode solutions.

The details of the applications of these techniques to low-loss dielectric earth models is discussed by Annan(1970, 1973), Tsang et al (1973) for various dipolar excitations. In the following discussions, the geometrical optics and the normal mode solutions are used. The reason for this is that sufficiently accurate results can be obtained in a very economical manner. The computation cost of numerical integration rules our this method for all be very particular cases under consideration. Of the two solutions obtained by normal countour integration, the normal mode solution is the more correct solution. The only approximations involved in the normal mode solutions are in the analysis of the branch-line contributions which yield lateral and inhomogeneous waves associated with the boundaries. The actual "normal mode" part of the solution is exact within the computational error of evaluating its contribution. The geometrical optics solution involves asymptotic expansions for each multiple

reflection and has built in approximations from the first step of analysis. The main advantage of the geometrical optics solution is that the response has a simple physical interpretation and is economically computed. As pointed out by Annan (1973), this solution can only be used when spatial dimensions are on the order of the wavelength, or attenuation distances in the media involved. In a low-loss dielectric medium, the attenuation distance (distance for a field to drop to 1/e of its value) is given by $W/\pi\sqrt{K'}\tan\delta$.

The theoretical solutions for the electric and magnetic fields on the surface of the 2-layer earth are summarized in Table 1; the fields are expressed in terms of electric and magnetic Hertz vectors which have only vertical (\hat{e}_3) components. The complex radial wavenumber plane and integration contours are shown in Figure 2. For the expressions in Table 1, the geometrical optics solution is obtained by expanding the expression in the denominators

$$\frac{1}{1 - R_{10} R_{12} \beta} = \sum_{n=0}^{\infty} R_{10}^n R_{12}^n \beta^n \quad (1)$$

whereas the mode solution is obtained by solving the transcendental equation

$$R_{10} R_{12} \beta = 1 \quad (2)$$

which yields the TE and TM normal mode horizontal wavenumbers of the layered earth. The contour of the integration is

deformed into a steepest descent contour through a saddle point for each term in the (geometrical series) expansion. Each term in the geometrical series can be expressed in an asymptotic series. The geometrical optics solution to final order is obtained by retaining only the first term in each asymptotic series. For the normal mode analysis, the contour is deformed to yield a sum over the normal modes of the system plus integrals along the branch lines.

Scale Model Description

For electromagnetic systems to be similar, the spatial dimensions in free space wavelengths and the loss tangents must be the same. In order to simulate the radio interferometry method in a reasonably sized laboratory, wavelengths in the centimeter range are necessary; this corresponds to radio frequencies in the GHz range. The 2-layer earth model and associated electronics are shown in Figures 3 and 4.

The transmitting (TX) and receiving (RX) antennas are tuned half-wavelength electric dipoles. The excitation frequency is 5.9 GHz. which corresponds to a free space wavelength $W = 5.08$ cm. The 2-layer earth is simulated by a tank of oil with very low electrical loss ($\tan\delta \ll 1$) with a plane reflector suspended at a depth d in the oil. The effects of the finite size of the tank (30W long x 15W wide x 15W deep at 5.9 GHz) are minimized by lining the inside with a microwave absorbing materials (Eccosorb). This reduces undesired spurious reflections from the walls of

the tank. The TX and TX antennas are mounted on a track suspended over the tank; the RX antenna is mounted on a mechanized carriage so that profiles of field strength versus TX-RX separation can be made automatically. The track and associated supports are also covered with microwave absorbing material.

Three sets of electrical properties of the 2-layer models were used in the model. The first set was an oil with dielectric constant $K_1 = 2.16$ and $\tan \delta_1 = 0.0022$, and an aluminum sheet, $\tan \delta_2 = \infty$, acting as a perfectly reflecting substratum. A second set of electrical properties were obtained by doping the oil with benzonitrile to increase its loss tangent. The third consisted of oil (undoped) underlain by a dielectric slab $K_2 = 6.75$ and $\tan \delta_2 = 0.11$. The slab was made of epoxy doped with carbon to increase its loss tangent. The slab was $2W$ thick and had a sufficiently high loss that it eliminated the possibility of spurious reflections from the bottom of the slab returning to the surface. The thickness of the oil layer was varied from $0.2W$ up to $10W$ and profiles of $\log_{10} |E\phi|$ versus TX-RX separation along the B profile are presented here.

The automatic traverse equipment and associated recording apparatus are sketched in Figure 4 (Waller (1973)). The field strength versus the distance is displayed on an X-Y recorder and at the same time can be recorded on a two-channel analog tape recorder. The recorded data was later digitized in order that data enhancement and automatic interpretation schemes could be tested.

Theoretical and Experimental Results

(a) Half-Space Earth: Radiation Pattern Directionality

Before discussing the 2-layer earth in detail the half-space response is briefly reviewed. The interaction of the dipole source with the air-earth interface drastically modifies the directionality of the antenna. This result is important when analysing 2-layer models with the geometrical optics solution. This effect has been discussed by Tsang et al (1973), Annan (1970, 1973), Cooper (1971).

The TE radiation from the horizontal electric dipole is considered in the following analysis. The radiation pattern for TE energy is the same as that for the electric field component E_{ψ} . Since E_{ψ} varies as $\sin\psi$ in the $X_1 - X_2$ and this variation is independent of the layered structure, the variation of E_{ψ} in the $X_2 - X_3$ plane at a fixed distance from the source yields the pertinent radiation pattern information. E_{ψ} in the $X_2 - X_3$ ($\sin\psi = 1$) plane for whole-space is simply given by

$$E_{\psi} = j\omega\mu_0 I dl \frac{e^{j2\pi R}}{4\pi RW} \quad (3)$$

while for the half space, as $R \rightarrow \infty$,

$$E_{\psi} = T_{10}^{TE} \left(\frac{|z|}{R}\right) j\omega\mu_0 I dl \frac{e^{j2\pi R}}{4\pi RW} \quad (z > 0) \quad (4)$$

$$E_{\psi} = T_{01}^{TE} \left(\frac{|z|}{R}\right) j\omega\mu_0 I dl \frac{e^{j2\pi\sqrt{K_1^*} R}}{4\pi RW} \quad (z < 0)$$

where

$$R = \left(\sum_{i=1}^3 (x_i)^2 \right)^{1/2} \quad (1)$$

I_{dl} = electric dipole moment

$$T_{ij}^{TE}(\alpha) = \frac{2\alpha}{\alpha + n_{ij} (1 - n_{ij}^2 (1 - \alpha^2))^{1/2}}$$

$$n_{ij} = (k_i / k_j)^{1/2}$$

μ_0 = free space permeability

The modified pattern is highly directional with a strong peak into the earth at the critical angle of the interface as illustrated in Figure 5. The patterns show radiated power versus direction in the $X_2 - X_3$ plane. The whole-space pattern is used to normalize the patterns for varying dielectric constants of the half-space. Similar analyses can be carried out for other field components; all show highly directional patterns.

Experimental measurements of the radiation pattern obtained with the scale model with no subsurface reflector confirm the directionality of the source in the presence of an interface. The radiation patterns were measured by mounting the receiving antenna on a specially constructed boom which moved the antenna in a circle of constant radius about the transmitted antenna. The amplitude of the received

signal and the angular position of the boom were fed to an X-Y recorder which produced directly plots of field intensity versus position in the $X_2 - X_3$ plane. The results of measurements of $|E_\varphi|$ are shown in Figure 6. The pattern for E_φ was measured on circles with radii of 3 W, 4.5 W, and 6 W. The "theoretical" pattern for the air-oil-dipole configuration computed by Cooper (1971) is shown with the experimental results. It should be noted that the experimental results are not normalized and that the shape of the patterns, not the magnitudes, should be considered.

The discrepancy between the theoretical response and observed response are primarily explained by the fact that the experimental measurements were made at a finite distance from the source. The theoretical pattern shown is valid only infinitely far from the source by definition. As the TX-RX separation is increased, the experimental pattern changes shape and becomes more like the theoretically predicted pattern.

The preceding solution for the theoretical response is obtained from the first term in an asymptotic expansion for the field. At finite source-receiver distances, higher order terms in the expansion become important. At the peak of the pattern, however, alternate solutions must be used since the higher terms of the asymptotic expansion are infinite. Brekhovskikh (1960) has studied the fields in the region of the peak of the pattern in detail and obtained a modified expansion with the first correction term decreasing

as $(1/r)^{5/4}$. A rough calculation shows that this term is significant out to distances of tens of wavelengths.

The physical rationale for the lobate pattern is quite simple. The explanation can be seen most easily if the waves radiated by the antenna are examined from the ray theory point of view. In a whole space the source radiates the waves uniformly in all directions in the $X_2 - X_3$ plane. The presence of the half-space modifies this, since rays which propagate horizontally are continually refracted downward at the critical angle of the interface. Combining the whole-space pattern of the antenna with the directional selectivity of the interface yields a complex radiation pattern with high directionality.

To first order, the fields along the interface are zero. If higher terms of the asymptotic expansions are retained, the fields fall off as $(1/r)^2$. There are two components in this second order effect; one which propagates with the phase velocity of the earth and one which travels with the phase velocity of the air. As a result the fields at the surface of the half-space exhibit a regular beating as a function of spatial distance from the antenna. This is discussed by Annan (1970, 1973).

(b) 2-Layer Earth: Perfectly Reflecting Substratum

The 2-layer earth can exhibit a wide variety of responses depending upon the range of electrical properties and layer thickness. In early analysis, the case of a

perfectly reflecting substratum was considered as a starting point. In order to demonstrate the general character of the 2-layer earth, a suite of responses for various values of d and a perfectly reflecting substratum obtained with the scale model and computed theoretically using both the normal mode and geometrical optics solution are shown in Figure 7. The layer thickness ranges from $0.5 W$ to $7 W$. The E_{ϕ} field strengths in decibels are plotted versus transmitter receiver separation in free-space wavelengths along the B profile. The scale model response is shown along with the mode and geometrical optics solution. The geometrical optics curve is shifted upward from the experimental curve while the mode solution is shifted downward. This offset of the curves is used to minimize the overlap of the various responses which tends to confuse the visual presentation of the data.

The results in Figure 7 span most of the important depth ranges and demonstrate most of the features of the 2-layer response. For the shallow depths of $0.5 W$, $1.0 W$, and $1.5 W$, the fields are expressible in terms of one, two, or three guided modes (see Appendix) plus the lateral and inhomogeneous waves given by branch-line contributions. The fields decay with distance as $(1/r)^{\frac{1}{2}}$ and exhibit a regular beating as the modes move in and out of phase. For $d = 0.5 W$, only one mode is guided and the only interference occurs near the source where the branch line and modal contributions are comparable in magnitude. The remainder of the infinite sequences of modes are either not excited or are leaky modes which decay exponentially with distance from the transmitter.

As the layer thickness increases more and more modes move into the guided regime and the field strength versus distance becomes more complicated as the various modes move in and out of phase.

Examination of the theoretical responses show that the geometrical optics solution and the model response are in good agreement for layer thicknesses greater than $3.0 W$. For shallower depths, the experimental and theoretical responses diverge from one another. The breakdown in the geometrical optics solution is to be expected from its asymptotic nature. The normal mode solution, however, shows excellent agreement at the shallow depths and becomes the same as the geometrical optics solution at the larger depths.

(c) Thin Layers and Critical Depths

The preceding discussion of the 2-layer earth with a perfectly reflecting substratum illustrates the general nature of the response. At very shallow depths and at various critical depths, the response changes quite drastically with layer thickness. The suite of curves for depths $d = 0.13 W$ to $0.88 W$ given in Figure 8 show this behaviour clearly. The critical depths (d_c) in wavelengths for the model electrical properties are given by $d_c = 0.23(2N + 1)$ TE modes) and $d_c = 0.46n$ (TM modes), $n = 0, 1, 2, \dots$ (see Appendix). For $d < 0.23$, (E_ψ is composed of TE modes only on B profile), no normal modes are excited since the

layer is too thin. As a result, the variation of the fields with distance is dependent on the branch-line integrals which describe the secondary waves associated with the interfaces and which fall off as $(1/r)^2$. As d increases past $0.23 W$ the first normal mode moves into the guided regime and the field strength falls off with distance as $(1/r)^{\frac{1}{2}}$. The plot of field strength versus distance varies only slightly with depth changes for $0.23 < d < 0.69$.

As $d \rightarrow 0.69$, the field strength versus distance plot begins to show a weak beating. For d just greater than 0.69 , the fields show very deep interference nulls at regular spacing. Two guided modes (TE) are now propagating in the layer for $0.69 < d < 0.88$, the profiles exhibit regular beating; however, the maxima and minima locations are very sensitive to the layer thickness. Although not presented here, data collected as $d \rightarrow 1.16$ shows the same behaviour as $d \rightarrow 0.69$. At $d = 1.16$, a third mode moves from the leaky to guided regime (see Appendix).

The theoretical responses computed by the normal mode method are shown along with experimental results. The mode solutions match the experiment results very well except at the critical depths. At the critical depths, two poles and a branch point merge together in the mathematical solution. The branch line contribution is evaluated approximately by steepest descent integration; the approximate solution fails at the critical depths. The results of evaluating the branch line contribution by numerical integration are also shown on the profile for $d = 0.69$. The agreement

between experiment and theory is much better at the critical depths with this improvement. (It should be noted that the depth of experimental signal nulls may not match those of the theoretical nulls due to the presence of spurious background signals and the low level characteristics of the log amplifier.)

(d) 2-Layer Earth: Dielectric Substratum

The response of a dielectric substratum is not greatly different from the previous responses for a perfectly reflecting substratum. The major difference is that there are no longer any unattenuated guided modes; all the modes are leaky since energy can always leak out of the layer into the substratum. As a result, the field shows the same basic behaviour but all responses have a strong attenuation with distance from the TX.

The data collected with the scale model experiment are shown in Figure 9. The experimental results are presented along with the theoretically (normal mode) computed responses. The results compare extremely well. The normal modes no longer have a sharp onset as they do for a perfectly reflecting substratum. The modes now move from a very leaky regime to a much less leaky regime with no sharp dividing line present. The accuracy of the theoretical solution is better than for the perfectly reflecting substratum case since there are no true critical depths and the mathematical approximations in evaluating branch-line contributions are greatly improved.

Summary and Conclusions

The results of theoretical and experimental work have led to a clear understanding of the physical mechanisms of wave propagation in a 2-layer dielectric earth. This detailed understanding of the waves propagations in such a system is necessary for the interpretation of radio interferometry data from geologic environments which can be simulated by a 2-layer model.

The practical aspects and limitations of constructing scale model experiments at GHz. frequencies are well understood and the reliability of the model makes it an ideal method of examining problems which are not tractable from a theoretical point of view. With such excellent agreement between theory and experiments, the model can be applied to the analysis more complex problems with confidence.

The scale model has proved to be invaluable in checking out the computer programmes which generate the theoretical responses. The mathematical formalism is very complex and its translation into a computational format is difficult; particularly when approximations are made in certain parts of the analysis.

The normal mode approach to analysing moderately to very thin layers has greatly improved the ability to interpret layered structures. The initial analysis of responses was made using the geometrical optics solutions which is invalid for thin layers. The model study confirming the mode analysis has already led to successful interpretation of radio interferometry data obtained in thin layer environments

Rossiter et al. (see accompanying paper).

Acknowledgements

This research has been supported by NASA grant no. NAS 9-11540 for model construction and collection of model data and by the Canadian Department of Energy, Mines and Resources grant no. 1135-D 13-4-16/73 for analysis and preparation of this manuscript. We wish to thank Mr. J. Proctor for his able assistance in the computational aspects of this work.

Appendix

TE and TM Mode Critical Depths for a 2-Layer Earth

The radial wave numbers of the normal modes of a plane stratified 2-layer earth are obtained by solving the transcendental equations (Annan (1973))

$$\text{TE Mode} \quad 1 - R_{10}^{\text{TE}} R_{12}^{\text{TE}} \beta = 0 \quad (\text{A-1})$$

$$\text{TM Mode} \quad 1 - R_{10}^{\text{TM}} R_{12}^{\text{TM}} \beta = 0 \quad (\text{A-2})$$

When A-1 or A-2 are satisfied, the TE or TM reflection coefficient for the 2-layer structure (see Table 1) is singular having a resonance (simple pole) at that particular value of horizontal wavenumber denoted by λ_p^{TE} or λ_p^{TM} . The wave nature of the problem is sketched in Figure A (a). A plane or cylindrical wave propagating with horizontal wavenumber bounces back and forth between the two interfaces. In one transit back and forth across the layer the wave suffers an amplitude and phase change given by $R_{10} R_{12}$ due to reflection at the interfaces plus an amplitude and phase change of $\beta^{\frac{1}{2}}$ while propagating across the layer in one direction. Equations A-1 and A-2 just express the requirement that the wave completes one transit of the layer with no change in amplitude and a phase change of $2n\pi$, $n = 0, 1, 2, \dots$. In general the λ_p^{TE} and λ_p^{TM} are complex and A-1 and A-2 have no purely real solutions. Only totally real λ_p^{TE} yield modes which are unattenuated radially.

True guided modes exist only when $|R_{10}| = |R_{12}| = 1$ which physically occurs only when the media are loss free and region 1 is a low velocity region (i.e. $K_1 > K_0$ and K_2) or the lower interface is a perfect reflection (i.e. $\tan \delta_2 \rightarrow \infty$). In addition d must exceed a minimum critical thickness. Analysis of equations A-1 and A-2 in the complex λ plane show that the λ_p^{TM} must lie along a line which intertwines the various Riemann surfaces defined by the branch lines of the $(K_i^* - \lambda^2)^{1/2}$ functions. The case of a perfectly dielectric slab ($\tan \delta_2 = \infty$) substratum is sketched in Figure A(b). The roots of the transcendental equation lie on the line indicated in A(b). The solid circles denote roots on the upper Riemann surface which are excited modes and the open circles indicate roots on the lower Riemann surfaces. The poles on the real axis between $\sqrt{K_0^*}$ and $\sqrt{K_1^*}$ are guided unattenuated modes while the poles $\lambda_p < \sqrt{K_0^*}$ are leaky modes and have a positive imaginary component. The branch-lines are chosen as indicated in Figure A(b) and run from $\sqrt{K_i}$ to $\sqrt{K_i} + j\infty$. The upper Riemann surface for the radical $(K_i - \lambda^2)^{1/2}$ where K is real is defined as the one where $(K_i - \lambda^2)^{1/2} = \delta$ for $\lambda < \sqrt{K_i}$ and $(K_i - \lambda^2)^{1/2} = j\delta$ where δ is a real positive number and λ is on the real axis. On the lower Riemann surface δ must be replaced by $-\delta$ in the preceding expressions. For complex K the Riemann surface definitions consistent with the real K definitions are obtained by examining the case of $\text{Im } K_i \rightarrow 0$.

The behaviour of the λ_p^{TM} with variations in d is twofold; the poles λ_p^{TM} move down the contours and are

more closely packed as d increases and the contour, on which the poles lie, swings towards the imaginary axis. As the depth varies, a pair of the poles coincide with the $\sqrt{K_0^*}$ branch point at regular depth spacings. These depths are the critical depths for the modes and mark the depth where a mode moves from the leaky to the unattenuated or guided regime.

The critical depths for the case of the perfectly reflecting substratum are obtained by noting that

$$R_{12}^{TE} = R_{12}^{TM} = -1 \quad (A-3)$$

and that for $\lambda = \sqrt{K_0}$,

$$R_{10}^{TE} = 1 \quad R_{10}^{TM} = -1 \quad (A-4)$$

Substituting into A-1 and 2 yields.

$$d_c^n = \frac{2n+1}{4(K_i-1)^{1/2}} W \quad n = 0, 1, 2, \dots \quad (A-5)$$

$$d_c^n = \frac{n}{2(K_i-1)^{1/2}} W$$

For finite loss tangents, and a dielectric bottom, the contours on which λ_p lies still pass through $\sqrt{K_1}$ but are displaced away from the real λ axis between $\sqrt{K_0}$ and $\sqrt{K_1}$ so that all modes have a finite imaginary component which corresponds to attenuation with distance.

Bibliography

- Annan, A.P., 1973, Radio Interferometry Depth Sounding: Part I - Theoretical Discussion, Geophysics, v. 30, no. 3, p. 557-580.
- Annan, A.P., 1970, Radio Interferometry Depth Sounding, M.Sc. Thesis, University of Toronto, Toronto, Ontario, Canada.
- Brekhovskikh, L.M., 1960, Waves in Layered Media: New York, Academic Press.
- Cooper, W.W., 1971, Patterns of Dipole Antenna on Stratified Medium, Technical Report TR71-3, MIT Centre for Space Research.
- Katsube, T.J., and Collett, L.S., 1971, Electrical properties of Apollo 11 and 12 lunar samples, in Proceedings of the Second Lunar Science Conference, Houston, Texas, edited by A.A. Levinson: Cambridge, Mass. Inst. Tech.
- Olhoeft, G.R., Strangway, D.W., and Frisillo, A.L., 1973, Lunar Sample Electrical Properties, Proc. Fourth Lunar Sci. Conf., (Suppl. 4, Geochim, Cosochim. Acta), v. 3, p. 3133-3149.
- Rossiter, J.R., LaTorraca, G.A., Annan, A.P., Strangway, D.W., and Simmons, G., 1973, Radio Interferometry Depth Sounding, Part II - Experimental Results, Geophysics, v. 38, no. 3, p. 581-599.

- Rossiter, J.R., Strangway, D.W., Annan, A.P., Watts, R.D.,
and Redman, J.D., Detection of Thin Layers by Radio
Interferometry, submitted to Geophysics, 1974.
- Simmons, G., Strangway, D.W., Bannister, L., Baker, R.,
Cubley, D., LaTorraca, G., and Watts, R., 1972,
The Surface Electrical Properties Experiment, in
Kopal, A. and Strangway, D., eds., Lunar Geophysics,
Proceedings of a Conference at the Lunar Science
Institute, Houston, Texas, 18-21, October, 1971,
D. Reidel, Dor drecht, p. 258-271.
- Strangway, D.W., Simmons, G., LaTorraca, G.A., Watts, R.D.,
Bannister, L., Baker, R., Redman, J.D., and
Rossiter, J.R., 1974, Radio-Frequency Interferometry -
A New Technique for Studying Glaciers, J. of Glaciology,
in press.
- Tsang, L., Kong, J.A., and Simmons, G., Interference Patterns
of a Horizontal Electric Dipole over Layered Dielectric
Media, J. Geophys. Res., v. 78, p. 3287-3300, 1973.
- Wait, J.R., 1970, Electromagnetic Waves in Stratified Media,
2nd Edition: New York, The Macmillan Co.
- Waller, W.M., 1973, Surface Electrical Properties of
Simulation Model, Lockheed Electronics Co. Final
Report. LEC/PESD 634-TR-139 for contract NAS 9-122200,
NASA-JSC, Houston, 1973.

Figure Captions

- Fig. 1 Sketch of a 2-layer earth geometry and the associated cartesian and cylindrical coordinate system.
- Fig. 2 Complex radial wavenumber plane illustrating integration contours and location of singular points:
- | | | |
|---------------|-----|-----------------------|
| branch points | ◆ | |
| TE poles | { ● | upper Riemann surface |
| | { ○ | lower Riemann surface |
| TM poles | { ▲ | upper Riemann surface |
| | { △ | lower Riemann surface |
- Hankel transform contour
- Geometrical optics path through saddle point
- _____ Normal mode contour
- - - - - Branch cuts
- Fig. 3 Schematic drawing of scale model 2-layer earth.
- Fig. 4 Schematic diagram of scale model electronics, display and recording system.
- Fig. 5 TE (E) radiation patterns for the horizontal electric dipole on the surface of a dielectric half-space for $K_1 = 1$. (whole-space pattern), 2., 3.2., 10.
- Fig. 6 Scale model experimental measurements of (E_ϕ) pattern in X_2 - X_3 plane compared with the theoretical pattern computed by Cooper (1971).

Fig. 7 Suite of 2-layer earth responses where the substratum is a perfect reflector; _____ scale model response, ----- normal mode theoretical response, geometrical optics theoretical response.

Fig. 8 Suite of 2-layer earth responses for a perfectly reflecting substratum and shallow reflector depths: — scale model response; ----- normal mode theoretical response; * * * normal mode with numerical integration of branch-line contributions.

Fig. 9 Suite of 2-layer earth responses for a dielectric substratum: — scale model response; ----- normal mode theoretical response.

Fig. A (a) Sketch of multiple reflections in thin layer.
 (b) Illustration of pole positions in complex λ plane as a function of d .

.-.-.-. Contour on which $|R_{10} R_{12} \beta| = 1$



Branch-point



Roots (λ_p) on the upper Riemann surface



Roots (λ_p) on the lower Riemann surface

Table of Contents

Table 1: Cylindrical components of the E and H fields about a Horizontal Electric Dipole (HED) on the surface of a 2-layer earth. The fields are expressed in terms of (electric and magnetic) Hertz (vector) potentials ($\bar{\pi}_e$ and $\bar{\pi}_m$) which have only a vertical (\hat{e}_3) component.

TE and TM Fields in Region i

TE: $\vec{H}_i^{TE} = \left[\hat{e}_3 + \frac{\nabla \partial}{k_i^2 \partial z} \right] \pi_m^i$ $\vec{E}_i^{TE} = \frac{\hat{e}_3 \times \nabla \pi_m^i}{j\omega \epsilon_i}$

TM: $\vec{E}_i^{TM} = \left[\hat{e}_3 + \frac{\nabla \partial}{k_i^2 \partial z} \right] \pi_e^i$ $\vec{H}_i^{TM} = \frac{\hat{e}_3 \times \nabla \pi_e^i}{-j\omega \mu_i}$

π_e^o & π_m^o for HED

$\pi_e^o = \frac{j\omega \mu_0 I d l \cos \varphi}{4\pi} \int_0^\infty \left\{ \pm e^{\pm j2\pi \gamma_0 (z-h)} - R^{TM} e^{j2\pi \gamma_0 (z+h)} \right\} J_1(2\pi \lambda \rho) d$

$\pi_m^o = \frac{I d l}{4\pi} \sin \varphi \int_0^\infty \frac{k_0^2}{-j\gamma_0} \left\{ e^{\pm j2\pi \gamma_0 (z-h)} + R^{TE} e^{j2\pi \gamma_0 (z+h)} \right\} J_1(2\pi \lambda \rho)$

2 Layer Earth Reflection Coefficients: R^{TE} & R^{TM}

$R = \left[\frac{1}{R_{01}} + \frac{R_{01} - 1/R_{01}}{1 + R_{01} R_{12} \beta} \right]$ $\beta = e^{j2\pi \gamma_1 2d}$

$R_{ij}^{TE} = \frac{\gamma_i - \gamma_j}{\gamma_i + \gamma_j}$ $R_{ij}^{TM} = \frac{k_j^* \gamma_i - k_i^* \gamma_j}{k_j^* \gamma_i + k_i^* \gamma_j}$

$T_{ij} = 1 + R_{ij}$

Parameter Definitions

h - height of Tx antenna

z - height of Rx antenna

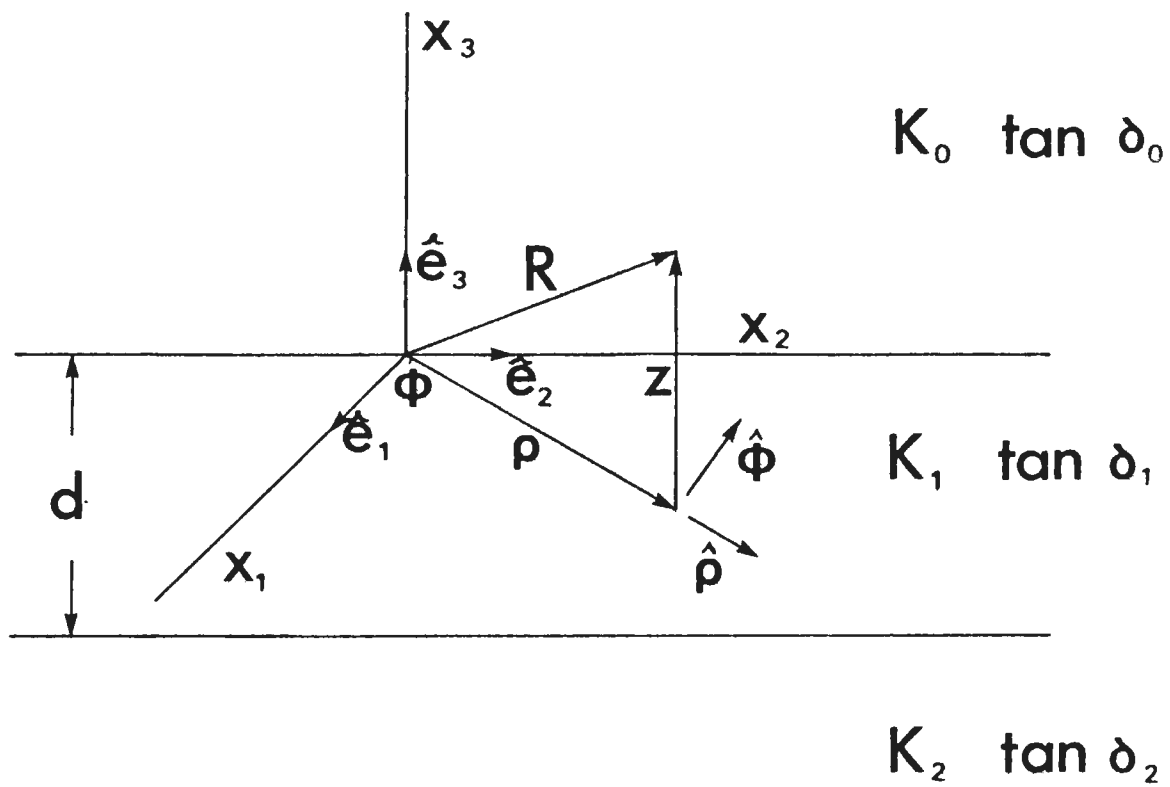
k_i - propagation constant in i^{th} region = $\omega \sqrt{\epsilon_i \mu_i} = k_0 (K_i^*)^{1/2}$

λ - horizontal wavenumber

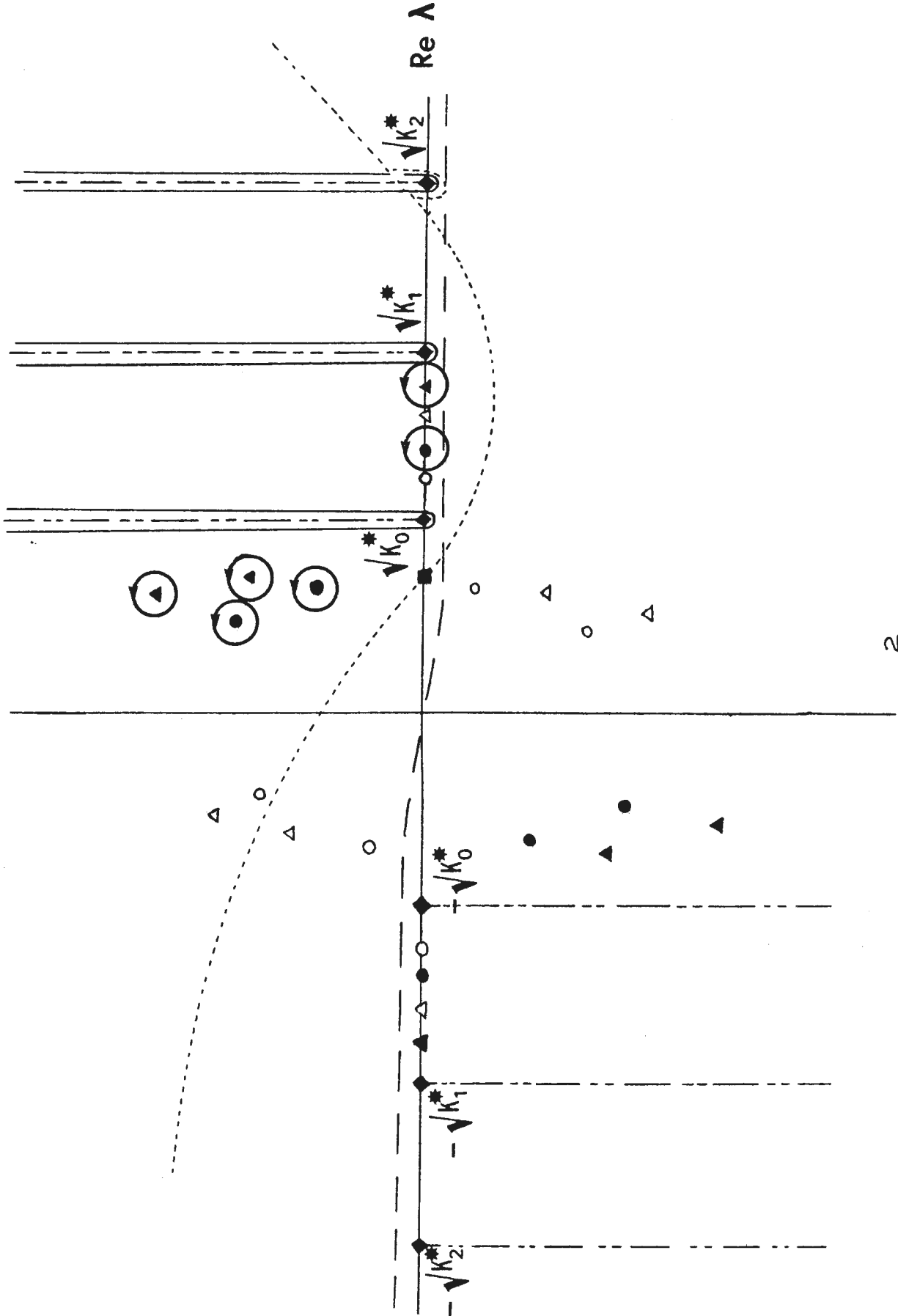
γ_i - $(k_i^2 - \lambda^2)^{1/2}$ vertical (\hat{e}_3) wavenumber

R^{TE} & R^{TM} TE and TM Fresnel reflection coefficients for an N-layered

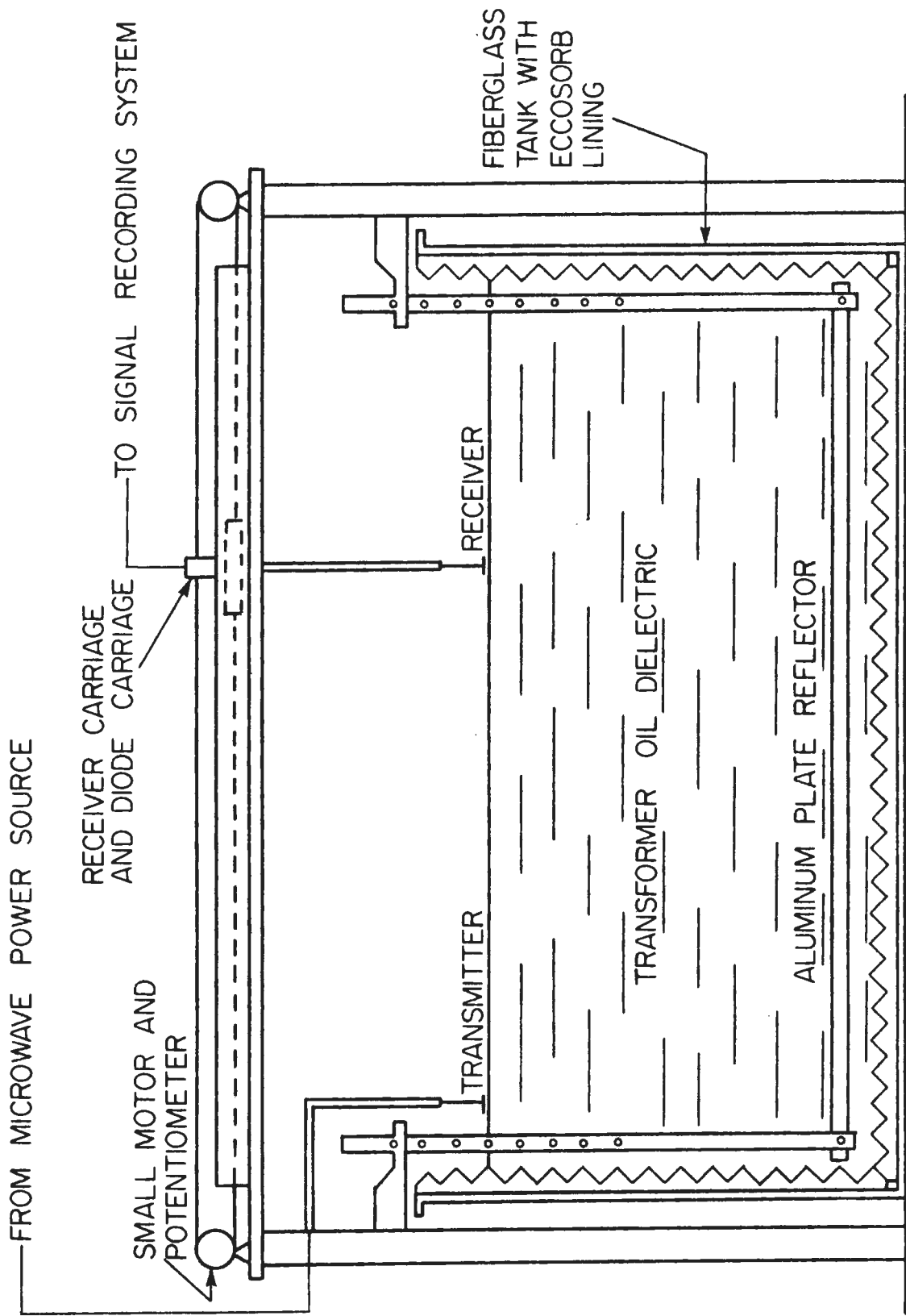
K_i^* - $K_i (1 + \tan \delta_i)$ - complex dielectric constant

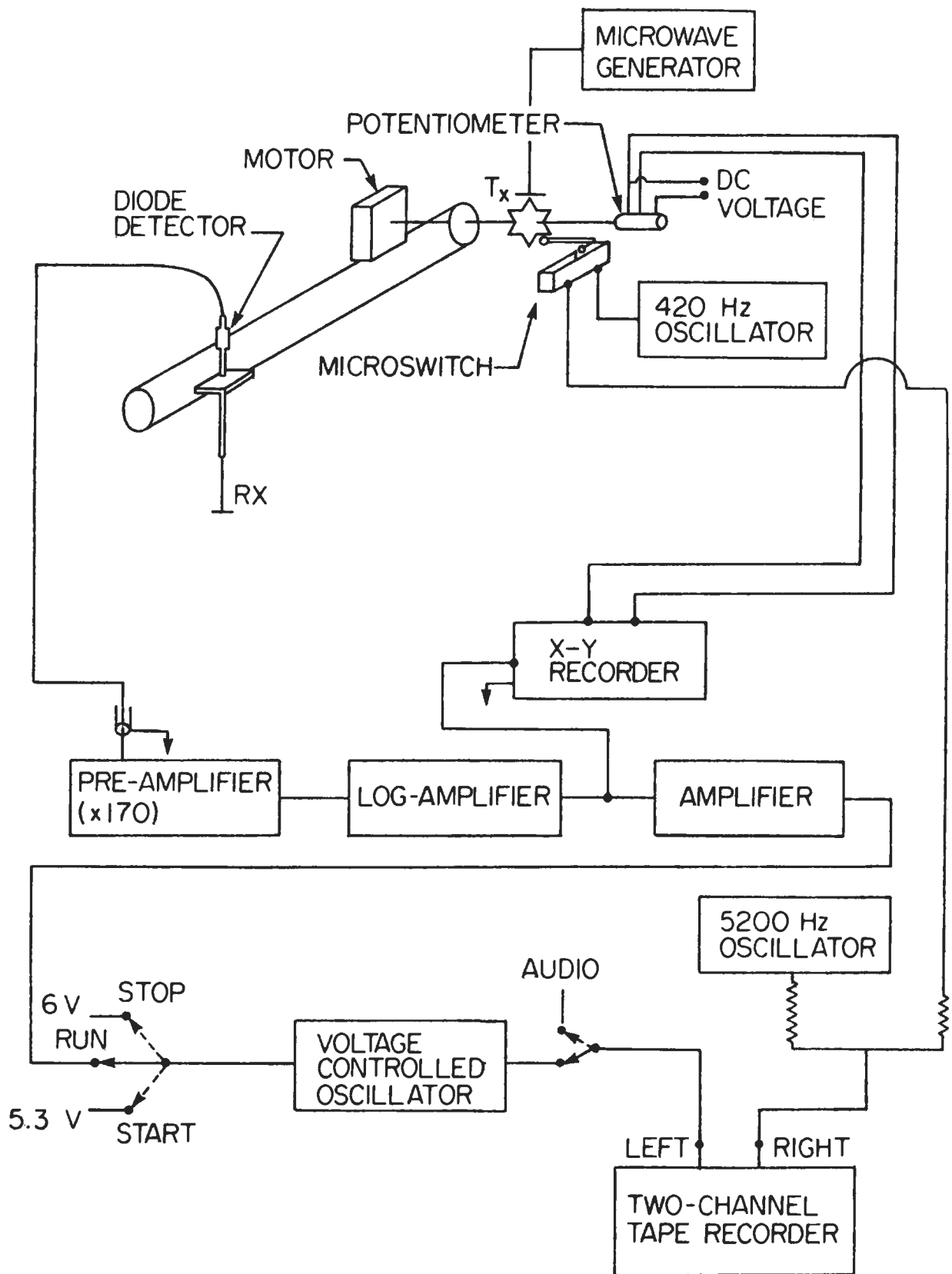


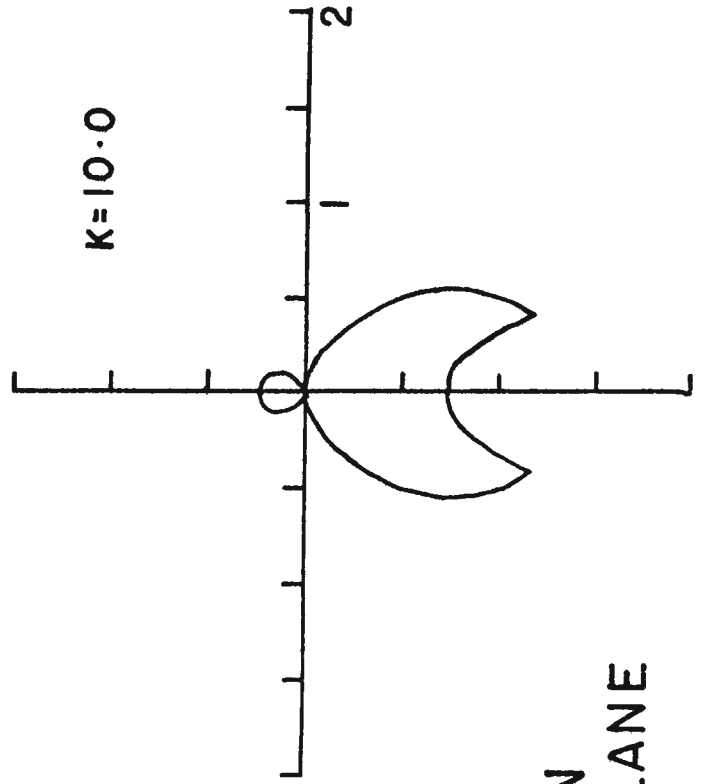
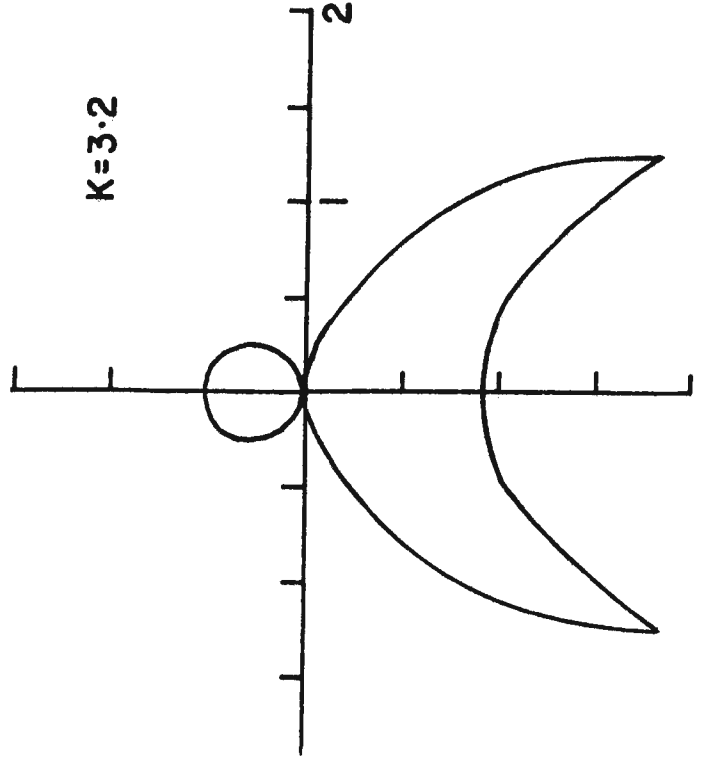
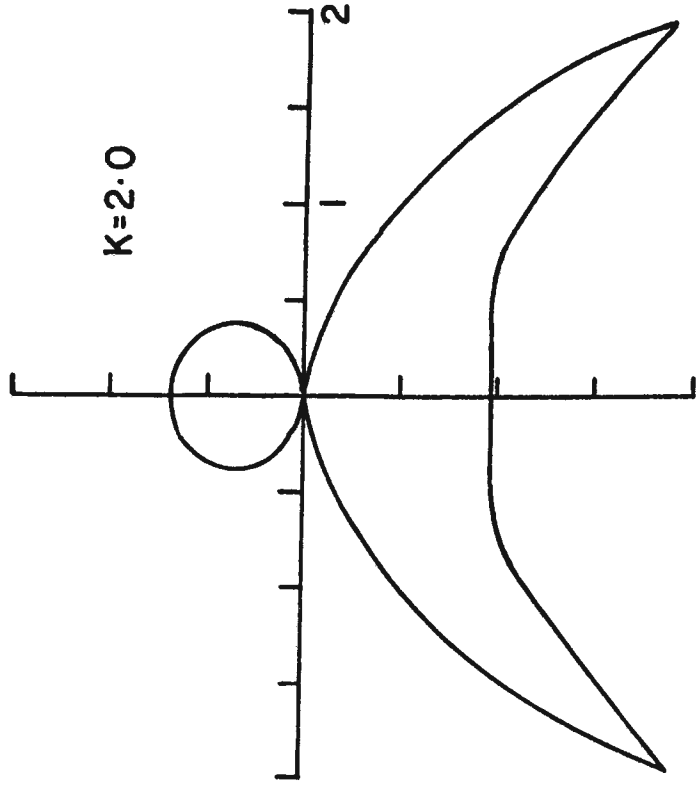
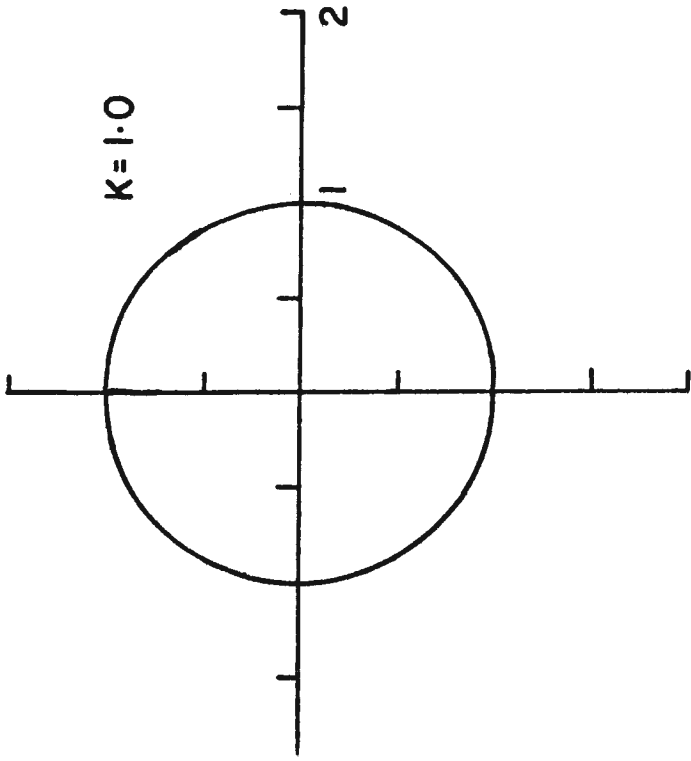
$\text{Im } \lambda$



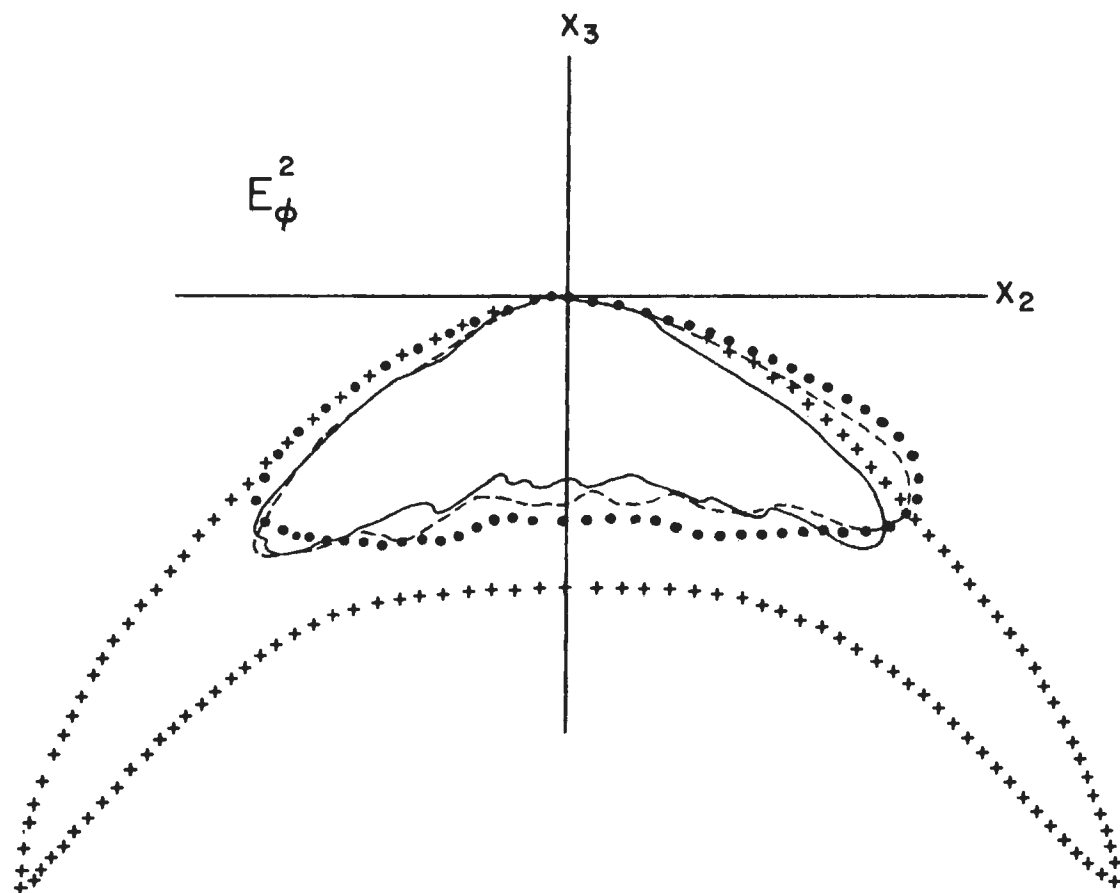
$\text{Re } \lambda$



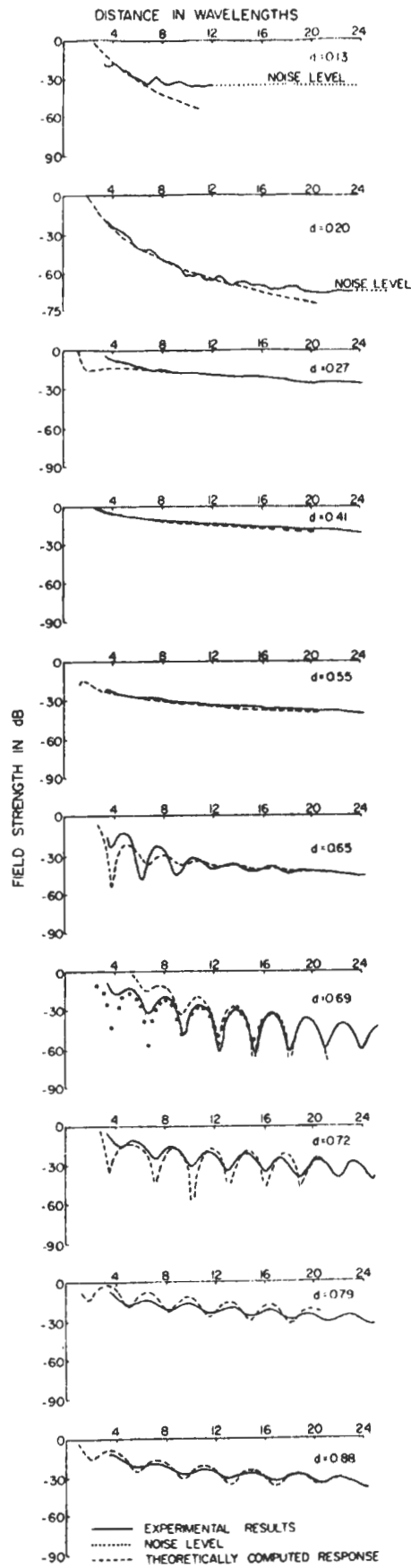


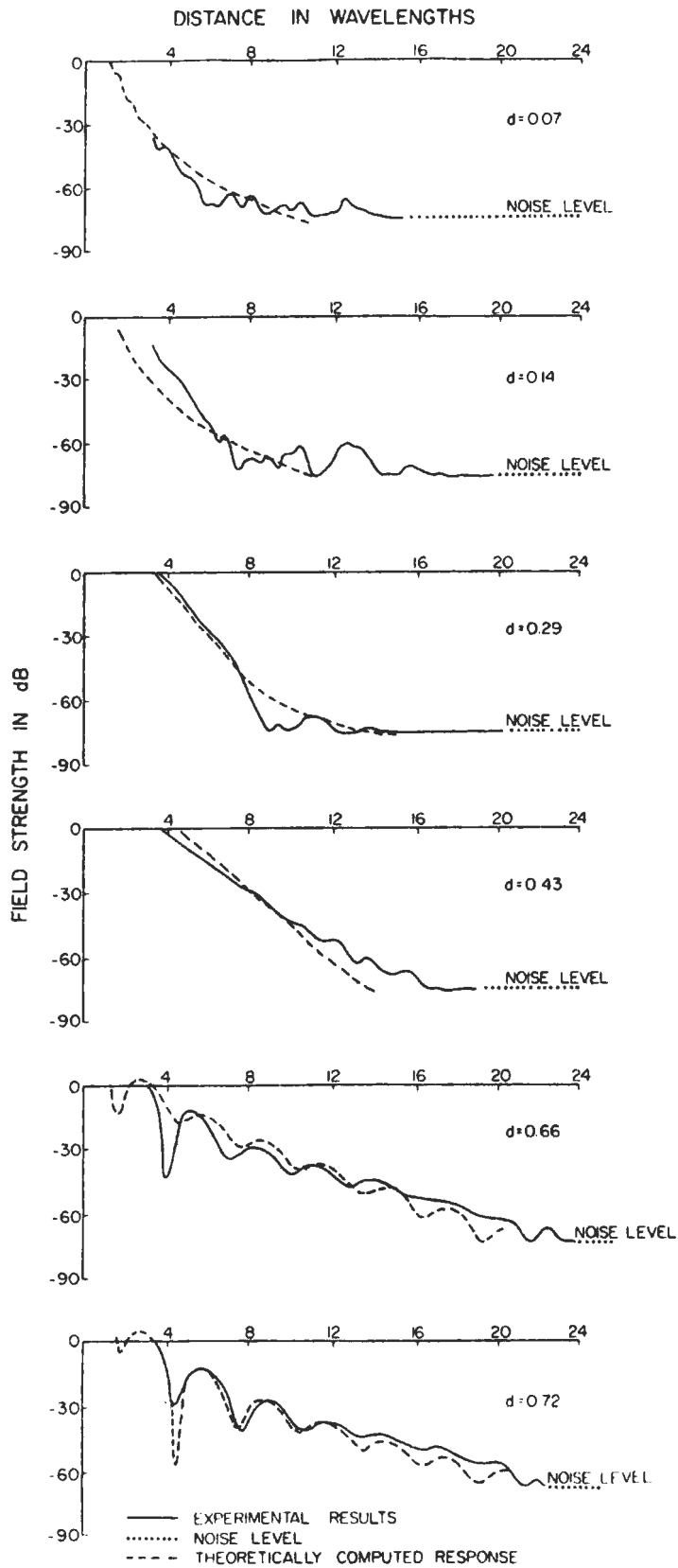


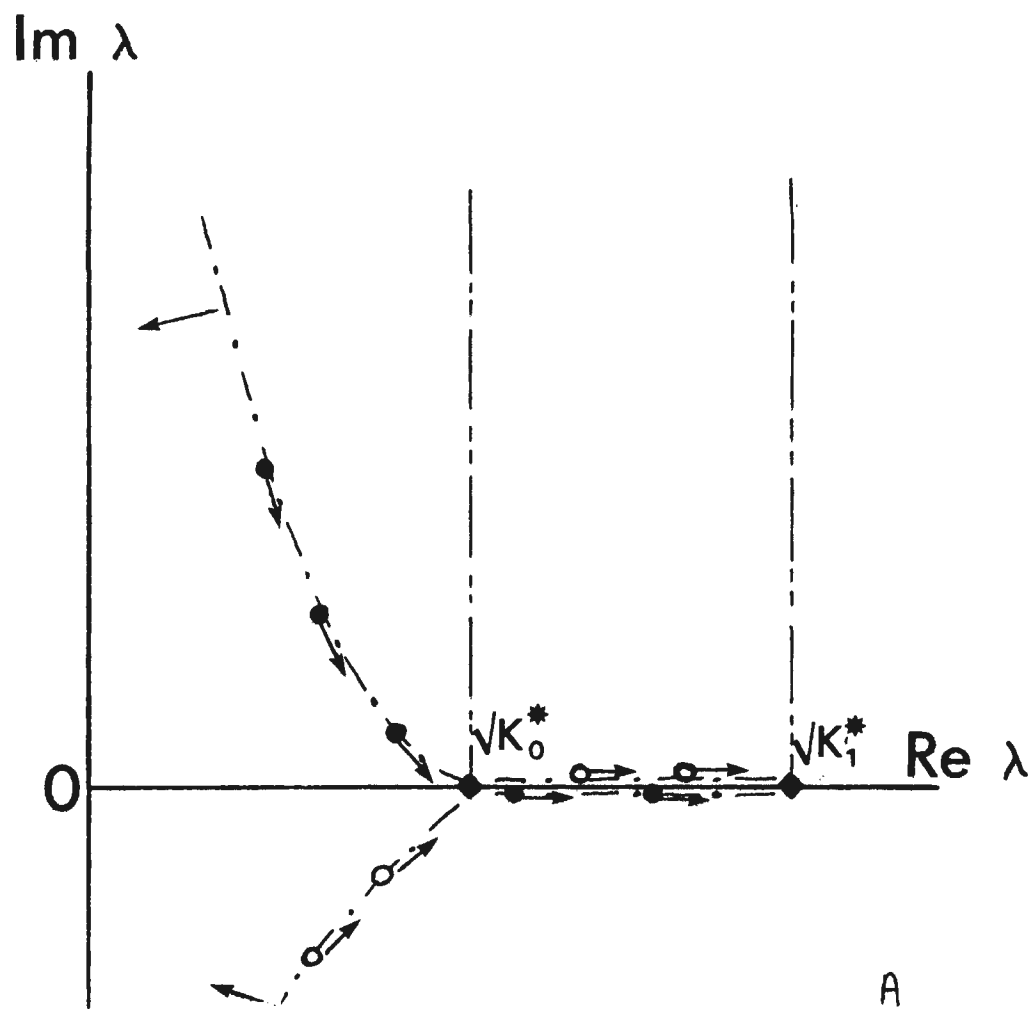
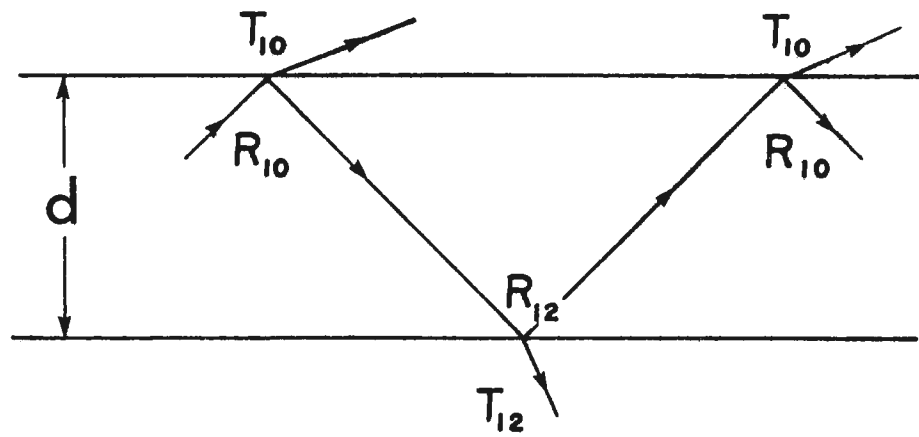
TE POWER
RADIATED IN
THE X_2 - X_3 PLANE



+++ COOPER -- $k' = 2.16$
 EXPERIMENTAL { — 6w RADIUS
 - - - 4.5w RADIUS
 3w RADIUS







A

DETECTION OF THIN LAYERS BY RADIO INTERFEROMETRY

J.R. Rossiter¹, D.W. Strangway², A.P. Annan¹,
R.D. Watts³, and J.D. Redman²

1. Department of Physics
University of Toronto
Toronto, M5S 1A7
Canada

2. Department of Geology,
University of Toronto,
Toronto, M5S 1A1
Canada

3. NAS/NRC Post-Doctoral Fellow,
Johnson Spacecraft Center,
Houston, Texas 77058, U.S.A.;

Presently at U.S.G.S.
Denver, Colorado, U.S.A.

April 18, 1974

ABSTRACT

Recent theoretical work on the radio interferometry technique for dielectric layers of less than one free space wavelength thick, has indicated that there is a thickness for which no interference is observed. This thickness is about 0.2 free space wavelengths for ice, and it lies between the thickness that allows one single mode to propagate in the layer (> 0.2 wavelengths) and a thickness that is essentially transparent to the wavelength being used (≤ 0.2 wavelengths).

Field work was done on the Juneau Icefield using frequencies from 1 to 32 MHz. At 1 and 2 MHz, an interference pattern typical of a half space of ice with a dielectric constant of 3.3 was observed, while at 4 MHz essentially no interference was seen. At higher frequencies, the interference observed is typical of that of a layer overlying a half space. The upper layer can be interpreted to have a depth of 15 or 20 m (0.2 wavelengths at 4 MHz) with a dielectric constant of 2.4. This is the result of a layer of snow over a half space of ice. The technique is therefore of potential interest in interpreting the nature of the snow layer overlying a glacier.

INTRODUCTION

Radio frequency interferometry depth sounding was originally developed to measure the dielectric properties and structure of highly resistive geological regions (Annan, 1970, 1973). It has been used successfully for sounding glaciers (Rossiter et al., 1973; Strangway et al., 1974), and on the moon (Simmons et al., 1972, 1974). The technique consists of setting a radio transmitter on the surface to be sounded, and measuring the field strength as a function of distance from the transmitter. Several waves propagate from the transmitter to the receiver, generating an interference pattern that is indicative of both the dielectric properties and the structure of the medium.

Theoretical studies have determined the fields to be expected over dielectric layers (Annan, 1973; Kong, 1972; Tsang et al., 1973). Early work used geometrical optics approximations in order to evaluate the integral expressions, but it can be shown that the method is highly inaccurate for layers less than about three free space wavelengths (abbreviated "W" throughout) thick. In more recent work, a normal mode approximation has been used that is particularly suitable for calculating the fields in the presence of a thin layer.

In a companion paper (Annan et al., 1974), theoretical and experimental data from an analogue scale model are compared. In the present paper, we will examine the particular case of a thin dielectric layer (0 to 1 W thick) overlying a thick dielectric layer (see Figure 1), using mode theory, and compare these results with field data collected on the Juneau Icefields, Alaska.

THEORY OF THIN LAYERS

Radio interferometry data show three distinct types of behaviour as the upper layer increases from being very thin and transparent, through a critical thickness, to being thick enough to allow propagating modes. We will examine each of these three cases.

(a) Very thin transparent upper layer

When the upper layer is very thin (less than about 0.2 W thick in ice), it is essentially transparent. Therefore, the observed interference pattern is independent of the properties of the upper layer, and looks like that of a half space with the properties of the lower layer (see Figures 2 and 3).

(b) Transition thickness - decoupled layer

As the upper layer becomes approximately 0.2 W thick

(the exact value is dependent on the dielectric constant), it effectively decouples any signal from the lower layer. However, if it is still too thin to allow free propagation within itself, the observed patterns will show no interference at all (see Figure 4). Since this transition band is narrow (and may be non-existent for very low losses), it is extremely diagnostic of upper layer thickness.

(c) Modal propagation in the upper layer

As the upper layer becomes thick enough to support freely propagating modes, the interference patterns again show clear beating (see Figures 5 and 6). Since the interference is generated by modes propagating along the thin layer guide, the spatial frequency of the beats is relatively low, and dependent on the properties of the upper layer (although occasionally a higher spatial frequency ripple, due to the lower layer, can be seen).

DIELECTRIC PROPERTIES OF ICE AND SNOW

The dielectric properties of ice and snow have been reviewed by Evans (1965). Ice has a strong relaxation at about 10^4 Hz at 0°C, but for frequencies well above this, the dielectric constant is 3.2, and is fairly independent of temperature. Since radio frequencies are on the high

frequency tail of the relaxation spectrum, the product $f \cdot \tan \delta$ is approximately constant. It has a value of about 0.2 MHz at 0°C, decreasing to 0.1 MHz at -10°C.

Snow is essentially a mixture of two dielectrics - ice and air. As such, it has dielectric properties that are between those of its constituents, and which depend primarily on its density. Thus snow of density 0.5 g/cm³ has a dielectric constant of about 1.9 and a loss tangent about half that of ice.

The effect of impurities is not well understood, although impurities tend to increase the loss tangent. The addition of a few percent water by volume to snow would increase the dielectric constant to perhaps 2.5 and increase the loss tangent perhaps several times. Few accurate studies have been done on this problem.

JUNEAU ICEFIELD DATA

During the summer of 1972, measurements were made at various locations on the Juneau Icefields (see Figure 7). We will examine two runs - Run 36 made from Site 6 on the Taku Glacier, and Run 92 made from Site 25, in the accumulation zone of the Matthes Glacier. At Site 6, the thickness of ice

has been determined seismically to be approximately 350 m. (Miller, 1952). The thickness of the ice at Site 25 is uncertain, but it is probably about 200 m.

Measurements were made at six frequencies - 1, 2, 4, 8, 16, and 32 MHz, so that the free space wavelength varied from 300 m to about 10 m. Six components of the magnetic field were measured - three from each of two transmitting antenna orientations. Of these components, we presently have theoretical solutions for two of them - the vertical (H_z) and radial (H_ρ) magnetic fields from a broadside transmitting antenna. These two components were compared to suites of theoretical curves and a best fit that gave consistent results for all frequencies was found.

For both runs, the data at 32 MHz were so scattered that interpretation in terms of layered structures was not possible. Some scattering is present at 16 and 8 MHz. This seems typical of temperate glaciers (Strangway et al., 1974; Davis, 1973). We attribute this scattering to random reflections from crevasses and other irregularities in the ice with typical sizes of about 10 m.

The parameters deduced from each frequency for the two runs are listed in Table 1. Theoretical curves for the best single set of parameters for each run are shown with the field data in

Figures 8 and 9 (i.e. one set of parameters was chosen for each run, although for any given frequency better fits might have been found with slightly different parameters). In each case, the two components (H_p and H_z) gave similar results. From the 1 and 2 MHz data, the dielectric constant and loss tangent of the lower layer can be estimated. From the 4 MHz curves, very tight limits can be put on the thickness of the upper layer. From 8 MHz and to some extent 16 MHz data, the properties of the upper layer can be determined.

Runs 36 and 92 differ in two basic respects. For Run 36, the loss tangents are typical for ice - $0.2 \pm 0.1/f$, where f is frequency in MHz (Evans, 1965). The values obtained for the thickness of upper layer are consistent from frequency to frequency. For Run 92, it was not possible to obtain a consistent thickness without letting the loss tangent drop to at least $0.1/f$. Even then, the depths obtained at the lower frequencies (especially 4 MHz) were less than 15 m while for 8 and 16 MHz a depth of about 20 m was required.

DISCUSSION

We interpret the thin upper layer at both sites as being snow about 15 to 20 m thick, with a dielectric constant of 2.4 ± 0.2 , overlying thick glacial ice, with a dielectric constant

of 3.3 ± 0.1 . The loss tangent at Site 6 (Run 36) is about $0.2 \pm 0.1/f$, while at Site 25 (Run 92), it is somewhat lower. These dielectric properties are typical for glacial ice and for snow of density 0.65 ± 0.15 (Evans, 1965). We attribute the lower loss tangent at Site 25 to the lower mean temperature at the higher site which reduces both the relaxation frequency and the amount of free water present. It is interesting that although the measurements were made in summer with runoff water abundant on the surface, these losses are not particularly high. Presumably, any free water is in too thin a layer or is too well disseminated to be noticeable at the frequencies used.

Inconsistency of the depth determinations from frequency to frequency (especially true at Site 25) is possibly due to the gradation of the snow-ice boundary. Examination of a crater pit some 5 m deep blasted on the Taku Glacier (see Figure 7(a)) confirmed the gradational nature of snow density (and hence dielectric constant) with depth. Since Site 25 is in the accumulation zone of the glacier, snow may be compacting even more gradually in that area.

CONCLUSION

Using radio-frequency interferometry, a thin layer can be detected and estimates of the thickness of the layer to within a few meters can be made. By using a range of frequencies, the dielectric parameters of both the upper and the lower layer can be obtained.

Acknowledgements

Field work, data collection and reduction was done under NASA Contract No. NAS 9-11540 to MIT and a subcontract to the University of Toronto for the Apollo Surface Electrical Properties Experiment. We thank Messrs. G. LaTorraca, R. Baker, and L. Bannister, and Dr. G. Simmons.

Support for the analysis and interpretation of the data from the Department of Energy, Mines and Resources, under Research Agreement 1135-D13-4-16/73, is gratefully acknowledged. Computational assistance was provided by Mr. J. Proctor.

References

- Annan, A.P., "Radio Interferometry Depth Sounding", M.Sc. thesis, Department of Physics, University of Toronto, 1970.
- Annan, A.P., "Radio Interferometry Depth Sounding: Part I - theoretical discussion", Geophysics, v. 38, pp. 557-580, 1973.
- Annan, A.P., Waller, W.M., Strangway, D.W., Rossiter, J.R., and Redman, J.D., and Watts, R.D. "The electromagnetic response of a low-loss, two-layer, dielectric earth for horizontal electric dipole excitation", submitted to Geophysics, 1974.
- Davis, J.L., "The Problem of Depth Sounding Temperate Glaciers", M.Sc. thesis, Trinity College, Cambridge, 1973.

- Evans, S., "Electrical properties of ice and snow - a review",
J. Glaciology, v. 5, pp. 173-192, 1965.
- Kong, J.A., "Electromagnetic fields due to dipole antennas over
stratified anisotropic media", Geophysics, v. 37, pp.
935-996, 1972.
- Miller, H.M., et al., "Scientific Observations of the Juneau Ice
Field Research Project, Alaska, 1949, Field Season",
J.I.R.P. Report No. 6, American Geographical Society,
New York, 1952.
- Rossiter, J.R., LaTorraca, G.A., Annan, A.P., Strangway, D.W.,
and Simmons, G., "Radio interferometry depth sounding
part III - experimental results", Geophysics, v. 44,
pp. 581-599, 1973.
- Simmons, G., Strangway, D.W., Bannister, L., Baker, R., Cubley, D.,
LaTorraca, G., and Watts, R., "The Surface Electrical
Properties Experiment", Lunar Geophysics, Proceedings of
a conference at the Lunar Science Institute, Houston,
Texas, 18-20 October, 1971, D. Reidel, Dordrecht, pp.
258-271, 1972.
- Simmons, G., Strangway, D.W., Annan, A.P., Baker, R., Bannister,
Brown, R., Cooper, W., Cubley, D., de Bettencourt, J.,
England, A., Groener, J., Kong, J., LaTorraca, G., Maynard,
Nanda, V., Redman, D., Rossiter, J., Tsang, L., Unger, J.,
and Watts, R., "The Surface Electrical Properties
Experiment", Apollo 17 Preliminary Science Report, NASA
SP-130, Washington, pp. 15-1 - 15-14, 1974.

Strangway, D.W., Simmons, G., LaTorraca, G., Watts, R.,
Bannister, L., Baker, R., Redman, D., and Rossiter,
J., "Radio-frequency interferometry - a new
technique for studying glaciers", J. Glaciology,
no. 67, 1974.

Tsang, L., Kong, J.A. and Simmons, G., "Interference
patterns of a horizontal electric dipole over
layered dielectric media", J. Geophys. Res.
v. 78, pp. 3287-3300, 1973.

TABLE 1: INTERPRETATION OF JUNEAU RUNS 36 AND 92 BY COMPARISON TO THEORY

RUN 36

Frequency (MHz)	d_1 w (m.)	k_1	$\tan \delta_1$	k_2	$\tan \delta_2$
1	<0.075(<23)	-	-	3.3±0.1	0.20±0.10
2	.100-.150(15-23)	-	-	3.3±0.1	0.10±0.05
4	0.2-0.3(15-22)	-	-	-	0.05±0.03
8	0.45-0.60(17-22)	2.4±0.1	.02±.01	-	-
16 ⁽¹⁾	0.9-1.2(17-22)	2.4±0.2	0.010±0.005	-	-
<u>Interpretation:</u>	19±4 m.	2.4±0.1	0.2±0.1/f ⁽²⁾	3.3±0.1	0.2 ±0.1/f ⁽²⁾

RUN 92

1	<0.1(<30)	-	-	3.3±0.1	0.10 ?
2	<0.125(<20)	-	-	3.3±0.1	0.05-0.10
4	.100-.175(7-13) .125-.200(9-15)	@2.4	-	-	@ .05 @ .02
8	0.5-0.7(19-26)	2.4±0.1	.02±.01	-	-
16 ⁽¹⁾	1.2±0.1(22±2)?	2.4±0.2	<.02	-	-
<u>Interpretation:</u>	18±8 m.	2.4±0.2	0.10/f ⁽²⁾	3.3±0.1	0.10±0.05/f ⁽²⁾

1. 16 MHz data are fairly scattered (see text)
2. f in MHz. Because of its dielectric mechanism, the loss tangent of ice essentially behaves as f . tan δ = constant (Evans, 1965).

FIGURE CAPTIONS

- Fig. 1 Configuration of a thin dielectric layer overlying an infinite dielectric half space. By varying the frequency, the thickness of the upper layer in wavelengths can be changed.
- Fig. 2 Theoretical curves of field strength (db) vs. range in wavelengths (λ) for a very thin upper layer, with the dielectric constant of the lower layer varying. The spatial frequency of the pattern increases with increasing k_2 . (a) H_y broadside component, (b) H_z broadside component.
- Fig. 3 Theoretical curves for a very thin upper layer with the loss tangent of the lower layer varying. The sharpness of the interference drops off with increasing $\tan \delta_2$. (a) H_y broadside component, (b) H_z broadside component.
- Fig. 4 Theoretical curves for the region of no interference showing the transition from a transparent upper layer to an upper layer that propagates freely. (a) H_y broadside component, (b) H_z broadside component.
- Fig. 5 Theoretical curves for a propagating upper layer, with the dielectric constant of the upper layer varying. (a) H_y broadside component, (b) H_z broadside component.
- Fig. 6 Theoretical curves for a propagating upper layer, with the loss tangent of the upper layer varying. (a) H_y

broadside component, (b) H_z broadside component.

Fig. 7 Maps of the Juneau Icefield (a) near Camp 10 and (b) near Camp 18. There is a gap of 2 km between the top of (a) and the bottom of (b). Radio interferometry was conducted at "R.F.I Sites". Seismic depths (from Miller, 1952) are indicated where known. Run 36 was made at Site 6 at an elevation of 1050 m. ASL on the Taku Glacier; Run 92, was made at Site 25 at an elevation of 1770 m. ASL, on the Matthes Glacier. The crater site is also shown in (a).

Fig. 8 Radio interferometry data, H_ρ and H_z broadside components, 1 to 16 MHz for Run 36, Site 6 (solid lines). At 16 MHz scattering is significant (see text). Theoretical curves are also shown (dashed lines) for the following parameters: $d_1 = 19$ m., $k_1 = 2.4$, $\tan \delta_1 = 0.2/f$, $k_2 = 3.3$ and $\tan \delta_2 = 0.2/f$.

Fig. 9 Radio interferometry data, H_ρ and H_z broadside components, 1 to 16 MHz, for Run 92, Site 25 (solid lines). At 16 MHz scattering is significant (see text). Theoretical curves are also shown (dashed lines) for the following parameters: $d_1 = 18$ m., $k_1 = 2.4$, $\tan \delta_1 = 0.2/f$, $k_2 = 3.3$ and $\tan \delta_2 = 0.1/f$.

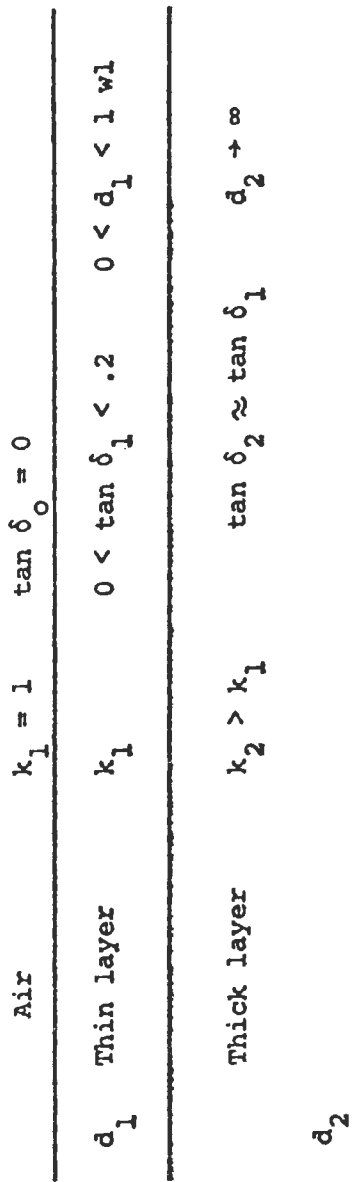


Fig. 1: Configuration of a thin dielectric layer overlying an infinite dielectric half-space.

D: 0.05 λ
LT1: 0.02 LT2: 0.05
K1: 2.4 K2: VARYING

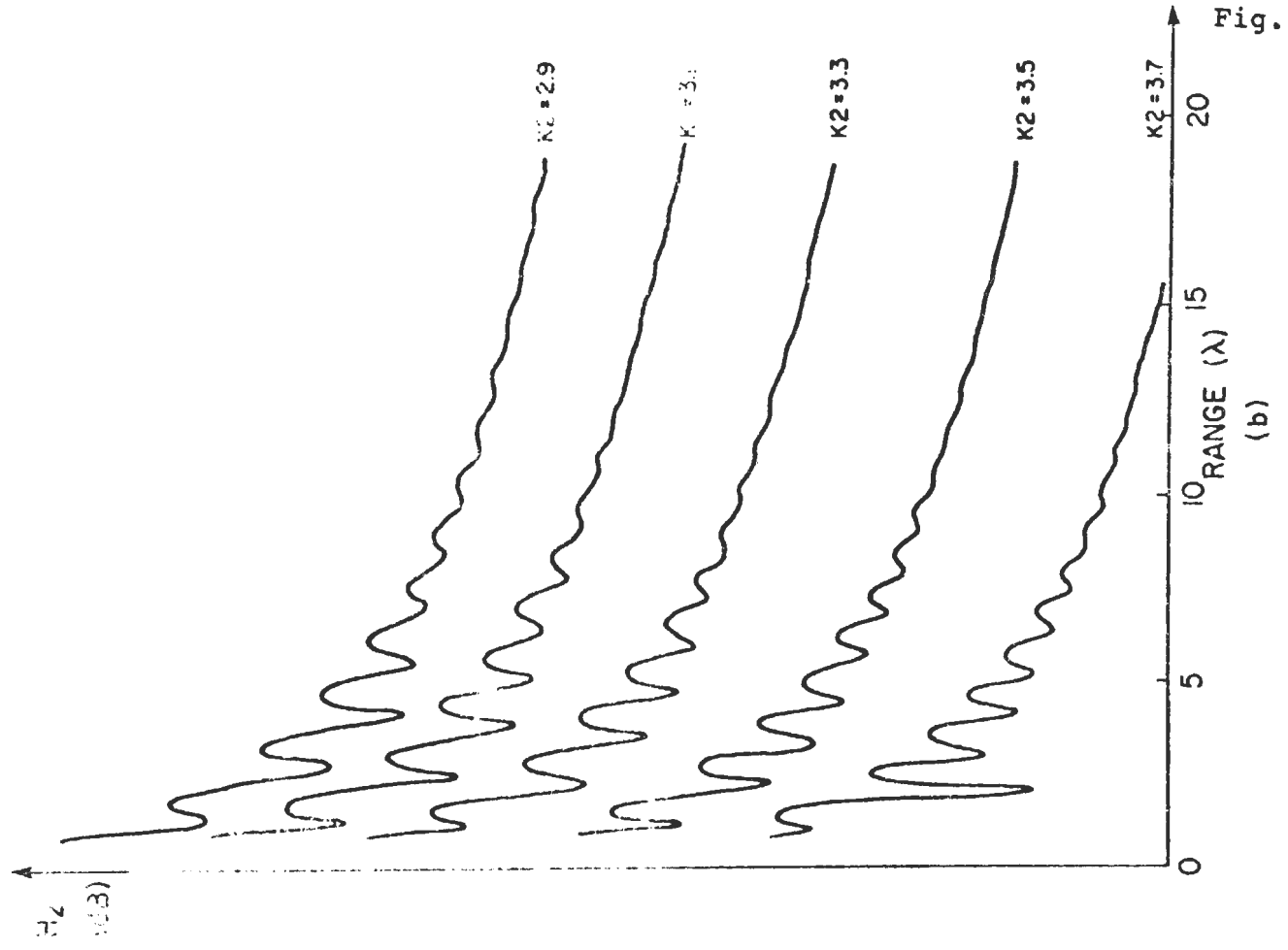
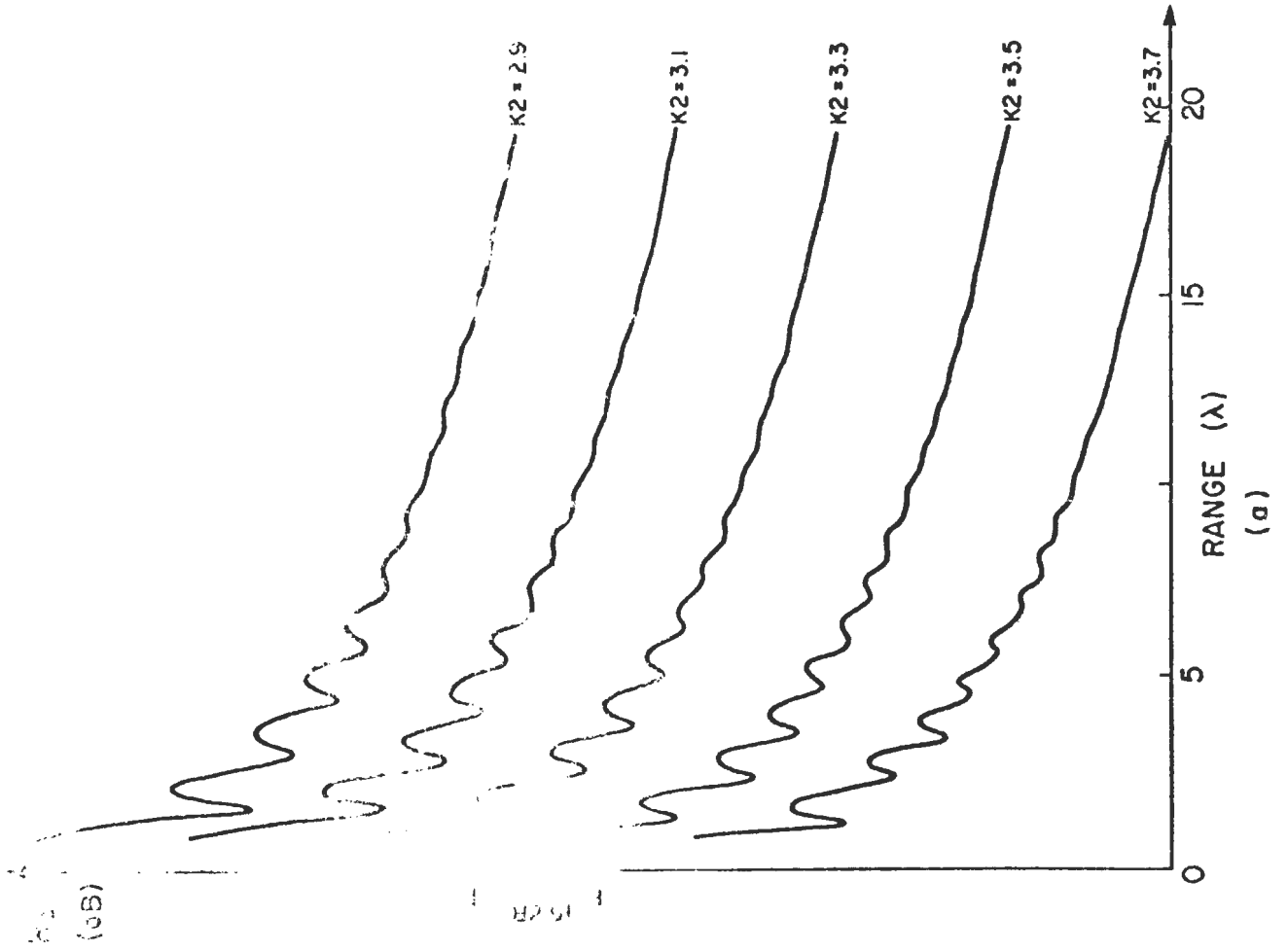


Fig. 2

$D: 0.05\lambda$
 $LT1: 0.02$ $LT2: \text{VARYING}$
 $K1: 2.4$ $K2: 3.3$

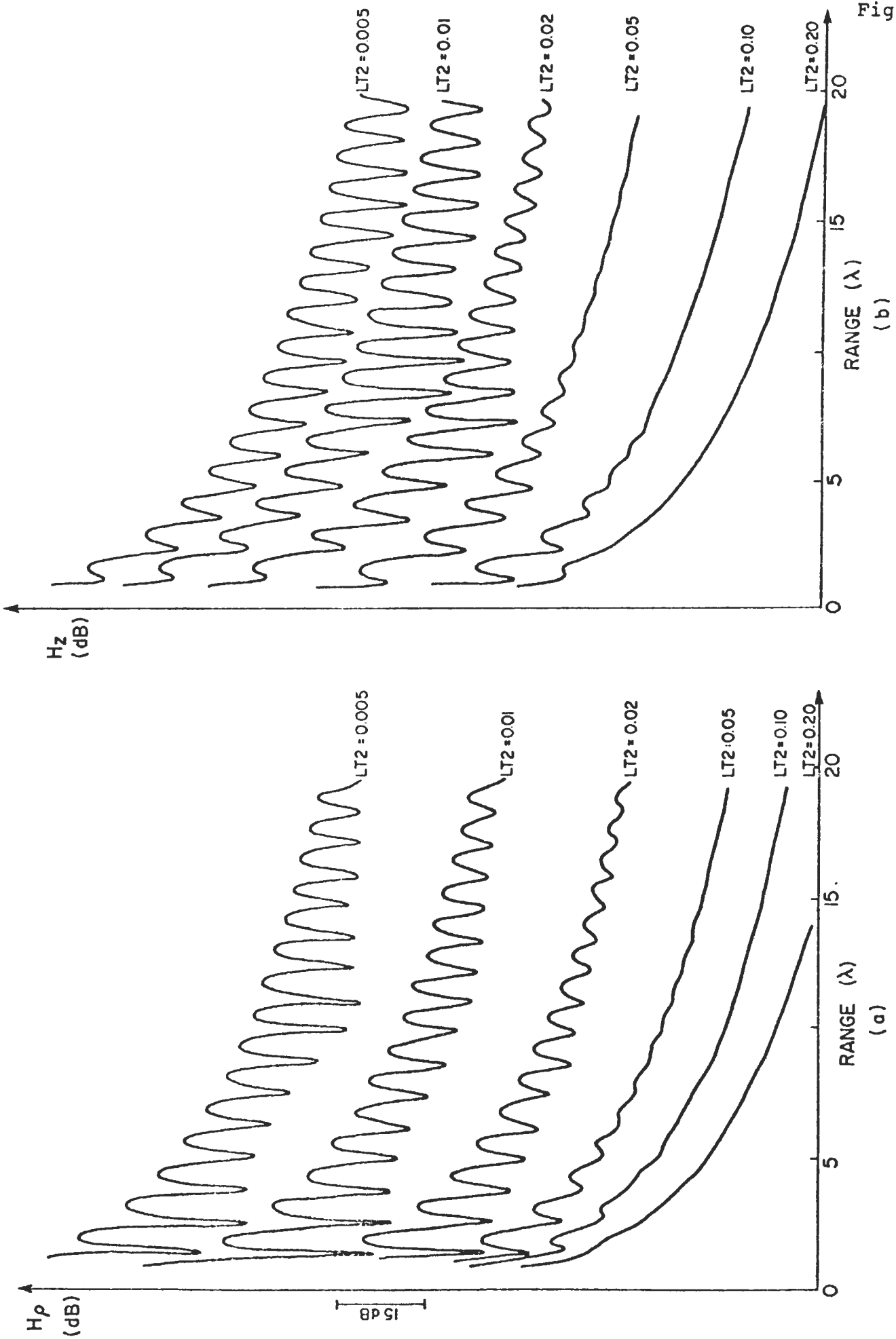
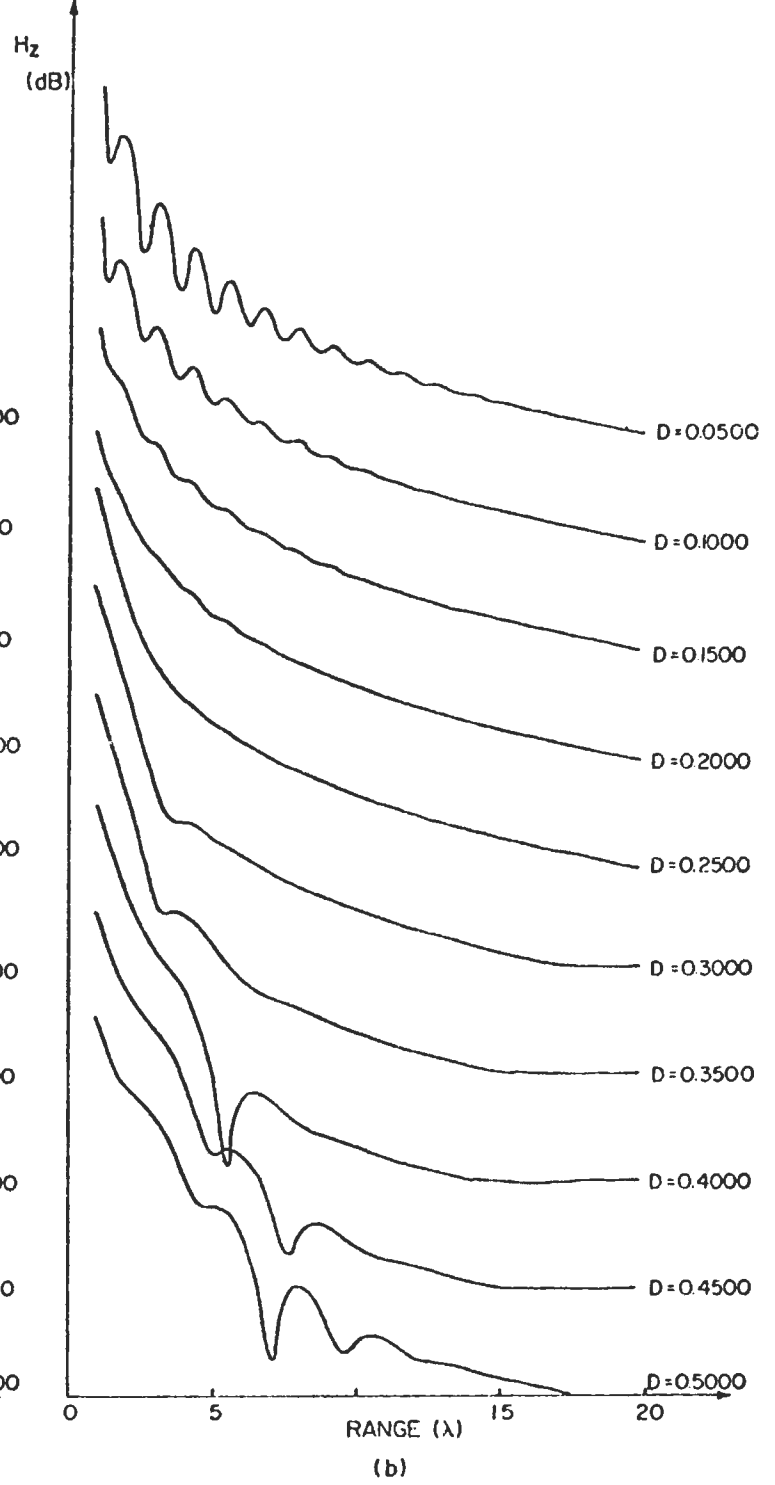
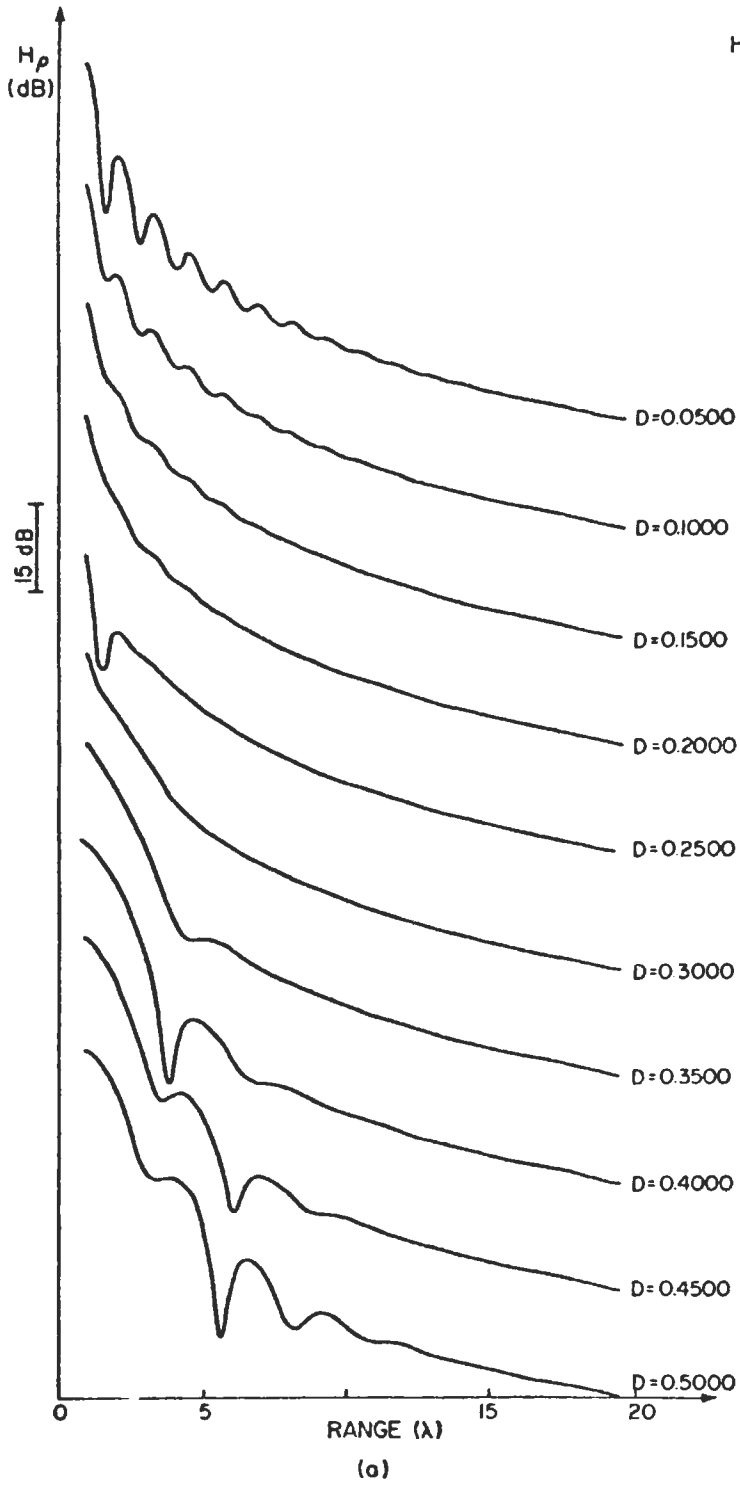
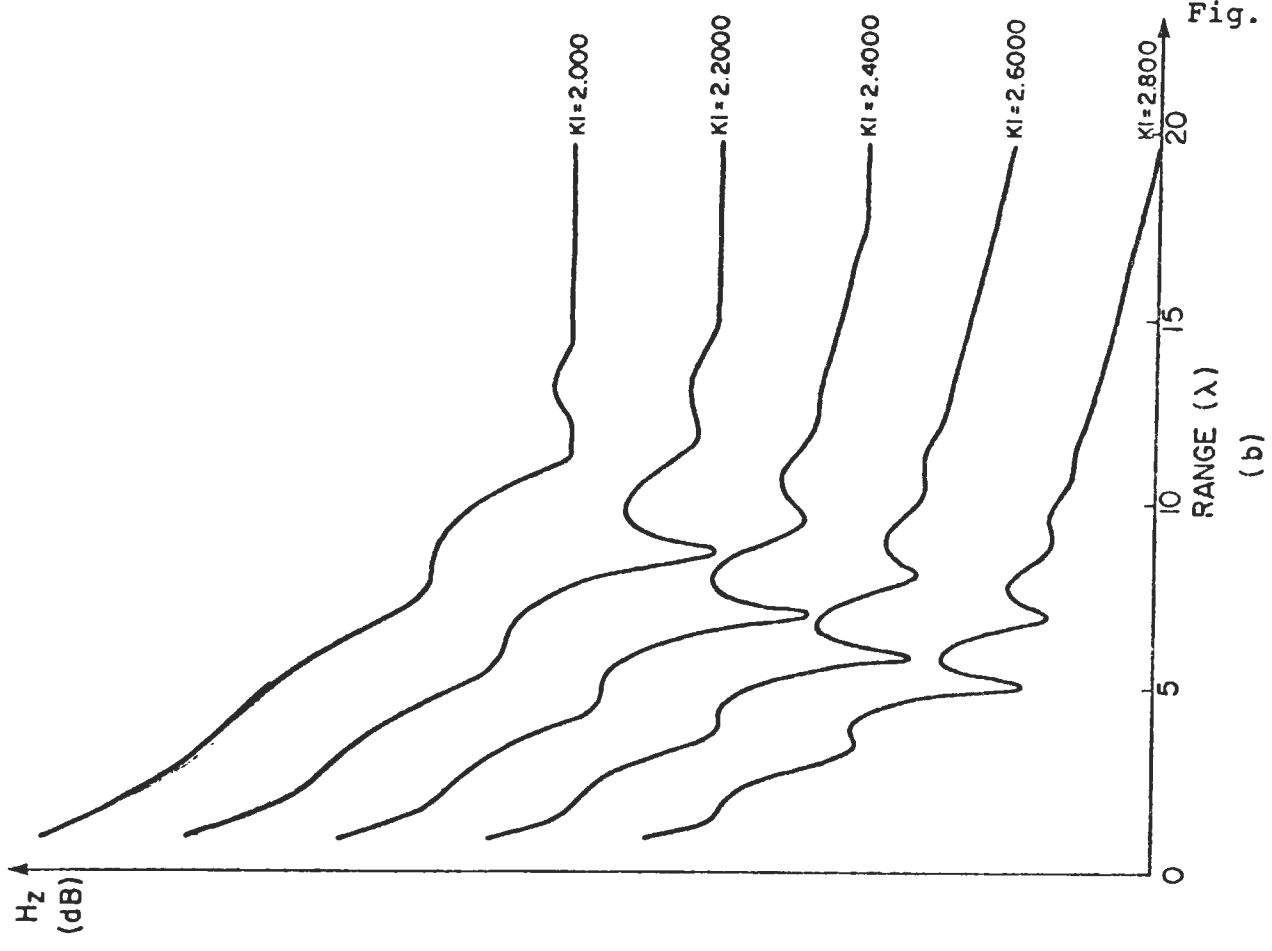
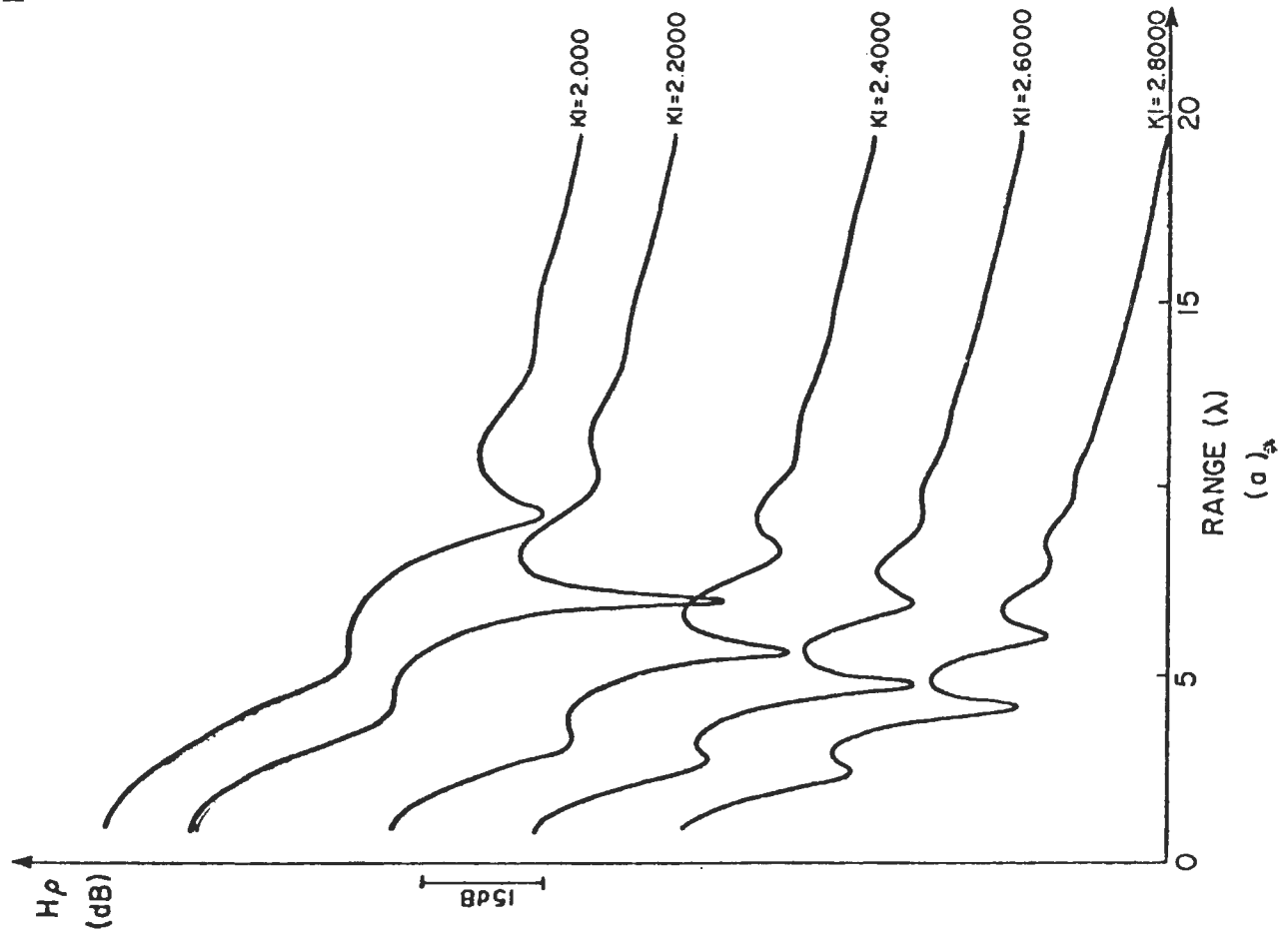


Fig. 3

DEPTH : VARYING
 LT1:0.0200 LT2:0.0500
 KI:2.400 K2:3.300



DEPTH : 0.500 λ
LT1 : 0.0200 LT2 : 0.0500
K1 : VARYING K2 : 3.300



DEPTH: 0.500 λ
LTI: VARYING LT2: 0.0500
KI: 2.400 K2: 3.300

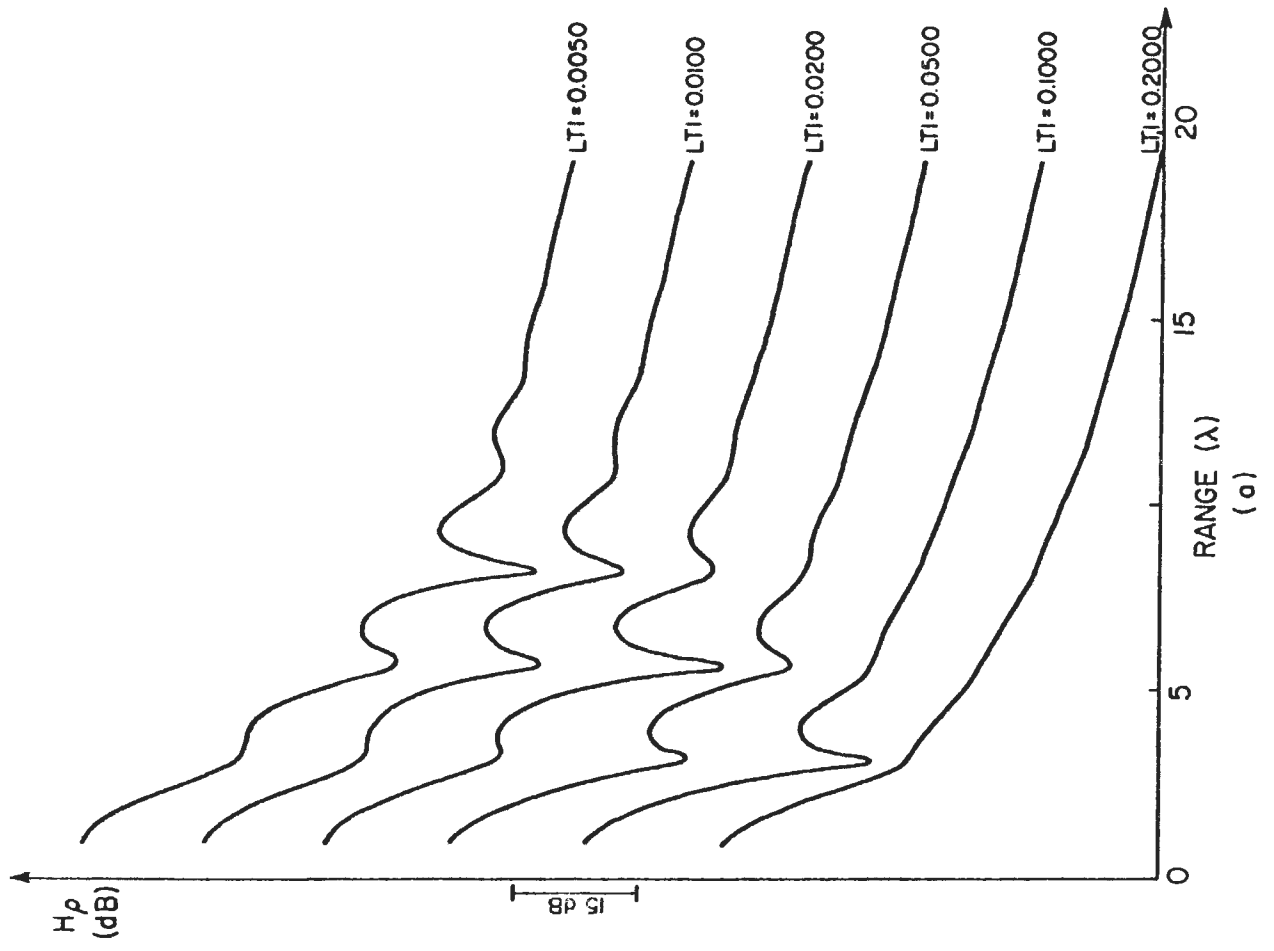
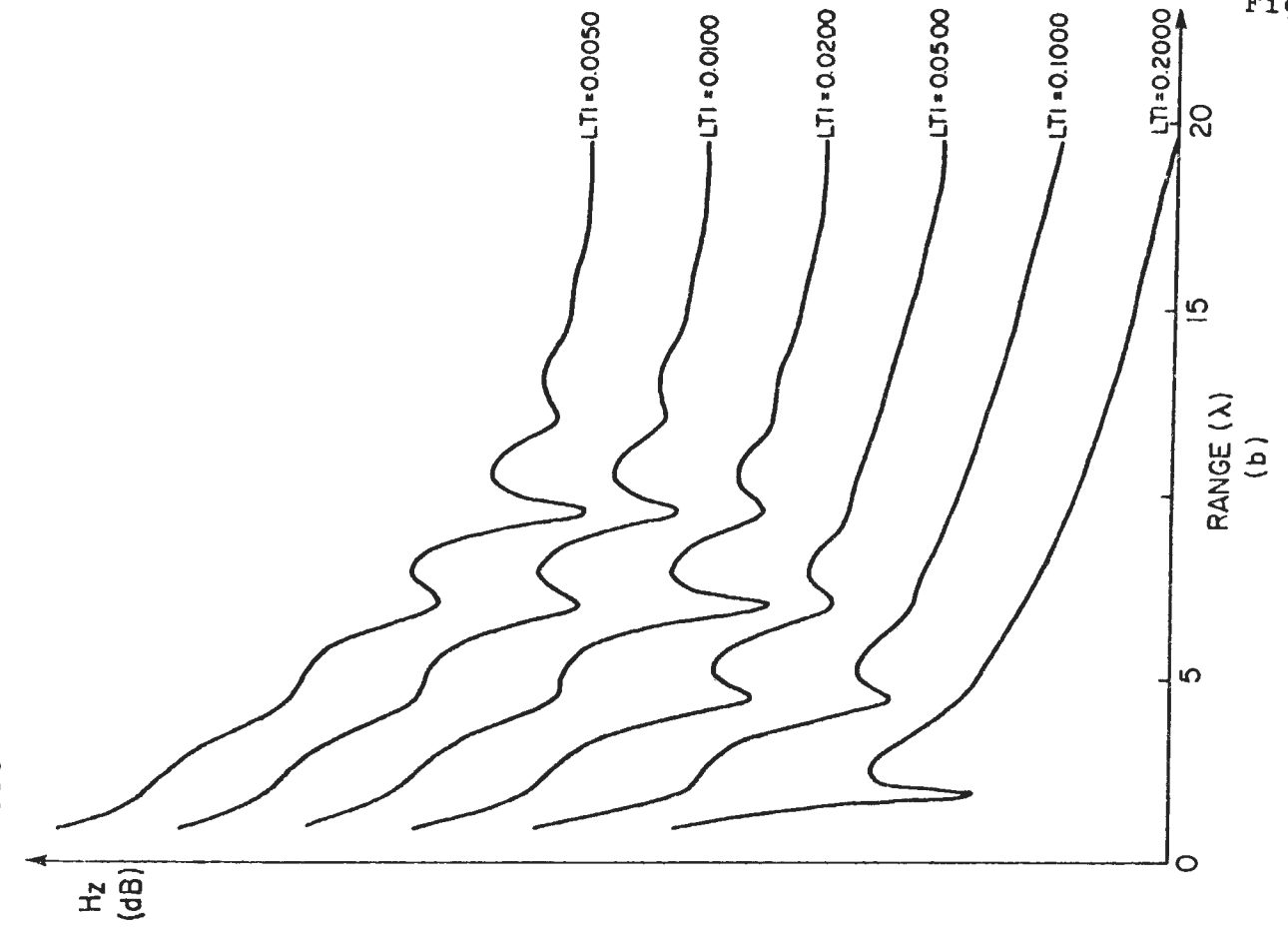


Fig. 6

Fig. 7a

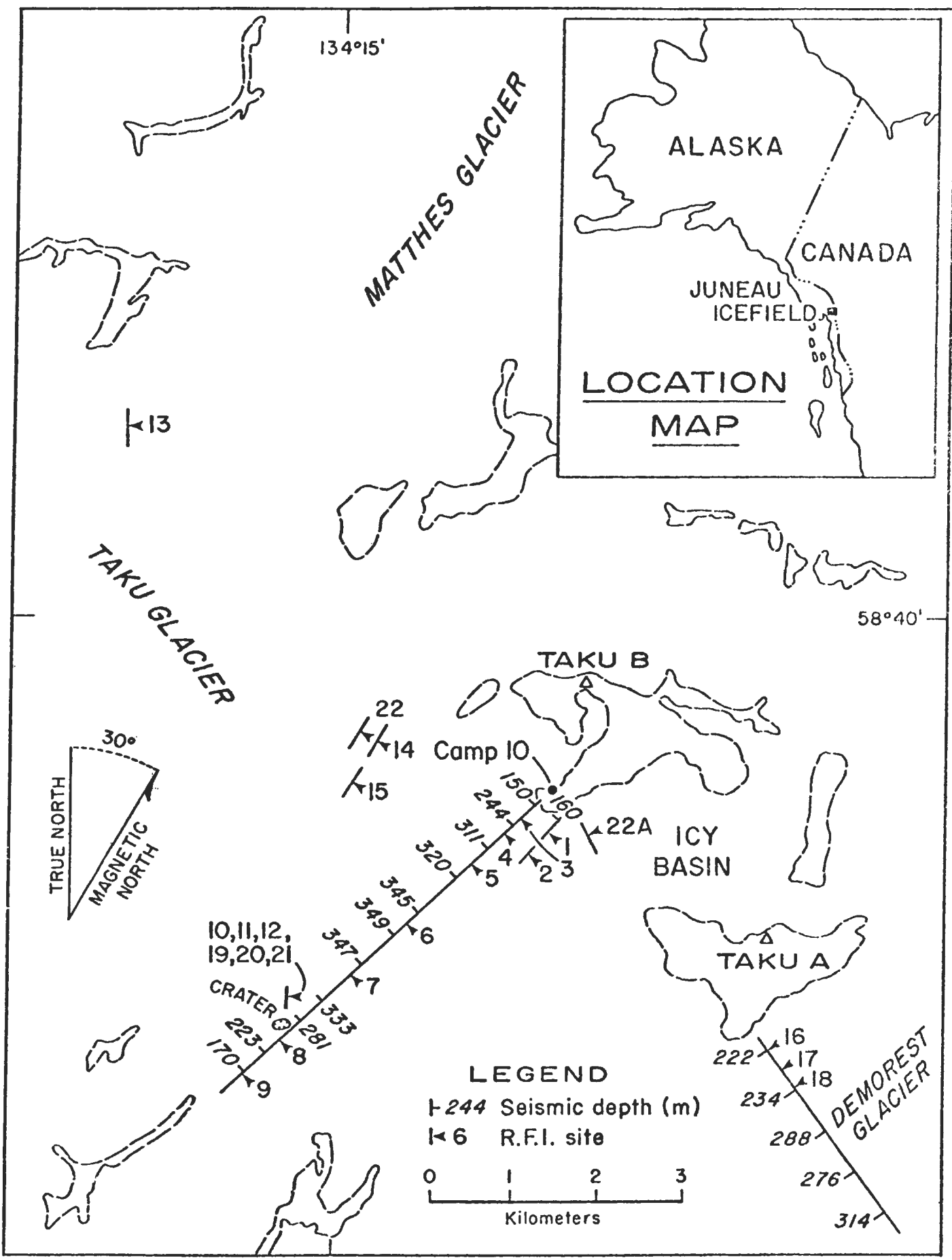
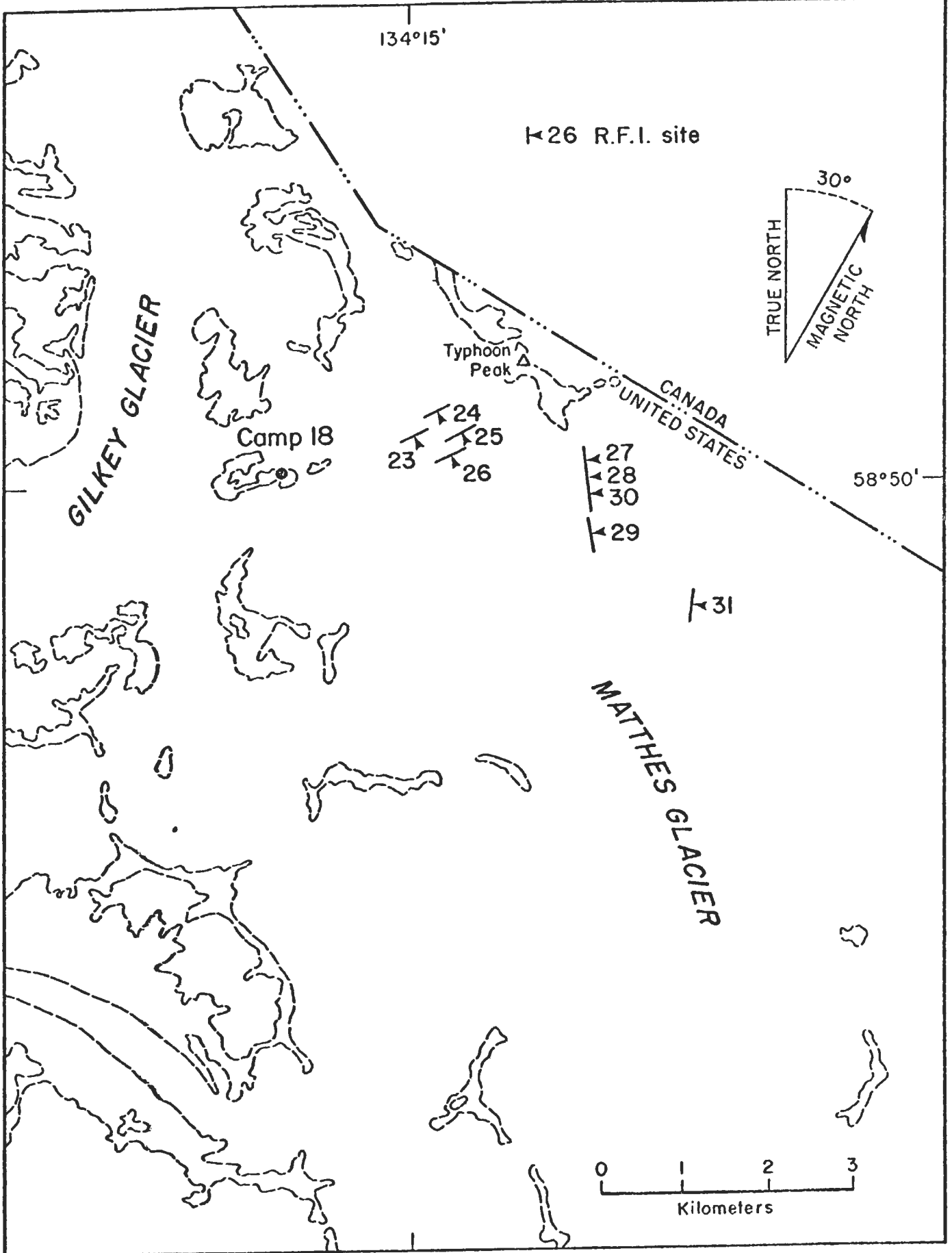


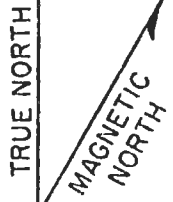
Fig. 7b



134°15'

←26 R.F.I. site

30°



GILKEY GLACIER

Typhoon Peak

Camp 18

- ←24
- ←25
- ←26
- ←27
- ←28
- ←29
- ←30

CANADA
UNITED STATES

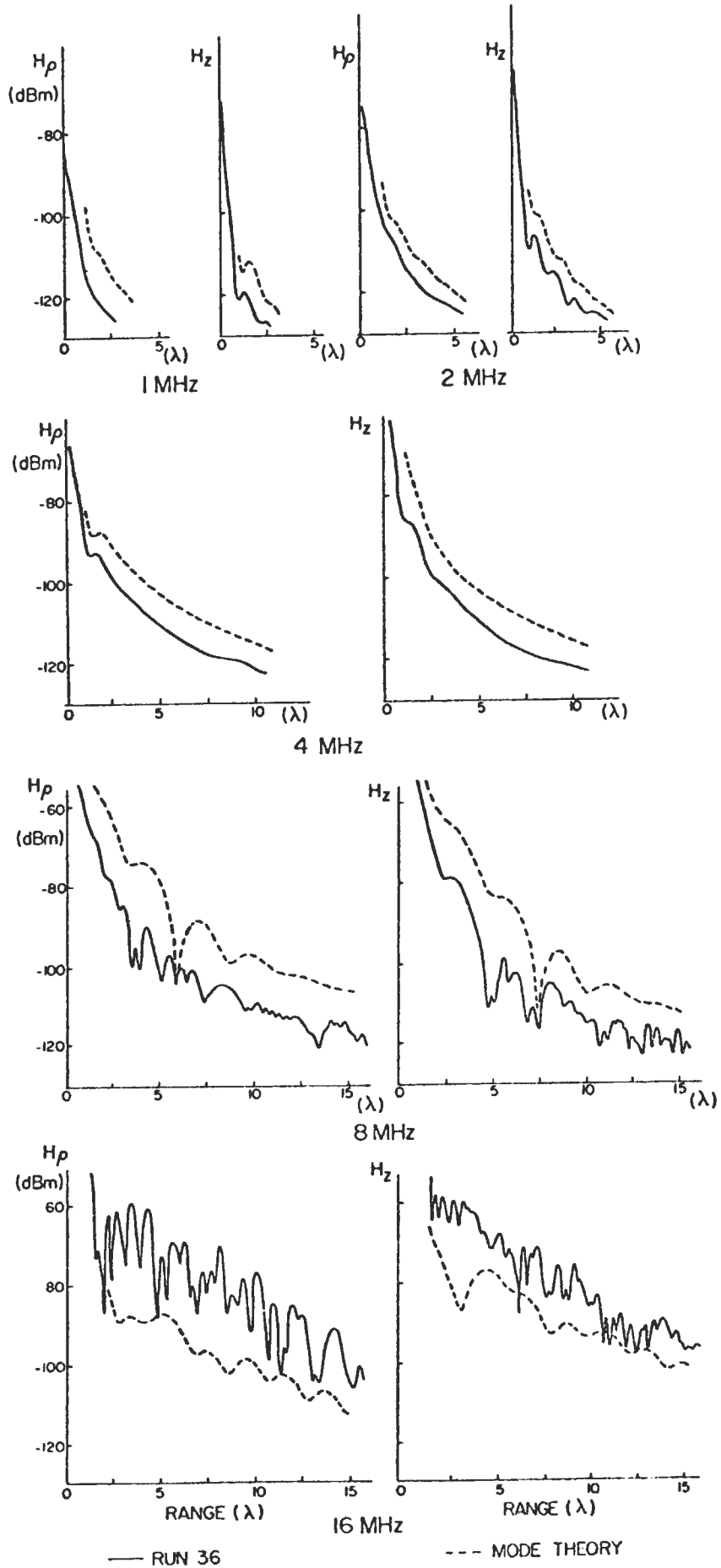
58°50'

←31

MATTHES GLACIER



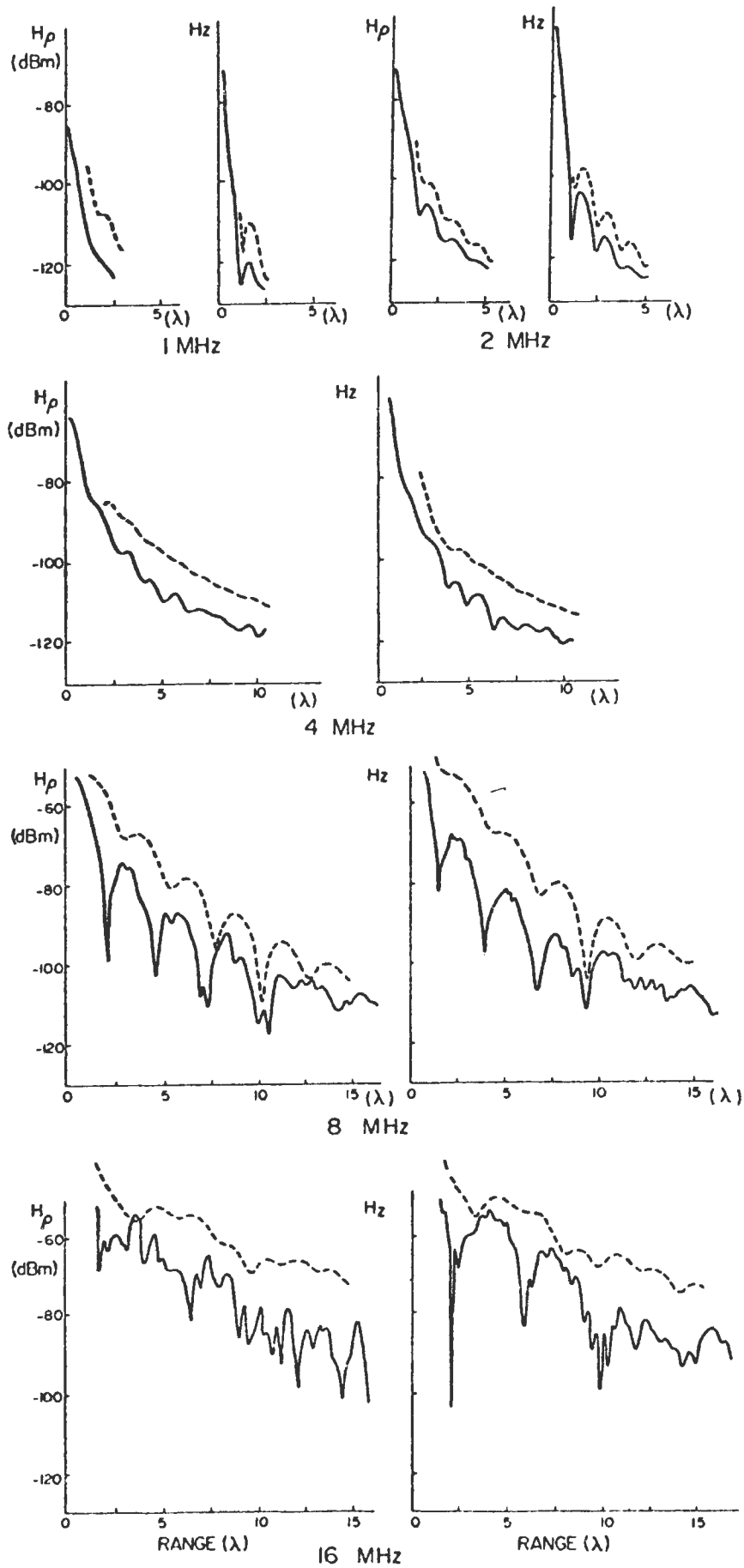
JUNEAU ICEFIELD - RUN 36



— RUN 36

--- MODE THEORY

JUNEAU ICEFIELD - RUN 92



— RUN 92

--- MODE THEORY

C-7

February 18, 1974

ELECTRICAL STRUCTURE AT TAURUS-LITTROW

by

D.W. STRANGWAY,^{1,2} A.P. ANNAN,³ J.D. REDMAN,²
J.R. ROSSITER,³ and R.D. WATTS⁴

- 1 NASA-JSC, Houston, Texas 77058; Currently at 2.
- 2 Dept. of Geology, University of Toronto, Toronto, Canada, M5S 1A1.
- 3 Dept. of Physics, University of Toronto, Toronto, Canada, M5S 1A7.
- 4 Lunar Science Institute, Houston, Texas, 77058; Currently at U.S.G.S., Denver, Colorado.

Introduction

The Surface Electrical Properties (SEP) Experiment was flown to the Taurus-Littrow region of the moon on Apollo 17. The experiment used megahertz radio frequencies in order to determine (i) electrical layering at the landing site, (ii) the dielectric properties of the surface material in situ, and (iii) the presence of scattering bodies.

In order to sound into the surface layers a relatively new technique, called radio interferometry, was employed. A transmitter was set out on the lunar surface and a receiver was carried on the Lunar Roving Vehicle. As the Rover moved along its traverse, the received magnetic field strength and the Rover's position with respect to the transmitter were recorded.

At any point on the traverse several waves reach the receiver, and these waves interfere, as shown in Figure 1. A plot of field strength as a function of transmitter-receiver separation therefore gives an interference pattern that is diagnostic both of the physical properties and of the structure of the upper layers. Field strength data for six frequencies and six combinations of receiving and transmitting antenna orientation, along with position, calibration, and temperature information, were recorded on

a magnetic tape which was returned to earth.

The basis for the interferometry concept and details of the SEP Experiment have been given elsewhere (Annan, 1973; Rossiter et al., 1973; Simmons et al., 1972; The SEP Team, 1974). In the present paper we will outline briefly the basis for our interpretation, present the lunar SEP data, and describe our most recent evaluation of the results.

Background Material

Because radio interferometry is a relatively new technique, most of our background experience with it was built up explicitly for the lunar experiment. This study had three main facets: (i) theoretical evaluation of the EM fields surrounding a dipole over a dielectric; (ii) experimental work using an analogue scale model; and, (iii) field trips to different glacier sites for full scale experiments in a real environment.

Although the integral expressions for the EM fields surrounding a dipole over a layered earth have been known for some time (e.g. Baños, 1966), their evaluation for low-loss layers is far from trivial. Straight numerical integration is prohibitively expensive. Therefore two complementary approximate methods were used - a geometric

optics approach and the theory of normal modes (Annan, 1970, 1973; Kong, 1972; Tsang et al., 1973). The former is most accurate for thick layers, and becomes invalid for distances less than about a wavelength. The latter is most easily calculated for thin layers in which only a few modes propagate.

In order to check these calculations, and to be able to study cases too complex for theoretical treatment, a scale model was constructed using microwave frequencies (Waller, 1973; Annan et al., 1974). The model used a layer of dielectric oil in which a reflecting plate could be set up in many different orientations. A typical suite of model curves for the layered case of a dielectric over a perfect reflector is shown in Figure 2, along with the corresponding theoretical curves. The inaccuracy of the geometric optics solution for thin layers is readily apparent.

Field experience with the interferometry technique was gained on trips to the Gorner and Athabasca Glaciers (Rossiter et al., 1973; Strangway et al., 1974), and to the Juneau Icefields (Rossiter et al., 1974), using prototype lunar hardware at various stages of development. Since most of the glacial sites were known, from independent work, to be close to a plane layered situation, we were

faced with the problem of finding the set (or sets) of parameters that best characterized the data collected. This was done by trial-and-error comparison of suites of theoretical curves with field data (although attempts at formal inversion are currently underway by Watts (1974)).

A typical set of field profiles and their corresponding "best-fit" theoretical curves is shown in Figure 3. Although no single frequency or component was uniquely indicative of the parameters (dielectric constant, loss tangent, and depth to reflector), by accepting only parameter sets that gave consistent, good fits for all frequencies, and for both of the maximum-coupled components for which we have theoretical solutions, an acceptable interpretation was always found.

SEP Operational History

The SEP experiment was carried out at the Taurus-Littrow landing site during EVA-II and III. The transmitting dipole antennas were deployed by the astronaut about 150 meters east of the Lunar Module in a north-south and in an east-west direction (see Figure 4). During EVA-II SEP data was recorded as the Rover moved in a westerly direction away from the SEP transmitter out to station #2. The traverse as reconstructed from the SEP-LRV navigation data is given in Figure 5.

From the SEP transmitter out to a range of 1.7 km the receiver operated normally. Between the range of 1.7 km and 4.3 km the receiver operated in an acquisition mode, attempting to acquire a synchronization signal from the transmitter. In this mode only partial data is collected. At a range of 4.3 km, because of the low received field strength, the receiver obtained a false resynchronizing pulse, causing an incorrect realignment of the receiver and transmitter timing, and a subsequent loss of field strength data from that point. At station #2 the receiver was turned off to aid in cooling. The receiver was operating again between stations #4 and #5; however, the signal levels were too low to allow a resynchronization with the transmitter. At the beginning of the station #5 stop the receiver was turned off, and, although the receiver was turned on again at the end of the station stop, because the internal receiver temperature was above a safe limit a thermal switch prevented it from operating for the remainder of EVA-II.

Data was to have been recorded during EVA-III from the SEP transmitter to station #6 but the astronauts failed to turn on the receiver. Therefore, the data which are used as a basis for this discussion are those taken from the SEP transmitter west to a range of 4.3 km.

SEP Data and Discussion

The configuration of the SEP transmitting and receiving antennas is shown in Figure 6. The six frequencies, 1, 2, 4, 8, 16 and 32 MHz, are transmitted sequentially by two orthogonal horizontal dipole antennas and received by three orthogonal loop antennas, resulting in 36 readings of the field strength during each measurement cycle.

Positional information from the Rover navigation system is recorded as increments and decrements of 1° in bearing, and 100 m in range, and as odometer pulses, each equivalent to a .49 meter change in position for the right-front and left-rear wheels of the Rover.

The Rover traverse derived from SEP data has been compared in Table 1 with traverse data produced by the U.S.G.S. (ALGIT, 1974) and with the traverse reconstruction created from the Goddard Very Long Baseline Interferometry Data (I. Salzberg, personal communication, January 1974). The VLBI data has absolute accuracy of approximately 40 m. The U.S.G.S. traverse is taken from photographic pans made at station stops, and are accurate to approximately 10 m for EP-4, LRV-1, and station 2, and to about 50 m for LRV-2 and 3.

The three traverses are plotted in Figure 7. The

maximum differences are about 500 m at stops LRV-2 and 3. The differences between USGS and VLBI traverses are larger than expected, and later data might be in better agreement. For the first 2 km, all three reconstructions are in good agreement.

TABLE 1. COMPARISON OF EVA-II TRAVERSE STOPS FROM USGS, VLBI AND SEP-LRV NAVIGATION DATA (See Figure 7).

STATION	RANGE (Km)			BEARING		
	VLBI	USGS	SEP-LRV NAV DATA	VLBI	USGS	SEP-LRV NAV DATA
EP-4	.500	.538	.508	80.4	80	83
LRV-1	2.603	2.603	2.645	80.9	78	82
LRV-2	3.750	3.729	3.811	81.4	86	83
LRV-3	4.248	4.253	4.325	80.2	87	82
HOLE IN THE WALL	5.638		5.683	79.5		81
STN. #2		7.46	7.6		68	71

A set of SEP field strength data is shown in Figure 8. Each plot contains either the endfire or the broadside components for one frequency, plotted as a function of range, in free-space wavelengths. The data are plotted to either 1.7 km or to 20 wavelengths.

For each frequency, six components are measured. Three components H_ϕ -endfire, and H_ρ and H_z broadside are maximum-coupled for a plane layered geometry, while the other three are minimum-coupled to the transmitted signal. For all six frequencies the maximum-coupled components have an average level from 5 to 15 dB greater than the minimum-coupled components. These results are in direct contrast to our glacial studies. In all our glacier runs the max and min components were approximately equal in level at 16 and 32 MHz (Strangway, et al., 1974). We attributed this to random scatterers (e.g. crevasses) in the ice of the order of a wavelength in size. We therefore conclude that there are few scattering bodies near the lunar SEP site with typical sizes of from 10 to 300 m. Scattering experiments both in the scale model and on glaciers support this conclusion.

Further confirmation is obtained, by an examination of the H_ϕ -endfire component. This component has a near-surface wave so large that it effectively masks any interference. However, if near-surface scattering is important, this component becomes erratic. As can be seen from Figure 8, this component is relatively smooth at all SEP frequencies. The residual peaks and nulls correlate well with those in the H_ρ -broadside component. Therefore we feel that these two components are slightly mixed because the traverse was not completely east-west (i.e. not directly off the end of the endfire antenna).

The other two maximum-coupled components (H_{ρ} and H_z broadside) have been the most important for interpretation (see Figure 9). At 16 and 32 MHz the number of peaks and troughs per free space wavelength of range is fairly low, indicating a dielectric constant of about 2 to 5. However, the lower frequencies show somewhat higher beating rates, indicating a dielectric constant of about 6 to 8, and certainly less than 9 or 10. These observations imply that the dielectric constant of the near-surface material is lower than that of deeper material. These results are consistent with the dielectric properties of a soil layer over solid rock, as measured on returned samples (e.g. Olhoeft et al., 1973).

The loss tangent is estimated from the sharpness of the peaks and nulls in the two major components. This analysis indicates that the average loss tangent of the surface layers to a depth of several hundred meters is less than about 0.05. The fact that the higher frequencies have strong signal levels for many tens of wavelengths from the transmitter, while the lower frequencies die out relatively quickly, indicates that the near surface material may have losses in the order of 0.01 or less. These low loss values confirm that there is no moisture in any form in the upper layers of the moon.

Structure is more difficult to determine unambiguously. By comparing the two major components to suites of theoretical curves for a plane two-layer geometry (i.e. dielectric layer over a dielectric half-space), no single set of parameters has been found that gives theoretical curves in good agreement with the data at all frequencies. Several perturbations from the two-layer model have therefore been suggested.

One possible variation is sketched in Figure 10(a), showing a thinning layer of soil over rock. The inferred parameters are a layer 20 m thick near the SEP site, with dielectric constant of about 3 or 4, thinning to 15 m thick a few hundred meters to the west. The lower material would have a dielectric constant of about 6 or 7. Results from the Lunar Seismic Profiling Experiment, conducted over the same region, show good agreement with this model (Watkins and Kovach, 1973). The basis for this interpretation is the curve for 2 MHz broadside (Figure 9(b)), which shows little interference out to about 4 wavelengths range, but then has several dramatic peaks. This behaviour suggests that the layer is just thick enough near the transmitter that little energy is transmitted either through the layer or through the subsurface. However, further from the transmitter the layer becomes so thin that it is essentially transparent. Although we have no rigorous proof that this

happens for sloping interfaces, we have seen similar behaviour for plane layers of different thicknesses.

Table 2 lists the parameters of a three-layer model, sketched in Figure 10(b). This model assumes, (i) that layer 1 is so thin that it is essentially transparent to all frequencies but 16 and 32 MHz; and, (ii) that the boundary between layers 2 and 3 is too deep to have much effect on 16 and 32 MHz. Theoretical curves for this model are shown for comparison to the data in Figure 9. Although the major features of the data are also in the theoretical curves, the details are not always in good agreement. This may be due to slight adjustments in loss tangent (the particular features in most curves are very dependent on the loss tangent), or due to slight dipping of the interfaces (as mentioned above). However, this model has provided the best fit to all the data.

TABLE 2. PARAMETERS FOR BEST-FIT 3-LAYER MODEL

(See Figures 9 and 10(b)).

	<u>Depth (m)</u>	<u>Dielectric constant</u>	<u>Loss tangent</u>
Layer 1	7 \pm 1	3.8 \pm 0.2	0.008 \pm 0.004
Layer 2	100 \pm 10	7.5 \pm 0.5	0.035 \pm 0.025
Layer 3	∞	9 ?	?

A third model which has been suggested (SEP Team, 1974) is that the dielectric constant increases gradationally with depth. This model is not at all supported by the LSPE seismic data (Watkins and Kovach, 1973); however, this type of phenomenon may be important, especially near the surface.

Conclusions

Although it is not yet possible to definitively outline the Taurus-Littrow structure from SEP data, the following conclusions can be made:

- (1) The low loss tangents required for interference indicate (less than 0.05) indicate that water in any form is not present in the Taurus-Littrow area to a depth of at least several hundred meters.
- (2) Scattering is not important at any of the SEP frequencies. This implies that there are not large numbers of scattering bodies with typical sizes from 10 to 300 meters in the area.
- (3) The dielectric constant is about 2 - 5 near the surface, becoming 6 - 9 at depth. This is consistent with soil overlying rock.
- (4) No plane two-layer theoretical model has been able to fit the data accurately. A thinning layer, a three-layer model or grading dielectric properties may explain the data better.

(5) The Rover navigation data recorded on EVA II to Station 2 is in good agreement with VLBI and USGS traverse reconstructions.

Acknowledgements

This work was carried out under a sub-contract to the Dept. of Physics, University of Toronto from MIT, under NASA Contract No. NA5 9-11540.

We thank Mssrs. J. Proctor and J. Rylaarsdam for computational and data processing assistance. Mr. G. Wagner designed and built the data reduction systems. Much of the data reduction was carried out at the Johnson Space Center and at the Lunar Science Institute, Houston, Texas.

References

- Annan, A.P., "Radio Interferometry Depth Sounding", M.Sc. thesis, Dept. of Physics, U. of Toronto, 1970.
- Annan, A.P., "Radio Interferometry Depth Sounding"; Part I - Theoretical Discussion", Geophysics, v. 38, pp. 557-580, 1973.
- Annan, A.P., Waller, W.M., Strangway, D.W., Rossiter, J.R., and Redman, J.D., "The Electromagnetic Response of a Two-Layer Dielectric Earth Excited by a Horizontal Electric Dipole", submitted to Geophysics, 1974.
- Apollo Lunar Geology Investigation Team, (U.S.G.S.), "Preliminary Geological Analysis of the Apollo 17 Site", Apollo 17 Preliminary Science Report, in press, 1974.

- Baños, A., "Dipole Radiation in the Presence of a Conducting Half-space", Pergamon Press, New York, 1966.
- Kong, J.A., "Electromagnetic Fields due to Dipole Antennas over Stratified Anisotropic Media", Geophysics, v. 37, pp. 985-996, 1972.
- Olhoeft, G.R., Strangway, D.W., and Frisillo, A.L., "Lunar Sample Electrical Properties", Proc. Fourth Lunar Sci. Conf., (Suppl. 4, Geochim. Cosmochim. Acta), v. 3, pp. 3133-3149, 1973.
- Rossiter, J.R., LaTorraca, G.A., Annan, A.P., Strangway, D.W., and Simmons, G., "Radio Interferometry Depth Sounding; Part II - Experimental Results", Geophysics, v. 38, pp. 581-599, 1973.
- Rossiter, J.R., Strangway, D.W., Annan, A.P., Watts, R.D., and Redman, J.D., "Detection of Thin Layers by Radio Interferometry", submitted to Geophysics, 1974.
- Simmons, G., Strangway, D.W., Bannister, L., Baker, R., Cubley, D., LaTorraca, G., and Watts, R., "The Surface Electrical Properties Experiment", in Kopal, Z. and Strangway, D., eds., Lunar Geophysics, Proceedings of a Conference at the Lunar Science Institute, Houston, Texas, 18-21 October, 1971, D. Reidel, Dordrecht, pp. 258-271, 1972.
- Strangway, D.W., Simmons, Gene, LaTorraca, G., Watts, R., Bannister, L., Baker, R., Redman, D., and Rossiter, J., "Radio-Frequency Interferometry - A New Technique for studying Glaciers", J. Glaciology, in press, 1974.

Figure Captions

Fig. 1. The three main waves used in radio interferometry. The surface wave travels above the surface of the dielectric and the subsurface wave travels just below it. Because these two waves travel at different velocities, their beat frequency is a function of the dielectric constant. Any reflected waves from a subsurface horizon also influence the interference pattern (after Strangway, et al., 1974).

Fig. 2. Theoretical solutions and scale model data for a dielectric over a perfect reflector. The inaccuracy of the geometric optics approach for thin layers is readily apparent. This type of comparison confirms that the theoretical solutions are correct (after Annan, et al., 1974).

Fig. 3. Interpretation of radio interferometry data from the Athabasca Glacier by comparison to theoretical curves. Although any single component may have many good matches to theory, by demanding good fits for all frequencies and both maximum coupled components, a unique interpretation could be made (after Strangway, et al., 1974).

Fig. 4. Map of the Taurus-Littrow site, showing the Apollo 17 Lunar Roving Vehicle traverses (marked I, II, and III), the major station stops, the SEP transmitter site, and the locations of the EP-4 deployment. SEP data were collected

along the first portion of traverse II (from NASA Apollo 17 traverse planning documents).

Fig. 5. Sketch of the EVA-II traverse recovered from LRV navigation data, from the SEP site to Station 2. The Rover stops are indicated.

Fig. 6. Orientation of the SEP antennas. Three orthogonal magnetic field components are measured from a transmitting antenna approximately broadside to the traverse, and three from an antenna endfire to the traverse. The two transmitting antennas were laid out on the surface in the form of a cross and activated alternately (after Strangway, et al., 1974).

Fig. 7a,b,c. EVA-II traverse reconstruction as compiled from (i) LRV navigation data recorded by SEP; (ii) Goddard Very Long Baseline Interferometry; and (iii) U.S.G.S. traverse reconstruction from photographic information. The three independent reconstructions are in good agreement out to 2 or 3 km, although they disagree more than expected near LRV-2 and 3 (see Table 1).

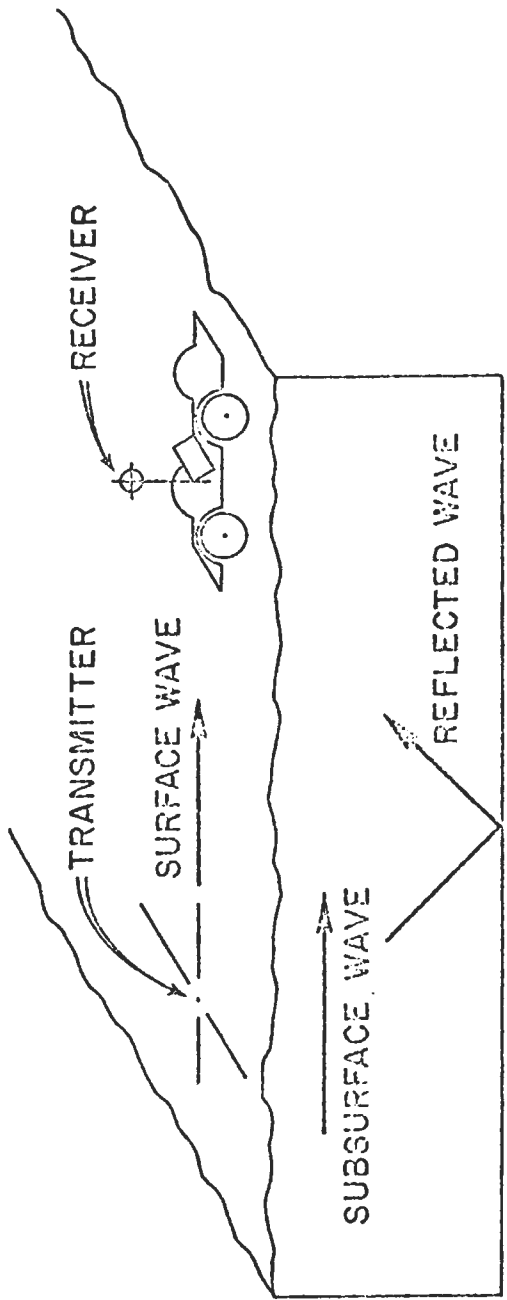
Fig. 8 (a-1). The surface Electrical Properties Experiment data for all 36 components. Each component has been plotted as a function of free space wavelength, out to 1.7 km or

20 wavelengths (whichever is smaller). The vertical scale is in dB, with a reference at -90 dBm, as shown. The component is labelled at the end of the curve; H_{θ} endfire, H_{ρ} and H_z broadside are maximum coupled; the others, minimum coupled. The position of the EP-4 deployment is indicated. Since a 360° turn was made at that point, the values during the turn have been removed. Note that since a standard x-y plot format has been used, west is to the right in these plots.

Fig. 9 (a-f). The two components used for interpretation - H_{ρ} and H_z broadside (solid lines). The theoretical curves for the parameters given in Table 2 and Figure 10(b) are also shown (dashed lines).

Fig. 10. Two possible deviations from a two-layer model: (a) a thinning layer that de-couples the subsurface near the SEP site, but is transparent further west; (b) a three-layer model (Table 2).

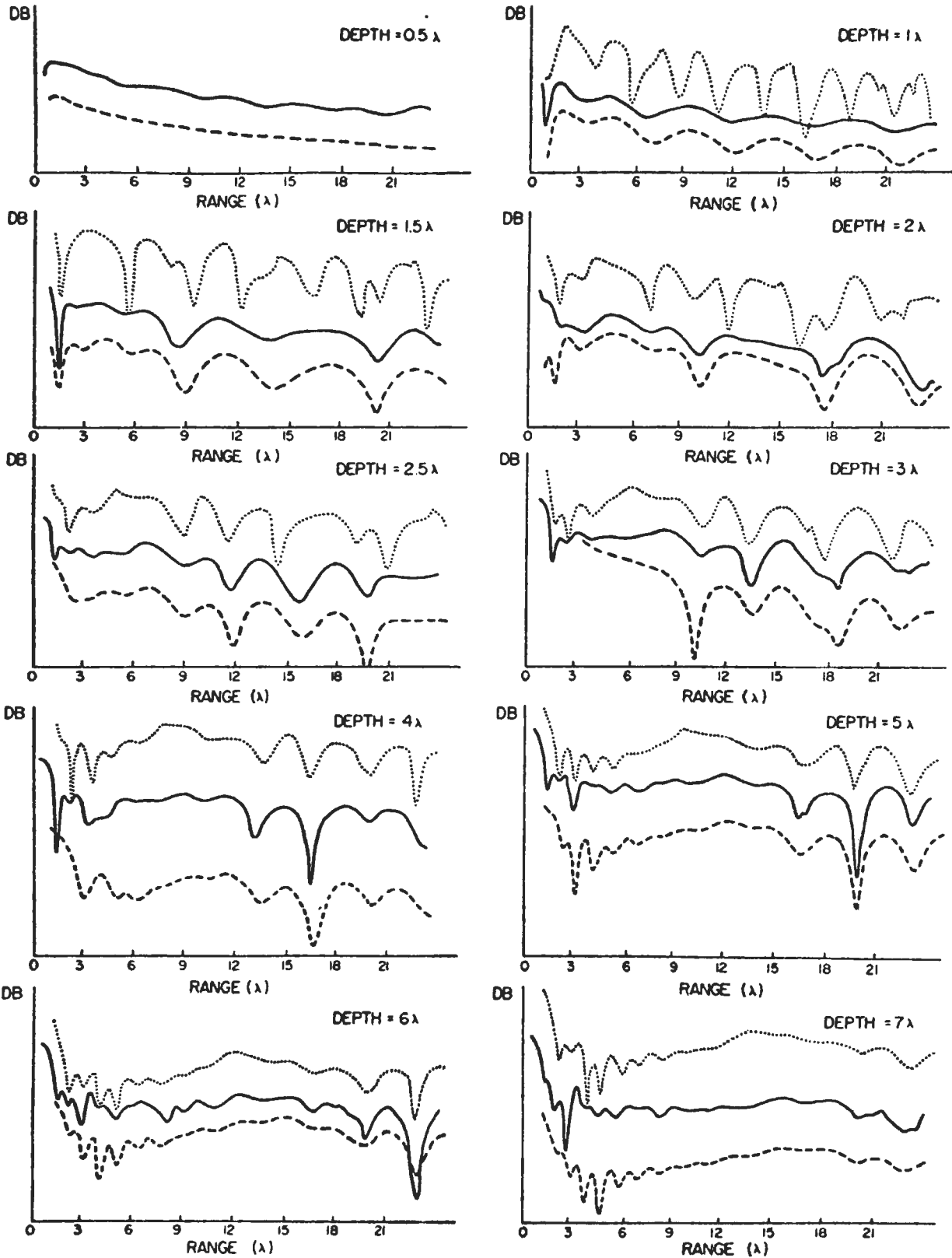
Fig 1.



1(a)

THEORETICAL SOLUTIONS AND SCALE - MODEL RESULTS
 PLANE LAYERED GEOMETRY, VARIOUS DEPTHS TO REFLECTOR

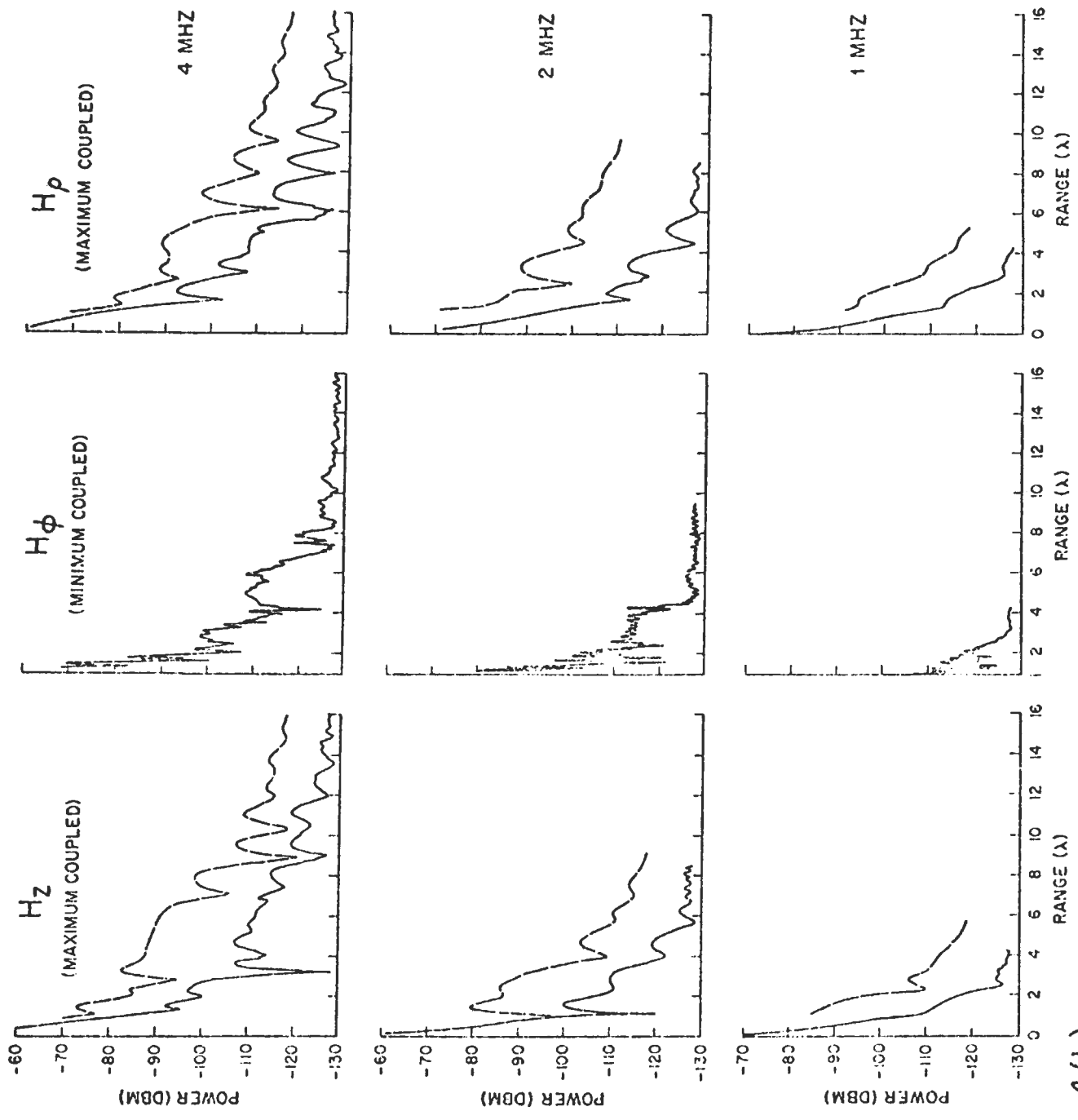
Fig 2.



SCALE - MODEL ———
 THEORETICAL ·····
 GEOMETRICAL OPTICS - - - -
 NORMAL MODES - · - · -

$k = 2.16$
 $\tan \delta = 0.0022$

Fig 4(b)



4(b)

Fig 4

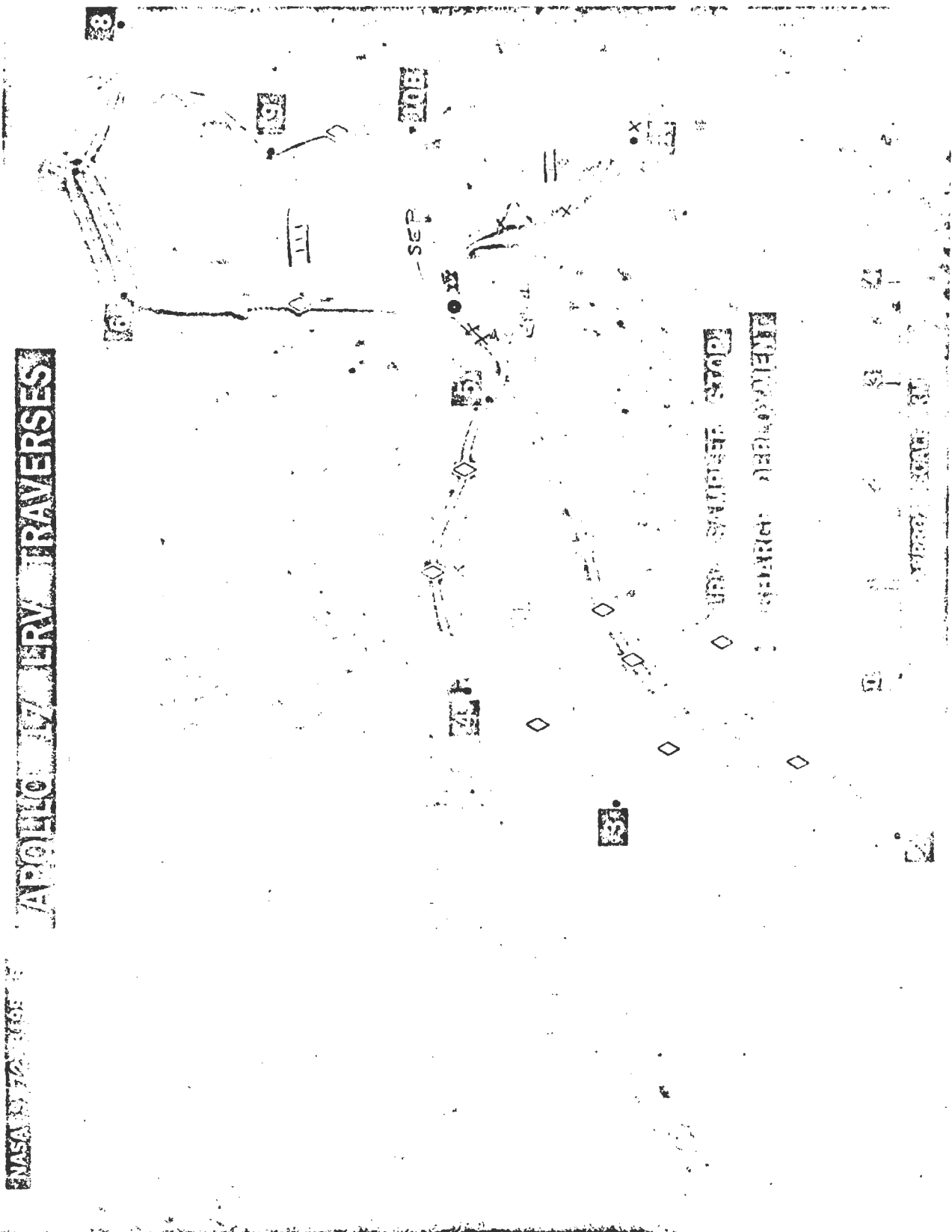


Fig. 17B - Pictorial view of the LRV traverses

FIG #5

FIG. #3 EVA-II TRAVERSE RECONSTRUCTION FROM SEP-LRV NAVIGATION DATA

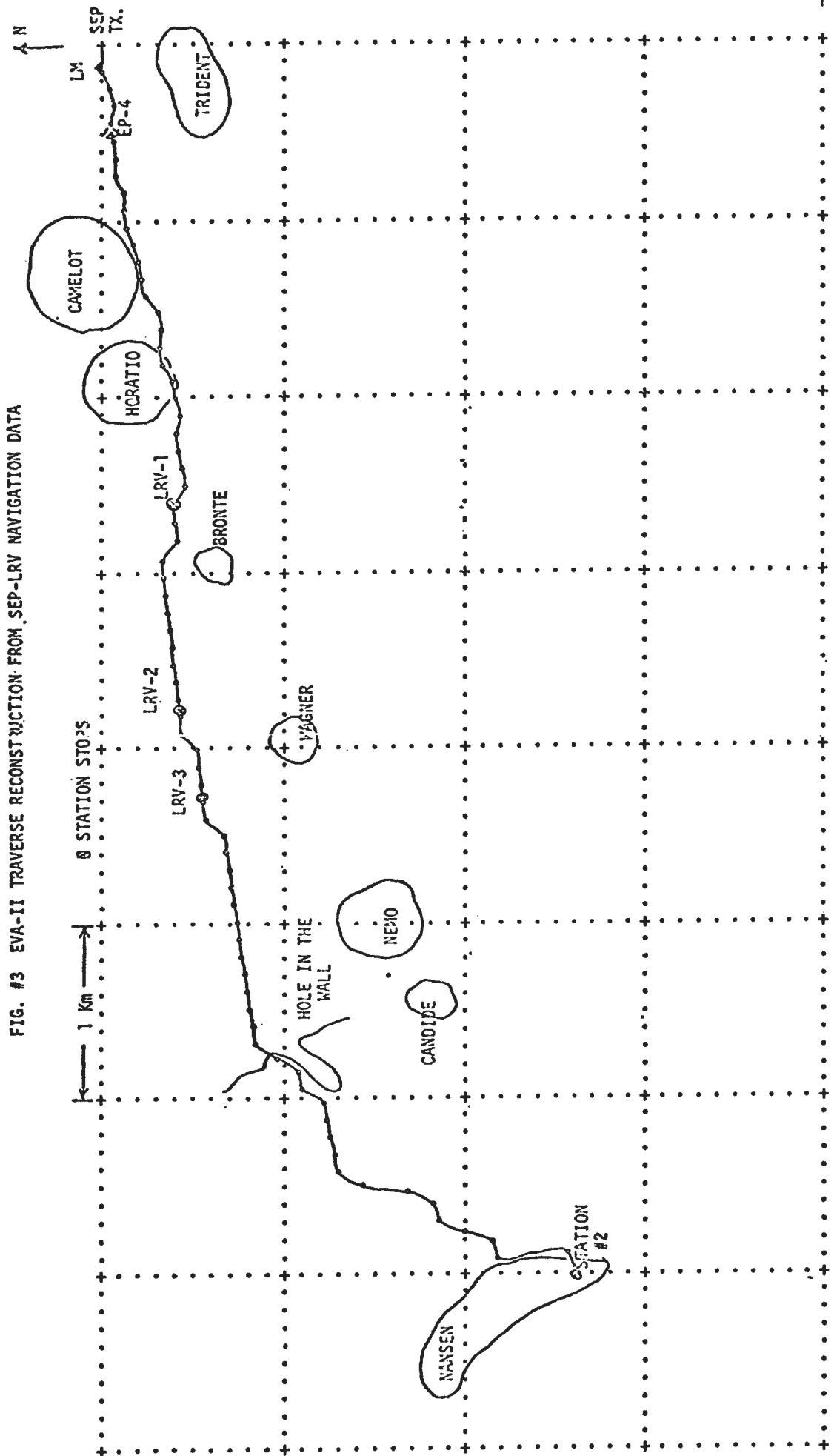
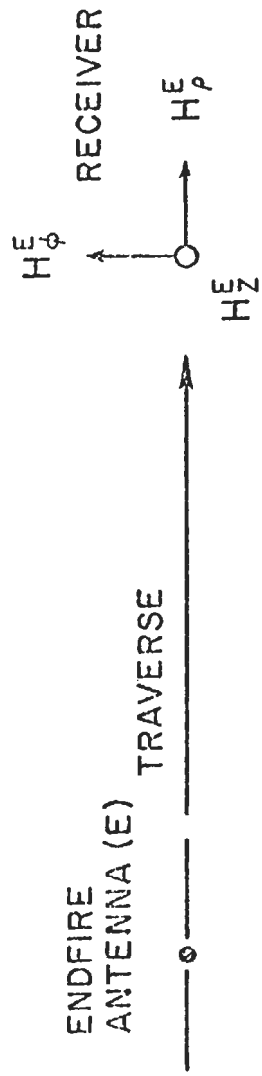
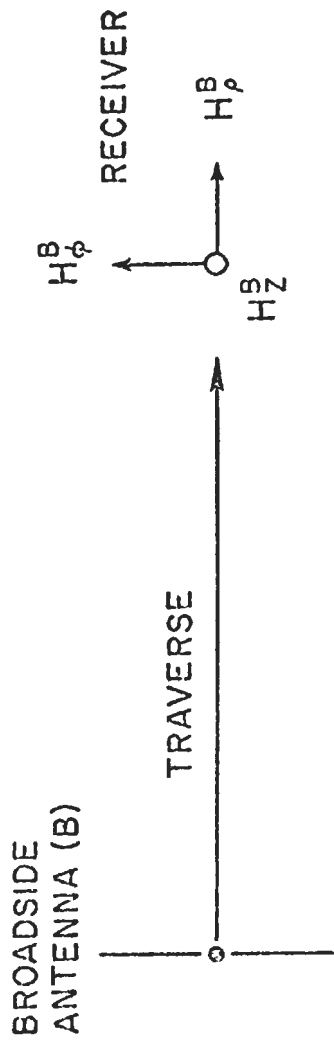


Fig. #3



†(b)

FIG. #4(a) COMPARISON OF EVA-II TRAVERSE RECONSTRUCTION FROM SEP-LRV NAVIGATION DATA WITH VLBI AND USGS TRAVERSE DATA

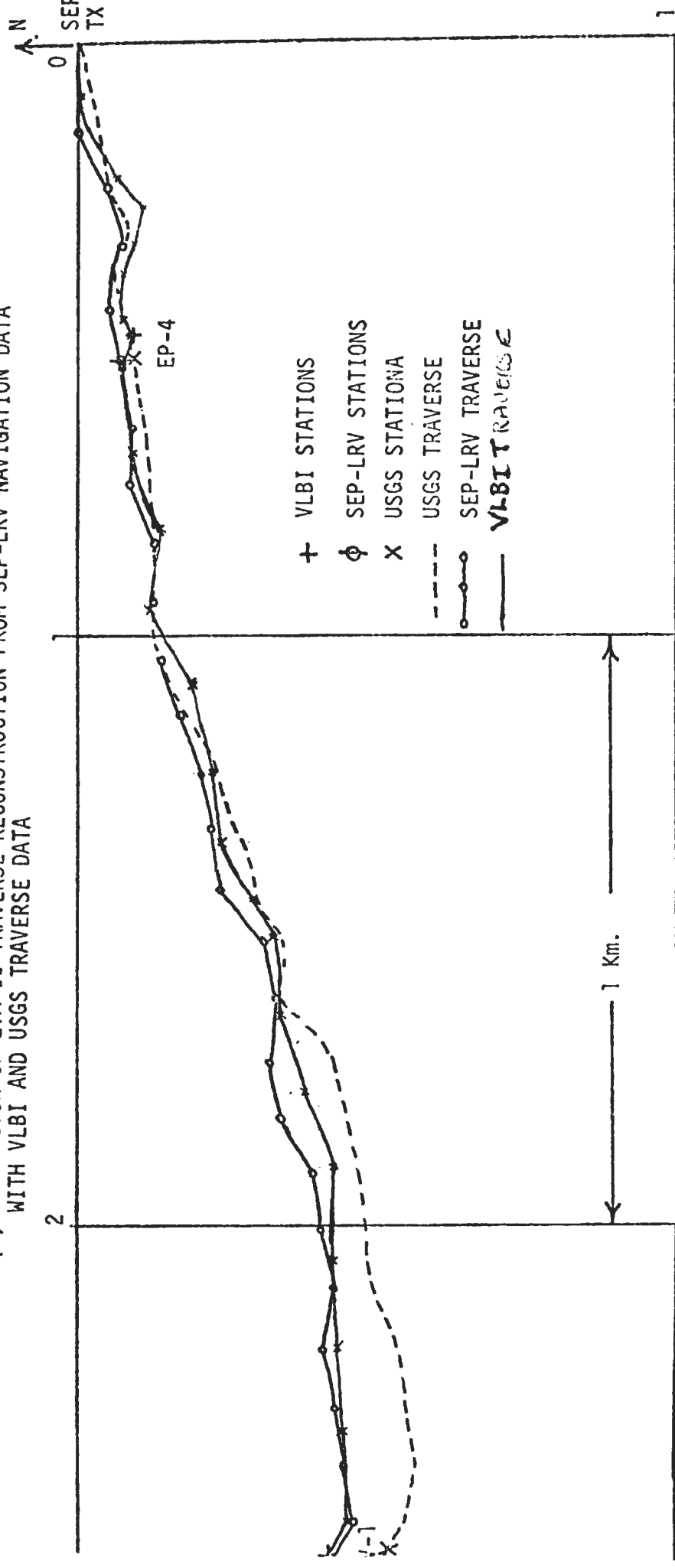
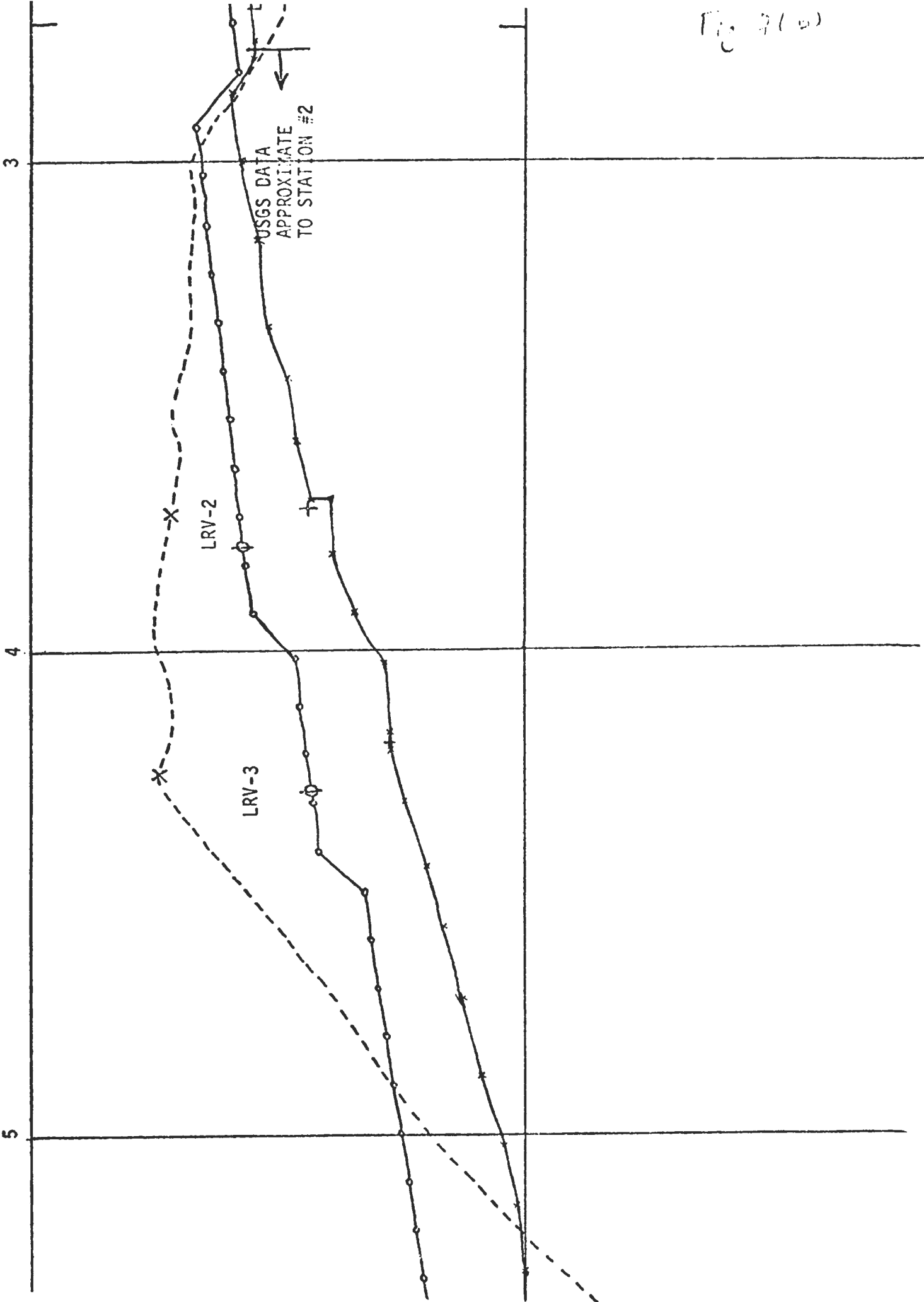


Fig 4(b)

FIG. # 4(b)



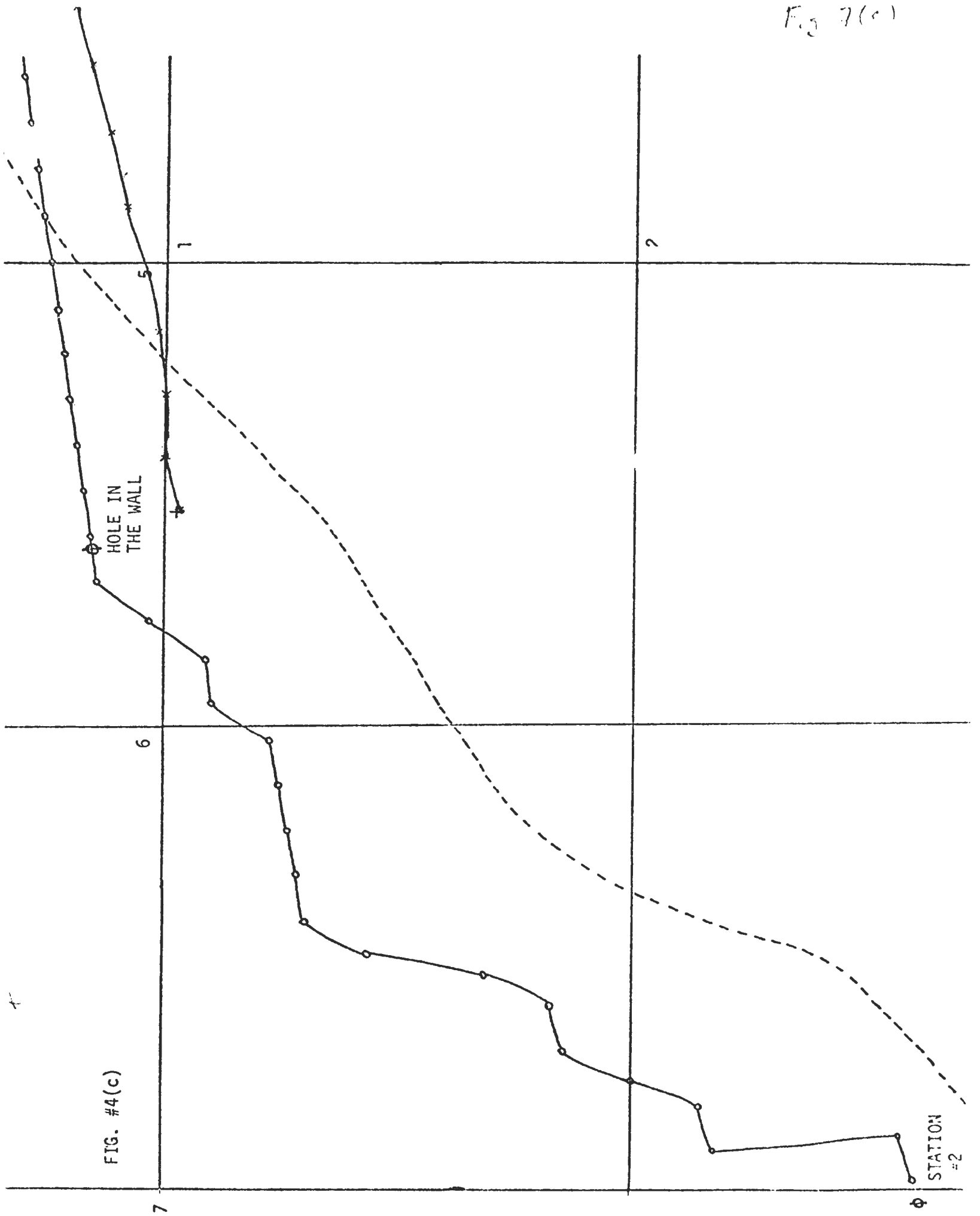


FIG. #4(c)

STATION = 2

1.0 MHz

APOLLO 17

TUNING REMOVED; NO INTERPOLATION

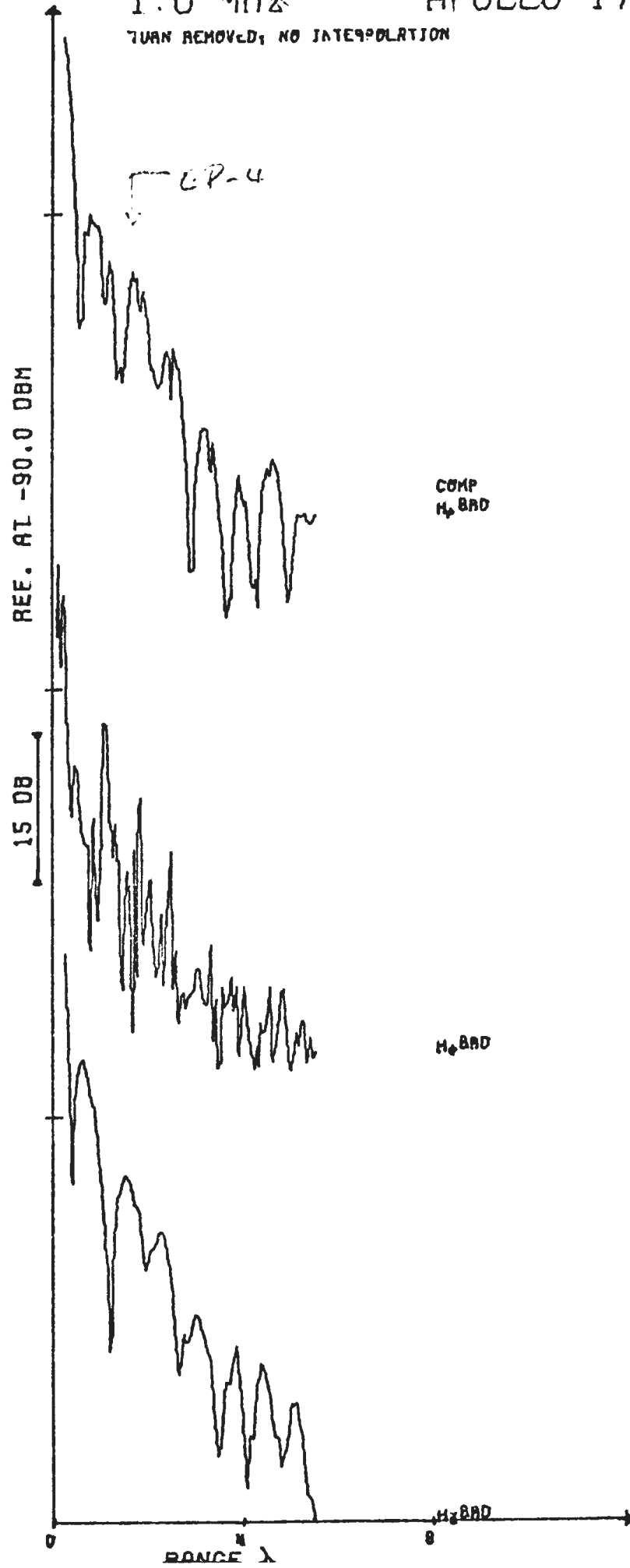
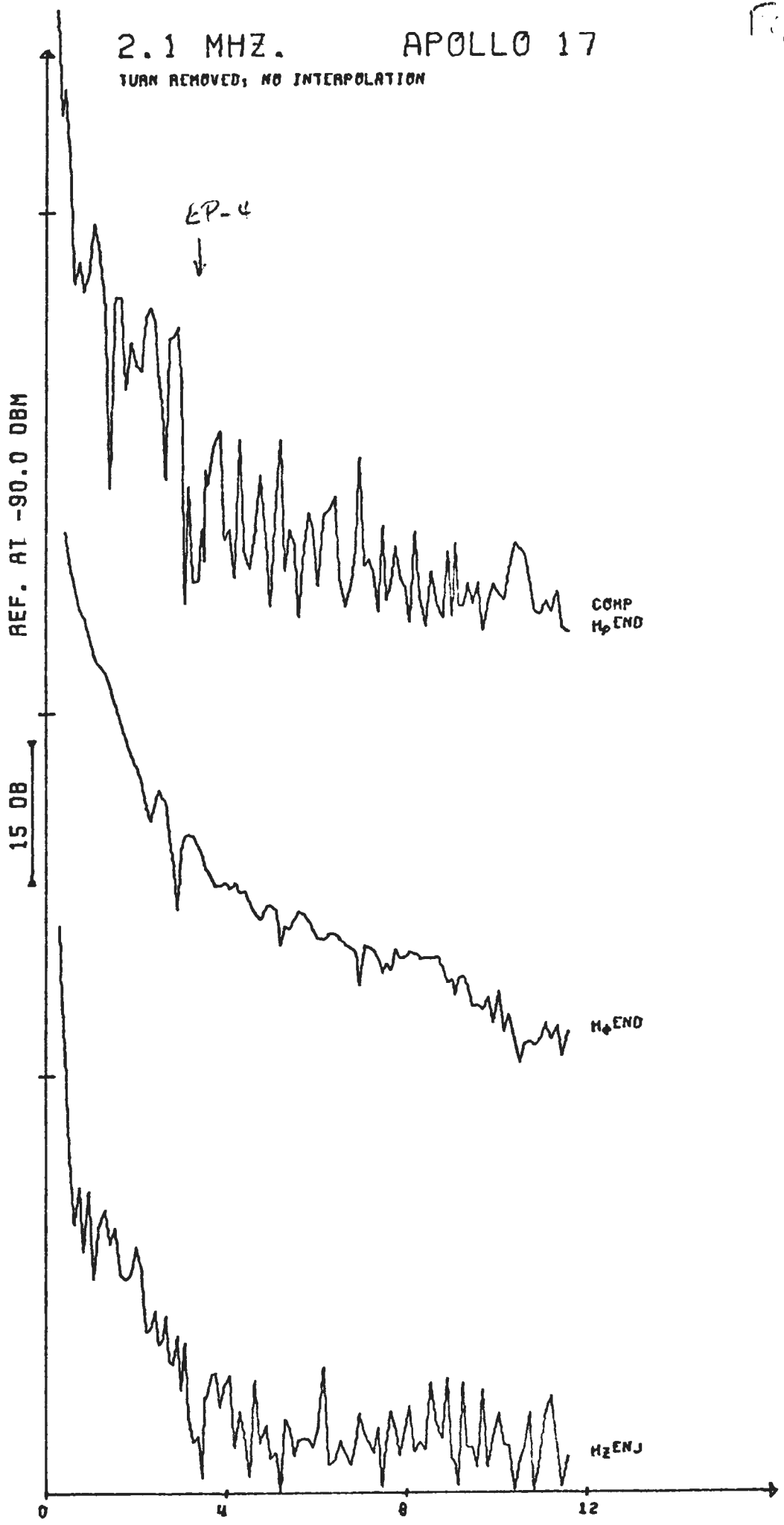


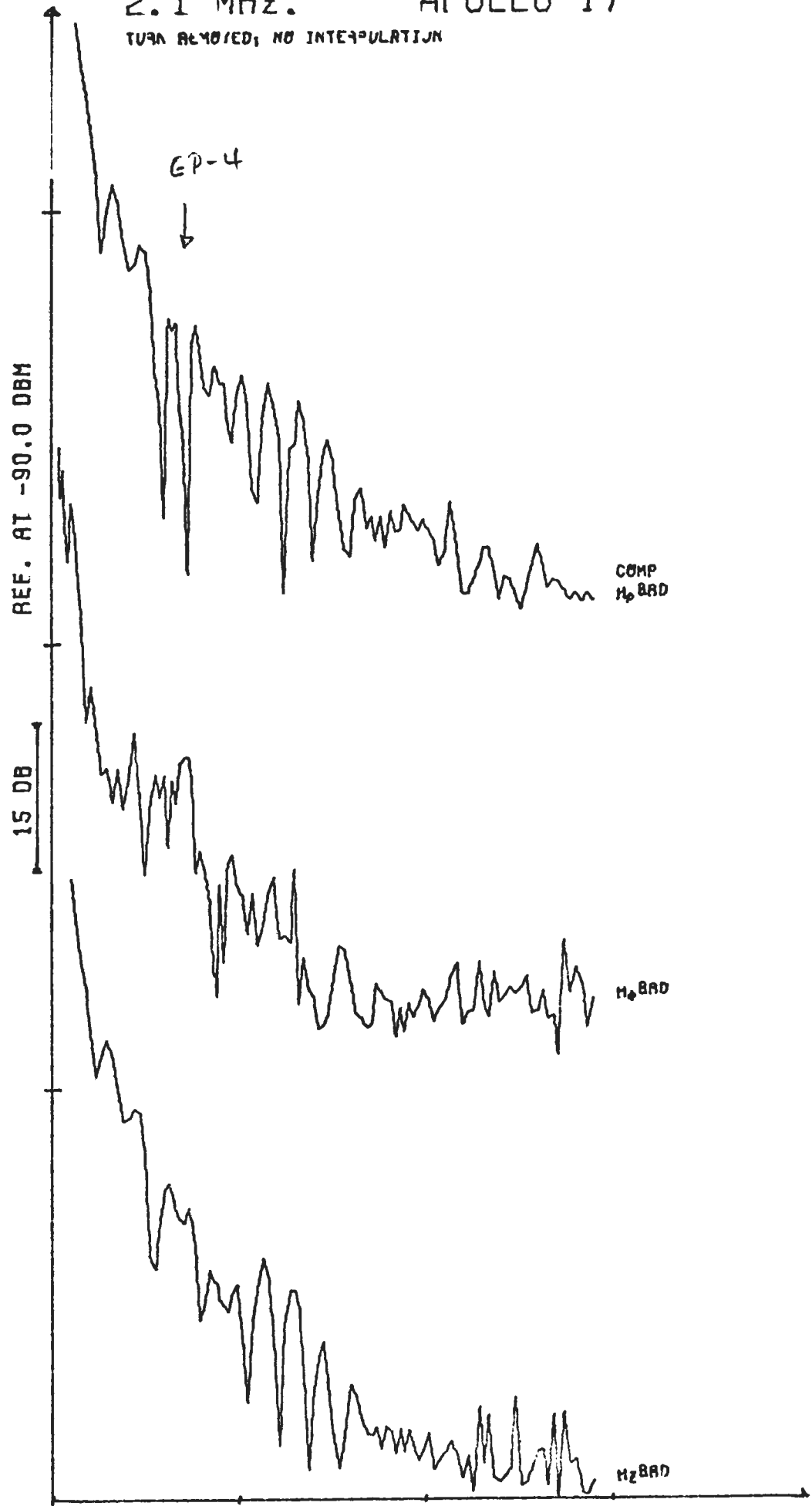
Fig 8(a)

2.1 MHz. APOLLO 17
TURN REMOVED; NO INTERPOLATION



2.1 MHz. APOLLO 17

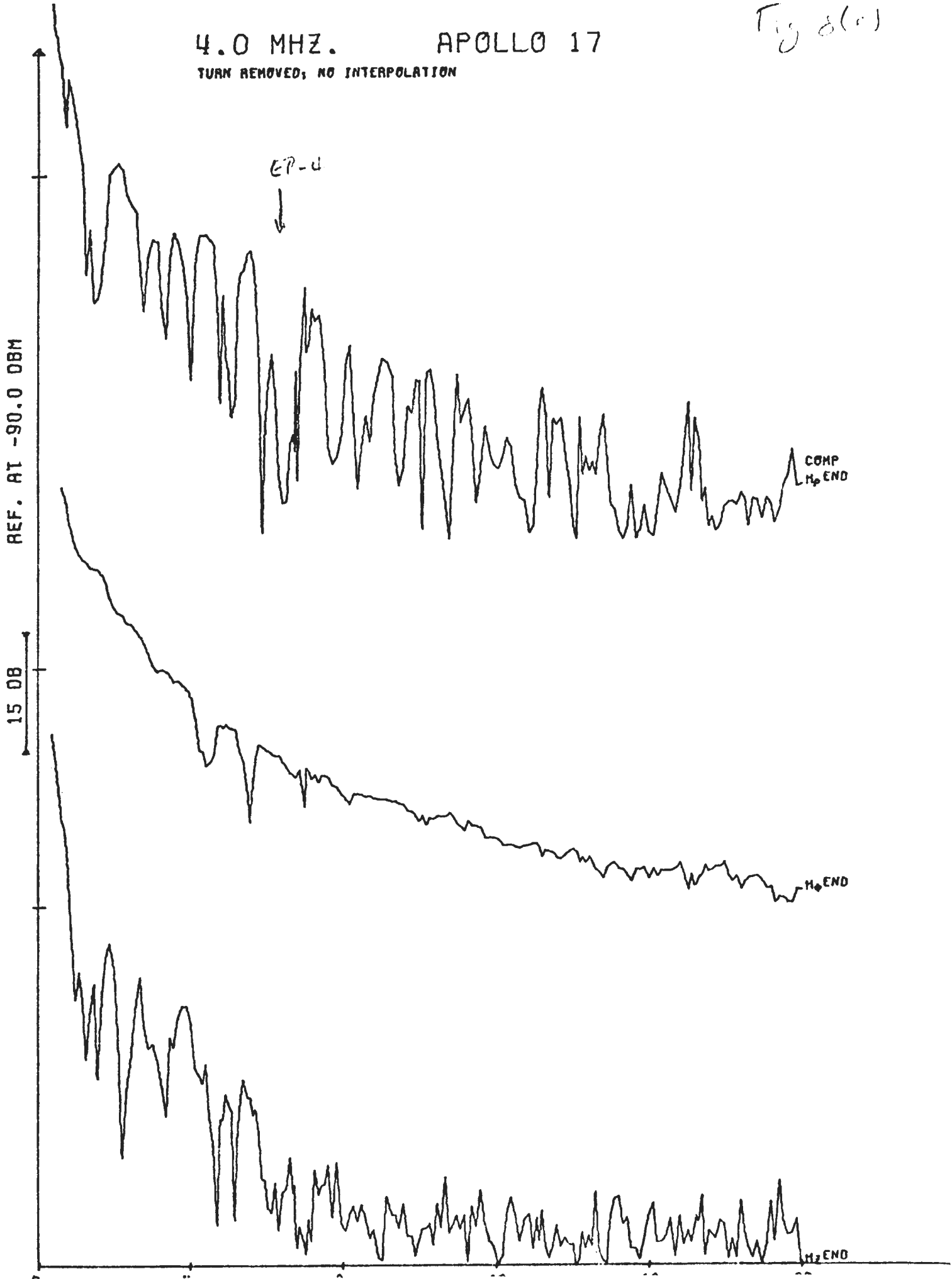
TUNER REMOVED; NO INTERPOLATION



4.0 MHZ. APOLLO 17

Fig 8(a)

TURN REMOVED; NO INTERPOLATION



4.0 MHZ. APOLLO 17

TURN REMOVED; NO INTERPOLATION

REF. AT. -90.0 DBM

15 DB

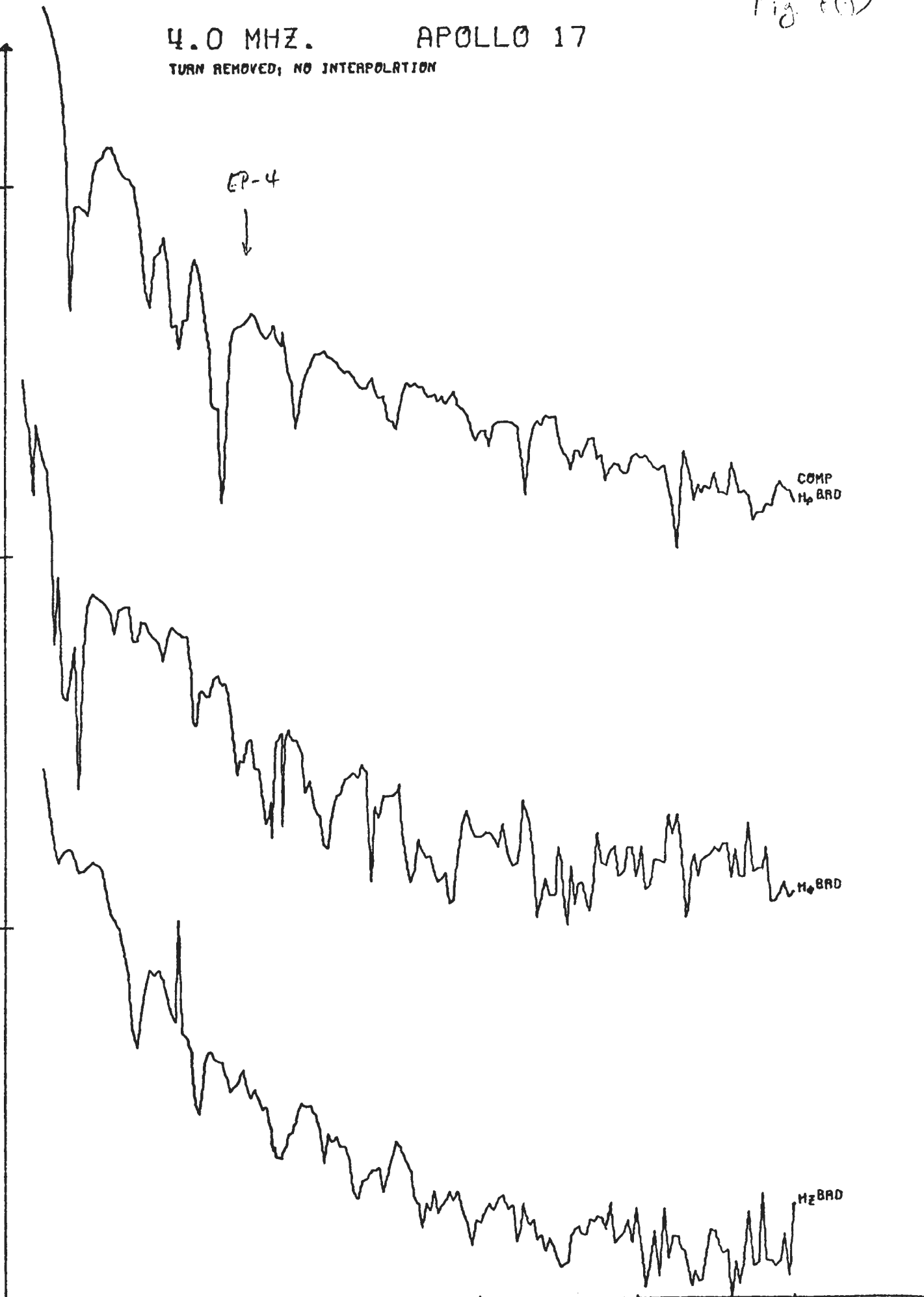
EP-4



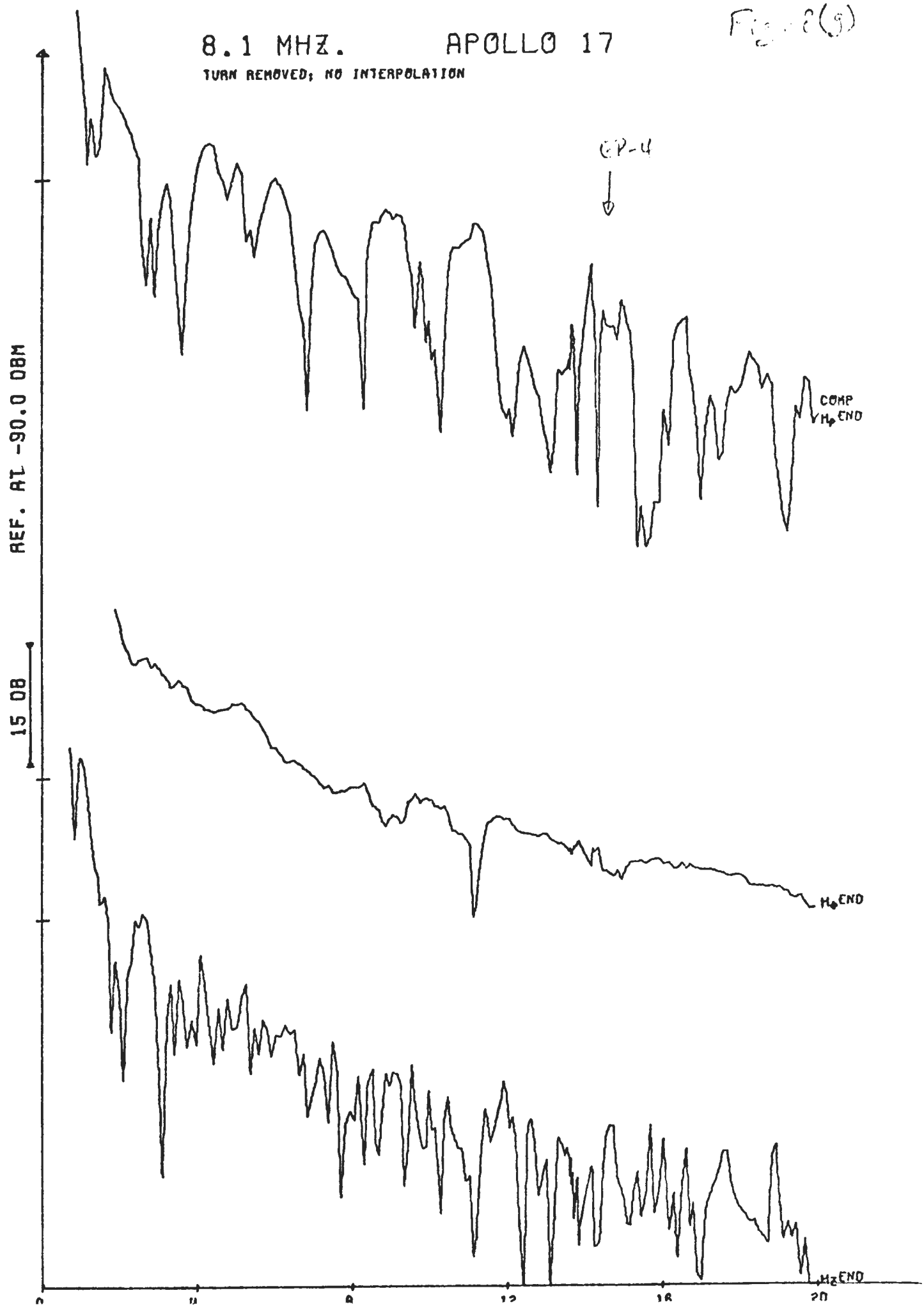
COMP
H_p BRD

H_p BRD

H_z BRD



8.1 MHz. APOLLO 17
TURN REMOVED; NO INTERPOLATION



8.1 MHZ. APOLLO 17
TURN REMOVED; NO INTERPOLATION

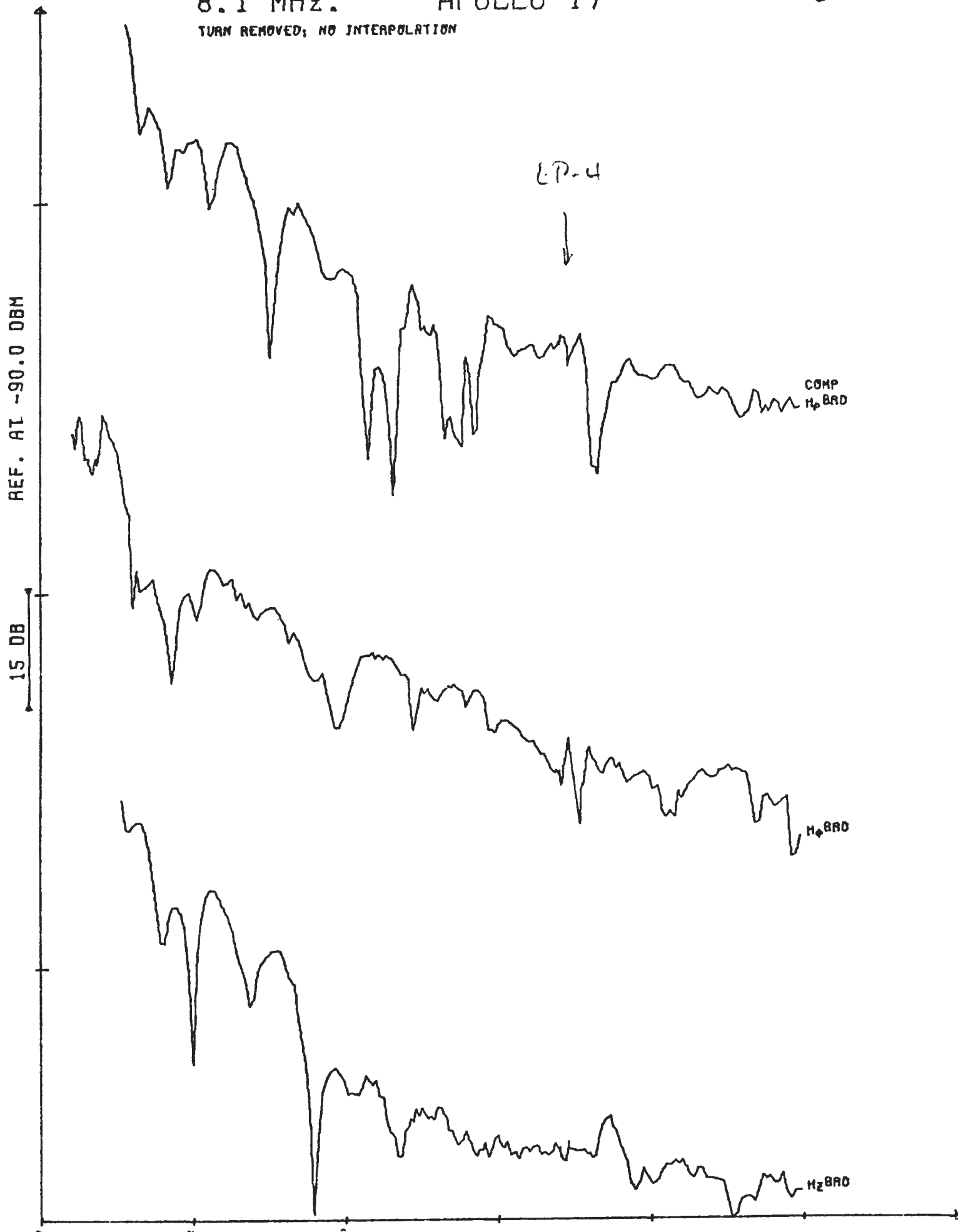


Fig 8(i)

16.0 MHZ. APOLLO 17

TURN REMOVED; NO INTERPOLATION

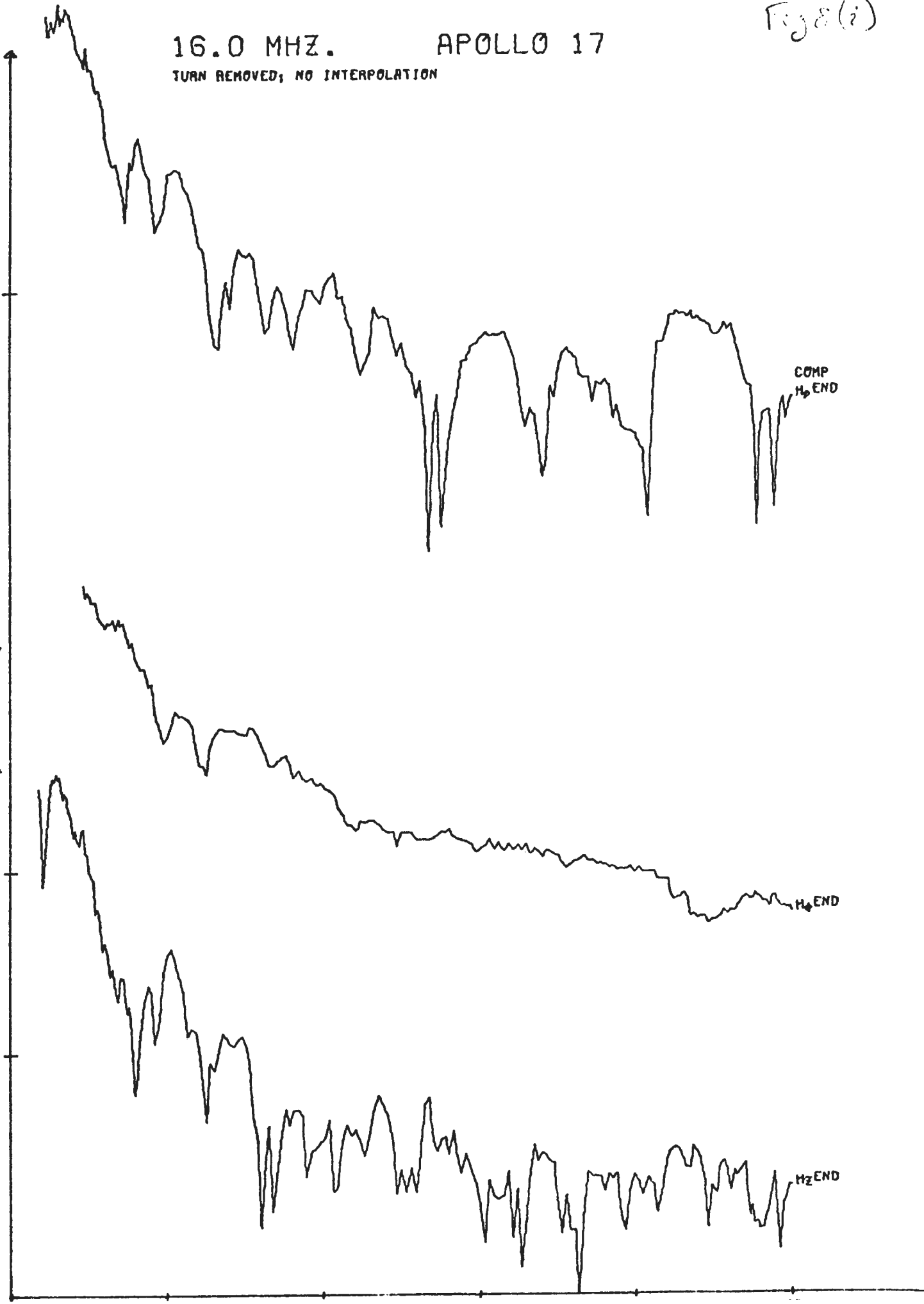
REF. AT -90.0 DBM

15 DB

COMP
H_p END

H₂ END

H₂ END



16.0 MHz. APOLLO 17

Fig. 8(j)

TURN REMOVED; NO INTERPOLATION

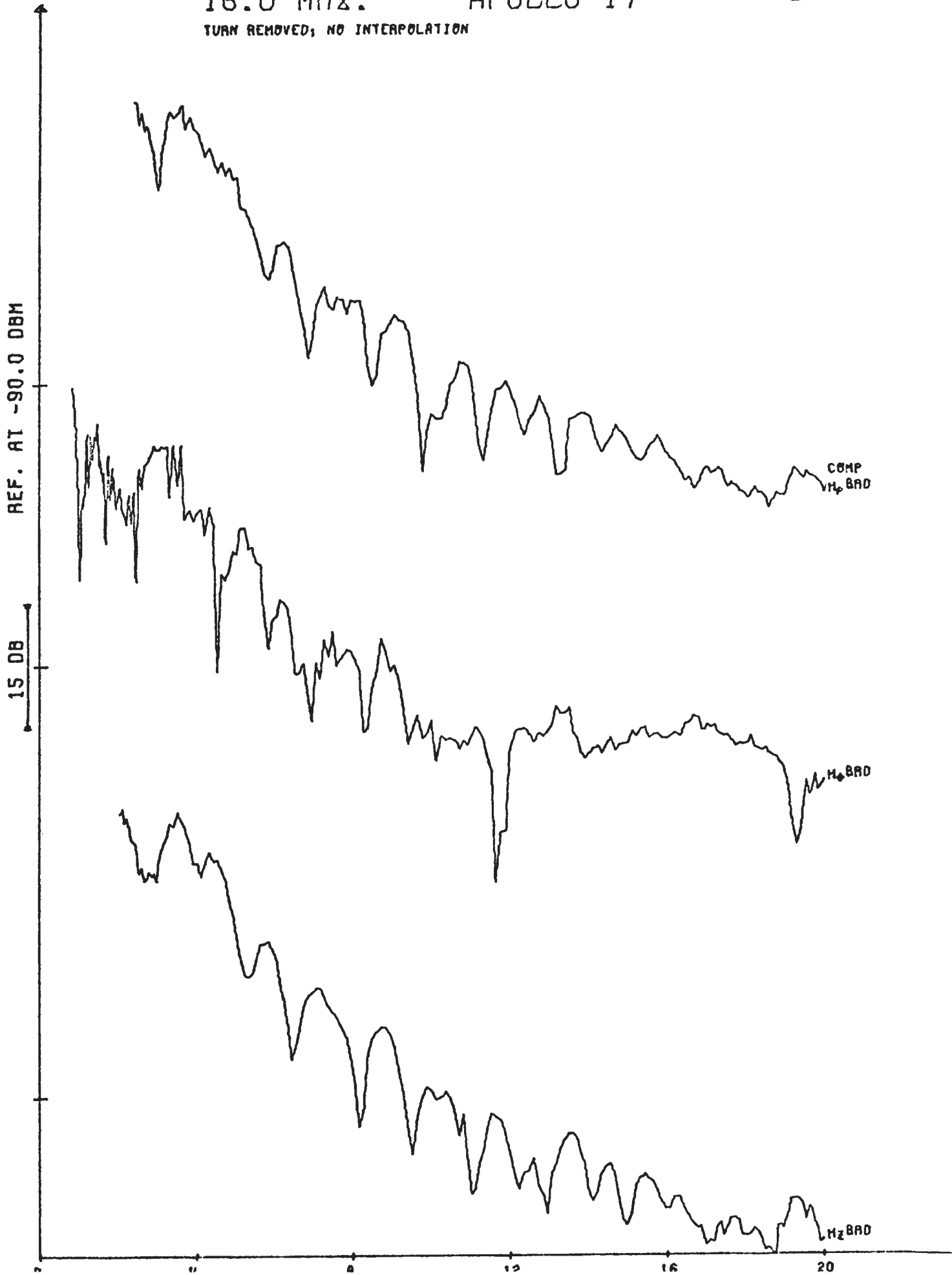


Fig 8 (k)

32.1 MHz.

APOLLO 17

TURN REMOVED; NO INTERPOLATION

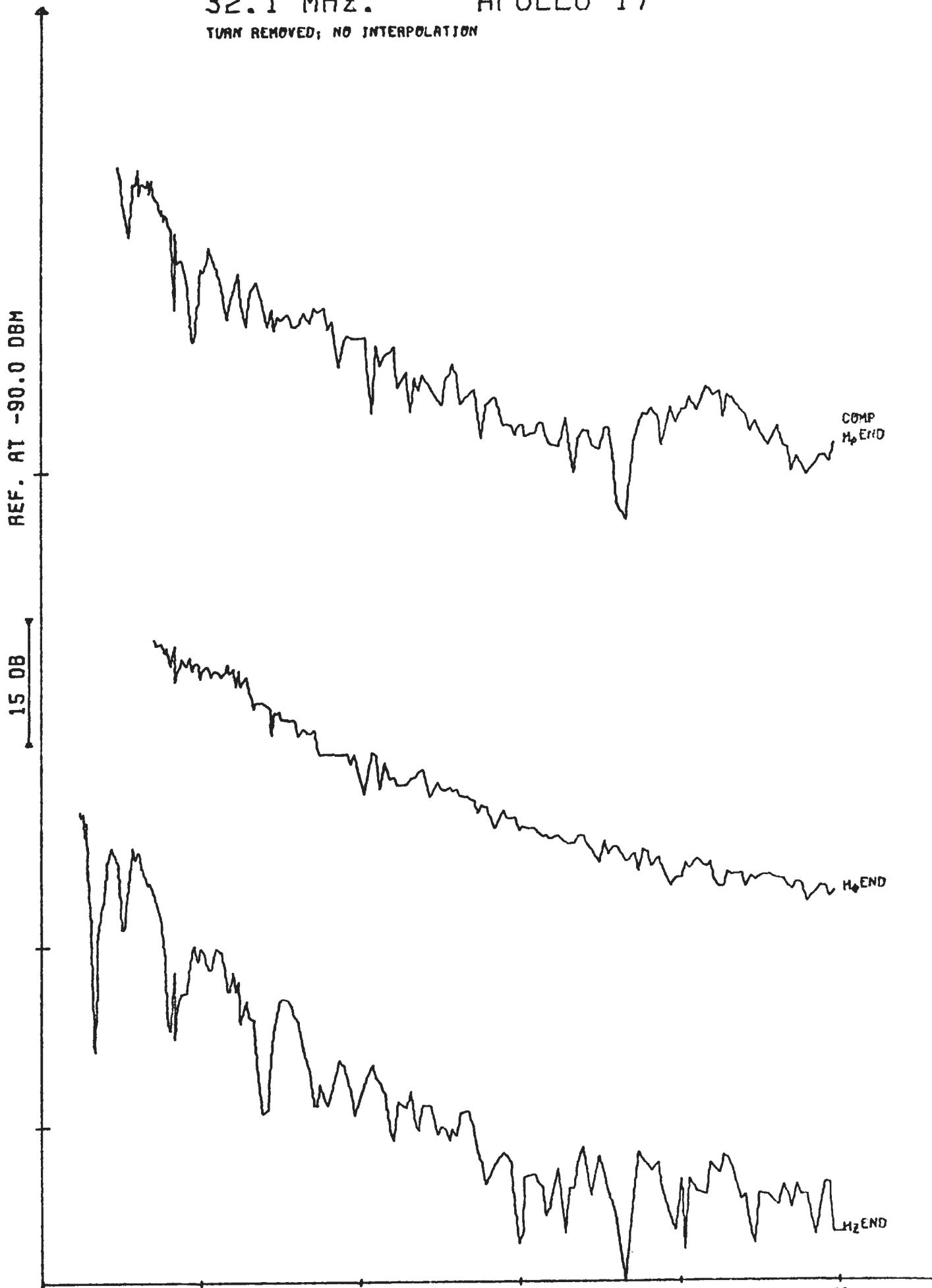
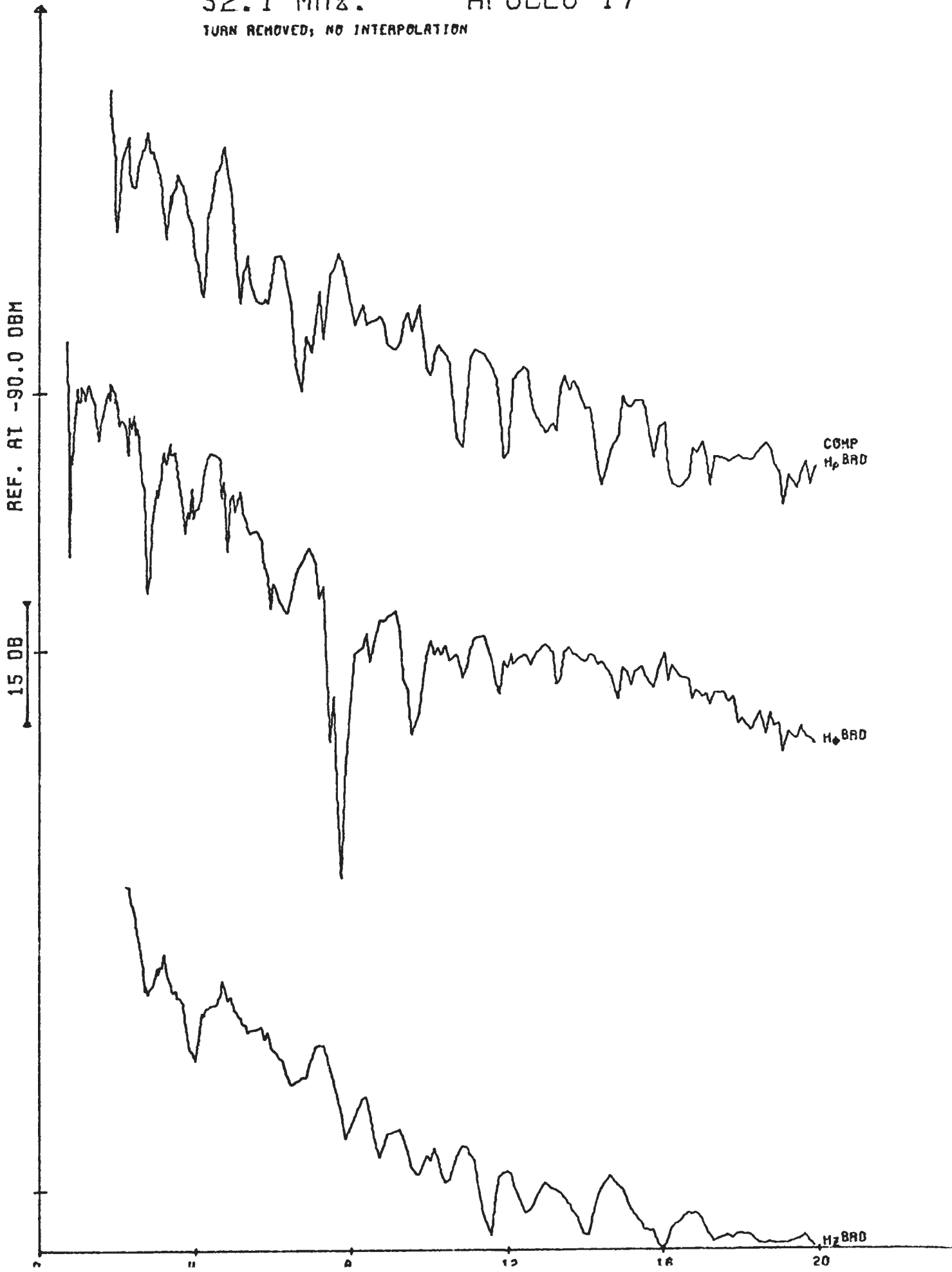


Fig 2(8)

32.1 MHz. APOLLO 17

TURN REMOVED; NO INTERPOLATION

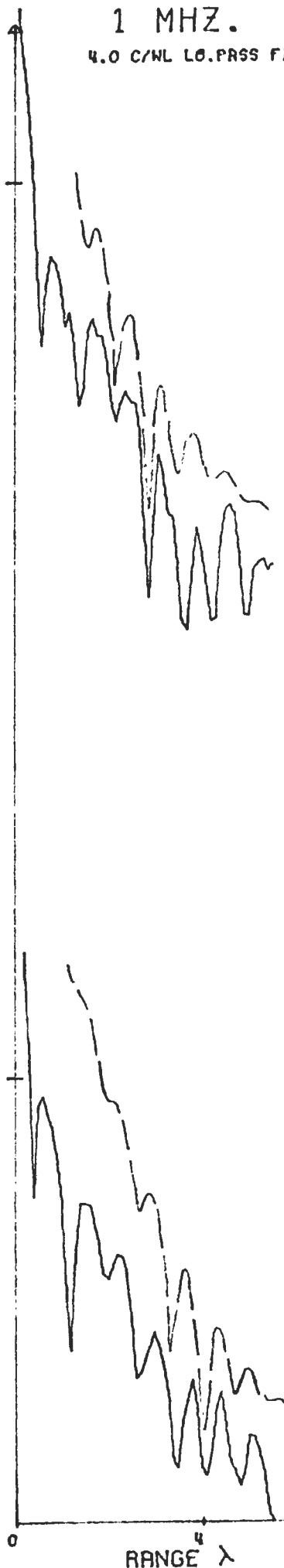


1 MHZ.
4.0 C/WL LB. PASS FILTER

Fig 9(a)

15 DB/INCH

1 MHZ.



COMP	MAX	SITE	RUN	FREQ
H _p BRD	66.00	17	1	1

H_p BRD 60.60 17 1 1

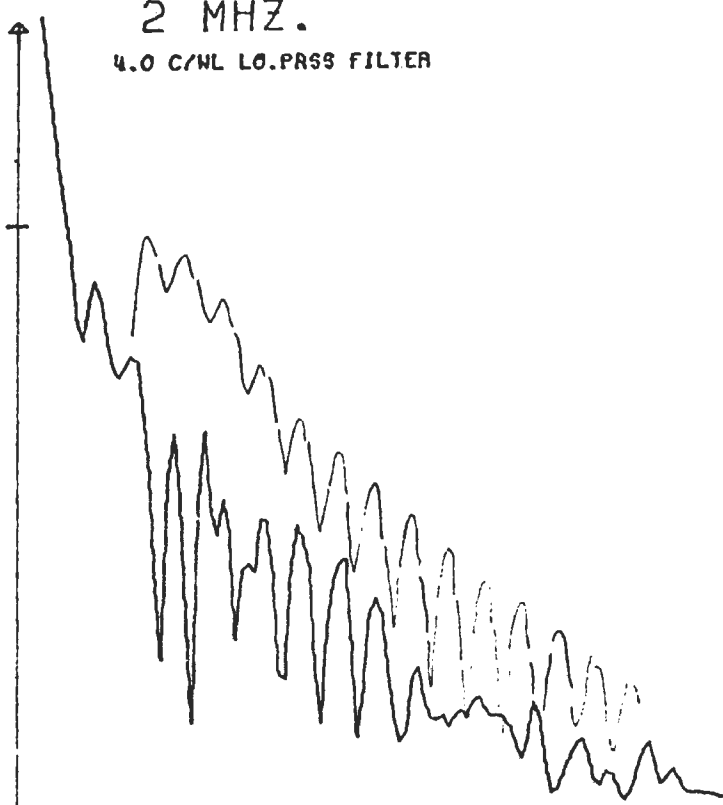
RANGE λ

2 MHZ.
4.0 C/NL LO.PASS FILTER

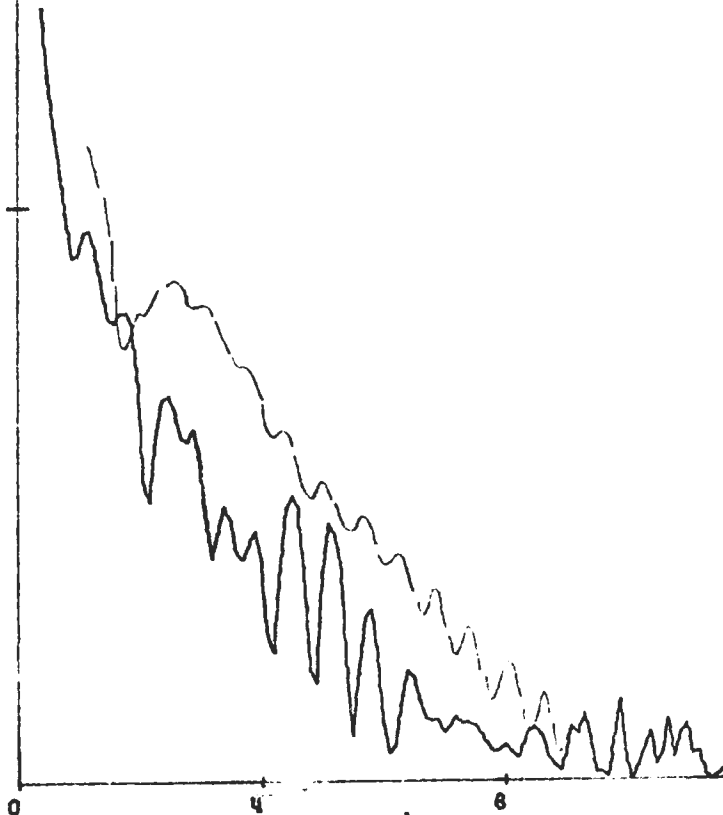
Fig 9(b)

15 DB/INCH

2 MHZ.



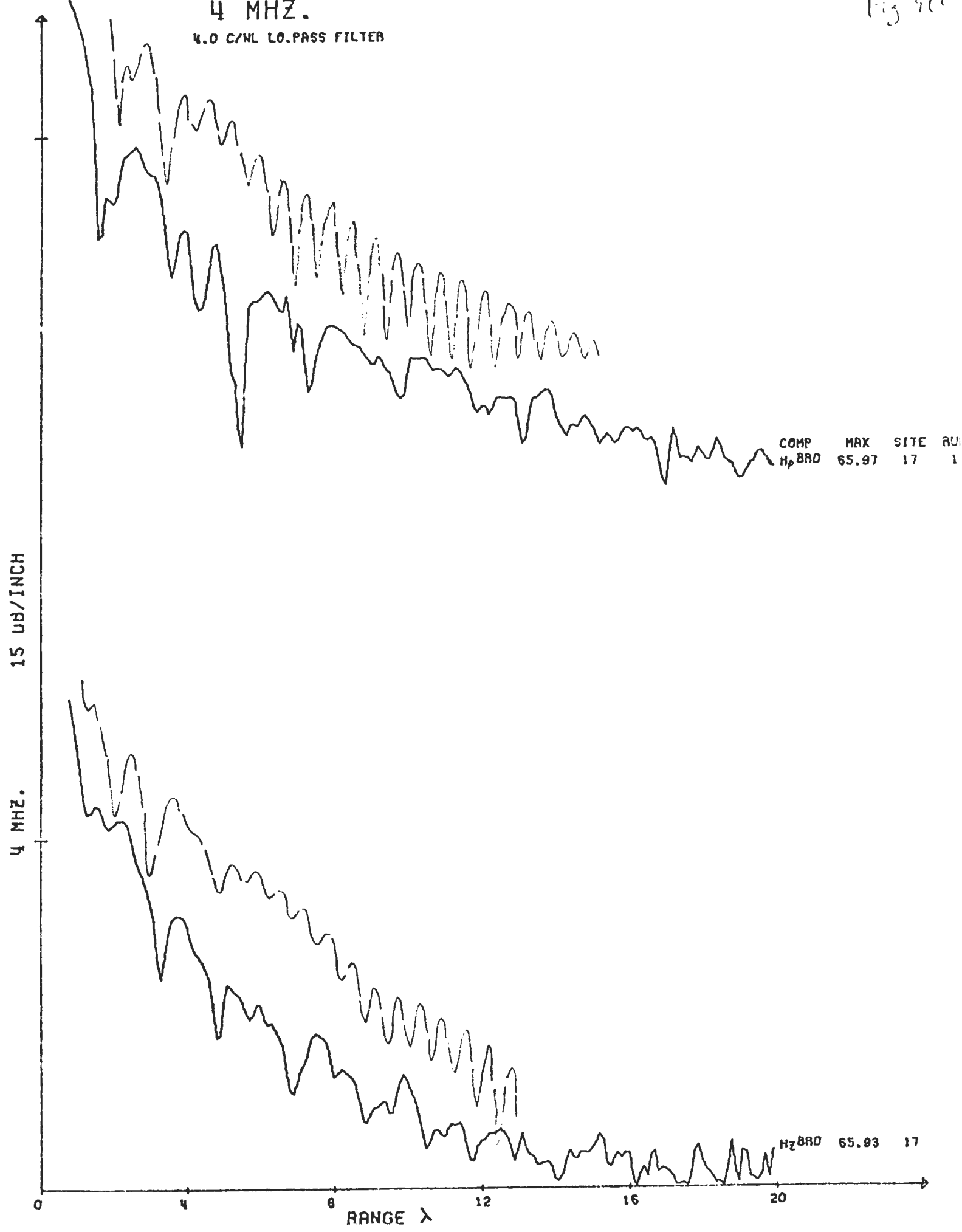
COMP	MAX	SITE	RUN	FREQ
H _p BRO	64.84	17	1	2



H ₂ BRO	63.74	17	1	2
--------------------	-------	----	---	---

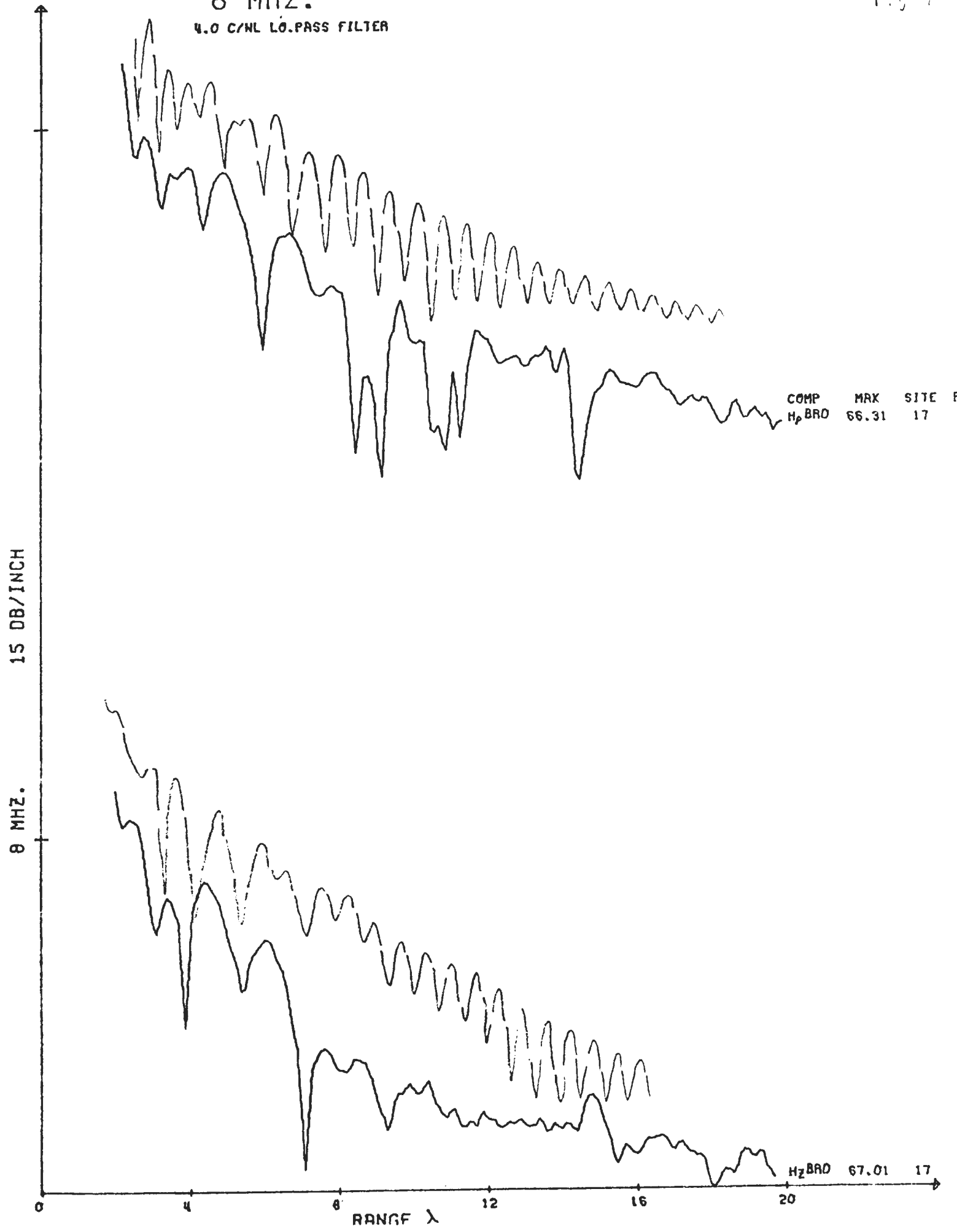
RANGE λ

4 MHZ.
4.0 C/ML LO.PASS FILTER



8 MHZ.

4.0 C/NL LO.PASS FILTER



COMP	MAX	SITE	RANGE
H ₂ BRO	66.31	17	17

H ₂ BRO	67.01	17
--------------------	-------	----

16 MHZ.

4.0 C/WL LO.PASS FILTER

Fig 9(c)

15 DB/INCH

16 MHZ.

COMP	MAX	SITE
H _p BRO	66.92	17

COMP	MAX	SITE
H _z BRO	66.79	17

0

4

8

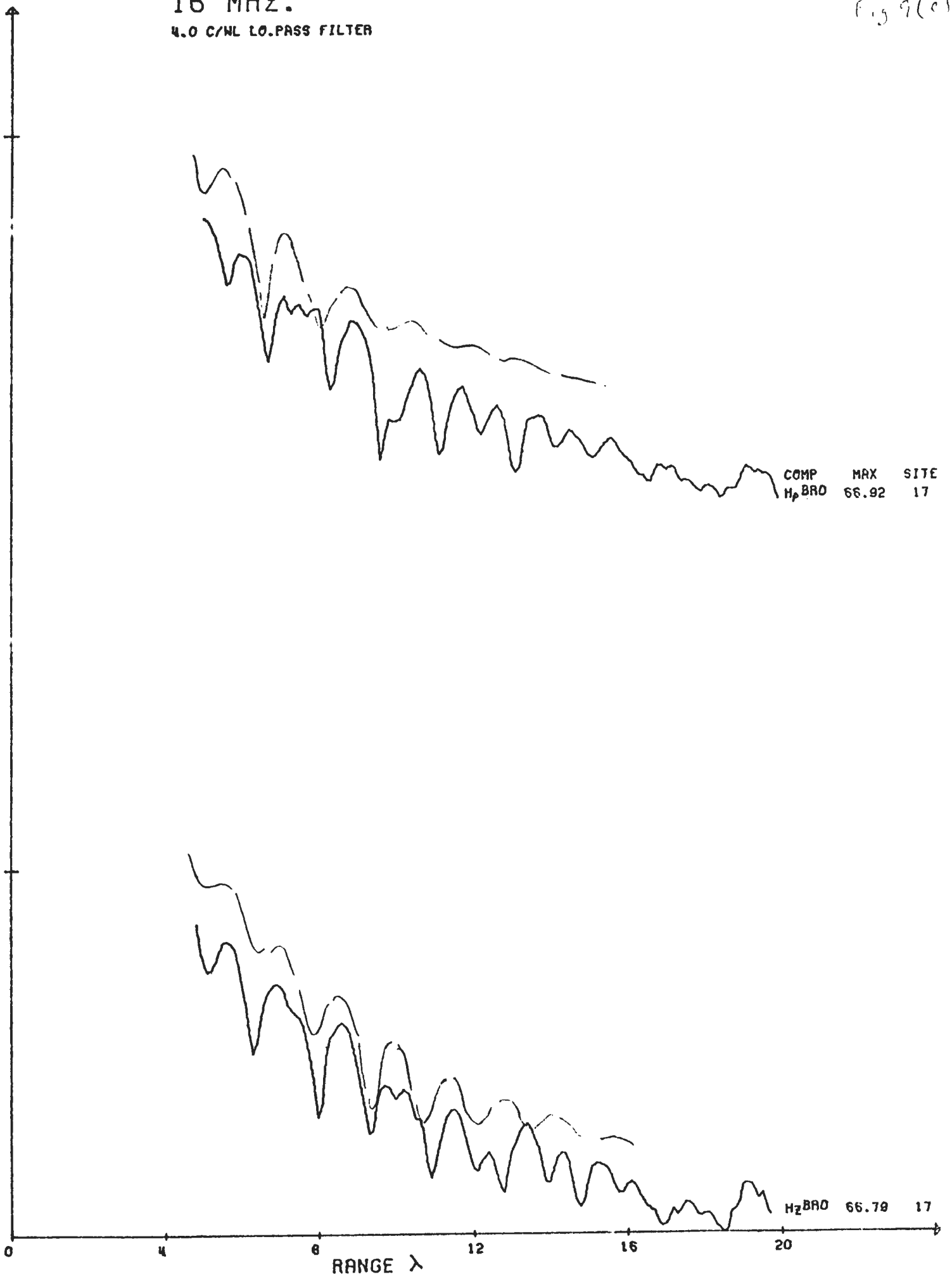
RANGE λ

12

16

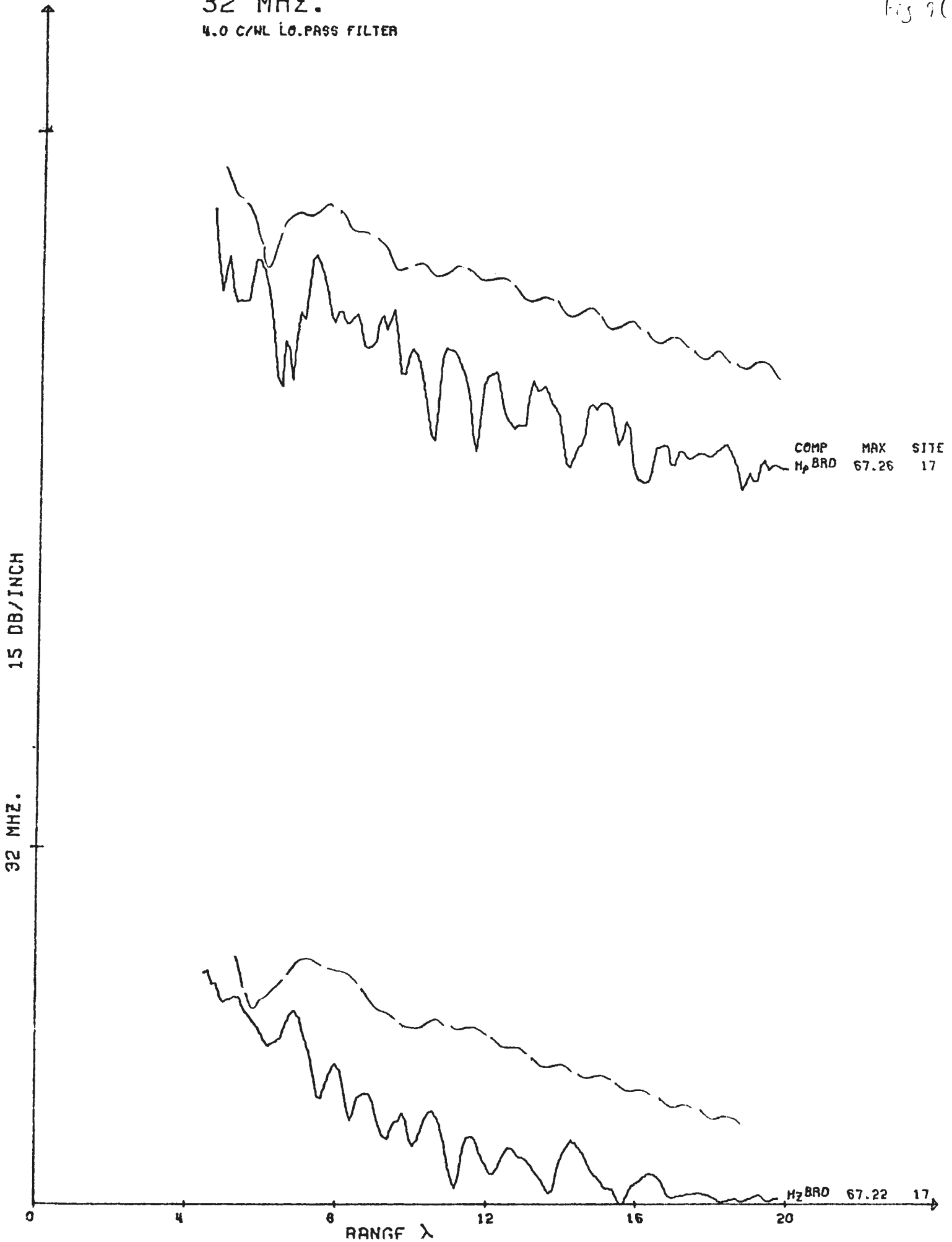
20

→

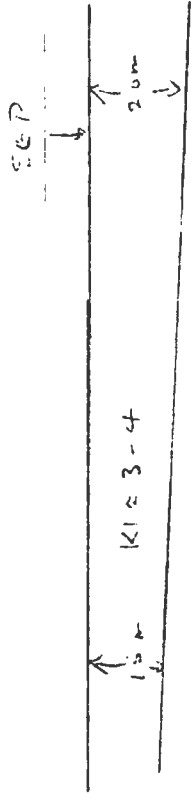


32 MHZ.
4.0 C/NL LO.PASS FILTER

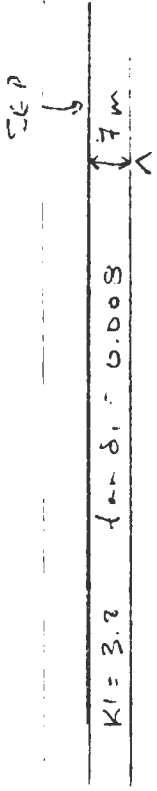
Fig 9(4)



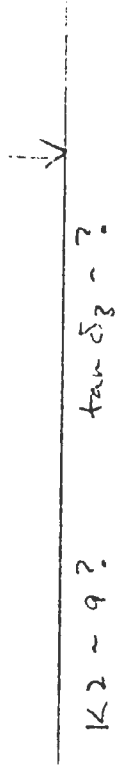
WIND



$K2 = 6-7$



$K2 = 7.5$ $\tan \delta_2 = 0.03$ $100m$



$K2 = 9?$ $\tan \delta_3 = ?$

10 (b)

10 (a)

Sloping interface method.

Three-layer model

15-2

15. Surface Electrical Properties Experiment

*Gene Simmons,^{a†} David Strangway,^{b‡} Peter Annan,^c Richard Baker,^a
Lawrence Bannister,^a Raymon Brown,^a William Cooper,^a Dean Cubley,^b
Joseph deBettencourt,^d Anthony W. England,^{e‡} John Groener,^a Jin-Au Kong,^a
Gerald LaTorraca,^a James Meyer,^a Ved Nanda,^a David Redman,^c
James Rossiter,^c Leung Tsang,^a Joseph Urner,^d and Raymond Watts^c*

The surface electrical properties (SEP) experiment was used to explore the subsurface material of the Apollo 17 landing site by means of electromagnetic radiation. The experiment was designed to detect electrical layering, discrete scattering bodies, and the possible presence of water. From the analysis of the data, it was expected that values of the electrical properties (dielectric constant and loss tangent) of lunar material in situ would be obtained.

The SEP experiment is important for several reasons. First, the values of the electrical properties of the outer few kilometers of rock and soil of the Moon, measured in situ for the first time, may help others interpret many observations already made with both Earth-based and lunar orbital bistatic radar. Second, the SEP experiment will provide data that are needed to interpret the observations made with the lunar sounder, an Apollo 17 orbital experiment. In the Apollo lunar sounder experiment, the time intervals required for electromagnetic waves to penetrate the Moon, be reflected, and return to the surface of the Moon were measured. Of more interest than times, however, are depths, which can be obtained from the lunar sounder delay times and the dielectric constant that is measured in the SEP experiment. Third, the results of the SEP experiment are expected to help define the stratigraphy of the Apollo 17 landing site. Visual observations made by the crewmen and recorded with cameras are restricted

to the surface of the Moon. The SEP experiment will extend to depth those visual observations made at the surface and perhaps reveal features at depth that do not reach the surface.

DESCRIPTION OF THE EXPERIMENT

The basic principle of the SEP experiment is interferometry. This principle involves only the interference of two or more waves to produce an interference pattern. The inversion of the interference pattern in terms of the spatial distribution of the electrical properties is the basic aim of the experiment (fig. 15-1). The experiment is most easily understood in terms of a single dipole antenna for radiating electromagnetic energy and a loop receiver for measuring the magnitudes of the fields. In the

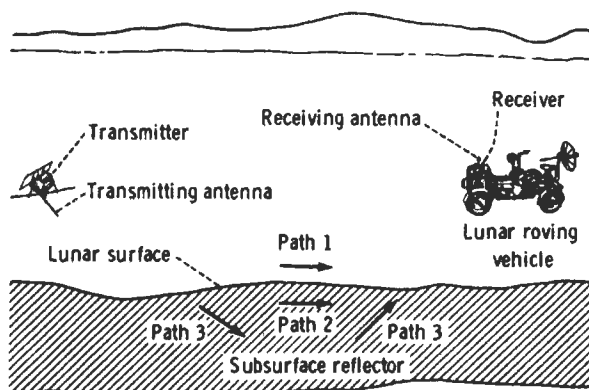


FIGURE 15-1.—Simplified schematic diagram of the SEP experiment. Electromagnetic radiation from the transmitting dipole antenna travels along path 1 (above the surface), along path 2 (below the surface), and, if reflectors are present, along path 3.

^aMassachusetts Institute of Technology.
^bNASA Lyndon B. Johnson Space Center.
^cUniversity of Toronto.
^dRaytheon Company.
^eU.S. Geological Survey.
[†]Principal Investigator.
[‡]Coinvestigator.

early developmental stages of this experiment, exactly this configuration was used (ref. 15-1).

The electromagnetic energy radiated from the transmitting antenna travels along various paths. In the "half-space" case, one wave travels above the interface through "free" space and another travels below the interface through subsurface material. Because the velocity of electromagnetic waves in a solid medium is different from that in free space, the two waves interfere and produce a distinctive interference pattern. This case has been studied extensively from both experimental and theoretical viewpoints since 1909 (ref. 15-2). The correct mathematical solutions, although somewhat complicated, are now well known (ref. 15-3). An example of a theoretical interference pattern for the half-space case is shown in figure 15-2. The spacing between successive maximums or successive minimums is related to the frequency of the wave and to the dielectric constant

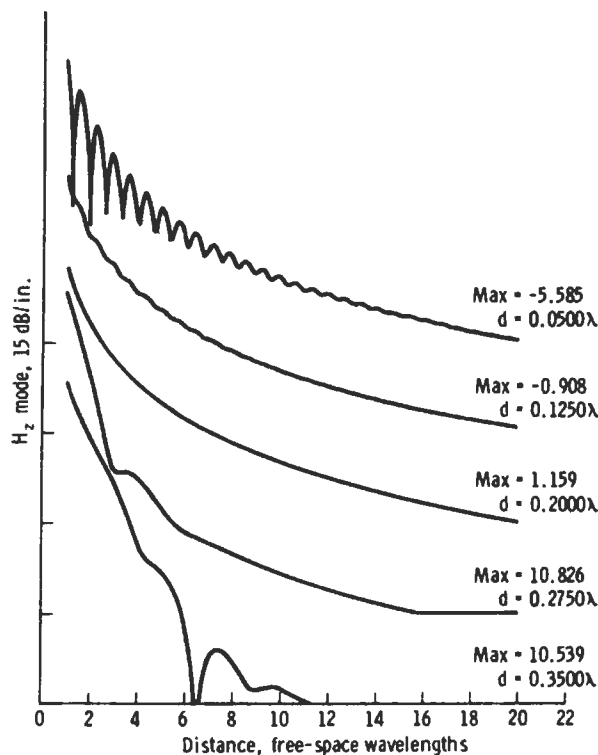


FIGURE 15-2.—Theoretical interference pattern for a half-space case, in which medium 1 is solid and medium 2 is free space; where depth $d = 0$, medium 1 loss tangent $p_1 = 0.0300$, medium 2 loss tangent $p_2 = \infty$, medium 2 dielectric constant $\epsilon_{r_2} = \infty$, and frequency $f = 299.8$ MHz. The symbol H_z represents the vertical component of the magnetic field. The points on the ordinate indicate the maximum (max) values of each wave pattern.

of the medium, and the rate at which the field strength decreases with distance is related to the loss tangent of the medium. This type of pattern is present in some of the lunar data.

If a reflecting horizon occurs at depth, such as the case shown schematically in figure 15-1, then a reflected wave will interfere at the surface of the medium with the other waves. Figure 15-3 is a theoretical curve showing the distinct interference pattern produced by a reflected wave. The presence of additional reflecting horizons in the subsurface would produce still more complicated interference patterns.

In the Apollo 17 SEP experiment, two crossed dipole antennas that radiated sequentially were used. In addition, several frequencies—1, 2.1, 4, 8.1, 16, and 32.1 MHz—were used. Because each transmitting antenna radiates at each frequency for a sufficiently long time, the experiment results can be analyzed in terms of continuous waves. The shortest sampling time at the lowest frequency includes approximately 33 000 cycles.

THEORETICAL BASIS

The SEP experiment is the first geophysical field technique to use the dielectric properties of rocks rather than the conductive properties. In that sense, the experiment is entirely new. Consequently, all the

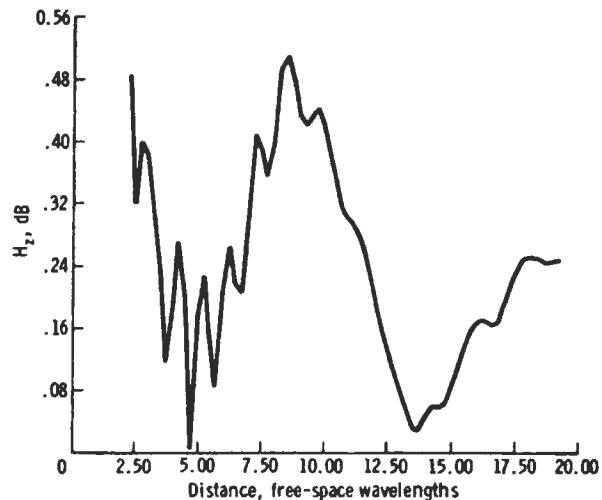


FIGURE 15-3.—Theoretical curve for the case of a single layer over a reflector. The layer is four free-space wavelengths ($4\lambda_0$) thick (ref. 15-8).

experimental techniques and most of the theoretical basis have been developed specifically for the lunar experiment. Descriptions of the early versions (circa 1968) of the technique are given in references 15-1, 15-4, and 15-5. In this report, the physical and mathematical basis of the experiment is outlined and the discussions in references 15-6 to 15-8 are followed. Theoretical work has been limited to the electric and magnetic fields that result from dipole antennas on plane, horizontal, layered media. For mathematical details, the reader is referred to the original sources.

In the theoretical development, consideration is given first to electromagnetic propagation in an unbounded, homogeneous, isotropic dissipative medium and next to propagation near the plane interface of two semi-infinite homogeneous media (specialized to a lossy dielectric below an empty (or free) space region, popularly called the half-space case). Then, the effects of inhomogeneous horizontal stratification are considered, specialized initially to a lossy dielectric region of two layers, the first of depth d and the second of infinite depth and having electrical properties differing from the adjacent layer and the semi-infinite space above.

UNBOUNDED, HOMOGENEOUS, LOSSY DIELECTRIC MEDIA

Electromagnetic propagation in unbounded dissipative media is treated adequately in references 15-3 and 15-9 to 15-13. Variation of electric and magnetic fields with time t is usually expressed as $\exp(j\omega t)$ where the rotative operator $j = \sqrt{-1}$ and the radian frequency $\omega = 2\pi f$ (where the frequency f is expressed in hertz); this exponential is hereafter suppressed. Meter-kilogram-second units are used where, in vacuo, the dielectric constant or permittivity $\epsilon_0 = 1 \times 10^{-9}/36\pi$ F/m and the permeability $\mu_0 = 4\pi \times 10^{-7}$ H/m. The phase velocity in vacuo is $c = 1/\sqrt{\mu_0\epsilon_0} = 3 \times 10^8$ m/sec. Mathematically, the field expressions are solutions to Maxwell's equations.

The dissipative medium is characterized by its electrical constants, real relative dielectric constant ϵ_r and conductivity σ (mho/m). (For a vacuum, $\epsilon_r = 1$.) The media are customarily considered to be nonmagnetic with permeability $\mu = \mu_0$. The finite value of σ gives rise to a complex relative dielectric constant ϵ_r' , a complex refractive index N , and a complex phase constant $k = \beta - j\alpha$ where β is the phase constant and

α is the attenuation constant. A typical component of electric field E at a large distance R from the radiating source varies with R according to

$$E = E_0 e^{-jkR} = E_0 e^{-\alpha R} e^{-j\beta R} \quad (15-1)$$

where E_0 is a reference value of E (independent of R).

The complex relative dielectric constant is

$$\epsilon_r' = \epsilon_r (1 - jp) = \epsilon_r - jx \quad (15-2)$$

where p is the loss tangent

$$p = \frac{\sigma}{\omega\epsilon_0\epsilon_r} = 60\sigma \frac{\lambda_0}{\epsilon_r} \quad (15-3)$$

with λ_0 the free-space wavelength in meters.

The refractive index relative to vacuum is

$$N = \sqrt{\epsilon_r'} = \sqrt{\epsilon_r} (1 - jp)^{1/2} \quad (15-4)$$

The evaluation of the complex radical may be accomplished by the 50-yr-old method of G. W. Pierce (ref. 15-14), recently revived by King (ref. 15-9), as follows.

$$\sqrt{1 - jp} = f(p) - jg(p) \quad (15-5)$$

where

$$f(p) = \cosh\left(\frac{1}{2} \sinh^{-1} p\right) = \left[\frac{1}{2} \left(\sqrt{1 + p^2} + 1\right)\right]^{1/2}$$

$$g(p) = \sinh\left(\frac{1}{2} \sinh^{-1} p\right) = \left[\frac{1}{2} \left(\sqrt{1 + p^2} - 1\right)\right]^{1/2}$$

Thus, the complex phase constant k may be written as

$$k = \beta - j\alpha = \beta_0 \sqrt{\epsilon_r'} = \beta_0 N = \beta_0 \sqrt{\epsilon_r} [f(p) - jg(p)] \quad (15-6)$$

where the phase constant (real) in vacuo $\beta_0 = 2\pi/\lambda_0 = \omega\sqrt{\mu_0\epsilon_0}$. Hence

$$\left. \begin{aligned} \beta &= \beta_0 \sqrt{\epsilon_r} f(p), \text{ rad/m} \\ \lambda &= \frac{3 \times 10^8}{f}, \text{ m} \\ \alpha &= \beta_0 \sqrt{\epsilon_r} g(p), \text{ Np/m} \end{aligned} \right\} \quad (15-7)$$

When the loss tangent p is small, say $p < 0.5$, then $f(p) = 1$ and $g(p) = p/2$; this is the case encountered in the lunar SEP experiment, so that

$$\left. \begin{aligned} \beta &= \beta_0 \sqrt{\epsilon_r} = \frac{2\pi}{\lambda}, \text{ rad/m} \\ \lambda &= \frac{\lambda_0}{\sqrt{\epsilon_r}}, \text{ m} \\ \alpha &= \frac{60\pi\sigma}{\sqrt{\epsilon_r}}, \text{ Np/m} \\ &= 1.64 \frac{\sigma}{\sqrt{\epsilon_r}}, \text{ dB/km} \end{aligned} \right\} (15-8)$$

and α is independent of frequency. If σ and ϵ_r are constant with frequency, then p is proportional to f ; if p is constant with f , then σ/ϵ_r is proportional to f .

Propagation in Layered Media

For propagation in semi-infinite space near and above a semi-infinite, homogeneous (nonlayered) lossy dielectric, see references 15-3, 15-9, 15-10, and 15-15 to 15-17. References 15-16 and 15-17 are especially useful for layered media. Earlier application was to ground-wave propagation along the surface of the Earth, generally where the loss tangent of the Earth is large. The mathematical solutions are involved; they were solved initially by Sommerfeld in 1909 (ref. 15-2) with later (1926) correction of the famous $\sqrt{-1}$ sign error (ref. 15-18). A complete history, with proof of the existence of Sommerfeld's controversial surface wave, is given by Baños (ref. 15-3). The resulting field equations (for electric field E and magnetic field H) depend on the nature of the source. In theory, there are four source dipoles: the horizontal electric dipole (HED) and vertical electric dipole (wires), the horizontal magnetic dipole, and the vertical magnetic dipole (VMD). In the SEP experiment, a tuned series of wire antenna radiators (thus extensions of the elemental HED) is used, and the cylindrical coordinate values of magnetic field H_ρ , H_ϕ , and H_z are measured.

The major difference in typical ground-wave propagation from that on the Moon (or in earthbound glaciers and deserts) is in the low values of ϵ_r and p for the latter. For the case of a semi-infinite Moon below semi-infinite space, the solution is that for the

so-called half-space case; the integral method of solution (ref. 15-3) involves general integrals of the type

$$I(a, b, r) = \int_{-\infty}^{\infty} F(\lambda) e^{-\gamma_1 a - \gamma_2 b} H_0^1(\lambda r) \lambda \, d\lambda \quad (15-9)$$

where the function $F(\lambda)$ is devoid of exponential behavior, H_0^1 is the zero-order Hankel function of the first kind, and $\gamma_i = (\lambda^2 - k_i^2)^{1/2}$ may be called a complex propagation factor ($i = 1$ denoting the lunar soil and $i = 2$ the space above). The variable λ used in equations (15-9) and (15-10) is a complex separation (or eigen) variable of integration and should not be confused with the wavelength.

In a cylindrical coordinate system with the source dipole at a height h above the origin of the coordinates (ρ, ϕ, z) , two essential integrals $U(a, b, r)$ and $V(a, b, r)$ are required to determine the vector potential Π from which the fields E and H are derived. The relationship of E and H is derived from Maxwell's equations and continuity relations at the space-dielectric plane boundary ($z = 0$). The U and V integrals differ in the value of $F(\lambda)$ used; thus, for the V integral

$$F(\lambda) = \frac{k_1^2 \gamma_2 - k_2^2 \gamma_1}{(k_1^4 - k_2^4)(\lambda^2 - k_0^2)} \quad (15-10)$$

where

$$\left. \begin{aligned} k_0^2 &= \frac{k_1^2}{N^2 + 1} \\ N &= \frac{k_1}{k_2} = \frac{k_z}{\beta_0} = \sqrt{\epsilon_r} \end{aligned} \right\} (15-11)$$

In equation (15-11), the refractive index N (eq. (15-4)) is the reciprocal of n used by Baños (ref. 15-3) and others.

For evaluating a component of the magnetic field (e.g., H_z) in the SEP experiment, the U integral is required (actually the partial derivative of U). Here, $a = 0$, $b = h + z$, and the exponential involving a in equation (15-9) is unity; thus, U is written as $U(0, b, r)$. If $h = 0$, then U becomes $U(0, z, r)$.

The integral solution involves, generally, saddle-

point or double-saddle-point approximation methods (ref. 15-3). However, if $h = z = 0$, the solution for $U(0,0,r)$ is exact, as found by Van der Pol. Thus, the expressions for H_z waves broadside to the horizontal wire (HED) are exact as are those for the tangential component of electric field E_ϕ (VMD) (first noted by Wait (ref. 15-16)). If h or z (or both) are nonzero values, approximate methods must be used; these methods are very laborious because complex contour integration must be used with consequent studies of poles and branch cuts in the integrals $I(a,b,r)$.

The resulting field expression for the half-space case consists of two components, one a wave traveling above the surface with the phase velocity of space and the second a lateral wave; these two waves interfere. An example is shown in figure 15-2 for H_z lateral waves broadside to an HED for several values of ϵ_{r1} and $p_1 = 0.03$. The lateral wave is that component of energy traveling in the dielectric but refracting across the boundary to reach the receiver at height $h = z$.

For typical terrestrial soils, the loss tangent p of the ground is so high that the lateral wave is relatively too small to be observed. However, in glaciers, polar regions, and deserts, such interference patterns as those shown in figure 15-3 may be observed.

Horizontal Stratification

Two Layers.—Wave propagation in stratified regions has been treated generally by Brekhovskikh (ref. 15-17) and Wait (ref. 15-16); the properties of antennas in such regions have been discussed by Galejs (ref. 15-15). As specified for the SEP experiment, the previously mentioned treatments in references 15-6 and 15-8 find useful application. The geometry is that of figure 15-4. The solutions are

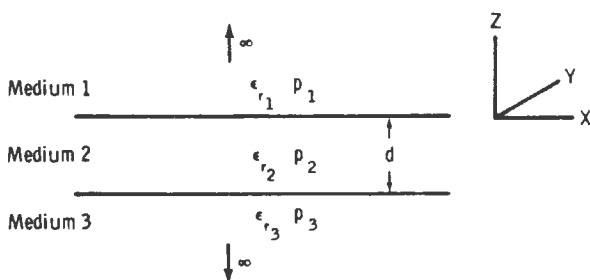


FIGURE 15-4.—Geometry for the case of a single layer over a half space. Medium 1, $a \geq 0$ (free space); medium 2, $-h \leq z \leq 0$; medium 3, $a < -h$.

integrals, similar to equation (15-9). The theoretical problem is reduced to that of solving the integrals. Three techniques have been used: (1) numerical integration on a digital computer, (2) asymptotic expansions that lead to geometrical optics approximations, and (3) contour integration to yield a normal mode solution (mode). In the geometrical optics approximation (GOA) method, the resulting field at the receiver consists of the space and lateral wave components (the half-space case) plus those attributable to reflections from the boundary between the upper layer of thickness d and the lower semi-infinite layer. (Lateral waves at this boundary and their effects have been generally neglected.) The formulation of reflections is approximate, but the GOA solution is considered satisfactory if the depth d is greater than the wavelength λ in the upper layer. An example is shown in figure 15-3, where $d = 4\lambda_0$, for lateral waves broadside to an HED. In the mode approach, the contributions to the integrals are identified in terms of the normal modes of wave propagation.

Multiple Layers.—Solutions to the various integrals (eq. (15-9)) for multiple layers can also be obtained by numerical integration and by using normal mode theory. The numerical integration method (refs. 15-8 and 15-19) provides quite exact solutions but requires much computer time; however, the method provides a check on other techniques and can be extended readily to large numbers of layers. In the GOA method, the problem is treated in terms of rays (thus, distances must be large compared with various wavelengths); therefore, solutions that are readily interpretable against a background of physical optics are provided. Unfortunately, the GOA is invalid for "thin" layers, the case for both glaciers and the Moon for at least some of the SEP experiment frequencies. The formulation and solutions for certain parameters are given in references 15-6 and 15-8. The theoretical curve for one set of parameters is shown in figure 15-5. The lack of agreement between the GOA and the numerical integration at distances less than 7λ is caused by the approximations in the GOA and indicates clearly that the proper solution must be chosen for a particular experimental situation. The normal mode solution, valid for thin layers such as appear to be present at the Apollo 17 site, was formulated by Tsang, Kong, and Simmons (ref. 15-8).

We are rather sure that our various formulations of the solution are correct. These formulations have

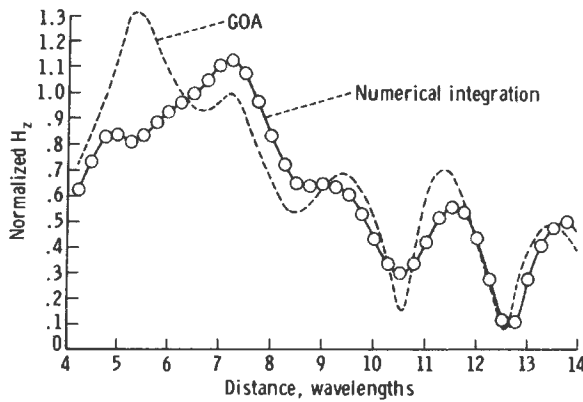


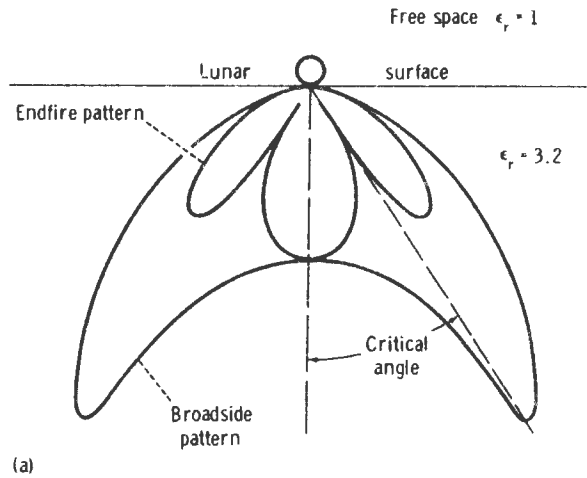
FIGURE 15-5.—Comparison of the geometrical optics approximation (dashed curve) with the Tsang exact solution (solid curve), obtained by numerical integration, for a single-layer case (ref. 15-8). Note the excellent agreement for all peaks except the first.

been tested against field data collected on glaciers for which the geometry was known from previous investigations using such other techniques as seismic, gravity, and drilling (refs. 15-1, 15-8, and 15-20). They have also been tested against laboratory data obtained with analog scale models.

The antenna radiation patterns of both the receiving loops and the transmitting dipoles are important in the analysis of the lunar data. The theoretical patterns for the transmitting antenna have been calculated (ref. 15-21), and the results are shown in figure 15-6. It has not been possible to calculate, with equal confidence, the patterns for the receiving antennas because of the effects of the lunar roving vehicle (LRV). From the data obtained on the Moon, however, it is deduced that the influence on the H_z component is minimal; thus, our preliminary data analysis is based on that component. In order to interpret the H_ρ and H_ϕ components, the effect of the radiation pattern of the receiving antenna must be removed.

THE EQUIPMENT

On the Moon, the crewmen deployed a small, low-power transmitter (fig. 15-7) and laid on the surface two crossed dipole antennas that were 70 m long tip to tip. The receiver and receiving antennas, shown in figure 15-8, were mounted on the LRV. Inside the receiver, there was a tape recorder which recorded the data on magnetic tape. The entire tape recorder, the data storage electronics assembly (DSEA), was returned to Earth. In addition to the



(a)

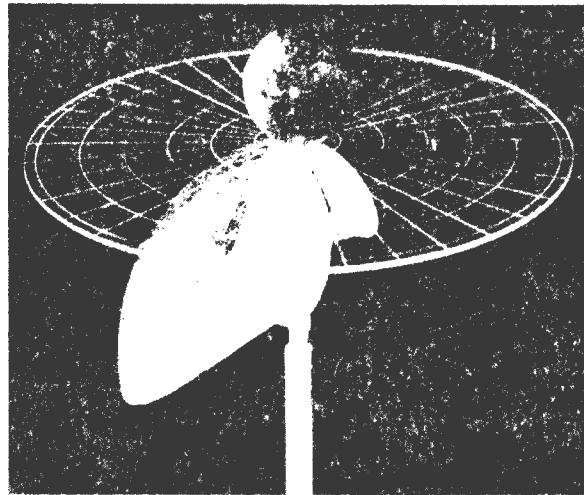


FIGURE 15-6.—Model of the theoretical radiation pattern for the SEP experiment transmitting antenna on the Moon (ref. 15-22). (a) Diagram. (b) Photograph.

SEP experiment data, information on the location of the LRV, obtained from the LRV navigation system, was also recorded on the tape.

Description

The electromagnetic radiation at the six SEP experiment frequencies is transmitted and received according to the scheme shown in figure 15-9. One data frame, which is 38.4 sec in duration, consists of six 6.4-sec subframes that are identical except for the receiver calibration and synchronization process. In subframe 1, for example, the receiver is calibrated at 32.1 and 16 MHz and the synchronization signal is

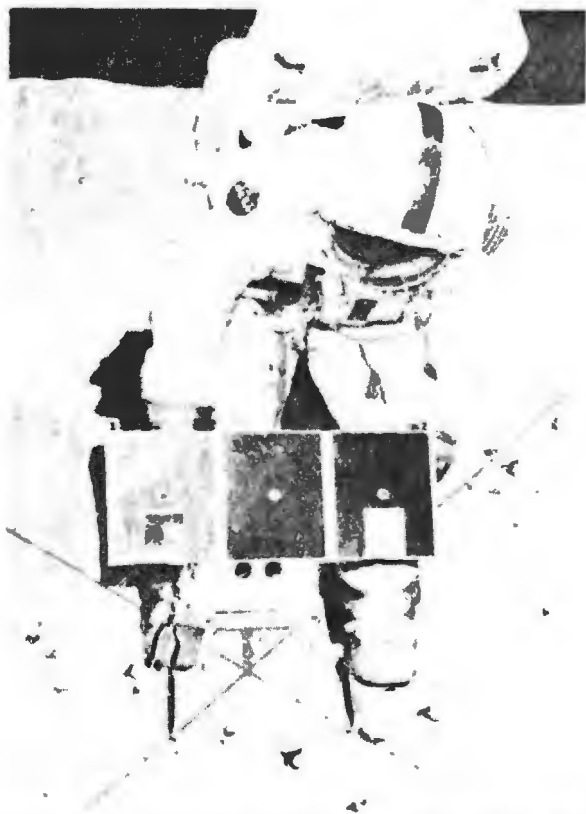


FIGURE 15-7.—The SEP experiment transmitter shown with the solar panel power source and dipole antennas deployed. The transmitter electronics package is covered on the bottom five sides with a thermal blanket. Because the top of the unit is shaded by the solar panel, the uncovered surface needs only a coat of thermal paint to provide adequate cooling for the enclosed electronics. The balance between heat lost to cold space by radiation and that generated inside the unit by the electronics equipment is very delicate and requires careful thermal design.

transmitted on the north-south (N-S) dipole antenna and received on the X antenna. In subframe 2, the receiver is calibrated at 8.1 and 4 MHz and the synchronization signal is transmitted on the east-west (E-W) antenna and received on the Y antenna. Each experiment frequency sequence is repeated exactly as shown in all six subframes. Each experiment frequency is transmitted first on the N-S antenna for 100 msec and then on the E-W antenna for 100 msec. During each 100-msec transmission interval, the receiver "looks" at the transmitted signal for a period of 33 msec with each of the three orthogonal (X,Y,Z) receiving loops. In addition to the preceding operations, once each subframe, the receiver observes environmental noise and records its amplitude.



FIGURE 15-8.—The SEP experiment receiver and antennas. The receiver electronics, including tape recorder and battery, are contained in the box (23 cm³), which usually is completely enclosed in a thermal blanket. The thermal blanket has been opened to show optical surface reflectors. The three-loop antenna assembly, folded during the journey to the Moon, is shown unfolded as it was used on the Moon.

The receiver acquires the transmitter signal sequence automatically as long as the signal exceeds a given threshold. Synchronization of the receiver is

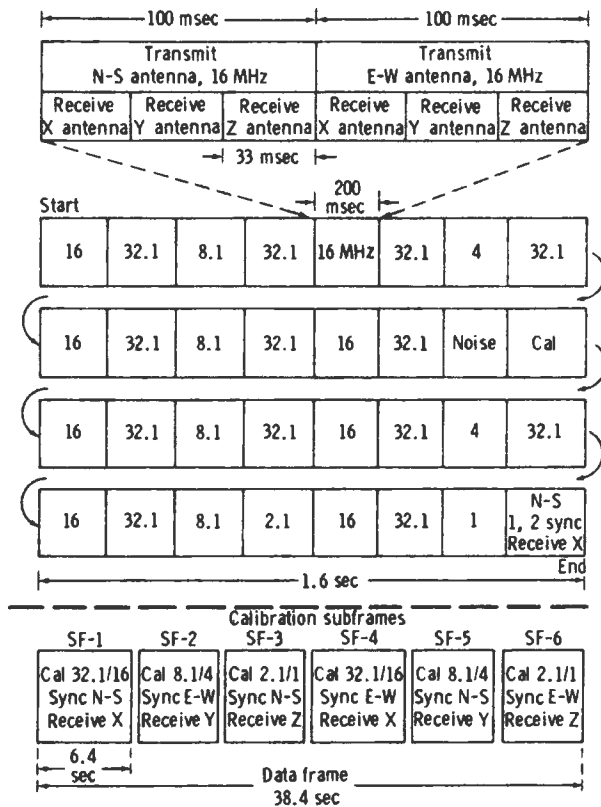


FIGURE 15-9.—The SEP experiment data format. The basic cycle, shown in the center of the diagram, starts with the 16-MHz signal and ends with the synchronization (sync) frame in the lower right corner. The cycle is 6.4 sec long. (Values are frequencies in megahertz.) The upper part of the figure shows a typical "data" frame. However, the single calibration (cal) frame changes successively through the subframe (SF) sequence shown at the bottom of the diagram.

accomplished when both (or either of) the 1- and 2.1-MHz signals exceed a given threshold. A block diagram of the SEP experiment receiver is shown in figure 15-10.

The loop antennas are connected sequentially to a low-noise amplifier section, which amplifies, converts (in frequency), and logarithmically compresses the amplitude of the received signal. A constant amplitude, variable frequency signal (in the band 300 to 3000 Hz) corresponding to the logarithm of the received signal amplitude was recorded on magnetic tape in the DSEA. The DSEA can record nearly 10 hr of data. Upon completion of the experiment, the DSEA was removed from the receiver for return to Earth.

Such functions as signal synchronization, frequency mixing, and antenna switching are controlled by the timing section, which is, in turn, crystal controlled for stability. The entire receiver assembly is battery powered using primary cells and is enclosed, except for the antenna assembly, in a thermal blanket. The thermal blanket has two flaps that may be opened to expose optical surface reflectors, which form a thermal radiator for internally produced heat while reflecting heat from the Sun, to control the internal temperature of the receiver.

The SEP experiment transmitter (figs. 15-7 and 15-11) is powered by solar cell panels that are designed to provide a minimum output of 10.0 W at 15 V and 1.10 W at 5 V. Like the receiver, the transmitter timing sequence is crystal controlled for stability. Also, separate stable crystal oscillators generate the signals that are radiated by the dipole antennas placed on the lunar surface. Because the antennas are required to radiate energy at six different frequencies, they are constructed in sections (fig. 15-12), and each section is electrically separated by electrical filters (signal traps). Each section of the antenna is of the proper electrical length for optimum performance. The dipole antennas, each 70 m long (tip to tip), are made of insulated wire between signal traps and were stored on reels until deployed.

Performance on the Lunar Surface

The crewmen deployed the SEP experiment equipment during the first period of extravehicular activity (EVA-1). Photographs of the receiver and of the transmitter and the transmitting antenna are shown in figures 15-13 and 15-14, respectively. Stereographic photographs will be used to obtain the location of the starting point of the SEP experiment profiles to within 1 m. The LRV, with its navigation system, was used to mark straight, orthogonal lines to be used as guides for deploying the antenna. Especially important for the analysis of the data was the fact that the arms of the transmitting antenna were laid out straight and at right angles to each other. The SEP experiment operations were nominal during EVA-1. During the rest period between EVA-1 and EVA-2, however, the temperature of the SEP experiment receiver increased; subsequent overheating hampered the SEP experiment operation until the DSEA recorder was removed in the middle of EVA-3 to prevent loss of data that had been recorded already

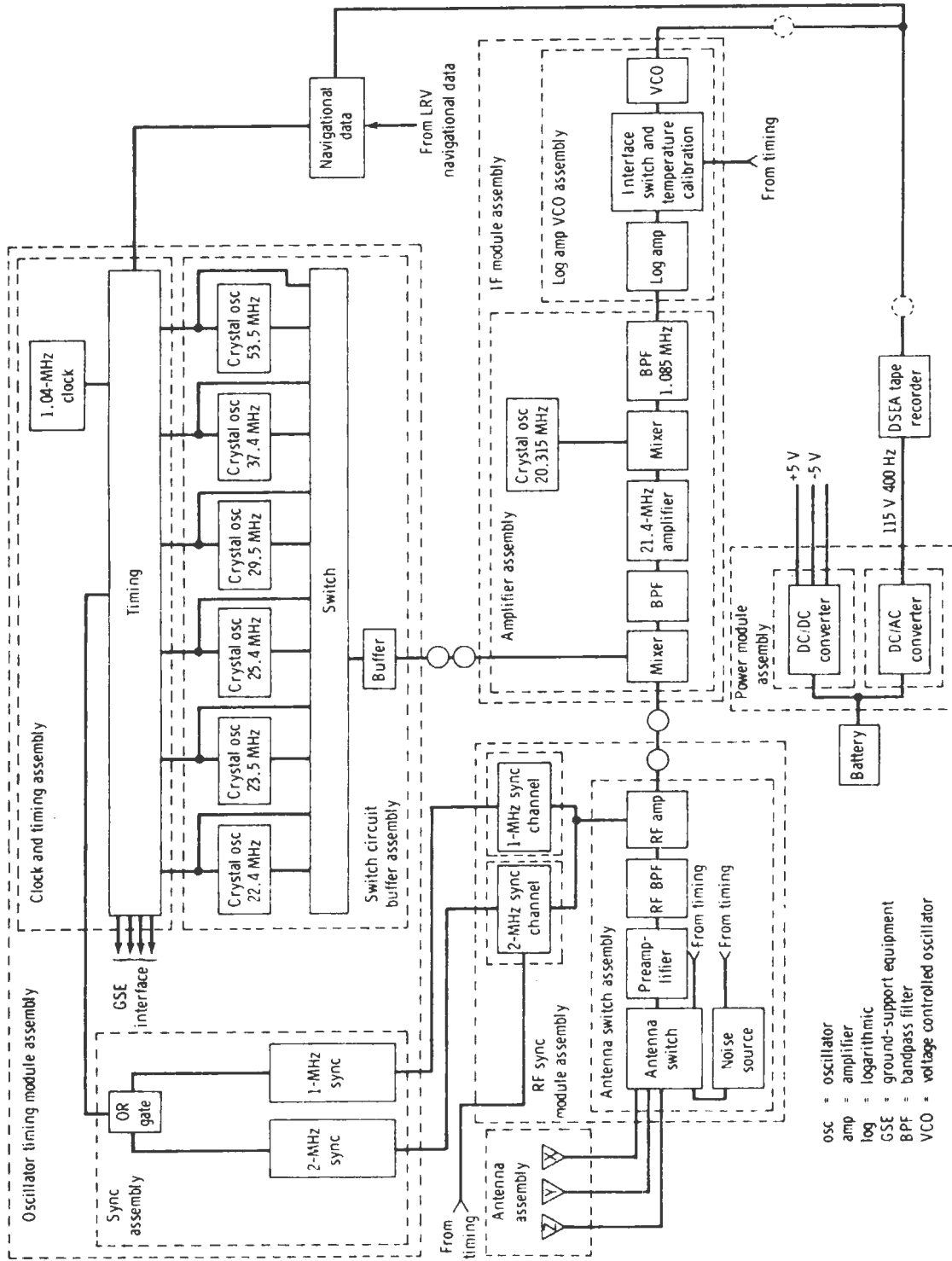


FIGURE 15-10.—Block diagram of the SEP experiment receiver.

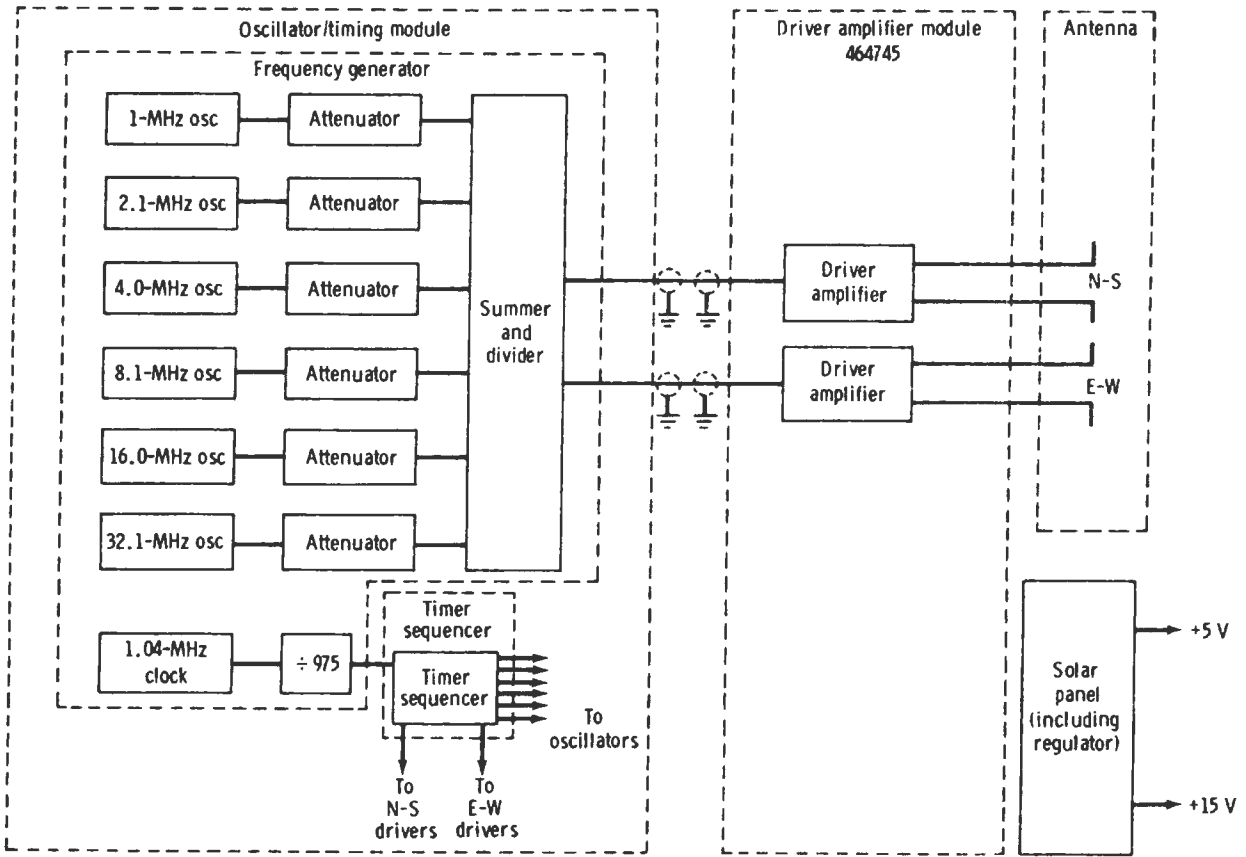


FIGURE 15-11.—Block diagram of the SEP experiment transmitter.

on the magnetic tape. The receiver contained a thermometer that was monitored by the crewmen. Despite the efforts of the crewmen to control the temperature, the receiver became too hot and was turned off by a thermally operated switch.

Data were obtained during EVA-2 on the traverses from the SEP experiment site toward station 2 and from station 4 toward the SEP experiment site. Data were not obtained during the early part of EVA-3 because the receiver switch was in the "standby" position rather than "operate." Apparently, the transmitter operated nominally throughout the mission.

THE DATA

Three kinds of data were recorded in the SEP experiment: navigational data, electromagnetic field strengths, and the internal temperature of the receiver. The navigational data, obtained from the LRV navigation system, included odometer pulses at 0.5-m increments from two wheels, the computed range to

the SEP experiment transmitter in 100-m increments, and the computed bearing to the SEP experiment transmitter in 1° increments. The navigational data are approximate because of wheel slippage on the lunar surface and will be improved greatly by including additional data on the LRV location obtained from photographs, crew comments, and long-baseline interferometry.

The second kind of data, the primary SEP experiment data, consists of the three orthogonal magnetic components H_z , H_ρ , and H_ϕ , recorded as a function of frequency and of transmitting antenna (N-S or E-W). An example of the field strength data is shown in figure 15-15.

The third kind of data, temperature of the SEP experiment receiver, was obtained for use in the postflight analysis of the experiment. Because of the sensitivity of all magnetic tape to temperature, the potential loss of data from excessive temperature in the SEP experiment receiver had been anticipated. Although protection against overheating had been

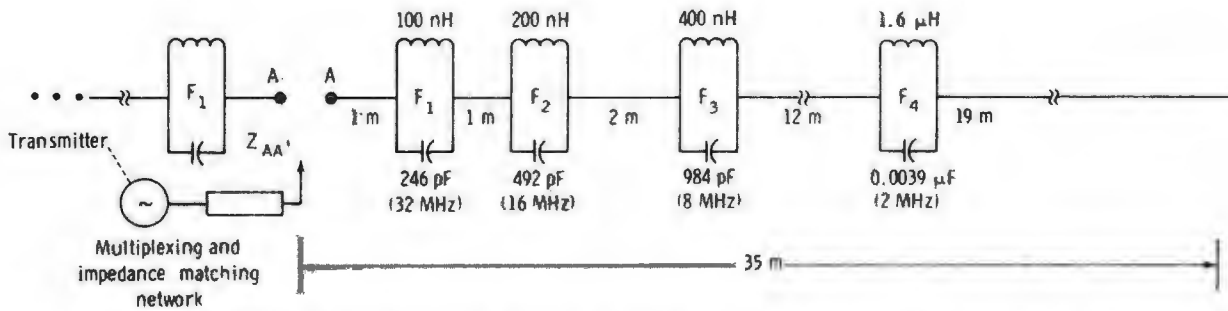


FIGURE 15-12.—Electrical schematic diagram of the SEP experiment transmitting antenna. Only one-half is shown because the antenna is symmetric about the midpoint (A', A). Total physical length (tip to tip) of each section of the antenna used for each SEP experiment frequency is 2, 4, 8, 32, and 70 m. The symbol Z represents impedance, and the components labeled F_1 to F_4 are filters.

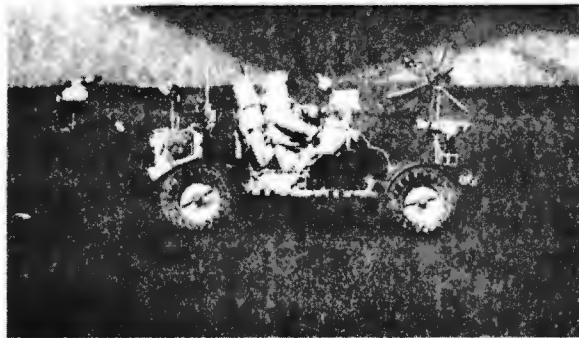


FIGURE 15-13.—The SEP experiment receiver mounted on the LRV (AS17-141-21512).



FIGURE 15-14.—The SEP experiment transmitter and antenna deployed at the Apollo 17 site (AS17-141-21517).

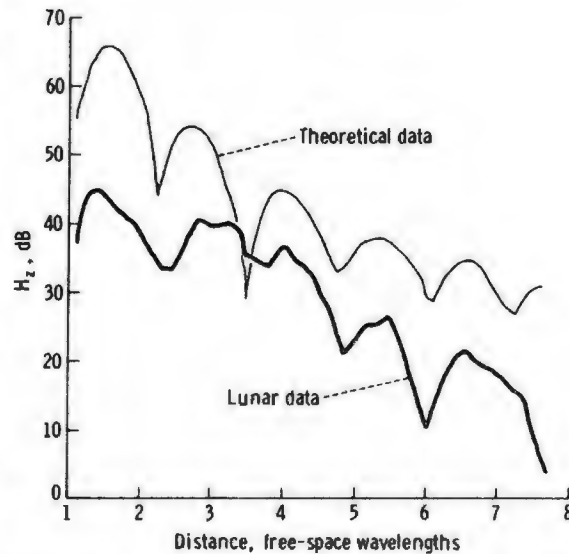


FIGURE 15-15.—Comparison of lunar data for H_2 , 16-MHz, N-S transmitting antenna with the theoretical curve calculated from mode theory. Parameters are given in table 15-1.

built in, it was desired to have data on the actual temperature. A portion of the temperature curve is shown in figure 15-16.

PRELIMINARY ANALYSIS

The analysis of each individual component at each frequency for each of the transmitting antenna orientations is quite straightforward. However, a single model that fits all the data has not been found, perhaps because of the limitations of our present

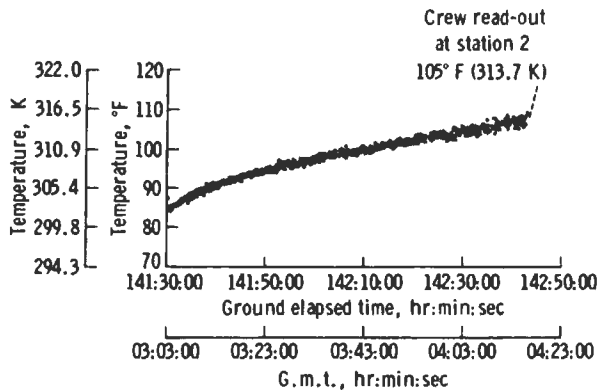


FIGURE 15-16.—Internal temperature profile of the SEP experiment receiver during the traverse from the SEP experiment site to station 2 on December 13, 1972.

theoretical development. For rigorous solutions, we are limited to models with homogeneous layers bounded by plane, horizontal surfaces. However, even within the limitations of our present theory, values of the properties of the lunar material in situ have been estimated, and some interesting conclusions about the electrical structure of the Taurus-Littrow site have been obtained.

The discussion in this report is based mainly on the analysis of H_z , the vertical component of the magnetic field, for two reasons. First, although the radiation patterns of the receiving antennas have not been measured, it is expected that the H_z data are less distorted than those of the other two components. Second, the appearance of the H_z data resembles more closely the glacier data, which comprise our background data.

Two quite different structural models of the Apollo 17 site have been developed to account for the observations. Although neither is based on rigorous theory, we believe that each is correct in the essential features. The first model, preferred by most members of the SEP experiment team, is one in which the dielectric constant increases with depth. Each of the lunar profiles can be matched quite well with the theoretical curves based on a single layer. The parameters for each of these six single-layer models are shown in table 15-I, and a typical example of the match between the theoretical and observed curves is shown in figure 15-15. The composite of these several models is shown in figure 15-17. We believe that the H_z data indicate that the dielectric constant increases with depth from a value of 2.5 to 3

TABLE 15-I.—Preliminary Results for H_z , N-S Transmitting Antenna

[$p = 0.003$]

Transmitter frequency, MHz	ϵ_{r_1} (a)	ϵ_{r_2} (b)	Layer depth, m
32.1	2.7	3.0	5.7
16	3.7	3.9	10
8.1	4.1	4.2	18
4	4.2	4.8	37
2.1	6.3	6.4	57
1	6.1	6.3	122

^aDielectric constant of layer.

^bDielectric constant of semi-infinite half space beneath layer.

near the surface to approximately 5 at a depth of 50 to 60 m. A discontinuity is present at 50 to 60 m, where ϵ_r increases to a value of 6 to 6.5. Because no reflection appears to be present in the 1-MHz data, we expect that ϵ_r does not increase between 60 m and at least 2.5 km. Compared to terrestrial values, the loss tangent is quite low (approximately 0.003) at all SEP experiment frequencies. On the basis of this low value of the loss tangent, we infer that water is probably not present at the Apollo 17 site.

In the alternate structural model, the cause of the apparent change of dielectric constant with depth is assigned to a sloping interface between a thin upper layer with $\epsilon_r = 3$ to $\epsilon_r = 4$ and $p < 0.04$ and a thick lower layer with $\epsilon_r = 6.5$ and $p = 0.04$. Rigorous theoretical expressions have not yet been obtained for this case either. However, we have confidence in the general effects attributed to a sloping interface because of the following limiting cases of horizontal interfaces.

1. For a very thin layer (thickness $< 0.1\lambda$), the interference pattern is equivalent to that of a half space in which ϵ_r and p have the values of the lower layer (fig. 15-18, upper curve).

2. For a layer with thickness between 0.1λ and 0.3λ , the individual "wiggles" of the interference pattern disappear (fig. 15-18, intermediate curves).

3. For a layer with thickness greater than approximately 0.3λ , the usual "reflected" wave appears in the pattern.

The sensitivity of the interference pattern of a thin

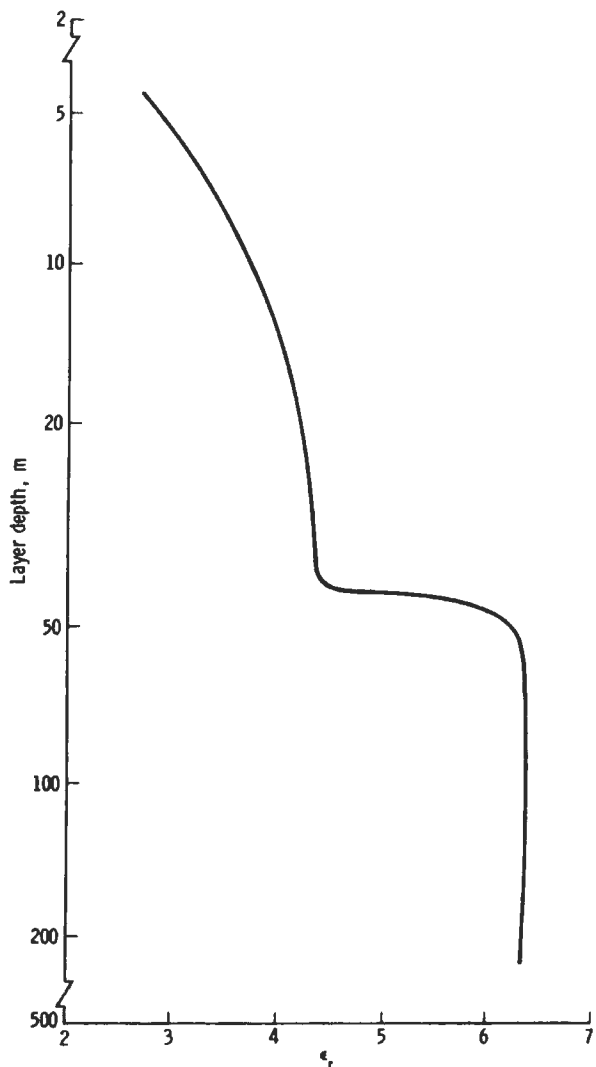


FIGURE 15-17.—Model for Apollo 17 site in which the dielectric constant varies with depth. The values of ϵ_r for each frequency are shown in table 15-1. In this figure, the approximate continuous function of ϵ_r is shown. Note that this interpretation is preliminary and, although the theoretical solution for each frequency is rigorous, the “solution” for the continuous variation of ϵ_r with depth is somewhat intuitive at present.

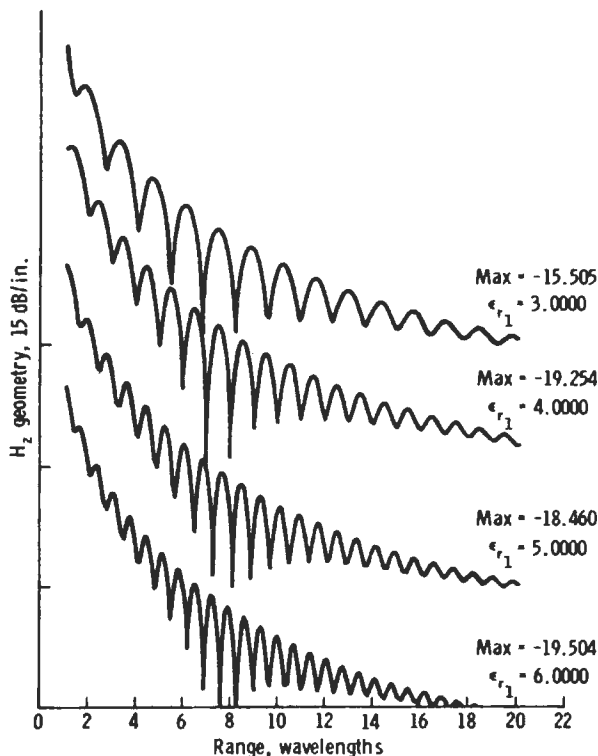


FIGURE 15-18.—Theoretical curves for thin layers, where $p_1 = 0.0300$, $\epsilon_{r_1} = 3.000$, $p_2 = 0.0400$, and $\epsilon_{r_2} = 6.000$. The points on the ordinate indicate the maximum values of each wave pattern. These plots are based on correct theory for horizontal layers, and they are used to “guess” a solution for an inclined interface.

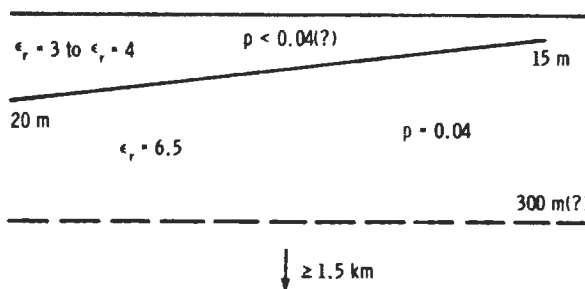


FIGURE 15-19.—The alternate model of the electrical structure at the Apollo 17 site. A layer of thickness between 0.2λ and 0.3λ is present at the SEP experiment site (left) and thins toward station 2 (right). The broken line at 300 m indicates a possible discontinuity in ϵ_r at that depth.

layer to the exact thickness is shown clearly in figure 15-18. The basis for this type of model is best seen in the 2.1-MHz profile, which resembles the intermediate theoretical curve of figure 15-18 near the SEP experiment site and resembles the upper theoretical curve of figure 15-18 farther away. The structure that best fits this analysis is shown in figure 15-19. The

layer is perhaps 20 m thick beneath the SEP experiment site and thins to 15 m at station 2. In addition, there is a hint of a discontinuity in ϵ_r at a depth of approximately 300 m.

CONCLUSIONS

1. The relative dielectric constant of the lunar material at Taurus-Littrow, at frequencies of 1 to 32 MHz, is approximately 3 to 4 near the surface and increases to 6 to 7 at a depth of approximately 50 m. The loss tangent is less than 0.04 and possibly as low as 0.003.

2. The electrical structure at Taurus-Littrow is not simple horizontal layering.

3. No liquid water is present in the outer 1 to 2 km.

4. Scattering of electromagnetic waves at frequencies of 1 to 32 MHz is insignificant.

5. Continuing postflight analysis of navigational data, photographs, and other data will provide location of the LRV on the EVA-2 traverse to an accuracy of a few meters.

6. Additional theoretical and scale model work is being done to solve the problem of continuous variation with depth of the dielectric properties and the problem of dipping interface.

ACKNOWLEDGMENTS

The experiment and equipment conceptual design was done at the Massachusetts Institute of Technology Center for Space Research. The flight hardware was designed and built by the Raytheon Company.

REFERENCES

- 15-1. Rossiter, J. R.; LaTorraca, G. A.; Annan, A. P.; Strangway, D. W.; and Simmons, G.: Radio Interferometry Depth Sounding: Part II—Experimental Results. *Geophysics*, vol. 38, no. 3, June 1973, p. 581.
- 15-2. Sommerfeld, A.: Über die Ausbreitung der Wellen in der drahtlosen Telegraphie. *Ann. Physik*, vol. 28, 1909, pp. 665-737.
- 15-3. Baños, Alfredo, Jr.: Dipole Radiation in the Presence of a Conducting Half-Space. Vol. 9 of International Series of Monographs on Electromagnetic Waves, Pergamon Press, Inc. (New York), 1966.
- 15-4. Annan, A. P.: Radio Interferometry Depth Sounding. M.S. Thesis, Univ. of Toronto, 1970.
- 15-5. Simmons, G.; Strangway, D. W.; Bannister, L.; Baker, R.; et al.: The Surface Electrical Properties Experiment. Lunar Geophysics: Proceedings of a Conference at the Lunar Science Institute, Houston, Tex., Oct. 18-21, 1971, D. Reidel Pub. Co. (Dordrecht, Holland), 1973, pp. 258-271.
- 15-6. Annan, A. P.: Radio Interferometry Depth Sounding: Part I—Theoretical Discussion. *Geophysics*, vol. 38, no. 3, June 1973, p. 557.
- 15-7. Kong, J. A.: Electromagnetic Fields Due to Dipole Antennas Over Stratified Anisotropic Media. *Geophysics*, vol. 37, no. 6, Dec. 1972, pp. 985-996.
- 15-8. Tsang, L.; Kong, J. A.; and Simmons, G.: Interference Patterns of a Horizontal Electric Dipole Over Layered Dielectric Media. *J. Geophys. Res.*, vol. 78, no. 17, June 19, 1973, pp. 3287-3300.
- 15-9. King, Ronald W. P.: *Electromagnetic Engineering, Vol. I—Fundamentals*. McGraw-Hill Book Co., Inc. (New York), 1945.
- 15-10. Jordan, Edward C.; and Balmain, Keith G.: *Electromagnetic Waves and Radiating Systems*. Second ed., Prentice-Hall, Inc. (Englewood Cliffs, N.J.), 1968.
- 15-11. Stratton, Julius Adams: *Electromagnetic Theory*. McGraw-Hill Book Co., Inc. (New York), 1941.
- 15-12. Smythe, W. R.: *Static and Dynamic Electricity*. McGraw-Hill Book Co., Inc. (New York), 1950.
- 15-13. Lorrain, Paul; and Corson, Dale R.: *Electromagnetic Fields and Waves*. W. H. Freeman (San Francisco), 1970.
- 15-14. Pierce, G. W.: A Table and Method of Computation of Electric Wave Propagation, Transmission Line Phenomena, Optical Refraction, and Inverse Hyperbolic Functions of a Complex Variable. *Proc. Am. Acad. Arts Sciences*, vol. 57, 1922, p. 175.
- 15-15. Galejs, Janis: *Antennas in Inhomogeneous Media*. Vol. 15 of International Series of Monographs on Electromagnetic Waves, Pergamon Press, Inc. (New York), 1969.
- 15-16. Wait, James R.: *Electromagnetic Waves in Stratified Media*. Vol. 3 of International Series of Monographs on Electromagnetic Waves, Pergamon Press, Inc. (New York), 1962.
- 15-17. Brekhovskikh, Leonid M. (David Lieberman, trans.): *Waves in Layered Media*. Vol. 6 of Applied Mathematics and Mechanics, Academic Press (New York), 1960.
- 15-18. Sommerfeld, A.: Über die Ausbreitung der Wellen in der drahtlosen Telegraphie. *Ann. Physik*, vol. 81, 1926, pp. 1135-1153.
- 15-19. Tsang, Leung: *Electromagnetic Near Fields of Horizontal Dipole on Stratified Lunar Surface*. B.S. Thesis, Mass. Inst. of Tech., 1971.
- 15-20. Strangway, D. W.; Simmons, G.; Watts, R.; LaTorraca, G.; et al.: Radio Frequency Interferometry—A New Technique for Studying Glaciers. *J. Glaciology*, vol. 12, 1973.
- 15-21. LaTorraca, Gerald A.: *Half Wavelength Dipole Antennas Over Stratified Media*. NASA CR-115561, 1972.
- 15-22. Simmons, Gene; Meyer, James W.; Baker, Richard H.; and Strangway, David W.: *Brief Introduction to the Surface Electrical Properties Experiment*. MIT Press (Cambridge, Mass.), Aug. 1972.

Line-Source Radiation over a Layered Dielectric:
Inversion of Radio Interferometry Data

by Raymond D. Watts¹

¹Physics Branch, Johnson Space Center, Houston, Texas and
Lunar Science Institute, Houston, Texas

Abstract

The radio interferometry technique described by Rossiter et.al, (1973) is used to study extremely resistive electrical structures. This paper describes an inversion procedure which can be applied to measurements of the fields radiated by a long-line current source. The measurements are the amplitude of one magnetic field component and the complex ratio of the two (vertical and horizontal) magnetic field components. Data can be directly inverted to the point of obtaining a plane-wave impedance spectrum. The Fréchet kernels (used to obtain the dielectric structure from the impedance spectrum by the Backus-Gilbert method) are derived. Processing the data to obtain the impedance spectrum should speed up the inversion process. The procedure for deriving the impedance spectrum indicates whether the data is inconsistent with a layered model. If there are several spectra which are consistent with the observations, they are all retrieved.

Introduction

Traverse measurements of radio waves from a stationary transmitter can be used to study the depth variation of electrical parameters in a sufficiently resistive electrical environment. This type of study (called radio interferometry) has been performed on glaciers (Rossiter et. al., 1973, Strangway et. al., 1973) and on the moon (Simmons et. al., 1973). It is also probably applicable to permafrost areas.

The principle feature of the data is the variation of signal strength with distance (Figure 2). The peak-and-null pattern is the result of interference of direct waves which have traveled through the air, with waves which have traveled through the dielectric. The distinct velocities create phase differences which lead to wave interference (Annan, 1973).

The advantage of this method over higher-frequency time-delay-measurement sounding methods is that a direct measurement of the wave velocity in the dielectric is obtained, and no assumption needs to be made about this parameter.

We assume a line-current source of radio energy. The source lies on the y-axis. The z-axis is vertical upward. Traverses are performed along the x-axis. Our model for the electrical structure of the earth is a generalized layered dielectric (Figure 1) with $\epsilon = \epsilon(z)$,

It would be highly desirable to measure the amplitude and phase of the various components as a function of distance from the transmitter. To optimize the effects of the structure on the data, however, frequencies are chosen such that the size of the structure and the wavelength are

nearly the same. For glacier and lunar problems this dictates frequencies in the megahertz range (Rossiter et. al., 1973). At these frequencies, no phase reference is available which can be carried in a traverse vehicle and which maintains transmitter phase for many minutes.

It is not difficult, though, to measure relative phase between two or more EM components. For this reason, we assume that a measurement of the ratio H_z/H_x is made along the traverse. This gives us an analytic function with which to work. It will be assumed that $H_x \neq 0$ anywhere on the traverse. Conditions for total destructive interference are quite stringent, and experience with glacier and lunar data indicates that H_x is unmeasurably small only on rare occasion. In such a case, the reciprocal ratio H_x/H_z can be used unless H_z is similarly ill-behaved.

The purpose of this paper is to show how a ratio measurement such as H_z/H_x can be processed for application of the Backus-Gilbert inversion algorithm. Derivations are carried to the point where the Backus-Gilbert theory may be applied, but the inversion process itself will not be discussed (see, for example, Wiggins, 1972, Gilbert, 1972, or Parker, 1970).

I. The Forward Problem

To develop a consistent notation, we will first solve the forward problem. We temporarily assume that the general layered dielectric defined by

$$\epsilon = \epsilon(z) \tag{1}$$

is in fact a piecewise constant function given by

$$\begin{aligned} \epsilon(z) = & \epsilon_0 & z \geq 0 \\ & \epsilon_1 & 0 > z \geq -d_1 \\ & \epsilon_2 & -d_1 > z \geq -d_2 \\ & \vdots & \vdots \end{aligned} \tag{2}$$

The various d_i are the (positive) depths to the dielectric interfaces.

Magnetic permeability is constant with $\mu \equiv \mu_0$.

The source current is given by

$$\bar{J}_s(x, z) = \hat{e}_y \delta(x) \delta(z) \tag{3}$$

This can be broken into component parts according to horizontal wavenumber:

$$\bar{J}_s(x, z) = \hat{e}_y \delta(z) \frac{1}{2\pi} \int_{-\infty}^{\infty} e^{ik_x x} dk_x \tag{4}$$

If we define \bar{J}_s by

$$\bar{J}_s(x, z; k_x) = \hat{e}_y \delta(z) e^{ik_x x} \tag{5}$$

then (4) becomes

$$\bar{J}_S(x, z) = \frac{1}{2\pi} \int_{-\infty}^{\infty} \bar{J}_S(x, z; k_x) dk_x \quad (6)$$

The approach we take to the forward problem is to find the fields which result from each partial source $\bar{J}_S(x, z; k_x)$, then integrate over k_x as in (6) to find the fields from the total source $\bar{J}_S(x, z)$.

Working with a single partial source $\bar{J}_S(x, z; k_x)$, all fields will vary as $e^{ik_x x}$. This factor will be suppressed until the final recomposition of the total fields. Time dependence is $e^{-i\omega t}$. Maxwell's equations are

$$H_y = E_x = E_z = 0 \quad (7)$$

$$\omega\mu H_z = k_x E_y \quad (8)$$

$$i\omega\mu H_x = -\frac{\partial E_y}{\partial z} \quad (9)$$

$$-i\omega\epsilon E_y = \frac{\partial H_x}{\partial z} - ik_x H_z \quad (10)$$

Equations (8) and (9) can be substituted into (10) to give the wave equation

$$\frac{\partial^2 E_y}{\partial z^2} + (\omega^2\mu\epsilon - k_x^2) E_y = 0 \quad (11)$$

There are two independent solutions to (11), representing up- and down-going waves. A well-known procedure assigns arbitrary amplitude and phase to the down-going wave at the bottom of the model, then

matches boundary conditions at successively higher interfaces until the waves are known at the surface $z = 0$. Because the wave at the bottom was arbitrarily chosen, the ratio of the upgoing to the downgoing wave at $z = 0$ is what has really been determined. By appropriate application of equations (8) - (10), this can be converted into a determination of the ratio E_y/H_x just below $z = 0$.

We define the impedance by

$$Z^{\pm}(k_x) = \frac{E_y^{\pm}(k_x)}{H_x^{\pm}(k_x)} \quad (12)$$

The superscripts refer to values just above (+) or just below (-) the surface $z = 0$. The impedance will later be generalized as a function of depth. The value Z^- has been found and is dependent only on the structure in the region $z < 0$. The value Z^+ is found for upgoing waves in $z > 0$:

$$Z^+(k_x) = -\frac{\omega\mu}{k_z} \quad k_z = \sqrt{\omega^2\mu\epsilon_0 - k_x^2} \quad (13)$$

The square root is chosen with the condition $\text{Im } k_z > 0$.

We now apply boundary conditions at $z = 0$. The electric field is continuous

$$E_y^+ = E_y^- \quad (14)$$

The magnetic field is discontinuous due to the partial source current \vec{J}_s .

$$H_x^+ - H_x^- = 1 \quad (15)$$

We rewrite (14) using (12):

$$Z^+ H_x^+ - Z^- H_x^- = 0 \quad (16)$$

This set of equations is solved for H_x^+ :

$$H_x^+ = \frac{Z^-}{Z^- - Z^+} \quad (17)$$

Application of (12) gives

$$E_y^+ = Z^+ H_x^+ = \frac{Z^+ Z^-}{Z^- - Z^+} \quad (18)$$

Application of (8) to (18) gives

$$H_z^+ = \frac{k_x}{\omega\mu} \frac{Z^+ Z^-}{Z^- - Z^+} = \frac{k_x Z^+}{\omega\mu} H_x^+ \quad (19)$$

We have derived the fields resulting from a source element $\bar{j}_s(x, z; k_x)$. To get the total fields due to the line source $\bar{J}_s(x, z)$, we reinstate the suppressed factor $e^{ik_x x}$ and integrate over k_x :

$$H_x^+(x) = \frac{1}{2\pi} \int_{-\infty}^{\infty} \frac{Z^-}{Z^- - Z^+} e^{ik_x x} dk_x \quad (20)$$

$$H_z^+(x) = \frac{1}{2\pi} \int_{-\infty}^{\infty} \frac{k_x Z^+}{\omega\mu} \frac{Z^-}{Z^- - Z^+} e^{ik_x x} dk_x \quad (21)$$

$$E_y^+(x) = \frac{1}{2\pi} \int_{-\infty}^{\infty} \frac{Z^+ Z^-}{Z^- - Z^+} e^{ik_x x} dk_x \quad (22)$$

II. Converting Field Measurements to Impedances

The next step in the inversion is to convert the measured ratio

$$M(x) \equiv \frac{H_z^+(x)}{H_x^+(x)} \quad (23)$$

into an impedance spectrum. Our goal is to retrieve $Z^-(k_x)$. This step is analogous to the surface harmonic decomposition which is performed on geomagnetic data prior to inverting it into a mantle conductivity structure. The result is a set of independent measurements in the sense that each might have been made without the others. In our case, such an experiment would consist of an impedance measurement for a single plane-wave. It is trivial to independently model a structure which satisfies each measurement: a halfspace of constant ϵ will do nicely. The difficult task, of course, is to find a model $\epsilon(z)$ which satisfies the entire spectrum of impedance measurements simultaneously.

We apply (20) and (21) to (23):

$$\int_{-\infty}^{\infty} dk_x e^{ik_x x} H_z^+(k_x) = M(x) \int_{-\infty}^{\infty} dk_x \frac{\omega \mu}{k_x Z^+} e^{ik_x x} H_z^+(k_x) \quad (24)$$

Since (24) must hold at each point x , it represents a cumbersome set of simultaneous integral equations for $H_z^+(k_x)$. A more useful form can be obtained by Fourier transforming both sides of (24):

$$H_z^+(l_x) = \int_{-\infty}^{\infty} dk_x m(l_x - k_x) \frac{\omega \mu}{k_x Z^+} H_z^+(k_x) \quad (25)$$

where

$$m(q) = \frac{1}{2\pi} \int_{-\infty}^{\infty} dx e^{-iqx} M(x) \quad (26)$$

is the Fourier transform of the measurements $M(x)$. Equation (25) is a homogeneous polar Fredholm equation of the second kind. The integral appears to be singular at $k_x = 0$, but $H_z^+(0) = 0$, representing a vertically-propagating wave with no vertical fields. Since k_x , Z^+ , and H_z^+ are all odd functions of k_x , the integral can be changed to a semi-infinite one with kernel $[m(l_x - k_x) - m(l_x + k_x)]$.

Since the kernel of equation (25) is observational and not mathematical, the solution will be a computational problem and (25) will become a matrix equation. The discrete approximation to (25) is

$$\bar{h} = \bar{m} \cdot \bar{d} \cdot \bar{h} \quad (27)$$

where \bar{m} is a Toeplitz matrix whose rows are the function $m(-k_x)$ shifted by l_x ; \bar{m} is antisymmetric. The diagonal matrix \bar{d} takes the values of $\frac{\omega \mu}{k_x Z^+}$.

Two problems confront us: 1) is there a solution to (27), and 2) is it unique? Since (27) is an eigenvalue form, the existence question is equivalent to asking whether the matrix $\bar{m} \cdot \bar{d}$ has an eigenvalue of 1. If the answer is yes, the uniqueness question is equivalent to asking whether the eigenvalue 1 is degenerate.

Since the data or the dielectric structure will probably not be perfect, we should try to satisfy (27) as closely as possible. We introduce the error vector

$$\bar{f} = (\bar{m} \cdot \bar{d} - \bar{I}) \cdot \bar{h} \quad (28)$$

and try to minimize its amplitude. If (27) can be solved we will get $\bar{f} = 0$. If it can't, then we will get a non-zero but minimal \bar{f} .

The power contained in \bar{f} is minimized:

$$E = \bar{f} \cdot \bar{f}^* \quad (29)$$

$$\delta E = 0 = (\delta \bar{f}^*) \cdot \bar{f} + \bar{f}^* \cdot (\delta \bar{f}) \quad (30)$$

let
$$\bar{N} = \bar{m} \cdot \bar{d} - \bar{I} \quad (31)$$

so
$$\bar{f} = \bar{N} \cdot \bar{h} \quad (32)$$

then

$$E = \bar{f}^* \cdot \bar{f} = \bar{h}^* \cdot \bar{N}^{*T} \cdot \bar{N} \cdot \bar{h} \geq 0 \quad (33)$$

let

$$\bar{P} = \bar{N}^{*T} \cdot \bar{N} \quad (34)$$

so \bar{P} is Hermitian and positive semi-definite.

Now

$$\delta E = (\delta \bar{h}^*) \cdot \bar{P} \cdot \bar{h} + \bar{h}^* \cdot \bar{P} \cdot (\delta \bar{h}) = 0 \quad (35)$$

if we let $\bar{h} = \bar{a} + i\bar{b}$, we have

$$(\delta \bar{a} - i\delta \bar{b}) \cdot \bar{P} \cdot \bar{h} + \bar{h}^* \cdot \bar{P} \cdot (\delta \bar{a} + i\delta \bar{b}) = 0 \quad (36)$$

We independently but simultaneously set the coefficients of $\delta\bar{a}$ and $\delta\bar{b}$ to zero:

$$\begin{aligned}\bar{p} \cdot \bar{h} + \bar{p}^* \cdot \bar{h}^* &= 0 \\ \bar{p} \cdot \bar{h} - \bar{p}^* \cdot \bar{h}^* &= 0\end{aligned}\tag{37}$$

which implies that

$$\bar{p} \cdot \bar{h} = 0\tag{38}$$

This equation may or may not have a solution. We do an eigenvalue analysis of the matrix \bar{p} . The eigenvalues are real and non-negative. If there are no eigenvalues considerably small than 1, then the observations are inconsistent with the mathematical model. If there is a single near-zero eigenvalue, the solution (eigenvector) is unique and \bar{h} has been obtained apart from a constant multiplicative factor.

If there are several near-zero but distinct eigenvalues, then the corresponding eigenvectors are orthogonal. Several possible \bar{h} vectors have been obtained which are consistent with the data. The disastrous case occurs when the near-zero eigenvalues are degenerate. The eigenvectors are not necessarily orthogonal, and \bar{h} can be taken as any linear combination of them. There is a whole range of possible impedance spectra depending on the choice of constants of combination.

The solution of equation (38), when it exists, gives the transform of the vertical magnetic field, $H_z^+(k_x)$, except for a multiplying factor. If the field-strength $\{H_z(x)\}$ has been measured in addition to the ratio $M(x)$, then Parseval's theorem can be used to determine the

amplitude of the missing factor. The power is forced to be equal in both domains. The phase of the factor cannot be recovered from the observations because it represents an absolute phase relative to the transmitter. However, when the receiver is practically coincident with the transmitter, the absolute phase of the magnetic fields is the same as the transmitter current phase (the fields are quasi-static for ranges $x \ll \lambda$). This condition can be used to determine the phase of the missing factor even though it does not come from the observations.

From equation (19),

$$H_x^+ = \frac{\omega \mu}{k_x Z^+} H_z^+ = \frac{Z^-}{Z^- - Z^+} \quad (39)$$

$$Z^- = \frac{H_x^+ Z^+}{H_x^+ - 1} \quad (40)$$

Z^+ is given by (13).

We have recovered the impedance spectrum.

III. Converting Z to ϵ

It is not the purpose of this paper to discuss the actual process of inversion, but rather to set the problem up for application of the Backus-Gilbert inversion method (Wiggins, 1972, Gilbert, 1972, Parker, 1970). The development is nearly identical to that of Parker (1970) for inversion of geomagnetic data into mantle conductivity information.

We return to equation (12), which is an expression of the wave impedance as it depends on of horizontal wavenumber and on the dielectric structure. We generalize $Z(k_x)$ to include its variation with depth, writing the generalized variable as $Z(z; k_x)$. We can substitute Maxwell's equations into (12) and obtain a non-linear differential equation for Z which can be solved numerically starting at the bottom of the model. This corresponds to the solution of the forward problem as discussed in section I.

It turns out to be algebraically advantageous, however, to introduce the wave admittance,

$$Y(z; k_x) = \frac{1}{Z(z; k_x)} = \frac{H_x(z; k_x)}{E_y(z; k_x)} \quad (41)$$

The variable Y separates from the variable $\epsilon(z)$ in the differential equation in a way which allows easy derivation of the Fréchet kernels which are required in the inversion iteration.

$$\frac{\partial Y}{\partial z} = \frac{1}{E} \frac{\partial H}{\partial z} - \frac{H}{E^2} \frac{\partial E}{\partial z} \quad (42)$$

$$\frac{\partial Y}{\partial z} = \frac{ik^2}{\omega\mu} - i\omega\epsilon + i\omega\mu Y^2 \quad (43)$$

Once (43) has been solved for a given $\varepsilon(z)$, then a perturbation in ε will generate a perturbation in $Y(z;k)$, particularly in the observable $Y(0^-;k)$. It is this property which allows iteration to a model for $\varepsilon(z)$ which fits the observations.

Taking perturbations on (43)

$$\frac{\partial}{\partial z} (\delta Y) = -i\omega(\delta\varepsilon) + z i\omega\mu Y(\delta Y) \quad (44)$$

Introducing the function

$$p(z) = z i\omega\mu \int^z dz' Y(z') \quad (45)$$

so that

$$\frac{\partial p}{\partial z} = z i\omega\mu Y \quad (46)$$

we get

$$\frac{\partial}{\partial z} [e^{-p} \delta Y] = -i\omega(\delta\varepsilon) e^{-p} \quad (47)$$

so

$$\delta Y(z) = -i\omega e^{p(z)} \int^z dz' [\delta\varepsilon(z')] e^{-p(z')} \quad (48)$$

For $z = 0$, this is

$$\delta Y(0) = -i\omega e^{p(0)} \int^0 dz' [\delta\varepsilon(z')] e^{-p(z')} \quad (49)$$

and thus the Frechet kernel for the observations is

$$F[\varepsilon(z)] = -i\omega e^{p(0) - p(z)} \quad (50)$$

where

$$p(0) - p(z) = 2i\omega \int_z^0 dz' Y(z') \quad (51)$$

It should be noted that the kernels defined by (50) and (51) can be derived in analytic form for a postulated structure of constant-dielectric layers. In this case the ratio of the analytic values for H and E defines Y, so the required integration in (51) can be performed exactly. Although a non-linear differential equation was used to derive the kernels, it is not necessary to continue treating them in that form.

If we regard the structure as a message which has to be transmitted through the kernels of (50) to become observable, we can see what structural information is found in what data. Let us assume a starting structure of a homogeneous halfspace, and investigate the observability of small perturbations to that structure.

The Fréchet kernels in this case are given by

$$F_{\text{homogeneous}} = -i\omega e^{-2iz \sqrt{\omega^2 \mu \epsilon_1 - k_x^2}} \quad (52)$$

As long as $k_x^2 < \omega^2 \mu \epsilon_1$, the exponential has an absolute value of 1 (assuming a lossless medium), and information content is uniform with depth. For $k_x^2 > \omega^2 \mu \epsilon_1$, the exponential decreases with depth. The attenuation distance is $\frac{1}{2\sqrt{k_x^2 - \omega^2 \mu \epsilon_1}}$. Therefore, the higher spatial frequencies yield information only for the uppermost part of the structure.

IV. Discussion and Conclusions

We have demonstrated that under ideal conditions it is possible to recover a single impedance spectrum from traverse observations of 1) the ratio (including phase) of vertical to horizontal magnetic field, and 2) the amplitude of either the horizontal or vertical field. Non-ideal conditions (data with errors, non-layered structures, and possibly some layered structures with unfortunate $\epsilon(z)$ functions) lead either to no spectrum which is consistent with the data or to several spectra. We have derived the Fréchet kernels which can be used to iteratively improve a model $\epsilon(z)$ until it fits the observed impedance spectrum as closely as possible. We have considered the possibility that several distinct impedance spectra may explain one set of observations. It is also possible that several distinct models $\epsilon(z)$ may explain one impedance spectrum.

A major contribution of this study is the demonstration of the usefulness of the phase measurement. Past applications of radio interferometry have used instrumentation which measured only the amplitude of the two components H_z and H_x . By making the phase measurement it is possible to work the data back to a quantity (the impedance) which is very closely tied to the structure. From a computational viewpoint, this is considerably more efficient (see Fig. 3) because we have eliminated a computational step in the iteration loop of the inversion procedure. The computer time investment in the eigenvector determination will pay off if many iterations are required to converge to the required structure.

The results of this paper have been derived for an impractical and non-existent energy source. The corresponding analysis for a dipole source is under way. In the meantime, inversion of synthetic line-source data is being attempted.

REFERENCES

- Annan, A. P. (1973), Radio Interferometry Depth Sounding, Part I - Theoretical Discussion, Geophysics (in press).
- Gilbert, Freeman (1972), Inverse Problems for the Earth's Normal Modes, in The Nature of The Solid Earth, E.C. Robertson, ed., McGraw-Hill, p 125-146.
- Parker, R. L., (1970), The Inverse Problem of Electrical Conductivity in the Mantle, Geoph. J., Vol. 22, p 121-138.
- Rossiter, J. R., et.al. (1973), Radio Interferometry Depth Sounding, Part II - Experimental Results, Geophysics (in press).
- Simmons, G., et.al. (1973), Surface Electrical Properties Experiment, in Apollo 17 Preliminary Science Report, National Aeronautics and Space Administration (in press).
- Strangway, D. W., et.al. (1973), Radio Frequency Interferometry - A New Technique for Studying Glaciers, J. Glaciology (in press).
- Wiggins, Ralph A. (1972), The General Linear Inverse Problem: Implication of Surface Waves and Free Oscillations for Earth Structure, Rev. of Geophys. and Space Phys., Vol. 10, No. 1, p 251-285.

FIGURE CAPTIONS

Figure 1

The line current transmitter lies along the y -axis on the surface of the dielectric halfspace. The receiver traverses in the x direction. Positive z is up.

Figure 2

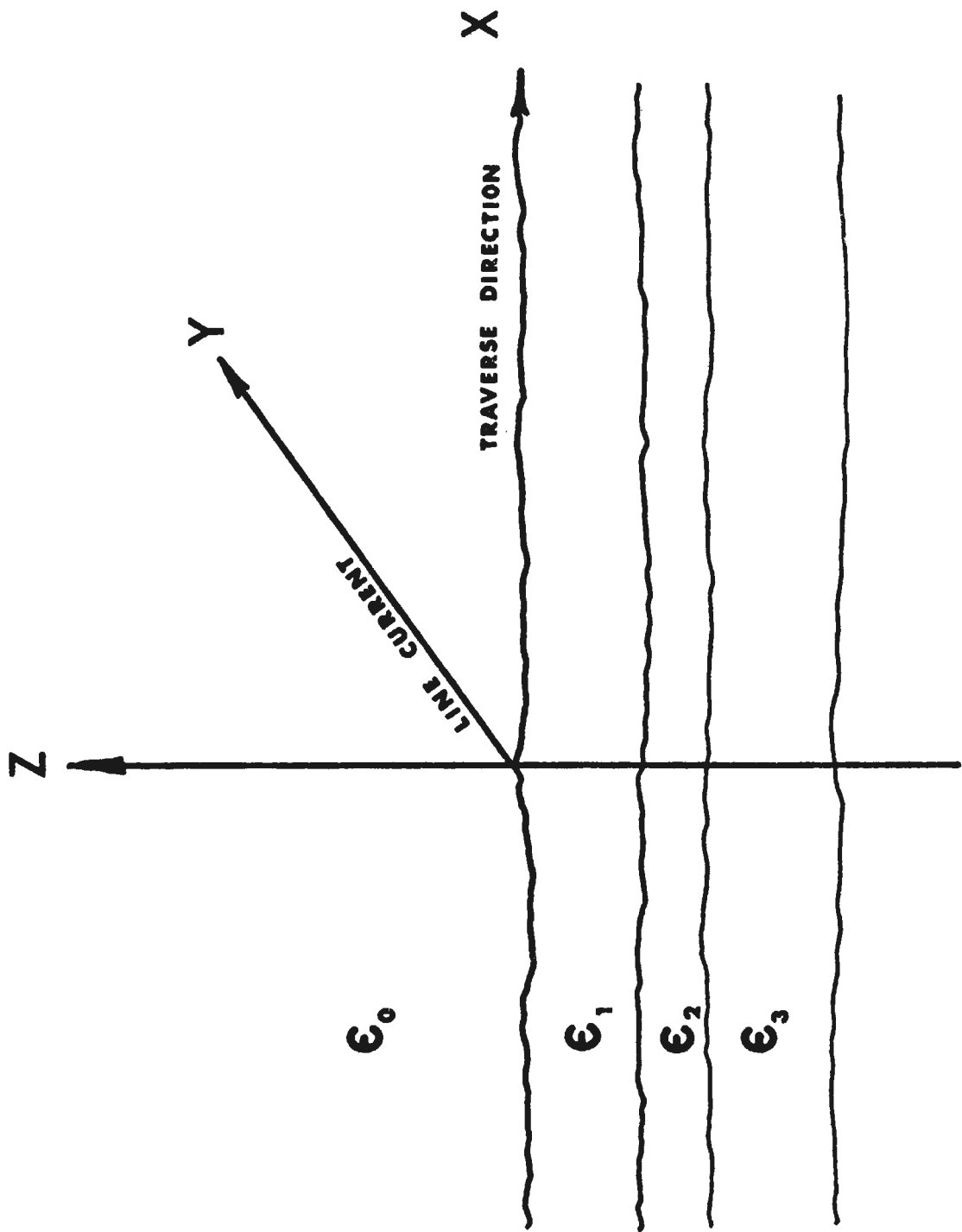
The received magnetic field strength varies with range from the transmitter. The peak-and-null pattern is due to interference between waves of different velocity traveling in the vacuum and dielectric halfspaces.

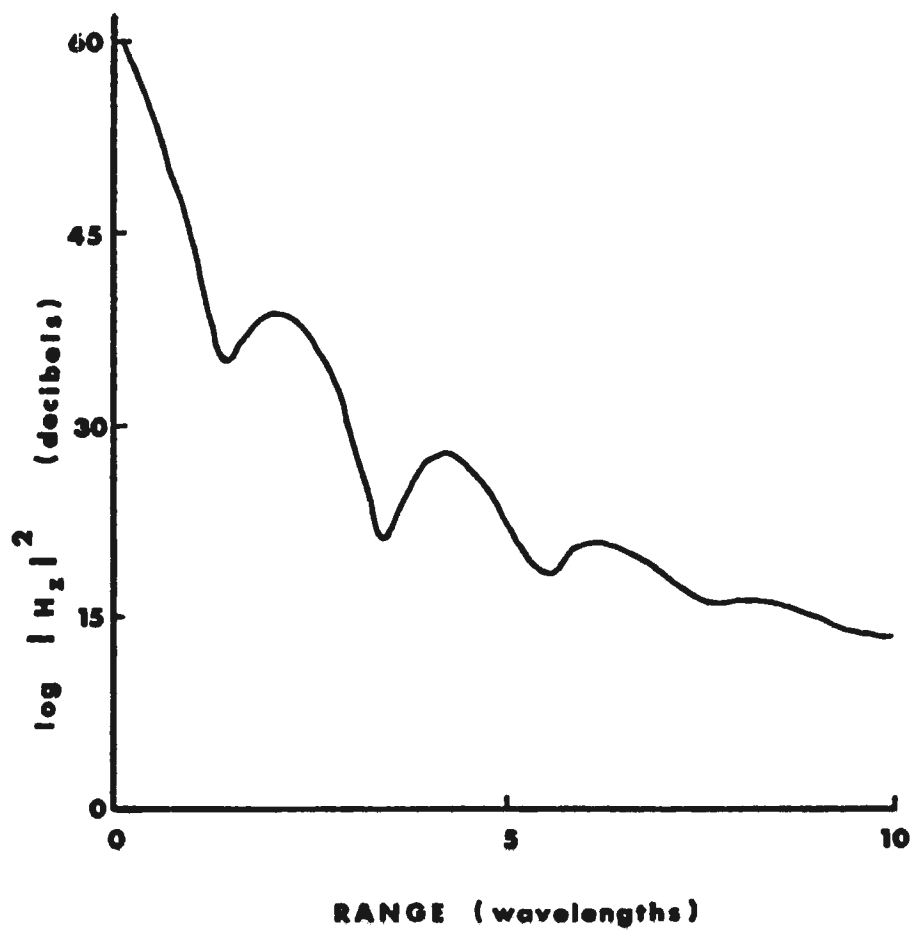
Figure 3a

Block diagram of data interpretation for measurements without relative phase between components. Fourier transforms are performed at each step of the inversion. There is no indication whether the data are consistent with a layered model.

Figure 3b

Data interpretation for measurements containing relative phase. Measurements are transformed one time rather than model parameters being transformed many times. Eigenvector analysis gives an indication of uniqueness and compatibility with a layered dielectric structure model.





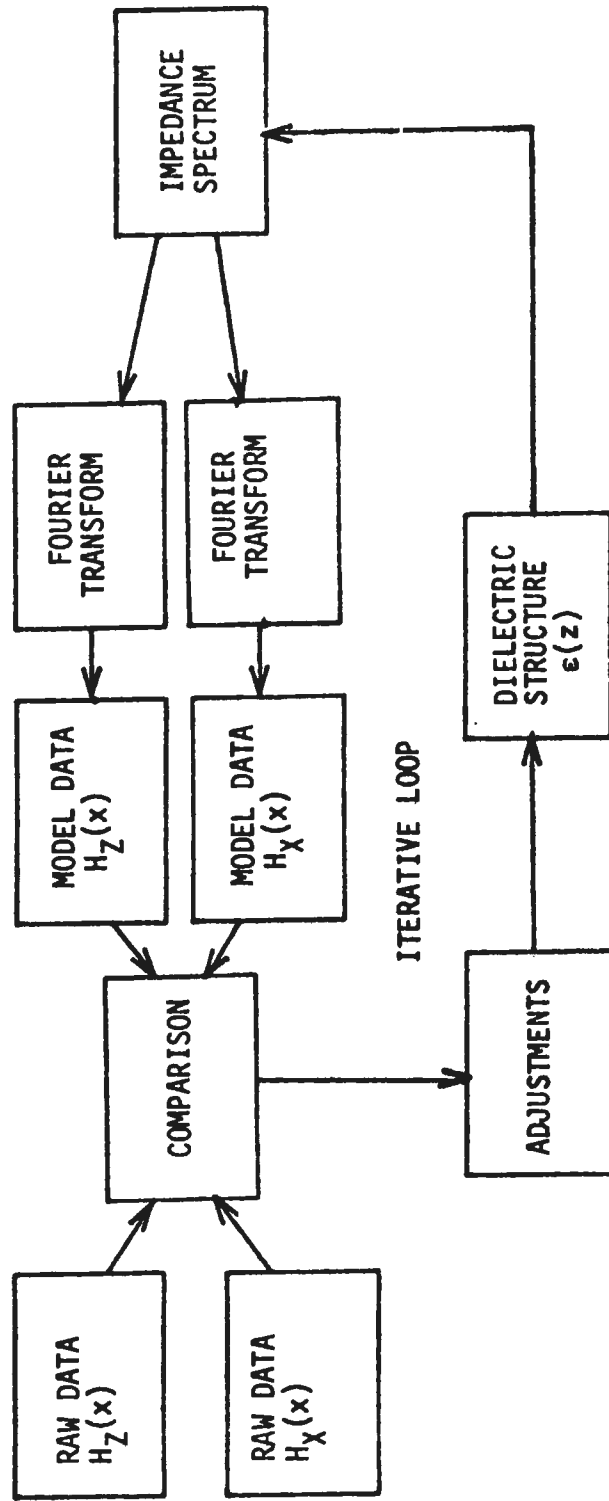


FIGURE 3a INVERSION OF PHASELESS DATA

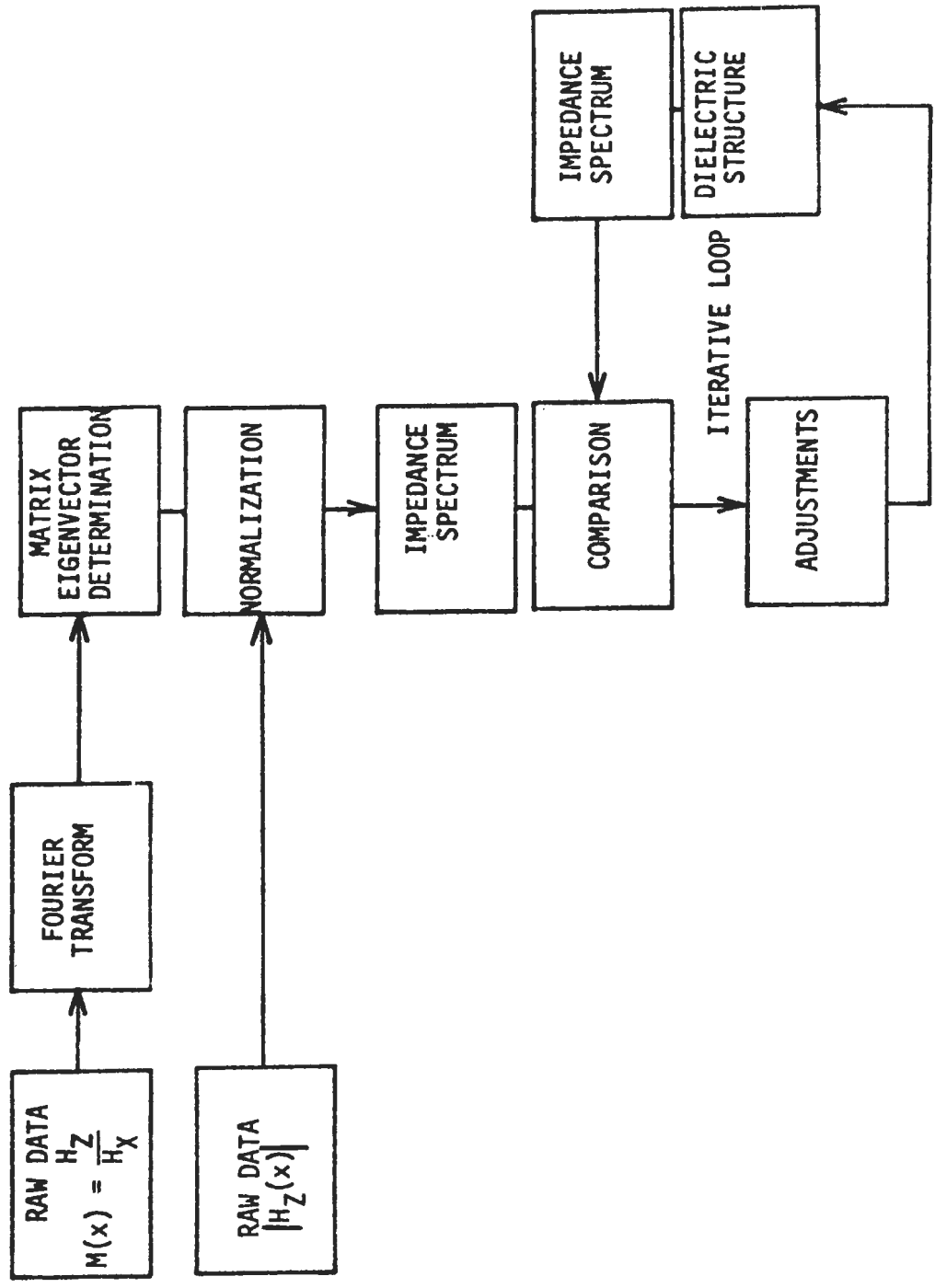


FIGURE 3b INVERSION OF DATA WITH PHASE

Distribution List

L. Beckley	MIT	30
G. Simmons	MIT	1
J. Kong	MIT	1
R. Baker	MIT	1
J. Meyer	MIT	1
A.P. Annan	U of T	1
J.D. Redman	U of T	1
J.R. Rossiter	U of T	1
J. Rylaarsdam	U of T	1
D.W. Strangway	U of T	7
R. Watts	USGS-Denver	1
A.W. England	USGS-Denver	1
J. de Bettencourt	Raytheon	1
W.F. Eickelman	NASA/JSC	1
D. Teegarden	NASA/JSC	1